

An International
Forum For
The AE Science
and Technology

JOURNAL OF ACOUSTIC EMISSION

Vol.29/January-December 2011



WCAE 2011 Beijing First International AE Conference in China

Endorsed by
AEWG
and
EWGAE

Published by
Acoustic Emission Group
Encino, CA USA

Journal of Acoustic Emission, Volume 29, 2011

VIEWING AN ARTICLE IN CD-ROM

You need a software that can read a pdf-file, such as Adobe Acrobat Reader®. Install one first before going further. You can download the latest version from www.adobe.com. Use of Adobe Acrobat® (not provided) allows one to utilize the Search function. This gives the power to search for a name or a word in the entire volume and is highly recommended.

PDF Files: Contents are listed below. Individual papers have file names of **29-xxx.pdf**, with xxx as their first page number.

CONTENTS

29-001 Modal AE Analysis of Fracture and Failure in Composite Materials, and the Quality and Life of High Pressure Composite Pressure Vessels

Michael R. Gorman

29-029 Imaging of Deep Structure Using Reflection Waves Detected by Spectral Matrix Analysis and Confidence Levels

Hirokazu Moriya

29-042 Effect of Loading Pattern on the Acoustic Emission Evaluation of Prestressed Concrete Girders

Francisco Barrios and Paul Ziehl

29-057 Dependence of AE Parameters on the Propagation Distance

D. Polyzos, A. Papacharalampopoulos, T. Shiotani and D. G. Aggelis

29-068 Identifying Quasi-Brittle Fracture by AE and Digital Imaging

Qing Lin and Joseph F. Labuz

29-078 Diesel Knock Combustion and its Detection Using Acoustic Emission

David P. Lowe, Tian Ran Lin, Weiliang Wu and Andy C.C. Tan

29-089 Detection of Transient Zones During Water Boiling by Acoustic Emission

Rami Carmi, Arie Bussiba, Galit Widenfeld, Yosi Aharon, Igal Alon and Igal Hochbaum

29-098 AE Monitoring of Lightning-Damaged CFRP Laminates during Compression-After-Impact Test

Jae-Ha Shin and Oh-Yang Kwon

29-106 Neural Network Techniques for Burst Pressure Prediction in Kevlar/Epoxy Pressure Vessels using Acoustic Emission Data

Eric v. K. Hill, Michael D. Scheppa, Zachary D. Sager, and Isadora P. Thisted

29-113 Monitoring of Metal Fatigue Damage using Acoustic Emission and Thermography

Dimitrios G. Aggelis, Evangelos Z. Kordatos and Theodore E. Matikas

29-123 Acoustic Emission Source Orientation Based on Time Scale

Didem Ozevin and Zahra Heidary

29-133 Detection of AE Signals against Background Friction Noise

V. Barat, D. Grishin and M. Rostovtsev

- 29-142** Guide for Development of Acoustic Emission Applications for Examination of Metal Structures
Boris Muravin and Mark F. Carlos
- 29-149** Acoustic Emission Measurements on Piezoelectric/ Ferroelectric Materials
Hideaki Aburatani
- 29-160** Intrinsically Safe Acoustic Emission Transducers
Ran Zhou, and Stan Hale
- 29-167** Re-Examination of NIST Acoustic Emission Sensor Calibration: Part I - Modeling the loading from glass capillary fracture
Brian Burks
- 29-175** Re-Examination of NIST Acoustic Emission Sensor Calibration: Part II - Finite element modeling of acoustic emission signal from glass capillary fracture
M. A. Hamstad
- 29-184** Investigation of Pencil Lead Breaks as Acoustic Emission Sources
Markus G. R. Sause
- 29-197** Necessary Condition for Delayed Fracture of Quasi-stable Type-304 Stainless Steel With Strain-induced Martensite
Mikio Takemoto, Shuichi Ueno, Motoaki Nakamura and Gunji Ueno
- 29-210** On the Strain Rate Dependence of Acoustic Emission during Hydrogen Assisted Cracking of High Carbon Steel
Evgeny D. Merson, Dmitri L. Merson, Mikhail M. Krishtal and Alexei Vinogradov
- 29-220** AE Technique for Detecting the Delayed Cracks Under Thermal Sprayed Coating
Mikio Takemoto, Gunji Ueno, Shuichi Ueno, Seiji Masano and Motoaki Nakamura
- 29-232** The Extraction Method for Dispersion Curves from Spectrograms using Hough Transform
D.A. Terentyev, V.A. Barat and K.A. Bulygin
- 29-243** Study of Acoustic Emission Data Analysis Tools for Structural Health Monitoring Applications
Manindra R. Kaphle, Andy C.C. Tan, David P. Thambiratnam, and Tommy H.T. Chan
- 29-251** Neural Network Fatigue Life Prediction in Notched Bridge Steel I-Beams from Acoustic Emission Amplitude Data
Fady F. Barsoum, Eric v. K. Hill, Jamil Suleman, Andrej Korcak and Yi Zhang
- 29-260** Numerical Simulation To Examine Accuracy of AE Source Location and Its Applications to In-Situ Rock Monitoring
Tsuyoshi Ishida and Shunji Sasaki
- 29-273** Research on Gas Pipeline Leak Location Method Based on Empirical Mode Decomposition
Xianyong Qin, Gongtian Shen, Renyang He, Tao Meng and Yong Xiao
- 29-284** Acoustic Emission in Materials Research – A Review
Kanji Ono
- 29-309** The Study of Pattern Recognition of Aircraft Fatigue Cracking Based on Waveform Analysis Method and Artificial Neural Networks of Acoustic Emission Signals
Zhen-Long Hu, Gong-Tian Shen, Guan-Hua Wu, Shi-Feng Liu and Zhan-Wen Wu

29-317 Acoustic Emission Response of Reinforced Lightweight Metal Matrix Composites during Tensile and Cyclic Loading

Matthias Merzkirch, Andreas Reeb, Kay André Weidenmann, Alexander Wanner and Volker Schulze

Frontal29	Contents of Volume 29 (2011)	I-1 – I-3
	Meeting Calendar	I-3
	Authors Index of Volume 29	I-4
	Policy/Author's Notes/ DVD/Subscription Information	I-5 – I-7
	AE Activity: World Conf. on AE, 2011, Beijing, China: Gongtian Shen	I-8
Cover illustration	Scenes from WCAE 2011 Beijing.	
JAE Index Folder*	Cumulative Indices of J. of Acoustic Emission, 1982 – 2011	
	JAE-Contents1-29 Contents of Volumes 1-29	
	JAE-Authors Index1-29 Authors Index Volumes 1-29	
	Comprehensive Authors Index (2011) is also included.	

* indicates the availability in CD-ROM only. Indices are also available for download from www.aewg.org.

Meeting Calendar

AEWG 54

The 54th Meeting on Acoustic Emission Working Group will be held on May 21-23, 2012 at Princeton, NJ. The host is Dr. Mark Carlos of Mistras Group/Physical Acoustics. More information is available at www.aewg.org. The first two days are for technical (and business) sessions and Wednesday, May 23, is for international committee meetings (RILEM TC-MCM & ISO TC135/SC9/WG4), half day each. For accommodation, call Hyatt Regency Princeton, +1 (609) 987-1234 or <http://www.Princeton.Hyatt.com>.

EWGAE 30 – ICAE 7

The 30th European Meeting on Acoustic Emission Testing and 7th International Conference on Acoustic Emission will be held on September 10-12, 2012 at Granada, Spain. The host is University of Granada and the organizing committee is co-chaired by Drs. Antolino Gallego and Amadeo Benavent-Climent. Key dates are, Abstract submission: March 25, 2012 and Submission of full papers: June 15, 2012. See more information at 2012.ewgae.eu. More can be requested from Leandro Morillas, Scientific Conference Secretariat, ewgae2012@ewgae.es, Tfl: +34 958241000 (Ext. 20411) Granada (Spain).

IAES 21

Japanese Committee on Acoustic Emission (JCAE) plans to hold 21st IAES on November 27-30, 2012, at the Okinawa Jichikaikan in Naha city, Okinawa, Japan. It is the 21st in a series that began in 1972. Key dates are, Abstract submission: June 30, 2012 and Submission of full papers: August 24, 2012. See more information at iaes21.org. More can be requested from

Dr. Manabu ENOKI,

Department of Materials Engineering, The University of Tokyo

7-3-1 Hongo, Bunkyo-ku, Tokyo, 113-8656 Japan

Email: info@iaes21.org; Phone: (+81)3-5841-7129; Fax: (+81)3-5841-7181

Authors Index, Volume 29 (2011)

Hideaki Aburatani	29-149	Motoaki Nakamura	29-197, 29-220
D. G. Aggelis	29-057, 29-113	Kanji Ono	29-284
Yosi Aharon,	29-089	Didem Ozevin	29-123
Igal Alon	29-089	A. Papacharalampopoulos,	29-057
		D. Polyzos,	29-057
V. Barat,	29-133, 29-232	Xianyong Qin,	29-273
Francisco Barrios	29-042		
Fady F. Barsoum,	29-251	Andreas Reeb	29-317
K.A. Bulygin	29-232	M. Rostovtsev	29-133
Brian Burks	29-167	Zachary D. Sager,	29-106
Arie Bussiba,	29-089	Shunji Sasaki	29-260
		Markus G. R. Sause	29-184
Mark F. Carlos	29-142	Michael D. Scheppa,	29-106
Rami Carmi,	29-089	Volker Schulze	29-317
Tommy H.T. Chan	29-243	Gongtian Shen,	29-273, 29-309
		Jae-Ha Shin	29-098
Michael R. Gorman	29-001	T. Shiotani	29-057
D. Grishin	29-133	Jamil Suleman,	29-251
Stan Hale	29-160		
M. A. Hamstad	29-175	Mikio Takemoto,	29-197, 29-220
Renyang He,	29-273	Andy C.C. Tan	29-078, 29-243
Zahra Heidary	29-123	D.A. Terentyev,	29-232
Eric v. K. Hill,	29-106, 29-251	David P. Thambiratnam,	29-243
Igal Hochbaum	29-089	Isadora P. Thisted	29-106
Zhen-Long Hu,	29-309		
Tsuyoshi Ishida	29-260	Gunji Ueno	29-197, 29-220
		Shuichi Ueno,	29-197, 29-220
Manindra R. Kaphle,	29-243	Alexei Vinogradov	29-210
Andrej Korcak	29-251		
Evangelos Z. Kordatos	29-113	Alexander Wanner	29-317
Mikhail M. Krishtal,	29-210	Kay André Weidenmann	29-317
Oh-Yang Kwon	29-098	Galit Widenfeld,	29-089
		Guan-Hua Wu,	29-309
Joseph F. Labuz	29-068	Weiliang Wu	29-078
Qing Lin	29-068	Zhan-Wen Wu	29-309
Tian Ran Lin,	29-078		
Shi-Feng Liu,	29-309	Yong Xiao	29-273
David P. Lowe,	29-078	Yi Zhang	29-251
		Ran Zhou,	29-160
Seiji Masano	29-220	Paul Ziehl	29-042
Theodore E. Matikas	29-113		
Tao Meng	29-273		
Dmitri L. Merson,	29-210		
Evgeny D. Merson,	29-210		
Matthias Merzkirch	29-317		
Hirokazu Moriya	29-029		
Boris Muravin	29-142		

JOURNAL OF ACOUSTIC EMISSION

Editor: Kanji Ono

Associate Editors: A. G. Beattie, T. F. Drouillard, M. Ohtsu and W. H. Prosser

1. Aims and Scope of the Journal

Journal of Acoustic Emission is an international journal designed to be of broad interest and use to both researcher and practitioner of acoustic emission. It will publish original contributions of all aspects of research and significant engineering advances in the sciences and applications of acoustic emission. The journal will also publish reviews, the abstracts of papers presented at meetings, technical notes, communications and summaries of reports. Current news of interest to the acoustic emission communities, announcements of future conferences and working group meetings and new products will also be included.

Journal of Acoustic Emission includes the following classes of subject matters;

A. Research Articles: Manuscripts should represent completed original work embodying the results of extensive investigation. These will be judged for scientific and technical merit.

B. Applications: Articles must present significant advances in the engineering applications of acoustic emission. Material will be subject to reviews for adequate description of procedures, substantial database and objective interpretation.

C. Technical Notes and Communications: These allow publications of short items of current interest, new or improved experimental techniques and procedures, discussion of published articles and relevant applications.

D. AE Program and Data Files: Original program files and data files that can be read by others and analyzed will be distributed in CD-ROM.

Reviews, Tutorial Articles and Special Contributions will address the subjects of general interest. Nontechnical part will cover book reviews, significant personal and technical accomplishments, current news and new products.

2. Endorsement

Acoustic Emission Working Group (AEWG), European Working Group on Acoustic Emission (EWGAE), have endorsed the publication of Journal of Acoustic Emission.

3. Governing Body

The Editor and Associate Editors will implement the editorial policies described above. The Editorial Board will advise the editors on any major change. The Editor, Professor Kanji Ono, has the general responsibility for all the matters. Associate Editors assist the review processes as lead reviewers. The members of the Editorial Board are selected for their knowledge and experience on AE and will advise and assist the editors on the publication

policies and other aspects. The Board presently includes the following members:

A. Anastasopoulos	(Greece)
F.C. Beall	(USA)
J. Bohse	(Germany)
P. Cole	(UK)
M.A. Hamstad	(USA)
R. Hay	(Canada)
K.M. Holford	(UK)
O.Y. Kwon	(Korea)
J.C. Lenain	(France)
G. Manthei	(Germany)
P. Mazal	(Czech Republic)
C.R.L. Murthy	(India)
A.A. Pollock	(USA)
F. Rauscher	(Austria)
J. Schmidt	(Poland)
T. Shiotani	(Japan)
P. Tschliesnig	(Austria)
H. Vallen	(Germany)
M. Wevers	(Belgium)
B.R.A. Wood	(Australia)

4. Publication

Journal of Acoustic Emission is published annually in CD-ROM by Acoustic Emission Group, PMB 409, 4924 Balboa Blvd, Encino, CA 91316. It may also be reached at 2121H, Engr. V, University of California, Los Angeles, California 90095-1595 (USA). tel. 310-825-5233. FAX 310-206-7353. e-mail: aegroup7@gmail.com or ono@ucla.edu

5. Subscription

Subscription should be sent to Acoustic Emission Group. Annual rate for 2012 is US \$111.00 including CD-ROM delivery, by priority mail in the U.S. and by air for Canada and elsewhere. For additional print copy, add \$40-49. Overseas orders must be paid in US currencies with a check drawn on a US bank. PayPal payment accepted. Inquire for individual (with institutional order) and bookseller discounts. See also page I-7.

6. Advertisement

No advertisement will be accepted, but announcements for books, training courses and future meetings on AE will be included without charge.

Notes for Contributors

1. General

The Journal will publish contributions from all parts of the world and manuscripts for publication should be submitted to the Editor. Send by e-mail or to:

Professor Kanji Ono, Editor - JAE
Rm. 2121H, Engr. V, MSE Dept.
University of California
420 Westwood Plaza,
Los Angeles, California 90095-1595 USA
e-mail: kanjiono1@gmail.com

Authors of any AE related publications are encouraged to send a copy to:

Acoustic Emission Collection
Grainger Engineering Library
University of Illinois at Urbana-Champaign.
c/o: Mary C. Schlembach, Engineering Physics &
Astronomy Librarian
154 Grainger Engineering Library Information Center
1301 West Springfield Ave. Urbana, IL 61801
Email: schlemba@illinois.edu

Only papers not previously published will be accepted. Authors must agree to transfer the copyright to the Journal and not to publish elsewhere, the same paper submitted to and accepted by the Journal. A paper is acceptable if it is a revision of a governmental or organizational report, or if it is based on a paper published with limited distribution.

The language of the Journal is English. All papers should be written concisely and clearly.

2. Page Charges

No page charge is levied. The contents of CD-ROM will be supplied to the authors free of charge via Internet site.

3. Manuscript for Review

Manuscripts for review need only to be typed legibly; preferably, double-spaced on only one side of the page with wide margins. The title should be brief. An abstract of 100-200 words is needed for articles. Except for short communications, descriptive heading should be used to divide the paper into its component parts. Use the International System of Units (SI).

References to published literature should be quoted in the text citing authors and the year of publication or consecutive numbers. These are to be grouped together

at the end of the paper. Journal references should be arranged as below. Titles for journal or book articles are helpful for readers, but may be omitted.

H.L. Dunegan, D.O. Harris and C.A. Tatro (1968), *Eng. Fract. Mech.*, 1, 105-122.

Y. Krampfner, A. Kawamoto, K. Ono and A.T. Green (1975), "Acoustic Emission Characteristics of Cu Alloys under Low-Cycle Fatigue Conditions," NASA CR-134766, University of California, Los Angeles and Acoustic Emission Tech. Corp., Sacramento, April.

A.E. Lord, Jr. (1975), *Physical Acoustics: Principles and Methods*, vol. 11, eds. W. P. Mason and R. N. Thurston, Academic Press, New York, pp. 289-353.

Abbreviations of journal titles should follow those used in the ASM Metals Abstracts. In every case, authors' initials, appropriate volume and page numbers should be included. The title of the cited journal reference is optional.

Illustrations and tables should be planned to fit a single page width (165 mm or 6.5"). For the reviewing processes, these need not be of high quality, but submit glossy prints or equivalent electronic files with the final manuscript. Lines and letters should be legible.

4. Review

All manuscripts will be judged by qualified reviewer(s). Each paper is reviewed by one of the editors and may be sent for review by members of the Editorial Board. The Board member may seek another independent review. In case of disputes, the author may request other reviewers.

5. Electronic Media

This Journal will be primarily distributed electronically by CD-ROM. In order to expedite processing and minimize errors, the authors are requested to submit electronic files of the paper. On the INTERNET, you can send an MS Word file and the separate figure files (in JPEG or other formats) to "aegroup7@gmail.com".

6. Color Illustration

With the new format, authors are encouraged to use them.

JAE DVDs: Vol. 1-28 (1982-2010)

Two DVDs contain all the articles from the past 28 years of Journal of Acoustic Emission. Cost is \$100 including shipping. Send an order to Acoustic Emission Group (address below).

Separate pdf files of Volume 1 through 28 are available for download from aewg.org without cost.

2012 SUBSCRIPTION RATES

Base rate (CD-ROM) for one year	\$111.00
CD-ROM + printed copy, US priority mail:	\$151.00
CD-ROM + printed copy, non-US priority mail:	\$160.00
Print copy only with priority shipping (US)	\$140.00
Print copy only with priority/air shipping (non-US)	\$149.00

Payment must be in U.S. dollars drawn on a U.S. bank. Bank transfer accepted at

California Bank and Trust, San Fernando Valley Office (Account No. 080-03416470)
16130 Ventura Blvd, Encino, CA 91436 USA (Swift code: CALBUS66)

PAYPAL payment is accepted. Inquire via e-mail.

Back issues available in CD only; Inquiry and all orders should be sent to (Fax no longer available):

Acoustic Emission Group
PMB 409, 4924 Balboa Blvd. Encino, CA 91316 USA

For inquiry through Internet, use the following address:

Editor-Publisher

Publication Date of This Issue (Volume 29):

kanjiono1@gmail.com

Kanji Ono Tel. (818) 849-9190

23 March 2012.

AE Activity: Report of WCAE-2011 Beijing:

Gongtian Shen

World Conference on Acoustic Emission - 2011 Beijing was held from Aug. 24 to Aug. 26, 2011 in Beijing, China. A total of 136 people from 19 countries attended this conference. The Proceedings published 88 papers*, including six keynote lectures, 44 orally presented papers and 20 poster presentation. Business meeting were held in the afternoon of Aug. 24, 2011. 114 delegates from 19 countries attended this meeting. A motion for establishment of the World Congress on Acoustic Emission, the name of which was changed later to International Society on Acoustic Emission (ISAE), was passed by the majority of the delegates. Allen Green (USA) was elected as the Honorary President of ISAE and Gongtian Shen was elected as the Interim President of ISAE. The constitution of ISAE is being drafted. The elected Interim Executive Board meeting in Aug. 26, 2011 decided that the next WCAE will be held in October, 2013, in Shanghai, China.

* Twelve papers from the Proc. of WCAE2011 are included in this Volume after revisions.



Dr. Gongtian Shen, Chairman of WCAE2011, presented one of the six keynote lectures.



Scenes from the WCAE2011 venue.

MODAL AE ANALYSIS OF FRACTURE AND FAILURE IN COMPOSITE MATERIALS, AND THE QUALITY AND LIFE OF HIGH PRESSURE COMPOSITE PRESSURE VESSELS

MICHAEL R. GORMAN

Digital Wave Corporation, 13760 E Arapahoe Rd, Centennial, CO 80112

Abstract

The use of modal acoustic emission testing and analysis techniques to determine the quality of newly manufactured vessels and to detect and analyze damage in vessels that are in service can provide the required confidence in the safety of high pressure composite (HPC) pressure vessels operated at pressures up to 103 MPa (15,000 psi). These vessels are made of composite materials, such as carbon fibers embedded in a resin matrix, the fiber content being approximately 60% by weight. A practical method for distinguishing fiber break and matrix cracking events by a combination of energy and frequency is described and a new rolling ball impact energy calibration technique provides a method for comparing source energies with wave energies. Background energy oscillation appears to give detailed insight into failure progression. Fiber-bundle tip vibration can reveal the presence of already broken fiber bundles. The curvatures of cumulative events and energy curves quantitatively measure pressure vessel stability and are used in the current ASME code as accept-or-reject criteria for HPC pressure vessels. These tools are useful for manufacturing acceptance, in-service testing, quality control, fatigue, stress rupture and composite repair applications.

1. Introduction

This work is compendium of results developed over the past twenty years on the study of acoustic emission (AE) in composite materials, particularly in high pressure composite pressure vessels fabricated with composite materials like carbon and glass fibers embedded in an epoxy or polyester matrix. All of the testing described herein was performed with wideband sensors, as opposed to the resonant types that have been traditionally used in practical AE testing, and all analysis was done on the recorded waveforms. Ever since the original discovery that plate waves [1] were the main practical waves to be studied in AE work on composite pressure vessels, and indeed metallic vessels and many other practical structures as well, all work done by this author has been based on the capture and analysis of wideband waveforms. Since the publication of [1], many articles by different workers have been published under various titles such as plate wave AE [2, 3], wideband AE, waveform-based AE [4, 5], guided wave AE or wave-based AE as can easily be seen by doing a web search using these key words. There are now many works published on the subject and this subject has come to be known in the literature more and more as modal AE [6]. Accept-or-reject criteria of high-pressure composite (HPC) pressure vessels in the current ASME code for newly manufactured vessels and under consideration by NBIC (National Board Inspection Code) for in-service vessels are based on this foundation.

1.1 Acoustic Emission in Composite Materials

Composite fracture mechanisms are manifold but consist mainly of matrix cracking, delamination between layers, fiber breakage, fiber to matrix debonding and fiber pull-out. These are the sources of AE in the material. Another very important source is friction between newly created fracture surfaces.

An AE event is an impulse or transient wave that propagates outwardly in all directions from a source. A source is a disturbance, such as a fracture or rupture in the material that gives rise to the transient stress wave. Sources and waves can be modeled using elastodynamic theory. As the wave propagates through a plate-like material it changes shape due to dispersion and attenuation. The wave is detected by one or more sensors coupled to the material at some distance from the source. The detected signal that is analyzed is called the waveform. Since there are multiple fracture mechanisms in composites, the waveform produced by a given fracture mechanism must be distinguished from all others if the fracture mechanism is to be uniquely identified.

An AE waveform is distinguished by 1) the wave (mode) shapes, 2) the wave (mode) energies and 3) the wave (mode) frequency spectrum. The waveforms can be calculated using elastodynamic theory. Stress and strain analysis, fracture mechanics and testing of composite materials provide additional insight into how to use the elastodynamic modeling to analyze measured waveforms. The waves are analyzed to determine whether the source is a delamination, small matrix crack event, fiber breakage event, frictional event or simply unwanted noise.

In propagating through the material AE waves behave much as any other sound waves. They can reflect, refract and diffract depending on the material and structural features encountered. The most salient feature of waves in plates is dispersion. Theory predicts that the different frequency components travel at different speeds. This means that the wave will change shape as it propagates. The waveforms shown in Fig. 1 are examples of the by now well-known E and F waves, or, extensional and flexural wave modes, respectively. The change in shape, or dispersion, can be readily seen between channels three and channel four some distance away. This is not just a reduction in amplitude, but an actual physical separation and recombination of the different Fourier components in the waves. Superposition of these components creates the shape of the wave modes at any given point in time and space.

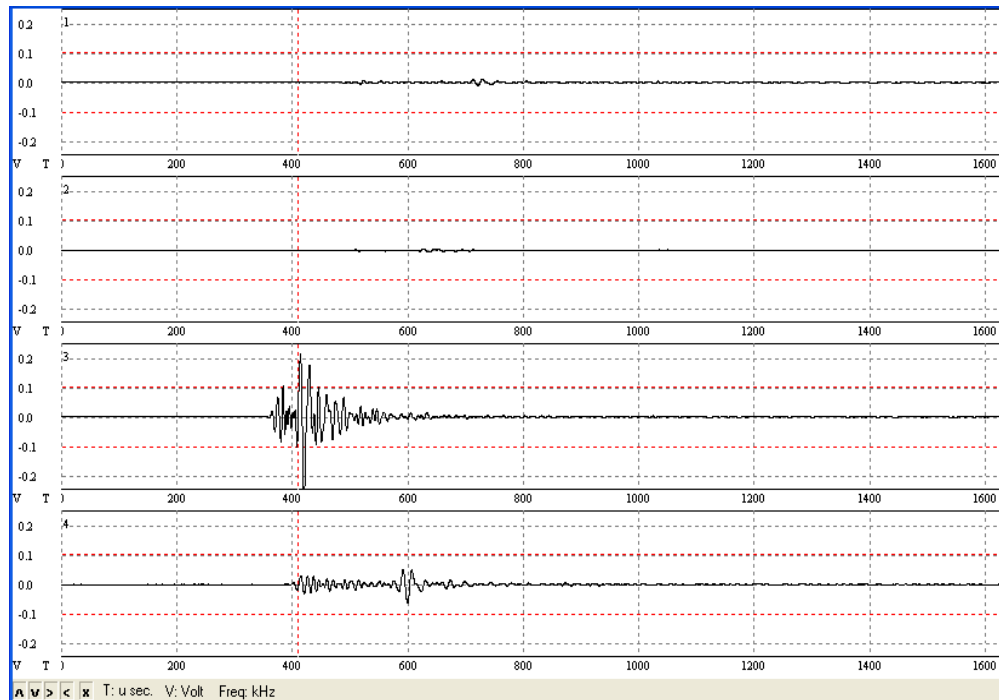


Fig. 1. The waveforms for an event in a composite pressure vessel. The wave arrives first at channel 3. Ordinate is volts and abscissa is time in μs .

1.2 Composite Pressure Vessels in Fatigue

Composite materials consist of many types of material systems such as fiberglass/polyester, fiberglass/epoxy, aramid fiber/epoxy and carbon fiber/epoxy, plus hybrid systems. The fatigue performance varies with the material system, structural design, ply angles or winding angles, laminate stacking sequence or winding pattern, cycle loads and loading pattern and so forth. Test specimens have survived hundreds of thousands or even millions of loading cycles. Composite materials are now used for the primary load bearing components of several military and civilian aircraft due to their long fatigue life and weight advantages. Composite materials have been used since the 1960s for construction of high-pressure rocket motor pressure vessels. Composite pressure vessels in CNG service have been around for a couple of decades. DOT approved 31 MPa (4500 psi) self-contained breathing apparatus (SCBA) cylinders made with composite materials are routinely used by firemen around the world.

It has been well-known and accepted since the late 1980s that there are literally thousands upon thousands of tiny matrix cracks in a typical composite pressure vessel after the first few loading cycles. Composite failure progresses in stages. A point is reached called matrix crack saturation. From this stage onward more critical fiber breakage occurs. Experience shows that *pressure vessel failure is mainly due to fiber failure.*

1.3 Literature Discussion – High Pressure Composite Vessels and Fatigue

There is a body of literature on AE monitoring during testing of pressure vessels going back to the 1970s. Perhaps the most referred to study of HPC pressure vessels under fatigue loading is the work by Chiao *et al.* that was performed at Lawrence Livermore and published in 1978 [7]. The fatigue tests were run at a fairly high maximum tensile stress of 91% of average burst pressure. This is very high compared to the operating pressures of ASME, DOT, and ISO pressure vessels where the fatigue stress ratio is normally less than 40%. AE monitoring was applied only to the specimens that were pressurized quasi-statically to burst. The 25 fatigue specimens tested in that program were not monitored by AE.

Awerbuch *et al.* published in 1984 [8] perhaps the most extensive laboratory study of AE in a composite material used for pressure vessels undergoing fatigue loading. In that work 96 coupon specimens cut from filament wound graphite/epoxy panels were tested. One-third of the panels were loaded quasi-statically to failure in tension and about one-third were cycled in tension to progressively higher loads until failure. The remaining one-third of the specimens were cycled at a fatigue ratio of 0.1 for either 5,000 cycles or 15,000 cycles. Some details of this study are worth mentioning here.

The specimens were examined under a 250x closed-circuit TV camera while undergoing loading. Damage development could be monitored in real-time along with the AE. After cycling, the specimens were loaded in tension to failure (rupture). Some of the specimens had damage inflicted in the form of notches. After failure, the specimens were examined by photomicrography and scanning electron microscopy to examine the fracture surfaces. Material from each plate, from which the specimens were machined was documented before testing to get a baseline of the material before any load was applied. X-ray radiographs and ultrasonic C-scans were taken of the original and tested condition. All these different examination provided details about the failure mechanisms.

During fatigue loading, the camera was focused on the edge of the specimen and matrix cracks were observed to initiate at the voids in the matrix. Gradually the cracks would link the voids together. Transverse cracks would also appear in the 90° plies. This was followed by delaminations between the helical plies, the 90° plies and the 0° plies. The opening and closing of the rugged fracture sur-

faces was easily observed to correlate with the AE. Indeed, most of the AE was clearly due to frictional rubbing of the fracture surfaces.

The emission events, E , were accumulated as a function of cycle number, N , and an interesting fact was that the emission would suddenly jump to a new level after so many hundreds of cycles. The events would then accumulate linearly for a while before another major increase would be seen. Despite all of the damage that occurred during cycling, an increase in the average remaining strength was observed. The specimens that were cycled 15,000 times at the highest absolute stress did show a slight reduction in strength of about 9%. All cycled specimens showed an increase in compliance over specimens that were not cycled.

Maximum fatigue load and stress had a dramatic effect on AE events. For example, an increase of maximum fatigue stress from 47% to 53% changed the event sum after 5,000 cycles from around 10,000 events to over 30,000 events for identical undamaged specimens, but there was no effect on strength. One would conclude that, left undamaged by any outside influences, the fatigue capabilities of filament wound graphite/epoxy composite material are very good.

Testing specimens in tension to failure after they had been cycled showed that AE events initiated at approximately 8 – 10% of the fatigue load. This was most likely due to frictional emission and not new damage. The data showed that it takes a higher load of about 120% of the fatigue load to stimulate emission from new damage.

The specimens that had damage inflicted, in the form of double edge notches, failed at lower loads, as expected due to the reduced cross section remaining after notching. AE also initiated at a lower load. All notched specimens failed close to the notches.

From this work we conclude that inflicted damage, not (low cycle) fatigue, is the key factor that will affect the strength of filament wound graphite/epoxy pressure vessels. The stress concentrations created by significant damage will cause crack growth and/or fiber breaks, which release AE impulses.

Fiber breakage and matrix cracking details were discussed in [2] and [4] and in a report by Failure Analysis Associates to General Motors Corporation, 1997 [9]. NGV Type II vessels had short cuts introduced across their carbon fibers and were subsequently pressure cycled for 15,000 cycles. The stress concentration at the ends of the cuts led to matrix cracks (splitting) that gradually worked their way completely around the circumference. The AE waveforms from the matrix cracks were captured and stored. Burst testing showed that the effect of the cracks on vessel strength was negligible. NGV Type IV vessels were cycle tested for 15,000 cycles. Impact damage had a large effect on strength reduction. As part of this test program, a laboratory study of fiber tow specimens elucidated the spectra of fiber breaks and matrix cracking. As expected from theoretical calculations [10], fiber breaks and matrix cracks had different frequency spectra. However, it was noted that the spectra can overlap and thus the spectrum alone is not sufficient to distinguish the two; their respective wave energies must be taken into account. A method for doing this is given in this paper.

Fultineer and Mitchell [11] discussed the results of testing carbon-fiber overwrapped pressure vessels that had been in service. They proposed a specific number of AE (ringdown) counts as a criterion, by which to remove vessels from service. ASTM E2191-10 for this type of vessel (size limited to 2.5 cubic feet of water volume) is a standard based on this. Interestingly, the notion of using the “knee” of the cumulative AE count curve is mentioned but not used; that is, it is not developed into a criterion for dispositioning vessels. Using the “knee” to disposition vessels

has been problematic. We propose, however, that the shape of the cumulative AE event curve at pressure holds can be used to determine if the vessel stabilizes appropriately. Our experience shows that the exponential fit to pressure hold “rollover” or curvature of the cumulative events curve for hundreds of identically manufactured vessels falls into a certain range of values. This is not unexpected for it is essentially a measure of the relaxation time of the material under load and a measure of the quality and repeatability of the manufacturing process.

2. Waveform Recording

The E and F waves are digitized and stored for analysis. The recording system, including sensors, or, transducers, must have proper sensitivity, fidelity, signal to noise ratio and bandwidth so that the E and F waves can be identified. The equipment needed for AE testing of HPC pressure vessels is quite straightforward.

A typical recording system consists of

1. sensor
2. preamplifier
3. high-pass and low-pass filters
4. amplifier
5. A/D (analog-to-digital) converter
6. a computer program for the collection of data
7. a computer monitor for the display of data
8. a computer program for the analysis of data

It is desirable that the front end of the E wave for a given event be distinguishable; i.e., that it has not been interfered with by superposition of another wave so much so that it cannot be clearly identified and used for analysis purposes. This is called a *clean front end*.

There is usually some amplification applied to the signal. Typically, for the first pressurization of a virgin vessel, an 80-dB threshold is used so that only the higher energy events are detected. A 56-dB threshold or lower is used for subsequent pressurization and fatigue cycling.

Sensors are coupled to pressure vessels by some viscous liquid or gel; for example, silicone vacuum grease. They are positioned by measuring the propagation and attenuation of waves excited by pencil-lead breaks. The displacement of the wave motion on the surface of a vessel is desired, so, ideally, sensor calibration would be in volts/meter of displacement over a specified frequency range. This can be done with a basic Michelson interferometer setup such as that used at NIST. This also aids in making comparisons with elastodynamic calculations. Sensor sensitivity is usually in the range of about 0.1 V/nm over the range from 50 to 400 kHz.

3. Fiber Breakage Events and High Frequency Components in the Frequency Spectrum

Fiber-bundle breakage is the most severe kind of event as far as pressure vessel strength is concerned. Reasoning is given below that suggests that AE waveforms due to fiber-bundle breakage can be distinguished in practical testing 1) by the presence of the highest frequencies available in AE signals, and 2) by the shape of the frequency spectrum; that is, by the relative energies of various spectral ranges within the frequency spectrum. The mode shapes are highly dependent on the exact material, thickness and location of the fiber breakage within the material but are of distinctive waveforms.

Since real composites are not transparent and individual fibers are small (~10 μm diameter) the conjecture that fiber breaks are occurring can only be proved indirectly, but the evidence comes from several directions, both theoretical and experimental. There are several pieces of evidence that fiber breakage is detected: 1) by elastodynamic modeling, 2) by simple physical considerations using typical fiber and matrix properties, 3) by the fact that the distinctive waveforms occur at the higher loads as predicted by statistical fiber failure (weakest link/shear lag) models and confirmed by experiment, 4) by the fact that the distinctive types of waveforms occur in great numbers at the higher loads but not at the lower load levels, 5) by the appearance of fiber broken end tip vibrations (more about this later) only after the fiber break waveforms appear, 6) by work - energy considerations based on the direct observation of fiber breaks in specially prepared coupon specimens.

A crack may look, for example, like a displacement jump. The jump in opening is some finite value and because of continuity the crack must begin and end in unruptured (but possibly stretched) material. A jump is often modeled as a step function or impulse or some other function. Any function can be considered as a sum of Fourier components so a simple way to think about a crack is to think of building it out of oscillators of varying material constants and stretches. In wave propagation theory, the source characteristics determine the wave frequencies, while the material dictates the velocity and wavelength. Considering a fiber as a spring, the oscillator force (F) can be written in length change (ΔL)

$$F = k\Delta L,$$

where the spring constant is $k = EA/L$. Taking mass $m = \rho V$ and $V = AL$, the angular frequency (ω) can be written

$$\omega^2 = k / m = AE / ml = AE / \rho VL = E / \rho L^2.$$

Using values for glass fibers,

$$\omega = \sqrt{22(10^9) / 2.6(10^3)} / L$$

or $f = 463/L$, while epoxy values yield

$$\omega = \sqrt{2(10^9) / 1.3(10^3)} / L$$

or $f = 197/L$. It can be seen that, all other things being equal, the (highest) frequency in a matrix crack is about half that of a glass-fiber break. Higher frequency ratios can be expected in CFRP composites. Relative frequency values similar to those calculated here are close to those found in experimental data.

Another physical approach to deciding if fiber breakage occurs in much shorter time than matrix ruptures is to consider the velocity of sound in the matrix versus the fiber. Crack speeds can be no faster than the speed of sound and, in fact, have been found to be far less. Theoretically, crack surfaces can be created at the Rayleigh surface wave speed. The velocity of sound is much faster in fiber than matrix.

To investigate the frequency spectrum further, the elastodynamic governing equations for a composite plate were coded in a computer program. Typical graphite/epoxy moduli were inserted and the waveforms due to different source motions were calculated. The forcing function was chosen to be an impulse and impulses of varying time lengths were studied. As expected, the highest frequencies were in the waveforms produced by the fastest source, confirming the physical reasoning above. Notably, the calculated waveforms resembled those in experimental data suspected of being fiber breaks.

Next, we turn to the experimental evidence. Hundreds of pressure vessel tests were investigated over many years, including both CFRP and FRP vessels, to determine when waves with the highest frequencies appeared as a function of load level, or pressure. Waveforms with the highest frequency components occur as the higher load levels are reached. Importantly, the number of these waveforms per unit time increases (greater rates) above 80% of ultimate stress in agreement with statistical fiber failure theory. Laboratory tests on impregnated fiber tows and on coupon specimens were carried out as well and show the same pattern as above; that is, at the higher load levels, waveforms containing higher frequencies begin to appear and increasingly so as the specimens are ramped to failure [9, 12].

Waveforms from the test of an FRP vessel are exhibited in Figs. 2 – 4. They show the differences between matrix cracking and fiber breakage waveforms by their frequency spectra and energy differences.

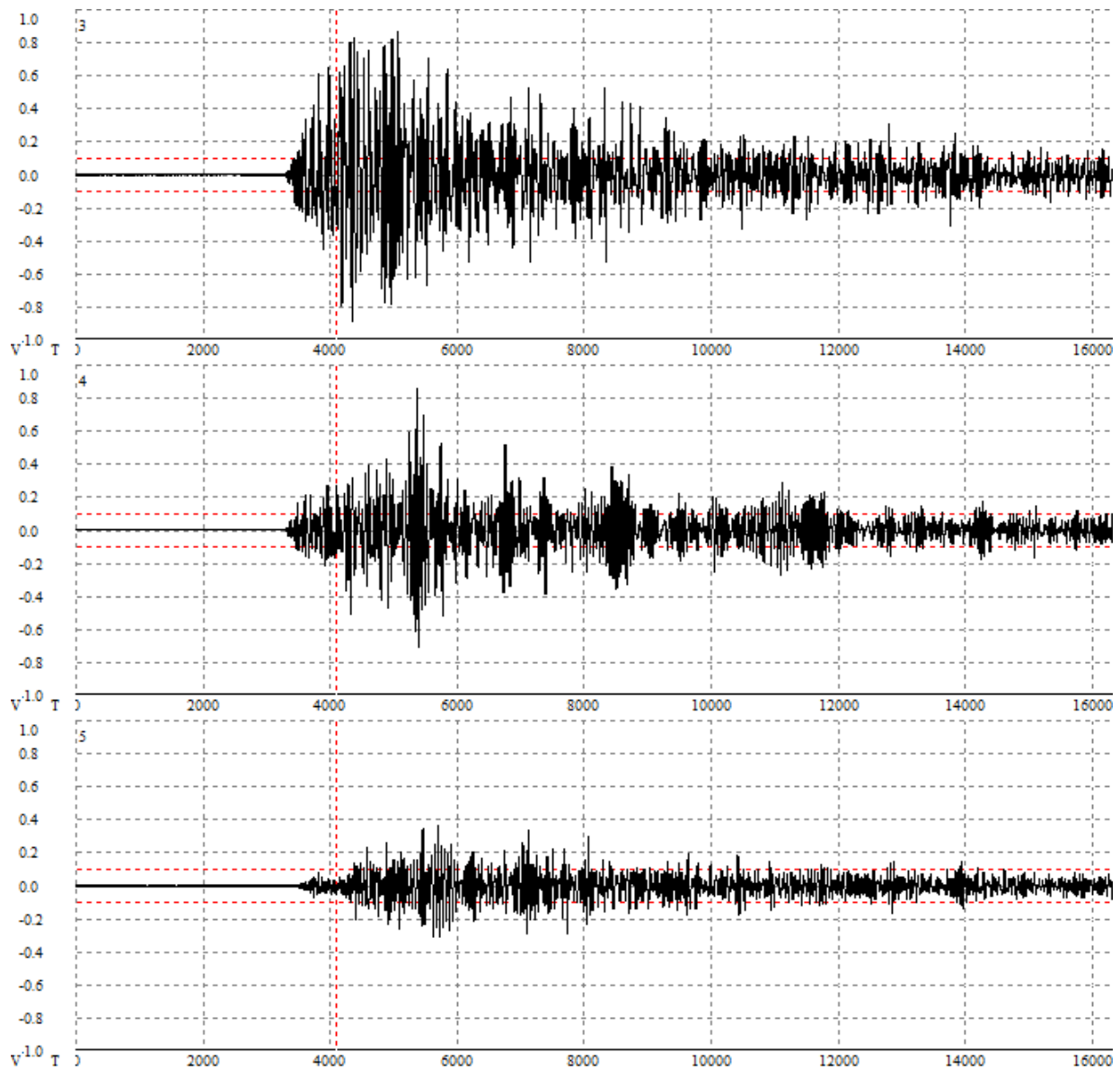


Fig. 2. Matrix splitting waveforms in a unidirectional FRP overwrapped vessel. The spectra for these waveforms (channel 3, 4, 5) are shown in Fig. 3 below.

The waveforms for matrix splitting, as shown in Fig. 2, are observed frequently throughout tests and they can be quite energetic achieving loud audible sounds. The cracks can be observed in many semi-transparent or translucent materials FRP materials. The frequencies of these very large energy matrix events are very low and it can be seen in Fig. 3 that they excite sound in the audible range below 10 kHz.

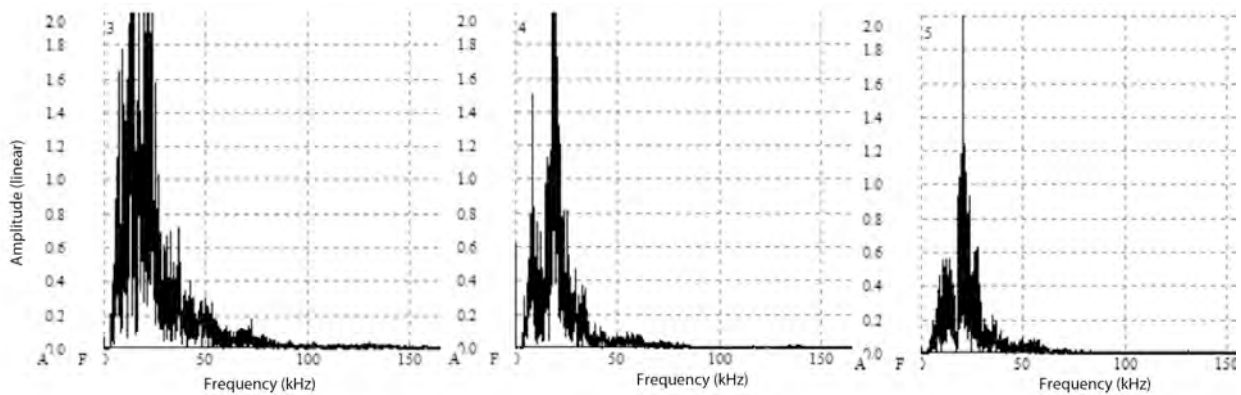


Fig. 3. Amplitude (linear, volts) versus frequency for channels 3, 4 and 5 on a fiberglass vessel showing the spectrum of the matrix cracking (splitting) occupies mainly the low frequency part of the spectrum below 50 kHz.

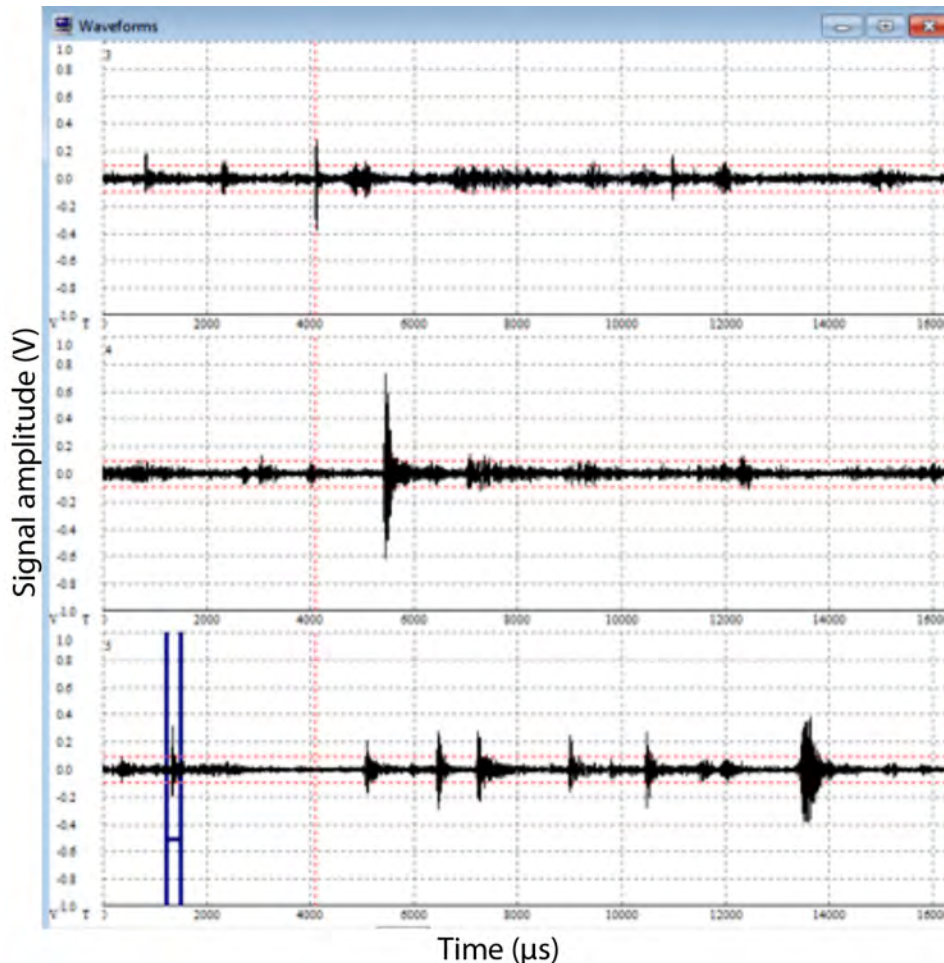


Fig. 4. a) Waveforms of fiber breaks on a ramp to burst at about 80% of ultimate load. Note multiple breaks. Broad spectrum uses entire range of the transducer response.

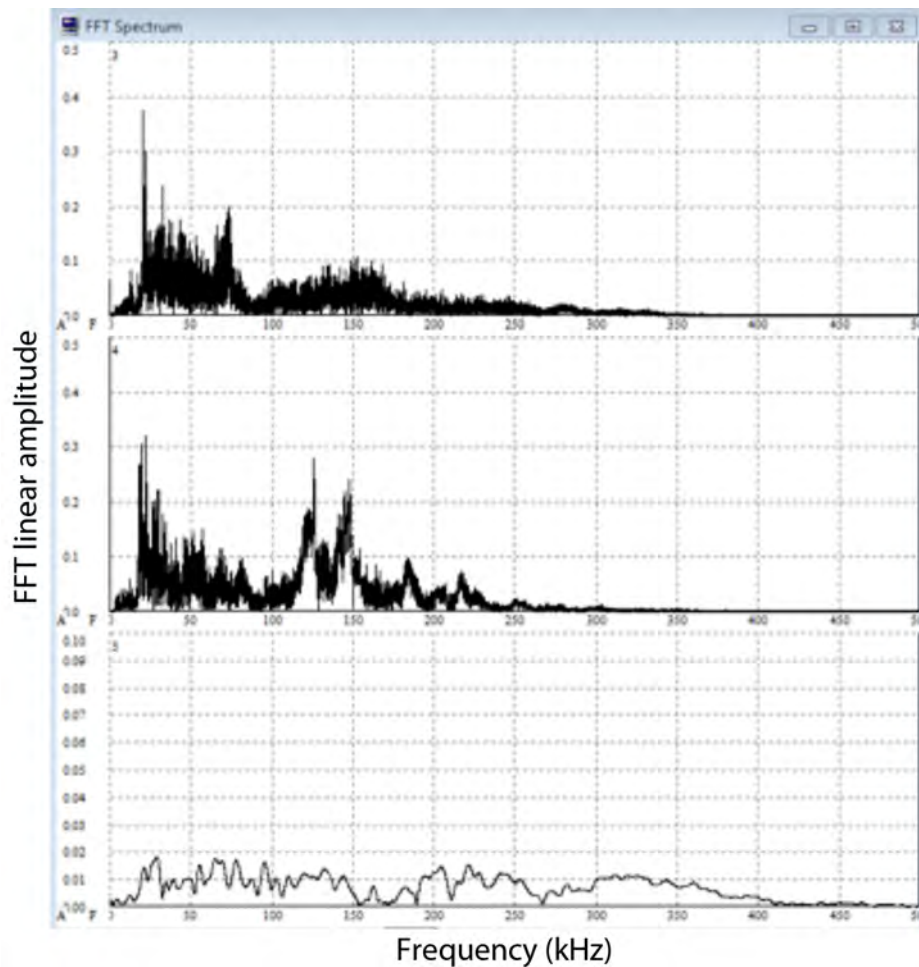


Fig. 4. b) Broad FFT spectra of fiber-break signals at 80% of ultimate load covering entire range of the transducer response. Channel 5 (bottom) data is from a short segment between blue lines in Fig. 4a.

Turning next to fiber-break waveforms in this same test, we can see the much broader spectrum. The wave window in Fig. 4a for this same vessel at about 80% of burst pressure shows several fiber breaks. These waveforms have sharp front ends and high frequencies, shown in Fig. 4b. These are events with much higher frequencies in the spectrum. The higher frequencies of a fiber break may even be superposed on the lower frequencies of a matrix crack. Fiber breaks may be present alone or they may occur during matrix fracture, in which case the waveforms will be superimposed on each other.

We conclude based on the experimental evidence and theoretical reasoning that we are observing fiber breaks. Based on reasoning about the energy involved in the source motion, we are likely observing (partial) fiber-bundle breaks. The energy in AE waveforms is discussed later after an energy calibration method is presented. The distribution of energy in the frequency spectrum, which is, of course, related to waveform shape, is required for unambiguous identification of fiber breakage.

Next, we discuss an interesting type of waveform that is observed only after fiber breakage has occurred, namely, an extremely narrowband waveform. This type of AE wave can be observed quite often in composite pressure vessel tests. The (center) frequency varies with different materials and geometries, but they typically look like the one shown in Fig. 5.

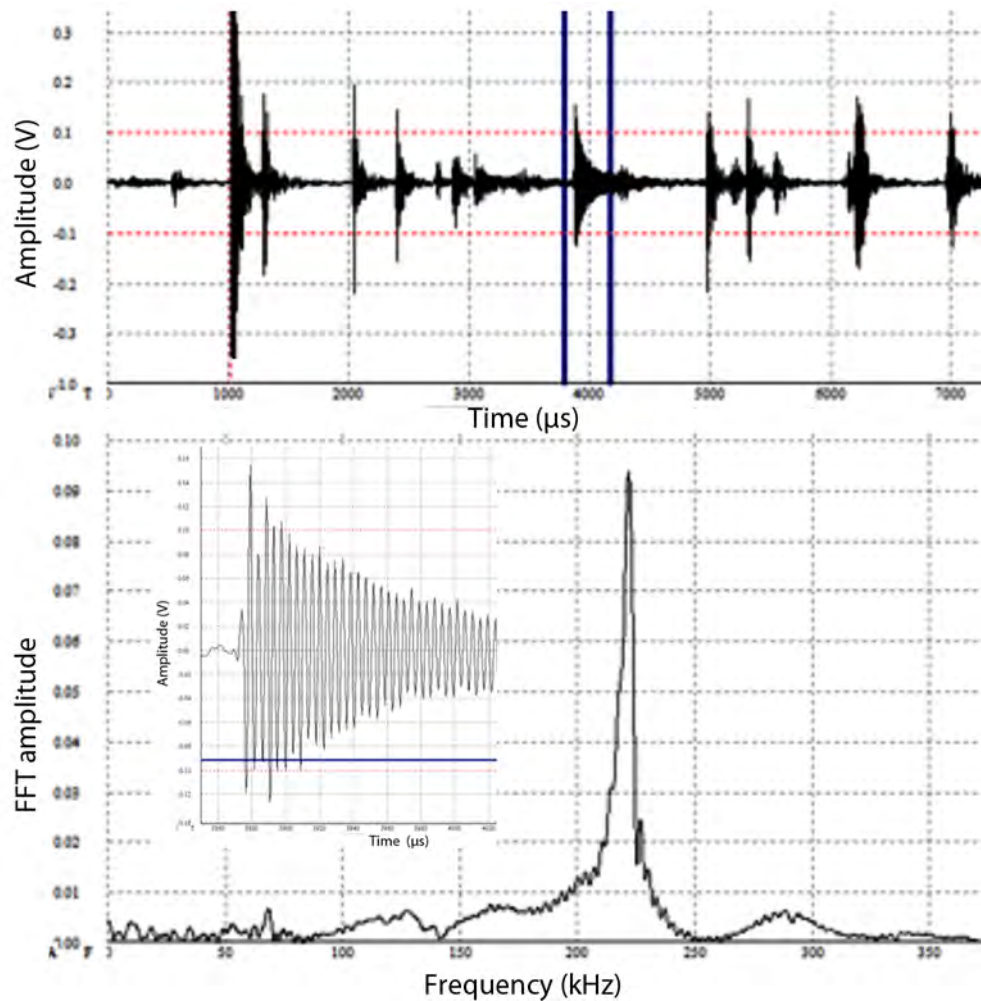


Fig. 5. The waveform and spectrum of a fiber-bundle vibration. The wave is between two vertical blue lines near 4000 μs on top figure and is shown expanded in the insert.

Thus, not all the sharp spikes are fiber breaks. Some are due to fiber vibration. These events can show up at just about any point in the pressurization after fiber (bundle) breaks have occurred arising as frictional events on pressurization and depressurization. They can accompany a fiber-break waveform as well.

4. Energy of AE Waves

The energy in an AE wave depends on the amount of motion at the source, i.e., the size of the disturbance to the wave propagation medium. Different fracture sources have larger and smaller motions (displacements) associated with them. For example, matrix splitting along the fiber direction in a unidirectional composite can be a large motion that creates high-energy waves. Individual fiber breaks do not involve significant motion and, therefore, according to work-energy considerations, should be relatively low energy events, especially below 80-90% of burst pressure. On the other hand, the motion of matrix cracks involves much greater volume of material, than a fiber break and would therefore be much more energetic. For example, matrix cracking along a fiber direction, sometimes called splitting, can be so energetic that it is audible.

Fiber-break waves have distinct features. Even when the wave appearance is similar to matrix fracture waves in time space, the difference is clear in the frequency domain. A fiber break

is a fast source, while a matrix crack evolves much more slowly due to greater than ten to one difference in their tensile moduli. The speed of the fiber break produces the high frequencies, much higher than a matrix crack event can produce. Frequencies higher than 2 MHz have been observed in proximity to a fiber break [12]. However, these very high frequencies are attenuated rapidly as the wave propagates. Practically speaking, the observation of frequencies above 300 kHz, combined with certain other characteristics of the frequency spectrum, is enough to confirm a fiber break. It should also be noted that it is fiber-bundle breaks that are usually detected in structural testing and not the breaking of individual fibers. The energies of individual fiber breaks are very small, about 30 nJ for a glass fiber, for example.

4.1 Scaling Fiber Break Energy

The wave energy is computed by the formula

$$U = \int V^2 dt / Z ,$$

which is the formula for computing energy in the AE signal, where V is the signal amplitude in V and Z is the input impedance at the preamplifier.



Fig. 6. Rolling ball impact calibration setup.

A rolling ball impactor was used to create an acoustical impulse in an aluminum plate. The measured energy in the wave was then used to scale the fiber-break energy. See Fig. 6. The impact setup uses a steel ball 12.7 mm (1/2") in diameter, made of chrome alloy steel hardened to Rc 63, precision ground and lapped to a surface finish of 38 nm, within 2.5 μm of diametral accuracy and sphericity within 0.63 μm. The plate of 7075-T6 aluminum was 1220 x 1830 x 3.2 mm size and simply supported by steel blocks. The inclined plane was aluminum with a machined square groove 9.5-mm wide, which supported the ball and guided it to the impact point. The top surface of the inclined plane was positioned next to the edge of the plate and stationed below the lower edge of the plate such that the ball impacted with equal parts of the ball projecting above and below the mid-plane of the plate. A mechanical release mechanism was used to release the ball down the plane. The ball roll length was 305 mm and the inclined plane angle was six degrees. The impact produced an impulse that propagated to sensors coupled to the surface of the plate 305 mm away from the edge. The sensors were coupled to the plate with vacuum

grease. The energy of the leading edge of the impulse, known as the wave front, was measured. The vertical position of the ball impact point was adjusted gradually in order to “peak up” the acoustical signal, much as is done in ultrasonic testing where the angle is varied slightly to maximize the response. The center frequency of the first cycle of the E wave was confirmed as 125 ± 10 kHz. See Fig. 7. The energy value in J of the first half cycle of the E wave was used to scale the fiber-break energy, as illustrated later in this work. This provided an “end to end” calibration meaning that the energy was measured using the complete AE instrumentation (sensor, cables, preamplifiers, amplifiers, filters and digitizer) that was used in actual test situations.

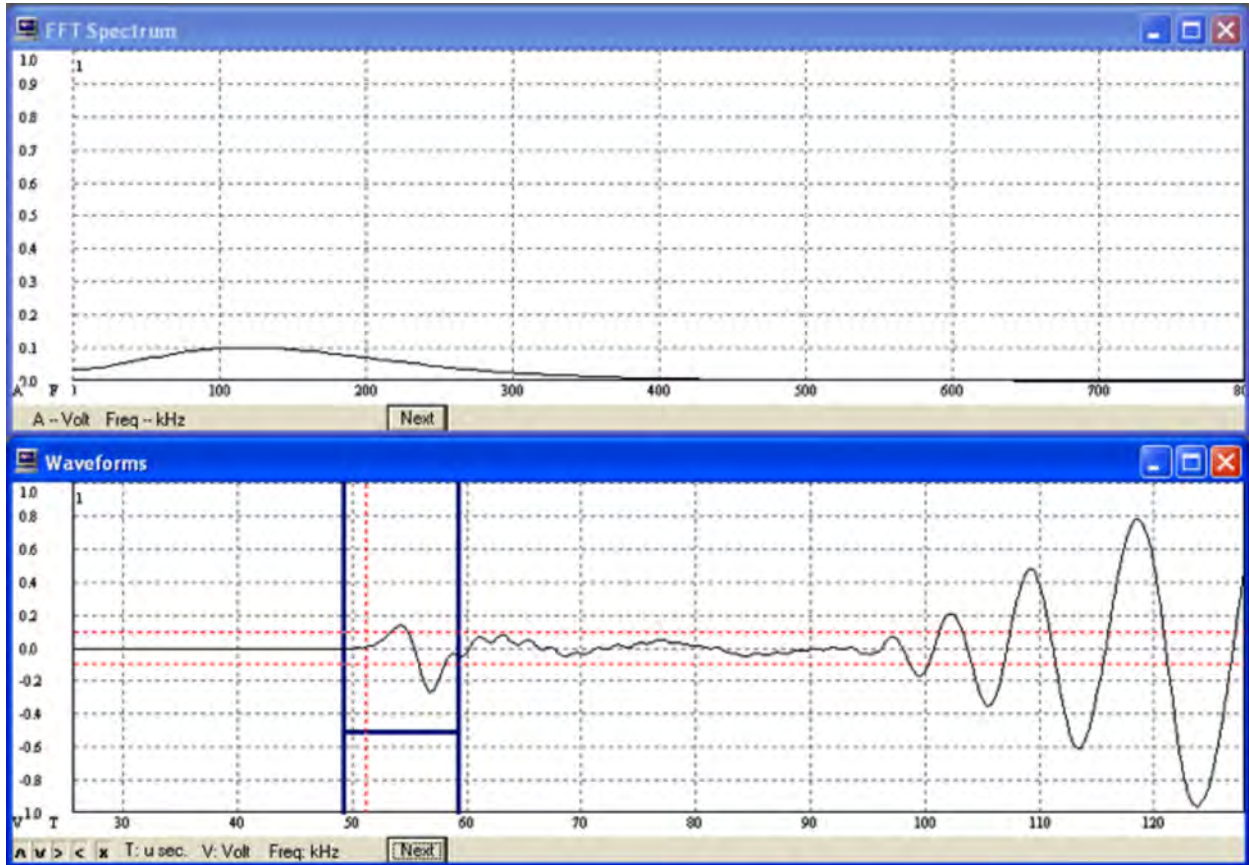


Fig. 7. Front end of waveform created by rolling ball impact calibration setup. FFT shows center frequency of first cycle (between two blue lines) is approximately 125 kHz.

The energy linearity of the complete AE instrumentation (sensor, cables, preamplifiers, amplifiers, filters and digitizer) was measured by using different roll lengths of 203, 305 and 406 mm. The start of the E wave was taken from the first cycle of the waveform recognizable as the front end of the E wave to the end of the E wave which was taken as $10 \mu\text{s}$ later. (The time was calculated from the dispersion curves for the specified aluminum plate.) A linear regression was applied to the energy data and a goodness of fit $R^2 > 0.9$ was obtained.

4.2 Fiber-bundle Breakage Energy Calculations and Accept/Reject Criteria

Now that scaling AE waveform energy has been covered, we can show how it is used to develop accept/reject criteria for pressure vessels. In order to determine if fiber-bundle breakage has occurred during the filling operation, the frequency spectra of the direct E and F waves are examined and the energies in certain frequency ranges are computed as given below.

Definitions

Energies (U) in the ranges are defined as

50 – 400 kHz:	U_0
100 – 200 kHz:	U_1
250 – 400 kHz:	U_2

The criteria for determining if high frequency spectrum events have occurred are given by the following formulas:

$$\begin{aligned} U_0 / (U_{FBB}) &\geq 10\% \\ U_2 / (U_1 + U_2) &\geq 15\% \\ U_2 / U_0 &\geq 10\% \end{aligned}$$

The percentages given are conservative and may mark some matrix fracture waveforms but not miss any fiber fracture waveforms. They can be adjusted if needed to accommodate a less conservative criterion for the detection of damage growth. U_{FBB} is the energy of a fiber-bundle break calculated using the average breaking strength found in the literature, either from the manufacturer's data or independent test data. The formula used for calculating average fiber break energy is

$$U_{FB} = \frac{E\varepsilon^2}{2} Al$$

where ε is the strain to failure of the fiber, E the Young's modulus of the fiber, A is area of the fiber and l is the ineffective fiber length for the fiber and matrix combination. If the ineffective length is not readily available, four (4) times the fiber diameter is conservative. We take $U_{FBB} = 100 \times U_{FB}$, where U_{FB} has been calculated and scaled by the rolling ball impact energy as in the examples below. If these criteria are met, fiber-bundle break damage has occurred during the test and the vessel should be removed from service. Common fiber-bundle sizes are 1000 and 3000 fibers per tow so 100 fibers represents a partial bundle break.

Example of Fiber Break Energy Calculation

Suppose $d = 7 \mu\text{m}$, $E = 69.6 \text{ GPa}$ and $\varepsilon = 0.01$ (average breaking strain) for some type of glass fiber. Using $A = \pi d^2/4$ and $l = 4d$, $U_{FB} = 30 \text{ nJ}$. Note that this is just an example for one composite material. The values used to calculate fiber-break energy need to be appropriate for the material being tested.

Example of Scaling Calculation

Suppose that the rolling ball impact (RBI) acoustical energy measured by a particular high fidelity AE transducer is $U_{RBI}^{AE} = 0.5 \text{ nJ}$ and the impact energy $U_{RBI} = 1.9 \text{ mJ}$ (due to gravity). Fiber break energy of a glass fiber $U_{FB} = 30 \text{ nJ}$ would correspond to a wave energy

$$\begin{aligned} U_{FB}^{AE} &= U_{FB} \times U_{RBI}^{AE} / U_{RBI} \\ &= 30 \text{ nJ} \times 0.5 \text{ nJ} / 1.9 \text{ mJ} = 7.9 \text{ fJ} \end{aligned}$$

This is the number used to calculate the value of U_{FBB} and is used as the fiber-break energy in the acceptance criterion above and the energy acceptance criterion illustrated below in Section 5.

Amplifier Gain Correction

All energies are corrected for gain. (20 dB amplifier gain increases apparent energy 100 times and 40 dB gain 10,000 times.)

Typically, the failure of a high-pressure composite vessel is fiber dominated but delamination also can be measured by modal AE techniques. The analysis methods are based on identifying the delamination events by the wave characteristics [13].

5. Frictional Acoustic Emission (FRAE)

Friction between fracture surfaces plays an important role in understanding AE in fatigue testing. It is an indicator of the presence of damage because it is produced by the frictional rubbing between existing and newly created fracture surfaces. Even the presence of fiber-bundle

breakage can be detected by examining the waveforms produced by frictional emission. Increasing FRAE intensity throughout a pressure cycle means more and more damage has occurred.

FRAE is also useful for detecting stress concentrations. For normal vessel behavior, FRAE is distributed fairly equally, channel by channel, over the entire vessel. An active channel points to a stress concentration near that sensor.

FRAE commonly consists of three types of waveforms, 1) broadband (both high and low frequencies in both the E and F waves), 2) low frequency rumbling (mainly F wave) and 3) narrowband waves. The narrowband waves have been observed in pressure vessel testing going back some years and are of particular significance. The tips of fiber bundles protrude into the void at a break and the bundle acts like a small, cantilevered beam. The fundamental vibration mode, and sometimes a couple of higher order modes, can be observed in the frequency spectrum. Experimental studies carried out on bundles and partial bundles at the edge of composite coupons and theoretical calculations of the beam frequencies corresponded well with fiber-bundle sizes and lengths measured. These results will be presented elsewhere, but see Fig. 5 for a characteristic waveform and singular spectrum appearance. These vibrations are often observed just after a fiber-bundle break event. They also are observed during depressurization as fracture surfaces recombine and sometimes are even detected on pressurization as fracture surfaces separate and activate the vibration.

The broad bandwidth FRAE waves are due to rubbing between fracture surface flanks. The asperities on the crack flanks often grab, stick and then give way rapidly which results in a broadband signal that can sometimes contain very high frequencies, though not as high as in the fiber break waveforms discussed previously. Sometimes the fracture surface rubbing excites waves of only low frequencies that have their own unique appearance. Usually, all three types of FRAE are excited during depressurization when all the fracture surfaces try to rejoin and fiber bundles are stimulated into vibration as the plastically deformed areas no longer fit precisely together, creating mechanical forces within the material.

It should be noted that a certain amount of FRAE is normal on every cycle both on loading and unloading. Large deviations in the intensity (numbers of waveforms and their energies) of frictional events from the average expected indicate that new damage has occurred. It should be noted that a certain amount of FRAE is normal on every pressure cycle, both on loading and unloading. Copious and energetic FRAE indicates the presence of extensive damage.

5.1 Acoustic Emission Allowance Factor, F

Friction between fracture surfaces plays an important role in understanding AE in fatigue testing. It is an indicator of the presence of damage because the frictional rubbing between existing and newly created fracture surfaces produced it. As noted above, even the presence of fiber-bundle breakage can be detected by examining the waveforms produced by FRAE. Increasing FRAE intensity throughout a pressure cycle means more and more damage has occurred. Therefore, for a vessel to pass, no AE event should have energy greater than $(F) \times U_{FB}$ at any time during the test. We call F the *acoustic emission allowance factor*. The smaller the allowance factor, the more conservative the test. For example, an $F = 10^4$ is the equivalent of more than three fiber tows, each tow consisting of 3,000 fibers, breaking simultaneously. This should be a conservative figure in most cases for vessels containing hydrogen, air, and other gases, such as natural gas.

6. Background Energy Oscillation

Damage decreases the ability of the composite material to redistribute load effectively. Composite materials work by redistributing load from broken, weaker fibers to stronger neighboring fibers that can carry the load. While this process is occurring the material is locally straining and producing scores of small tremors. If these small tremors continue, strong emissions will eventually follow because the composite is unable to handle the load as normally expected. The small tremors are numerous and form an almost continuous signal that is observed as an increase in the *background energy*. We define background energy as the minimum of the average energy over a preset length of time in the waveform window. The moving average of the energy data is plotted against time, along with the pressure. The number of points in the average depends on the type of vessel and test.

As a composite pressure vessel progresses towards failure under increasing pressure, an interesting effect appears. As a vessel is loaded to higher pressure, the background energy begins to oscillate. In a monotonic loading to burst it seems to indicate the precise point in the cumulative events curve, at which significant damage begins to occur. Background energy oscillation appears to be associated with the onset of significant fiber breakage, which primarily dictates composite (pressure vessel) failure.

The data in Figs. 8a and b are for two fiberglass-overwrapped vessels that burst at 114.6 and 102.9 MPa (16683 and 14972 psi) or about 11.7 MPa (1700 psi) apart. The oscillations began at 62.4 and 51.9 MPa (9082 and 7551 psi), respectively. A 50- μ s window was stepped through each waveform window recorded during the test and the energy was computed. Then, the minimum was found. The energy in the pre-trigger portion of the waveform window is a good way to observe the fluctuations in the background energy, and the pre-trigger energy (PTE) also shows the background energy oscillation effect. A 30-point moving average of the energy minima is plotted in the right figures of Figs. 8a and b. See three more examples in Figs. 9a-c. The data in Figs. 9a, b, and c, are for carbon-fiber overwrapped pressure vessels. The background energy oscillation points are 60.7, 69.9, and 77.3 MPa (8837, 10180, and 11264 psi), respectively. Oscillation of background energy is observed at much lower pressures than burst pressure if a vessel is weak and starting to fail prematurely. Background energy can be used as an accept/reject criterion

Background energy at high pressure is compared to the quiescent background energy. The quiescent background energy can be determined by doing a pencil-lead break on the vessel at steady, low (preferably zero) pressure prior to commencing the pressurization (or filling operation for, say, hydrogen vessels) and calculating the energy of the pre-trigger portion of the waveform window in the usual manner (integral of voltage squared over time). At the start of a test, the (quiescent) background energy is usually measured before load is applied. In a good vessel, background energy may increase by a factor of ten or more on pressurization to proof pressure, and then it decreases significantly during a load hold because the driving force of pressure increase is halted. If the vessel is depressurized at this point, the background energy will return to quiescent levels. This behavior is shown in Fig. 10 for a CFRP vessel, which performed normally to design pressure. Note that background energy rises during pressurization, but falls during both pressure holds. If the vessel is weak, the background energy will rise by a factor of 40 or more from the quiescent level and if the vessel is very weak and progressing to failure the background energy will begin to oscillate. This behavior is shown in Fig. 11, which is a CFRP vessel of the identical design to the vessel in Fig. 10, but which failed prematurely. Note that the

magnitude of the rise was higher in this composite material than typically found in vessels like CNG and SCBA vessels. Typical rise in a good vessel was around four times, while in poor vessels, it was about ten.

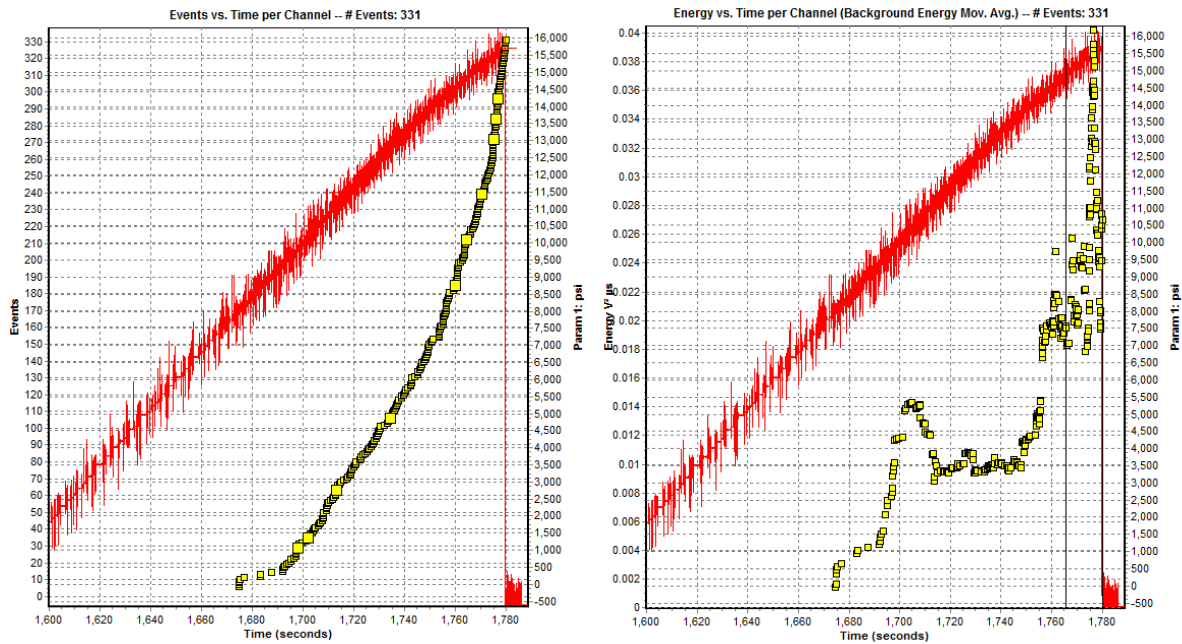


Fig. 8a. Fiberglass-overwrapped vessel (FRP5914) that burst at 114.6 MPa (16683 psi). Left figure shows events and pressure vs. time. Right, Background energy vs. time.

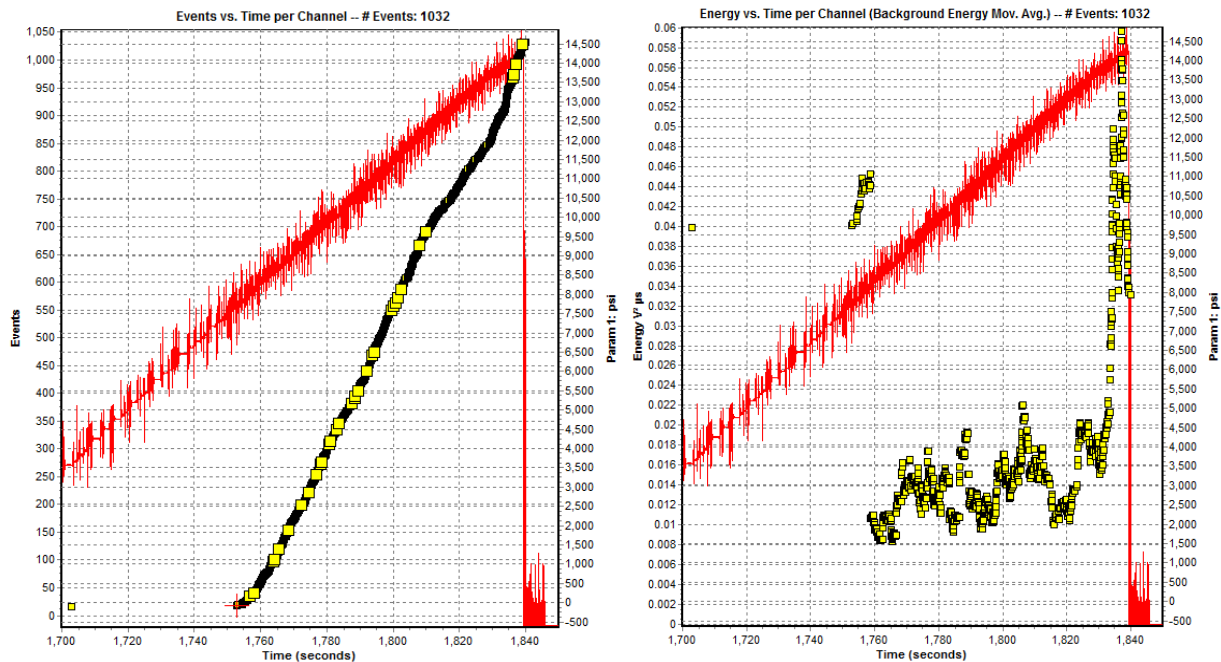


Fig. 8b. As above for vessel FRP9050: 102.9 MPa (14972 psi) burst.

The background energy drops during the load hold, as it should, although the large increase in background energy before the first hold is significant and indicates that the vessel is weak from the start. As the pressure is increased the background energy begins to oscillate as the weakness in the vessel is exhibited as the load is redistributed. As the pressure rises, the oscillation of the background energy indicates that the vessel is struggling with the increased load. In all vessels studied, the background energy begins to oscillate as burst pressure is approached.

Background energy appears to give some warning time that a vessel is progressing to failure, so it may also find use in stress rupture monitoring.

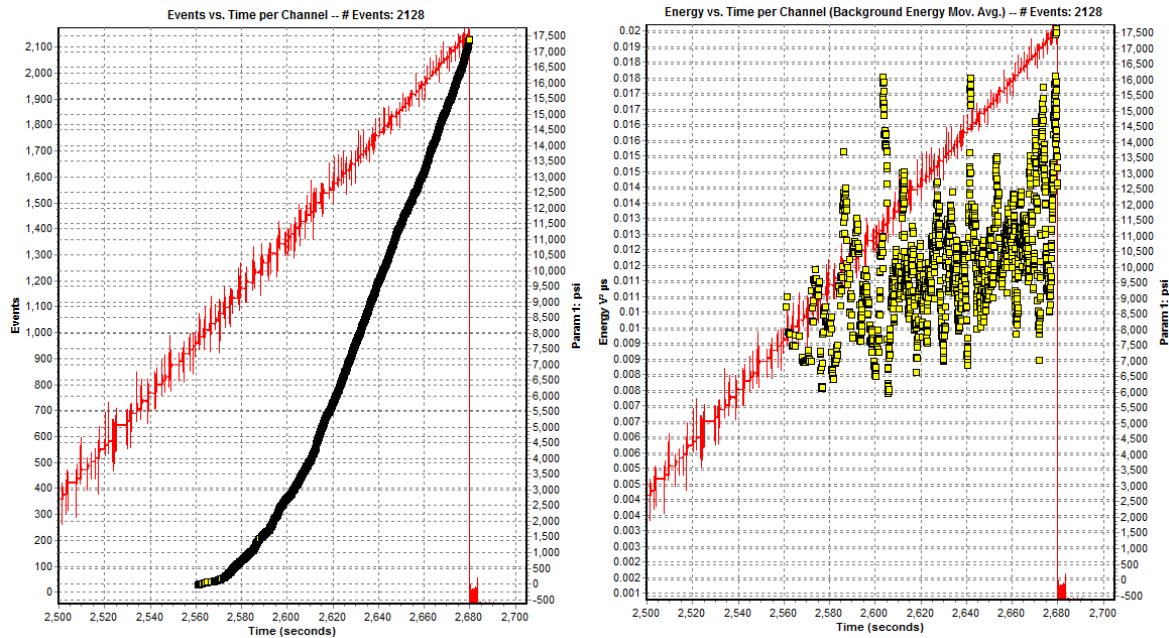


Fig. 9a. Carbon-fiber overwrapped vessel (CFRP 138059) that burst at 125.9 MPa (18,333 psi). Left figure shows events and pressure vs. time. Right, Background energy vs. time.

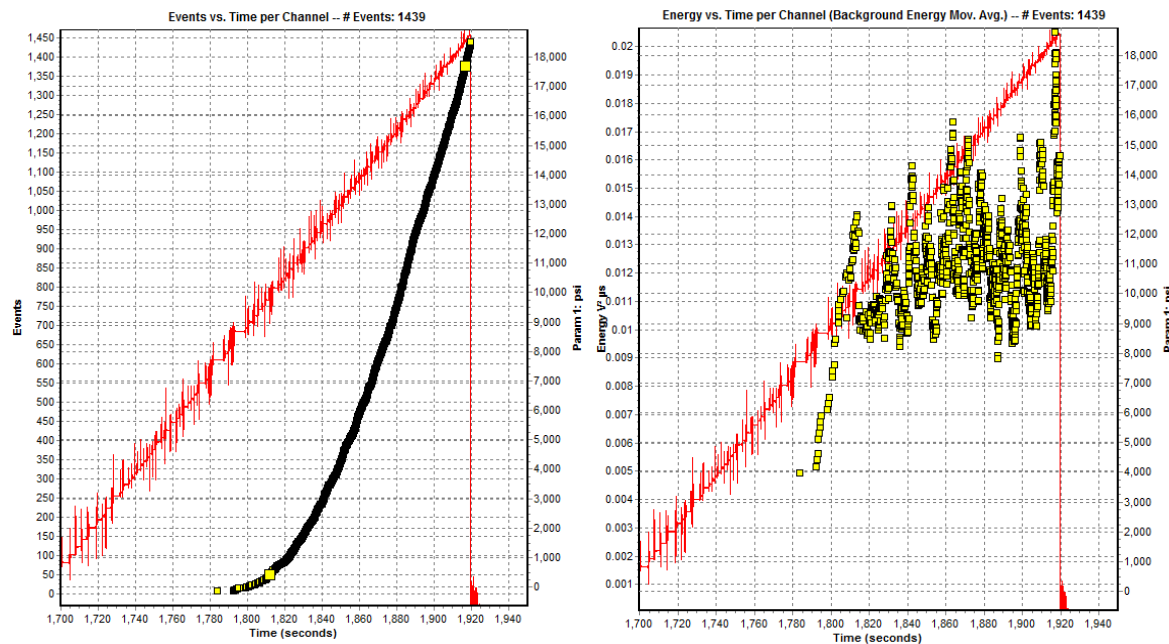


Fig. 9b. As above for vessel CFRP130029: 130.1 MPa (19,952 psi) burst.

During a test, if the background at one sensor is high compared to quiescent background energy, it indicates that that section of the vessel has difficulty handling the load. Matrix and fiber failures occur within that section as load transfer progresses over a surrounding region of the material. Load transfer continues until a strong region is encountered and the progression of the damage stops. However, if the load is increased further, the scenario may repeat and failure may soon result. There seems to be a peak in the background energy oscillation. As the load is increased beyond a certain point, the background energy oscillation begins to diminish in magni-

tude. This occurs just before burst. As the vessel comes apart the background energy may increase dramatically once again. Before this point, when the oscillations diminish slightly, there appears to be enough time to halt the test. At the point when the first oscillations begin, the load is generally about 75% of burst pressure. This effect has been observed in both fiberglass and carbon fiber vessels with various different matrix materials.

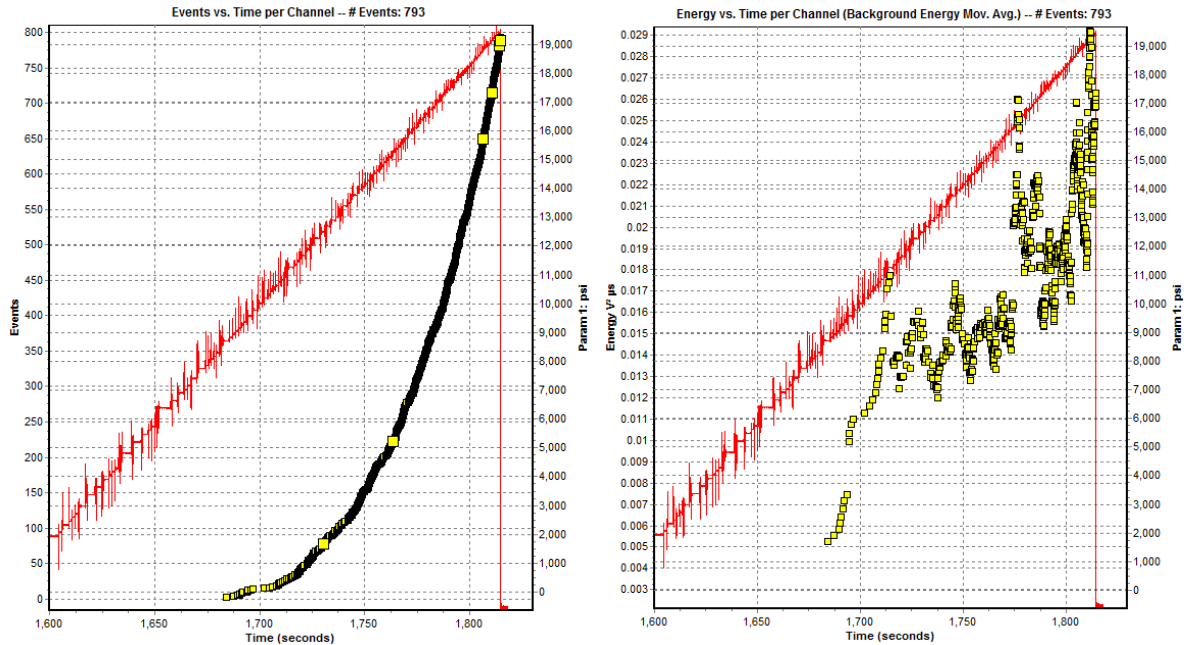


Fig. 9c. As above for vessel CFRP139536: 137.8 MPa (20,075 psi) burst.

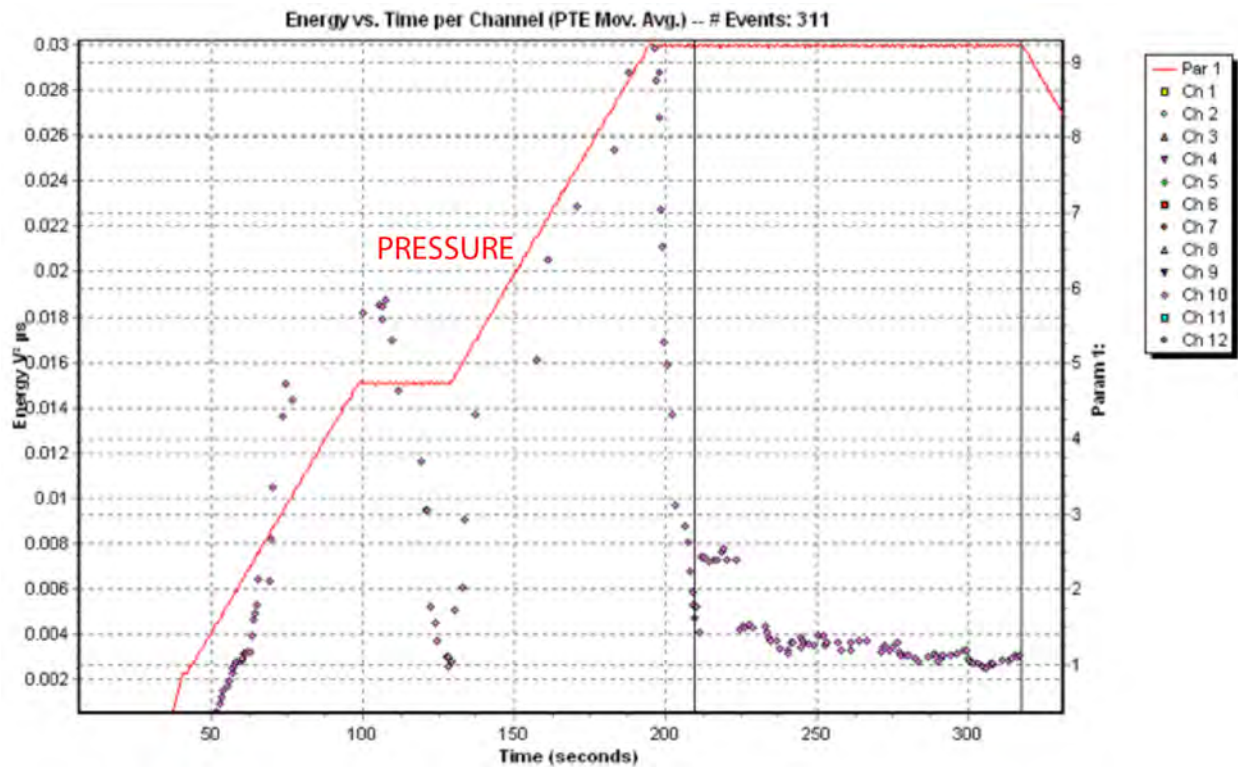


Fig. 10. Background energy and pressure vs. time for a CFRP vessel that held the design pressure. Note that the maximum energy level was below 0.03 V²-μs.

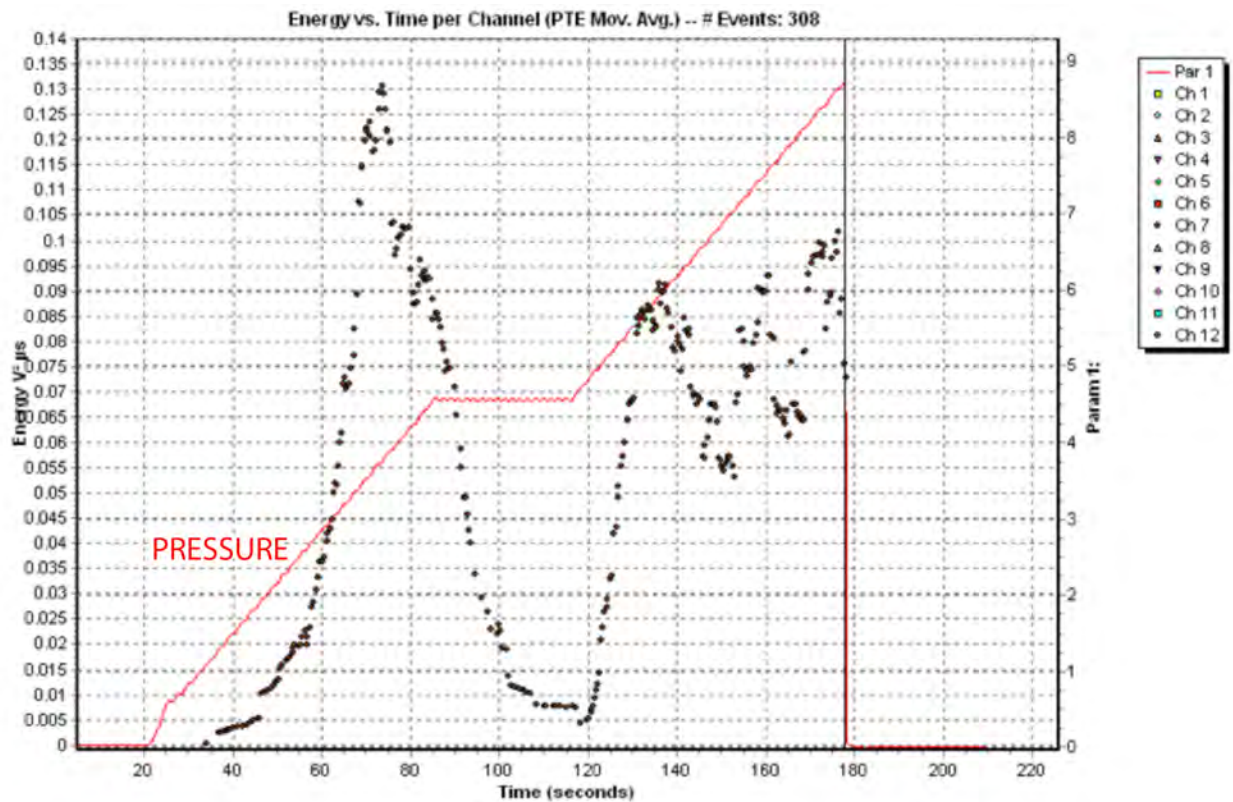


Fig. 11. The background energy vs. time for channel 7 for a CFRP vessel that burst below design pressure. The peak background energy value ($0.13 \text{ V}^2\text{-}\mu\text{s}$) was $>4x$ that of good vessel. The observation of a steep rise in background energy is a definite warning of vessel weakness.

Pre-trigger energy (PTE) is a good practical indicator of background energy as shown in Figs. 12b-g. Figure 12a shows changes in cumulative events for different channels and pressure. Marks of #1 to #6 indicate the pressure levels that correspond to the waveform windows in Fig. 12b-g. At the beginning of a test (Fig. 12- Mark1), the PTE is essentially zero and signal before the trigger (broken vertical red lines in Fig. 12) shows a flat line. Pre-trigger energy or PTE increases early in the pressurization when a weak vessel is pressurized as shown in Fig. 11. In Fig. 12-1, the tenth event in this test is shown. This was the first pressurization of this vessel. The background energy must be followed for each sensor. In this case $\text{PTE} = 0.003 \text{ V}^2\text{-}\mu\text{s}$ for channel 7. Channel 7 is the uppermost cumulative event curve containing the large circle in Fig. 12a. The succeeding figures (Figs. 12b to g) give examples for PTE at increasing pressure level in a weak vessel. Figure 12-c shows the waveforms for the 63rd event. The pressure is still very low, but the (channel 7) $\text{PTE} = 0.034 \text{ V}^2\text{-}\mu\text{s}$. The vessel shows weakness early on. Figure 12-d shows the waveforms for the 120th event. A pressure hold is about to occur. Background energy (channel 7) $\text{PTE} = 0.0959 \text{ V}^2\text{-}\mu\text{s}$. In Fig. 11-e, an event that occurred during a pressure hold is shown and the background energy is once again low; $\text{PTE} = 0.0029 \text{ V}^2\text{-}\mu\text{s}$ (channel 7). The small tremors have vanished for the moment. Figure 11-f shows event #235, which occurred just after the pressure hold as the pressure began to increase once again. The small tremors begin again and background energy or $\text{PTE} = 0.0817 \text{ V}^2\text{-}\mu\text{s}$ (channel 7). PTE continues to increase, on average, until burst is imminent. The average is important. The number of small tremors varies, of course, as the load is redistributed due to material variations. At higher pressures, PTE reaches a saturation value of about $0.2 \text{ V}^2\text{-}\mu\text{s}$ (channel 7).

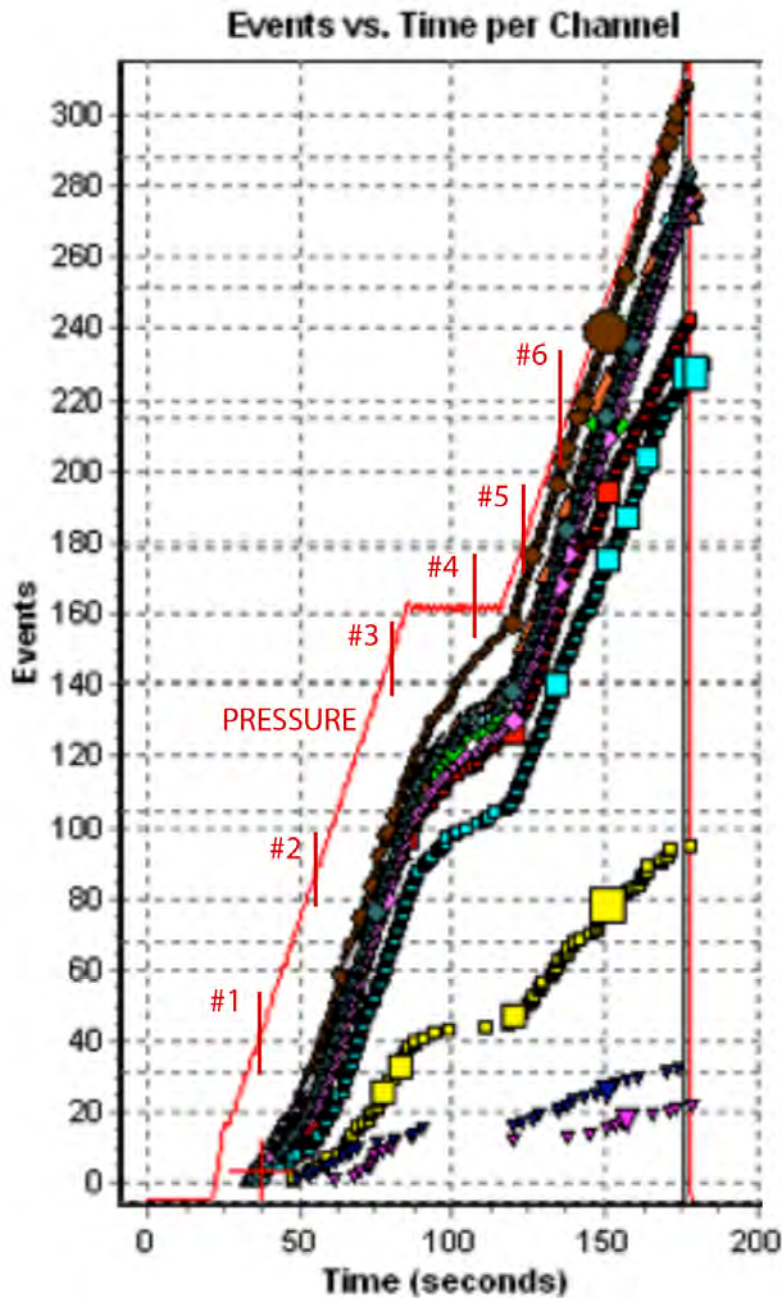


Fig. 12a. Pressure and cumulative events vs. time for a vessel that failed below design pressure. Marks of #1 to #6 give the pressure levels when six events in Fig. 11 were recorded.

Here is another example of background energy behavior on an FRP vessel that was hoop-wrapped over a steel liner (G1091, June 18, 2009), as opposed to the fully-wrapped vessels above in Figs. 8-12. Cumulative events and pressure versus time are plotted in Fig. 13a for one of the channels on the FRP vessel. The data are for the burst run; i.e., pressure was raised till burst as indicated. Note that the event energy (given as the size of triangles on the cumulative event plot) gradually diminishes. Corresponding plot of background energy is shown in Fig. 13b. We see that the background energy oscillation begins at about 75% percent of the burst pressure.

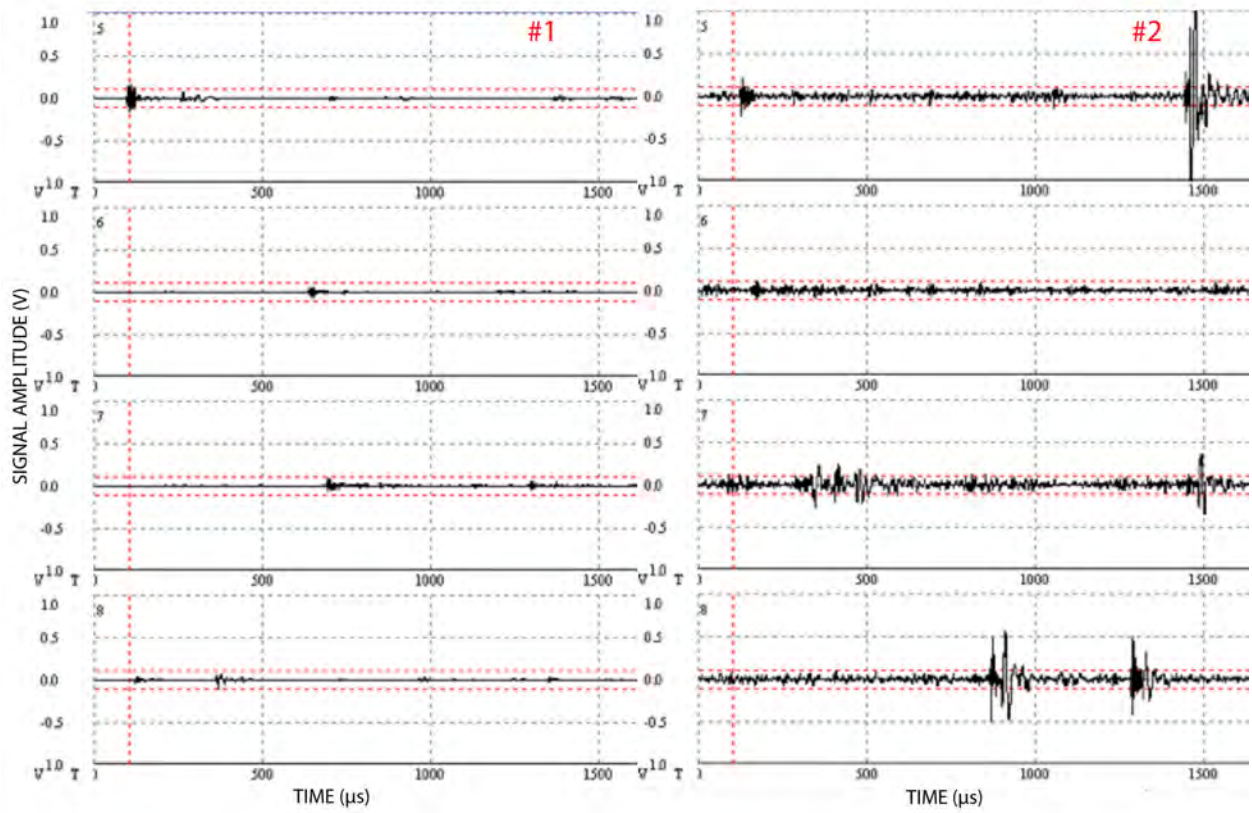


Fig. 12b, c. Waveforms for channels 5, 6, 7, and 8 showing voltage vs time. Pre-trigger line is the vertical dotted line at $\sim 100 \mu\text{s}$. #1: 10th event, #2: 63rd event,

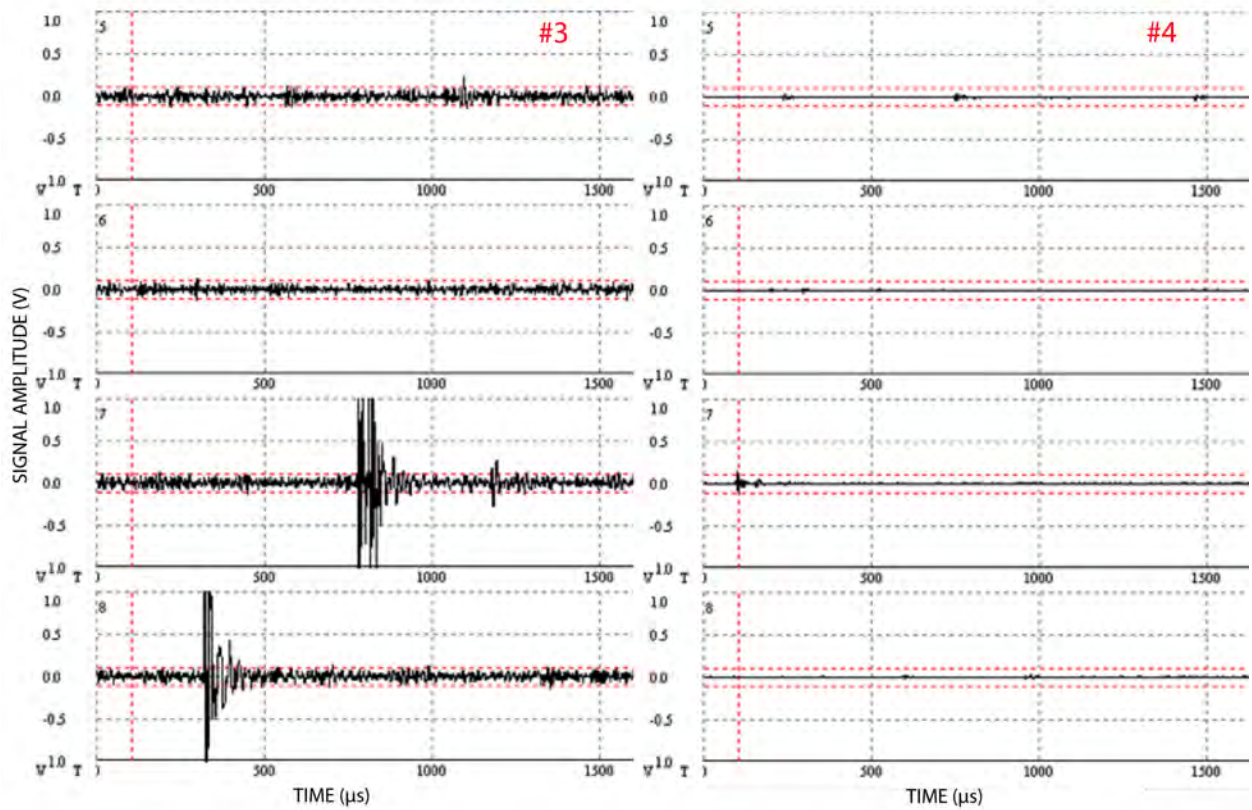


Fig. 12d, e. As above. #3: 120th event, #4: 191st event during pressure hold.

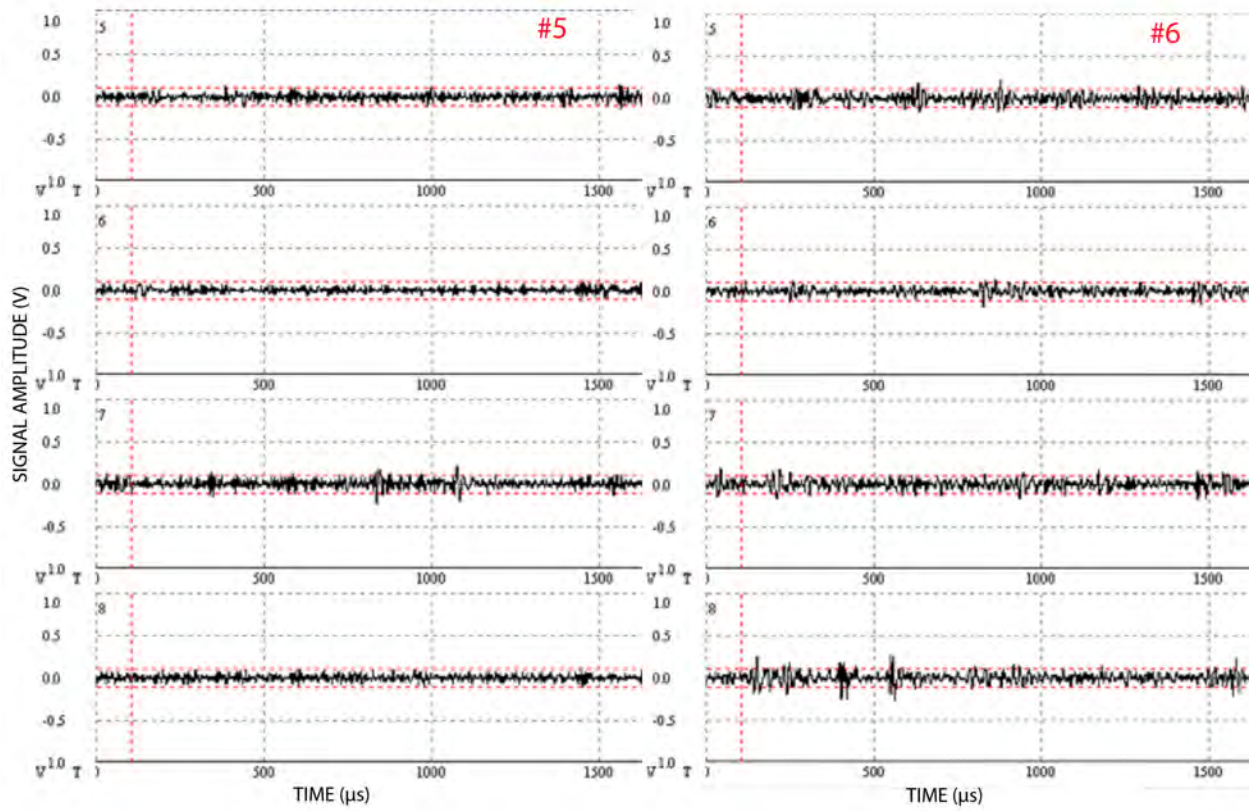


Fig. 12f, g. As above. #5: 235th event, #6: 263rd event.

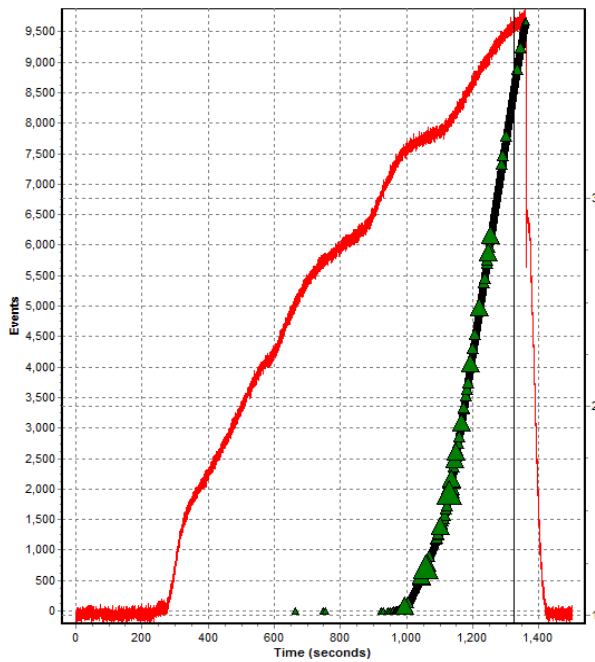


Fig. 13a. Cumulative events and pressure vs. time for a burst test of a hoop-wrapped fiberglass pressure vessel with a steel load-sharing liner.

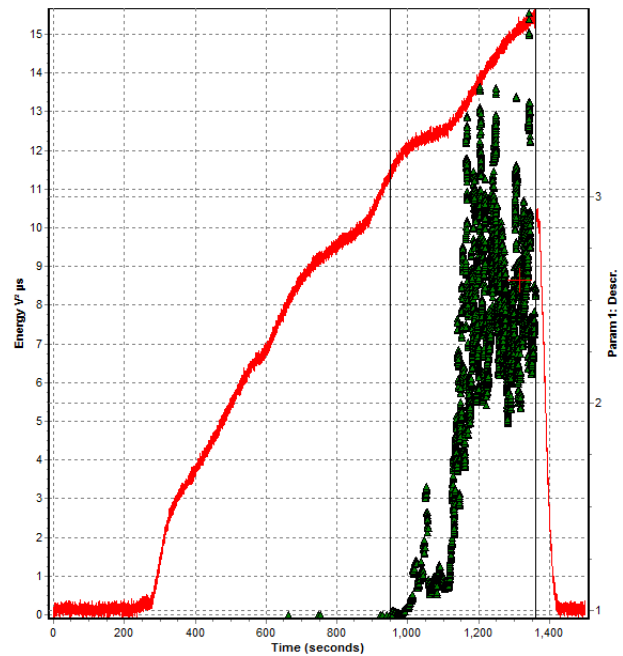


Fig. 13b. Background energy oscillation effect during the pressurization to burst. Fig. 13a at left shows the cumulative event curve.

6.1 Background Energy Accept/Reject Criteria

In the in-service code (ASME/NBIC), which was written for high-pressure vessels that are in-service, the background energy of any channel should not exceed 10 times the quiescent background energy of that channel. During a load hold, background energy should reduce to quiescent levels. Any oscillation in background energy during a load hold shows that the vessel is struggling to handle the pressure. Pressure should be reduced immediately and the vessel removed from service. For vessels that have been cycled many times, there should be almost no change in the background energy at loads up to operating pressures and no oscillation whatsoever. Any oscillation in background energy means that the vessel is weak and the pressure should be reduced immediately.

7. Cumulative Events Analysis

Acoustic emissions are generally copious in number on the first loading of a new vessel. It is well known that thousands of matrix micro-cracks develop in composite vessels during the initial pressurization as the composite material adjusts to the load. This is in fact beneficial, much as shakedown testing of a metal vessel is beneficial to the metal vessel.

It is proposed here that the shape of the cumulative events curve is more informative about the integrity of the vessel than the absolute number of events. This conjecture is guided by reasoning from weakest link fiber strength theories and shear lag models of composite behavior, and it has been borne out in experimental testing. Weakest link theories are progressive failure models and shed a lot of light on why AE events accumulate as they do with increasing pressure. They also suggest that not all AE events are deleterious to vessel strength and why simple counting, although important, may not always be as reliable an indicator of vessel condition as desired.

High-pressure composite vessel failure is fiber dominated. Weakest link theory maintains that fibers can be considered as a chain of links. When the tension reaches the strength of the weakest link, the fiber breaks. If the fiber is bonded in a matrix, the matrix transfers the stress through shear to the neighboring parts of the fiber. Also, neighboring fibers experience a stress concentration since the stress is higher near the break. The stress reduces to the imposed stress at a distance called the ineffective fiber length. When the tension is increased the next weakest link breaks. The weak links are randomly distributed due to the manufacturing process. This is analogous to Griffith's theory of flaws in glass fibers, which, in turn, led to Fracture Mechanics, which has proven very successful in understanding material failure. In fact many codes and standards are based on it.

Fibers in a tow are considered a bundle of chains. When the tension is increased the next weakest link breaks. This could be a link in the same fiber or it could be a link in a neighboring fiber. The stress concentration at a break could force a link in a neighboring fiber to break. The stress concentration compounds on neighboring fibers and they may break further compounding the stress concentration. At a certain point, this process continues and the composite proceeds rapidly to failure. The work of the weakest link mathematicians is to model this process and predict composite failure. The models work well for small samples but there is a volume effect in large composite structures that is difficult to model. Nevertheless, the significant variation in burst pressures of identical vessels lends support to the weakest link theory. Typically, many weak links fail throughout a composite structure before a stress concentration becomes large enough to initiate general failure. Many studies have shown that the majority of fibers do not

begin to fail until the stress reaches approximately 80 - 90% of ultimate stress, i.e., burst pressure.

Similarly to cracks being blunted in a metal pressure vessel that sustains a given pressure, the composite material rapidly adapts to the stress concentrations due to all the fiber breaks (and matrix fractures) by redistributing the stresses to stronger sections. Unlike with steel where the crack blunting occurs nearly instantaneously (there is no known creep behavior in steel at room temperature), in composites there is time dependent behavior. The point of AE monitoring is to verify that stable redistribution is taking place. This is why counting AE events and observing the shape of the cumulative events vs. time curve during load hold demonstrates the stability of a composite and is a very important technique. A vessel that passes this test will behave as expected.

Some composites stabilize rapidly and other more slowly. The shear lag driven stress redistribution does not take place instantaneously but takes some time as the matrix creeps in the vicinity of a stress concentration. The time dependence of the load transfer is reflected in the shape of the cumulative events vs. time curve. A stable vessel will exhibit a cumulative curve with exponentially decaying curvature.

A model that works well is an exponential equation of the form

$$y = A \exp(B t) + C,$$

where B defines the shape of the cumulative event curve and, for a stable vessel, B must be negative. Some values of B for comparison are

B = -0.02 is for rapid stabilization (~1 min.)

B = -0.00001 is for slow stabilization (~ 166 min.)

B = -0.0017 – 0.006 is for moderate stabilization (~5 min. to 30 min.)

The HPC pressure vessels all exhibit a fiber dominated failure mode, and follow the exponential characteristics. The numbers also agree with stress relaxation studies [14]. The shape of the cumulative events curve is similar for HPC pressure vessels made of glass, Kevlar and carbon fiber. The cumulative energy of the AE impulses vs. time and pressure should also decay exponentially. The same equation can be used to fit the curve and once again the exponent must be negative and be within a certain range of values.

A 3 to 6 meters long vessel is large. Each section on a large pressure vessel essentially behaves like an independent specimen in the sense that fibers failing at one end do not create a stress concentration at the other end. The cumulative events and energy curves must be plotted for each channel and events must be sorted by first arrival to verify the stability of that section of the vessel.

If engineering failure analysis states that delamination detection is important, delamination can be measured by monitoring AE by identifying the delamination events by the wave characteristics specific to delamination type failure. Delamination waveforms in composite materials have been described in detail elsewhere [13].

A specific analysis procedure is given below so it is clear how the analysis of cumulative events and energy curves is carried out. Note that waveforms from matrix splits, matrix cracks, fiber breaks and frictional emission due to fracture surface fretting are all included. These can be distinguished and separated out if desired, but this is not required for simple stability analysis. Wave analysis is used when plotting cumulative events vs. time mainly to distinguish signals

from noise and to verify or audit that the first arrival channel was determined by the computer program correctly. Typical steps to do composite stability analysis are:

1. Filter data to eliminate any external noise such as EMI, mechanical rubbing, and flow noise. EMI is characterized by a lack of any mechanical wave propagation characteristics, particularly a lack of dispersion being apparent. EMI can be further identified by coincidental arrivals on more than one channel. The two criteria should be considered together to ensure it is not simply an event that happened to be centered between the sensors. The appearance of the modes, or mode shape, is determined by the material, thickness and propagation distance and will be obvious when observed during test setup. Mechanical rubbing frequencies are usually very low frequency and can be determined by experiment. Flow noise is characterized by waves that fill the waveform window. It can be filtered out by setting a pre-trigger/post-trigger energy ratio.
2. Use only events that have clean front ends and in which first arrival channel can be determined. Clean means a pre-trigger energy of less than $0.01 \text{ V}^2\text{-}\mu\text{s}$, which is computed by the integral of the voltage squared over time for the pre-trigger portion of the waveform window.
3. Plot X versus t on the filtered data, where X = first arrival cumulative events and energy. Plots should always show the pressure data.
4. Identify pressure hold times.
5. Extract data from cumulative events-time plots just for pressure hold times. Apply exponential fits by channel for pressure hold and display both data and fit. The values are determined by the fit to $y = A \exp(B t) + C$. The B value is the shape of the cumulative events curves. C is an intercept and A is a scale factor. B values for some composites range from -0.00001 to -0.1 . See notes on analysis below. A prototype vessel provides the initial B value, provided that it behaves as expected, i.e., the cumulative AE events and energy decay with time in the load hold and the vessel burst pressure is satisfactory.
6. B should be negative and R^2 at least 0.80. A positive B value indicates that the event frequency was not decreasing and the vessel is not normal.

Example of Cumulative Events Analysis

A typical cumulative events vs. time and pressure curve is shown in Fig. 14a. Four sensors were used in this test. Hold pressure was 124 MPa, which was 1.8 times operating pressure. The vertical lines mark the pressure hold region (320-570 s). This is the behavior of a good vessel. The cumulative events plot exhibits a strong negative exponential curvature with time during pressure hold. Each point represents an event and the four waveforms recorded for the event. Channel 1 is chosen and the

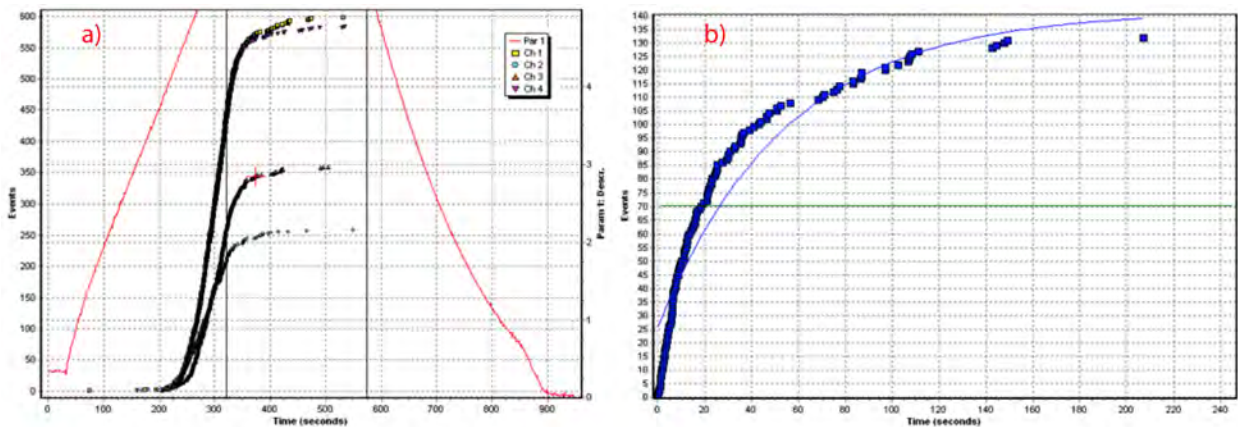


Fig. 14 a) Cumulative events and pressure vs. time. b) Exponential fitting of the cumulative events vs. time for channel 1 during pressure hold period.

result of an exponential fit is shown in Fig. 14b. Exponent B is -0.01827 and goodness of fit is $R^2 = 0.91$. Exponents are similar for similar vessels and fall within a range. The observed exponent shows that this vessel stabilizes rapidly.

A typical result of the first (virgin) loading of a fiberglass-overwrapped steel liner vessel in Fig. 15 shows that the cumulative events curve stability test can be performed during autofretting. When this same analysis is done on event energy, a result similar to Historic Index [15] is produced.

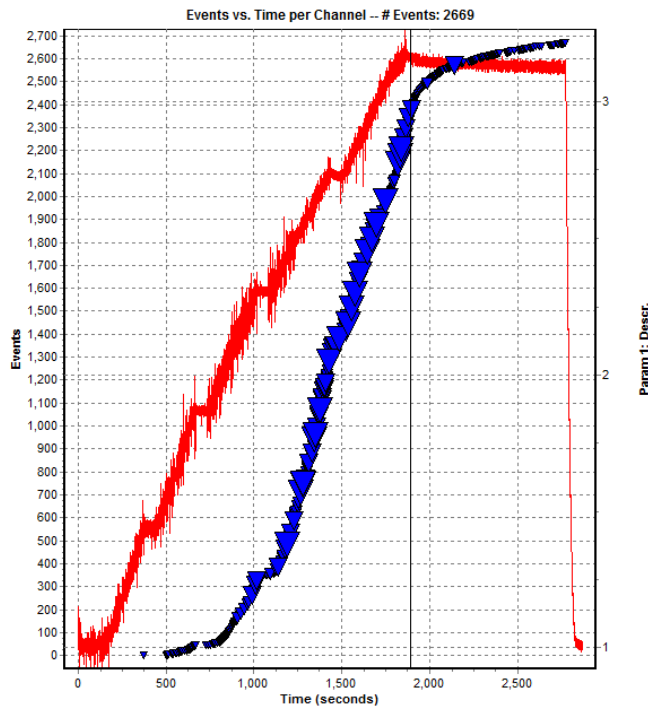


Fig. 15. Autofretting showing cumulative events and pressure vs. time for the virgin test of the vessel. (G1091 AF June 18 2009)

When doubt exists about the stability of the composite material, that is, the emission persists and does not decay at a specified rate, or the energies of the emissions are not decaying during a load hold, then there is evidence that a serious stress concentration exists. This is not normal HPC pressure vessel behavior. However, it is important to realize that events with higher energies can occur anytime during a pressure hold and little energy jumps may be detected. This is part of the nature of composite materials and is not of concern as long as the overall rate of appearance of energy jumps is decreasing and the energies do not exceed specified limits. If the energy of an event is very large, it is a good idea to use waveform analysis to identify the fracture source and then assess vessel integrity through engineering analysis of stress and strain, FEA and failure analysis that incorporates the types of flaws and their locations determined by modal AE analysis.

8. Conclusions

- Integrity of high-pressure composite (HPC) pressure vessels can be assessed against specific accept/reject criteria by modal AE methods, including fiber break energy, background energy oscillations, frictional AE (FRAE) and cumulative events and energy curves. The

accept/reject criteria can be tied to engineering analysis, for example, the amount of fiber breakage allowed by finite element analysis or perhaps netting analysis for a given section.

- Fiber-break events are determined better by a combination of energy and frequency spectrum than by the presence of high frequencies alone.
- The background energy oscillation effect begins at approximately 60-75% of burst pressure and is a clear indicator of gradual reduction in local load carrying capacity of the material as stresses are redistributed to bear the pressure.
- Energy in AE waves can be scaled by using the rolling ball impactor method. The scaling method also gives good agreement with the energy of crack growth in metals [16].
- An AE allowance factor, similarly to the factor of safety for stress, can be adjusted to be more or less conservative in dispositioning vessels.
- The use of modal AE and the effects described herein, such as determining fiber breakage, matrix cracking and so forth, can be extended to composite materials in various applications besides pressure vessels such as aircraft and aerospace structures, automobiles and so forth.

9. Suggestions for Further Research

- 1) Does the background energy oscillation effect show itself in stress rupture tests and what load levels?
- 2) Is burst pressure predicted by the background energy oscillation effect?
- 3) Do the broken fiber tip vibrations indicate composite condition?
- 4) What factor of safety should be applied for fiber breakage?
- 5) What are the best ways to determine the acoustic emission allowance factor?

Acknowledgements

The author would like to acknowledge that he was greatly aided by discussions over the years with many colleagues including Steven Ziola, William Prosser, Donald Gardiner, Edward Wu, Timothy Fowler, Kanji Ono, Marvin Hamstad, Steve Carpenter, Ajit Mal, Jonathan Awerbuch, Eric Madaras and Thomas Drouillard.

References

For those unfamiliar with AE testing in composite, see a review by M.A. Hamstad, "A Review: Acoustic Emission, A Tool for Composite-Materials Studies," *Exper. Mech.*, **26** (1986), 7–13. Proceedings of six International Conferences on Composite Materials (1982, 1986, 1989, 1992, 1995, 1998) are also good references.

For a recent review of *metal fatigue*, in which AE was monitored with 55 references, see M. Huang et al., "Using Acoustic Emission in Fatigue and Fracture Materials Research", *JOM*, **50** (11), 1998. <http://www.tms.org/pubs/journals/JOM/9811/Huang/Huang-9811.html>

1. M.R. Gorman, "Plate Wave Acoustic Emission," *J. Acoust. Soc America*, **90**(1), (1991), 358-365.
2. M.R. Gorman and S.M. Ziola, "Plate Waves Produced by Transverse Matrix Cracking," *Ultrasonics*, **29** (1991), 245–251.

3. M.R. Gorman and W.H. Prosser, "AE Source Orientation by Plate Wave Analysis," *Journal of Acoustic Emission*, **9**(4), (1991) 283-288.
4. W.H. Prosser et al., "Advanced Waveform-Based Acoustic Emission Detection of Matrix Cracking in Composites," *Mat. Eval.*, **53** (9) (1995), 1052–1058.
5. M. Shiwa, S. Carpenter, and T. Kishi, "Analysis of Acoustic Emission Signals Generated During the Fatigue Testing of GFRP," *J. Comp. Mat.*, **30** (18) (1996), 2019–2041.
6. G.N. Morscher, "Modal acoustic emission of damage accumulation in a woven SiC/SiC composite. *Comp. Sci. Technology*, **59** (1999), 419–426.
7. T.T. Chiao, M.A. Hamstad, E.S. Jessop, and R.H. Toland, High-Performance Fiber/Epoxy Composite Pressure Vessels, Lawrence Livermore Laboratory UCRL-52533, NASA CR-159512. December 12, 1978.
8. J. Awerbuch, M. Madhukar, M.R. Gorman, *Journal of Reinforced Plastics and Composites*, **3**, 1984, 2-38.
9. 'Development of Inspection Technology for NGV Fuel Tanks,' Failure Analysis Associates, FaAA-SF-R-97-05-04, May 1997.
10. W. Huang, S. M. Ziola and M. R. Gorman, Review of Progress in Quantitative Nondestructive Evaluation, **18** (1999) 797-804.
11. R.D. Fultineer and J.R. Mitchell, ASTM STP 1353, 1999, pp. 224-235.
12. M. Surgeon, Ph.D. thesis, Katholieke Universitat Leuven, 1999.
13. M.R. Gorman, "Acoustic Emission", *Encyclopedia of Structural Health Monitoring*, C. Boller, F-K. Chang and Y. Fujino, Editors, ISBN 978-0-470-05822-0, March 2009. Vol. 1, Ch. 4, pp. 79-100.
14. F.W. Crossman et al., ASTM STP 658, J.R. Vinson, Ed., 1978, pp. 205-220.
15. T.J. Fowler, J.A. Blessing and P.J. Conlisk, New Directions in Testing, *Proc. 3rd International Symposium on AE from Composite Materials*, Paris, France, 1989.
16. Steven M. Ziola, private communication, 2011.

IMAGING OF DEEP STRUCTURE USING REFLECTION WAVES DETECTED BY SPECTRAL MATRIX ANALYSIS AND CONFIDENCE LEVELS

HIROKAZU MORIYA

Graduate School of Engineering, Tohoku University,
6-6-04 Aramaki, Aza Aoba, Aoba, Sendai 980-8579, Japan

Abstract

A new spectral matrix method for detecting the arrivals of linearly or elliptically polarized waves was developed and applied to reflection imaging of the earth's crust and upper mantle. In this method, parameter values representing the confidence levels of the detection of the arrivals of linearly or elliptically polarized waves are used to image the reflectors. This paper describes the theory for the detection of polarized waves and discusses their detectability in relation to a synthetic three-component signal. The dependence of detectability on time-window length and on the center frequency of the analysis was quantitatively evaluated for this signal. Next, earthquake data for events around Sendai, Japan with magnitudes ranging from 2.0 to 5.6 were analyzed and the reflectors imaged by a migration technique based on the confidence levels of polarized wave arrival detection. By assuming P-P and S-S reflections, reflectors due to characteristic changes in the mantle were identified at depths of 350–500 km, demonstrating the feasibility of using a spectral matrix to detect polarized waves and to image the earth's crust and upper mantle.

Keywords: Spectral matrix, reflection survey, repeating similar earthquake

1. Introduction

Estimation of the structure of the earth's crust and upper mantle such as the region of phase change is important for revealing the evolution of the lithosphere. In this regard, laboratory experiments have clarified the phase changes of rock in relation to temperature in the upper mantle, and theoretical and seismic tomography studies have addressed the stagnant slab in the mantle [e.g. 1 - 4]. The measurement method used to explore the earth's crust and mantle is a critical aspect of such studies, and the development of various reliable imaging methods based on different principles is important for verifying and understanding the detailed structure of the earth. A reflection survey, which uses reflection waves for imaging structures, is a powerful method for identifying acoustic anomalies and boundaries, and various techniques to measure reflectors and process the collected data have been developed [e.g. 5]. The detection of reflection waves, however, can be difficult because of their relatively low energy and because of ambient noise. It is easier to detect reflection waves by using three-component seismic measurements rather than one-component signals because a three-component seismic signal makes it possible to evaluate three-dimensional (3-D) polarization, allowing the discrimination of wave modes such as P-wave, S-wave, and Rayleigh wave modes [6 - 11]. Polarized seismic waves contain information about the earth's crust and upper mantle, and characterization of the polarization is a key subject in seismology and geophysical exploration, where reflected and converted seismic waves are used to evaluate subsurface structures.

A method using a three-component signal for the detection of reflections has been applied to induced micro-earthquakes/AE in geothermal fields. In such studies, linearly polarized coherent waves are detected in coda waves by principal component analysis of the spectral matrix. The

parameter representing the linearity of the polarization is migrated by the diffraction stack migration technique, and the feasibility of the method for extracting reflectors such as fractures has been demonstrated [12 - 14]. This result implies that a similar analysis applied to polarized seismic waves might be useful in reflection surveys, even without the use of many observation points or artificial seismic sources. Moriya et al. [15, 16] and Moriya [17] proposed a method to detect the arrivals of polarized waves and to calculate the statistical confidence of the arrival detection. They evaluated the linearity and ellipticity of the polarization by spectral matrix analysis and examined the feasibility of the method to analyze both synthetic and earthquake signals.

Recently, many seismic observatories have been established, and seismic networks of three-component seismic detectors with broad-band frequency characteristics have been used for seismic observations, allowing the representation of the 3-D particle motion of seismic waves by the locus of the three-component signal. Unknown structures in the earth's crust might be detectable by these networks if the different polarization states and arrival times of polarized seismic waves can be identified. The detection of reflected waves as waveform data is a fundamental technique that is a key to successful reflection imaging. This paper describes a statistical method for detecting the arrival times of polarized seismic waves in a three-component seismic signal. The application of the method to earthquake data follows in order to image reflectors in the earth's crust and upper mantle and to demonstrate the feasibility of the method for estimating subsurface structure.

2. Statistical Detection of Polarized Seismic Waves Using Spectral Matrix Analysis

The particle motion of seismic waves represents the polarization and the analysis of polarization makes it possible to detect the arrival time of waves. The arrivals of linearly or elliptically polarized waves can be detected using spectral matrix analysis [17]. A statistical parameter that represents the confidence level for the detection of the arriving wave for the migration is introduced here. The spectral matrix is defined as a function of time and frequency as follows:

$$\mathbf{S}_p(t_j, f_k) = \begin{pmatrix} S_{xx}(t_j, f_k) & S_{xy}(t_j, f_k) & S_{xz}(t_j, f_k) \\ S_{yx}(t_j, f_k) & S_{yy}(t_j, f_k) & S_{yz}(t_j, f_k) \\ S_{zx}(t_j, f_k) & S_{zy}(t_j, f_k) & S_{zz}(t_j, f_k) \end{pmatrix}, \quad (1)$$

where $S_{aa}(t_j, f_k)$ ($a = x, y, z$) are the power spectra; $S_{ab}(t_j, f_k)$ ($a, b = x, y, z, a \neq b$) are the cross-spectra. These are calculated using time series from a finite time window of the three-component signal; t_j is a representative time corresponding to the center of the time window; and f_k denotes the frequency [17]. The linearity and ellipticity of the polarization can be evaluated using the eigenvalues (λ_i) of the spectral matrix. We introduce two parameters to characterize the particle motion of the waves as follows [18 - 20]:

$$C_{Linear}(t_j, f_k) = \frac{(\lambda_1 - \lambda_2)^2 + (\lambda_1 - \lambda_3)^2 + (\lambda_2 - \lambda_3)^2}{2(\lambda_1 + \lambda_2 + \lambda_3)^2}, \quad (2)$$

and

$$C_{Elliptical}(t_j, f_k) = 1 - \frac{2\lambda_3}{\lambda_1 + \lambda_2}, \quad (3)$$

where $\lambda_i = \lambda_i(t_j, f_k)$ ($\lambda_1 > \lambda_2 > \lambda_3$, $i = 1, 2, 3$) are the eigenvalues, and $C_{Linear}(t_j, f_k)$ and $C_{Elliptical}(t_j, f_k)$ are parameters that characterize the linearity and ellipticity, respectively. We introduce a method that uses two moving time windows and has the ability to distinguish the arrival times of different coherent waves that closely overlap in time but have different frequency contents. To judge the arrivals of polarized waves statistically, we define the following function:

$$Z_{mode}(t_q, f_r) = \sqrt{(2m+1)n-3} (Z_{T,mode}(\overline{C_{R1}(t_q, f_r)}) - Z_{T,mode}(\overline{C_{R0}(t_q, f_r)})) \quad (4)$$

where (*mode* = *Linear* or *Elliptical*) and

$$Z_{T,mode}(\overline{C_{R0}(t_q, f_r)}) = \frac{1}{2} \log \left(\frac{1 + \overline{C_{R0,mode}(t_q, f_r)}}{1 - \overline{C_{R0,mode}(t_q, f_r)}} \right), \quad (5)$$

$$Z_{T,mode}(\overline{C_{R1}(t_q, f_r)}) = \frac{1}{2} \log \left(\frac{1 + \overline{C_{R1,mode}(t_q, f_r)}}{1 - \overline{C_{R1,mode}(t_q, f_r)}} \right). \quad (6)$$

The subscript “*mode*” represents the polarization type, either “*Linear*” or “*Elliptical*”, referring to linear or elliptical polarization, respectively. $\overline{C_{R0,mode}(t_q, f_r)}$ and $\overline{C_{R1,mode}(t_q, f_r)}$ are the mean values of $C_{mode}(t_j, f_k)$ for $(2m+1)n$ samples taken from $C_{mode}(t_j, f_k)$ over a representative time t_q and with a frequency f_r , where t_q is the boundary time between the two moving time windows used for calculating the spectral matrices, m is the number of sample frequencies, and n is the number of discrete sample times used to calculate the mean values [21]. $\overline{C_{R0,mode}(t_q, f_r)}$ is the value before time t_q and $\overline{C_{R1,mode}(t_q, f_r)}$ is the value after time t_q (Fig. 1). The parameter $Z_{T,mode}(t_q, f_r)$ has an approximately normal distribution because $\overline{C_{R0,mode}(t_q, f_r)}$ and $\overline{C_{R1,mode}(t_q, f_r)}$ are transformed by Fisher’s transformation into equations (5) and (6). $\overline{C_{R0,mode}(t_q, f_r)}$ and $\overline{C_{R1,mode}(t_q, f_r)}$ show the degree of polarization before and after a representative time t_q , and a statistical test can be introduced to judge whether the difference between $\overline{C_{R0,mode}(t_q, f_r)}$ and $\overline{C_{R1,mode}(t_q, f_r)}$ is significant or not. When a polarized wave with frequency f_r arrives at time t_q , the difference between $\overline{C_{R0,mode}(t_q, f_r)}$ and $\overline{C_{R1,mode}(t_q, f_r)}$ becomes larger and $Z_{mode}(t_q, f_r)$ has a peak. Significance levels are commonly used in statistical tests to determine whether to reject or accept the null hypothesis. The significance level α is defined as follows:

$$\alpha = \int_{z(\alpha)}^{+\infty} P(z) dz, \quad (7)$$

where $P(z)$ has a standard normal distribution in which the random variable z has the values of $Z_{mode}(t_q, f_r)$. When the following inequality is satisfied,

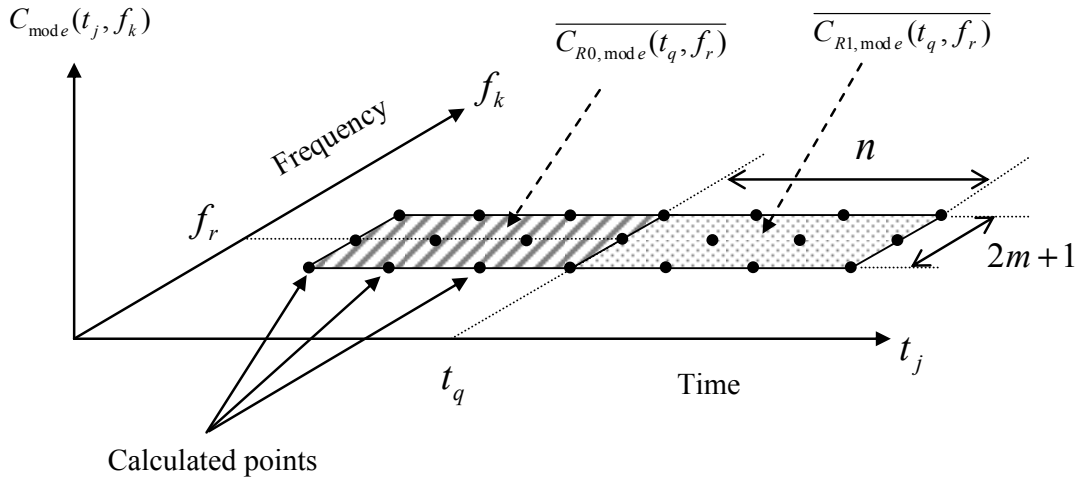


Fig. 1. Concept of mean values in the time–frequency domain. $\overline{C_{R0,mode}(t_q, f_r)}$ and $\overline{C_{R1,mode}(t_q, f_r)}$ are the mean values of $C_{mode}(t_j, f_k)$ for $(2m+1)n$ samples taken from $C_{mode}(t_q, f_r)$ over a representative time t_q and frequency f_r , where t_q is the boundary time between two moving time windows used for calculating the spectral matrices.

$$Z_{mode}(t_{arrival}, f_{arrival}) > z(\alpha), \quad (8)$$

the hypothesis that a wave with linear or elliptical polarization has arrived is accepted, and the arrival of a polarized wave is estimated to have a significance level α . For instance, when $z(\alpha)$ is 1.96, then the arrival of a wave is detected with a significance level of 95%. In practice, the value of $Z_{mode}(t_a, f_r)$ indicates wave arrival and the confidence level of the detection.

3. Evaluation of the Method using Synthetic Waves

Previously, we evaluated the detectability using a synthetic wave signal consisting of sinusoidal waves and random noise and showed that the arrival times of linearly and elliptically polarized signals can be detected within 10 sampling points at a signal-to-noise ratio (S/N) of -7 dB [17]. In this study, we evaluated the dependence of detectability on the time-window length used in the analysis, and its dependence on frequency, before applying the method to earthquake data. It is known that the results of a polarization analysis are affected by the time-window length used for the calculation of a co-variance matrix. In this study, the co-variance matrix is replaced by a spectral matrix in order to analyze polarization in the time and frequency domains. Thus, the evaluation of time-window length dependence is important because the time-window length influences the reliability of the spectral estimation, and also affects the linearity and ellipticity evaluated using the eigenvalues of the spectral matrix.

A synthetic three-component signal was produced by an attenuated tone-burst sinusoidal wave and a computer-generated random number. The synthetic three-component signal comprised three linearly polarized waves (at 20, 70, and 120 s) and one elliptically polarized wave (at 170 s), each one a sinusoidal wave with a frequency of 5 Hz, assuming a sampling frequency of 100 Hz, where the S/Ns of the three linearly polarized waves and the one elliptically polarized wave were 25.0, 6.3, 1.6, and 1.8 dB, respectively. S/N was defined in the time domain as the ratio of the root mean square of the sinusoidal wave to that of the noise. This synthetic wave was divided into three components by multiplying by the directional cosine after assuming an arrival direction. The principal direction of polarization (that is, the assumed arrival direction) was N30°E and $\phi = 60^\circ$ for the first sinusoidal wave and N40°E and $\phi = 70^\circ$ for the other three sinusoidal waves, where $\phi = 0$ is horizontal. Figure 2 shows the synthetic three-component signal and $Z_{Linear}(t_q, f_r)$ and $Z_{Elliptical}(t_q, f_r)$ as a function of the time-window length used in the analysis, where the time-window length varies from 0.5 to 3 s. The given frequency of the sinusoidal wave was 5 Hz and its period was 0.2 s; thus, the time-window length varies from 2.5 to 15 periods of the given sinusoidal wave. The center of frequency used for the calculation was 5 Hz, with m and n set to 3 and 10, respectively. The data length of the fast Fourier transform (FFT) was 1024 sampling points in all cases; therefore, the frequency resolution for the spectral estimation was constant at 0.098 Hz. Peaks appear at 20, 70, 120, and 170 s, and the onset of the sinusoidal wave can be detected at all time-window lengths, although the half-width of the peaks becomes broader as the time-window length becomes longer. Thus, as shown in Figs. 2(b) and 2(c), the arrival of the polarized wave can be detected using the parameters $Z_{Linear}(t_q, f_r)$ and $Z_{Elliptical}(t_q, f_r)$ even when the time-window length for the analysis is changed. This result suggests that the dependence of arrival detectability on time-window length can be neglected when the time window used in the analysis covers several periods of the targeted wave. Therefore, the time window should be long enough to encompass several periods of the polarized wave components. In this method, the polarized waves are analyzed in the time and frequency domains. The advantage of performing the analysis in the frequency domain is that the frequency range for the

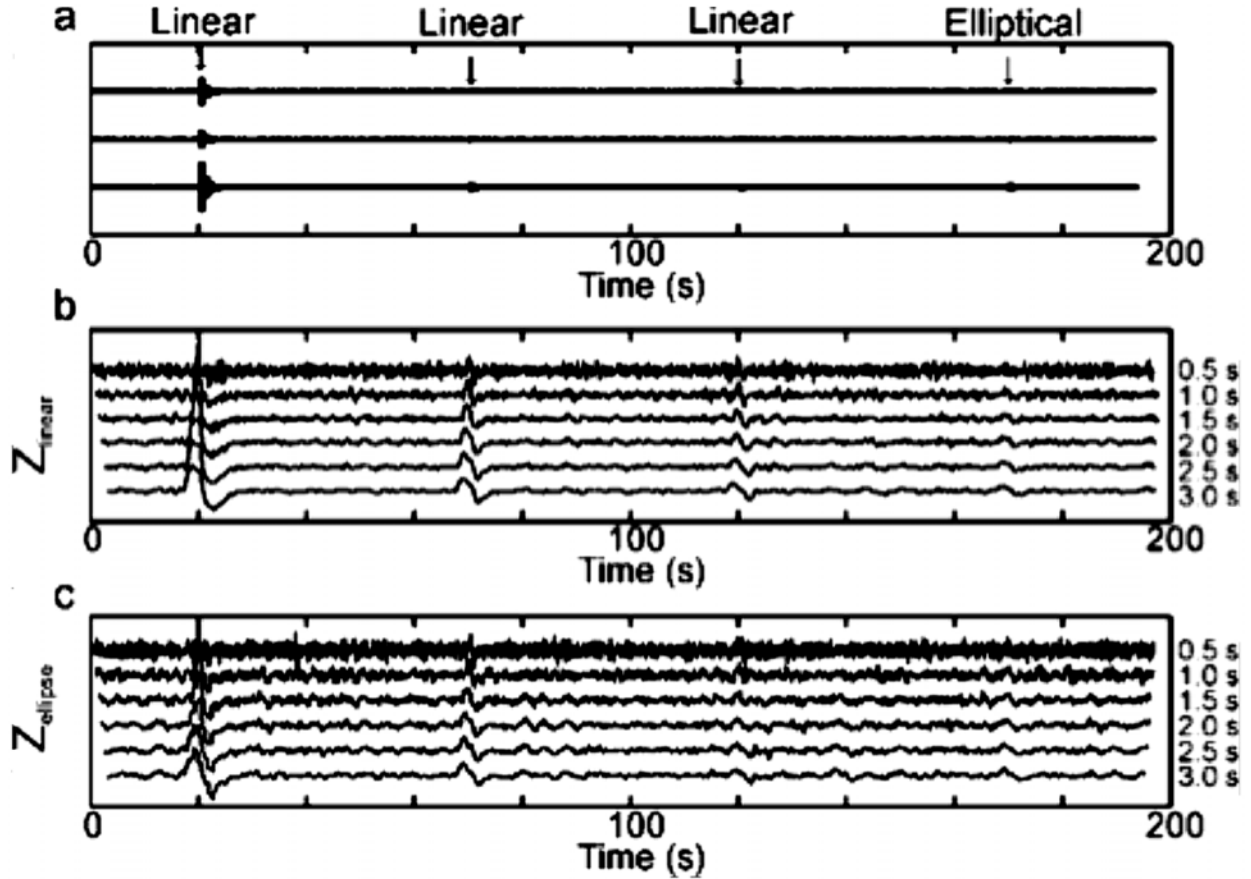


Fig. 2. (a) Synthetic three-component signal, (b) $Z_{\text{Linear}}(t_q, f_r)$ and (c) $Z_{\text{Elliptical}}(t_q, f_r)$, where the time window length for analysis is changed.

detection of the polarized waves can be selected in relation to the spectral content and also to reduce the influence of noise. It is important, however, to choose a suitable frequency for the detection of the targeted polarized waves. Therefore, we evaluated the dependence of detectability on the frequency selected for the analysis. Figure 3 shows the synthetic three-component signal and $Z_{\text{Linear}}(t_q, f_r)$ and $Z_{\text{Elliptical}}(t_q, f_r)$ as a function of the center frequency, which varies from 5 to 30 Hz. The frequency resolution of the estimated spectrum is 0.98 Hz because the time-window length for the FFT is 10.24 s (1024 sample points), and the parameter m , which represents the frequency range for calculating the mean value of $\overline{C_{R0,mode}}(t_q, f_r)$ and $\overline{C_{R1,mode}}(t_q, f_r)$, is given as 3. Thus, the frequency width is 0.6 Hz, centered on the center frequency. For instance, the frequency range for the analysis is 5 ± 0.3 Hz when the center frequency is 5 Hz. The onset of the sinusoidal wave can be detected when the center frequency is 5 Hz (Figs. 3(b) and 3(c)). However, the peaks are small or absent when the center frequency used in the analysis does not correspond to the frequency component of the signal. This result suggests that a frequency range, in which the center frequency is close to the dominant frequency of the polarized wave, should be chosen so that the polarized waves can be distinguished from noise in the frequency domain. Therefore, the method can be used to detect the polarized wave component with low S/N if a suitable center frequency is chosen for calculation of the parameter $Z_{\text{mode}}(t_q, f_r)$, but it is necessary to evaluate the spectral content of the signal to determine the center frequency to be used in the analysis.

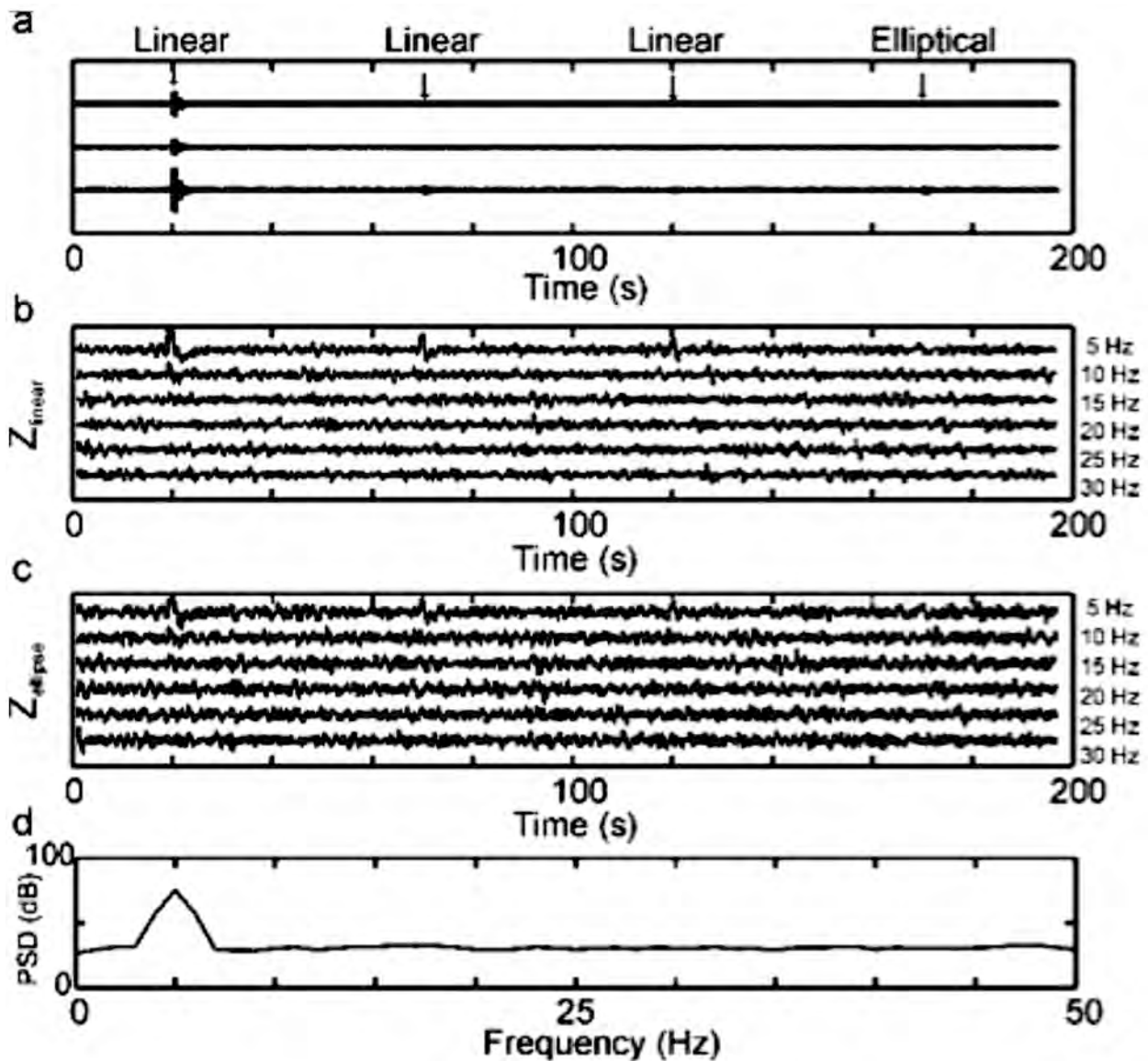


Fig. 3. (a) Synthetic three-component signal, (b) $Z_{Linear}(t_q, f_r)$, (c) $Z_{Elliptical}(t_q, f_r)$ and (d) power spectrum, where the parameters $Z_{Linear}(t_q, f_r)$ and (c) $Z_{Elliptical}(t_q, f_r)$ as a function of the center frequency is changed from 5 Hz to 30 Hz.

4. Application to the Imaging of Subsurface Structures by using Earthquakes

The earthquake events used for the analysis were collected at 31 stations by the Hi-net system of the National Research Institute for Earth Science and Disaster Prevention (NIED) of Japan and observatories of the Japan Meteorological Agency (JMA) and Tohoku University (Fig. 4). Six earthquakes with high S/N were selected from waveforms collected between 1 December 2003 and 29 February 2008.

Their magnitudes ranged from 2.0 to 5.6, their source locations were distributed from longitude 140.365E to 142.435E and latitude 37.828N to 38.776N, and their depths were from 27 to 128 km. Figure 5 shows the source locations of the earthquakes studied. The P-wave velocity V_p was given as 7.0 km/s, and V_p/V_s was assumed to be 1.7. Although the migration velocity is sensitive to the imaging depth of the reflectors, we did not attempt to model the velocity structure.

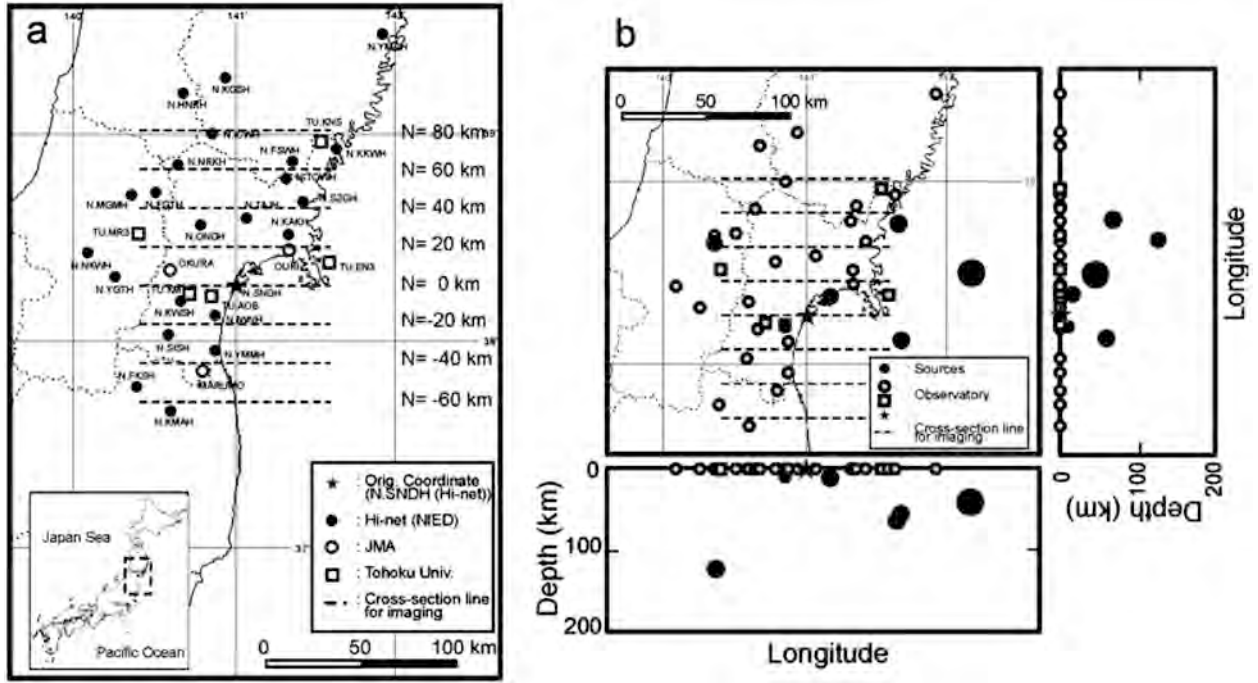


Fig. 4. (a) Earthquake observatories used for the analysis. The map shows the northeastern part of Japan, and the broken lines denote the cross sections used in the reflection imaging. (b) Source locations of used earthquakes, where closed circles represent the source location and the larger size means the larger magnitude. The symbols \circ , \square and \star represent the observation points.

The calculation of $Z_{mode}(t_q, f_r)$ was carried out after estimation of the spectrum to determine the center frequency for the analysis; we chose 5 Hz as the center frequency because the power spectral density ranged from 2.5 to 15 Hz and because using a relatively low frequency component in the analysis has the advantage of extracting reflection waves with lower attenuation. The time-window length was set at 1.0 s because the lowest frequency component of the signal was 2.5 Hz and the time-window length should be larger than one period of the frequency component to satisfy the marginal conditions for spectral estimation.

The imaging was carried out as follows. First, virtual reflection points were assumed every 1 km within a range of 50 km in both the E-W and N-S directions and between 0 and 700 km depth. The theoretical arrival time of each reflected wave originating from P- and S-waves reflected from a virtual reflection point was calculated, and the calculated value of parameter $Z_{mode}(t_q, f_r)$ at the time corresponding to the theoretical arrival time of the reflections was assigned to that virtual reflection point. The same operation was performed for data for all six earthquakes from all of the earthquake observatories, and the values were accumulated at each reflection point. Finally, the ensemble averages of the parameter values were calculated at each virtual reflection point.

This process is based on the same concept as the Kirchhoff migration method, which draws a reflection-time surface by using the amplitude of waves or reflection coefficients. In this study, the amplitude was replaced by the parameters $Z_{mode}(t_q, f_r)$, which represent the confidence levels of the polarized wave arrival. The average of $Z_{mode}(t_q, f_r)$ at each virtual reflection point was calculated to show the imaging result as the mean value of the confidence levels, because the value of $Z_{mode}(t_q, f_r)$ indicates the confidence level for the acceptance of the hypothesis that a polarized seismic wave has arrived. Therefore, the mean value of $Z_{mode}(t_q, f_r)$ at each virtual re-

flexion point can be regarded as the likelihood that the wave has been reflected at that point. Determination of the confidence level is thus useful for evaluating the validity of the reflectors implied in the result. For instance, a mean value of 1.65 for $Z_{mode}(t_q, f_r)$ at a virtual reflection point can be statistically interpreted to mean that the confidence level of the hypothesis that the reflector exists at that point is 90%.

5. Results and Discussion

Figure 5 shows a three-component signal and the calculated parameters for detecting linearly and elliptically polarized waves at a confidence level of 90% ($Z_{mode}(t_q, f_r) = 1.65$). In Fig. 6(a), waves with large amplitude can be identified in the coda wave, but it is impossible to judge visually whether these waves represent the polarized waves. Therefore, we applied the method described here to this waveform data and chose the center frequency and the time-window length for calculation of $Z_{mode}(t_q, f_r)$ by considering the power spectral density of the waveform (Fig. 6(d)), which shows that the frequency component is dominant from 2.5 to 15 Hz. Thus, the center frequency for the analysis was set at 5 Hz and m and n to 3 and 10, because the center frequency should include the dominant frequency component of the waves and because the use of a lower frequency favors the detection of reflection waves owing to less attenuation during the wave propagation. The length of the moving time window was set to 3.0 s (300 points of discrete time-series data) because several periods of the frequency component of 5 Hz are included in that time window. The Fourier transform was calculated using the FFT algorithm, which requires less calculation time than other spectral estimation methods. Several peaks could be identified (Fig. 5(b) and 5(c)) after the arrival of the P- and S-waves. The hypothesis that polarized waves have arrived at a particular time gains confidence as the parameter $Z_{mode}(t_q, f_r)$ becomes larger. Here, we examine reflection imaging using the arrivals of linearly and elliptically polarized waves, under the assumption that these polarized components originated from P-P and S-S reflection waves, respectively. Reflection images were determined by the method described above, and images were calculated by assuming P to P reflections and S to S reflections at the cross sections set every 20 km from -60 to $+80$ km in the N-S direction as shown in Fig. 4 (Figs. 6 and 7). The ensemble average of the parameters $Z_{mode}(t_q, f_r)$ has a value below around 0.45, and the confidence level corresponds to 17% if we consider that value as α in equation (7). The reason for the low mean value of the parameters is that the polarized waves were detected with a low S/N. The basic principles underlying the method described in this paper allow the contrast in the images (Figs. 6 and 7) to be interpreted as indicating differences in reflectivity. In the P-P reflection imaging, several zones of higher confidence levels can be seen within the depth range from 350 to 700 km (Fig. 6, indicated by red bands). Seismic wave velocities are thought to change rapidly at around 400–1000 km depth owing to phase transitions in the mantle, and discontinuities at depths of 410 and 660 km in the transitional region are well known. Seismic tomography studies have also suggested that subducting slabs of lithosphere tend to become stagnant in the transition zone [2, 22]. Therefore, the red and yellow bands from 350 to 700 km depth in Fig. 6 are likely to indicate acoustic impedance changes associated with characteristic changes in the mantle. On the other hand, the region of higher confidence levels from 100 to 150 km results from virtual images formed by the detection of S-waves when linearly polarized waves were searched for in the P-wave coda portion, because the S-wave arrival is also detected by the analysis using the parameter in equation (2) (Fig. 5(b)). In the S-S reflection imaging (Fig. 7), a zone

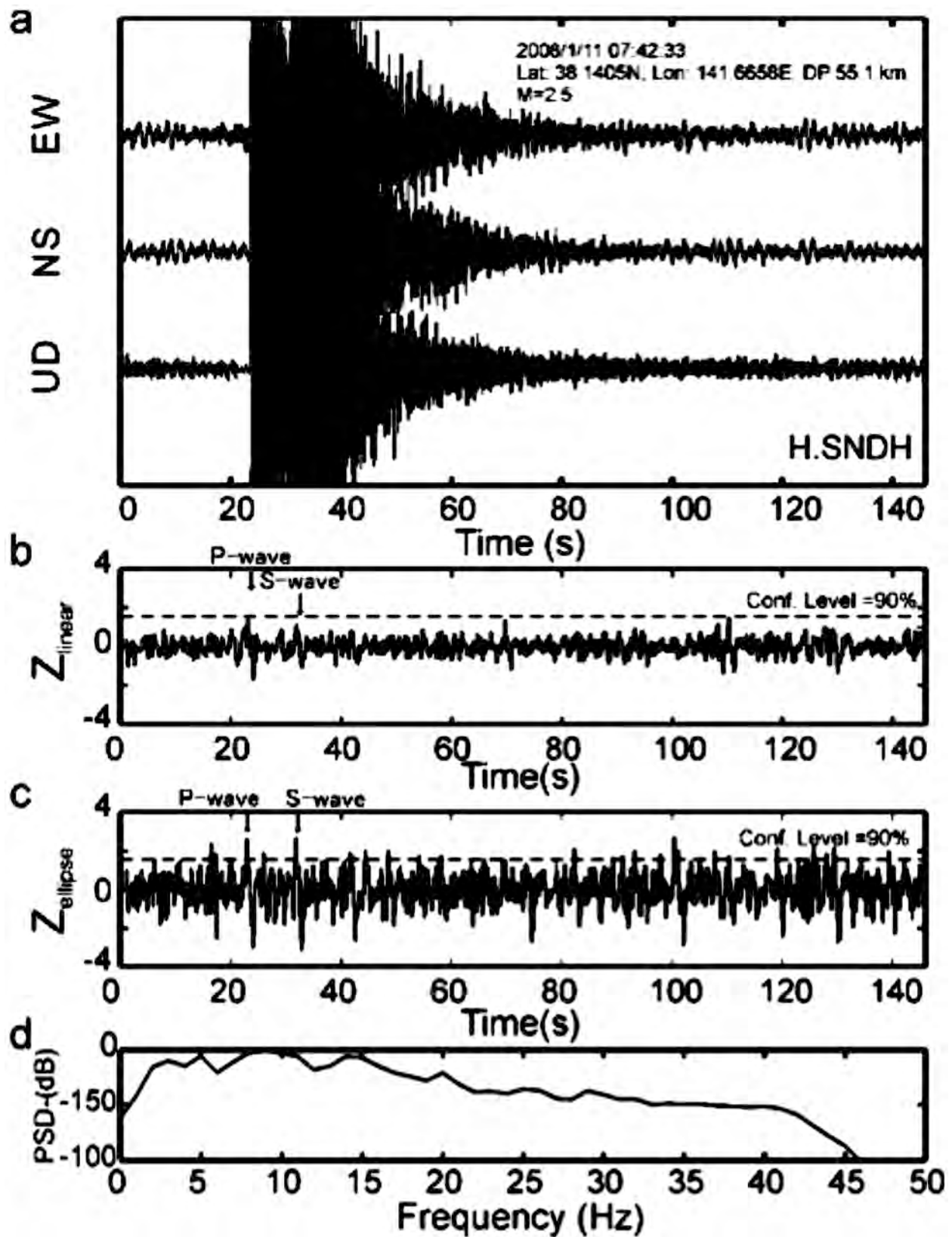


Fig. 5. Example of waveforms from observation N.SNDH (indicated by the symbol \star in Fig. 4) and parameters for the detection of linearly and elliptically polarized waves. The three-component signals (U-D, E-W, N-S) and the parameters for linear and elliptical polarization are shown. The sampling frequency of the waveform was 100 Hz.

of higher confidence can be seen at around 350 km in depth (indicated by the blue arrow). This zone is also seen in Fig. 6, and is a common reflector of linearly and elliptically polarized waves. Many zones of higher confidence can be seen at depths shallower than around 150 km, suggesting that the boundary between the lithosphere and the asthenosphere is approximately at that depth. Depths below 500 km could not be imaged owing to the limited recording duration of the event data. The results suggest that the proposed method can delineate reflectors and that, from an acoustic point of view, the method is useful for revealing metamorphic conditions and structures in the plate convergence region in the upper mantle.

6. Conclusion

We proposed a statistical method for detecting the arrival of polarized seismic waves in three-component seismic observations and applied the method to a reflection survey using local earthquake data to image the earth's crust and upper mantle. Analysis of the spectral matrix in the time and frequency domains identified linearly and elliptically polarized waves. Imaging performed by using a statistical parameter that reflects the confidence level of the arrival of polarized waves succeeded in delineating reflectors, which are represented as discontinuities in acoustic impedance. Thus, this method is feasible for detecting polarized waves in a three-component seismic signal.

Advantages of the method are that wave polarization is evaluated by using three-component signals in the time and frequency domains and that the polarized waves can thus be detected with low S/N, allowing linear and elliptical polarization to be distinguished, whereas it is difficult to identify the reflected waves by direct use of the waveform because of its very low amplitude. With this new method it will be possible to detect polarized waves and also to image the earth's crust and upper mantle.

Acknowledgments

The author would like to thank the National Research Institute for Earth Science and Disaster Prevention (NIED), the Japan Meteorological Agency for providing the earthquake waveform data that were downloaded from the website of the NIED (<http://www.hinet.bosai.go.jp/>).

References

- [1] D.L. Anderson and J.D. Bass: Transition region of the Earth's upper mantle, *Nature*, **320**, 321–328 (1986).
- [2] Y. Fukao, M. Obayashi, H. Inoue and M. Nenbai: Subducting Slabs Stagnant in the Mantle Transition Zone, *J. Geophys. Res.*, **97**, 4809-4822 (1992).
- [3] E. Ohtani, K. Litasov, T. Hosoya, T. Kubo and T. Kondo: Water Transport into the Deep Mantle and Formation of a Hydrous Transition Zone, *Phys. Earth Planet. Inter.*, **143**, 255-269 (2004).
- [4] T. Irifune, Y. Higo, T. Inoue, Y. Kono, H. Ohfuji and K. Funakoshi: Sound velocities of majorite garnet and the composition of the mantle transition region, *Nature*, **451**, 814-817 (2008).
- [5] W.M. Telford, L.P. Geldart, and R.E. Sheriff: *Applied Geophysics*, 2nd ed., Cambridge University Press, (1990).
- [6] E.A. Flinn: Signal analysis using rectilinearity and direction of particle motion, *Proceedings of the IEEE*, **59** (1965), 1234–1237.

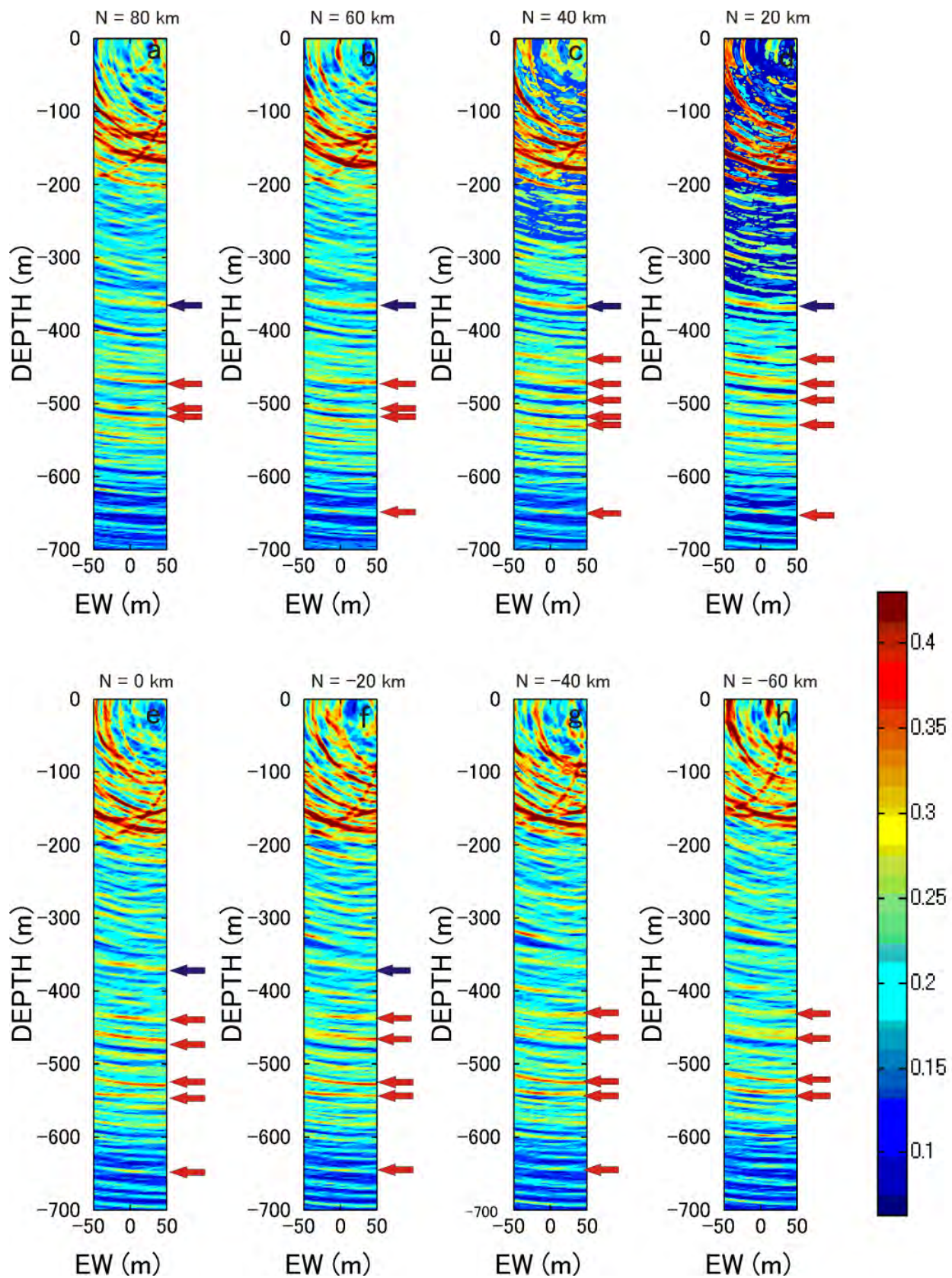


Fig. 6. Reflection imaging using linearly polarized waves assuming P-P reflection waves. Different cross sections of the image are shown. The origin of the coordinate system is the observation N.SNDH (indicated by the symbol \star in Fig.4). The images are aligned from north to south.

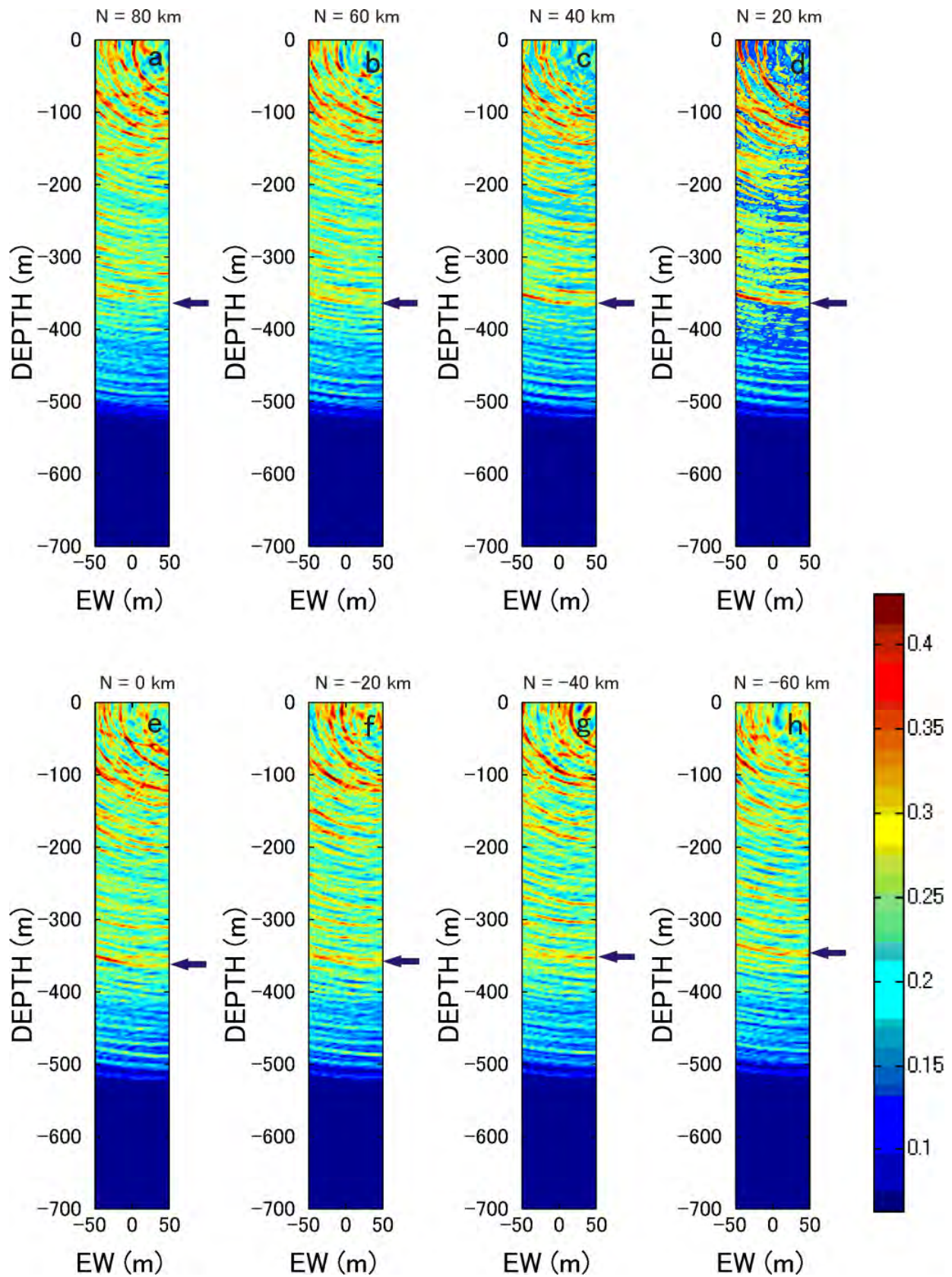


Fig. 7. Reflection imaging using elliptically polarized waves assuming S-S reflection waves. Different cross sections of the image are shown.

- [7] H. Moriya, K. Nagano and H. Niitsuma: Precise source location of AE doublets by spectral matrix analysis of triaxial hodogram, *Geophysics*, **59**, 36–45 (1994).
- [8] H. Moriya, H. Niitsuma and R. Baria: Multiplet-clustering analysis reveals structural details within the seismic cloud at the Soultz geothermal field, *Bull. Seism. Soc. Am.*, **93**, 1606–1620 (2003).
- [9] S. Greenhalgh, I. M. Mason and B. Zhou: An analytical treatment of single station triaxial seismic direction finding, *Journal of Geophysical Engineering*, **2**, 8–15 (2005).
- [10] M. Diallo, M. Kulesh, M. Holschneider, K. Kurennaya and F. Scherbaum: Instantaneous polarization attributes based on an adaptive approximate covariance method, *Geophysics*, **71**, V99–V104 (2006).
- [11] M. Kulesh, M.S. Diallo, M. Holschneider, K. Kurennaya, F. Krüger, M. Ohrnberger and F. Scherbaum: Polarization analysis in the wavelet domain based on the adaptive covariance method, *Geophysical Journal International*, **170**, 667–678 (2007).
- [12] N. Soma, H. Niitsuma and R. Baria: Estimation of deeper structure at the Soultz Hot Dry Rock field by means of reflection method using 3C AE as wave source, *Pure Appl. Geophys.*, **150**, 661–676 (1997).
- [13] N. Soma, H. Niitsuma and R. Baria: Reflection technique in time-frequency domain using multicomponent acoustic emission signals and application to geothermal reservoirs, *Geophysics*, **67**, 928–938 (2002).
- [14] N. Soma, H. Niitsuma and R. Baria: Reflection imaging of deep reservoir structure based on three-dimensional hodogram analysis of multicomponent microseismic waveforms, *J. Geophys. Res.*, **112** (2007), B11303, doi:10.1029/2005JB004216.
- [15] H. Moriya, K. Nagano and H. Niitsuma: Precise estimation of AE source direction by spectral matrix analysis, *Progress in Acoustic Emission* **5**, 244-251 (1990).
- [16] H. Moriya and H. Niitsuma: Precise detection of P-wave in low S/N signal by using time-frequency representations of a triaxial hodogram, *Geophysics*, **61**, 1453–1466 (1996).
- [17] H. Moriya: Precise arrival-time detection of polarized seismic waves using the spectral matrix, *Geophysical Prospecting*, **56**, 1-10 (2008).
- [18] J.C. Samson: Description of the polarization states of the vector processes: application to ULF magnetic fields, *Geophysical Journal of Research Astronomy Society*, **34**, 403–419 (1973).
- [19] A. Benhama, C. Cllet and M. Dubesset: Study and applications of spatial directional filtering in three-component recordings, *Geophysical Prospecting*, **36**, 591–613 (1988).
- [20] R. De Franco, and G. Musacchio : Polarization filter with singular value decomposition, *Geophysics*, **66**, 932–938 (2001).
- [21] H. Moriya: Spectral matrix analysis for detection of polarized wave arrivals and its application to seismic reflection studies using local earthquake data, *Earth, Planets and Space*, **61**, 1287-1295 (2009).
- [22] R.D. Van der Hilst, R. Engdahl, W. Spakman and G. Nolet: Tomographic imaging of subducted lithosphere below northwest Pacific island arcs, *Nature*, **353**, 37-43 (1991).

EFFECT OF LOADING PATTERN ON THE ACOUSTIC EMISSION EVALUATION OF PRESTRESSED CONCRETE GIRDERS

FRANCISCO BARRIOS¹ and PAUL ZIEHL²

¹ School of Civil engineering and Geomatics, Universidad Del Valle, Cali, Colombia,

² Department of Civil and Environmental Engineering, University of South Carolina, 300 Main Street, Columbia, SC 29208

Abstract

This investigation studies the effects and potential inconsistencies that can arise when acoustic emission (AE) criteria are applied to a cyclic load test (CLT) for damage evaluation of prestressed concrete girders. The CLT with AE criteria has recently been proposed for damage detection and structural evaluation of reinforced concrete flexural members. Attempts to develop the evaluation criteria placed limited attention on the effectiveness of the AE criteria within a CLT loading profile, resulting in apparent contradictions of AE criteria when applied for damage assessment in concrete members. The contradictions are sometimes produced by the lack of standardization in the application of the evaluation criteria throughout the loading profile. Results of the current study emphasize the necessity of calculating the Calm and Load Ratio values in a consistent manner when applying a cyclic load test loading profile. More consistent evaluation can also be obtained if parameters such as signal strength or energy are utilized.

Keywords: Calm ratio, load ratio, cyclic load test, pre-stressed concrete.

Introduction

AE evaluation is a promising alternative for structural assessment and damage detection for civil structures [1]. AE techniques have demonstrated superior sensitivity for damage detection over traditional approaches but still lack the holistic means required for a coherent integrity evaluation. This investigation aims to identify and address potential inconsistencies caused by application of AE criteria to a cyclic load test profile, similar to the one used for the CLT method as described in ACI 437 [2], and to others that have been used in previous AE investigations. The outcomes seek to improve the application of current AE assessment criteria for structural evaluation, and will constitute an important step towards the integration of AE techniques with CLT methodologies for pre-stressed concrete structures.

AE evaluation has been applied to a variety of civil engineering materials including steel, reinforced/pre-stressed concrete, and fiber-reinforced plastics (FRP) [1, 3]. The loading profile associated with the AE method is generally applied in a load-set fashion (Fig. 1a) that facilitates the detection of changes in activity during loading and reloading. Several types of loading profiles can be found in the literature and they generally correspond to special conditions involved in the particular study (type of material, static or dynamic loading, expected failure mode, etc.). Load is applied in a stepwise fashion to minimize noise and to facilitate evaluation of the data.

The Cyclic Load Test (CLT) method of structural evaluation as fully described in ACI 437 [2] is solely based on load versus displacement behavior and does not incorporate AE data. With the CLT method of evaluation, the stepwise loading pattern is executed to enable assessment of *deviation from linearity* in the load versus displacement response (Fig. 1b). With this method of

evaluation, each load-set consists of two identical load cycles to enable evaluation of the *permanency* and *repeatability* criteria. Loading profiles for both methodologies (cyclic load test and AE) are similar, but challenges exist to integrate both procedures.

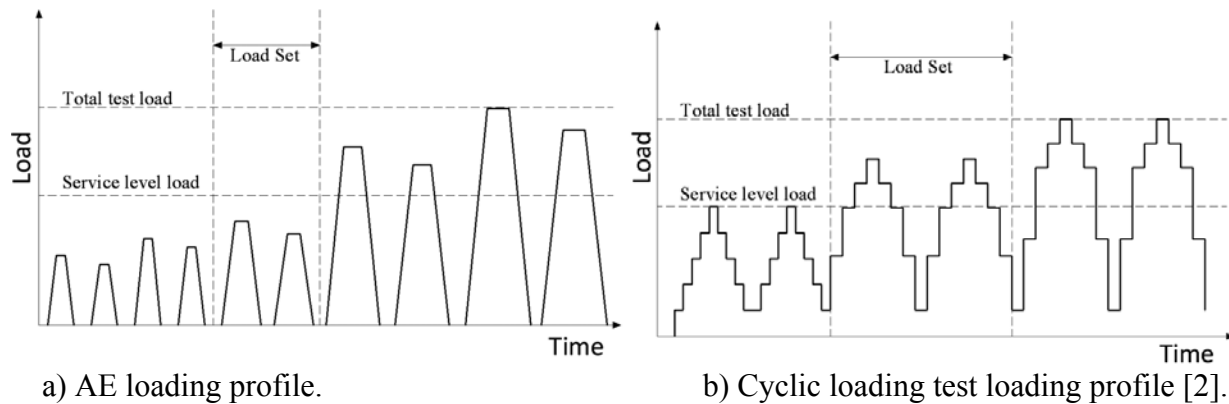


Fig. 1. Schematic of loading profiles.

For bridge and building elements two primary approaches to evaluation of AE data have been proposed. The first can be referred to as the Calm Ratio versus Load Ratio plot as described in Ohtsu et al. and elsewhere [4, 5]. See also [6-11]. The majority of investigations have been carried out on passively reinforced concrete specimens. However, the investigation described in Xu [9] focused on reduced-scale pre-stressed specimens. The second method is referred to as Intensity Analysis (plot of Severity versus Historic Index) as first proposed by Fowler et al. [12] for fiber reinforced vessels and later described in Golaski et al. for concrete bridge elements [13]. A variation on this approach that utilized high amplitude hits was later proposed by Tinkey et al. [14] for concrete box girders. This study concluded that Intensity Analysis may not be appropriate for distributed heavy damage.

Background

Loading profiles for evaluation of AE data are generally designed to account for the Kaiser effect. This is achieved through the application of a stepped loading pattern, which subjects the structure to multiple load steps at increasing levels until the maximum test load is attained. For civil engineering structures in general and for pre-stressed concrete members in particular, standardized procedures to determine the adequate number of steps, load levels, rate of loading and unloading, duration of the load holds, and the maximum test load are still in development. These parameters are crucial for the development of a practical testing methodology and for acquisition of meaningful AE data.

Calm Ratio versus Load Ratio (NDIS-2421): The Japanese nondestructive inspection standard 2421 (NDIS-2421) [5] proposes a combination of Calm Ratio (CR) and Load Ratio (LR) values as an evaluation criterion to assess the level of damage in reinforced concrete flexural members. This approach plots values of Calm Ratio versus Load Ratio for each load-set (or for individual load cycles), and later divides the graph into four zones of damage (Fig. 2). This method has been studied in reinforced concrete [6, 8, 11] and its application has been extended to pre-stressed members with promising results [7, 9]. However, this method of damage assessment faces a few inherent challenges. First, the manner in which the graph is partitioned allows for two far distant damage levels (Minor and Heavy) in very close proximity to one another. This does not correspond to physical reality and therefore impedes a straightforward quantification of

damage. Additionally, a paucity of published experimental data combined with significant dispersion of the data found in previous investigations has impeded the location of damage thresholds in the absence of an external criterion, such as crack mouth opening displacement.

Load Ratio: Also referred to as Felicity ratio or Concrete Beam Integrity (CBI) ratio, Load Ratio is a critical parameter for AE monitoring. The Load Ratio has been observed to decrease with the accumulation of damage. This ratio is inversely related to the reduction in AE activity during loading until the material is stressed beyond its previous stress level, also known as the Kaiser effect [4].

Calm Ratio: Calm Ratio is calculated as the ratio of total cumulative acoustic emission activity during the unloading phase to total cumulative AE activity during the entire loading cycle. One crucial aspect related to computation of the Calm Ratio is the type of AE parameter selected for evaluation. Some authors [6, 8, 9] have used the total number of hits during loading and unloading for this purpose. Data gathered from the flexural specimens of pre-stressed concrete in the current investigation indicates that the number of hits may not be appropriate for calculation of this ratio and may result in disruption of the cumulative damage trend.

A consideration of equal importance is the selection of the load cycles in the loading profile where the Calm Ratio is to be computed. When AE techniques are implemented along with the CLT method, the Calm Ratio can be either calculated on the initial loading cycle or the reloading cycle of the load-set. In some cases the AE data of the loading cycle has been combined with the activity of the reloading cycle [10]. There is currently little agreement about which of these alternatives constitutes the better approach. As shown later, this consideration has a significant impact on the Calm Ratio evaluation criterion, and also the Load Ratio criterion to a lesser degree.

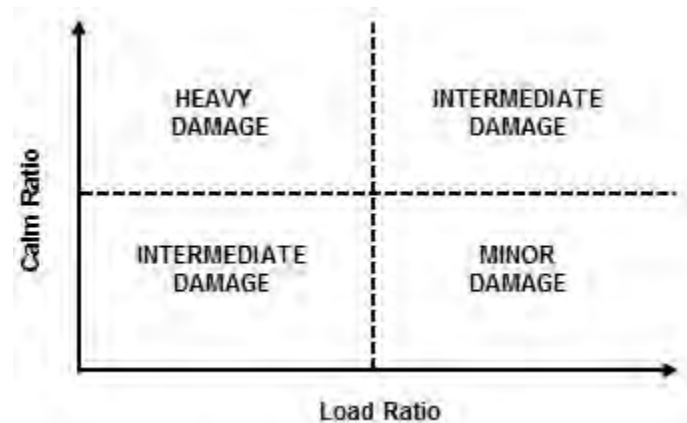


Fig. 2. Calm Ratio versus Load Ratio [6] (redrawn for clarity).

Experimental Procedure

This investigation analyzes experimental data gathered from the four-point flexural testing of six full-scale pre-stressed girder specimens. The first set of specimens consists of two self-consolidating concrete girders (SCC-1 and SCC-2) and one high early-strength concrete girder (HESC). The second set of specimens contains two self-consolidating lightweight concrete girders (SCLC-1 and SCLC-2) and one high early strength lightweight concrete girder (HESLC). The specimen nomenclature was chosen as follows: ‘concrete type (SCC, HESC, SCLC, or HESLC) - specimen number associated with concrete type’.

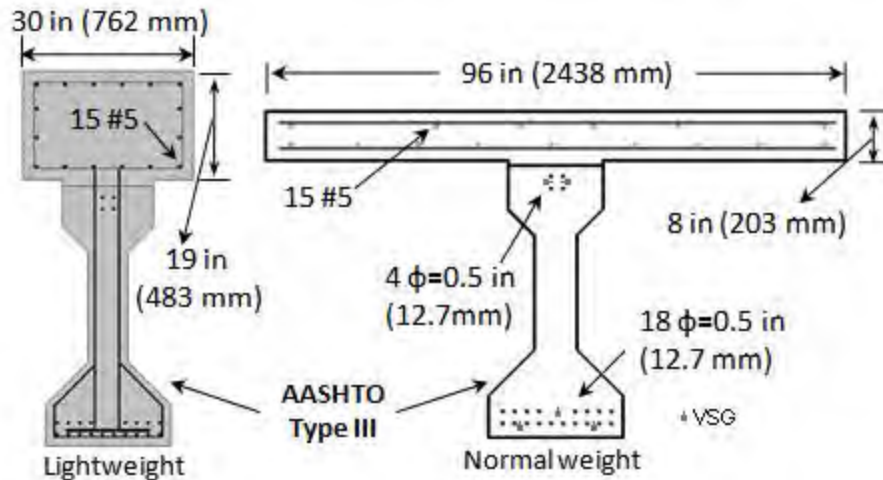


Fig. 3. Cross section details.

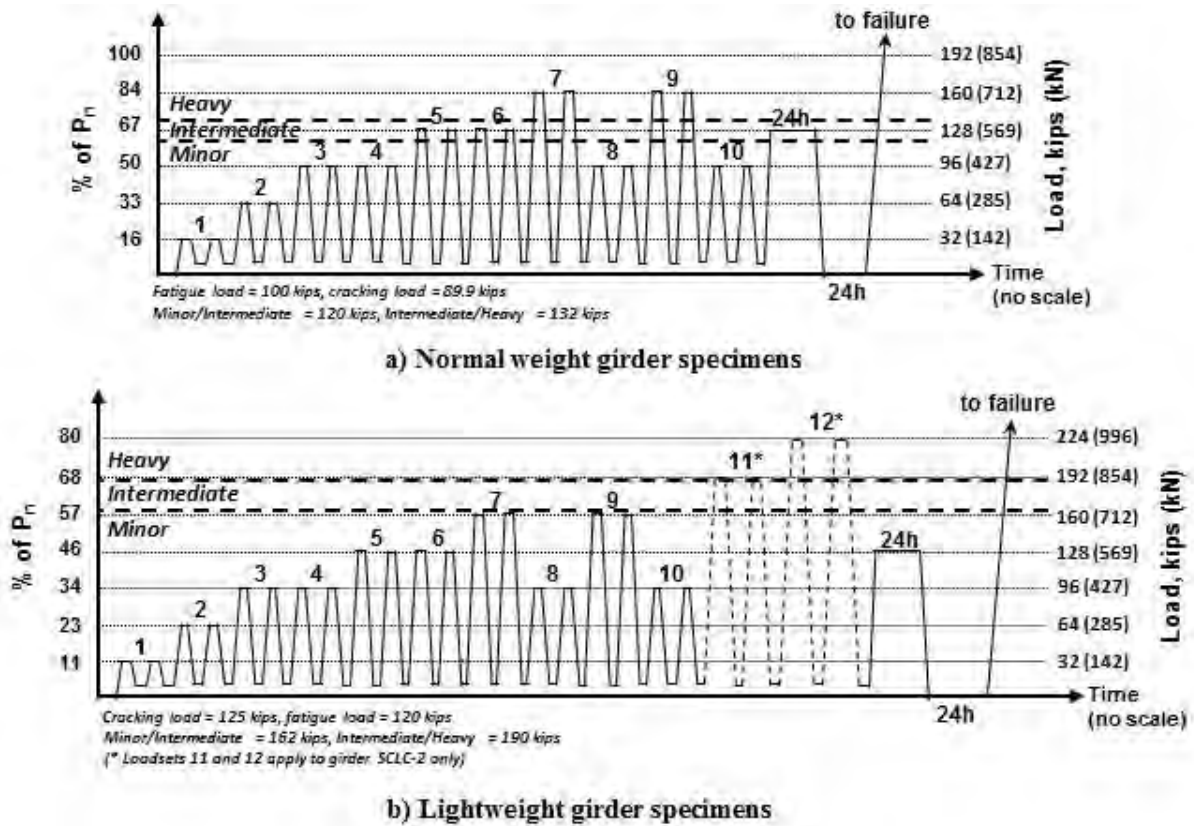


Fig. 4. Loading profiles

Specimen details: All girder specimens were AASHTO Type III with a span of 17.7 m and a depth of 1,143 mm. A concrete mix with a 28-day design compressive strength of 55.2 MPa was used to cast the girders, and a 27.6 MPa concrete deck (design strength at 28 days) was cast in the laboratory on top of each girder prior to testing. The concrete deck was 2.44-m wide and 203-mm deep for the normal weight girder specimens and 762-mm wide by 483-mm deep for the lightweight concrete girder specimens (Fig. 3). All girders were pre-stressed using 22 low relaxation strands having 12.7-mm nominal diameter and a tensile strength of 1.86 GPa. A 138-kN pre-stressing force was applied to each strand prior to release.

Internal and external instrumentation: Five vibrating-wire strain gages were installed within the girders to monitor long-term strain for pre-stress losses and other variables. Instrumentation was outfitted externally on both the girder and deck to measure and record displacement and concrete strain data. Two draw-wire transducers placed at mid-span were used to measure deflection of the girder.

Strain gages were adhered to the top of the deck and at the bottom of the girder. The strain gages were oriented in the longitudinal direction in relation to the deck and girder, and were located at the midpoint between the hydraulic rams. Cracks were marked on the girders with permanent markers as they developed, so cracking patterns at different load levels could be readily identified. Further information can be found in the related SCDOT research reports for both normal and lightweight concrete girder types [15, 16].

Loading patterns: The loading profiles for both sets of girders are shown in Figs. 4a and b. The loading values were developed with consideration to the calculated nominal capacity of the normal weight concrete girder specimens. A total test load (maximum load applied) of 712 kN was selected, which is approximately 73% of the measured load capacity of these girder specimens, and 84% of the calculated load capacity. Prior to loading according to the above loading profiles, girders SCC-2 and SCLC-2 were subjected to fatigue loading for 2,000,000 cycles. A summary of the girder specimens used for this investigation is provided in Table 1 and numerical values of each load-set are shown in Table 2.

Table 1: Summary of girder specimens.

Specimen Name	Loading Type	Cracking Load (kips)	Fatigue Load (kips)	Age of girder at release (days)	Age of girder at testing (days)	Age of deck at testing (days)
SCC-1	Static	89.9	-	2	270	200
SCC-2	Fatigue	89.9	100	2	900	300
HESC	Static	89.9	-	2	470	100
SCLC-1	Static	125	-	16	315	50
SCLC-2	Fatigue	125	120	16	555	90
HESLC	Static	125	-	16	490	60

Table 2: Load-set values.

Load-set	Load, kip (kN)
1	32 (142)
2	64 (285)
3, 4	96 (427)
5, 6	128 (569)
7, 9	160 (712)
8, 10	96 (427)
11	192 (854)
12	224 (996)

The total test load for the normal weight girders was also applied for lightweight girder specimens SCLC-1 and HESLC. The lightweight girders had a higher calculated nominal capacity (P_n) of approximately 1.25 MN due to the modified deck geometry. Therefore, for SCLC-1 and the HESLC girder, the maximum test load was approximately 57% of the calculated load capacity. The total test load applied to girder SCLC-2 was increased to include load-sets 11 and 12 (at 68% and 80% of calculated capacity) as shown in Fig. 4b.

AE monitoring: AE activity was monitored continuously during the application of the CLT procedures. Six R6i AE sensors (resonant in the vicinity of 60 kHz with integrated pre-amplification of 40 dB, manufactured by Mistras Group, Inc.) were mounted on one side of each girder specimen. The soft-

ware used for data collection and visualization was AEWin. All data was collected on a DiSP system, also manufactured by Mistras Group, Inc. The sensor layout was symmetric about an axis located midway between the loading points (Fig. 5). A 48-dB test and evaluation threshold was used for all specimens.

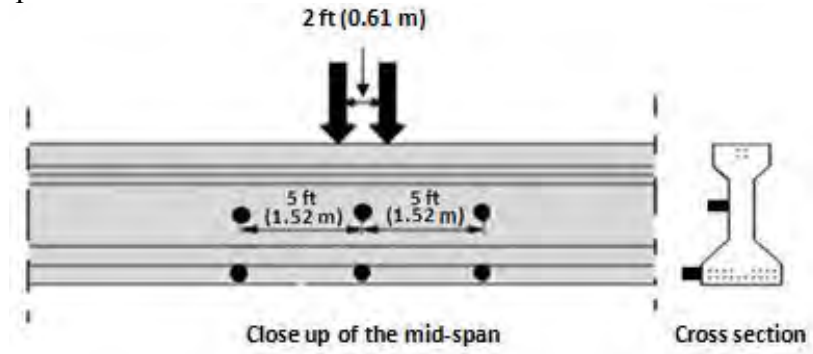


Fig. 5. Acoustic emission sensor layout.

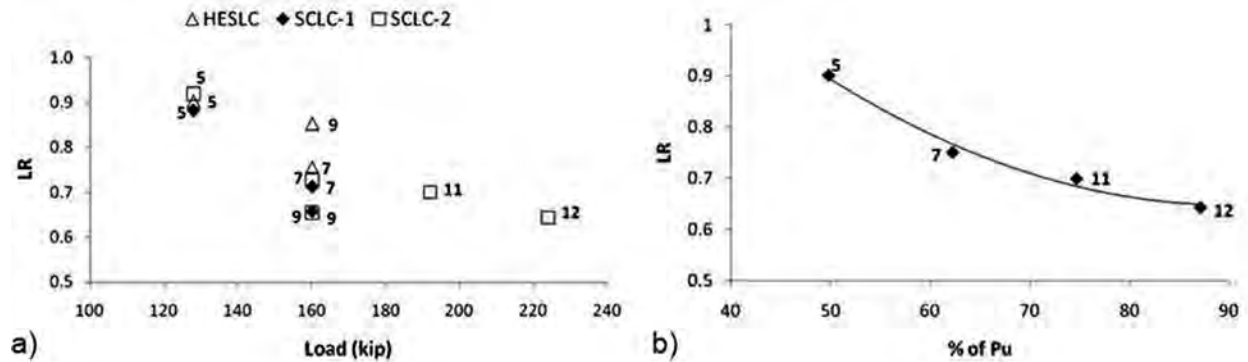


Fig. 6. Effect of repeat loadsets on Load Ratio (lightweight girder specimen). a) Effect of repeat loadsets, b) Averaged data without repeat loadsets.

Experimental Results

The experimental results are discussed in terms of the damage state of each set of girder specimens. The effect of repeated load-sets on the Load Ratio evaluation is first discussed, followed by a discussion of the trends in the Calm Ratio versus Load Ratio plots. Cumulative energy was used instead of total hits for calculation of the Calm and Load ratios.

For both sets of girder specimens, the Minor, Intermediate, and Heavy damage zones were determined based on load versus displacement behavior. Detailed descriptions related to the assessment of the damage zones for the specimens used in this investigation are provided in [7]. For the normal weight girder specimens, the lines of delineation for Minor/Intermediate and Intermediate/Heavy damage are 533 kN and 587 kN. For the lightweight girder specimens, the lines of delineation for Minor/Intermediate and Intermediate/Heavy damage are 720 and 845 kN. These damage zones are superimposed on the loading profiles shown in Figs. 4a and b.

Load ratio: Values of Load Ratio as a function of the applied load for the lightweight girder specimens are shown in Fig. 6a. Load-sets 6 and 8 are not shown because they experienced little AE activity due to the Kaiser effect. As expected, as the load is increased the Load Ratio is reduced. Oscillations in this general trend occur for load-set 9, which is a repeat of load-set 7. For comparison, a similar plot utilizing averaged values of the Load Ratio versus applied load (as a

percentage of calculated load capacity) is shown in Fig. 6b, where a more consistent trend is obtained in the absence of repeat load-sets.

For the Load Ratio, the effect of repeat load-sets on the criterion can be difficult to identify due to the subjective determination of the *load at the onset of significant AE during reloading*. The reduction in the AE activity during reloading cycles flattens the curve of released energy, impeding the unambiguous location of this point [7, 10]. Even though there can be differences in the values of the Load Ratio when calculated based on initial load-sets, the oscillations are more significant when repeat cycles are used for evaluation. The Load Ratio has been observed to be a more stable criterion than the Calm Ratio in this and other investigations [6].

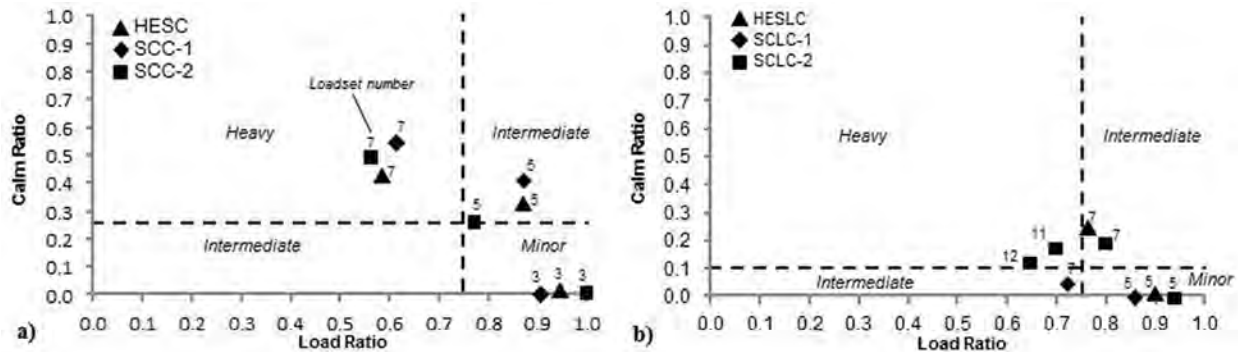


Fig. 7. Damage trend with Calm Ratio based on initial load cycle. a) Normal weight girder specimens, b) Lightweight girder specimens.

Calm Ratio versus Load Ratio (NDIS-2421): A plot of Calm Ratio versus Load Ratio is shown in Fig. 7a for the normal weight girder specimens and in Fig. 7b for the lightweight girder specimens. For these figures the Calm Ratio was calculated using the initial loading cycles, and results from only the initial load-sets are plotted (load-sets 3, 5, and 7 for the normal weight girder specimens; and load-sets 5, 7, 11, and 12 for the lightweight girder specimens).

For the normal weight girder specimens (Fig. 7a) the delineations between Minor, Intermediate, and Heavy damage zones were determined based on the load versus displacement behavior of the specimens combined with visual observation of cracking patterns [7]. For these specimens, load-set 3 is well within the Minor zone, load-set 5 is in the middle of the Intermediate zone, and load-set 7 falls within the Heavy zone. For the lightweight girder specimens, load-set 5 falls within the Minor zone, load-set 7 is at the boundary of the Minor and Intermediate zones, load-set 11 is at the boundary of the Intermediate and Heavy zones, and load-set 12 falls well within the Heavy damage zone. Damage zone classifications are summarized in Table 3.

Normal weight girder specimens: For the normal weight girder specimens (Fig. 7a), the limits for the damage zone classifications on the Calm Ratio versus Load Ratio plot were established based on the observation that load-set 3 is well within the Minor zone, load-set 5 is in the Intermediate zone, and load-set 7 is in the Heavy zone. The lines of demarcation that correspond to this observed behavior are at Load Ratio = 0.75 and Calm Ratio = 0.25. With these values established, the behavior of increasing damage is apparent on the Calm Ratio versus Load Ratio plot for all three specimens, and the results are well grouped for the specimens (HESC, SCC-1, and SCC-2).

Table 3: Damage zone classifications.

Specimen Type	Damage Zone Classification				
	<i>Minor</i>	<i>Minor/Intermediate</i>	<i>Intermediate</i>	<i>Intermediate/Heavy</i>	<i>Heavy</i>
Normal weight girders	loadsets 1-4, 8, 10	none	loadsets 5, 6	none	loadsets 7, 9
Lightweight girders	loadsets 1-6, 8, 10	loadsets 7, 9	none	loadset 11	loadset 12

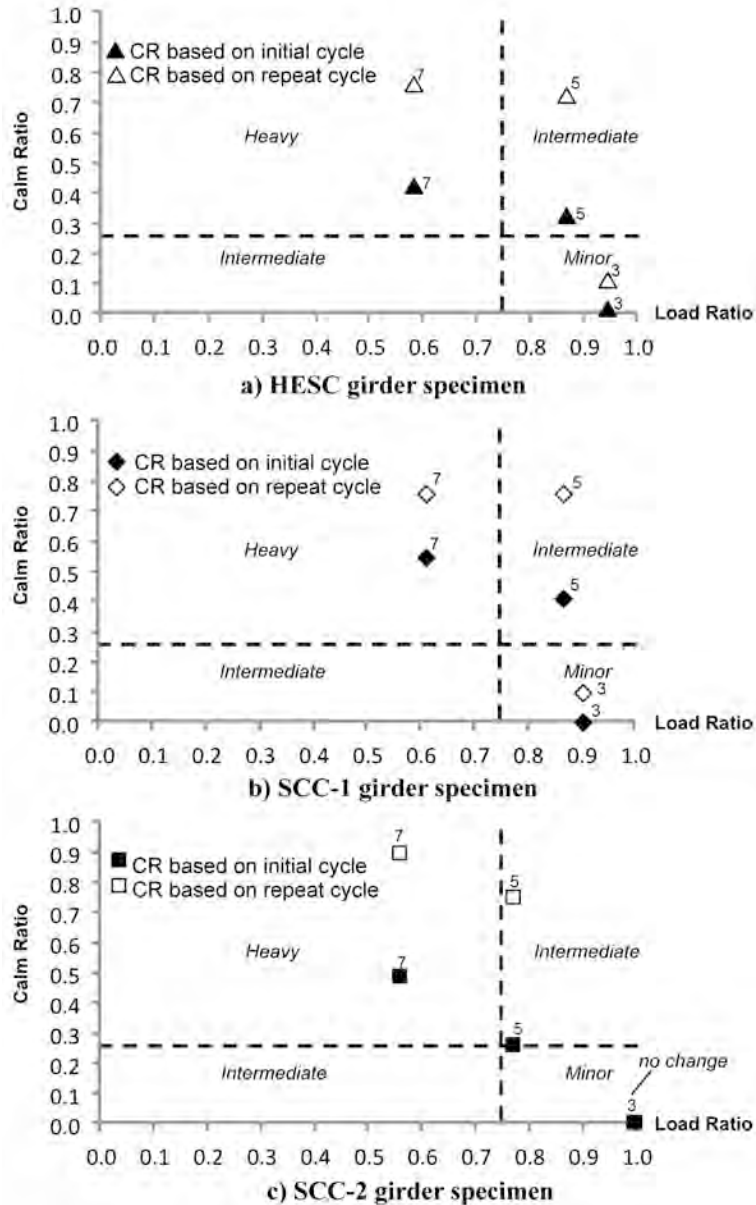


Fig. 8. Effect of calculating Calm Ratio based on repeat cycle (Normal weight girder specimens).

The values for both Load and Calm ratio are slightly lower than those described in Schumacher [6] and Lovejoy [11]. This is not surprising as those studies focused on passively reinforced specimens with a failure mode dominated by diagonal tension. It also seems that the Calm Ratio values in those studies may have been calculated based on the cumulative number of hits during unloading/cumulative number of hits during loading (as opposed to using the cumulative

number of hits during the entire loading cycle/cumulative number of hits during loading). Additionally, the ratios were calculated only for the overloads in the Schumacher study [6].

Figure 7a was established with calculation of the Calm Ratio based on the initial load cycle of a particular load-set. Figures 8a–c illustrate the effect of calculating the Calm Ratio based on the repeat load cycle of a particular load-set. Here an important phenomenon can be observed; Calm Ratio values when calculated based on load cycles at the same load level as the preceding load-set (referred to as ‘repeat’ load cycles) result in substantially increased values of the Calm Ratio for all three specimens. This is true even though the damage in the specimen has not changed. This is caused by the Kaiser effect, producing a drastic reduction in the AE activity during loading of the repeat load cycle in comparison to the activity during loading of the initial load cycle. The AE activity during unloading of these pre-stressed concrete specimens is relatively unchanged between the initial and repeat load cycles, thereby creating the amplification in the Calm Ratio values when calculated based on the repeat load cycle.

The amplification of the Calm Ratio values is particularly strong in pre-stressed beams because strong activity is present during unloading regardless of whether the cycle is a repeat cycle or initial cycle. Emission during unloading is largely due to friction that is caused by the prestressing force as the cracks close. Magnification of the Calm Ratio within repeat load-sets is more predominant when the girder has been loaded substantially beyond cracking. The cracking load for the normal weight girder specimens was approximately 400 kN (89.9 kips), corresponding to load-set 3 and above. The amplification for load-set 3 is significantly less than for load-sets 5 and 7 for all three specimens.

Calm Ratio values for load-set 3 of SCC-2 were not amplified in the repeat load cycle. This is attributed to the fact that this girder was subjected to fatigue loading at a level of 445 kN (100 kips) prior to conducting the loading protocol, and this level of load was slightly in excess of load-set 3. The fatigue loading served as a previous loading, and therefore the activity during loading of the initial load cycle was similar to that of the repeat load cycle for this case. It is also noted that the Load Ratio for load-set 3 was higher than for the other two girders, most likely because this girder was subjected to fatigue loading. This effect is as expected for this level of load and similar behavior has been reported elsewhere [11]. For load-sets above load-set 3 the Load Ratio for SCC-2 was reduced compared to the two girders that were not loaded in fatigue.

Lightweight girder specimens: For the lightweight girder specimens (Fig. 7b), the limits for the damage zone classifications on the Calm Ratio versus Load Ratio plot were established based on the observation that load-set 5 is within the Minor zone, load-set 7 is at the Minor/Intermediate zone threshold, load-set 11 is at the Intermediate/Heavy zone threshold, and load-set 12 is in the Heavy zone. The lines of demarcation corresponding to observed behavior are at Load Ratio = 0.75 (as for the normal weight girders) and Calm Ratio = 0.10 (differing from 0.30 for the normal weight girders). The behavior of increasing damage is not as clear on the Calm Ratio versus Load Ratio plot for the lightweight girder specimens. In particular it would be expected that load-set 12 would be more clearly placed in the Heavy damage zone. The results are relatively well grouped for each of the different specimens, with the exception of load-set 7 for SCLC-1. In this case, the Calm Ratio is lower than for the other two specimens at this same load-set. Published studies related to AE for lightweight pre-stressed concrete girders are scarce and further investigations related to this subject would be beneficial.

Figure 7b was established with calculation of the Calm Ratio based on the initial load cycle. Figures 9a – c illustrate the effect of calculating the Calm Ratio based on the repeat load cycle. The Calm Ratio values when calculated based on repeat cycles again result in substantially increased values for all specimens. As for the normal weight girder specimens, it is expected that the amplification of the Calm Ratio within repeat load-sets will be more predominant when the girder has been loaded substantially beyond cracking. The cracking load for the lightweight girder specimens was approximately 556 kN (125 kips), corresponding to load-set 5 and above. All load-sets plotted are therefore above the cracking load.

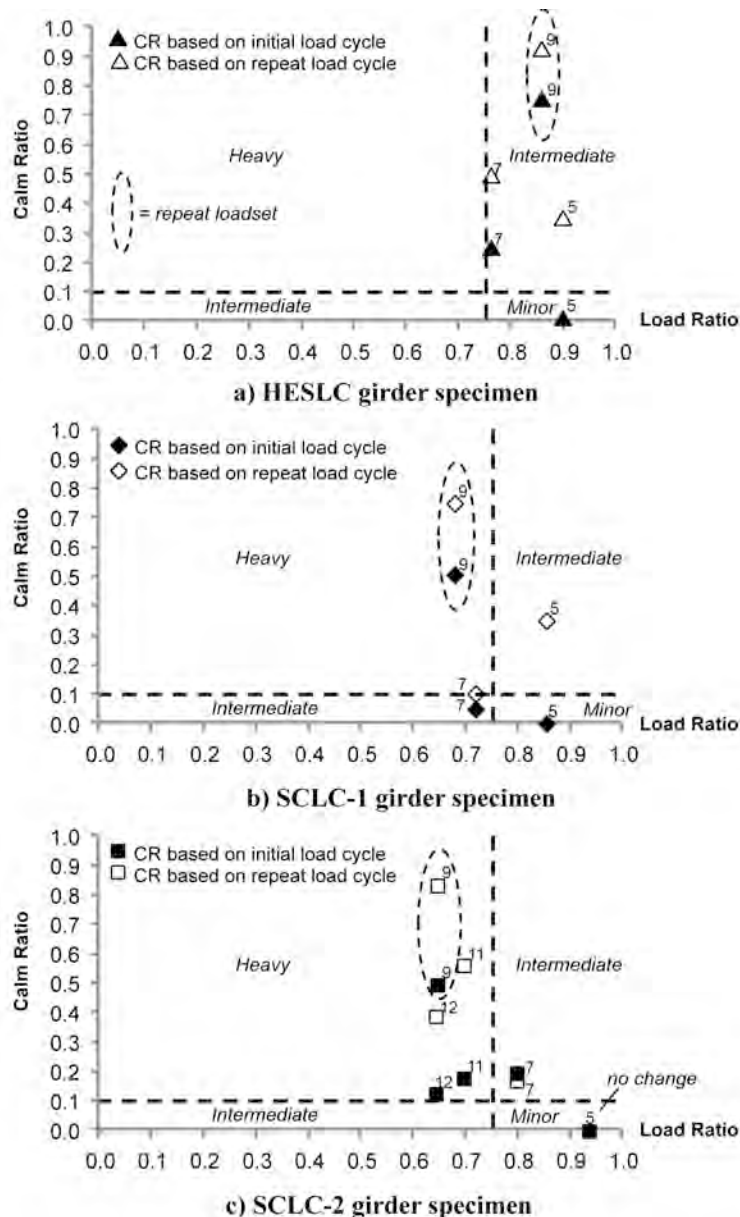


Fig. 9. Effect of calculating Calm Ratio based on repeat cycle. (Lightweight girder specimens).

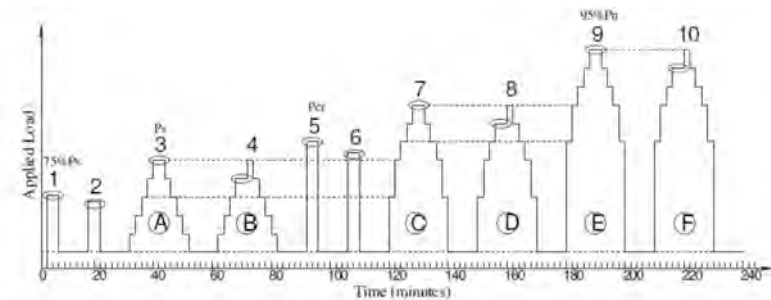
For the lightweight specimen that was loaded in fatigue (SCLC-2) prior to implementing the loading protocol, the Calm Ratio is not amplified for load-set 5. This specimen was loaded in fatigue to a level of 533 kN (120 kips), which approaches the level of load-set 5. Load-set 7, which lies at the Minor/Intermediate threshold, does not consistently demonstrate a significant

and noticeable increase in Calm Ratio when calculated based on the repeat load cycle, perhaps because this load-set only slightly exceeds the cracking load. As for the normal weight specimens, repeat load-sets well above the cracking load more clearly exhibit the amplification of the Calm Ratio.

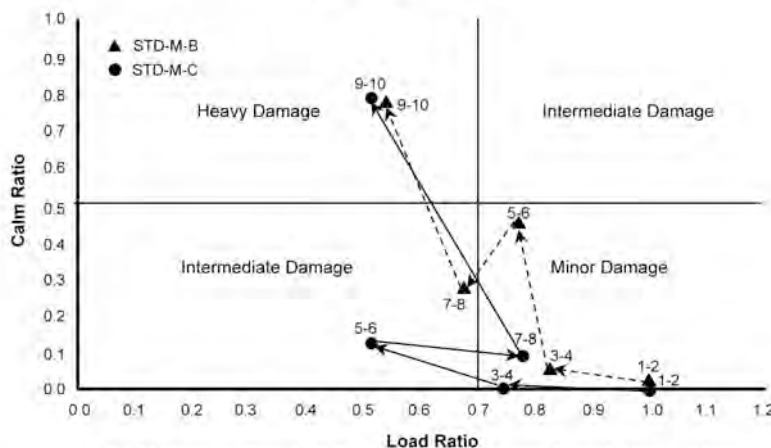
Similar to the normal weight specimen loaded in fatigue (SCC-2), for load-set 5 of SCLC-2 the Load Ratio was slightly higher than for the other two specimens. Load-set 7 was also slightly higher than the other two specimens, with load-sets 11 and 12 exhibiting decreasing values of Load Ratio. However, the Load Ratios for load-set 11 and 12 were not reduced as much as would be expected, particularly given the level of damage present at load-set 12.

Load-set 9 is a repeat of load-set 7. The results for this repeat load-set are shown in Figs 9a – c within a dashed ellipse. The effect of this repeat load-set is similar to the effect of a repeat load cycle. The magnification of the Calm Ratio for load-set 9 is pronounced for all three lightweight specimens, and is even more pronounced when calculated based on the repeat load cycle of the repeat load-set.

For evaluation of actual building or bridge structures the level of previous loading may not be available. In such cases high values of the Calm Ratio may prove useful as an indication of previous damage, provided that the values are calculated based on the initial load cycle. It is also mentioned that Load Ratio computations may be complicated by a lack of knowledge of prior load history. This is more of a consideration for bridges as opposed to buildings, because bridge load testing is typically carried out far below the design capacity of the structural system. For bridge applications an RTRI ratio approach has been proposed [17, 18]. For building systems the



a) Loading profile



b) Damage trend in Calm Ratio versus Load Ratio plot

Fig. 10. Loading profile and damage trends based on Xu [9].

situation is quite different and the full factored load is often prescribed for load testing [2]. This level of load is well beyond what the system is likely to experience in service.

Total number of hits versus cumulative energy: Another important consideration when evaluating the Calm and Load Ratios is the parameter used for computation. Several authors [6, 8, 9] have used the total number of hits for this purpose. Inspection of the data gathered from this investigation indicates that the total number of hits may not be the most appropriate parameter for either Calm or Load Ratio calculations. This can be explained by the fact that the amount of damage exerted to a material is not only a function of the number of hits. Rather, it is dependent on the amount of energy associated with the hits. Computation of the Calm Ratio based on the number of hits does not assure a complete description of deterioration and may prove to be misleading in some cases.

Figures 10a and b present the loading profile and the associated Calm Ratio and Load Ratio values obtained from reduced-scale pre-stressed girders by Xu [9]. Calm Ratio values were computed during the loading cycle of the load-sets, keeping all the points within reasonable values for their location on the Calm Ratio versus Load Ratio plot. Figure 10b, however, illustrates the erratic behavior of two specimens when subjected to the loading pattern.

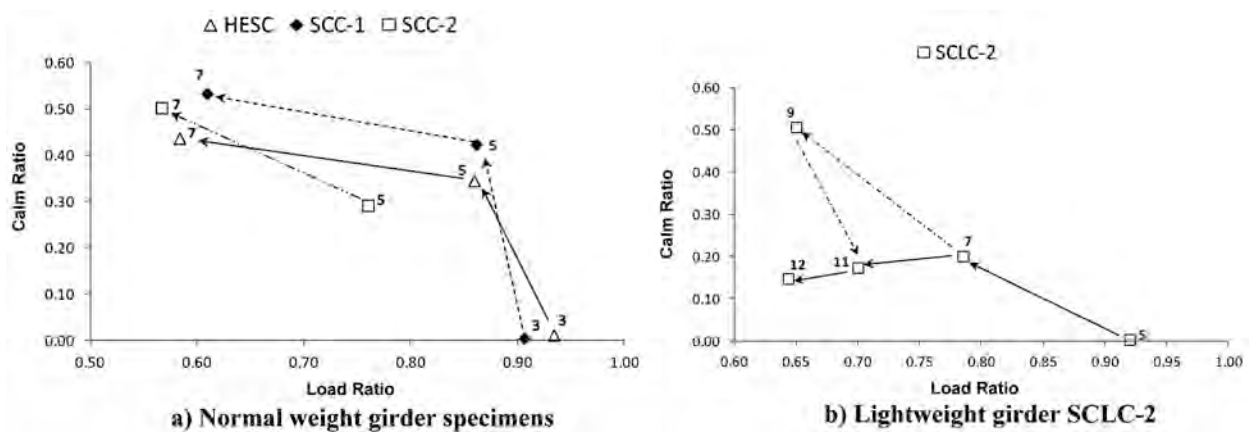


Fig. 11. Damage trends based on energy.

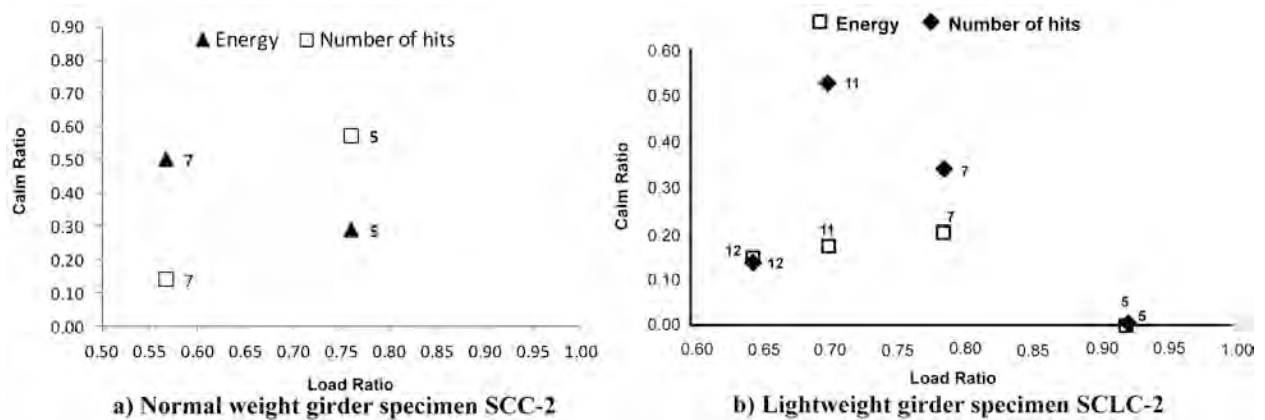


Fig. 12. Damage trends based on energy and number of hits.

These results differ from the more consistent trend exhibited for the girders described in the current investigation (Figs. 11a and b), where Calm Ratio values were computed using cumula-

tive energy in place of total hits. Figure 11b also shows the disturbance that the inclusion of a repeat load-set will cause (load-set 9 is a repeat of load-set 7). For a more direct comparison of the data gathered in this investigation, differences in the plots using cumulative energy and total number of hits are shown in Figs. 12a and b for girder specimens SCC-2 and SCLC-2, respectively.

The unstable trend of the Calm Ratio in the results reported by Xu [9] has been reported in other investigations where the number of hits has been used for computation of the Calm Ratio. Another example is shown in Fig. 13 from Colombo [8], where the Calm Ratio versus Load Ratio plot was developed for passively reinforced concrete beam specimens.

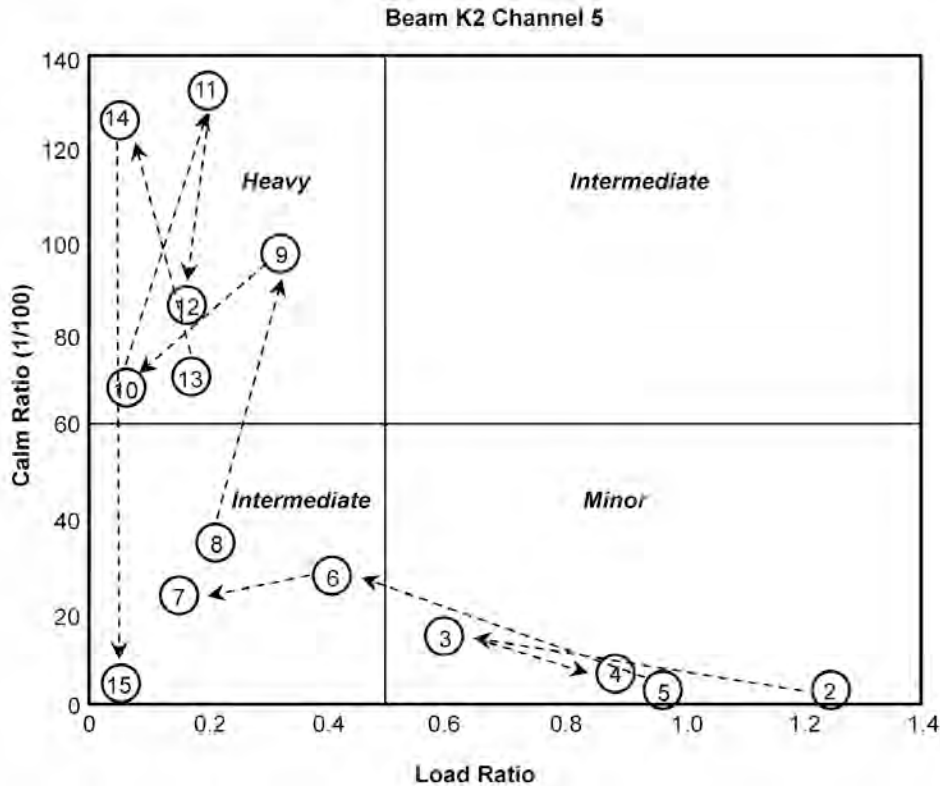


Fig. 13. Damage trend from Colombo [8] (redrawn for clarity).

Summary and Conclusions

The cyclic load test method of structural evaluation as described in ACI 437 [2] is based solely on load versus displacement behavior. Differing approaches have been proposed to incorporate AE into the CLT method of structural evaluation [7, 9, 10, 19, 20]. The objective of a combined approach is to develop a more sensitive and robust nondestructive evaluation methodology than achieved by either method alone. Only limited attention has been placed to date on AE evaluation criteria when applied within a CLT loading profile.

Results of the current study emphasize the necessity of calculating the Calm and Load Ratio values in a consistent manner when applying a CLT loading profile. The presence of repeat cycles, and repeat load-sets, can alter the behavior of both the Calm Ratio and Load Ratio. The effect of repeat load cycles is particularly strong for the Calm Ratio values for pre-stressed flexural members.

For Load Ratio versus applied load, in order to obtain a curve that varies monotonically with the accumulation of damage, the effect of repeated load-sets should be excluded from the evaluation. Regarding the Calm Ratio, repeat load cycles can produce increased values that may mistakenly result in the interpretation of a higher amount of damage than is present. The presence of repeat load cycles can also hinder the appropriate location of the damage boundaries in the Calm Ratio versus Load Ratio plot. The data obtained from the current investigation indicates that for a consistent damage assessment AE evaluation is best performed based on initial loading cycles.

The data further suggests that a more consistent evaluation can be obtained if parameters such as signal strength or energy are utilized in place of hits or counts. This is because signal strength and energy reflect the energy released by a member as both the amplitude and duration of the events are considered within these parameters. The erratic behavior in the Calm Ratio versus Load Ratio plots found in some previous investigations may be partially associated with the computation of these values based on the total number of hits.

In terms of assessment of damage with the Calm Ratio versus Load Ratio plots, the normal weight girder specimens exhibited clear indications of Minor, Intermediate, and Heavy damage and the plots corresponded to the recorded load versus displacement behavior as well as visual observations of damage. For the lightweight girder specimens, the correlation of damage as determined through load versus displacement behavior and the Calm versus Load Ratio plots was not as clear. Because very little information related to AE evaluation of lightweight concrete prestressed girders has been published, this is suggested as an area for further investigation.

References

1. Ziehl, P. (2008), "Applications of Acoustic Emission Evaluation for Civil Infrastructure," *SPIE Smart Structures and Materials and Nondestructive Evaluation and Health Monitoring*, March 9-13, San Diego, California, 9 pp.
2. ACI Committee 437 (2007), "Test load magnitude, protocol and acceptance criteria", *ACI 437.1R-07*, American Concrete Institute, Farmington Hills, Michigan.
3. Ono, K. (2010), "Application of Acoustic Emission for Structure Diagnosis", *Diagnostyka, monitoring i modernizacja eksploatowanych obiektów*, Conference proceedings, Kielce, Poland.
4. Ohtsu, M., Uchida, M., Okamoto, T., and Yuyama, S. (2002), "Damage assessment of reinforced concrete beams qualified by acoustic emission", *ACI Structural Journal*, Volume 99, No. 4, pp. 411–417.
5. JSNDI (2000), "Recommended Practice for In Situ Monitoring of Concrete Structures by Acoustic Emission", *Japanese Society for Nondestructive Inspection, NDIS 2421*, 6 pp.
6. Schumacher, T. (2008), "Acoustic Emission Techniques Applied to Conventionally Reinforced Concrete Bridge Girders", *Final Report submitted to the Oregon Department of Transportation*.
7. Barrios, F. (2010), "Acoustic emission techniques and cyclic load testing for integrity evaluation of self-compacting normal and self-compacting lightweight prestressed concrete girders", Dissertation, Dept. of Civil and Environmental Engineering, University of South Carolina, Columbia, SC.
8. Colombo, S., Forde, M., Main, I., and Shigeishi, M. (2005), "Predicting the ultimate bending capacity of concrete beams from the 'relaxation ratio' analysis of AE signals", *Construction and Building Materials*, Volume 19, pp. 746–754.

9. Xu, J. (2008), "Nondestructive evaluation of prestressed concrete structures by means of acoustic emission monitoring." Dissertation, Dept. of Civil Engineering, Auburn University, Auburn, Alabama.
10. Ziehl, P., Galati, N., Nanni, A., Tumialan, J. (2008), "In-situ evaluation of two concrete slab systems. Part II: Evaluation criteria and outcomes", *ASCE Journal of Performance of Constructed Facilities*, Volume 22, No. 4, pp. 217–227.
11. Lovejoy, St., C. (2006), "Development of Acoustic Emissions Testing Procedures Applicable to Conventionally Reinforced Concrete Deck Girder Bridges Subjected to Diagonal Tension Cracking", *Ph.D. Dissertation*, Oregon State University, Corvallis, Oregon.
12. Fowler, T.J., Blessing, J.A., Conlisk, P.J., and Swanson, T.L. (1989), "The MONPAC system", *Journal of Acoustic Emission*, Volume 8, pp. 1-10.
13. Golaski, L., Gebiski, P., and Ono, K. (2002), "Diagnostics of Reinforced Concrete by Acoustic Emission", *Journal of Acoustic Emission*, Volume 20, pp. 83-98.
14. Tinkey, B.V., Fowler, T.J., and Klingner, R.E. (2002), Texas DOT Report, FHWA/TX-03/1857-2, 108 pp.
15. Ziehl, P., Rizos, D., Caicedo, J., Colmorgan, A., Howard, R., and Barrios, F. (2010), "Investigation of the Performance and Benefits of Self-Consolidating Concrete for Prestressed Bridge Girders", *Final Report submitted to the South Carolina Department of Transportation*, 212 pp.
16. Ziehl, P., Rizos, D., Caicedo, J., Barrios, F., Howard, R., and Colmorgan, A. (2009), "Investigation of the Performance and Benefits of Lightweight SCC Prestressed Concrete Bridge Girders and SCC Materials", *Final Report submitted to the South Carolina Department of Transportation*, 182 pp.
17. Luo X., Haya H., Inaba T., Shiotani T. and Nakanishi Y. (2002), "Experimental study on evaluation of breakage in foundations using train-induced acoustic emission", Proc. Structural Engineering World Congress, Paper No. T9-1-e-3.
18. Shiotani T., Luo X., and Haya H. (2006), *Journal of Acoustic Emission*, Volume 24, pp. 205-214.
19. Liu, Z. and Ziehl, P., (2009), "Evaluation of RC Beam Specimens with AE and CLT Criteria", *ACI Structural Journal*, Vol. 106, No. 3, pp. 1-12.
20. Ridge, A., and Ziehl, P. (2006), "Nondestructive evaluation of strengthened RC beams: Cyclic load test and acoustic emission methods." *ACI Structural Journal*, Volume 103, No. 6, pp. 832–841, 2006.
21. Galati, N., Nanni, A., Tumialan, G., and Ziehl, P. (2008), "In-Situ Evaluation of Two RC Slab Systems – Part I: Load Determination and Loading Procedure", *ASCE Journal of Performance of Constructed Facilities*, **22**, No. 4, pp. 207-216.

DEPENDENCE OF AE PARAMETERS ON THE PROPAGATION DISTANCE

D. POLYZOS¹, A. PAPACHARALAMPOPOULOS¹, T. SHIOTANI²
and D. G. AGGELIS³

¹ Department of Mechanical Engineering and Aeronautics, University of Patras, Rio 26500, Greece. ² Graduate School of Engineering, Kyoto University, Kyoto 615-8540, Japan. ³ Department of Material Science and Engineering, University of Ioannina, Ioannina 45110, Greece.

Abstract

Acoustic emission (AE) technique is used to monitor the fracture process in engineering materials and structures. The pulse emitted during a cracking incidence depends on the motion of the crack tip and supplies information on the mode of active cracking. Therefore, AE data are used for classification of the dominant cracking mode. This is significant since nucleation of shear cracks generally follows tensile ones on an existing failure surface and crack characterization gives insight in the current stage of the fracture process. The differences in the microscopic motion of the crack sides for the distinct crack modes results in noticeable changes in the AE signals, concerning their shape and frequency content. However, due to inherent inhomogeneity of the materials the pulse is strongly distorted until reaching the AE sensor on the surface. This effect is accumulated with propagation distance and renders crack classification troublesome for large structures. In the present study, the Boundary Element Method (BEM) is employed and numerical simulations dealing with the propagation of AE signals generated by the loading of straight and inclined surface breaking cracks are conducted. This study includes both the generation of the pulse from a crack propagation incidence of a surface breaking crack and reception of the corresponding wave at several different positions. The relative motion of the crack sides is varied in order to simulate different crack modes, while different crack tip geometries are investigated. Waveform analysis reveals the strong dependence of AE parameters on the distance between the source crack and the receiving point, stressing out that the influence of distance is crucial and should be taken into account for successful cracking mode characterization.

Introduction

Acoustic emission (AE) is a method widely used for real time monitoring of the structural condition of different materials and structures. It is based on the elastic energy, which is released after each crack propagation incidence. This energy is transmitted through the material in the form of elastic waves and can be detected by appropriate sensors on the surface of the material [1]. The accumulated activity recorded by the sensors is indicative of the severity of cracking, since the existence of cracks is usually the prerequisite for AE generation. Certain indices based on the magnitude or the number of the AE signals has been employed successfully in the health monitoring of heterogeneous structural materials like concrete and composites [2-4]. When multiple sensors are applied, apart from the number of AE hits, significant information concerning the location of the source events can be derived based on the time delay between acquisition of the corresponding signals at different sensors [5]. This allows estimation of which part of the material needs repair, which is of paramount importance for large-scale structures.

However, there are other important aspects of the AE testing, which are based on the qualitative parameters of the received signals. It has been seen that the shape of the waveforms is indicative of the fracture type, something very important for the classification of cracks in different

materials [6-9]. Shear cracks follow tensile cracks as damage is being accumulated within the material. Therefore, the characterization of the cracking mode can act as a warning against final failure. It has been shown that tensile events are linked to higher frequency content and higher RA value (rise time/amplitude, $\mu\text{s}/\text{V}$; see Fig. 1) than shear [7, 8, 10]. This kind of classification has proven useful in laboratory conditions concerning corrosion cracking in concrete [7], fracture of cross-ply laminates [6, 9, 11], as well as discrimination between tensile matrix cracking and fiber pull-out during bending of steel-fiber reinforced concrete [12]. However, it should be kept in mind that the AE signals are elastic waves, which are scattered while propagating from the source to the sensors. The shape of the waveform will change depending on the heterogeneity of the path, either due to the constituent phases if a composite material is examined or/and due to the existence of cracks [13, 14]. Since the shape of the wave changes, it is expected that the calculation of AE parameters will be affected. This practically means that one specific event will be recorded as having different waveform shapes for sensors placed at close or further distances from the source. Therefore, the influence of the distance in the measurement of AE parameters should be studied especially in relation with standardization, which is currently being attempted for the field of concrete [10, 15].

In the present paper, the relation between the measured AE parameters and the fracture mode and propagation distance through a concrete-like elastic medium is numerically studied. Simulations are used to examine the waveform shape change due to the simultaneous propagation of distinct wave modes with different velocities on the surface. The transient waveforms are recorded at different locations to simulate different AE sensors on the surface of the material.

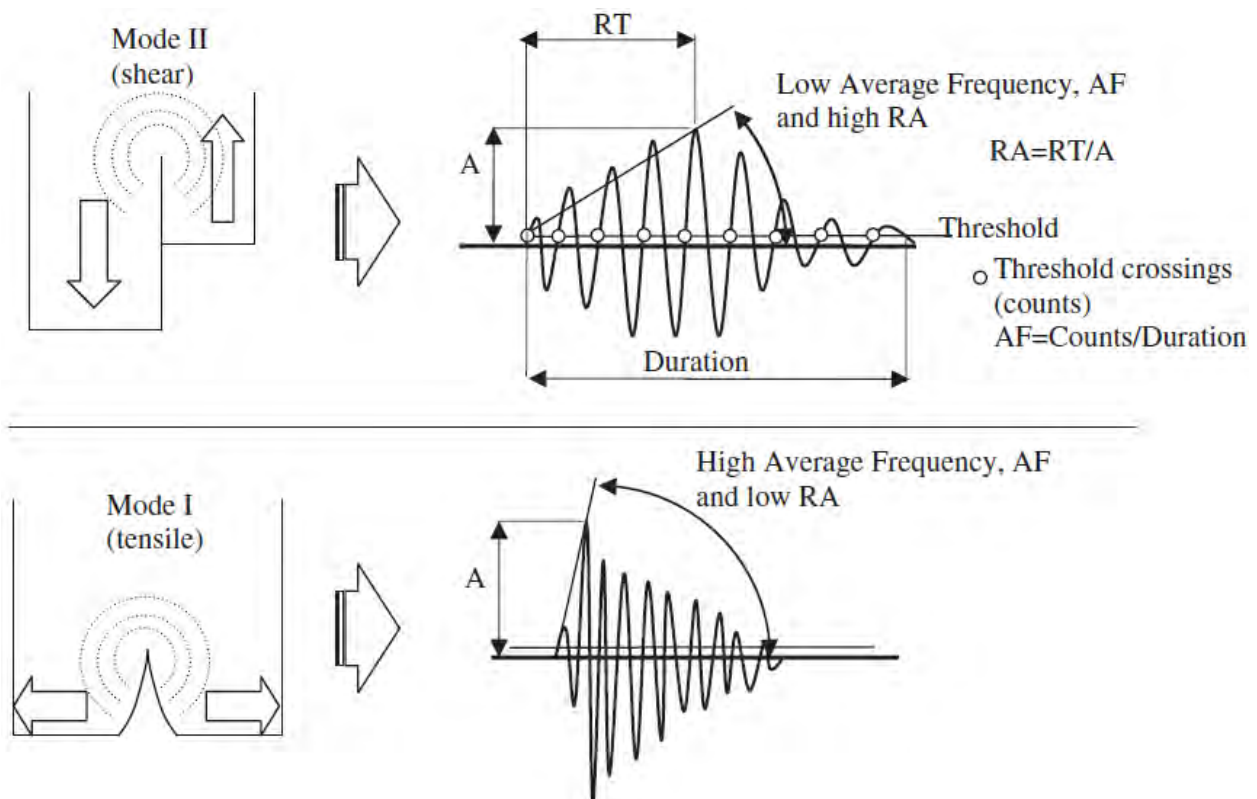


Fig. 1. Schematic view of RA and average frequency, AF.

Numerical Simulation of AE Signals via BEM

In the present section the boundary element method (BEM) is exploited for the numerical simulation of AE signals created by straight and inclined surface breaking cracks subjected to Mode I & II loading.

Consider a two-dimensional linear elastic half-space of surface S and a straight or inclined surface breaking crack subjected to Mode I or Mode II loading as shown in Fig. 2. The excitation of the tip of the crack through a suddenly applied displacement field creates AE pulses captured by equally spaced transducers located on the free surface of the considered concrete space, also depicted in Fig. 2. Applying fast Fourier transform (FFT) on the excitation signal, the above time domain problem is decomposed to a sequence of harmonic boundary value problems that can be solved with the aid of the BEM.

For each frequency ω the corresponding displacement vector \mathbf{u} satisfies the Navier–Cauchy differential equation:

$$\mu \nabla^2 \mathbf{u} + (\lambda + \mu) \nabla \nabla \cdot \mathbf{u} + \rho \omega^2 \mathbf{u} = \mathbf{0} \quad (1)$$

where λ, μ and ρ stand for the Lamé constants and the mass density, respectively, ∇, ∇^2 represent the gradient and Laplace operator, respectively and ω the excitation angular frequency. Considering the fundamental displacement tensor \mathbf{u}^* and the corresponding fundamental traction \mathbf{t}^* of the above differential equation and employing Betti's reciprocal identity, one can obtain the integral representation of the harmonic problem in the form [16]:

$$\frac{1}{2} \mathbf{u}(\mathbf{x}) + \int_S \mathbf{t}^*(\mathbf{x}, \mathbf{y}, \omega) \cdot \mathbf{u}(\mathbf{y}) dS_y = \int_S \mathbf{u}^*(\mathbf{x}, \mathbf{y}, \omega) \cdot \mathbf{t}(\mathbf{y}, \omega) dS_y \quad (2)$$

For the present problem where both the surface of the crack and the surface of the half space are traction free, i.e. $\mathbf{t}(\mathbf{y}, \omega) = \mathbf{0}$ the integral equation (2) is written as

$$\frac{1}{2} \mathbf{u}(\mathbf{x}) + \int_{S+S_1} \mathbf{t}^*(\mathbf{x}, \mathbf{y}, \omega) \cdot \mathbf{u}(\mathbf{y}) dS_y = \int_{S_2} \mathbf{t}^*(\mathbf{x}, \mathbf{y}, \omega) \cdot \mathbf{U}(\mathbf{y}, \omega) dS_y \quad (3)$$

with \mathbf{x} being the point where the corresponding displacement vector \mathbf{u} is evaluated, \mathbf{U} is the excitation displacement vector corresponding to frequency ω , S is the free surface of the half space, S_1 the traction-free surface of the crack and S_2 the tip of the crack where \mathbf{U} is imposed.

Integral equation (3) is solved numerically by discretizing S, S_1, S_2 into continuous, isoparametric, quadratic line elements, while a combination of continuous–discontinuous or partially discontinuous elements is used for corners and discontinuous boundary conditions. The truncation of the free surface is accomplished by considering that the reflected Rayleigh waves do not affect the transient signal at the observation point [17]. Collocating the discretized integral Eq. (3) at each node, one obtains a system of linear algebraic equations having the form

$$[\mathbf{H}] \cdot \{\mathbf{u}\} = \{\mathbf{b}\} \quad (4)$$

where vector $\{\mathbf{b}\}$ contains all the known displacements of the excited nodes of surface S_2 , $\{\mathbf{u}\}$ is a vector with all the unknown displacements at S, S_1 and $[\mathbf{H}]$ is a matrix comprising regular, weakly singular and hypersingular integrals all numerically evaluated through advanced integration techniques explained in [16]. The linear algebraic system (4) is solved numerically through a LU decomposition algorithm and the evaluated displacements are converted to time domain through the inverse FFT procedure.

In order to minimize the aliasing phenomena, the exponential window method proposed by Kausel and Rössset [18] is utilized, where complex frequencies with a small imaginary part of the form: $\omega_c = \omega - jc$ are used. The constant c is set equal to $0.65\Delta\omega$ where $\Delta\omega$ is the frequency step used in FFT. After numerically solving the problem in the frequency domain and then applying the inverse Fourier transform, the time response is rescaled with the aid of the exponential factor e^{ct} .

Figure 2 depicts the basic geometry including the surface breaking crack and the recording transducers. The simulation of Modes I and II was accomplished by accordingly changing the direction of the applied displacement field on the crack tip. Two different types of excitation waveforms were used, namely short (1 cycle) and long (20 cycles). The basic excitation frequency was 150 kHz. The case of slightly curved crack tips was also considered in order to explore the effect of crack geometry on the received signals. The specific material properties were $\lambda = 11$ GPa, $\mu = 17$ GPa and $\rho = 2.3$ Mg/m³, resulting in a longitudinal wave velocity of 4735 m/s.

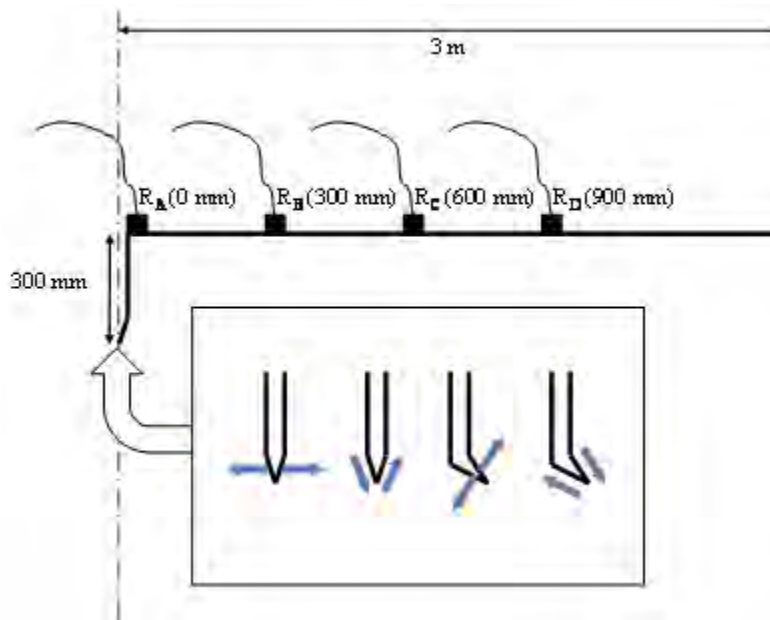


Fig. 2 Geometry of the problem solved via BEM.

Results

Influence on Waveform Shape

Two types of pulses were used for excitation: short (one cycle) and long (several cycles). The short pulse enables the separation of the different wave modes after propagation. This helps one understand wave propagation and identification of different modes and reflections that would not be possible for a long-pulse excitation. On the other hand, experimental AE signals are quite long, as also influenced by the resonance behavior of AE sensors, which limit the bandwidth, causing an increase in time domain duration. Before the main analysis of the long realistic signals is presented and analyzed, it is essential to discuss some qualitative aspects of propagation, which are clearer for the short pulse.

Figure 3a shows the waveforms captured by the four receivers after Mode I short pulse excitation on the curved crack geometry. These waveforms stand for the vertical motion of the surface nodes that correspond to each “receiver”. The initial weak burst belongs to the longitudinal

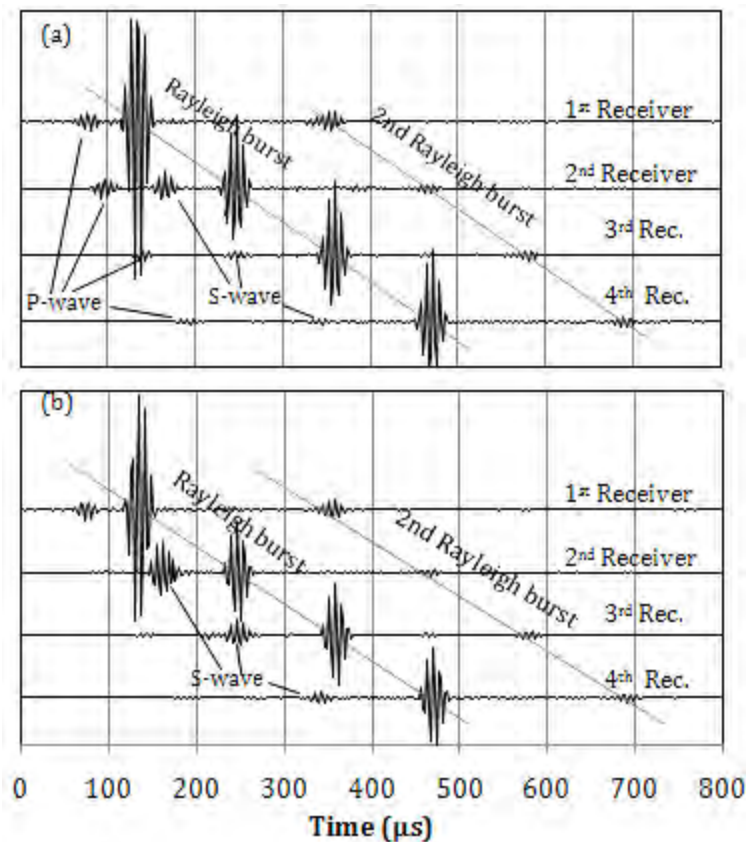


Fig. 3 Waveforms for the four receiver points after short pulse (a) mode I excitation, (b) mode II excitation in the inclined crack.

(P-) wave, which is the fastest mode and can be seen in all four waveforms. Focusing on the waveform of the first receiver, a stronger burst is obtained after 100 μs , corresponding to the Rayleigh wave that contains most of the energy after excitation. Until reaching the 1st receiver, all different wave modes travel along the crack side. A part of the energy is reflected from the surface back to the crack tip while another continues on the horizontal surface line. Therefore, the Rayleigh burst can be easily identified at the successive receivers after equal intervals of 110 μs , which is the transit time needed for the Rayleigh wave to propagate the distance of 300 mm between receivers. Another Rayleigh burst can be identified, approximately 220 μs after the first in all waveforms (Fig. 3a), due to reflection from the surface to the tip and back reflection from the tip to the surface. The 2nd Rayleigh burst is considerably weaker since in each reflection point a part of energy is converted to P- and S- wave modes. Rayleigh waves can be identified even after long propagation because of negligible spreading, since in the two-dimensional space, Rayleigh waves are limited to the surface of the material. On the other hand, P-wave suffers spreading even in two-dimensions and therefore, it can be identified only by the initial propagation and not after possible reflections. The shear wave is located between the P- and R- components for all receivers, except for the 1st, where it has still not separated from the Rayleigh, which travels at almost the same speed. On the other receivers, the S- components are well separated mainly because they travel to the receivers on a straight line, while the Rayleigh has to traverse the crack side until reaching the top surface and thus covers more distance before being felt by receivers 2 to 4. This is the reason why the delays between the Rayleigh burst at successive receivers are equal, while this is not the case for P- and S- waves.

Figure 3b shows the corresponding waveforms at the exactly same geometry (inclined crack) after shear (Mode II) excitation. The main features of the waveforms are similar to the previous case, with the main wave components recorded at the same intervals. It is seen, therefore, that in the event of a surface crack, most of the energy propagates in the form of Rayleigh waves. The mode of the source excitation seems to have only slight qualitative effect on the received waveform. However, one distinct difference between the waveforms collected after Mode I or II excitation is the proportion between P- and S- waves. In the second case (Fig. 3b, Mode II) the shear component is apparently stronger than the P-wave, which is negligible after the 2nd receiver. This shows that according to the mode of excitation the energy is reasonably translated to different modes and as a result of the different wave speeds, the shape of the acquired waveform is expected to differ.

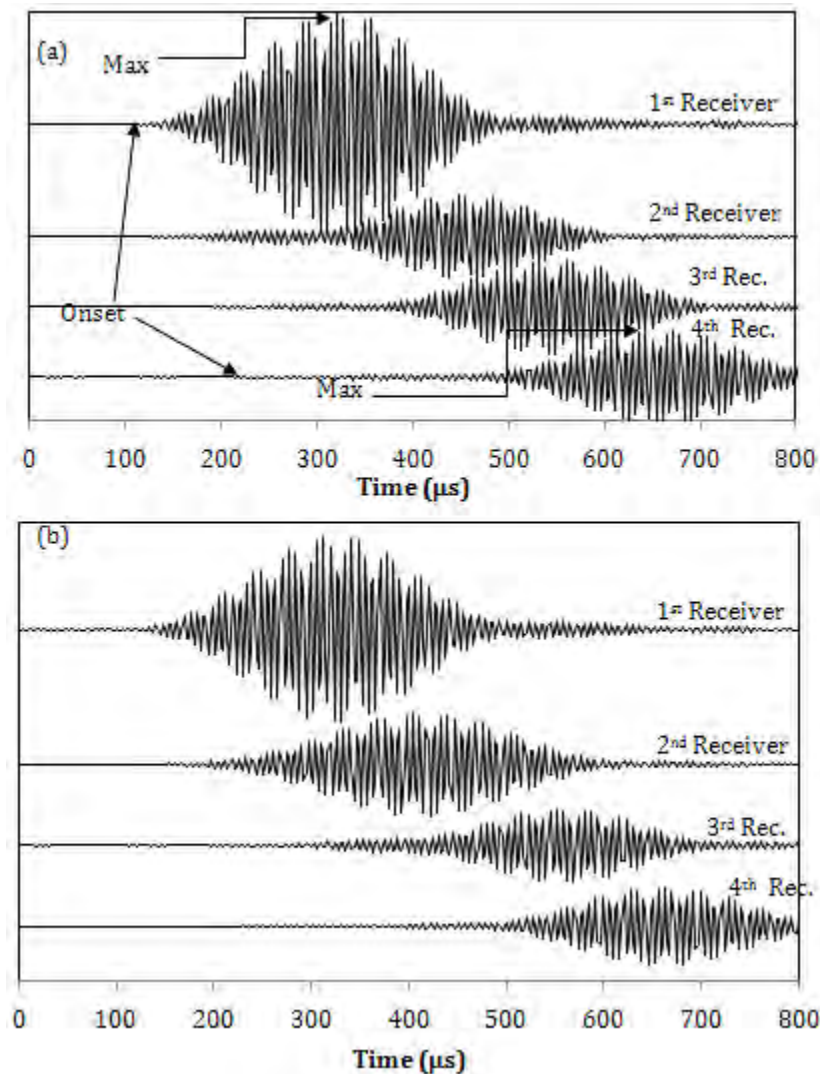


Fig. 4 Waveforms for the four receiver points after long pulse (a) Mode I excitation, (b) Mode II excitation in the inclined crack.

In order to produce realistic results and measure AE parameters as commonly done in AE practice, longer pulse excitation was applied. The excitation consisted of 10 cycles of 150 kHz in a sinusoidal envelope, in order to resemble the resonance frequency of commercially used transducers [8, 12], while other central frequencies are also applicable. The waveforms for Mode I and II excitations are seen in Fig. 4a and 4b respectively for the geometry of the inclined crack.

Seemingly there are no strong differences between the two modes. As a general comment, the different wave types are not separated and the waveform is a long burst of several cycles. One of the visible differences as the distance from the crack increases, is that the main energy of the wave envelope is translated backwards compared to the onset of the pulse (see Fig. 4a). This is mainly due to the Rayleigh component that arrives later compared to the initial P-wave and thus the calculated AE parameters shall differ considerably. In order to calculate the specific AE parameters the threshold was set equal to 2% of the maximum amplitude of each waveform, while comparisons using threshold of 5% are also conducted.

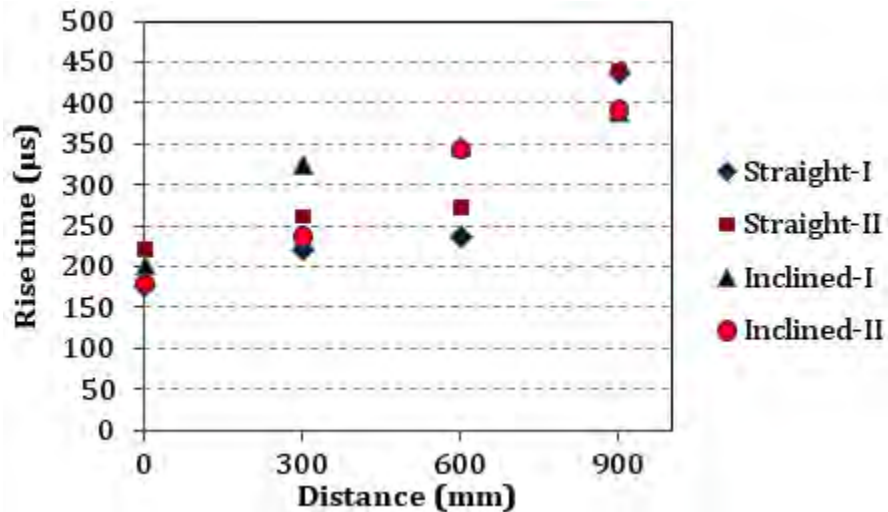


Fig. 5 Rise time vs. horizontal distance from the crack for different crack geometries and excitations and threshold 2% of maximum.

AE Parameters

Figure 5 shows the rise time of the waveforms. For all simulated cases the rise time of the waveform exhibits a steadily increasing trend with distance. RT starts at approximately 200 μs , while for the furthest receiver is calculated at 400-450 μs . This increasing trend is already indicative of the strong dependence of the AE parameters on the propagation distance to the sensors. Since RT is the delay between the time of maximum amplitude and the onset, it is confirmed that the main energy of the waveform is continuously delaying relatively to the weak P-wave component. Figure 6a shows the RA value ($RA=RT/A$) with respect to distance. In this case there is an also increasing trend vs. distance for all of the simulated cases. Concerning the excitation mode in both geometries (straight and inclined cracks), Mode II results in much higher RA even for the closest receiver. For the nearest receiver on the straight crack geometry, mode I results in RA equal to 33 $\mu\text{s}/\text{V}$, while mode II in 247 $\mu\text{s}/\text{V}$. As the wave propagates to the furthest receiver, RA for Mode II reaches 1500 $\mu\text{s}/\text{V}$ while Mode I, although increases, is limited to below 300 $\mu\text{s}/\text{V}$. This is in accordance with and confirms the experimental evidence of several recent studies, where shear cracking induces higher RA than tensile [7, 8, 10-12].

However, the cracking mode is not the unique parameter that influences RA. One other interesting outcome of the simulations that has not been noted before is that the RA values depend also on the geometry of the crack. For Mode I cracking, the straight crack results in RA lower than 300 $\mu\text{s}/\text{V}$ even for the furthest sensor, while the curved crack induces higher RA for any sensor up to 1100 $\mu\text{s}/\text{V}$. Similarly, for Mode II, the curved geometry results in RA values of more than 2500 $\mu\text{s}/\text{V}$, while for the straight crack RA does not exceed 1500 $\mu\text{s}/\text{V}$. The above shows that the geometry of the crack is also important and that a slight inclination of the crack

may interfere with the recorded pulse. The significance of this dependence to distance is that RA values of different mode waveforms overlap; as an example a shear event (Mode II) on the straight crack measured by the closest receiver (horizontal distance of 0 mm) exhibits an RA of 250 $\mu\text{s}/\text{V}$. This is approximately the RA of Mode I excitation on the same geometry measured at the distance of 900 mm. Therefore, a tensile event may be misclassified as shear if the waveform is captured at a long distance from the source. This may well be the case in-situ where long separation distances between sensors are usually applied in order to cover as much volume of the structure as possible with a limited number of sensors. In laboratory, still the influence should not be negligible, since the values of RA change much for 300 mm. In order to check the influence of threshold, Fig. 6(b) shows the RA vs. distance for a different level of threshold, specifically, 5% of the maximum amplitude. Since the threshold is higher, the first few cycles of the waveform may not exhibit threshold crossings. Therefore, RA is in any case lower than the corresponding value measured with lower threshold. This shows that the selection of the threshold should always be taken into consideration because it moderately influences the calculated values. Nevertheless, since contemporary AE equipment can record the whole waveform, analysis with any desired threshold is possible at post-processing stage.

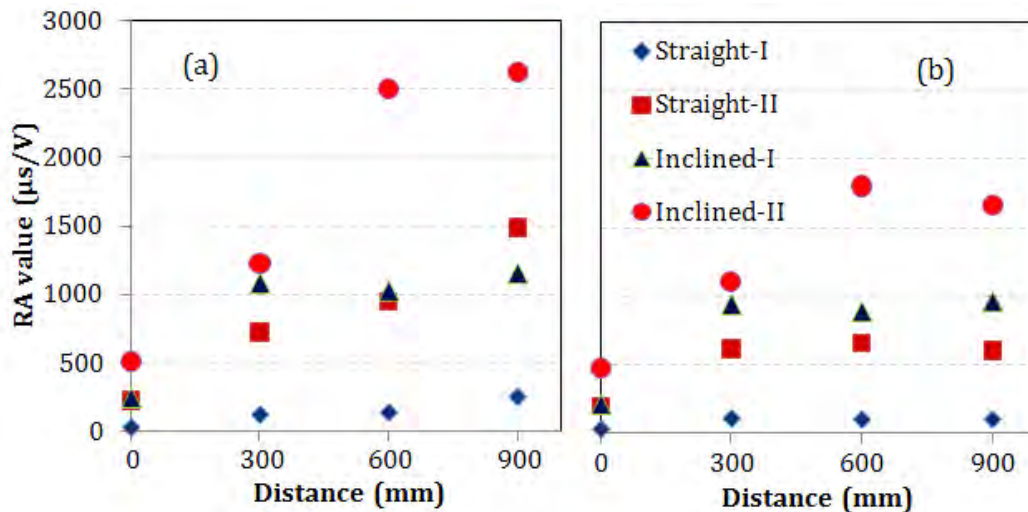


Fig. 6. RA value vs. horizontal distance from the crack for different crack geometries and excitations and threshold (a) 2% of maximum and (b) 5% of maximum amplitude.

In order to evaluate the RA dependence on distance, the results are presented normalized to the RA value of the 1st receiver in Fig. 7. For all simulated cases a strong increase is depicted of the order of 5 to 8 times. This shows that any classification scheme should definitely incorporate the distance information since the measured values that will be used to characterize a cracking event may well differ as measured by adjacent sensors. As an example, it is mentioned that an increase of approximately 4 to 10 times has been measured for the transition between tensile matrix cracking and fiber pull out in steel-fiber reinforced concrete [12], roughly from 500 $\mu\text{s}/\text{V}$ to 2000 $\mu\text{s}/\text{V}$. It is reasonable, therefore, that a shift by a factor of 5 or more due to propagation distance would mask the change due to the source crack mode.

Average frequency, AF, is another AE parameter that has been related to the cracking mode. It is calculated as the ratio of the threshold crossings over the duration of the waveform. Figure 8a shows the measured AF values vs. distance. The results do not show any clear trend as a function of distance, the cracking mode or the geometry. In a certain extent, this is reasonable since the geometry corresponds to undamaged material, without any cracks that are strong scatterers of

elastic waves. In case distributed cracks are present in the matrix, the effect of waveform distortion should be more evident and the frequency would be downshifted [19].

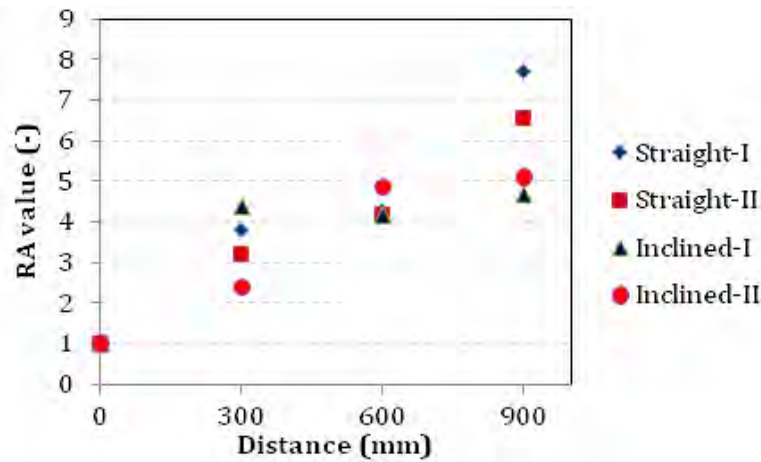


Fig. 7 Normalized RA value vs. horizontal distance from the crack for different crack geometries and excitations at threshold of 2% of maximum.

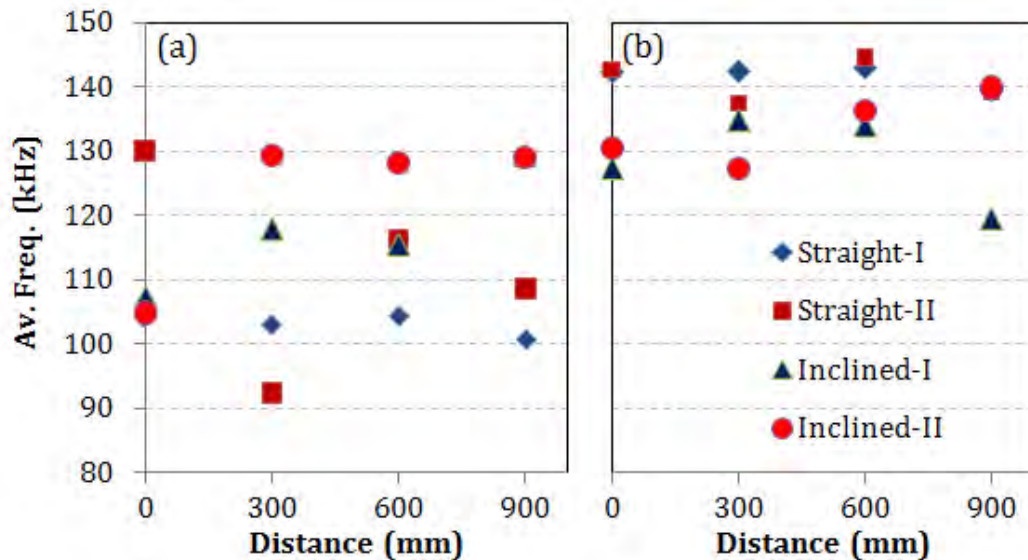


Fig. 8. Average frequency vs. horizontal distance from the crack for different geometries and excitations and threshold (a) 2% and (b) 5% of maximum.

As mentioned earlier, most of the AE parameters are threshold dependent. In order to examine the influence of threshold in the calculation of AF, another threshold of 5% of maximum amplitude was applied. The results are shown in Fig. 8b, again with no specific correlation to distance or mode. The values of AF for the more sensitive lower threshold (2%, Fig. 8a) are slightly lower due to the inclusion of the initial and final weaker parts of the waveform. There, several cycles after the 1st threshold crossing do not cross the threshold and do not “qualify” as crossings (counts), leading to lower frequency measurement. This comparison can be seen in Fig. 6 concerning the RA value. When the higher threshold of 5% is applied, the qualitative conclusions do not change, see Fig. 6b; the values are just translated to lower levels. However, lower and therefore more sensitive threshold is more adequate as it results in wider range of values and stronger discrepancies between the different cases, which allows better characterization. Low ambient noise is crucial therefore in order to allow application of a low and sensitive threshold.

Conclusions

This study presents wave propagation simulations inside an elastic medium after a propagation incidence in a surface-breaking crack. It aims at the better understanding of the effect of different conditions in the calculation of AE parameters. This is important even for small scale applications, since geometry imposes strong influence on the waveforms even for small distances. Consequently, starting from laboratory conditions, and in order to expand the application of AE classification schemes to real structures, the dependence of AE parameters on distance should be further studied. The received signals are compared regarding their original cracking mode (tensile or shear), surface crack geometry (straight or curved), as well as the propagation distance to the sensor, while several other parameters like distributed damage content and microstructure should also be studied in the future. Shear excitation results in higher RA values, as numerous experimental studies suggest. Additionally, the crack geometry seems to strongly influence the shape of the waveforms since higher RA is measured for the curved crack tip, compared to the straight one. The RA value follows an increasing trend with propagation distance, attributed mainly to the lower velocity of Rayleigh waves, which contain most of the energy of the excitation. This increasing trend is strong and should be certainly taken into account in crack classification schemes, since for long distances even “tensile” waveforms would be mistaken as “shear”. The importance of a sensitive low threshold is also depicted, while the frequency content does not seem to crucially depend on the distance since the attenuation was not included.

References

- [1] Grosse, C. U. and Ohtsu, M. (2008). *Acoustic Emission Testing*, Springer, Heidelberg.
- [2] Kurz, J. H., Finck, F., Grosse, C. U., and Reinhardt, H. W. (2006). “Stress Drop and Stress Redistribution in Concrete Quantified Over Time by the B-Value Analysis,” *Structural Health Monitoring*, **5**: 69-81.
- [3] Aggelis, D.G., Shiotani, T., Momoki, S., and Hiram, A. (2009). “Acoustic Emission and Ultrasound for Damage Characterization of Concrete Elements”, *ACI Materials J.*, **106**(6): 509-514.
- [4] Ono K., Mizutani Y., Takemoto M. (2007). “Analysis of acoustic emission from impact and fracture of CFRP laminates”, *Journal of Acoustic Emission*, **25**, 179-186.
- [5] Grosse, C., Reinhardt, H., and Dahm, T. (1997). “Localization and classification of fracture types in concrete with quantitative acoustic emission measurement techniques”, *NDT&E Int.*, **30**(4): 223-230.
- [6] Anastassopoulos, A.A., and Philippidis, T.P. (1995). “Clustering methodology for evaluation of acoustic emission from composites”, *Journal of Acoustic Emission*, **13**(1/2): 11-22.
- [7] Ohtsu, M., and Tomoda, Y. (2007). “Phenomenological model of corrosion process in reinforced concrete identified by acoustic emission”, *ACI Mater J.*, **105**(2): 194–200.
- [8] Shiotani, T., Ohtsu, M., and Ikeda, K. (2001). “Detection and evaluation of AE waves due to rock deformation”, *Construction and Building Materials*, **15**(5-6): 235-246.
- [9] Mizutani Y., Nagashima K., Takemoto M., Ono K. (2000). “Fracture mechanism characterization of cross-ply carbon-fiber composites using acoustic emission analysis”, *NDT&E International* **33**: 101–110.
- [10] Ohtsu M. (2010). Recommendation of RILEM TC 212-ACD: acoustic emission and related NDE techniques for crack detection and damage evaluation in concrete, Test method for classification of active cracks in concrete structures by acoustic emission. *Materials and Structures*, **43**(9): 1187-1189.

- [11] Aggelis, D.G., Barkoula, N.M., Matikas, T.E., and Paipetis, A.S. (2010). “Acoustic emission monitoring of degradation of cross ply laminates”, *Journal of the Acoustical Society of America*, **127**(6): EL246-251.
- [12] Aggelis, D.G., Soulioti, D.V., Sapouridis, N., Barkoula, N.M., Paipetis, A.S., and Matikas, T.E. (2011). “Acoustic emission characterization of the fracture process in fibre reinforced concrete”, *Construction and Building Materials*, **25**: 4126-4131.
- [13] Aggelis, D.G. (2009). “Numerical simulation of wave propagation in material with inhomogeneity: inclusion size effect”, *NDT&E Int*, **42**: 558-563.
- [14] Aggelis D. G., Shiotani T., Papacharalampopoulos A., Polyzos D. (2011). “The influence of propagation distance on elastic waves as measured by acoustic emission parameters”, *Structural Health Monitoring*, doi:10.1177/1475921711419992.
- [15] RILEM Technical Committee MCM. On-site measurement of concrete and masonry structures by visualized NDT. (<http://www.rilem.net/tcDetails.php?tc=MCM>).
- [16] Polyzos D., Tsinopoulos S. V., Beskos D. E. (1998). “Static and Dynamic Boundary Element Analysis in Incompressible Linear Elasticity”, *European Journal of Mechanics A/Solids*, **17**(3): 515-536.
- [17] Kattis S. E., Polyzos D., Beskos D. E. (1999). “Vibration Isolation by a Row of Piles Using a 3-D Frequency Domain BEM”, *International Journal of Numerical Methods in Engineering*, **46**: 713-728.
- [18] Kausel E., Rössset J. M. (1992). “Frequency domain analysis of undamped systems”, *Journal of Engineering Mechanics ASCE*, **118**: 721–734.
- [19] Aggelis, D. G., and Shiotani, T. (2007). “Experimental study of surface wave propagation in strongly heterogeneous media”, *Journal of the Acoustical Society of America*, **122**(5): EL 151-157.

IDENTIFYING QUASI-BRITTLE FRACTURE BY AE AND DIGITAL IMAGING

QING LIN¹ and JOSEPH F. LABUZ²

¹Department of Energy and Resources Engineering, College of Engineering, Peking University, Beijing, P. R. China. ²Department of Civil Engineering, University of Minnesota, Minneapolis, MN 55455, USA

Abstract

Fracture of rock and other quasi-brittle material exhibits significant microcracking, so the identification of crack growth is well suited for AE, although interpretation of detailed features often relies on supplemental measurements or analyses. By recording the time histories and determining the arrival time of the P-wave in each waveform, it is possible to locate an AE event in a laboratory specimen with an error of a few mm. Opening and mixed-mode fracture experiments were performed within a closed-loop, servo-controlled testing system using a three-point bend specimen with a central or an eccentric notch, resulting in a combination of Mode I and II stress intensity factors (K_I and K_{II}). The experimental setup included AE monitoring and digital image correlation (DIC), a particle tracking method that can be used to determine displacements of a speckle pattern in a digital image. The matching process is the identification, between two images, of a small area called a subset, which has a unique intensity pattern. Cross-correlation with a fast Fourier transform method was used to search the intensity values in a region of interest such that the displacement vector was obtained for each subset. A cluster of microcrack locations clearly identified the fracture and its growth. Complimentary analyses from DIC provided (1) a detailed position of the crack tip, and (2) a zone of increased tangential displacement but no differential movement near the crack tip, suggesting that the process zone in “slight mixed-mode loading ($K_{II}/K_I = 5\%$) is governed by Mode I opening.

Keywords: Digital image correlation (DIC), mixed-mode fracture, process zone, quasi-brittle material.

Introduction

Fracture of a quasi-brittle material such as rock generates microcracking, clearly identified by AE [1]. Indeed, the existence of a process zone is often directly related to the locations of AE, and crack growth can be monitored by tracking the event hypocenters. Furthermore, numerical analyses of fracture experiments suggest that AE locations are associated with the process zone [2].

Opening and mixed-mode fracture tests were performed using a three-point bend specimen with either a center or an off-center (eccentric) notch within a closed-loop, servo-controlled load frame. A mixed-mode loading condition was achieved by changing the notch position along the tensile region of the beam, resulting in different combinations of Mode I and II stress intensity factors. The experimental setup included AE monitoring with eight sensors at known positions, and digital image correlation (DIC) with a charge-coupled device (CCD) camera and a corresponding image acquisition system. The resolution of measurements from AE is on the order of mm for the laboratory experiment, and the locations are three-dimensional. In contrast to AE, DIC, with displacement accuracy of a few microns, provides a detailed picture of the

fracture process by determining the displacement fields. However, a limitation of DIC, at least with the use of surface photographs, is the two-dimensional nature of the observations, whereas AE gives information through the volume. Thus, the two techniques are complimentary in the study of rock fracture.

Background

AE locations

A common type of source location algorithm involves the arrival time of the P-wave [3]. Microseismic activity due to a change in stress or environment is recorded by each sensor with a known position at a given time. From the relative arrival times of the P-wave and a known (separately measured) P-wave velocity of the material, the event hypocenter can be determined with a minimum of five sensors. The problem contains four unknowns: the spatial coordinates x , y , z of the event and the time t , at which the event occurred, but a fifth sensor (or other information) is needed to remove ambiguities arising from the quadratic nature of the distance equation. Because some error is associated with arrival-time detection of low amplitude signals and with the P-wave velocity model, the number of sensors should be increased so that the location problem becomes over-determined. Then an algorithm can be developed whereby the error is minimized to obtain a best-fit type of solution, and statistical methods can be used to evaluate the goodness of the fit.

The distance r_i between the source and the i^{th} sensor is related to the P-wave velocity c_P by

$$r_i = c_P(t_i - t) + \varepsilon_i \quad (1)$$

where t = time at which the event occurs, t_i = arrival time at the i^{th} sensor, and ε_i = residual of computed distances. From equation 1, it can be seen that a time shift does not affect the source location, so an arbitrary time base can be selected. The travel distance r_i can be expressed by the unknown source coordinates (x, y, z) and the known sensor coordinates (x_i, y_i, z_i) by

$$r_i = \sqrt{(x_i - x)^2 + (y_i - y)^2 + (z_i - z)^2} \quad (2)$$

The sum of the squares of the residuals ε_i can be written

$$I = \sum_{i=1}^N \varepsilon_i^2 \quad (3)$$

where N = the number of sensors. The unknowns x , y , z and t can be determined using a least-squares method by minimizing I . However, the equations are nonlinear in the source coordinates x , y , z , so the minimization is carried out numerically using the Levenberg-Marquardt algorithm. The first estimate of x , y , z is obtained by a linearization of the equations [4].

Digital Image Correlation (DIC)

DIC refers to a group of non-contacting approaches that can extract full-field displacements through imaging analysis, based on the acquired digital photograph of an object [5, 6]. The determination of displacement relies on matching a subregion that has a unique intensity pattern between the two images. This subregion, named a subset, acts as a target during the matching process. Generally, a subset is small as compared to the corresponding specimen surface, such that it is not practical to search the whole field to find a subset. Also, the displacements involved in the measurement are generally small too, so it is not necessary to examine the whole image to find it. Thus, a relatively larger area surrounding a subset, named the region of interest (ROI), can serve as a domain for the identification of the subset.

For DIC processing, two digital images are selected, where the image before deformation is called the reference image and the image of the deformed surface is called the objective or current. Based on the prepared speckle pattern of the specimen surface or simply the natural surface characteristics, the size of the subset and corresponding ROI are selected, as shown in Fig. 1. The purpose of DIC is to correlate the original and displaced subsets through the best matching of the intensity patterns. In other words, if the intensity patterns of the two subsets in the reference and objective images are best matched, the two subsets are considered the same, before and after deformation.

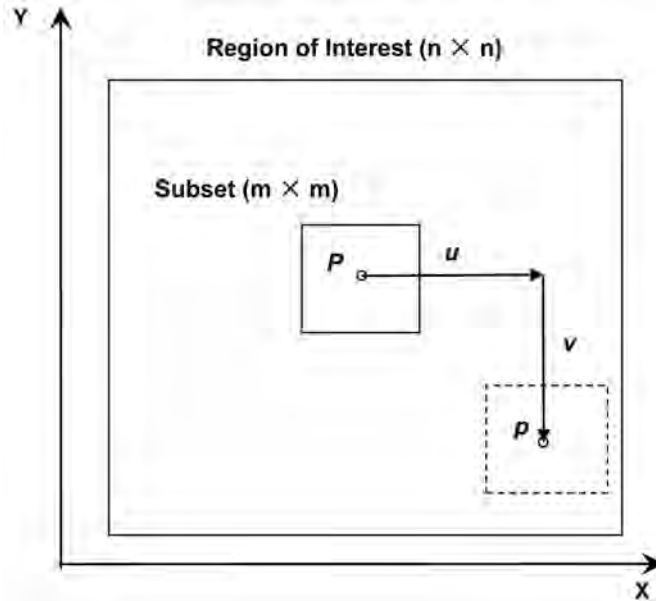


Fig. 1. Displacement (u and v) of a subset in the region of interest.

Figure 1 shows the subset and ROI within the reference image, and the original subset is at the center of ROI at position $P(X, Y)$. The intensity values that are located at position P can be represented as

$$I(P) = I(X, Y) \quad (4)$$

After deformation, point P is displaced to position p and the intensity values are changed to

$$I'(p) = I'(X + u, Y + v) \quad (5)$$

To find the best match of the two subsets, cross-correlation with a fast Fourier transform (FFT) method is used to search the intensity values in the ROI. The cross-correlation function R is defined as the two-dimensional spatial convolution of I and I' with the separation vector s in the correlation plane:

$$R(s) = \int I_1(P) I'(P + s) dP \quad (6)$$

There is a sharp peak of the cross-correlation function on the correlation plane. For a given subset of a pattern involving several speckles, the peak of the cross-correlation $R(s)$ will reach a maximum in the ROI under the condition $\vec{s} = \vec{u}$. Actually, this highest peak in the correlation plane represents the most probable match of the subset between reference and current images. Note that the principle of correlation-based DIC determines the average displacement of a small group of speckles that form a unique speckle pattern within the subset, rather than determination of the displacement of an individual speckle [7]. The DIC processing divides a digital image into subsets. Then, the cross correlation is calculated over all subsets, such that one displacement vector is obtained for each subset. A full-field displacement within the image is determined through assembly of the displacement vectors.

Experimental Procedure

A simple testing approach to achieve opening or mixed-mode fracture is a beam under three-point bending (Fig. 2), with a center ($\beta = 0\%$) or off-center ($\beta = 30\%$) notch, where the eccentricity factor β is the normalized distance, with respect to the half-span, from the centerline. The nominal size of the beams were height $H = 60$ mm, span $S = 147$ mm, and thickness $B = 26$ mm; one notch length was used, $a/H = 0.1$, with $\beta = 0$ or 30% . Crack initiation and propagation were controlled with a closed-loop, servo-hydraulic system and crack mouth opening displacement (CMOD) as the feedback signal. The sedimentary rock used for testing, Berea sandstone, consists of uniformly sized grains ranging from 0.1 – 0.8 mm, with an average grain size of 0.2 mm. For the material tested, the P-wave velocity measured perpendicular to bedding (natural layering) was 2160 m/s and parallel to bedding it was 2290 m/s; the rock is anisotropic, but only slightly (less than 10%), meaning that the ray direction of the P-wave can be approximated by the wave front normal, or that the group and phase velocities are approximately the same.

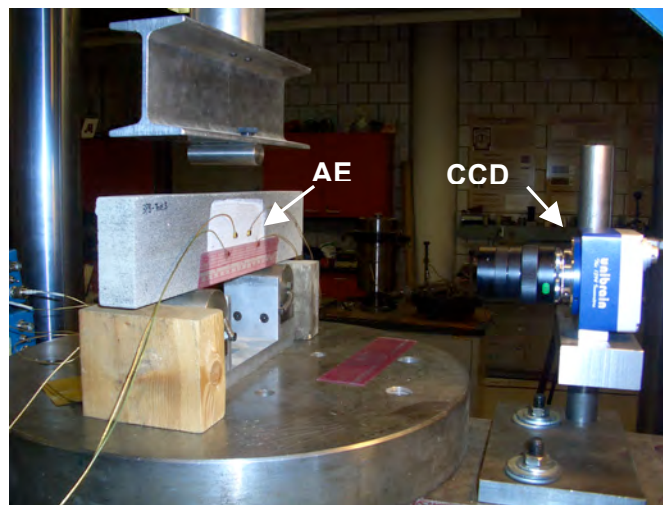


Fig. 2. Experimental configuration.

Eight piezoelectric transducers (Physical Acoustics model S9225), four on each side, were glued to a beam to cover a region of approximately 40 mm in radius surrounding the notch (Fig. 2). The AE signals were recorded by a computer automated measurement and control data acquisition system, equipped with four DAQ cards (National Instruments model PCI-5112). Each card has two individual 8-bit analog-to-digital converters, and a sampling rate of 20 MHz was set to record AE signals that are conditioned by bandpass filters from 0.1 – 1.2 MHz and 40dB gain. The transducers have a diameter of approximately 3 mm, with the frequency response from 0.1 – 1 MHz. All channels were triggered when the signal amplitude exceeded a threshold on the anchor sensor. A program coded with LabView controls the signal acquisition over a 200- μ s window, with a 100- μ s pre-trigger.

An isotropic velocity model was assumed, even though the rock possesses slight anisotropy. An “average” velocity measurement was performed on the specimen before it was tested, so that the sensors were attached in exactly the same way as for the experiment. An artificial AE event was produced on the surface of the specimen by breaking a 0.5-mm pencil lead at a marked location, and this was repeated a number of times. The first arrivals were then determined for these signals and the velocity was varied until the event locations matched, with minimum error, the known coordinates of the artificial events.

One surface was selected to produce the speckle pattern for the image matching (Fig. 3). To achieve a random pattern of speckles, the general procedure of preparation is (1) lightly coat the specimen surface with white paint; (2) after the white paint is dry, overspray the coated surface with a dark mist by a spray paint; (3) continue misting and re-misting until the speckle pattern is unique. A charge-coupled device (CCD) digital camera is used to acquire the digital images (Fig. 2), specifically a Unibrain (San Ramon, CA) Fire-I 810 IEEE-1394 CCD camera with 1600×1200 effective square pixels in combination with a Computar lens (Model M3Z1228MP, Commack NY) with manual control of aperture, focus, and zoom. The fastest rate the camera could acquire digital images is 15 frames/s. The camera is connected to the computer by an IEEE-1394 or “firewire” cable, which is a standardized specification that allows for data transfer speed of up to 400 Mb/s. The image acquisition toolbox inside *Matlab* was used as the control software to acquire the digital images.

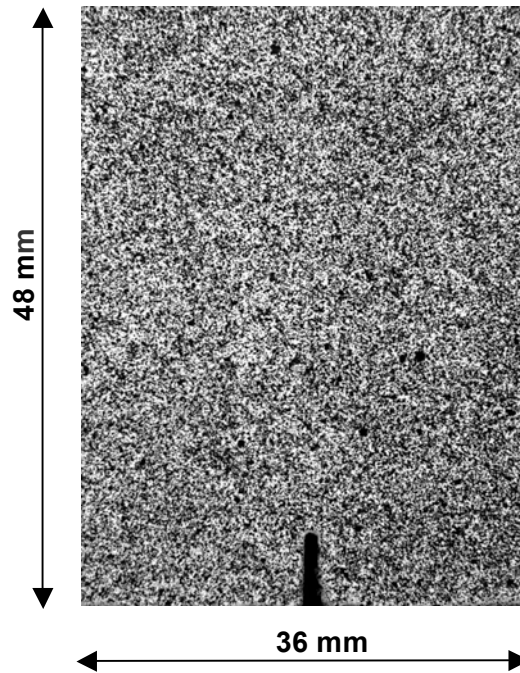


Fig. 3. Digital image of the speckle pattern.

The matching process was performed on intensity values of the digital images, and the unit of measure from the computational analysis is pixel-based. Thus, a magnification factor M is introduced to transform the results from the digital image to the physical dimension on the specimen surface:

$$u = Mu^D \quad \text{and} \quad v = Mv^D \quad (7)$$

where M is a constant magnification factor associated with the experimental setup, which is largely dependent on the digital camera; u^D and v^D are the pixel-based displacements from the image analysis. The magnification factor relates a physical dimension on the specimen surface to a corresponding dimension on the digital image. Different magnification factors can be obtained by the adjustment of lens magnification and/or the camera position. However, since the CCD array of the digital camera is fixed (1200×1600), there are limitations in setting M because of the importance of the field of view. Since the height of the specimen was about 60 mm, $M = 30.0 \mu\text{m}/\text{pixel}$ was selected, with the observation area of $36 \times 48 \text{ mm}$ (Fig. 3).

The other important parameter for the image matching process is the subset size, where it is optimal to have 8 – 10 speckles inside the subset and a balance of intensity distribution between

the speckles and background [6]. With the surface preparation producing speckles 100 – 200 μm in diameter and $M = 30 \mu\text{m}/\text{pixel}$, the speckle size on the image ranged from 3×3 to 7×7 pixels. Thus, the subset was selected to be 20×20 pixels or a 0.6 mm square.

Identification of Fracture

Mode I fracture

Using CMOD as the feedback signal, fracture propagation can be well controlled by the servo-hydraulic system even though crack growth is unstable. The results are presented at increments of post-peak load, both for AE locations and incremental displacement contours (AE or displacement measured between two load levels).

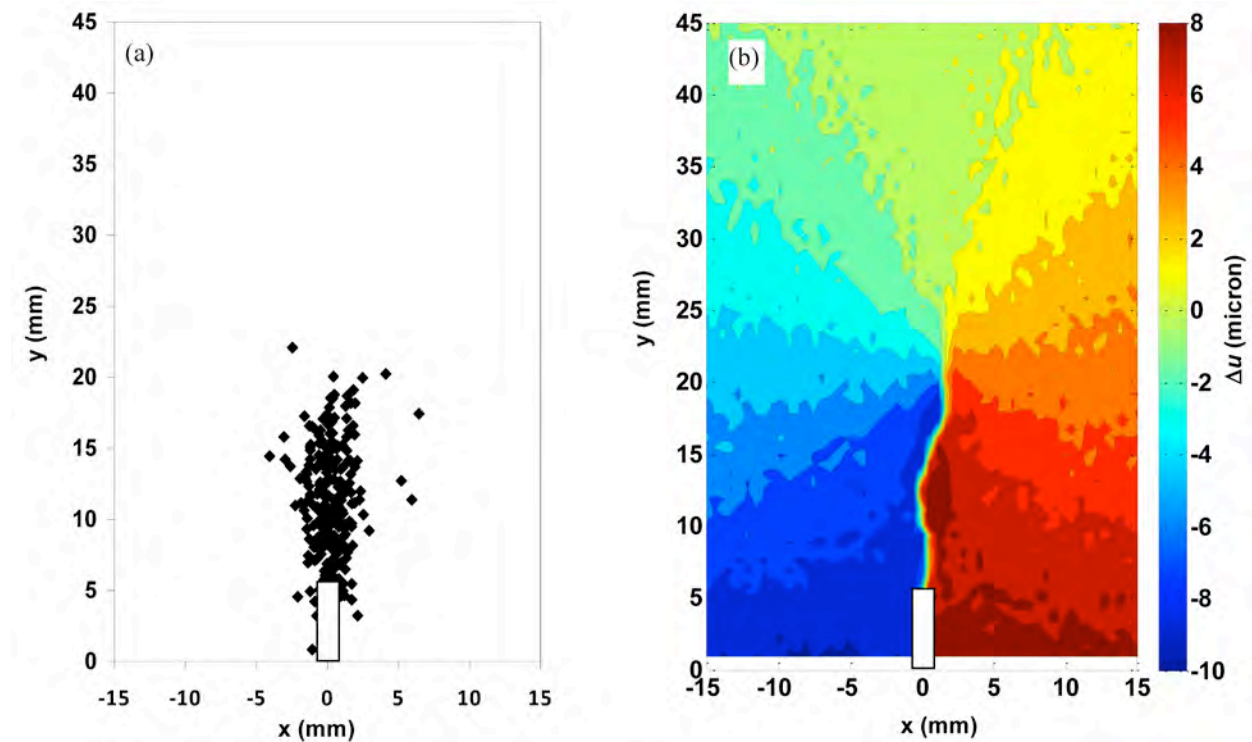


Fig. 4. Mode I fracture test of specimen CN-1: 95-90% of peak load. (a) AE locations. (b) Incremental horizontal displacement contours Δu .

Figure 4a shows the post-peak AE locations from 95–90% of peak load during crack propagation for specimen CN-1 with a center notch. A clustering of AE is clearly identified along the entire fracture developed by Mode I loading; AE extend from the notch $y = 6 \text{ mm}$ to the position $y = 20 \text{ mm}$. The AE locations are 3D, representing damage processes through the thickness, but for convenience, the locations are projected on the viewing plane; the zone width is about 5 mm, although it is influenced by crack tortuosity. Figure 4b displays the incremental horizontal displacement Δu contours in the same post-peak stage of loading (95 – 90% of peak load). Because of the loading configuration, the horizontal displacement exhibits a symmetric pattern and the center vertical cross section $x = 0 \text{ mm}$ represents the line of symmetry. The Δu contours merge at $x = 0 \text{ mm}$, $y = 20 \text{ mm}$, which indicates the tip of a displacement discontinuity. For example, a few mm below the tip, the incremental opening displacement is about $8 \mu\text{m}$, *i.e.* $-4 \mu\text{m}$ to the left and $+4 \mu\text{m}$ to the right. As indicated by the AE activity, it can be interpreted that cohesive traction was acting in this region [2].

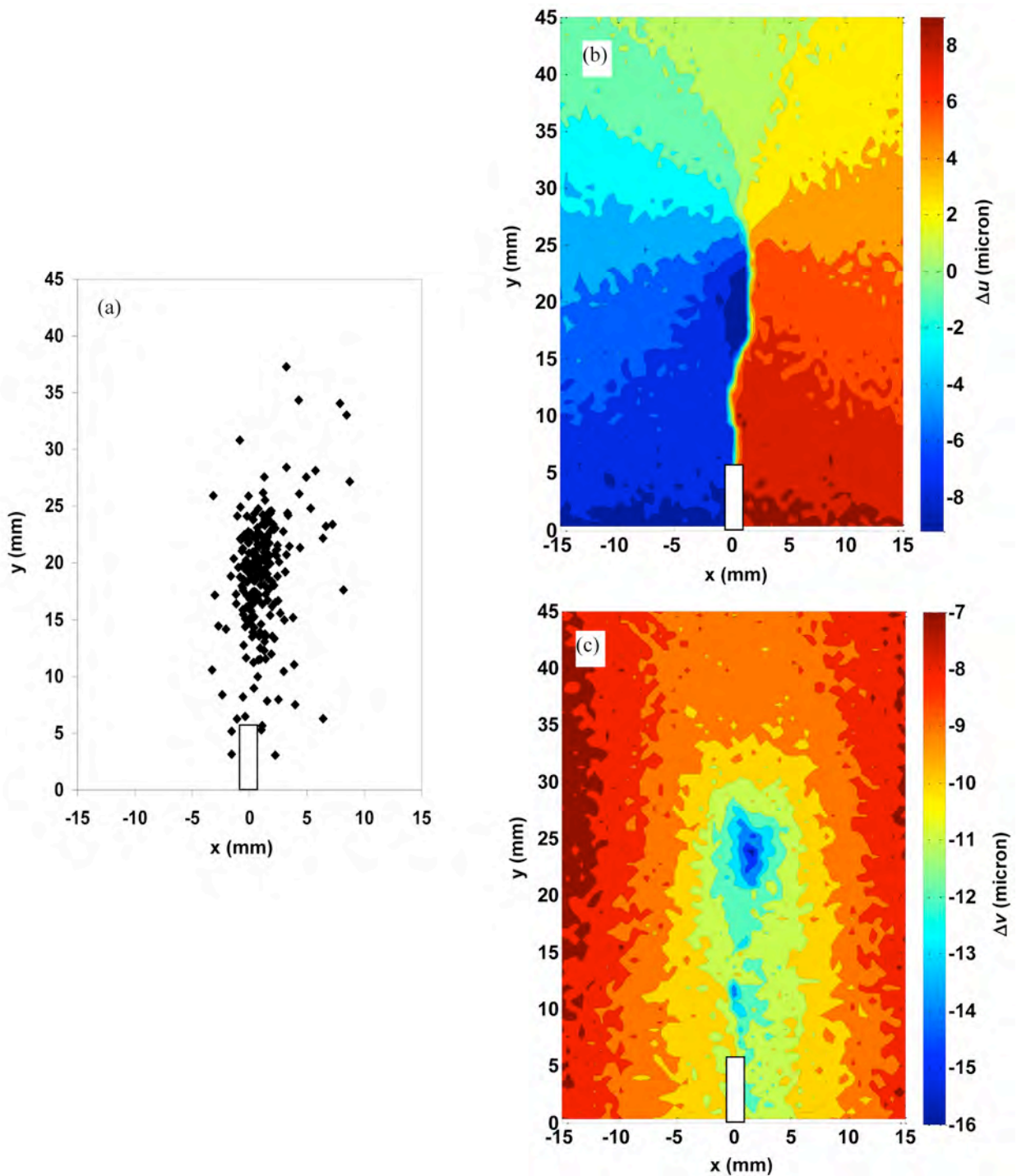


Fig. 5. Mode I fracture test of specimen CN-1: 80-70% of peak load. (a) AE locations. (b) Incremental horizontal displacement contours Δu . (c) Incremental vertical displacement contours Δv .

With an increase of CMOD, the crack propagated as the applied load reduced. Figure 5 shows the AE locations and the incremental displacement contours for 80 – 70% of post-peak load. Note that 85% of AE locations were from a region between $y = 10$ mm and $y = 25$ mm along the symmetry line, and the width of the region is about 5 mm (Fig. 5a). Very few AE events were observed at positions of $y < 10$ mm, suggesting that this region is traction-free [2]. The incremental horizontal displacement contours indicate the tip at position $x = 0$ mm, $y = 25$

mm (Fig. 5b). An interesting observation concerns an island of incremental vertical displacement of $\Delta v = -13 \mu\text{m}$ near the region of the crack tip, which may be associated with the process zone (Fig. 5c); this vertical displacement can be thought of as tangential displacement of the crack, which displays no differential movement, meaning that $K_{II} = 0$, an obvious result for the symmetric loading.

Mixed-mode fracture

Specimen EN-1 with an eccentric notch of $a/H = 0.1$ and $\beta = 30\%$ exhibits mixed-mode fracture, where sliding displacement occurs along (a portion of) the crack and symmetry is not maintained. A linear elastic stress analysis based on a boundary element code [8] gives a combination of Mode I and II stress intensity factors with $K_{II}/K_I = 5.4\%$.

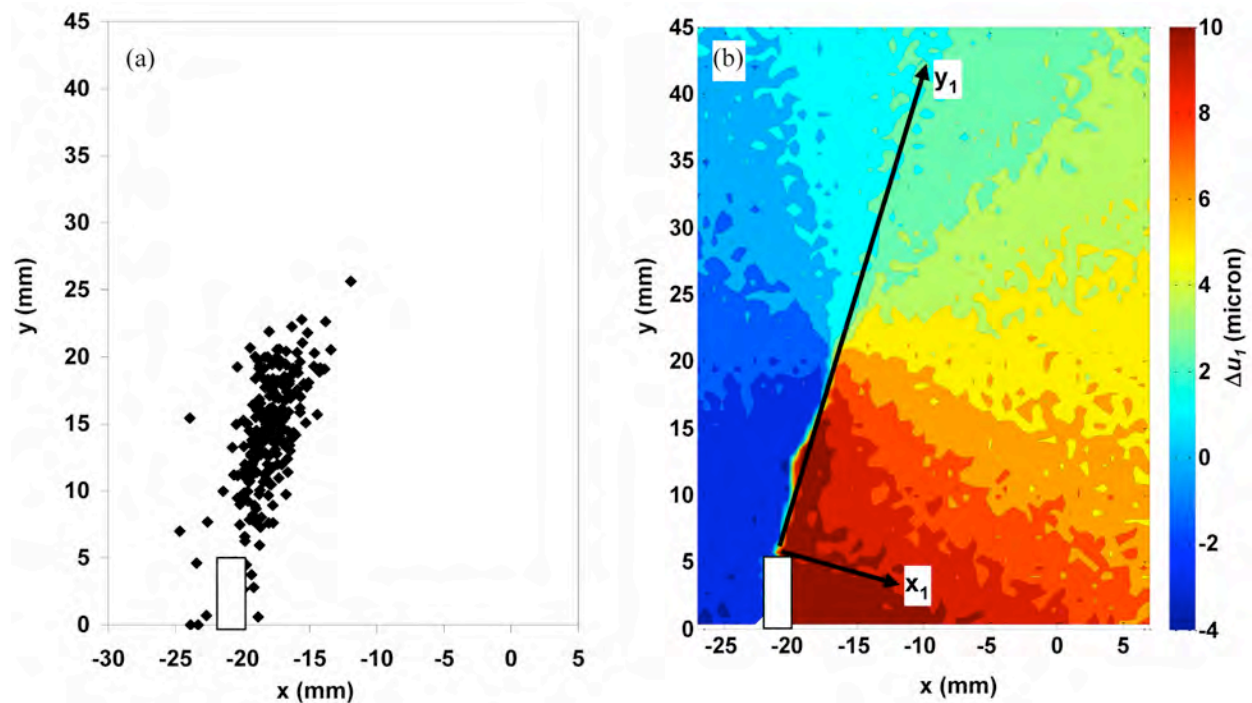


Fig. 6. Mixed-mode fracture test of specimen EN-1 from 100-90% of peak load. (a) AE locations. (b) Incremental normal displacement contours Δu_I .

For 100–90% post-peak load, the AE locations (Fig. 6a) cluster within a zone that is slightly longer than that shown for Mode I loading (Fig. 4a), and the fracture is inclined at 20° from the vertical. Thus, it is convenient to establish a new coordinate system (x_I, y_I) positioned at the notch tip and inclined at 20° along the fracture direction (Fig. 6b), such that the normal and tangential (and possibly sliding) displacements can be identified from the measured horizontal and vertical displacement fields. The incremental displacements $\Delta u_I, \Delta v_I$ based on the new coordinate system can be computed through a transformation of the incremental horizontal and vertical displacements $\Delta u, \Delta v$. Note that the contours of transformed displacements are still plotted in x, y coordinates, in order to compare to the AE locations; the merging of the contours identifies the tip, which coincides well with the AE.

For 90–80% of post-peak load, the AE locations (Fig. 7a) cluster within the range from $y = 10$ mm and $y = 26$ mm, with a traction-free length suggested where very few ($< 10\%$) AE are located. Figure 7b shows the incremental normal displacement Δu_I along the fracture, and the tip is at $x = -14$ mm, $y = 26$ mm. The incremental tangential displacement contours again show

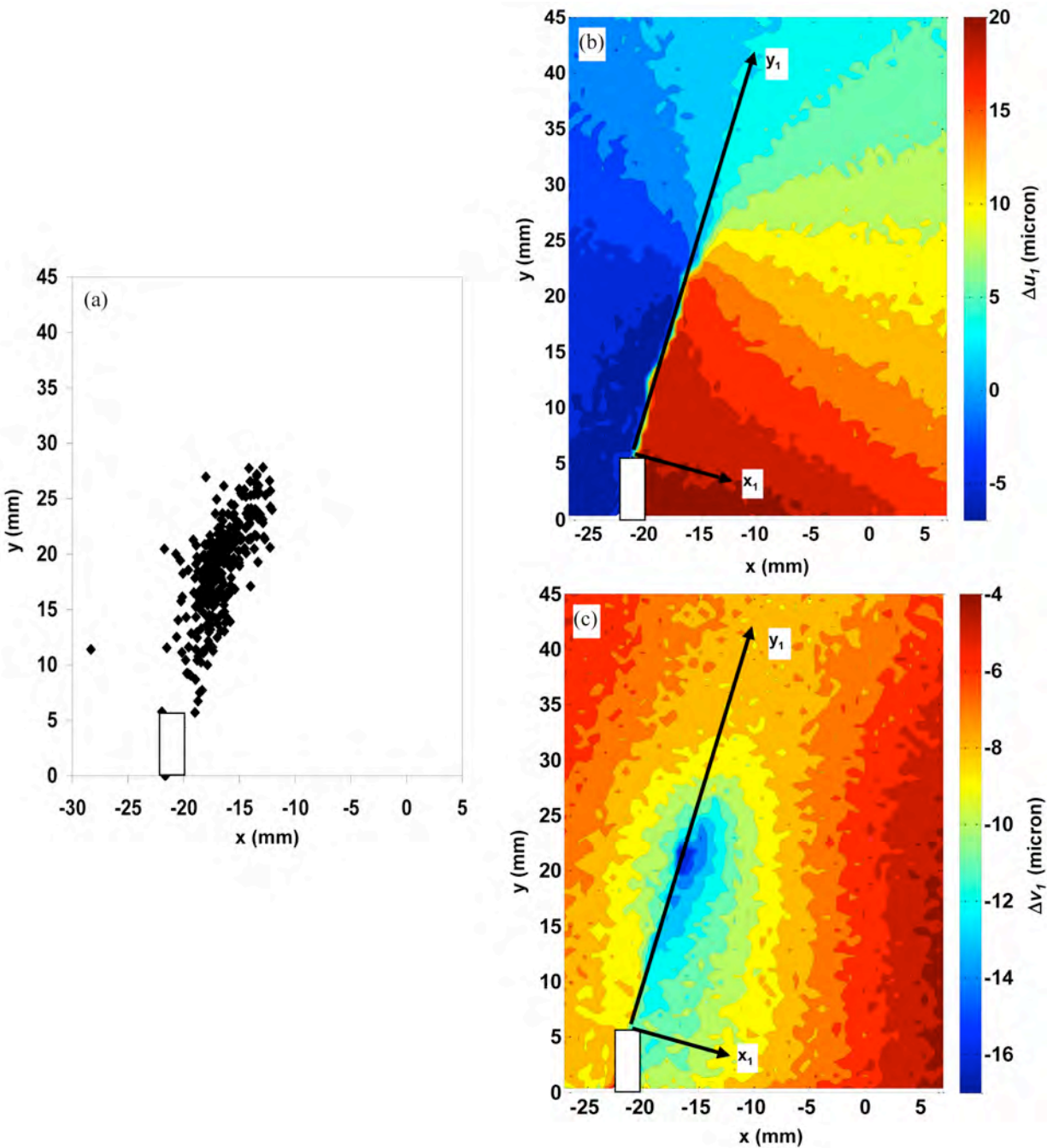


Fig. 7. Mixed-mode fracture test of specimen EN-1 from 90-80% of peak load. (a) AE locations. (b) Incremental normal displacement contours Δu_I . (c) Incremental tangential displacement contours Δv_I .

an island (Fig. 7c), similar to the opening mode behavior, but it is important to notice that the island in the mixed-mode experiment shows no differential tangential displacement – no sliding – and consequently $K_{II} = 0$ in the island. Furthermore, sliding displacement is displayed along a portion of the crack, as displayed by the contours varying in color between the upper and lower parts of the fracture. Thus, the island in mixed-mode loading is an opening region where no sliding occurs. Indeed, the observation of slip below the position $y_I = 20$ mm confirms an assumption concerning the process zone in mixed-mode loading [9], where slip is absent until a critical amount of opening displacement takes place. It appears that the process zone, for a

mode-mixity (K_{II}/K_I) of approximately 5%, is associated with opening, and AE activity is concentrated in this zone.

Summary

Two techniques, AE and digital image correlation (DIC), were used to identify fracture of rock under opening and mixed-mode loading conditions. Experimental results demonstrated that both techniques provided similar measurements on the length and character of the fracture. A grouping of microcrack locations clearly identified the cohesive-nature of a portion of the fracture, and crack growth. DIC provided a position of the crack tip, and a zone of increased tangential displacement but no differential movement near the crack tip, suggesting that the process zone for slight mixed-mode deformation is governed by Mode I opening.

Acknowledgement

Partial support was provided by NSF grant CMMI-0825454 and the MSES/Miles Kersten Chair.

References

1. J.F. Labuz and L. Biozi, (1998). *Int. J. Solids Struct.*, **35**, 4191-4203.
2. Z.P. Bažant, (2002). *Engng Fract. Mech.*, **6**, 165-205.
3. M.D.G. Salamon and G.A. Wiebols, (1974). *Rock Mech. Rock Engng*, **6**, 141-166.
4. S.A. Budavari, (1971). *Aust. Geomech. J.*, **1**, 15-17.
5. T.C. Chu, W.F. Ranson, M.A. Sutton and W.H. Peters, (1985). *Exp. Mech.*, **25**, 232-244.
6. M.A. Sutton, J. Orteu and H.W. Schreier, (2009). *Image Correlation for Shape, Motion and Deformation Measurements*. Springer, New York.
7. D.J. Chen, F.P. Chiang, Y.S. Tan and H.S. Don, (1993). *Appl. Opt.*, **32**(11), 1839-1849.
8. I.A. Ostanin, S.G. Mogilevskaya, J.F. Labuz and J. Napier, (2011). *Eng. Anal. Bound. Elem.*, **35**, 623-630.
9. Z.P. Bažant and P. Gambarova, (1980). *J. Struct. Div. ASCE.*, **106** (ST4), 819-842.

DIESEL KNOCK COMBUSTION AND ITS DETECTION USING ACOUSTIC EMISSION

DAVID P. LOWE¹, TIAN RAN LIN^{1,2}, WEILIANG WU¹ and ANDY C. C. TAN¹

¹ School of Engineering Systems, Queensland University of Technology, GPO Box 2434, Brisbane, QLD 4001, Australia, ² CRC for Infrastructure and Engineering Asset Management

Abstract

This paper presents an experimental investigation into the detection of excessive diesel knock using acoustic emission (AE) signals. Three different dual-fuel diesel engine operating regimes were induced into a compression-ignition (diesel) engine operating on both straight diesel fuel and two different mixtures of fumigated ethanol and diesel. The experimentally induced engine operating regimes were; normal, or diesel only operation, acceptable dual-fuel operation and dual-fuel operation with excessive diesel knock. During the excessive diesel-knock operating regime, high rates of ethanol substitution induced potentially damaging levels of diesel knock. AE data was captured along with cylinder pressure, crank-angle encoder, and top-dead centre signals for the different engine operating regimes. Using these signals, it was found that AE signals clearly distinguished between the two acceptable operating regimes and the operating regime experiencing excessive diesel knock. It was also found that AE sensor position is critical. The AE sensor positioned on the block of the engine clearly related information concerning the level of diesel knock occurring in the engine whilst the sensor positioned on the head of the engine gave no indication concerning diesel knock severity levels.

Keywords: Diesel knock, dual-fuel, condition monitoring

1. Introduction

It is the high pressure-rise rates associated with the auto-ignition of fuel during the premixed combustion stage that produces the characteristic “knocking” noise widely associated with diesel engines. This noise is often referred to as *diesel knock* [1] or *combustion roughness* [2]. When excessive, diesel knock results in the propagation of high amplitude pressure waves at frequencies governed by combustion chamber resonance and as is the case with spark-ignition knock, can be extremely detrimental to engine life [2, 3]. Diesel knock has not been a fundamentally limiting factor in the same manner as spark-ignition knock in terms of engine design, however, diesel knock is recognized as a considerable problem associated with the use of alternative fuels in dual-fuel type diesel engines [4]. The increasing use of bio-fuels and the performance limitations associated with excessive diesel knock in dual-fuel engines combine to make diesel knock an important parameter to monitor from both, engine performance, and health viewpoints.

Knock detection in spark-ignition engines is undertaken using both piezoelectric accelerometers and spark plug ion-current sensors. Spark plug ion-current sensors detect knock using an applied spark plug gap voltage whilst piezoelectric accelerometers detect knock by sensing engine vibrations excited by the knock phenomena in a frequency range of 4-8 kHz [5]. Although effective for spark-ignition knock detection, the increased vibration levels associated with normal diesel engine operation result in unreliable excessive diesel knock detection using piezoelectric accelerometers.

Being fundamentally related to cylinder pressure, it is no surprise that cylinder pressure sensors are the most effective for detecting diesel knock. However, pressure sensors are not commonly used in production engines as engine designs having extra recesses into individual combustion chambers are considered undesirable [5]. Acoustic emission (AE) sensors, however, have the potential to monitor multiple cylinders, are non-intrusive [6], and are easily installed and AE based monitoring methods have been successfully demonstrated in many diesel engine monitoring applications. For example, Fog et al. [6 - 8] detail the detection of large marine diesel engine exhaust valve faults as well as misfire using AE signals. Other investigations have demonstrated AE based methods for the detection of injector faults [9] and for monitoring the piston ring and cylinder liner interface [10 - 13]. El-Ghamry et al. [14] have also shown that AE signals contain information relating to combustion. This work demonstrates an indirect method of cylinder pressure measurement using AE signals.

Section 2, provides a concise overview of the cause of diesel knock and the closely related phenomena of combustion chamber resonance. In addition, Section 2 describes the methods used to quantify knock severity. Section 3 briefly describes the test rig and data acquisition systems used during the experimental investigation. Section 4 presents and discusses the results from the investigation and finally, Section 5 provides a summary of the main findings from this investigation.

2. The Diesel Knock Phenomena

Knock, pinging or *detonation* are all terms that have been widely used to describe the characteristic “metallic rattling” noise associated with abnormal combustion in spark-ignition engines. Spark-ignition knock is caused by the spontaneous ignition of gas ahead of the propagating flame front (the end gas) within the combustion chamber. This spontaneous ignition results in a rapid release of chemical energy and an accompanying rapid rise in cylinder pressure [15]. Unlike spark-ignition knock, diesel knock occurs when injected fuel auto-ignites and combusts in the premixed stage of combustion. Whilst this process is a normal part of diesel engine operation, various circumstances can lead to excess quantities of fuel combusting in a premixed fashion. This situation often develops if the parameters governing combustion lead to abnormally long ignition delay periods. As a consequence, excessive diesel knock can often be a symptom of underlying faults such as poor or contaminated fuels, injection system problems or unsuitable rates of alternative fuel substitution.

The rapid pressure increases associated with both spark-ignition and diesel knock result in the propagation of high amplitude pressure waves at frequencies governed by combustion chamber resonance. The combustion-chamber resonance frequencies are in turn determined by the geometry and the velocity of sound within the combustion chamber [3]. Figure 1 highlights the effects of spark-ignition knock on cylinder pressure. As seen, the knock phenomenon causes high frequency pressure fluctuations, which are recorded by the pressure sensor. It is also seen that the amplitude of the high frequency pressure fluctuations increases as the severity of the knock increases [15].

Whilst discussing spark-ignition knock, Heywood [15] points out that due to the highly variable nature of engine knock, fundamental definitions of knock intensity is extremely difficult to make. However, a method whereby cylinder pressure signals are used to calculate an average pressure rise rate (PRR) is described. Another method, also described by Heywood [15], uses

pressure signals, which are filtered to remove the low frequency components. The maximum amplitude of the knock-induced pressure oscillation is then used as the knock intensity measure.

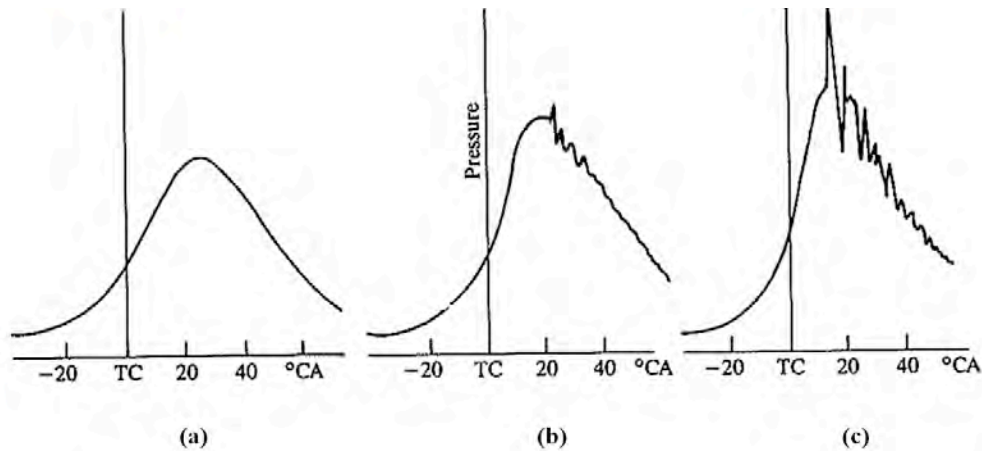


Fig. 1: Cylinder pressure vs. crank angle plots for (a) normal spark-ignition combustion, (b) light knock and (c) intense knock [15].

Whilst discussing diesel knock specifically, Hsu [2] mentions that maximum pressure rise rate (MPRR) has been used to quantify knock intensity when the frequency response of pressure measurement system is such that the system is unable to sense the individual pressure oscillations. Hsu [2] also points out that MPRR measurements can be misleading when modern instrumentation is used as peak MPRR values may not be associated with premixed combustion. Hsu [2] suggests that the best way to quantify diesel knock is to measure the combustion pressure wave energy at the characteristic frequency.

In addition to the previously mentioned measurement techniques, measurements using rates of heat release, such as those shown by Shiga et al. [16], can also provide insight regarding the relationship between the rapid releases of chemical energy, the accompanying rapid rise in cylinder pressure and the knock severity levels.

3. Combustion Chamber Resonance

As discussed, knock phenomena lead to the propagation of high amplitude pressure waves at frequencies governed by combustion chamber resonance. Therefore, the determination of the resonant frequencies is an important step in the quantification of diesel knock.

The pressure fluctuations within the combustion chamber are acoustic in nature as their amplitude is small compared to the mean in-cylinder pressure at the time they occur [17] and the geometry of a direct injection-type combustion chamber can be approximated as cylindrical cavity having plane ends [3]. The combustion chamber resonance frequencies can be calculated using equation (1).

$$f_R = c [(\alpha_{mn}/B)^2 + (p/2L)^2]^{1/2} \quad (1)$$

where m , n , and p denote circumferential, radial and axial mode numbers, respectively, and B is the bore diameter. L is the axial length and the value α_{mn} is determined using the Bessel function. The speed of sound (c) is determined using the following thermodynamic relationship with R being the gas constant, T is the temperature and γ is the ratio of specific heats.

$$c = \sqrt{\gamma RT} \quad (2)$$

Although axial, circumferential and radial modes are associated with cylindrical cavity resonance, the axial modes can be excluded in terms of knock intensity as the frequencies associated with this mode are generally above the audible range [18]. This is due to the small axial dimensions when the piston is close to top-dead centre (TDC), and the high speed of sound at combustion temperatures [19]. When the axial term in equation (1) is set to zero ($p = 0$), equation (1) can be rewritten as equation (3):

$$f_{mn} = (c/B)\alpha_{mn} \quad (3)$$

Equation (3) was used to calculate the first four transverse (radial and circumferential) mode frequencies. Based upon other bulk gas values detailed previously [18, 20], a bulk combustion temperature estimate of 2000 K was used. The calculated resonant frequencies are listed in Fig. 2 along with graphical representations of the corresponding modes.

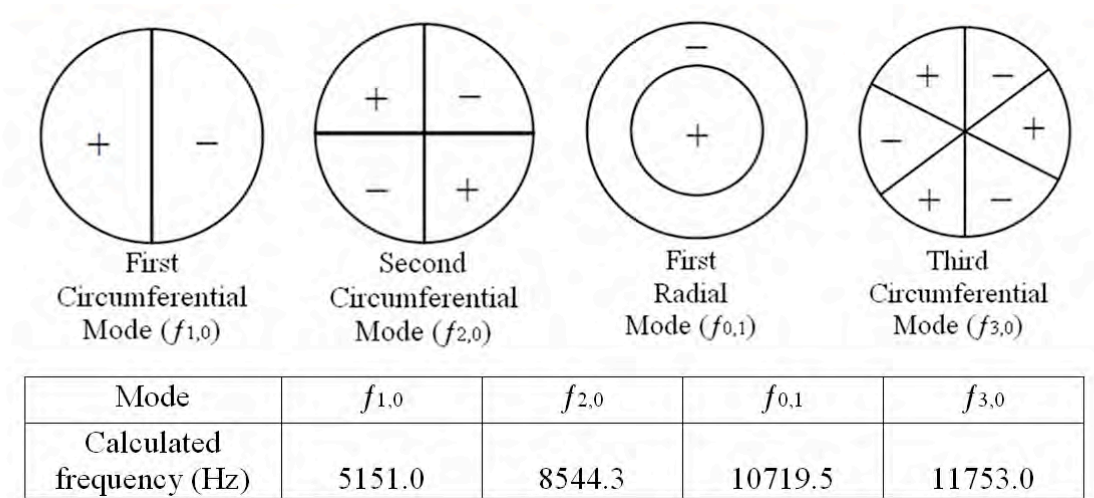


Fig. 2: The first four transverse modes with corresponding calculated resonant frequencies.

Fundamental frequency ($f_{1,0}$) values for the test engine were determined from the recorded pressure signals by spectral analysis using fast Fourier transforms. Measured fundamental frequency ($f_{1,0}$) values ranged between 5100 -5700 Hz.

It was found that the majority of the signal energy associated with cylinder resonance was contained within the lowest ($f_{1,0}$) mode. This finding has also been noted by other researchers such as Eng [20]. Once a fundamental frequency range directly relating to the level of diesel knock was determined, pressure signals were then used to quantify diesel knock levels.

4. Experimental Methodology

The test facility used in this experimental investigation consisted of a 5.9 litre, six-cylinder turbo-charged Cummins diesel engine coupled to a Froude water dynamometer. The engine and dynamometer are controlled electronically via a Dynalog control system. The test facility is shown in Fig. 3 and the relevant engine specifications are listed in Table 1.

A PAC MicroDisp AE system was used to record AE signals from two PAC 15 α sensors mounted on both engine block and head in close proximity to cylinder 1. These signals were amplified using PAC 2/4/6 AE pre-amplifiers. Figure 4 shows the position of the AE sensors on the front face of the engine. In addition to the AE signals, TDC and crank angle encoder



Fig. 3: Photograph showing the test facility.

Table 1: Relevant Cummins diesel engine specifications.

Engine Cycle	Four Stroke, Turbocharged
Cylinders	Six (Inline)
Firing Sequence	1, 5, 3, 6, 2, 4
Bore	102 mm
Stroke	120 mm
Displacement	5.9 Litres
Compression Ratio	17.3:1
Combustion System	Direct Injection

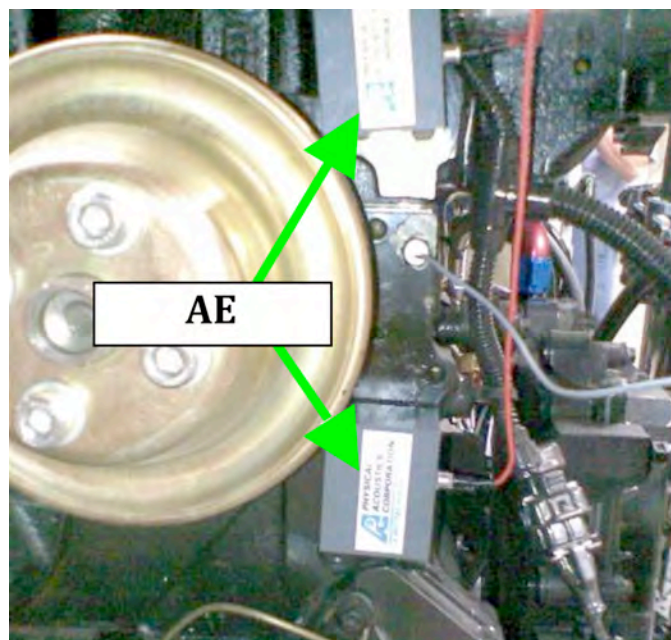


Fig. 4: AE sensor positions.

signals were recorded simultaneously. A National Instruments data acquisition system was used to record cylinder pressure, TDC and crank angle encoder signals, using LabView software. The cylinder pressure was recorded using a high-temperature Kistler pressure transducer installed on cylinder 1.

Three different engine-running conditions were induced during the experimental investigation. These running conditions were based on the rate of ethanol substitution. The rates used were; 0% ethanol (diesel fuel only), 30% ethanol and 50% ethanol by energy, respectively. These three engine-running conditions were chosen to represent three different operational regimes. The 0% ethanol (e0) running condition is representative of normal diesel engine operation. The 30% ethanol case (e30) represents acceptable dual-fuel diesel engine operation whilst the 50% ethanol (e50) case represents a case of unacceptable dual-fuel diesel knock. The ethanol was introduced into the engine by injecting the ethanol into the incoming air stream. This substitution technique is widely known as ethanol fumigation. The tests were all undertaken using an applied torque of 700 Nm at an engine speed of 2000 rpm. This loading condition represents approximately 90% of the maximum load.

The diesel knock levels induced during this experimental investigation were quantified using two techniques. The first technique involved the calculation of average amplitudes of pressure oscillation directly from recorded pressure signals by averaging the five highest amplitudes of pressure oscillation within an individual combustion cycle. The second technique involved the decomposition of the combustion window portion of the pressure signal using a three-level discrete wavelet decomposition. The wavelet decomposition was performed using a Daubechies (Db2) wavelet. The results from this signal decomposition were used to calculate the energy levels of the frequency bands associated with the different frequency modes. The results from this signal decomposition are detailed in the following section.

4. Results and Discussion

Figure 5 shows typical pressure traces for the three different ethanol substitution rates. These pressure traces are plotted with respect to crank angle. The pressure traces shown correspond to the final 60° of the compression stroke and the first 100° of the power stroke. The window encompassed by the dashed green outline highlights the portion of the signal where premixed combustion occurs and where the resonant pressure fluctuations are at a maximum. This window, referred to as the “combustion window” in the following discussion, is shown in Fig. 6. The combustion window extends from the combustion TDC to 25° after combustion TDC.

The dashed oval shown in Fig. 6 highlights the distinctive high amplitude pressure fluctuations associated with the e50 pressure curve. These pressure fluctuations are characteristic of excessive diesel knock. Acceptable dual-fuel combustion is shown by the e30 pressure curve and although different to the normal diesel (e0) curve in terms of underlying signal pressure form, the high amplitude pressure fluctuations characteristic of excessive diesel knock are absent.

Comparison of the amplitudes of the high frequency pressure fluctuations from each of the three different engine operating regimes was undertaken by calculating average pressure fluctuation amplitudes for each operational regime. The average pressure fluctuation amplitude values were 187, 139 and 587 kPa for e0, e30 and e50 operating regime, respectively. These values are shown graphically in Fig. 7. The average pressure fluctuation amplitude for the e50 case represents over three times increase from the normal regime.

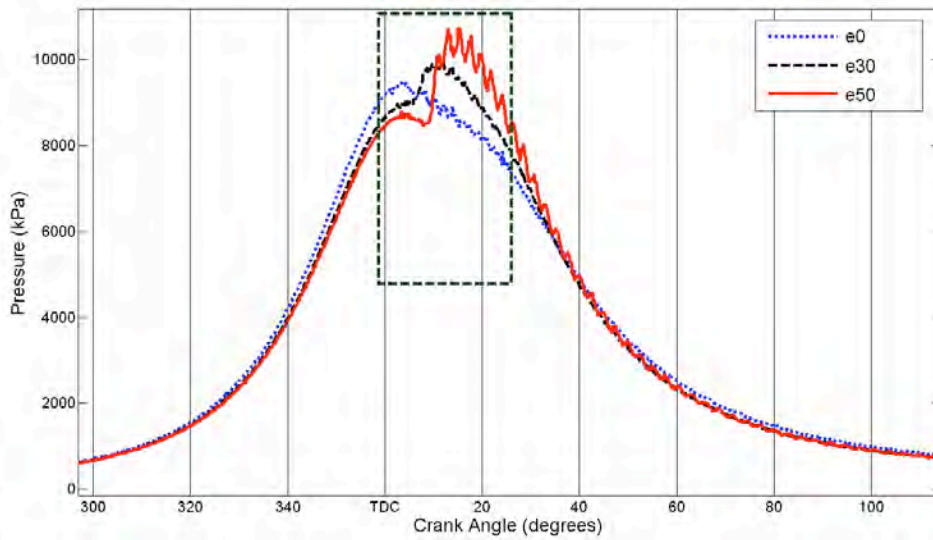


Fig. 5: Cylinder pressure traces for the three different ethanol substitution rates.

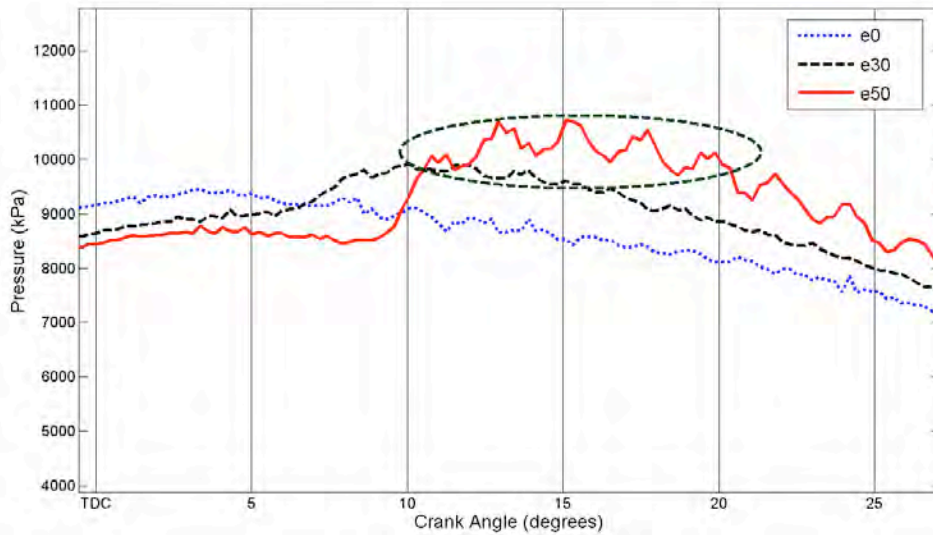


Fig. 6: Close-up view of the combustion window portion of the pressure curves for the three different ethanol substitution rates.

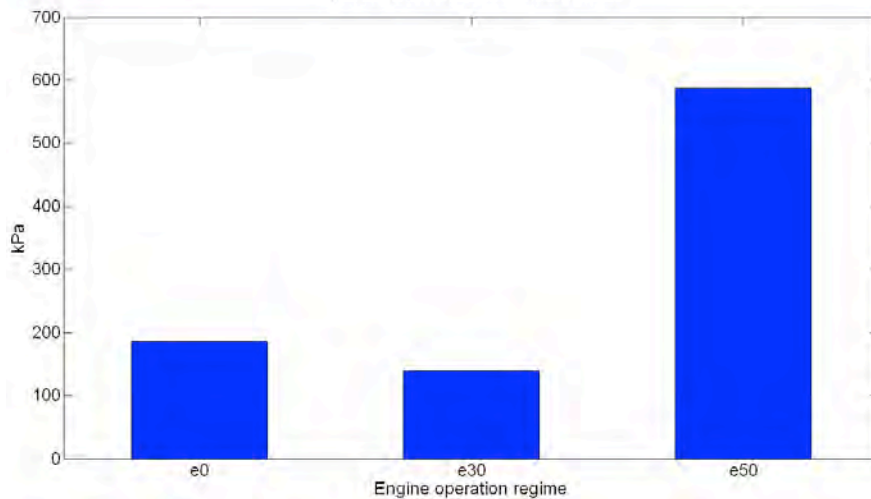


Fig. 7: Average cylinder pressure fluctuation amplitudes.

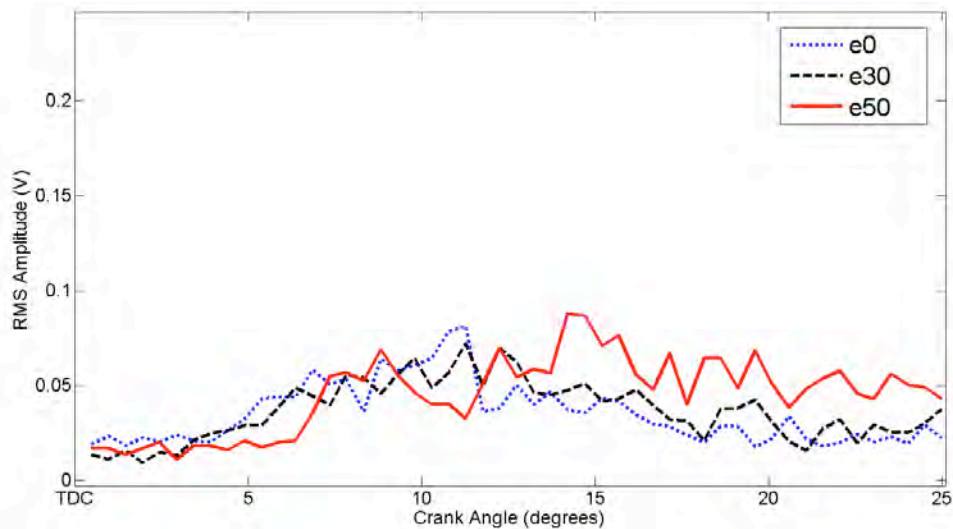


Fig. 8: Combustion window AE RMS from the engine head

A second diesel knock level technique was also used. This technique involved performing a three level discrete wavelet decomposition of the pressure signals. The results of this decomposition were used to calculate the combustion window energy associated with specific frequency ranges for the different operating regimes. The combustion window energy content for the 3.125 to 6.25 kHz frequency range showed a similar trend in terms of diesel knock severity to that shown in Fig. 7.

Factors such as engine block geometry, cooling system galleries and gaskets all drastically effect the transmission of AE [21]. In order to determine the most effective sensor position for diesel knock detection, AE sensors were attached to both the engine block and head in close proximity to cylinder 1. The AE signals were then truncated using the combustion window described previously. The resultant signals were used to calculate RMS energy (RMS). As shown in Fig. 8, the total combustion window AE energy (RMS) levels from the engine head for the e0, e30 and e50 cases are all similar. It is clear that the total energy (RMS) values calculated from the engine head show no clear indication regarding the unacceptable knock experienced during the e50 operating regime. Figure 9 shows the combustion window AE energy (RMS) calculated from the engine block. A sharp increase in the AE RMS level for the e50 case commences at approximately 10° after TDC. The increase in AE RMS energy during the e50 case corresponds to the start of the high amplitude pressure fluctuations highlighted in Fig. 6. This increase in AE RMS gives a clear indication that excessive diesel knock is occurring.

Figure 10 shows a trend comparison between the two techniques used to quantify the diesel knock level and the total energy (RMS) values for the engine block AE signal. The various values have been normalized in terms of the normal operation (e0) case. This figure shows that the total AE signal energy (RMS) from the engine block sensor gives a good indication regarding the level of diesel knock as indicated by the two diesel knock quantification techniques. The increased AE energy (RMS) detected during the e50 regime appears directly related to the transverse (circumferential and radial) wave propagation modes associated with diesel knock.

5. Conclusion

Three different diesel engine operating regimes were induced into a (diesel) engine operating on both straight diesel fuel and two different mixtures of fumigated ethanol and diesel. Compar-

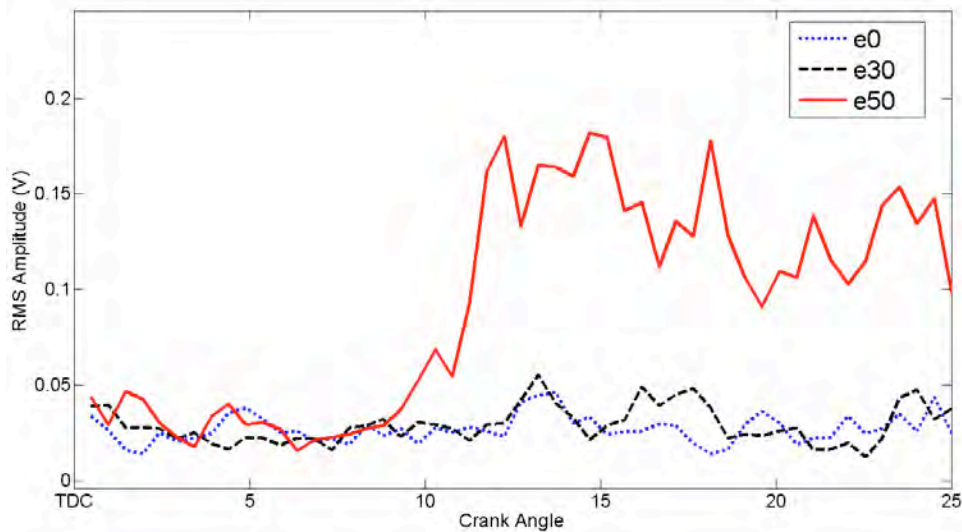


Fig. 9: Combustion window AE RMS from the engine block.

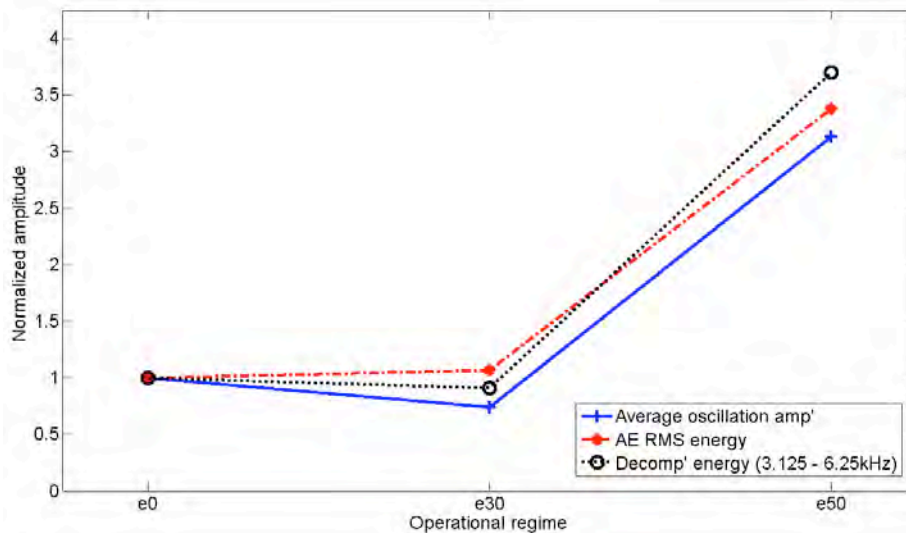


Fig. 10: A trend comparison between the Diesel knock level quantification techniques and the total AE energy (RMS) values from the engine block

isons of the diesel knock levels associated with the operational regimes showed that the e0 and e30 operating regimes had acceptable levels of diesel knock. The excessive levels of diesel knock induced during the e50 operational regime was shown to have pressure fluctuations more than three times higher than the e0 and e30 regimes.

The detection of the excessive diesel knock operational regime was possible using AE signals recorded from a sensor located on the engine block. A sensor located on the head of the engine, however, gave no indication regarding the unacceptably high levels of diesel knock.

The findings show that AE recorded from the block contains information concerning the propagation of high amplitude pressure waves at the combustion chamber resonant frequencies. This AE activity originates as a result of the interaction between the pressure oscillations and the combustion related components of the engine.

Acknowledgements

This paper was developed within the CRC for Infrastructure and Engineering Asset Management, established and supported under the Australian Government's Cooperative Research Centre Program. The authors gratefully acknowledge the financial support provided by the CRC.

References

- 1) B. Challen and R. Baranescu. Editors. *Diesel Engine Reference Book*, 2nd Edition. Butterworth-Heinemann, Oxford, UK. 1999.
- 2) B.D. Hsu. *Practical Diesel-Engine Combustion Analysis*. Society of Automotive Engineers, Inc. Warrendale, PA, USA. 2002.
- 3) Y. Ren, R. B. Randall, B. E. Milton. Influence of the Resonant Frequency on the Control of Knock in Diesel Engines. In: *Proceedings of the Institution of Mechanical Engineers, Part D: Journal of Automobile Engineering*. 1999.
- 4) M. H. Saidi and K. Eisazadeh Far. *Analysis of Combustion Process in Dual Fuel Diesel Engines: Knock Phenomenon Approach*. SAE Tech. Paper Series, Paper # 2005-01-1132. 2005.
- 5) W. J. Flemming. Overview of Automotive Sensors. *IEEE Sensors Journal*, **1**, (4), 296-308, 2001.
- 6) T. Fog. Condition Monitoring and Fault Diagnosis in Marine Diesel Engines. Ph.D. Thesis. Technical University of Denmark. 1998.
- 7) T. L. Fog, E. R. Brown, H. S. Hansen, L. B. Madsen, P. Sorensen, E. R. Hansen, J. A. Steel, R. L. Reuben, and P. S. Pedersen. Exhaust Valve leakage Detection in Large Marine Diesel Engines. In: B. T. Kuhnell and B. K. N. Rao (Ed.), *COMADEM '98 Proceedings of the 11th International Conference on Condition Monitoring and Diagnostic Engineering Management, Volume I*. CCMCM, Monash University. 1998.
- 8) T. L. Fog, E. R. Brown, H. S. Hansen, L. B. Madsen, P. Sorensen, E. R. Hansen, J. A. Steel, R. L. Reuben, and P. S. Pedersen. On Condition Monitoring of Exhaust Valves in Marine Diesel Engines. In: *Proceedings of the IEEE Workshop on neural Networks for Signal Processing IX*. Piscataway, New Jersey, pp 554-563. 1999.
- 9) A.K. Francis, J. D. Gill, R. L. Reuben, J. A. Steel. Investigation into Identification of Faults in a Small HSDI Diesel Engine Using Acoustic Emission, *DGZfP-Proceedings BB 90-CD*, Lecture 30, EWGAE, 2004.
- 10) N. H. Pontoppidan. Condition Monitoring and Management from Acoustic Emissions, PhD Thesis, Technical University of Denmark, Kongens Lyngby, Denmark. 2006.
- 11) N. H. Pontoppidan, J. Larsen and T. Fog, Independent Component Analysis for Detection of Condition Changes in Large Diesel Engines, *International Journal of COMADEM*, 2005.
- 12) R. M. Douglas, J. A. Steel, R. L. Reuben. A Study of the Tribological Behavior of Piston Ring/Cylinder Liner Interaction in Diesel Engines Using Acoustic Emission, *Tribology International*, **39** (12), 2006, 1634-1642.
- 13) R. McAllister Douglas. Monitoring the Piston Ring-Pack and Cylinder Liner Through Acoustic Emission Measurements. PhD Thesis, Heriot-Watt University, UK. 2007.
- 14) M. El-Ghamry, J. A. Steel, R. L. Reuben, T. L. Fog. Indirect Measurement of Cylinder Pressure from Diesel Engines Using Acoustic Emission. *Mechanical Systems and Signal Processing* **19**. (2005). 751-765.
- 15) John B. Heywood. *Internal Combustion Engine Fundamentals*. McGraw-Hill Inc. 1988.
- 16) S. Shiga, H. Ehara, T. Karasawa and T. Kurabayashi. Effect of Exhaust Gas Recirculation on Diesel Knock Intensity and its Mechanism. *Combustion and Flame*, **72**: 225-234 (1988).

- 17) R. Hickling, D. A. Feldmaier, F. H. K. Chen and J.S. Morel. Cavity Resonances in Engine Combustion Chambers and Some applications, *J. Acoust. Soc. Am.*, **73** (4), 1170-1178, 1983.
- 18) R. Hickling, D. A. Feldmaier, and S. H. Sung. Knock-induced Cavity Resonances in Open Chamber Diesel Engines, *J. Acoust. Soc. Am.*, **65**(6), 1474-1479, 1979.
- 19) A.J. Torregrosa, A. Broatch, X. Margot, V. Marant and Y. Beaugé, Combustion Chamber Resonances in Direct Injection Automotive Diesel Engines: A Numerical Approach. *Int. J. Engine Res.* **5** (1), 83-91, 2004.
- 20) J. A. Eng. *Characterization of Pressure Waves in HCCI Combustion*. SAE Technical Paper Series, Paper 2002-01-2859. Society of Automotive Engineers, Inc. 2002.
- 21) P. Nivesrangsan. Multi-Source, Multi-Sensor Approaches to Diesel Engine Monitoring Using Acoustic Emission. PhD Thesis, Heriot-Watt University, UK. 2004.

DETECTION OF TRANSIENT ZONES DURING WATER BOILING BY ACOUSTIC EMISSION

RAMI CARMİ, ARIE BUSSIBA, GALIT WIDENFELD, YOSI AHARON,
IGAL ALON and IGAL HOCHBAUM

NRCN, P.O. Box 9001, Beer-Sheva, 84190, Israel

Abstract

The capability to predict parameters and to develop quantitative predictive models in sub-cooled boiling flow is considerable importance to nuclear reactor safety and in many other industrial processes. Such predictions are based on heat transfer mechanisms derived from theoretical models and from experimental data on bubble dynamics from growth and motion aspects. In practice, it is essential to predict the complete boiling curve in system with specific conditions, which performs an accurate description of the boiling process, and to point out the transition between the regions. The prediction of the boiling curve is based on temperature measurements on the surface of the heating element using thermocouples or thermographic and high speed cameras [1, 2]. The accuracy of these measurements could be improved by applying acoustic emission (AE) method especially in complicated geometries. The current study adopts the AE techniques in order to examine the potential of the AE in detection of bubbles during boiling process and to point out the transition zones. Preliminary AE work has been conducted in order to determine the appropriate AE parameters, and to eliminate mechanical and electromagnetic interferences.

The AE findings in terms of counts, amplitude, peak frequency, etc., as a function of the applied current, revealed the early stages of bubble formation during boiling process. The AE data also indicates the transition between the different regions of the boiling curve. The AE results were analyzed by spectrum analysis and wavelet analysis in order to determine characteristic frequencies and sequences of the water boiling processes. The AE results show a great potential to detect in situ the early stages of boiling process and can be used as an efficient tool for monitoring continuously possible boiling in industrial pipes where the boiling might be critical and damage process.

Keywords: Boiling, bubbles, boiling curve, sub-cooled boiling flow, transient zones

Introduction

There is a growing interest in boiling process characterization from both engineering point of view and from fundamental research in various aspects. From practical side, boiling heat transfer is used in many industrial processes such as: refrigerator, heat exchanger in the chemical industry, steam power plants and electronic devices, either to generate vapor or because of its effectiveness in cooling. On research side, development of comprehensive quantitative predictive models is still long-term goals, since they are based on heat transfer mechanisms derived from theoretical models and from experimental data on bubble dynamics from growth and motion aspects. The latter has been focused since the development of advanced characterization techniques with powerful data processing. The most popularly used methods are the high-speed video camera [2, 3]. Recently, AE is being utilized as a complementary method in the characterization of micro-mechanisms of boiling process as implemented in the current study.

As a background, macroscopic boiling process is well known and defined since the first discovery of boiling curve by Nukiyama [4], and it is classified as pool boiling or flow boiling depending whether the fluid flow by natural movement or forced to flow by external pump. Further, classification concerns the average temperature of the fluid and divides into sub-cooled and superheating boiling. The classical boiling curve for water boiling condition is illustrated in Fig. 1a and the corresponding suggested micro-mechanisms are listed in Fig. 1b. Up to Point A (Stage I), the heat flows from the heating element to the water by natural convection. From Point A to C, bubbles form on preferred surface sites on the heating element due to local superheat conditions. Towards Point B the bubbles that form and depart from the heating surface collapse in the surrounding water due to heat exchange with the cool fluid. Beyond Point B to C, bubbles form in vigorous rates colliding with each other and combine to become numerous continuous bubbles, depart from the heating surface and continue to float all the way up to the free surface, where they pop up and release their vapor to the environment. From C to D, continuous vapor film is growing until it covers all the surface of the heating element, becoming Stage V or film boiling. As a result, a decrease in the heat flux is observed. From Point D, the dominant mechanism of heat transfer is radiation that increases the transfer rate.

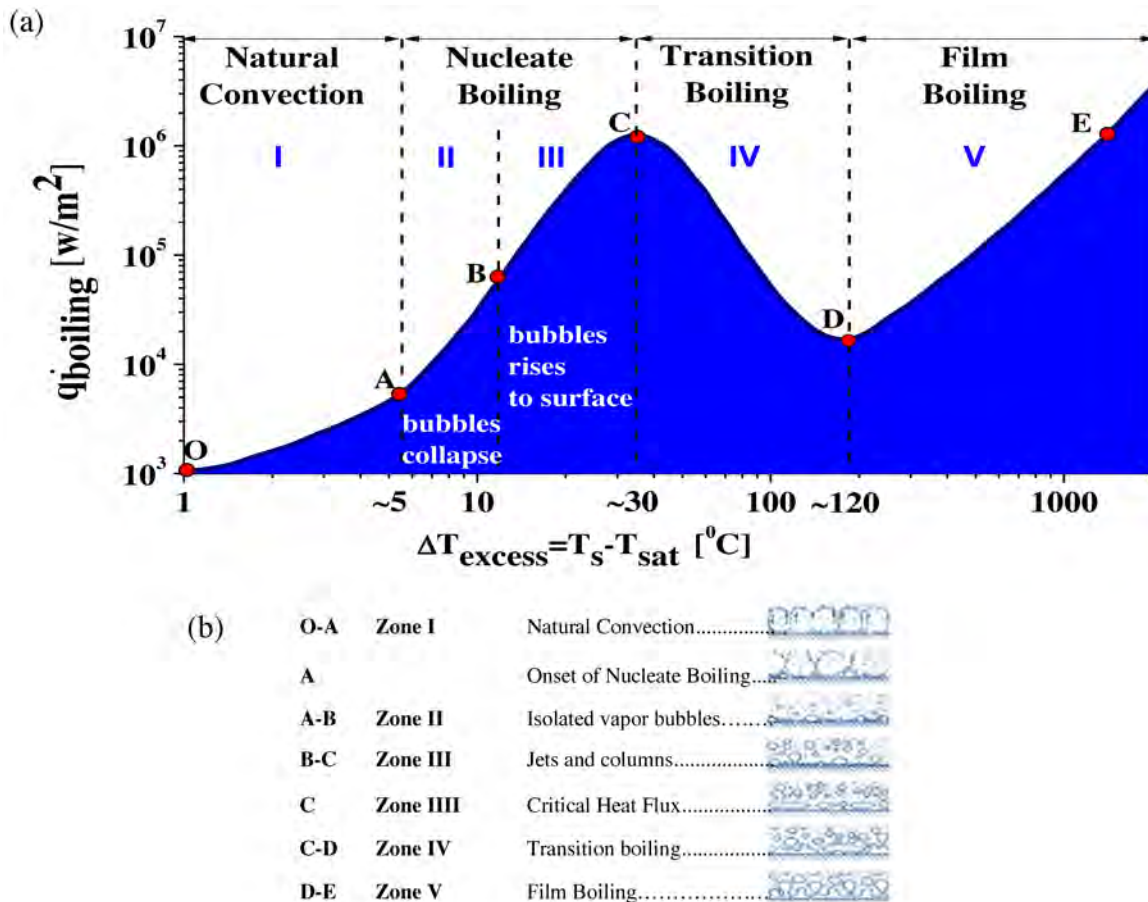


Fig. 1. (a) Typical boiling curve regimes for water in pool boiling 1 atm. [5], (b) The corresponding mechanisms at the different zones.

Boiling process produces acoustic pressure waves of above 50 kHz resulting from several mechanisms: bubble initiating, growth, departure [6], neck detachment accompanied by turbulent stream [7], bubble collapse due to heat transfer from the fluid [8], bubble natural oscillation due to fluctuation in the equilibrium state and bubble blast due to bursting in water surface [9]. Based

on these mechanisms, one can assume that the boiling process involves sequences of pulses, whose amplitude, length and time intervals vary randomly. Thus, AE technique has a good potential in revealing and distinguishing between different boiling regimes in the boiling curve. Accordingly, one can presume that early stage of boiling nucleation involved bubble formation and departure separately from the heating surface. The separation of the signals that contain all the characteristic information of the sources is expected. However, in vigorous boiling where bubbles collide each other and combine while growing, overlap of the impulses results in signals with continuous emission nature. Therefore, amplitude, frequency, phase and time information of the original signal are lost in the process. Other experiments [6, 10] revealed relation between the self-oscillation of the bubble to its size, and it was concluded that bubble in order of $6\ \mu\text{m}$ will produce sound in 500 kHz and $10\ \mu\text{m}$ yields 300 kHz. Acoustic signals pass quite easily in the medium of water or metal, but when steam is involved attenuation could reach up to 6 orders of magnitude. Thus, in stage I boiling, bubbles may be detected as separate acoustic waves while steam production will attenuate the amplitude, power and signal counts in a very sharp form.

The present study is an additional research attempt in applying acoustic emission (AE) to explore more on the main mechanisms involved during boiling process, as well to detect the transition between the various regimes of the boiling curve.

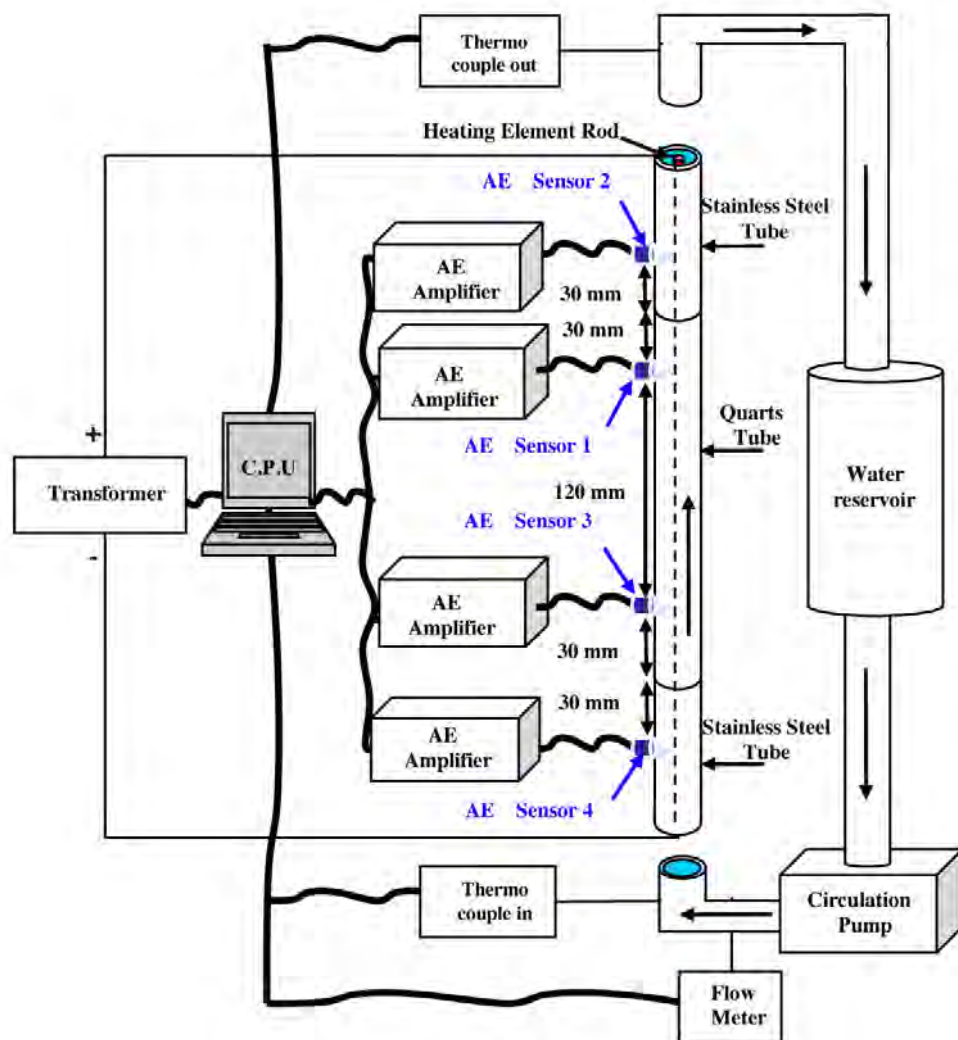


Fig. 2. A schematic illustration of the experimental set-up.

Experimental Procedures

The schematic experimental set-up is depicted in Fig. 2, including a reservoir of water heated initially to 55°C by steam and forced by circulation pump to the test system. The system had three segments: glass tube with diameter of 32 mm and height of 180 mm and two tubes made of stainless steel on both sides. A special joint between the metal and glass was designed in order to achieve smooth flow. Through the entire length of the tube, a central stainless steel rod served as the heater and was connected to the variable current electrical supply. Just above the upper side of the glass tube an immersion thermocouple of type K was located at the middle of the metallic tube and measured the average temperature of the water flow.

The AE arrangement included four resonant sensors, PAC micro-80. The two data sensors were located near the edges of the outer surface of glass tube and the two guard sensors were positioned 60 mm away. In order to have a good signal path, silicone gel was used as the couplant between the sensors and the tube surfaces. The sensors were attached by special tape and were connected to amplifiers with 40 dB of amplification combined with analog filter of 100-1200 kHz. The amplifiers were connected to the computerized AE system. Preliminary work has been performed in order to obtain the appropriate parameters of HDT, LDT and PDT as well as the threshold level, which was selected to be 32 dBae. AE activity was tracked continuously with current flow. The AE data such as counts, amplitude, duration, peak frequency and more, were analyzed in order to detect the very early stage of bubble formation and to distinguish the stage transition. Waveforms were analyzed using FFT and AGU-Vallen wavelet analysis functions [11], in order to find the characteristics frequencies of boiling mechanisms.

Results and Discussion

Figures 3a-c depicted the AE activity with the stepwise applied current during boiling process in terms of AE counts and cumulative counts, respectively. As shown up to 150 s, minor AE activity is being observed with almost constant counts of about 20. This AE activity is for the stage known in the boiling curve as natural convection, and originates from sources such as water flow, friction, heating element expansion and adjustments of glued interfaces of the glass/metal tubes. At 150 s, a sharp transition in the AE activity occurs (Fig. 3a) when the heater current is increased to above 900 A. This effect also appears in the cumulative display (lower arrow in Fig. 3b). This dramatic change indicates the initiation of the boiling process (referred to transition point (A) from stage I to II), which mainly occurs at the surface defects of the heating element. Normally, the water temperature at the vicinity of the heating element is about 105°C. By expanding this stage (Fig. 3c) one can notice that the AE activity followed a sinusoid-like behavior with increasing amplitude with time. Figure 3d shows the expanded pattern of one of the sinusoidal wave (marked by an arrow on Fig. 3c) with a profile of alternate burst and decay. This characteristic pattern indicates the discontinuity in the boiling process at the transient zone between stage I and II, although with the increasing trend in the AE activity. In cumulative count display (not shown), corresponding stepwise behavior was noticed. This AE response indicates that the boiling process evolution occurs gradually and not in a spontaneous manner. As such, approaching to asymptotic behavior will specify the end of this stage, which is an important finding in bubble initiation and growth event sequence.

The results on peak frequency are shown in Fig. 4a. Several distinct frequencies are found in stage I, but we notice only limited events had dominant peak frequency in stage II. This result may indicate that this stage is mainly attributed to continuous emission with sporadic burst signal.

This AE response is a result of two sources: the major one is related to signals overlapping produced by massive amounts of bubbles forming and their breakaway from the heating element surface due to imposed water flow. The second one is associated with bubble collapse due to heat exchange with the cooled surrounding liquid. As the current increases, almost linear behavior in the AE cumulative events is observed up to 1000 A (stage II in the boiling curve). Figures 4b-c illustrates the typical waves related to continuous (stage II) and burst signals (stage III). A change in the slope is also observed (2nd arrow in Fig. 3b), which may point out the transform from discrete boiling of bubbles (stage II) to coalescence process (referred to stage III).

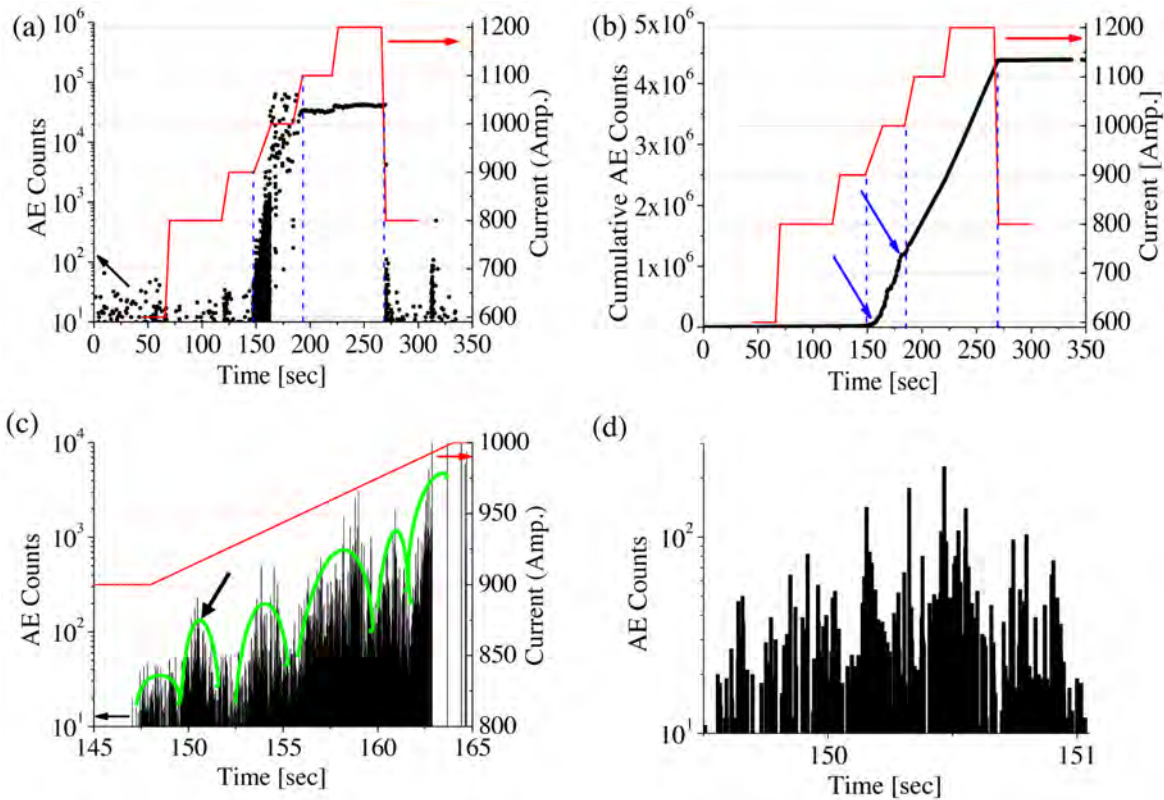


Fig. 3. AE activity with heating current during boiling process in terms of: (a) AE counts, (b) Cumulative AE counts, (c) Expanded region between 145 to 165 s, (d) Characteristic profile of one of the sinusoidal wave shown by the arrow in (c).

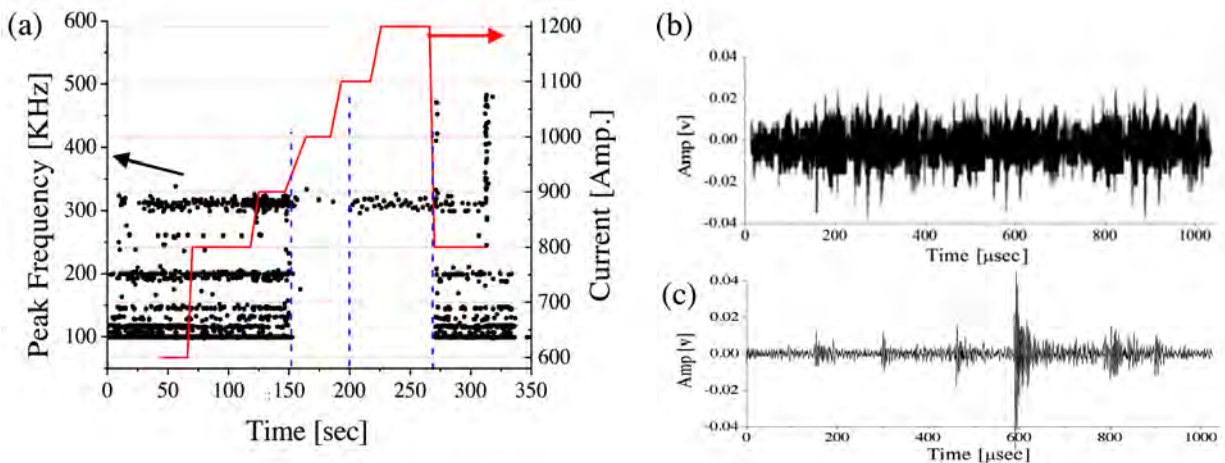


Fig. 4. (a) Peak frequency with applied current during boiling process, (b) Continuous-type wave associated with stage II, (c) Burst-type waves associated with stage III.

Figures 5a-d express the signal amplitude and the heater current vs. test time for the entire test, and individually for stage II and III, respectively. As shown in Fig. 5a the main stages and the transition zones from one to another are well reflected. In addition, the amplitude level reference (30 to about 45 dB) is observed up to 40 s after the test was initiated. Although the current was increased the amplitude levels up to 145 s remain almost unchanged as compared to the reference one. However, by refining the data using density function (not shown) signals with 35 dB become dominant. Figure 5b emphasizes a dramatic change in the amplitude level in stage II regime from 35 dB up to 70 dB. In stage III in the boiling curve, the increase of the amplitude further up to 85 dB (Fig. 5c) indicates a change in the mechanism, which may be associated with bubble coalescence. Figure 5d depicted stage III with almost constant amplitude of 85 dB up to the final test time.

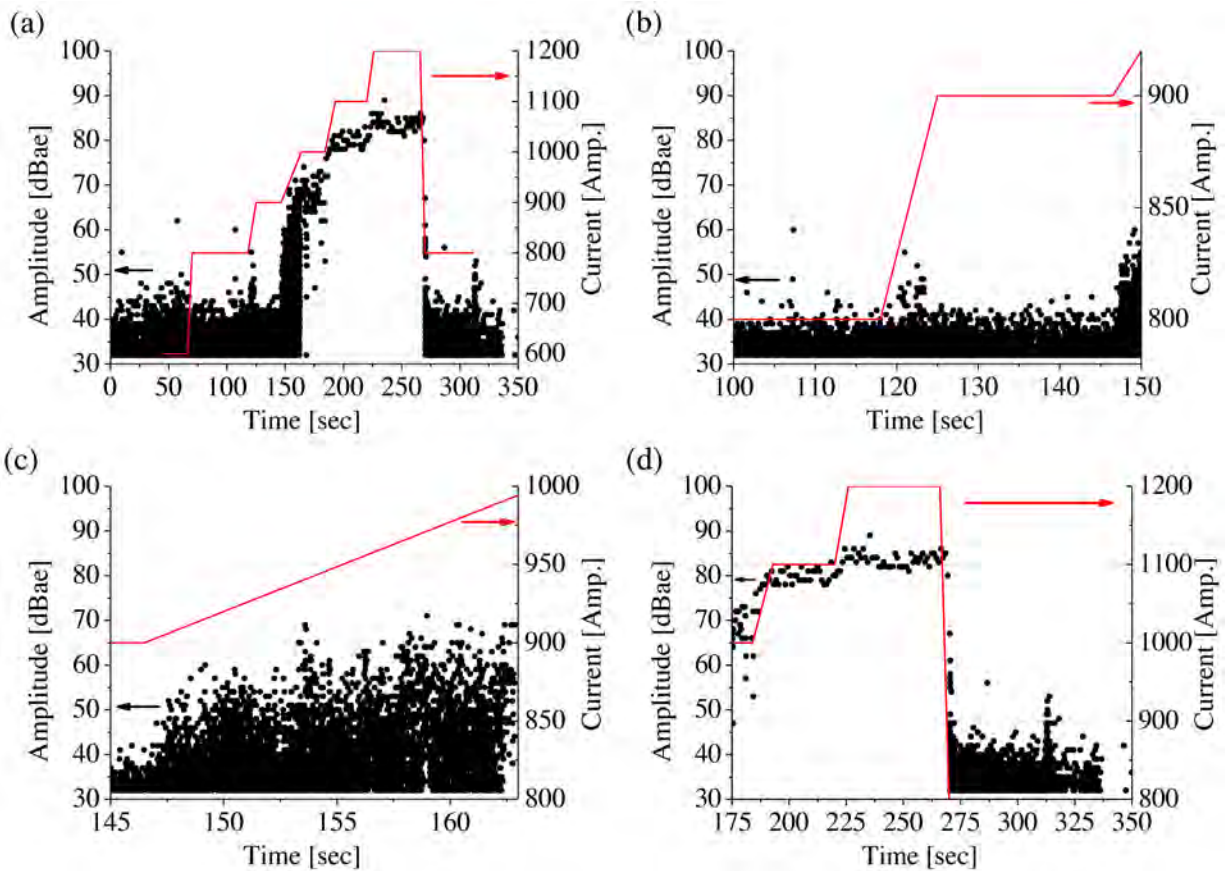


Fig. 5. Signal amplitude vs. time: (a) entire time set, (b) Stage I, (c) Stage II, (d) Stage III.

In order to assess the relation between the known mechanisms and the AE signals, a wavelet analysis was applied using AGU-Vallen software [11]. This analysis helped us distinguish between various types of boiling regime in terms of frequency and amplitude distribution in time domain. Those analyses showed that continuous emission (see Fig. 4b) from stage II of the boiling curve is not characterized by any significant peak frequency (not shown here). This type of emission is attributed to the initiation stage of the boiling process accompanied by bubble formation in the range of microns followed by collapse mechanism. In contrast, the column region (Stage III) is manifested by discrete AE burst signals as displayed in Fig. 6a. As shown, the wavelet analysis is depicted in two and three dimensions indicating on the main peak frequencies with the dominated one at 300 kHz. Noise signals that derived from undesired sources, such as heating shut-off and contraction of the heating element were around 1000 kHz and easily recognized (Figs. 7 a-b). Again the wavelet analysis was shown in two and three dimensions with the

dominant noise frequencies. Although the sensors were resonance type, we could distinguish the mechanisms based on the fact that the true signal frequency is around the wavelet frequency and near one of the resonant of the sensor, but not necessarily the exact one.

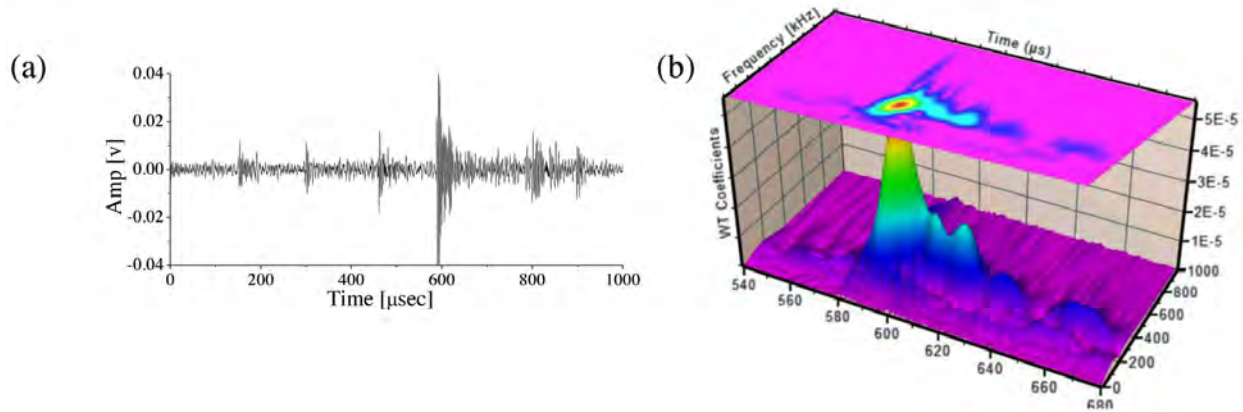


Fig. 6. (a) Typical burst wave associated with stage III, (b) Wavelet analysis with dominant frequency around 300 kHz.

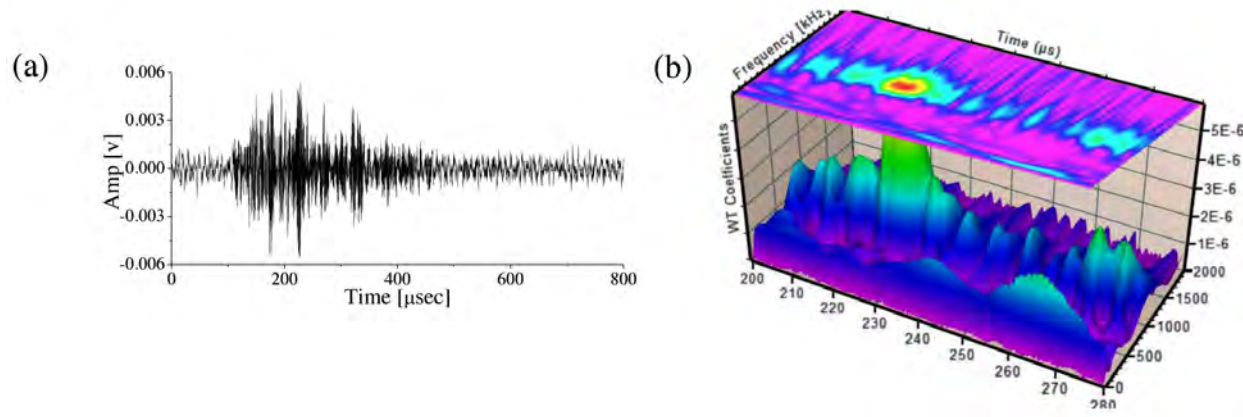


Fig. 7. (a) Typical noise wave, (b) Wavelet analysis with dominant frequency around 1 MHz.

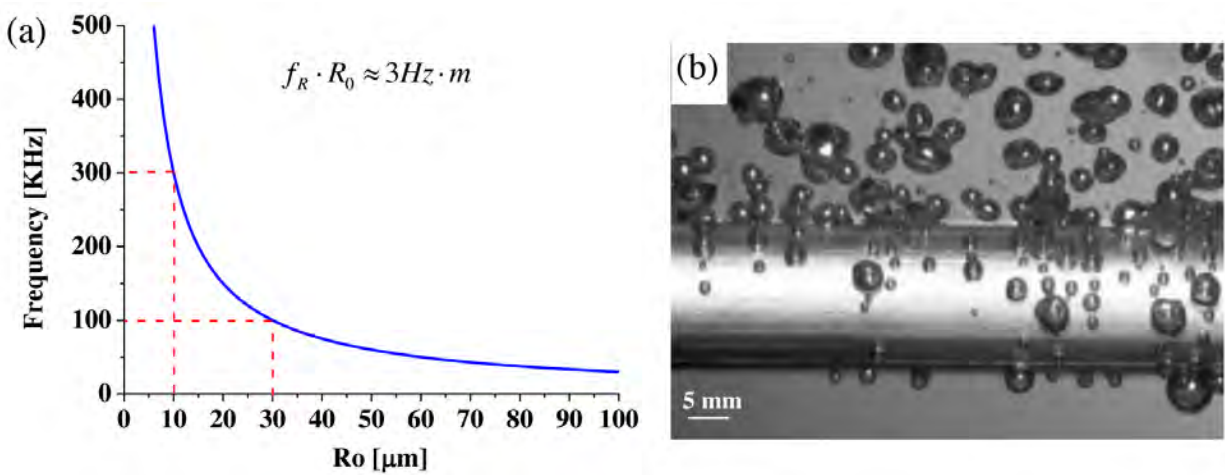


Fig. 8. (a) First approximation of Minnaert equation for bubble sizes vs. frequency, (b) Bubbles on heating element surface.

Similar frequency of bubble formation and detachment around 300 kHz was reported by Husin and Mba [12]. They were the first to correlate the AE energy of bubble burst with bubble size. In addition, they showed that with increasing bubble size, the AE of bubble burst also

increases. Statistically, it was found that the best AE parameter indicator for bubble study was AE amplitude. Based on the Minnaert equation [10] (Fig. 8a) one can estimate the bubble size with regard to the frequency range at stage II of water boiling process, to be in the range of 10-20 μm . As mentioned by Manasseh [1] bubbles size during formation are in the range of tens to hundreds of microns and only active acoustic method may be best to detect such small bubble size. Figure 8b shows an example of bubble formation in the range of 0.1-5 mm during boiling process at and near the heating element surface [13].

Conclusions

Based on the preliminary AE results, the following conclusions may be drawn:

1. Good feasibility in detecting very early stage of bubbles formation.
2. Transitions in mechanisms during boiling process can be distinguished clearly. The transition is well observed and characterized by discontinuity, burst and decay profile.
3. Sequence events during specific boiling stage can contribute to the analysis of dynamic bubbles growth, collapse and coalescence.
4. Peak frequency around 300 kHz is assumed to relate to bubble detachment micro-mechanism.
5. AE data can serve as complementary information to other characterization techniques in detecting the initiation and progression stages in boiling process monitoring.

Finally, more need to be done in order to incorporate this powerful technique in predicting the incidence of boiling in nuclear reactors. This is also the case for monitoring heat exchanger systems in the industrial chemical processes, detecting gas bubbles in the petrochemical industry and detecting gas layers in oil drilling [14].

References

- [1] R. Manasseh. Passive acoustic analysis of complex bubbly flows, *16th International Congress of Chemical and Process Engineering*, 22-26 August 2004, Prague - Czech Republic, Paper No. 1272.
- [2] V. Höller, M. Ruzicka, J. Drahos, L. Kiwi-Minsker, A. Renken. Acoustic and visual study of bubble formation processes in bubble columns staged with fibrous catalytic layers. *Catalysis Today*. **79-80**, 2003, 151-157.
- [3] G. Hetsroni, A. Msyak, E. Pogrebnyak, I. Sher, Z. Segal. Bubble growth in saturated pool boiling in water and surfactant solution. *International Journal of Multiphase Flow*. **32**, 2006, 159-182.
- [4] S. Nukiyama. The maximum and minimum values of heat transmitted from metal surface to boiling water under atmospheric pressure. *Journal of Japan Society of Mechanical Engineers*. **37**, 1937, 367-364.
- [5] Y.A. Cengel. *Heat Transfer a Practical Approach*. 2nd ed. McGraw-Hill, 2003.
- [6] T.G. Leighton. *The Acoustic Bubble*. Academic press, London, 1997.
- [7] R. Manasseh, G. Riboux, A. Bui, F. Risso. Sound emission on bubble coalescence: imaging, acoustic and numerical experiments. *16th Australasian Fluid Mechanics Conference*, 2007, 167-173.
- [8] C.Y. Han, P. Griffith. The mechanism of heat transfer in nucleate pool boiling - part I., *International Journal of Heat and Mass Transfer*. **8**, 1965, 887-904.
- [9] T. Divoux, V. Vidal, F. Melo, J.C. Géminard. Acoustic emission associated with the bursting of a gas bubble at the free surface of a non-Newtonian fluid. *Physical Review E*, **77**. 056310, 2008, 1-7.

- [10] M. Minnaert. On musical air bubbles and the sound of running water. *Philosophical Magazine*. **16**, 1933, 235-248.
- [11] AGU-Vallen Wavelet software, Vallen Systeme GmbH, November 2011. URL: <http://www.vallen.de/wavelet/>.
- [12] S. Husin and D. Mba. Acoustic emission of a single bubble activities. *Proceedings of the World Congress on Engineering 2010 Vol. II*, June 30- July 2, 2010, London, U.K.
- [13] URL: http://www.thefullwiki.org/Nucleate_boiling.
- [14] R.H. Telling, A.J. Walton, Bernoulli excitation and detection of gas bubbles, *Ultrasonics*, **39**, 2001, 455-459.

AE MONITORING OF LIGHTNING-DAMAGED CFRP LAMINATES DURING COMPRESSION-AFTER-IMPACT TEST

JAE-HA SHIN and OH-YANG KWON

Department of Mechanical Engineering, Inha University, Incheon 402-751, Korea

Abstract

Carbon-fiber reinforced plastic (CFRP) laminates made of nano-particle-coated carbon fibers and damaged by a simulated lightning strike were tested under compression-after-impact (CAI) mode, during which the damage progress due to compressive loading has been monitored by acoustic emission (AE). The impact damage was induced not by mechanical loading but by a simulated lightning strike. Conductive nano-particles were coated directly on the fibers, from which CFRP coupons were made. The coupon were subjected to the strikes with a high voltage/current impulse of 10~40 kA within a few μ s. The effects of nano-particle coating and the degree of damage induced by the simulated lightning strikes on AE activities were examined, and the relationship between the compressive residual strength and AE behavior has been evaluated in terms of AE event counts and the onset of AE activity with the compressive loading. The degree of impact damage was also measured in terms of damage area by using ultrasonic C-scan images. The assessment during the CAI tests of damaged CFRP showed that AE monitoring appeared to be useful to differentiate the degree of damage hence the mechanical integrity of composite structures damaged by lightning strikes.

Keywords: Carbon-fiber reinforced plastic (CFRP), electrical conductivity, lightning-strike damage, nano-particle coating, compression-after-impact (CAI)

Introduction

Composite materials are increasingly used in aircraft structures because of their high specific stiffness and strength, good fatigue and corrosion resistances [1]. Recently, the application of carbon-fiber reinforced plastics (CFRP) in commercial airframes becomes in reality even for primary structures such as fuselage as well as main wings. Excellent specific properties are the major driving forces to structural application of CFRP, but the sensitivity of laminated composites to impact loading in the thickness direction has been a serious obstacle to more widespread use of this class of materials. This is because the energy dissipated during impact is mainly absorbed by a combination of matrix damage, fiber fracture and fiber-matrix debonding, thus leading to significant reductions in the load-carrying capability of the material. In particular, compressive strength of brittle composite system is reduced remarkably after impact loading such as tool dropping and/or low-speed foreign object crashing [2]. Therefore, the damage tolerance becomes a major concern of reliability assessment. Since these types of damage are virtually invisible, the evaluation of residual strength under the compression-after-impact (CAI) condition has been considered as a critical step in damage-tolerant design of numerous composite structures [3].

Another issue newly raised due to the use of composites in commercial airframe is their vulnerability to lightning-strike damage. Every commercial airplane can be exposed to lightning strikes on average about twice a year [4]. With composites employed as the major structural materials for fuselage, a serious concern about the lightning-strike damage becomes in reality due to the poor electrical conductivity of composites comparing to that of aluminum alloys [5]. When

the fuselage is exposed to lightning strike, they shall suffer direct damages, such as puncture, spark propagation, local heating effect as well as indirect damages such as electromagnetic interference. If the external pressure acts on the surface of damaged area of fuselage, it will increase the severity of damages due to pressure from outside than the surface of the normal area. A study found that CFRP laminates made of carbon fibers coated with conductive nano-particles could reduce the lightning-strike damage by increased electrical conductivity [6].

In this study, CFRP coupons previously subjected to a simulated lightning strike were tested under the CAI condition and the damage progress due to compressive loading was monitored by acoustic emission (AE) activity.

Specimens and Experimental Setup

Six types of materials in total were tested; two types of prepregs, UD-CFRP and woven-CFRP were used and for each of them, three different laminates were prepared; the uncoated, the ITO 30% coated, and the ITO 40% coated. The uncoated UD-CFRP coupons were prepared as a reference from a unidirectional (UD) prepregs (USN125C, SK Chemicals). For the ITO-coated CFRP coupons, first the matrix resin was removed by soaking the prepregs in methyl-etherketone (MEK) and then indium-tin oxides (ITO) nano-particles of 30% and 40% concentrations in colloidal suspension were spray-coated directly on carbon fibers and dried. The ITO-coated carbon fiber bundles were placed between resin films on a hot press to reproduce a nano-particles-coated CFRP prepregs. The stacking sequence of CAI test coupons was $[0/90]_{8s}$, with the lateral dimension of 100 x 150 mm and the nominal thickness of 3.6 mm. The woven-CFRP coupons were prepared similarly from a plain weave, dry graphite fabric (BMS 9-8 3K-70-PW, Pacific Composites) except there was no need to remove the resin by soaking it in MEK. After the fabric was spray-coated with ITO nano-particles, CAI test coupons were prepared at hot press by using the same resin films as in the UD-CFRP coupons. The uncoated woven-CFRP coupons were also prepared as a reference.

Simulated Lightning Strikes and CAI Tests

The impact damage was induced by the simulated lightning strikes with an impulse current generator (ICG). The center of CFRP coupons was shot by the high voltage/high current ICG at 10, 20, 30 and 40 kA with a waveform of 8 μ s in rise time and 20 μ s in total duration. Damaged area of woven-CFRP coupons were virtually invisible even after the impulse current of 40 kA was applied. The CAI test fixture was prepared based on ASTM D7137 as shown in Fig. 1 [7], but was modified slightly from previous experiences of compression tests of CFRP. CAI tests were performed with a screw-driven mechanical test machine as shown in Fig. 2 where a CFRP coupon was in the CAI test jig. The crosshead speed was set to 1.25 mm/min for all tests under displacement control.

Four small AE sensors (B1025, Digital Wave) were mounted at each quadrant, with their location 36 mm away from the corner and toward the center of the CFRP coupon. They were fixed to the surface by using a spring-assisted attachment and grease couplant. Outputs of AE sensors were pre-amplified 40 dB and filtered by a band-pass filter of 100 kHz to 1.2 MHz, then processed recorded by using AE data acquisition boards (MISTRAS 2001, PAC). Threshold was set at 45 dB after pre-amplifier for the tests of UD-CFRP coupons, but was adjusted at 35 dB for woven-CFRP coupons since it appeared to be losing some low amplitude AE signals arrived before the maximum compressive load was reached.

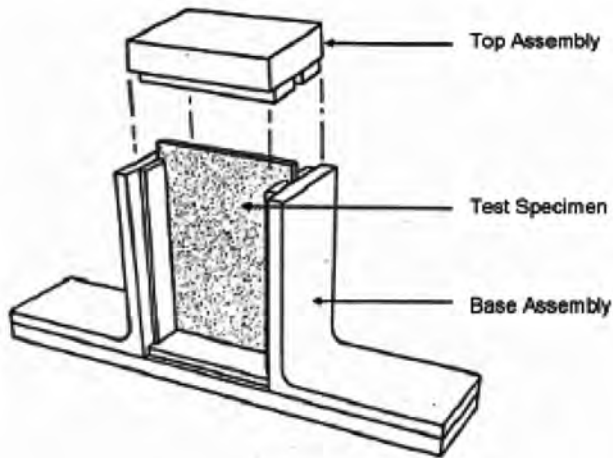


Fig. 1 CAI test fixture, ASTM D7137 [7].



Fig. 2 CFRP coupons in place for CAI test.

Degree of Damages and AE Activities

Figure 3 shows the photographs of UD-CFRP coupons after the completion of CAI tests. The left coupon was broken along the centerline containing the lightning-strike damaged area. The right coupon was broken along a line slightly above the damaged area. The latter is commonly observed as acceptable failure modes under ASTM 7137, however. Those of woven-CFRP coupons showed similar behavior but the broken surface was not as clear as shown in Fig. 3.

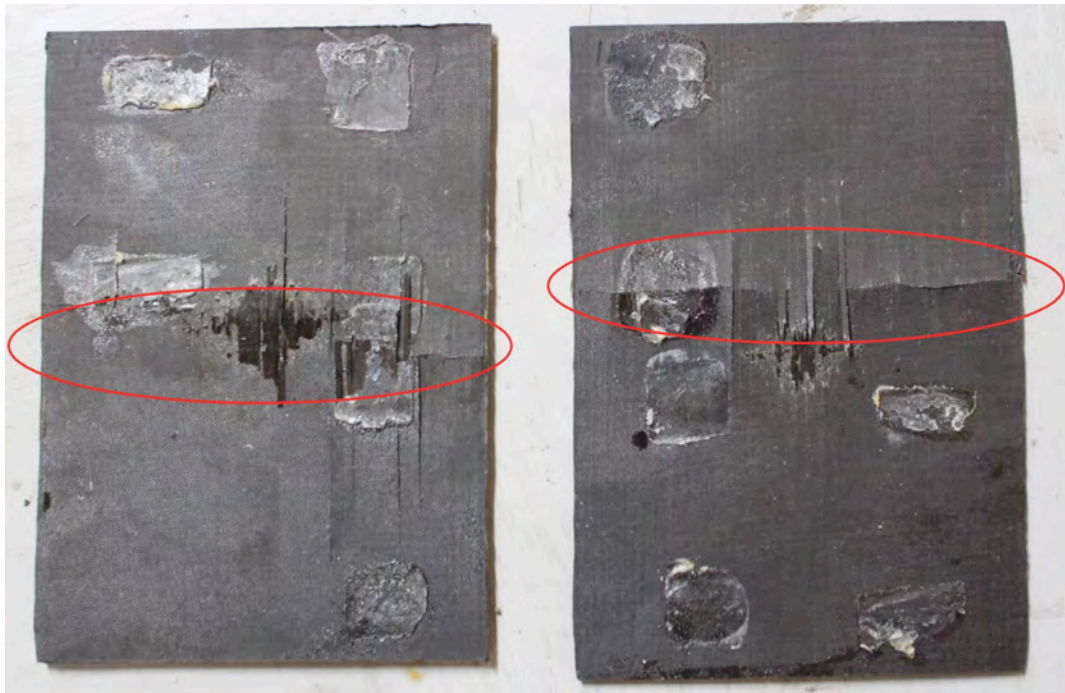
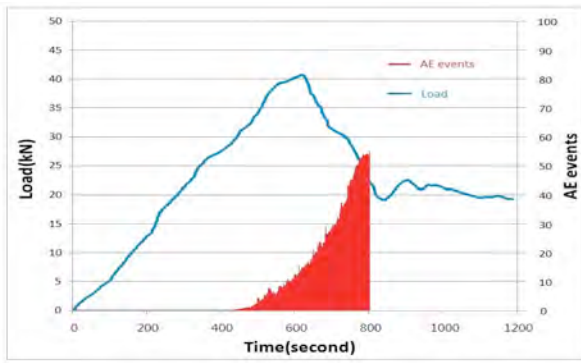
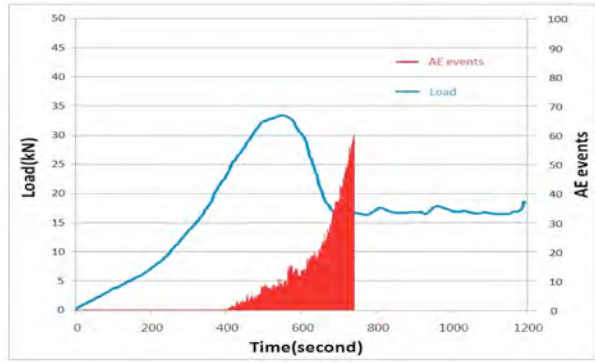


Fig. 3 Photographs of CFRP specimens after the CAI tests.

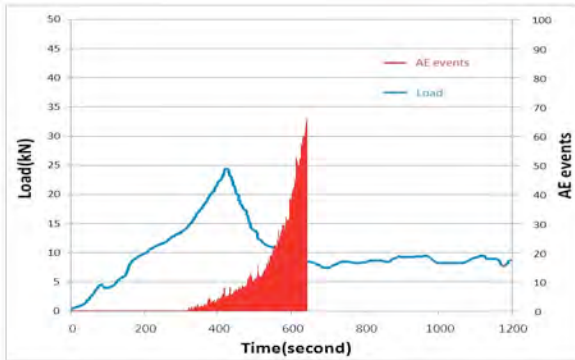
In Fig. 4, the primary data obtained during the CAI tests are shown as the relationship between compressive load and AE events with time for the uncoated, whereas the same data are shown in Fig. 5 for the ITO 40% coated. For both cases AE activity started earlier with the increasing level of impulse current applied, which corresponds to the severity of impact damage, but the onset of AE activity was significantly delayed with the ITO 40% coated in Fig. 5 regardless of the level of impulse current applied. In general, the maximum and residual compressive



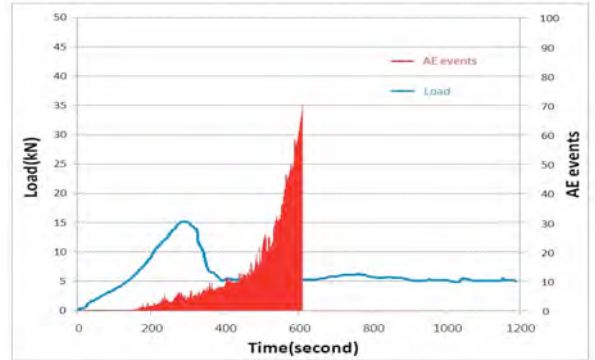
(a) Uncoated and 10 kA



(b) Uncoated and 20 kA

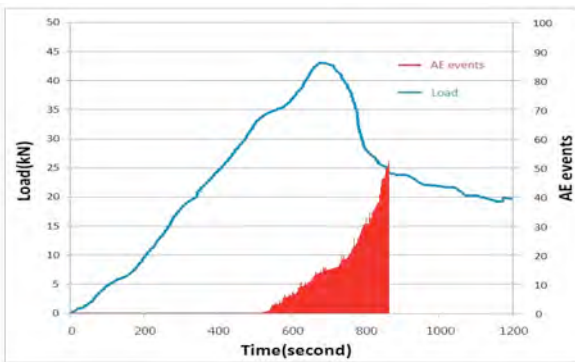


(c) Uncoated and 30 kA

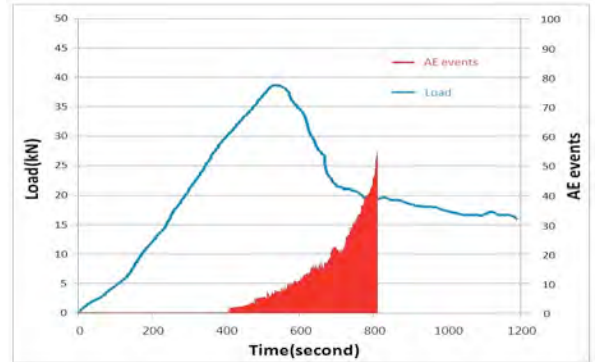


(d) Uncoated and 40 kA

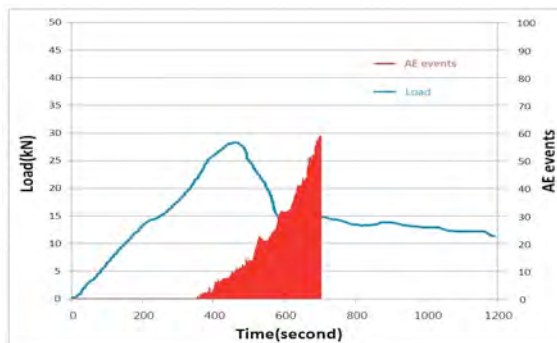
Fig. 4 Relationship between load and AE events with time for uncoated woven-CFRP.



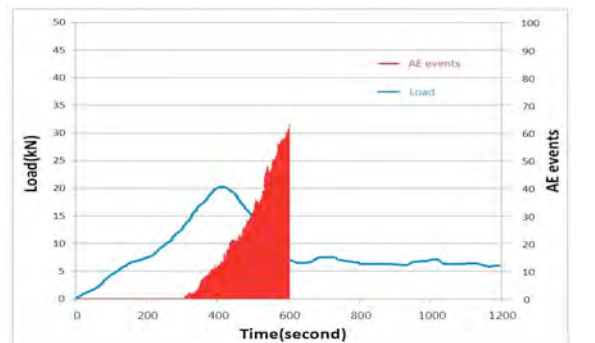
(a) ITO 40% coated and 10 kA



(b) ITO 40% coated and 20 kA



(c) ITO 40% coated and 30 kA



(d) ITO 40% coated and 40 kA

Fig. 5 Relationship between load and AE events with time for ITO 40% coated woven-CFRP.

strengths were also lower for the uncoated and damaged than for the ITO 40% coated and damaged. This is because higher degree of damage was induced for the uncoated CFRP coupons with lower electrical conductivity at the same level of impulse current. On the other hand, more AE events were observed overall with increasing level of impulse current applied.

It appeared that the severe damage induced by stronger electrical shocks produced more sources of AE when the coupons were tested under CAI test mode. It becomes even clearer if one can combine the relationship between the maximum compressive strength and the level of impulse current given in Fig. 6, and the impact-damaged area measured by ultrasonic C-scan in Fig. 7. It could also be shown as the direct relationship between the damaged area and AE total event as given in Fig. 8.

In Fig. 6, the relationship between the maximum compressive strengths and the level of impulse current are shown for woven-CFRP. The maximum compressive strength appeared to be almost inversely proportional with the level of impulse current applied for all types of CFRP coupons; UD- and woven-CFRP, and the uncoated, the ITO 30% coated, and the ITO 40% coated. At the same level of impulse current applied, the uncoated showed always the lowest strength whereas the ITO 40% coated showed the highest strength. For UD-CFRP coupons, a similar behavior was observed although the maximum compressive strength was generally lower, and the detailed data was reported elsewhere [8].

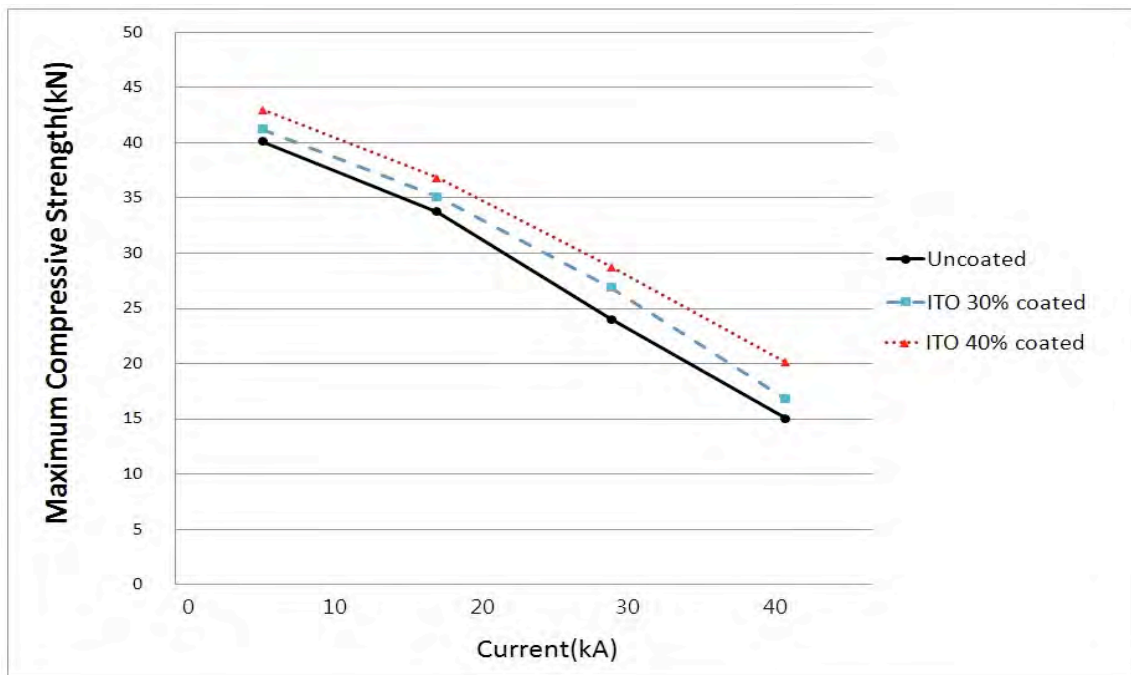


Fig. 6 Relationship between the maximum compressive strength and the level of impulse current applied for Woven-CFRP

The ultrasonic C-scan images of impact-damaged area are shown in Fig. 7 for UD-CFRP coupons. They were measured by using an ultrasonic scanning unit with 64-channel linear phased array transducer working at the center frequency of 5 MHz (Matrixeye EX, Toshiba) with a built-in function of area calculation. A visual image of damaged area for the uncoated (d) is also shown as a reference. The impact-damaged area was the largest for the uncoated, intermediate for the ITO 30% coated, and the smallest for the ITO 40% coated. The damaged area increased with increasing level of impulse current applied. For woven-CFRP coupons, a similar

trend was observed although the impact-damaged area was virtually invisible and generally much smaller than those shown here for UD-CFRP.

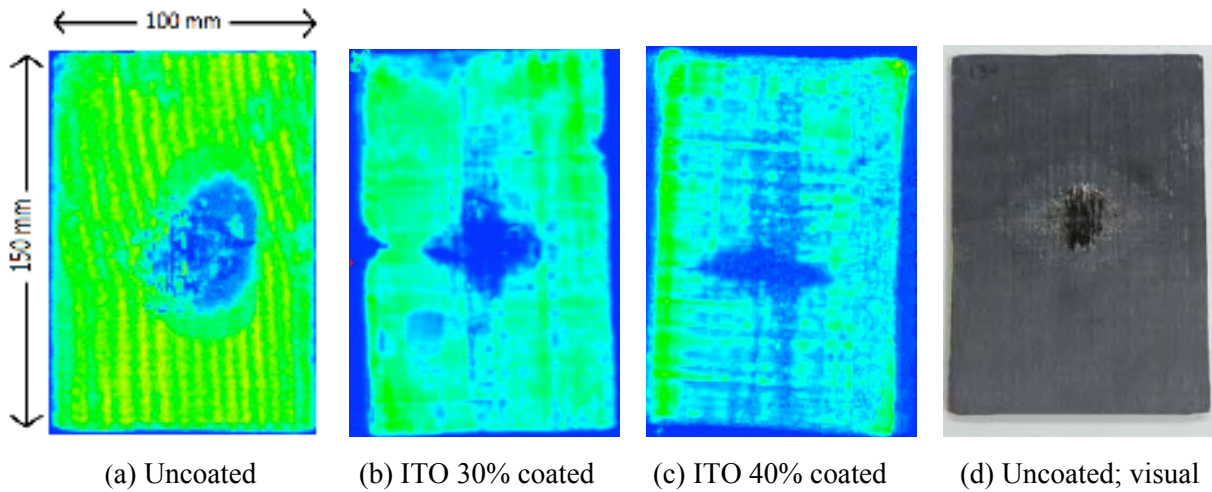
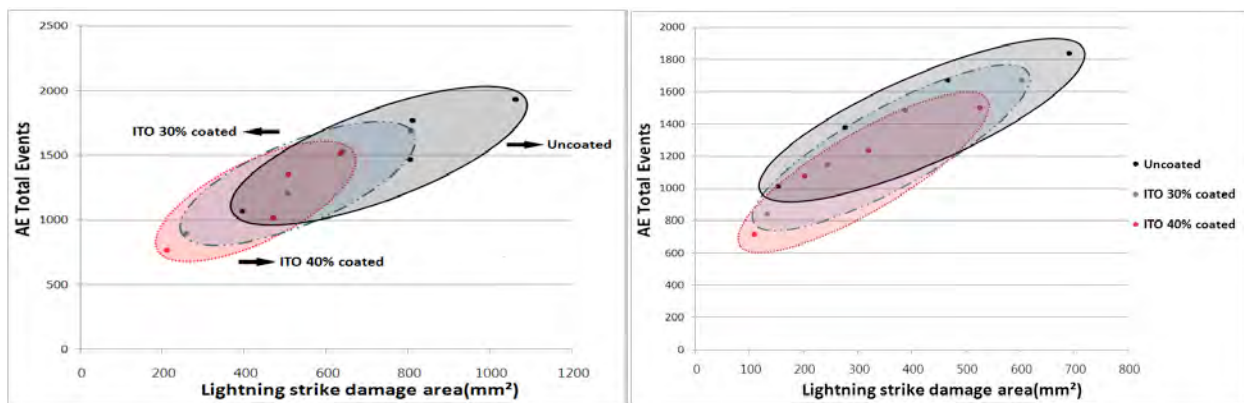


Fig. 7 Impact-damaged area measured by ultrasonic C-scan images for UD-CFRP coupons after the impulse current of 40 kA was applied. A visual image for the uncoated is also shown as a reference.

The overall AE activity for each type of CFRP coupons are summarized in Fig. 8 (a) and (b) in terms of AE total events versus the impact-damaged area for three different conditions of CFRP's in terms electrical conductivity. AE event counts appeared to be almost proportional to the impact-damaged area, which is again proportional to the level of impulse current applied for both types of CFRP coupons. The good correlation between AE events and the impact-damaged area induced by the impulse current can be utilized as a useful indicator of the degree of lightning-strike damage in composite airframes.



(a) UD-CFRP coupons (b) Woven-CFRP coupons
Fig. 8 Relationship between AE total events and lightning-strike damaged area.

The relationship between AE total events and the maximum compressive strength with the level of impulse current applied is shown in Fig. 9 for woven-CFRP coupons. With increasing level of impulse current, AE total events increased regardless of the condition of CFRP coupons, whereas the maximum compressive strength decreased. A similar behavior was observed for UD-CFRP coupons and reported elsewhere [8]. Therefore, smaller counts of AE total events implied smaller impact-damaged area and the higher maximum compressive strength.

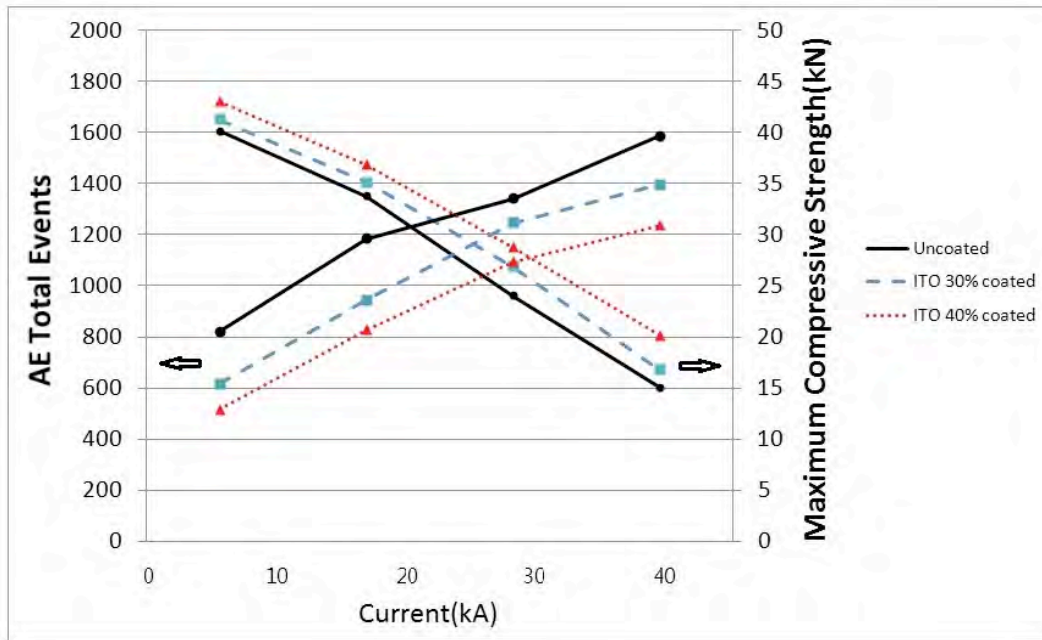


Fig. 9 Relationship between maximum compressive strength and total AE counts with the level of impulse current applied for Woven-CFRP coupons

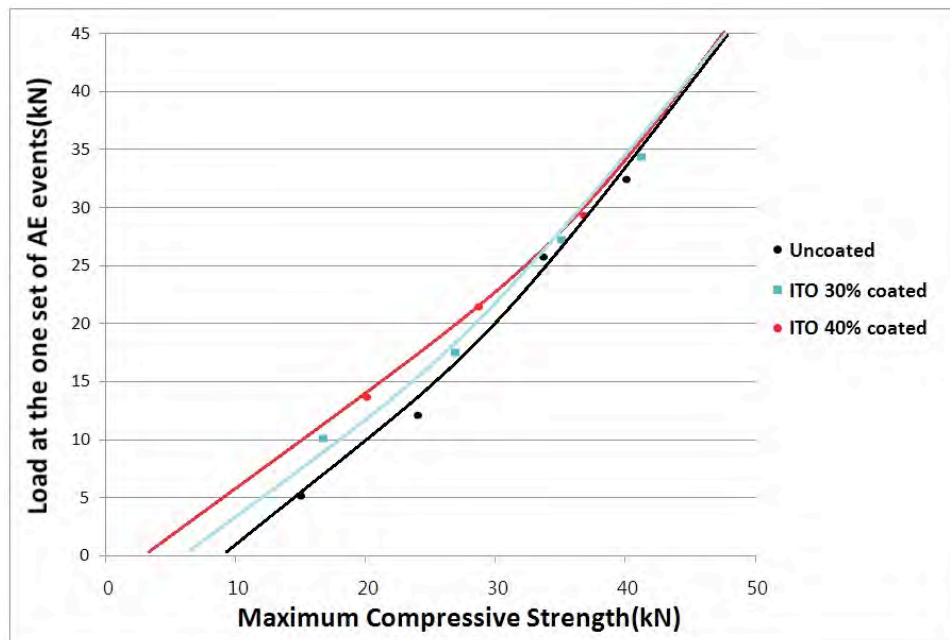


Fig. 10 Relationship between the maximum compressive strength and the stress level at the onset of AE activity.

In Fig. 10, the stress level at which AE activity started were calculated from the data shown in Figs. 4 and 5 and correlated with the maximum compressive strength for each condition of woven-CFRP coupons. The onset of AE activity was based on the detected of AE events with the pre-determined threshold level. Since the maximum compressive strength appeared almost inversely proportional to the levels of impulse current as shown in Fig. 6, the lower maximum compressive strength means higher degree of the impact-damage. The lower left part of Fig. 10 represents this condition. The stress level at the onset of AE activity appeared much lower for the

uncoated than for the ITO 40% coated. On the other hand, the upper right part of Fig. 10 represents the higher maximum compressive strength, hence lower degree of the impact-damage. In this case, the difference between different conditions of woven-CFRP was smaller. A similar behavior was observed for UD-CFRP coupons [8]. Therefore, this could be another useful indicator of the degree of damage induced by lightning strikes in composite airframes.

Conclusions

AE activity of CFRP coupons made of nano-particles-coated carbon fibers and then subjected to a simulated lightning strike by using a high voltage/high current impulse current generator was monitored under CAI test mode. AE data were evaluated in terms of the level of impulse current applied to simulate the lightning strike, hence the degree of impact-damage and the maximum compressive strength measured by the CAI tests. Coating of ITO nano-particles up to 40% in colloidal suspension appeared to be an effective means to prevent from lightning-strike damage in composite airframes. Compressive strength after the impact has close correlation with the level of impulse current applied and the lightning-strike damaged area. A good correlation between AE total events and the impact-damaged area induced by the impulse current applied can be utilized as a useful indicator of the degree of lightning-strike damage in composite airframes. The correlation between the maximum compressive strength and the stress level at the onset of AE activity could be another useful indicator of the degree of lightning-strike damage.

Acknowledgement

This work was supported by Inha University Research Grant.

References

- [1] J.R. Kollgaard and S.G. LaRiviere, "NDE Challenges with Future Commercial Aircraft – A Boeing Perspective", *Review of Progress in Quantitative NDE*, **27**, 2008, 23-28.
- [2] F. Aymerich and P. Priolo, "Characterization of fracture modes in stitched and unstitched cross-ply laminates subjected to low-velocity impact and compression after impact loading", *International J. of Impact Engineering*, **35**, 2008, 591-608.
- [3] I. Ohsawa, I. Kimpara, K. Kageyama, T. Suzuki, and A. Yamashita, "AE Characterization of Compressive Residual Strength of Impact-Damaged CFRP Laminates", *Progress in Acoustic Emission VII*, JSNDI, 1994, pp. 511-516.
- [4] F.A. Fisher, J.A. Plumer and R.A. Perala, *Aircraft Lightning Protection Handbook*, Federal Aviation Administration, DOT/FAA/CT-89/22, September 1989.
- [5] J. Guo, Y. Tang, F. Liang, Z. Zhao, D. Firsich and J. Fielding, "Carbon nanofiber paper for lightning strike protection of composite materials", *Composites Part B: Engineering*, **41**, (2), 2010, 192-198.
- [6] S.-W. Seo, M.-S. Ha, O.-Y. Kwon and H.-S. Choi, "Improvement of Electrical Conductivity of Carbon-Fiber Reinforced Plastics by Nano-Particles Coating", *J. of the Korean Soc. for Composite Materials*, **23**, (6), 2010, 1-6.
- [7] ASTM D7137/D7137M-07 "Standard Test Method for Compressive Residual Strength Properties of Damaged Polymer Matrix Composite Plates", American Soc. for Testing and Materials, 2007.
- [8] J.-H. Shin, O.-Y. Kwon and S.-W. Seo, "Acoustic Emission Monitoring of Compression-After-Impact Test of CFRP Laminates Damaged by Simulated Lightning Strikes", *Progress in Acoustic Emission XV*, JSNDI, 2010, pp. 115-120.

NEURAL NETWORK TECHNIQUES FOR BURST PRESSURE PREDICTION IN KEVLAR/EPOXY PRESSURE VESSELS USING ACOUSTIC EMISSION DATA

ERIC v. K. HILL, MICHAEL D. SCHEPPA, ZACHARY D. SAGER
and ISADORA P. THISTED

Aerospace Engineering Department, Embry-Riddle Aeronautical University
600 S. Clyde Morris Blvd, Daytona Beach, FL 32114

Abstract

The intent of this research project was to improve upon current nondestructive evaluation techniques for predicting the burst pressures of Kevlar/epoxy pressure vessels from acoustic emission (AE) data. AE data were recorded during the first step of hydro-burst testing of twelve unfilled and eleven inert-propellant-filled Kevlar/epoxy pressure vessels. These vessels were first impact damaged to varying degrees, after which the initial part of AE data up to 25% of the burst pressure was input to a back-propagation neural network (BPNN) capable of predicting the vessels' burst pressures. This raw AE amplitude distribution histogram data resulted in worst case predictions of 19.04% for the unfilled bottles and 5.70% for the inert propellant filled bottles. A Kohonen self organizing map (SOM) neural network was subsequently used to classify the raw AE data into the four distinct failure mechanisms typical of filament-wound composite pressure vessels. Using the matrix cracking only amplitude histogram data as input to the BPNN improved the worst case burst pressure predictions from 19.04% to 8.81% for the unfilled bottles and 5.70% to 3.85% for the inert propellant filled bottles, respectively. The greater than $\pm 5\%$ worst case error for the unfilled bottles was attributed to the scarcity of AE data available up to 25% of the expected burst pressure for BPNN processing. Thus, by inputting the amplitude histogram for the matrix cracking only data into a BPNN rather than the entire amplitude distribution histogram, the technique for predicting burst pressures in impact-damaged filament-wound Kevlar/epoxy pressure vessels was made significantly more accurate in spite of a scarcity of AE data.

Keywords: Back-propagation, neural networks, burst pressure prediction, Kevlar/epoxy pressure vessels, Kohonen self organizing map

Introduction

As the role of composite materials becomes more prominent in the aerospace industry, a nondestructive evaluation technique for ultimate load prediction for such materials arises. Composite materials are widely used in the fabrication of aerospace pressure vessels due to their high strength-to-weight ratios. Because of variability in the manufacturing process of these structures, however, there can be large variability in the ultimate strength of the finished product [1]. This uncertainty requires engineers to be able to accurately predict the burst pressures of composite pressure vessels after they are manufactured. Prediction of burst pressures is the best way to non-destructively ensure that the pressure vessels will be able to perform safely.

A major factor in the service life of composite vessels is impact damage. Impact of any magnitude can have adverse affects on the burst pressure [1]. To account for this, tests are run on damaged bottles with a variety of impact energies in order to study the effect of the damage on the burst pressure. This allows manufacturers to decide whether or not a damaged vessel will

be able to maintain its structural integrity. In many cases, destructive testing can be dangerous and not cost-effective. Using a neural network to predict ultimate failure, based on a small sample of AE data collected from the beginning of hydro-burst testing, is an effective way of solving both concerns.

Prediction Method

Until recently, our analysis of AE data has been accomplished primarily through the use of Neuralware's NeuralWorks Professional II/Plus neural network software since its release in the late 1980's. This program's ability to generate a variety of networks in a developed user interface promoted its wide usage. Recently, Mathwork's MATLAB has incorporated a Neural Network Toolbox, which includes many of the same networks. In an effort to determine whether the MATLAB neural networks could generate comparable results to NeuralWorks Professional II/Plus, the same data that was originally collected and used for predictions by Walker et al. [2] was analyzed utilizing the MATLAB Neural Network Toolbox. The low proof pressure AE data utilized came from the destructive pressurization of impact damaged Kevlar/epoxy pressure vessels. The burst pressure predictions obtained by Walker were generated utilizing NeuralWorks and the worst-case prediction error was 50% for the empty vessels and 31% for the inert filled samples. When using any neural network, the parameters of that network can be varied to yield better results. This process is called optimization, and when completed will provide the best results. Considerable optimization work was done here to determine the minimum worst case burst pressure prediction error for both sets of bottles.

Experimental Set-Up and Data Preparation

Two sets of Kevlar/epoxy pressure vessels were tested. The first was comprised of empty vessels and will be referred to as "KBD". The second set was filled with Hydroxyl Terminated Polybutadiene rubber, an inert propellant. These bottles will be referred to as "KBID". In order for the KBID bottles to be pressurized, a void in the shape of a cylinder 25.4 mm in diameter was left running along the central axis from top to bottom. The testing process remains the same for both types of vessel. To simulate damaged pressure vessels in service, Kevlar/epoxy pressure vessels were impacted by using a dead-weight drop test fixture. Two tips were used to simulate different types of impact, and each impact used a different energy magnitude. For the pressurization and configuration of data retrieval, see [1]. In order to simulate the pressurization during use, the vessels were ramped up to approximately 25% of the expected burst pressure and then dropped to zero. Each vessel was subsequently pressurized to burst.

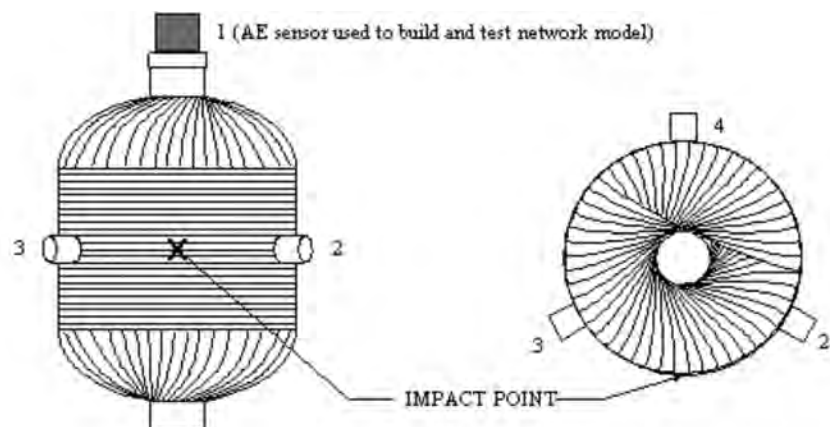


Fig. 1. Position of AE transducers on Kevlar/epoxy pressure vessels [1].

In order to record the AE information, four transducers were placed around the vessel. The first was placed on the polar boss, and the remaining three were placed around the center of the hoop region (Fig. 1). The waveform and hit data from the four AE transducers and the pressure transducer were imported into the Physical Acoustics Corporation (PAC) SPARTAN-AT computer, which converts the waveform into AE parameter data and creates dta and text files. [1]. The result was converted to an Excel file with a table of AE data from all four channels next to the corresponding pressure (in volts) sorted by time of hit. Multiple sheets were utilized to aid in the filtering process. The first sheet directly copied all the AE and pressure data. It was then split into sheets showing data from each individual channel.

To conduct the predictions on AE data from 25% of burst pressure, the data were split further. The first 25% of the data from each channel were separated onto a new sheet. Due to the approximation of the actual pressure at the top of the ramp up, another program was written to optimize the amount of data to be kept. Data recorded up to the drop in pressure were split from the ramp-to-burst data and put into their own Excel sheet (this will be referred to as the ramp up data). Neural network analysis and predictions were then determined from these AE data.

Artificial Neural Networks

An artificial neural network (ANN) is a way to take the analytical process of the human mind and allow computers to replicate it. Sets of data are input in parallel to a layer of processing neurons through weighted connections to return a desired output. Two kinds of neural networks were employed for classification and prediction in this research: a Kohonen self-organizing map and a back-propagating neural network (BPNN).

Kohonen Self-Organizing Maps

A Kohonen self-organizing map (SOM) is a competitive neural network where the input objects are compared to each other and then assigned weights based on their specified traits. The AE hits were grouped together based on their quantification parameters. This experiment used only three quantification parameters, energy, duration, and amplitude, from each AE hit as inputs. The resulting groupings were compared to known failure mechanisms from composite materials, e.g., matrix cracks, delaminations, and fiber breaks. Anything that did not fit into one of the three categories was categorized into a fourth classification known as multiple hit data (MHD), noise and data that are typically generated during the final failure of the composite structure. A depiction of the SOM used here and the resulting classifications vs. amplitude are shown in Figs. 2 and 3. A 3D plot of the SOM classifications for KBD169 is shown in Fig. 4.

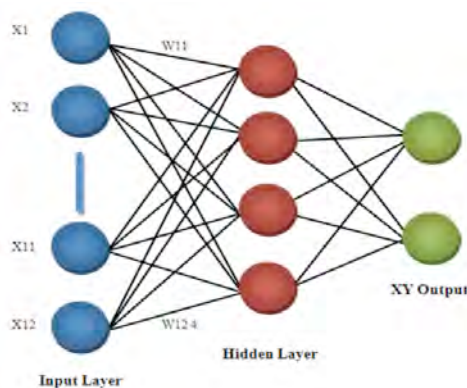


Fig. 2. Kohonen self-organizing map used.

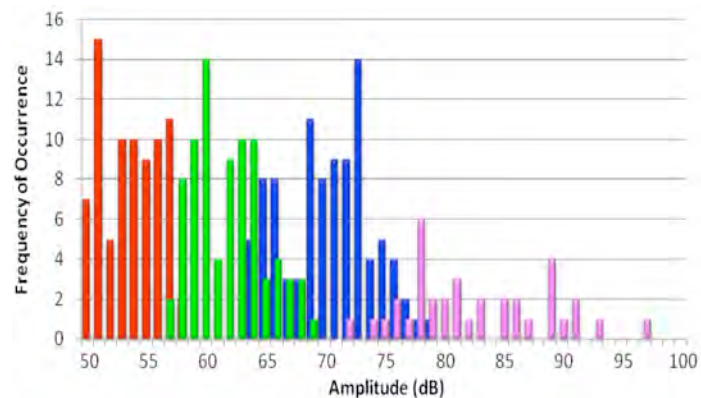


Fig. 3. Histogram of SOM result for KBD169.

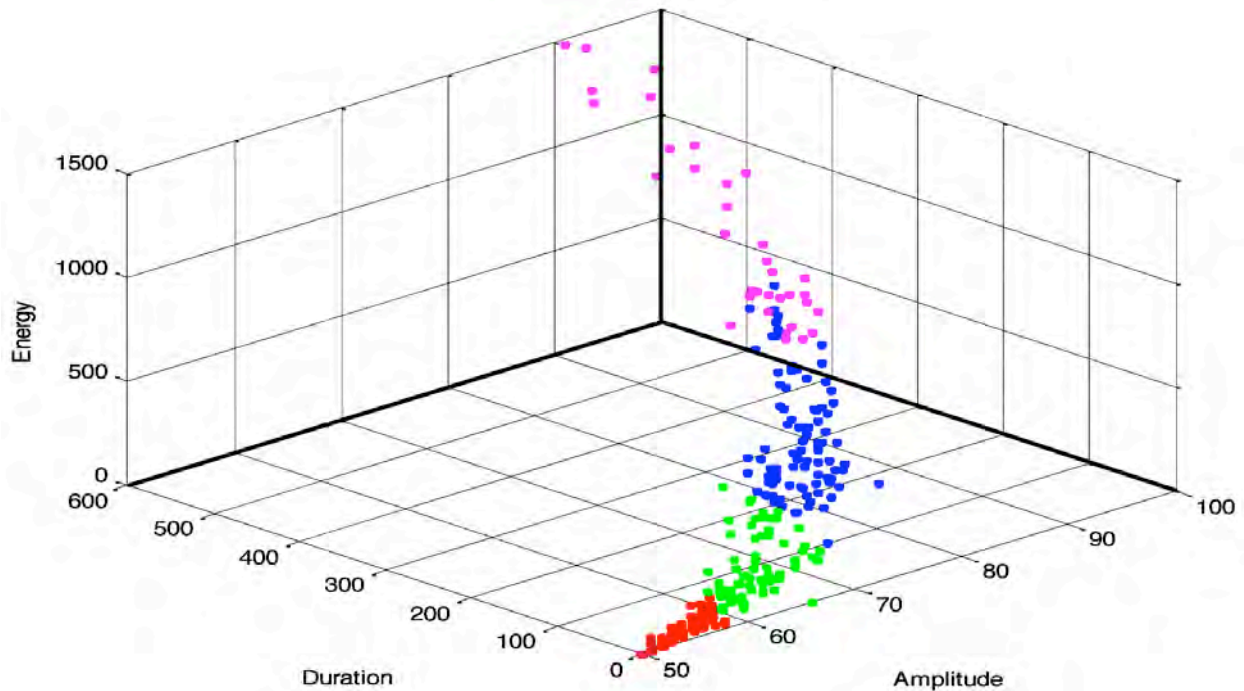


Fig. 4. 3-D plot of AE hits from KBD169 with four categories after SOM.

Back Propagation Neural Networks

A back propagation neural network (BPNN) can be used to predict outcomes based on previous results called training files. Similar to the human mind, past experiences are compared to the current situation. As training progresses, a pattern is recognized, and an accurate prediction of the end result can be made. The BPNN uses histogram data from each input and attempts to match the points with one or more transfer function(s) using weighted coefficients. The complexity of the transfer function is determined by the number of middle or hidden layer neurons. In some cases, a second hidden layer is required to accurately model the data. The output layer consists of a single neuron, which is the prediction for the final result. If the prediction is off by more than a user specified amount, the network adjusts the middle layer weights by an amount depending upon the learning coefficient and the error then runs again. The learning coefficient is kept small so that the most accurate results can be obtained [1]. This process continues for each set of data until all errors are within acceptable limits. The architecture of a typical BPNN is shown in Fig. 5.

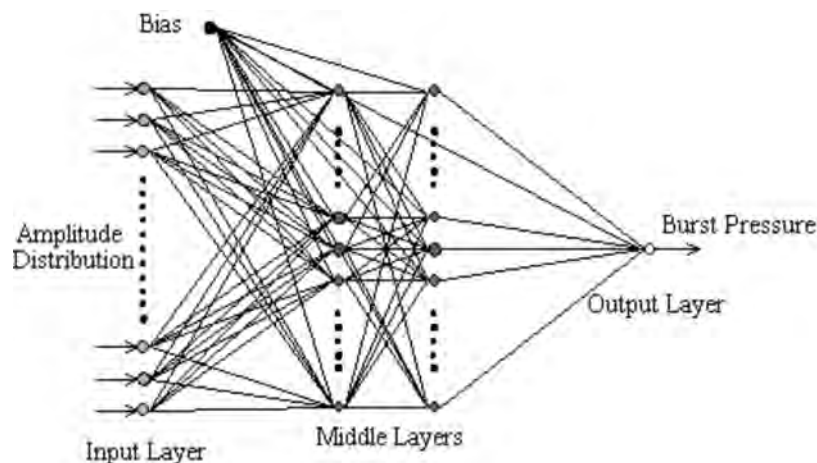


Fig. 5. Typical BPNN with multiple middle or hidden layers [1].

Optimization Process

Inputting channel-1 data only is a method used to produce the most accurate results [1]. The channel-1 transducer, located at the polar boss, was capable of receiving signals propagating both around the periphery of the vessel and those propagating through the liquid. This assumption is revisited here. Ramp-up data from each channel were individually used as input into a BPNN and used for burst prediction. The input amplitude histogram represents the frequency of hits at each amplitude. Table 1 illustrates that channel-1 data actually did produce the best results. Hence, in subsequent analyses only channel-1 data will be utilized.

Table 1. Worst-case error by channel.

Channel	Worst Case Error (%)	Bottle with Predicted Worst Case
Channel 1	5.70	KBID205
Channel 2	11.31	KBID191
Channel 3	7.09	KBID191
Channel 4	13.90	KBID245

Table 2. Ramp-up data predictions (KBD).

Bottle ID	Target	Output	Percent Error
KBD169	17.98	17.98	0.01
KBD213	16.24	15.82	2.57
KBD235	11.73	11.76	0.25
KBD187	16.60	16.60	0.01
KBD254	10.62	10.65	0.28
KBD233	21.08	21.08	0.00
KBD239	12.38	12.39	0.05
KBD241	16.23	19.32	19.04
KBD177	15.42	12.67	17.82
KBD225	14.82	12.87	13.17
KBD201	17.91	17.91	0.01
KBD215	17.26	17.25	0.06

Table 3. Ramp-up data predictions (KBID).

Bottle ID	Target	Output	Percent Error
KBID243	17.84	17.88	0.23
KBID205	21.17	19.96	5.70
KBID223	20.53	20.09	2.14
KBID249	17.65	17.19	2.60
KBID231	14.29	14.78	3.40
KBID181	16.48	16.30	1.12
KBID191	14.47	13.65	5.64
KBID185	20.86	21.44	2.80
KBID175	13.77	13.46	2.22
KBID245	15.51	15.21	1.95
KBD255	18.49	18.20	1.59

Classification of failure mechanisms through the use of SOM was not employed by Walker et al. [2]. Utilizing SOM classifications has previously demonstrated to improve the results obtained by a BPNN [3]. Thus, the first step in the optimization process was to pass the channel-1 data through SOM in an attempt to isolate the matrix cracking data. In order to determine the number of failure mechanisms, channel-1 data were classified into an increasing number of groups until each group had meaningful statistics. Classifying the channel-1 data into four groups appeared to be the most accurate. Amplitude histogram result can be seen in Fig. 3 for KBD169 case. This decision was also verified graphically by making a 3-D amplitude-energy-duration plot (Fig. 4). The overlap between the mechanisms was reduced using histograms. The groups of classified data were then sorted according to the general characteristics known to be associated with specific modes of failure and classified as such. Matrix-cracking-only data,

typically low in amplitude, energy, and duration (shown in red in Figs. 3 and 4), were then passed into the BPNN for prediction. The results can be seen in Tables 4 and 5. By inspection it can be seen that classifying the data with SOM pre-sorting and BPNN yielded better results than inputting raw channel-1 data directly into the BPNN.

Table 4. Filtered ramp-up data predictions (KBD).

Bottle ID	Target	Output	Percent Error
KBD169	17.98	17.99	0.03
KBD213	16.24	16.13	0.68
KBD235	11.73	11.87	1.16
KBD187	16.60	16.62	0.13
KBD254	10.62	11.33	6.70
KBD233	21.08	17.51	16.91
KBD239	12.38	13.20	6.65
KBD241	16.23	14.98	7.68
KBD177	15.42	16.08	4.26
KBD225	14.82	15.47	4.41
KBD201	17.91	18.12	1.17
KBD215	17.26	18.12	4.98

Table 5. Filtered ramp-up data predictions (KBID).

Bottle ID	Target	Output	Percent Error
KBID243	17.84	17.39	2.55
KBID205	21.17	20.14	4.85
KBID223	20.53	19.89	3.10
KBID249	17.65	18.13	2.71
KBID231	14.29	14.24	0.34
KBID181	16.48	16.39	0.58
KBID191	14.47	15.11	4.40
KBID185	20.86	20.46	1.90
KBID175	13.77	13.96	1.40
KBID245	15.51	15.56	0.30
KBID255	18.49	18.49	0.03

The next step in the optimization process was to determine the ideal number of hidden layer neurons. This was accomplished by using a BPNN to predict failure using varying numbers of hidden layer neurons. The number of hidden layer neurons was varied from 3 to 25. Due to the randomness associated with the initial weights in the BPNN, it was necessary to cycle through the range of neurons four times and then to compute the average of the resulting errors. From this procedure it became clear that the optimum number of hidden layer neurons for predicting burst pressures in the unfilled KBD bottles was 14, while 19 were optimal for the filled KBID bottles. The parameters used in the BPNN are shown in Table 6. Using these newly optimized parameters, the BPNN was able to predict with greater accuracy as seen in Tables 7 and 8.

Table 6. Optimized network parameters.

Network Parameter	KBD Parameter Setting	KBID Parameter Setting
Middle Layer Neurons	14	19
Learning Coefficient	0.003	0.003
Momentum	0.4	0.4
Epoch Size	9	9
Transition Point	5000	5000
Transition Ratio	0.5	0.5
F' Offset	0.1	0.1
Convergence Threshold	0.8	0.8
Transfer Function	Hyperbolic Tangent	Hyperbolic Tangent
Learning Rule	Normalized-Cumulative-Delta	Normalized-Cumulative-Delta

Through the optimization process, it was obvious that the scarcity of the Kevlar vessel AE data severely limited the accuracy of the neural network predictions. In order to offset the scarcity of data, a larger percentage of the AE data hits were input to the BPNN with SOM pre-sorting. This improved the accuracy of the predictions considerably.

Table 6. Optimal Results (KBD).

Bottle ID	Target	Output	Percent Error
KBD169	17.98	18.01	0.17
KBD213	16.24	14.81	8.81
KBD235	11.73	10.70	8.78
KBD187	16.60	16.81	1.29
KBD254	10.62	11.07	4.21
KBD233	21.08	19.45	7.74
KBD239	12.38	11.85	4.27
KBD241	16.23	15.74	3.04
KBD177	15.42	14.52	5.81
KBD225	14.82	13.66	7.85
KBD201	17.91	18.39	2.67
KBD215	17.26	17.28	0.14

Table 7. Optimal Results (KBID).

Bottle ID	Target	Output	Percent Error
KBID243	17.84	17.63	1.19
KBID205	21.17	21.03	0.68
KBID223	20.53	20.87	1.65
KBID249	17.65	17.96	1.74
KBID231	14.29	14.84	3.85
KBID181	16.48	16.84	2.18
KBID191	14.47	14.85	2.64
KBID185	20.86	20.73	0.63
KBID175	13.77	14.30	3.85
KBID245	15.51	16.00	3.15
KBID255	18.49	17.92	3.07

Conclusions

A reasonably accurate neural network procedure was developed for predicting burst pressures in impact-damaged filament-wound Kevlar/epoxy pressure vessels. Through optimization techniques, BPNN with SOM pre-sorting was able to reduce the worst-case error of its predictions from 49.84% to 8.81% on the KBD (unfilled) bottles and from 30.84% to 3.85% on the KBID (filled) bottles, respectively. Previous work [2] used NeuralWorks Professional II/Plus to predict burst pressures. After optimization, the present results were satisfactory for the scope of this evaluation. The greater than $\pm 5\%$ worst-case error for the unfilled bottles was attributed to the scarcity of AE available up to 25% of the expected burst pressure for BPNN processing.

Acknowledgements

Thanks must be extended to James L. Walker II, Chief, Non-Destructive Evaluation Branch, NASA Marshall Space Flight Center, EM20, MFSC, Alabama 35812 for providing the original AE data and experimental setup information for this research

References

1. E. Lanzarone, E.v.K. Hill, B.K.R. Manuel, J. Iizuka, A. Stepuro, and J.L. Walker II, "Self-Optimized Neural Network Burst Pressure Prediction in Composite Overwrapped Pressure Vessels," ASNT Fall Conference & Quality Testing Show, American Society for Nondestructive Testing, Columbus, OH, 2010, 8 p.
2. J.L. Walker II, S.S. Russell, G.L. Workman and E.v.K. Hill, "Neural Network/Acoustic Emission Burst Pressure Prediction for Impact Damaged Composite Pressure Vessels" *Materials Evaluation*, **55** (8), 1997, 903-907.
3. A. Gunasekera, E.v.K. Hill, M.W. Langdon, and W.D. Rice, "Compression After Impact Load Prediction in Graphite Epoxy Laminates," Nondestructive Evaluation of Aerospace Materials and Structures II Conference, St. Louis, MO, 24-25 May 2010, 6 p.

MONITORING OF METAL FATIGUE DAMAGE USING ACOUSTIC EMISSION AND THERMOGRAPHY

DIMITRIOS G. AGGELIS, EVANGELOS Z. KORDATOS
and THEODORE E. MATIKAS

Dept. of Materials Science and Engineering, University of Ioannina, Ioannina 45110, Greece

Abstract

Acoustic emission (AE) supplies information on the fracture behavior of different materials. In this study, AE activity was recorded in metal coupons with a V-shape notch, which were loaded in fatigue until final failure. AE parameters exhibit a sharp increase approximately 1000 cycles before final failure. The use of AE parameters is discussed both in terms of characterization of the damage mechanisms and as a tool for the prediction of ultimate fatigue life. Additionally, a nondestructive methodology based on lock-in thermography is applied to determine the crack growth rate using thermographic mapping of the material undergoing fatigue. The thermographic results on the crack growth rate of aluminum alloys were then correlated with measurements obtained by the conventional compliance method, and found to be in agreement.

Keywords: Aluminum, fatigue, nondestructive evaluation, tension, shear, thermography

Introduction

Acoustic emission (AE) is a method widely used for real time monitoring of the structural condition of materials and structures [1]. The cumulative AE activity, as recorded by the sensors is indicative of the severity of cracking, since crack propagation is a prerequisite for AE in most cases. High rate of incoming signals implies the existence of several active crack sources, while low or zero activity is connected to healthy material. When several sensors are used, apart from the number of AE signals (hits), the geometric location of the cracks can be extracted due to the delay between the arrivals of the waves at different measurement points [2, 3]. This allows the estimation of which part of the structure has suffered more extensive deterioration in order to take the necessary repair action, especially for large-scale structures.

However, there are other important aspects of AE measurements, which are based on qualitative parameters of the received signals. The waveform shape depends on the cracking mode, enabling the classification of cracks in different materials [4-6]. Shear cracks generally follow tensile type as the material approaches to final failure. Therefore, crack characterization may lead to an early warning. In general, when a tensile event is occurring, the sides of the cracks move away from each other, leading to a transient volumetric change of the material and consequently most of the energy is transmitted in the form of longitudinal waves, while only a small amount in shear waves, which propagate with a lower velocity. Therefore, most of the energy is recorded quite early within the received waveform. Figure 1a shows an example of AE waveform emitted by a tensile event. The delay between the onset and the highest peak (called Rise Time, RT), is short, leading to a large rise angle of the wave. In case of a shear crack (Fig. 1b), the shape (and not the volume) of the material in the vicinity of the crack changes, shifting the proportion of energy in favor of the shear waves. Therefore, the most important part of the waveform arrives much later than the fast longitudinal arrivals, leading to longer RT and consequently a small rise angle. Recently the shape of the initial part of the waveform is examined by the RA value, which is defined as the RT over peak amplitude, A, or $RA = RT/A$ and is measured in $\mu s/V$, as suggest-

ed by relevant recommendations [7]. Additionally, tensile events are characterized by higher frequency content, as expressed by the average frequency (AF) defined by the number of threshold crossing over the signal duration [7]. It is mentioned that these measurements depend on the “threshold”, which is a value set by the user high enough in order to avoid low environmental or other noise, but at the same time sensitive enough to allow recording of the actual AE hits due to crack propagation or other material processes.

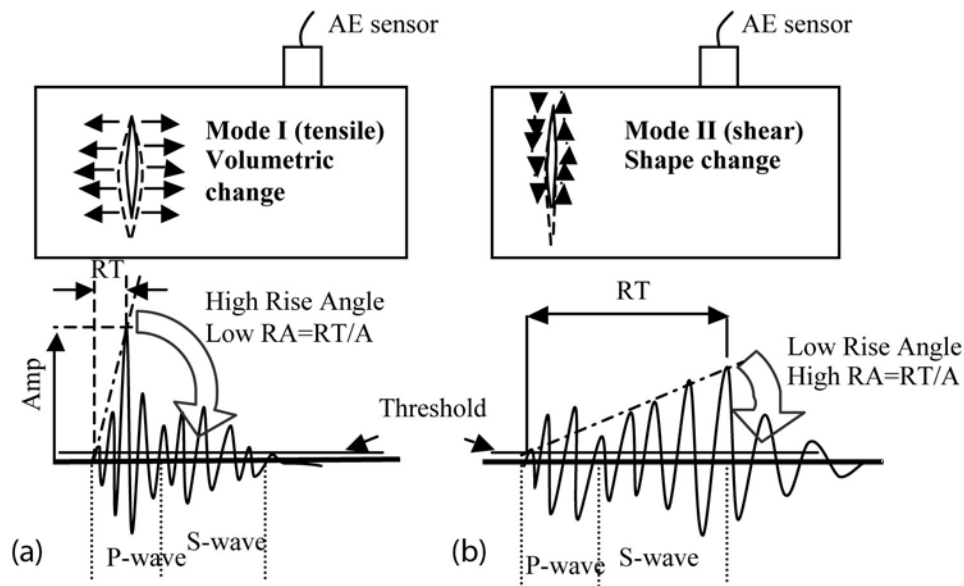


Fig. 1. Cracking modes and corresponding AE signals.

This classification scheme has proven powerful in case of laboratory applications concerning concrete cracking due to corrosion of metal reinforcing bar [5], fracture of composite laminates [4, 8], as well as the discrimination between matrix cracking and pull-out during bending of fiber reinforced concrete [9]. Specifically for the fields of metals and composites, mainly the cumulative AE activity is utilized being related to strength in single fiber-fragmentation tests [10], as well as to the remaining life in fatigue tests of steel specimens with notches [11]. Amplitude and cumulative activity have been monitored during bending of metal composite foams [12], while, concerning aluminum, AE parameters like rise time and duration have been considered in an attempt to correlate with crack growth [13, 14] and corrosive processes [15].

In this study, aluminum specimens with notches were fractured in fatigue tests. Measurements of the crack propagation rate were conducted with simultaneous AE monitoring in order to correlate the parameters obtained nondestructively with mechanical results and propose certain features as the most promising for fatigue damage characterization in metals.

Complementary to AE, infrared thermography was applied to monitor the cracking procedure during the fatigue of the same specimens. Infrared thermography is a powerful nondestructive evaluation tool, which can be effectively used for defect detection in materials such as aluminum alloys. In the industry, where inspection is of paramount importance in all fabrication stages, there is a need for fast, reliable nondestructive assessment techniques. Infrared lock-in thermography can fulfill this need because it is a quick, full-field and real-time inspection tool, which can examine a relatively large area of a structure. It is also a noncontact technique; the equipment is fairly portable and hence can be used reasonably easily in the field [16]. Lock-in thermography provides a powerful tool to study thermo-mechanical mechanisms. Instead of a simple tempera-

ture rise measurement, which depends on environmental conditions, lock-in thermography locates and measures thermal sources, which are proportional to thermo-mechanical energy, under harmonic loading and adiabatic conditions [17]. A major advantage of IR thermography applications is the detection and monitoring of sub-surface cracking [18-20].

In this paper, the fatigue crack propagation was monitored using a method, which was developed in previous work [21, 22] based on infrared lock-in thermography. The crack-tip stress field has been mapped using thermoelasticity principles. This technique is based on the fact that stresses within a solid material result in variations of the temperature. When the material is under tensile load, its temperature decreases proportionally to the load. However, when it is under compressive load, its temperature increases proportionally to the load. This behavior is known as the thermoelastic effect [17]. The setup included a radiometric camera, which measured the infrared radiation produced on the surface of the material undergoing cyclic loading, and a real-time correlator called “lock-in module”, which measured the change of temperature extracting it from the noise that is specified by the thermal resolution of the camera. Lock-in refers to the necessity to monitor the exact time-dependence between the output signal and the reference input signal [23]. This was done using a lock-in amplifier so that both phase and magnitude images become available. When the material becomes deformed, a part of the energy necessary to propagate the damage is transformed into heat [24, 25]. The heat wave, generated by the thermo-mechanical coupling and the intrinsic dissipated energy during mechanical loading of the sample, was detected by the thermographic camera.

Experimental Procedure

Materials and mechanical testing

The material was aluminum (AA7075). This material exhibits good resistance to corrosion, and high strength in environment as well as at high temperatures. Test specimens were manufactured according to ASTM E399-09e1. For the determination of the crack propagation rate (CPR) a crack opening displacement (COD) gage is fixed in the notch opening. The determination of crack propagation rate followed ASTM E647-08e1. The fatigue tests were conducted on an Instron servo-hydraulic machine with maximum static and dynamic load of ± 100 kN. The fatigue cycle was sinusoidal with frequency of 3 Hz, the stress ratio ($\text{Load}_{\max}/\text{Load}_{\min}$) was set to $R = 0.2$ and the amplitude ($\text{Load}_{\max} - \text{Load}_{\min}$) = 4 kN.

Acoustic emission

Two piezoelectric sensors (Pico, Physical Acoustics Corp., PAC) were attached on one side of the specimen (see Fig. 2). The sensors were attached using wax, which enhanced acoustic coupling, while supporting the sensors throughout the experiment. The frequency bandwidth is within 50 to 800 kHz and therefore, the sensors are suitable for monitoring of different sources. The AE signals were recorded on two channels in a PAC-PCI-2 board with a sampling rate of 5 MHz. The software used was PAC AEWIn, with AE activity and the signal parameters monitored in real time. The whole waveform data were recorded for post-processing.

Thermography

Lock-in IR thermography was used for non-contact monitoring of the crack propagation during the test. Thermographic assessment of fracture enabled determination of the crack growth rate. An infrared camera was placed at a distance from the specimen. The IR camera was connected with the lock-in amplifier and the amplifier with the main servo-hydraulic controller (see Fig. 3). Therefore, synchronization of the frequency through the lock-in amplifier and the testing

machine could be achieved and lock-in images and data capture during the fatigue testing were enabled. The experiments were conducted using an infrared camera CEDIP (MIW) with a cooled indium antimonide (InSb) detector (3-5 μm), a frame rate of 150 Hz and a focal plane array (FPA) with pixel format of 320 (H) x 240 (V). The resolution of the IR camera was 20 mK and the integration time is 1.5 ms.

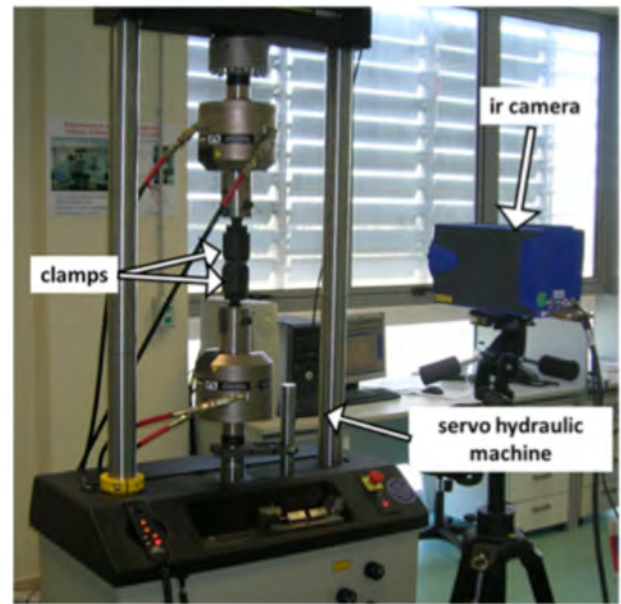
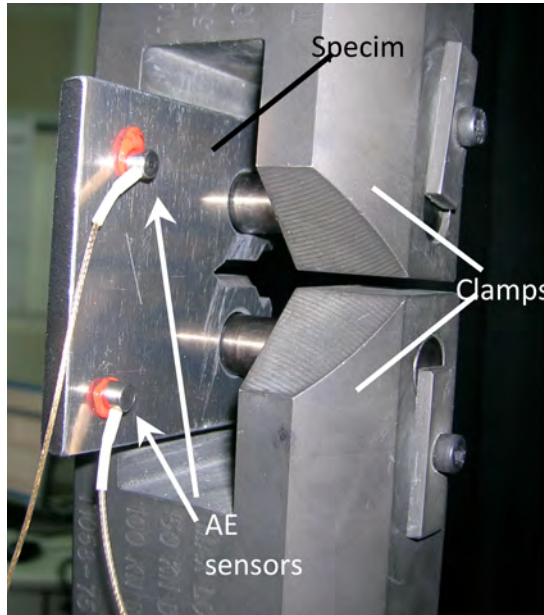


Fig. 2. Photograph of the sensors on the specimen. Fig. 3. Photograph of the experimental setup.

Results

Acoustic emission

Figure 4 shows the crack propagation rate (da/dN) as a function of time. As typically expected in metal fatigue the rate increases exponentially. The final failure of the specimen occurred at 3231 s. AE monitoring presented a more or less constant activity throughout the experiment. AE signals are recorded shortly after the start of the test. Without many fluctuations, the AE hit rate can be characterized as constant leading to a total number of almost 20000 hits.

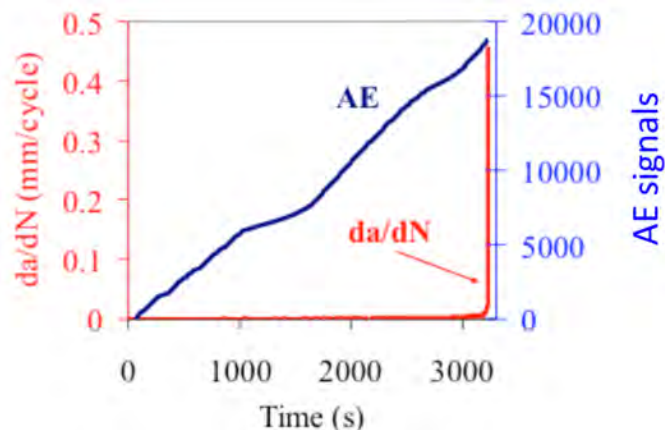


Fig. 4. Time history of CPR (or da/dN) and cumulative AE.

However, other AE parameters show a very distinct and clear trend. Figure 5 presents the duration and rise time of the signals. It is clear that approximately 200 to 300 s before the final

fracture, the duration and RT start to increase sharply. Specifically, until 3000 s the duration of the acquired signals was typically less than 3000 μs , while the RT less than 500 μs . After that point, AE signals with much longer duration and RT are recorded, as seen by the cloud of points rising to the top of the figure before the final fracture.

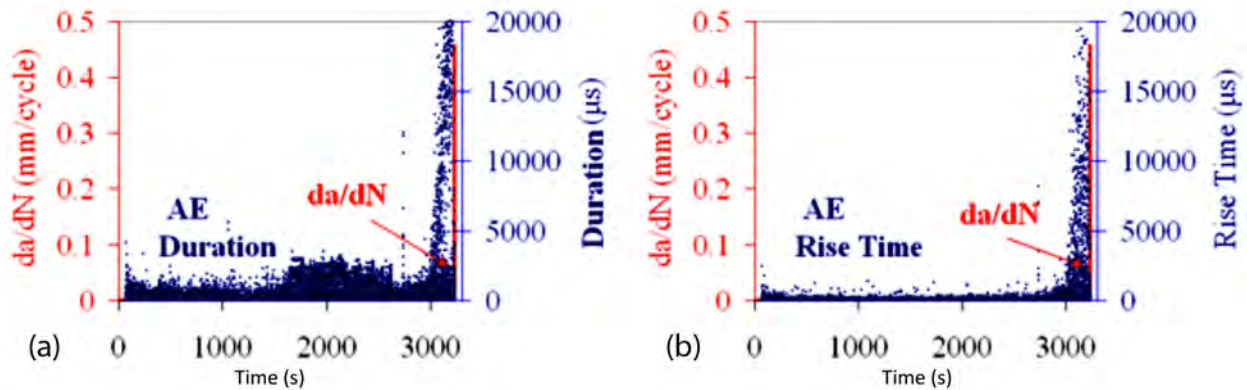


Fig. 5. Time history of CPR and (a) AE duration (b) RT.

The increasing duration and RT indicate possible shift of the cracking mode from tensile to shear. As mentioned above, this transition between different cracking modes can be examined by the RA value [7], which also takes into account the signals' amplitude. RA history in relation to the CPR can be seen in Fig. 6 for the last stage of the specimen's life (after 2500 s).

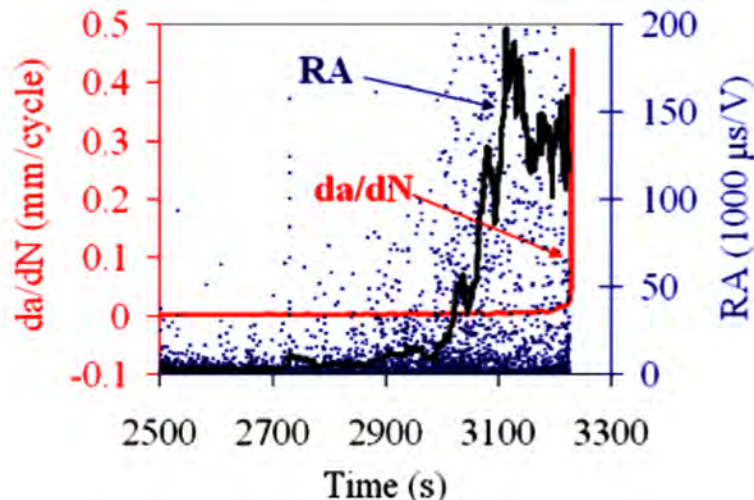


Fig. 6. Time history of CPR and RA.

Before 2700 s, RA values higher than 50 ms/V are infrequent. However, after 2900 s, the population of points expand to values higher than 75 ms/V. The solid line stands for the moving average of the recent 150 hits, which shows a clear increase at 3000 s, much earlier than the specimen's fracture. As discussed above, this shift of the RA value implies also the shift between the tensile and shear fracture modes; actually this is the sequence of the cracking modes within a typical fatigue specimen of this kind. Figure 7a shows a photograph of the fracture surface after the end of the experiment. The crack propagates horizontally for approximately 20 mm from the notch. Later, the fracture surface becomes curved. This is attributed of the local plane stress field. Due to the small thickness of the plate, the stress perpendicular to the surface (σ_z) is zero (Fig. 7b). Therefore, although the crack starts to propagate horizontally dictated by the notch, under the application of the tensile stress (σ_Y), final fracture occurs due to the shear stresses,

which are maximum at 45° . This cracking mode sequence is responsible for the behavior of the AE parameters. The small specimen size and the sensitivity of the sensors enable the capture of these changes accurately as the crack propagates.

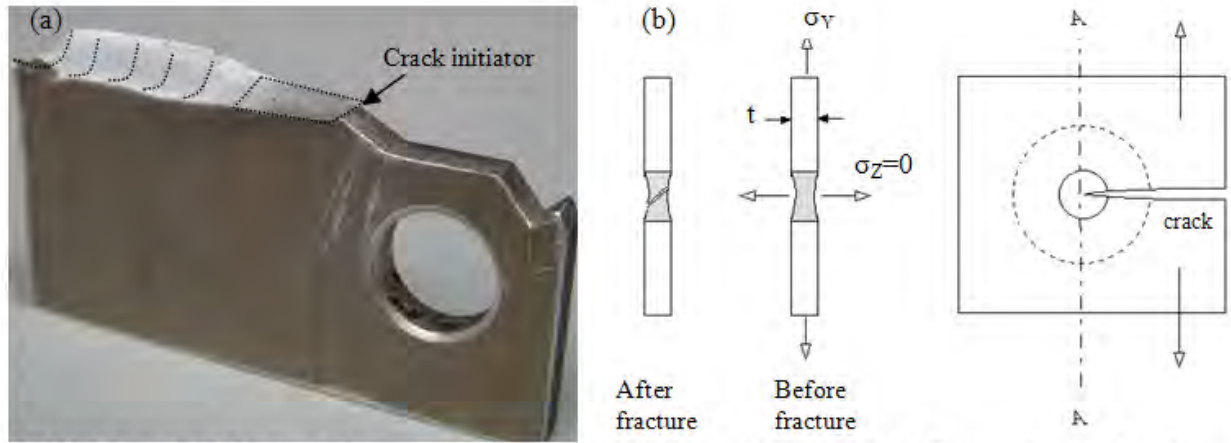


Fig. 7. (a) Part of the specimen after fatigue failure. (b) Plane stress fracture.

Another AE parameter that has been employed in cracking mode classification is the average frequency, AF, as mentioned earlier. In the present study, this parameter exhibits shifting trends, but in a much smoother way than RA. Figure 8 shows the AF of all hits as well as the linear fit to the data. The linear fit is produced to show the smooth but clear decreasing trend, which cannot be visually evaluated by the dispersed cloud of points. Indeed, there is a shift from an average value of 83 kHz at the beginning of the loading to approximately 50 kHz at fracture. This decrease can be again connected to the change of the dominant crack mode from tension to shear. The observed AE behavior is repeatable for all five specimens tested with parameters, such as RT, RA and AF.

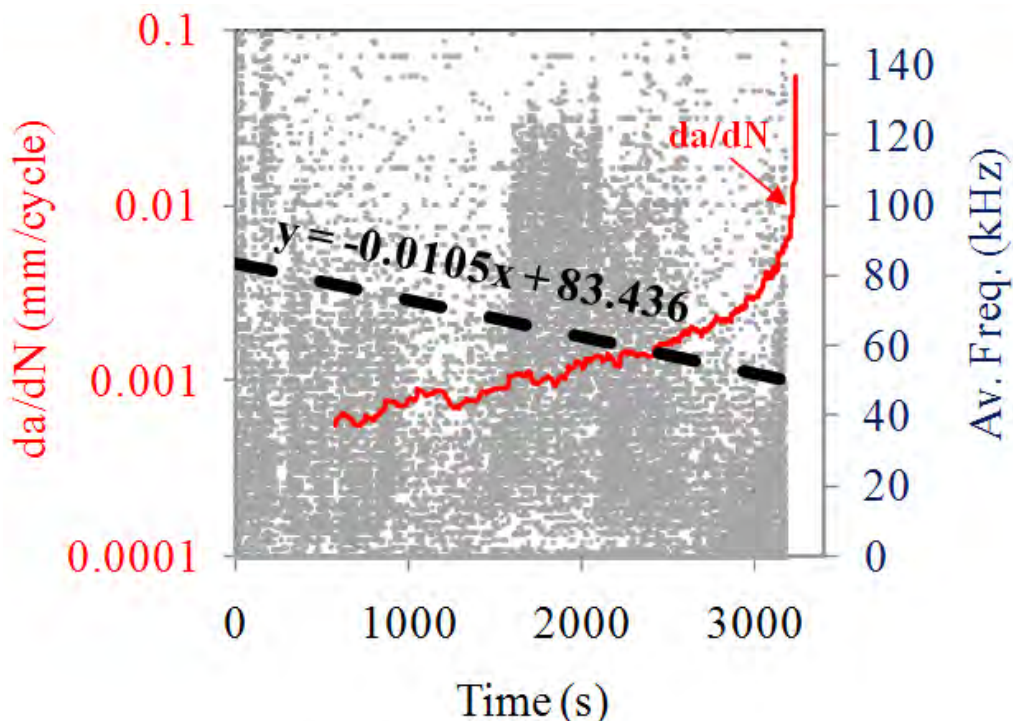


Fig. 8. Time history of CPR and AF.

Lock-in thermography results

In order to determine the crack growth rate using thermographic mapping of the material undergoing fatigue, we applied a specific procedure, which was described extensively in previous work [20]. According to this procedure, the distribution of temperature and stresses at the surface of the specimen was initially monitored during the test. The thermal images were obtained as a function of time (cycles). The stresses were determined in a post-processing mode based on thermoelasticity theory, as stated in the introduction, and the thermal variations monitored on the surface of the coupon. Local stresses versus time were measured along each of the fifteen reference lines (see Fig. 9a) drawn on the thermograph in front of the notch. The method was applied in five AA7075 specimens.

The maximum values of stress for three different reference lines of the fifteen are depicted against the number of fatigue cycles in Fig. 9b. The local stress is monitored at the location of each line. First, it increased while the crack approached the line, and attained a maximum value when the crack tip crossed the line. After the crack crossed the line, the local stress decreased.

The exact time and the corresponding fatigue cycle that each line attains a maximum value of stress can be defined by the plot of Fig. 9b (see arrows). All the reference lines had been drawn on the thermograph at fixed position in front of the crack-starting notch. Therefore, the crack growth rate (da/dN) can be calculated from the exact positions (mm) of reference lines and the fatigue cycle when the crack reaches each reference line.

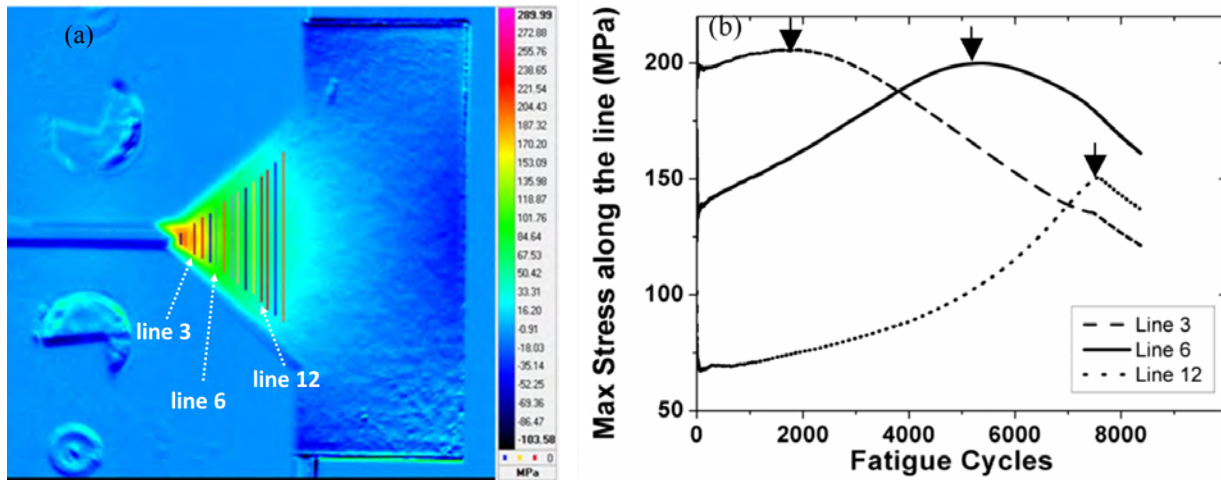


Fig. 9. (a) thermograph of 3 plotted reference lines s, (b) Diagram of max stress along 3 typical reference lines vs. fatigue cycle.

The crack growth rate values of aluminum alloy AA7075 obtained by the conventional compliance method were correlated with the damage parameters obtained using lock-in thermography (see Fig. 10). As can be seen by the thermographic data there is an abrupt change of the damage parameter after approximately 8000 cycles, indicating the upcoming failure of the specimen at approximately 80% of its total fatigue life. Observing this figure, it can be concluded that the lock-in thermography index can be regarded as a prediction of the crack propagation rate measured by the compliance method in AA7075 aluminum alloys. Specifically IR thermography indicates incipient catastrophic failure at approximately 80% of the fatigue life.

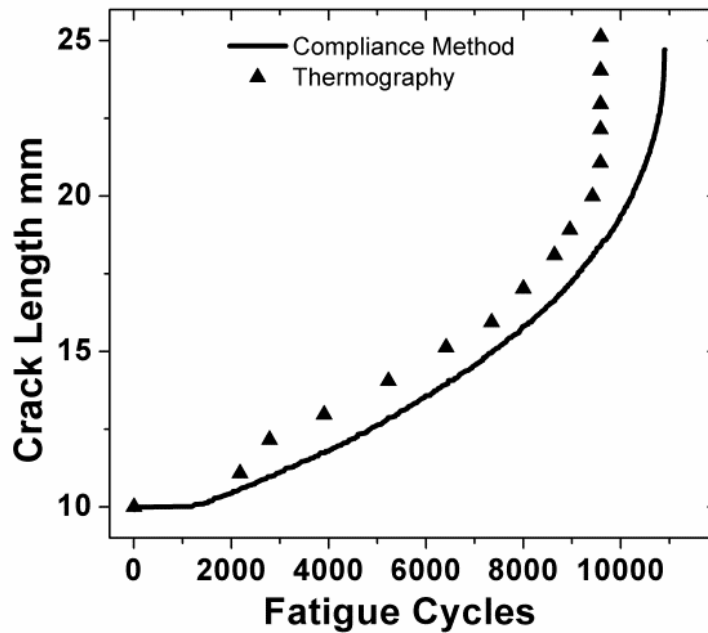


Fig. 10. Crack length vs. fatigue cycles determined by the compliance method and thermography.

Conclusion

This paper presents preliminary results on the AE monitoring during fatigue of aluminum coupons. The aim is the correlation of AE parameters with damage accumulation and the fracture mode. Study of the AE behavior shows that certain characteristics undergo clearly measureable changes much earlier than final fracture. Specifically, among others, the duration and the rise time of the signals, as well as the RA value of the waveforms increase sharply approximately 1000 to 1200 cycles before final failure. The mechanism, which is responsible for this change, seems to be the shift from the tensile to shear fracture mode. Such shift typically occurs in thin metal coupons with a notch. This is well known by visual observation of the specimen's fracture surface. It is concluded that these AE parameters should be further studied in order to establish early warning sign against final fracture and to characterize the damage status at any point of the materials life.

Additionally, this work demonstrated that crack growth rate can be effectively monitored by using lock-in thermography in metallic materials undergoing cyclic loading. The results obtained using this nondestructive technique were in agreement with the conventional compliance method. Thermographic monitoring is a noncontact, full-field, method able to assess accurately crack growth even in cases that cracking is not visible on the specimen's surface and propagates inside the material. In addition, it can be concluded that the new method, based on IR thermography, enables prediction of upcoming catastrophic failure of the specimen at an early state of damage. Lock-in IR thermography has a significant advantage since it can be used in situations which the conventional compliance method cannot be applied.

References

- [1] Grosse, C. U. and Ohtsu, M., 2008. *Acoustic Emission Testing*, Springer, Heidelberg.

- [2] Aggelis D.G., Shiotani T., Momoki S. and Hirama A., 2009. "Acoustic Emission and Ultrasound for Damage Characterization of Concrete Elements". *ACI Materials J.* **106**(6), 509-514.
- [3] Grosse, C., Reinhardt, H. and Dahm, T., 1997. "Localization and classification of fracture types in concrete with quantitative acoustic emission measurement techniques", *NDT&E Int.* **30**(4), 223-230
- [4] Anastassopoulos, A.A. and Philippidis, T.P., 1994. "Clustering Methodology for Evaluation of Acoustic Emission from Composites". *J. Acoustic Emission* **13**(1/2), 11-22.
- [5] Ohtsu, M. and Tomoda, Y., 2007. "Phenomenological model of corrosion process in reinforced concrete identified by acoustic emission". *ACI Mater J.* **105**(2), 194-200.
- [6] Shiotani, T., Ohtsu, M. and Ikeda, K., 2001. "Detection and evaluation of AE waves due to rock deformation". *Construction and Building Materials*, **15**(5-6), 235-246.
- [7] Ohtsu M., 2010. Recommendation of RILEM TC 212-ACD: Acoustic emission and related NDE techniques for crack detection and damage evaluation in concrete: Test method for classification of active cracks in concrete structures by acoustic emission, *Materials and Structures*, **43**(9), 1187-1189.
- [8] Aggelis, D.G., Barkoula, N.M., Matikas, T.E. and Paipetis, A.S., 2010. "Acoustic emission monitoring of degradation of cross ply laminates". *J. Acoust. Soc. Am.* **127**(6), EL246-251.
- [9] Soulioti, D.V., Barkoula, N.M., Paipetis, A.S., Matikas, T.E., Shiotani, T. and Aggelis, D.G., 2009. "Acoustic emission behaviour of steel fibre reinforced concrete under bending". *Construction and Building Materials* **23**, 3532-3536.
- [10] Rousset, G., Martin, E. and Lamon J., 2009. "In situ fibre strength determination in metal matrix composites", *Composite Science and Technology* **69**, 2580-2586.
- [11] Roberts, T.M. and Talebzadeh, M., 2003a. "Acoustic emission monitoring of fatigue crack propagation". *Journal of Constructional Steel Research* **59**, 695-712.
- [12] Brown, J., A., Vendra, L. J. and Rabiei, A., 2010. Bending Properties of Al-Steel and Steel-Steel Composite Metal Foams. *Metallurgical and Materials Transactions A*, **41A**, 2784-2793.
- [13] Aggelis, D. G., Kordatos, E. Z., Matikas, T. E. 2010. Monitoring of acoustic emission during fatigue of metal plates, *Progress in Acoustic Emission XV*, ed. Wakayama et al. JSNDI 2010, pp. 73-78.
- [14] Aggelis, D. G., Kordatos, E. Z., Matikas, T. E. 2011. Acoustic emission for fatigue damage characterization in metal plates, *Mechanics Research Communications*, **38**, 106-110.
- [15] Boinet, M., Bernard, J., Chatenet, M., Dalard, F. and Maximovitch, S., 2010. "Understanding aluminium behaviour in aqueous alkaline solution using coupled techniques Part II: Acoustic emission study", *Electrochimica Acta* **55**, 3454-3463.
- [16] Wong, B.S., Tui, C.G., Bai, W., Tan, P.H., Low, B.S., Tan, K.S. 1999. Thermographic evaluation of defects in composite materials. *Insight: Non-Destructive Testing and Condition Monitoring*, **41**(8), 504-9.
- [17] Brémond, P., Potet, P. 2001. Lock-in thermography: A tool to analyse and locate thermo-mechanical mechanisms in materials and structures. In: *Proc. SPIE 4360, Thermosense XXIII*. Rozlosnik, A.E., Dinwiddie, R.B., editors. SPIE Press, Orlando, FL, 2001, 560-566.
- [18] Yang, B., Liaw, P.K., Wang, G., Peter, W.H., Buchanan, R.A., Yokoyama, Y. 2004. Thermal-Imaging Technologies for Detecting Damage during High-Cycle Fatigue. *Metallurgical and Materials Transactions A: Physical Metallurgy and Materials Science*, **35A**(1), 15-23.

- [19] Plekhov, O., Palin-Luc, T., Saintier, N., Uvarov, S., Naimark, O. 2005. Fatigue crack initiation and growth in a 35CrMo4 steel investigated by infrared thermography. *Fatigue and Fracture of Engineering Materials and Structures*, **28**(1-2), 169-178.
- [20] Ait Aouit, D., Ouahabi, A. 2008. Monitoring crack growth using thermography. *Suivi de fissuration de matériaux par thermographie*, **336**(8), 677-683.
- [21] Kordatos, E.Z., Myriounis, D.P., Hasan, S.T., Matikas, T.E. 2009. Monitoring the fracture behavior of SiCp/Al alloy composites using infrared lock-in thermography. *Proc. SPIE 7294*, 72940X.
- [22] Myriounis, D.P., Kordatos, E.Z., Hasan, S.T., Matikas, T.E. 2011. Crack-Tip Stress Field and Fatigue Crack Growth Monitoring Using Infrared Lock-In Thermography in A359/SiCp Composites. *Strain*, **47**, e619-e27.
- [23] Maldague, X.V. 2001. *Theory and practice of infrared technology for nondestructive testing*, John Wiley & Sons Inc, New York.
- [24] Choi, M-Y., Park, J-H., Kang, K-S., Kim, W-T. 2006. Application of thermography to analysis of thermal stress in the NDT for compact tensile specimen. *Proc 12th PCNDT 2006*.
- [25] ASM Handbook. 1989. *Nondestructive Evaluation and Quality Control*, Vol.17.

ACOUSTIC EMISSION SOURCE ORIENTATION BASED ON TIME SCALE

DIDEM OZEVIN and ZAHRA HEIDARY

Civil and Materials Engineering, University of Illinois at Chicago
842 W. Taylor Street, Chicago, IL 60607

Abstract

This paper presents the identification of the acoustic emission (AE) source orientation using the time reversal or the phase shift. The methodology requires a data acquisition system that does not modify the phase information directly detected from the AE transducers; however, it is applicable to any kinds of sensor, resonant or broadband. Using finite element simulations, the relative time reversal and scaling values of the AE transducers are evaluated to develop a correlation between the relative data and the source orientation. The numerical results are evaluated using an experimental scheme and pencil-lead break simulations at different angles. Understanding the source orientation provides the directions of the acoustic wave patterns, which can be used to improve the source location accuracy with proper wave velocity selection and the source characterization.

Keywords: Source orientation, time scale, phase shift

Introduction

The AE method has various successful applications for detecting and locating the damage in many field testing of civil structures (e.g. Nair and Cai, 2010). However, the method's ability to identify the source orientation with available techniques requires diligently recorded AE signals without influenced by the sensor's transfer function, electronics and reflections as well as noise. Ohtsu and Ono (1986) used the generalized theory to identify the source representations of AE at different angles and modes. The theory requires the deconvolution of waveform signature and Green's function of the medium to find out the source representation. The authors showed the effect of crack orientation on the amplitude of the first wave arrival. This approach requires precise AE signature detection directly from the source. Ohtsu and Ono (1988) demonstrated the dependence of the amplitude of the incident P-wave to the crack orientation. However, the P wave amplitude may be influenced by other factors such as source intensity. Gorman and Prosser (1991) demonstrated that the source orientation can be extracted from the in-plane and out-of-plane displacement components of waves in plate-like structures. However, separating the amplitudes of two wave motions requires sufficiently long source-sensor distance, and the waveform should not be affected by extraneous noise and reflections.

The identification of source orientation with respect to the sensor coordinate can be critical for the accurate source localization and the source characterization. For example, depending on the crack growth direction and the sensor location, the acoustic radiation patterns control the amplitudes of longitudinal and shear wave amplitudes as angle and source dependent such as normal tear, transverse shear or longitudinal shear (Lysak 1996). The approach in this study to understand the AE source orientation is based on the time scales (i.e., phase differences) of the first arrival waveforms recorded at various sensor positions. As the source orientation depends on the first wavefront, the approach is not affected by reflections or resonating behavior of conventional AE transducers. The approach has been demonstrated with numerical models and experimental

studies. Current AE instruments require electronics at the pre-amplification level that modify the phase of the waveform. Therefore, in this study, the data was recorded using an oscilloscope without any pre-amplification.

Basis of the Correlation

The discrete time signals \mathbf{x} can be represented as $\mathbf{x}[\alpha t + \beta]$ where α represents time scaling and reversal, and β represents time shift. If α is less than 0, the signal is reversed in time. If β is nonzero, the signal is shifted in time (Oppenheim and Willsky 1997). The time scaling and shift for a signal to match with the reference signal \mathbf{y}_2 is calculated using the following correlation:

$$\mathbf{x}[\alpha t + \beta] \rightarrow \mathbf{y}[t] \quad (1)$$

where \mathbf{x} represents the original output of an AE sensor, and \mathbf{y} represents the modified form of \mathbf{x} to match with \mathbf{y}_2 . If two signals, \mathbf{y} and \mathbf{y}_2 match, their cross correlation coefficient should be equal to 1 with 0 time delay using the following formulation:

$$R_{\mathbf{y}\mathbf{y}_1}(\tau) = \sum_{t=1}^N \mathbf{y}(t)\mathbf{y}_1(t + \tau) \quad (2)$$

where $R_{\mathbf{y}\mathbf{y}_1}(\tau)$ is the cross correlation coefficient of two signals, \mathbf{y} and \mathbf{y}_1 , as a function of a time delay τ , N is the length of signals. The time scale of two AE sensor responses is dependent on the AE source orientation. This is related to the radiation pattern of elastic waves released at different angles with respect to the sensors. As the complete AE waveforms are influenced by many factors such as the sensor response, source-sensor distance and path, only the first wave arrivals of two AE sensor responses placed relative to the AE source are analyzed in order to demonstrate the correlation of the time scale and the source orientation.

Numerical Simulations

Finite element simulations are conducted using the structural module of COMSOL 4.2 Software. The structural geometry is made of aluminum with 5-mm thickness. The finite element model is approximated as 2D plane stress model. The source simulation function is applied at the right side of the hole placed at the center as shown in Fig. 1a (distance given in m). The source angle is varied from 90° (relative to the horizontal axis) to -90° with 15° increments. The source simulation function is defined by equation 1 and plotted in Fig. 1b for 100 kHz excitation signal.

$$F(t) = \sin(2\pi f_o t)(1 - e^{-t^2/t_{rise}})e^{-t/t_{decay}} \quad (3)$$

where t_{rise} is rise time, t_{decay} is decay time and f_o is frequency. The time step Δt and element size l for finite element calculations of propagating elastic waves for a stable and accurate solution without any numerical pollution (Hill et al. 2004) are

$$\Delta t = \frac{1}{20f_{max}} \quad l = \frac{\lambda_{min}}{20} \quad (4)$$

where f_{max} is the maximum frequency of interest and λ_{min} is the minimum wavelength involved. Three frequencies are studied in order to demonstrate the frequency independence of the time scale-source orientation relationship: 50 kHz, 100 kHz and 200 kHz. The mesh size and the time step for each frequency are given in Table 1.

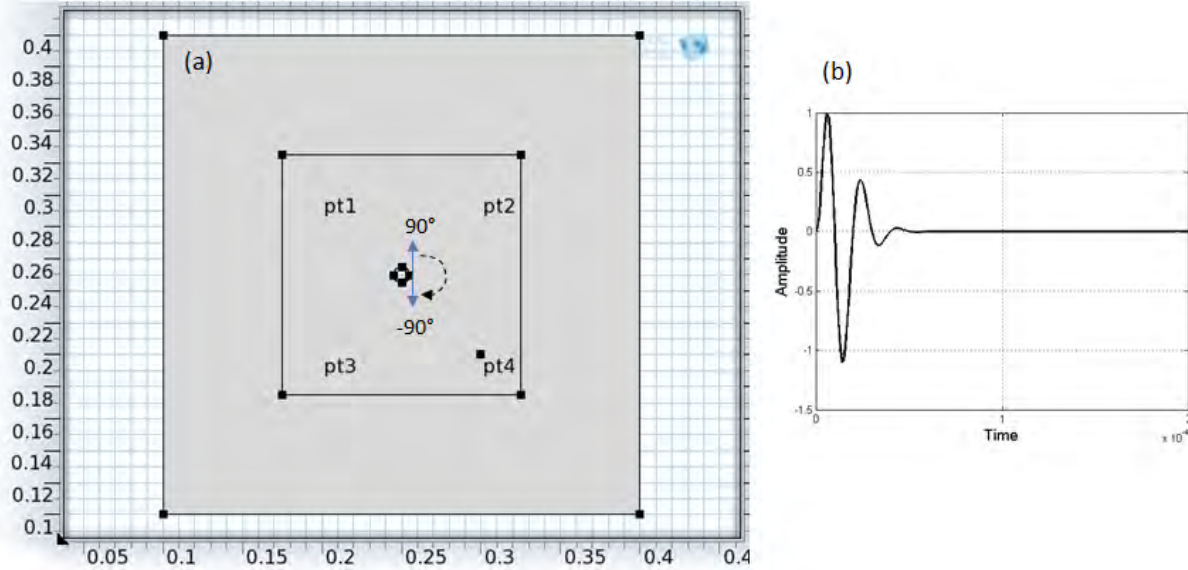


Fig. 1. Numerical model (a) geometry and source angles, (b) loading function for 100 kHz.

Table 1. Time step and mesh sizes for three AE source frequencies.

Frequency (kHz)	Time step (sec)	Mesh size (mm)
50	1E-6	5
100	0.5E-6	2.5
200	2.5E-7	1

The oscillatory nature of the wave equation requires fine meshing, which increases the computational time significantly when the target frequency increases as shown in Table 1. Therefore, the geometry in this study is divided into two regions: near field for the observation points pt1 to pt4 as shown in Fig. 1a and far field outside the observation points. For the near field region (inside the small square shown in Fig. 1a with solid lines), the mesh size for the target frequency is selected using equation 2, given in Table 1. The far field region (between two squares shown in Fig. 1a) is included into the model in order to prevent any reflections from boundaries to the observation points during the simulation duration. However, the second region is coarsely meshed as shown Fig. 2 as the numerical accuracy is not intended.

A total of 39 finite element simulations are studied (13 different angles and 3 different source frequencies). Figure 3 shows the simulation results of three angles (i.e. 90°, 60° and 30°) for each AE source frequency. The solid line shows the strain history in $-z$ direction (perpendicular to the planar view) for the observation point pt2 as shown in Fig. 1a; the dashed gray line shows the strain history in $-z$ direction for the observation point pt4. For the 50 kHz AE source simulation signal, the first wave arrival is at 1.1 μs which is equivalent to 6120 m/s wave velocity as the distance between the excitation location and the observation points is 0.067 m. The second wave arrival occurs about 48 μs , which is equivalent to 1400 m/s wave velocity. For the 100 kHz excitation signal, the first wave arrival is at 1.1 μs , while the second wave arrival is at 41 μs . For the 200 kHz excitation signal, the first wave arrival is at 1.1 μs , while the second wave arrival is at 32.5 μs . The reason for the variation of the second wave arrival with the excitation frequency is the dispersion characteristic of the flexural mode. The first wave arrival is the same for all three frequencies as the extensional mode is non-dispersive here. As the source excitation in

planar direction, the extensional wave mode has higher amplitude than the flexural wave mode. When the excitation frequency is increased from 50 kHz to 200 kHz, the arrival times of two wave modes are separated further due to smaller cycle duration of higher frequency excitation. The separation of two wave modes for low frequency source is more difficult than high frequency sources.

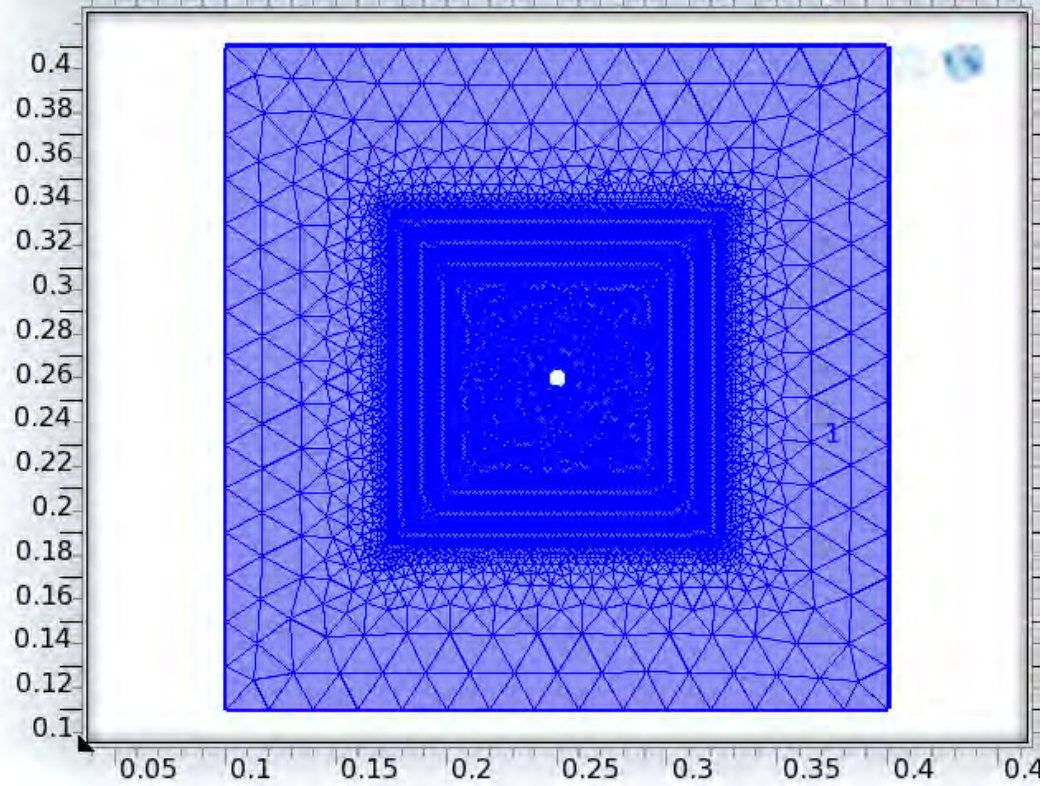


Fig. 2. Meshed geometry with two different mesh sizes. Distances in m.

There is a clear time scale difference of the waveforms at pt2 and pt4 depending on the source orientation or the angle with respect to each sensor. For 90° simulation, the angle between the source and the observation pt2 is 42°; the angle between the source and the observation pt4 is 138°. For 60° simulation, the angle between the source and the observation pt2 is 12°, the angle between the source and the observation pt4 is 108°. For 30° simulation, the angle between the source and the observation pt2 is 18°, the angle between the source and the observation pt4 is 78°. If the angle is less than 90°, the waveform has positive slope at the first wave arrival, while it has negative slope if the angle is greater than 90°.

The time scale value of two sensor responses under the given simulation angle is calculated by finding the linear curve fit of the first wave arrival. Figure 4 shows an example of two sensor waveforms (solid line for pt2, dashed line for pt4) together with the curve fit to the first wave arrival. The ratio of the slopes provides the time scale α of two sensors.

$$\alpha = \left(\frac{df_2}{dt}\bigg|_{t=t_0}\right) / \left(\frac{df_1}{dt}\bigg|_{t=t_0}\right) \quad (3)$$

where f_1 indicates the reference waveform that has the highest positive slope, f_2 indicates the second AE sensor response. Time scale is represented by the derivatives of waveforms at the first wave arrival at t_0 .

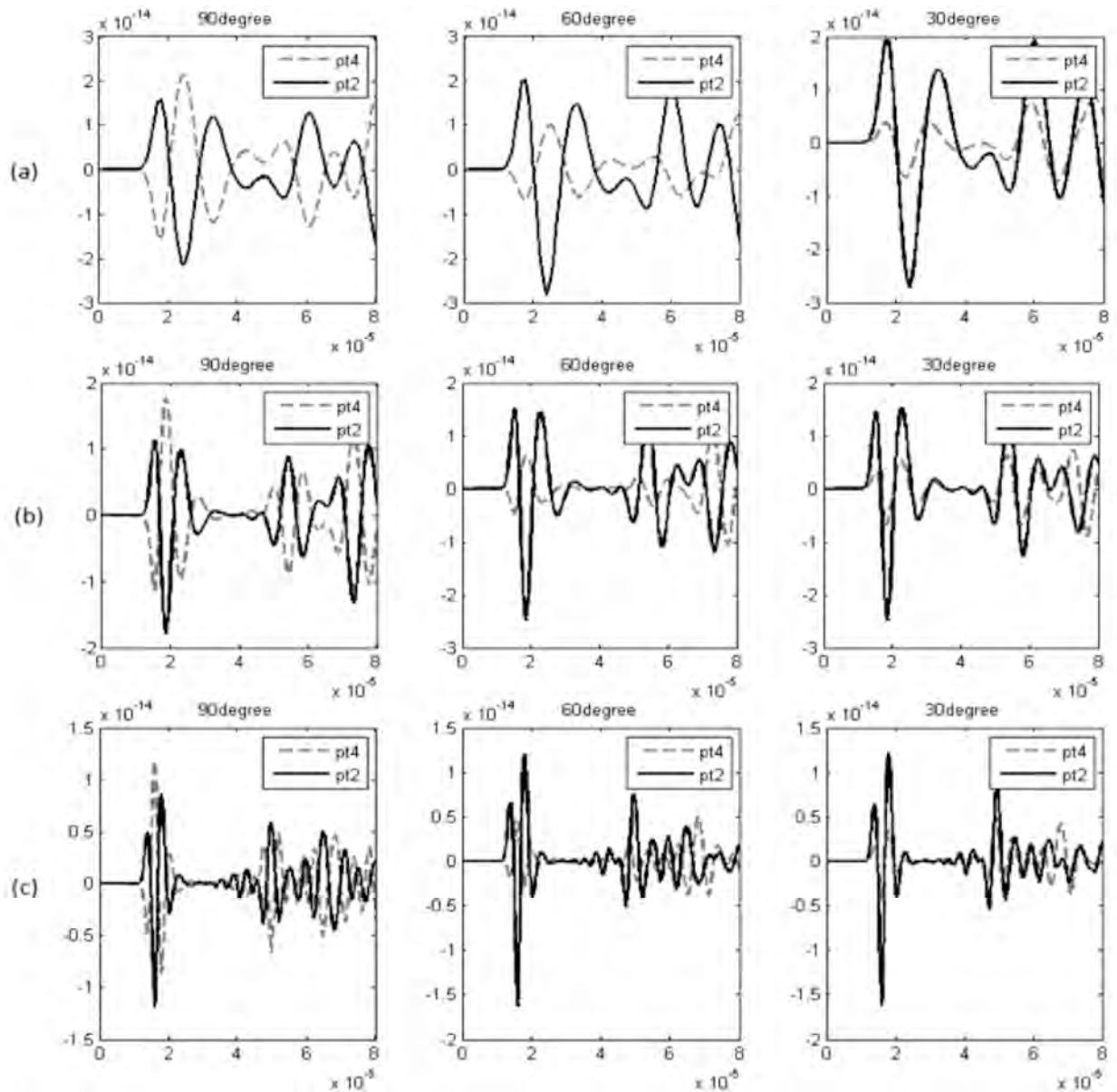


Fig. 3. The simulation results of 90°, 60° and 30° source angles for (a) 50 kHz excitation, (b) 100 kHz excitation, (c) 200 kHz excitation.

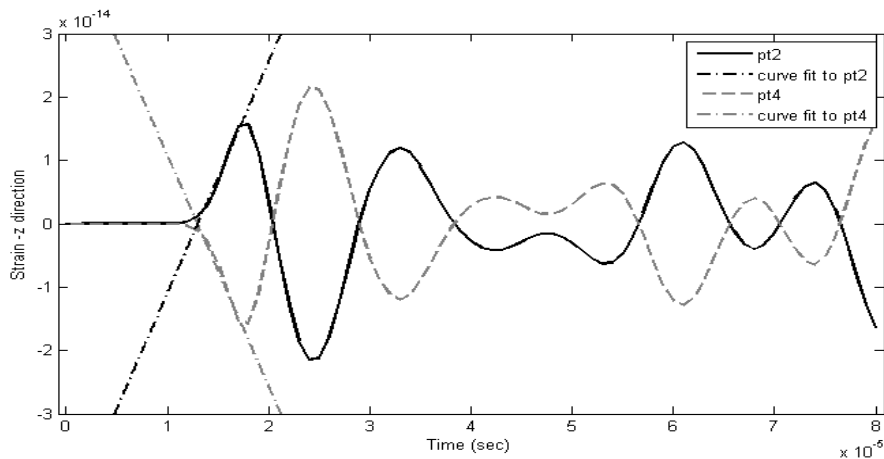


Fig. 4. The linear curve fits to the first wave arrivals.

Table 2 shows the slopes of the waveforms recorded at pt2 and pt4 locations under 13 different simulation angles and three different simulation frequencies. As discussed above, if the angle between the source and the sensor is less than 90° , the slope has positive value (e.g., 90° to -30° for the location pt2). If the angle between the source and the sensor is greater than 90° , the slope has negative value. This is the reason for the sign changes of the waveforms at pt2 at -45° and the waveforms at pt4 at 45° . The slopes for each simulation angle under three simulation frequencies are different; however, their ratios (i.e., time scales) are the same. Figure 5 shows the time scales with respect to the simulation angles for three frequencies. The figure indicates that the time scale to identify the source orientation is independent of the frequency. For unknown source orientation, the graph in Fig. 5 can be used together with the time scale of two AE sensors in order to identify the source orientation.

Table 2. The slopes of the first wave arrivals and their time scales for 3 excitation frequencies.

Ext. Angle	Excitation Frequency								
	50 kHz source			100 kHz source			200 kHz source		
	pt2	pt4	Time scale	pt2	pt4	Time scale	pt2	pt4	Time scale
90	4.07E-09	-4.40E-09	-1.08	3.83E-09	-3.36E-09	-0.88	2.30E-09	-2.20E-09	-0.96
75	5.00E-09	-3.00E-09	-0.60	4.62E-09	-2.80E-09	-0.61	2.78E-09	-1.41E-09	-0.51
60	5.77E-09	-1.85E-09	-0.32	3.87E-09	-1.67E-09	-0.43	3.00E-09	-9.14E-10	-0.30
45	5.11E-09	-5.32E-10	-0.10	5.00E-09	-2.50E-10	-0.05	3.36E-09	-1.45E-10	-0.04
30	5.93E-09	1.42E-09	0.24	5.26E-09	1.13E-09	0.21	3.13E-09	7.06E-10	0.23
15	5.23E-09	2.84E-09	0.54	3.81E-09	2.30E-09	0.60	2.20E-09	1.41E-09	0.64
0	4.46E-09	4.46E-09	1.00	2.27E-09	2.27E-09	1.00	2.46E-09	2.46E-09	1.00
-15	2.60E-09	5.24E-09	0.50	2.30E-09	4.41E-09	0.52	1.69E-09	3.13E-09	0.54
-30	1.32E-09	5.35E-09	0.25	1.08E-09	4.30E-09	0.25	8.15E-10	8.21E-09	0.10
-45	-4.96E-10	5.88E-09	-0.08	2.30E-10	4.06E-09	0.06	-1.48E-10	3.35E-09	-0.04
-60	-1.63E-09	5.77E-09	-0.28	-1.66E-09	4.88E-09	-0.34	-1.00E-09	3.61E-09	-0.28
-75	-3.00E-09	4.88E-09	-0.61	-2.43E-09	4.42E-09	-0.55	-1.93E-09	2.87E-09	-0.67
-90	-4.40E-09	4.40E-09	-1.00	-3.69E-09	3.69E-09	-1.00	-2.46E-09	2.23E-09	-1.10

Experimental Simulation

The numerical results are validated with the experimental simulation. A thin aluminum plate with dimensions of 610 x 432 x 1 mm was utilized for the experimental study. The plate was instrumented on its top surface with two nano AE sensors, which were mounted on the plate using high vacuum grease. The sensors were placed with their centers at 156 mm from the long edge and 406 mm from the short edge of the plate. They were connected directly to a digital oscilloscope (MSO2014 oscilloscope with 100 MHz bandwidth and 1 GS/s sample rate) for data collection without any pre-amplifier. As the oscilloscope has high input impedance of $1\text{ M}\Omega$, it does not require any impedance matching electronics between the data acquisition unit and the AE sensors. The AE simulations were conducted using 0.7-mm pencil-lead breaks at a location of 216 mm from the long edge and 165 mm from the short edge on the top of the plate (Fig. 6). The source-sensor distance in the experimental simulations is the same as the numerical simulations.

The angle of the pencil with respect to the surface was about 30° . Ten lead breaks were generated at five different angles (two repetitive simulations at each angle). Another set of experiments were conducted for longer sensor-source spacing in order to understand whether the distance affects the measurement. Similar test results were obtained, which is due to non-dispersive characteristics of extensional wave mode (the first wave arrival).

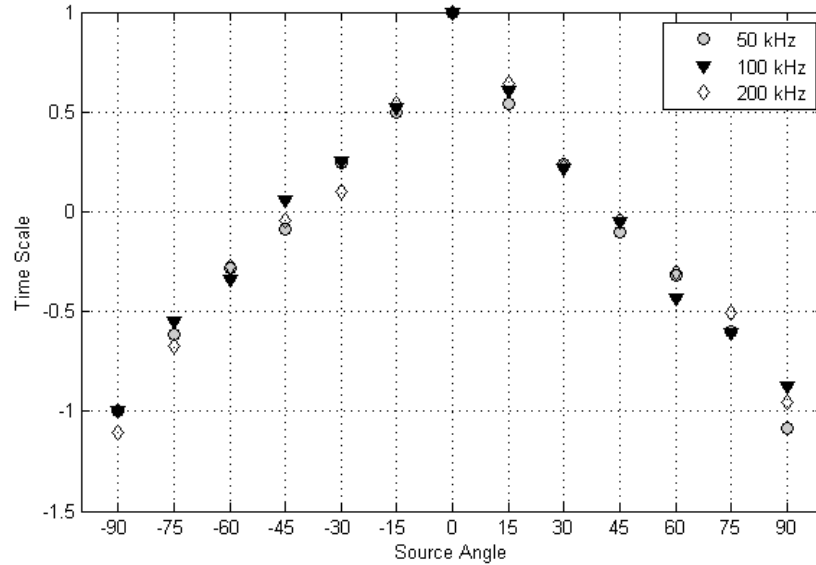


Fig. 5. Time scale change with respect to the source angle for three source frequencies.

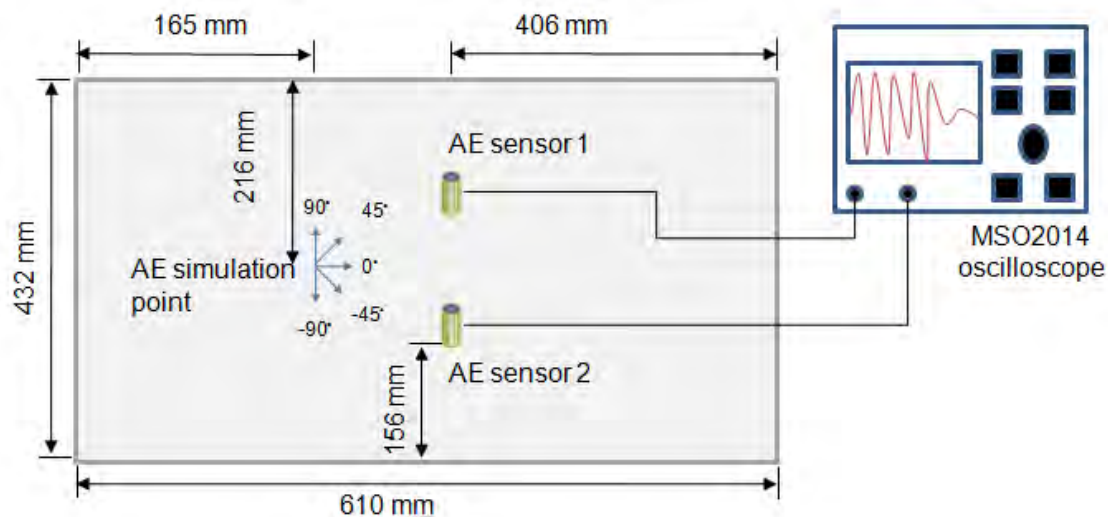


Fig. 6. Experimental setup.

Figure 7 shows the waveforms of two AE sensors, windowed to the first wave arrival, under the AE source simulation at 90° . The ratio of the slopes to the first wave arrival of sensor 1 and sensor 2 is -1 , which agrees with the numerical time scale. The frequency of the first wave arrival is identified as 293 kHz using the windowed frequency spectrum analysis. While the numerical simulations are conducted up to 200 kHz, the experimental result for 293 kHz frequency agrees with the numerical simulations. This reconfirms the independence of the approach from the frequency. The waveform signatures of two AE sensors are not identical while their distances to the simulation point are the same and the AE sensors are the same type. This may be because

of small variations of sensor responses or the coupling thickness. Therefore, the approach in this study is to find the correct time scale value to match the first wave cycles of two AE sensors, instead of matching two complete waveform histories.

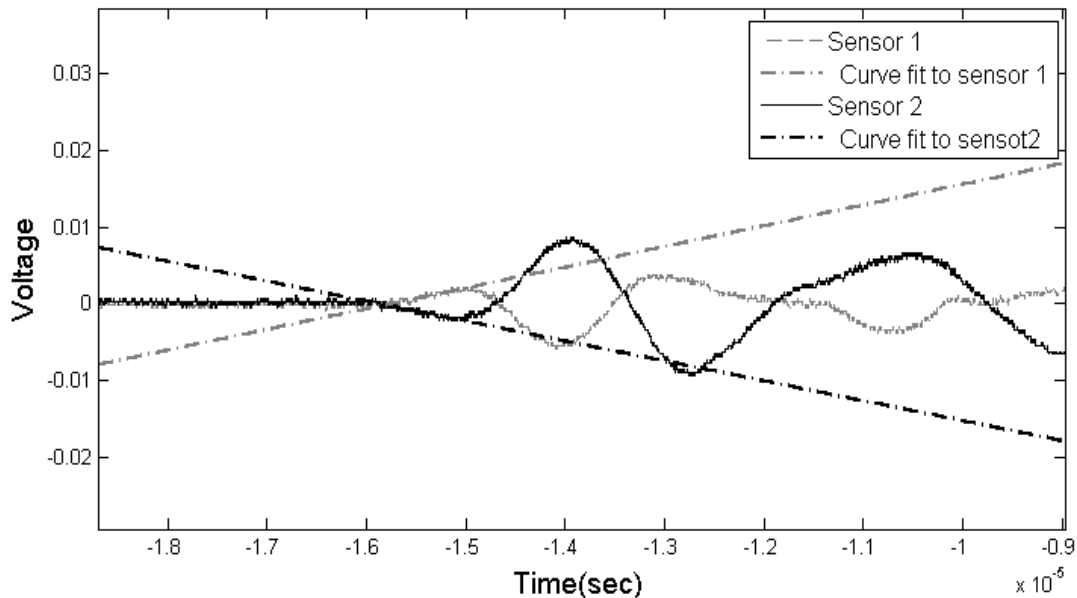


Fig. 7. The linear curve fits to the first wave arrival.

Table 3. The slopes of the first wave arrivals and their time scales for two sets of experimental result.

Source Angle	Test 1			Test 2		
	Sensor 1	Sensor 2	Time scale	Sensor 1	Sensor 2	Time scale
90	2704	-2599	-1.04	2403	-2648	-1.10
45	4838	-189.6	-0.03	4706	-403	-0.08
0	2634	2516	1.04	2758	2600	1.06
-45	-601	5189	-0.11	-336	4117	-0.08
-90	-3326	3607	-1.08	-1201	1320	-1.09

Figure 8 shows the waveforms of the AE sensors as the positions of sensor 1 and sensor 2, which are recorded by the digital oscilloscope and re-plotted in Matlab with time shifts in order to match the arrivals of the first wave fronts. There are slight differences in the arrivals of two sensors. The time shift values β for each source angle simulation are reported in the plots. There are no distinct arrival differences of extensional and flexural wave modes due to the proximity of the source to the sensors. However, the extensional wave mode amplitude is less than the flexural wave mode amplitude as the simulations are conducted on the surface of the plate with 30° angle and the sensors are more sensitive to the out-of-plane direction.

As an example of the analysis of the time scale as related to the source angle, Fig. 8c shows the simulation for 0° (the source oriented at the same angle to the sensor 1 and the sensor 2). After the first wave arrivals are matched with the time shift, the slopes of the first wave of two sensors are identical, which indicates that the time scale value is 1. For each angle the experiment conducted twice in order to minimize the error. Also for each of five source angles, time shift

and scale factor are calculated and shown in Fig. 8 and Table 3. The time scale factors for each source simulation angle agree with the numerical results.

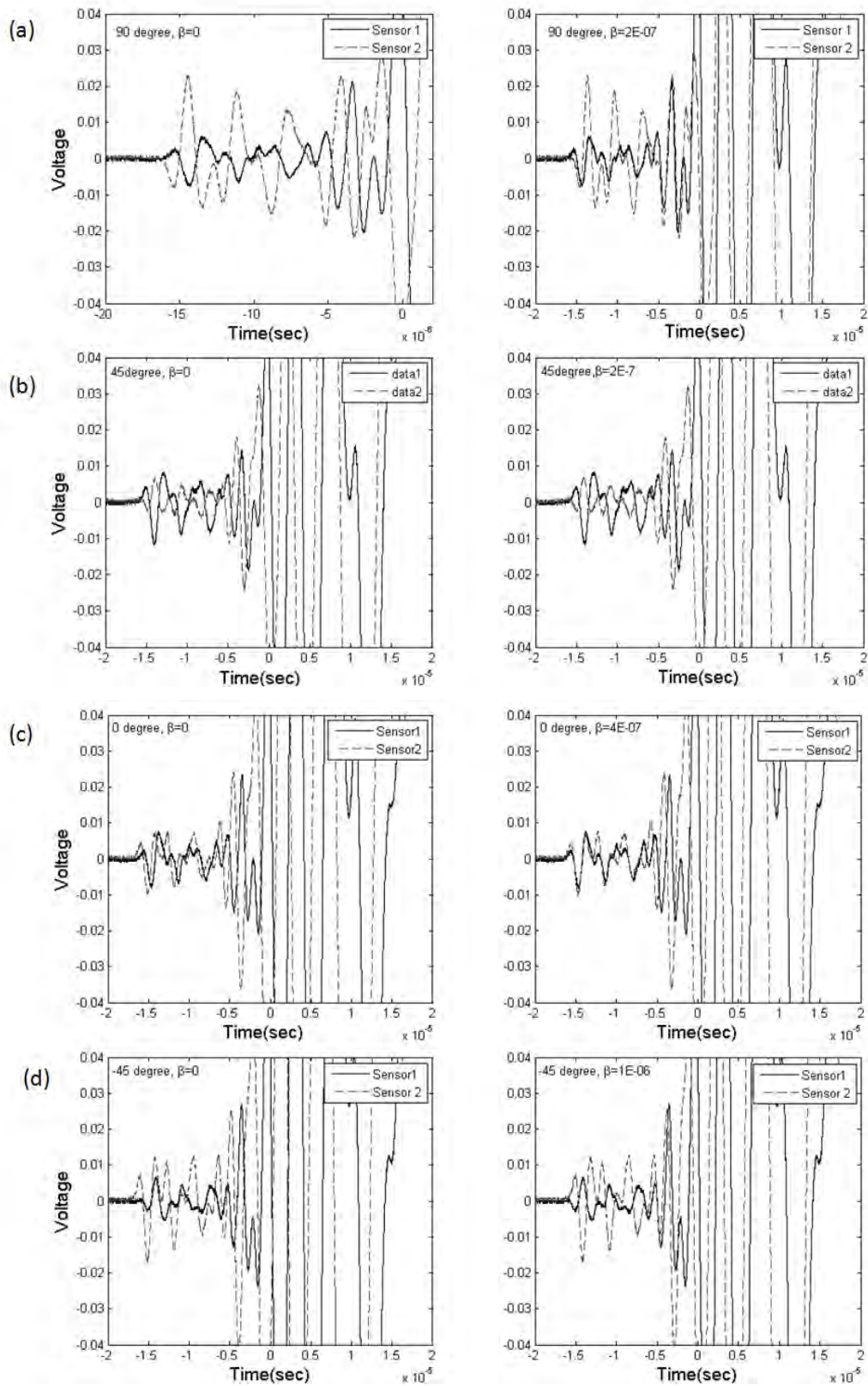


Fig. 8. The experimental results of various source angles and time shift: a) 90° , $\beta = 2E-07$, b) 45° , $\beta = 2E-07$, c) 0° , $\beta = 4E-07$, d) -45° , $\beta = 1E-06$.

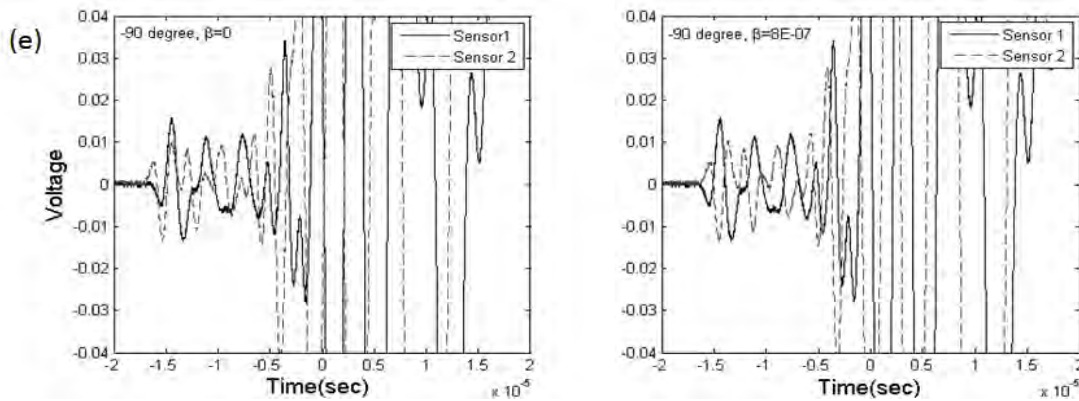


Fig. 8. (continued) The experimental results: e) 90° , $\beta = 8E-07$.

Conclusions

This paper demonstrates the identification of the AE source orientation based on the time scale of two AE sensors located relative to the AE source. The methodology requires no phase deformation due to the components of the data acquisition system, such as pre-amplifier and AE hardware. The source angle identification is demonstrated numerically for various frequencies in order to show that the time scale factor due to the source orientation is independent from the frequency. The experimental results validate the methodology, which can be used to increase the accuracy of source location with correct velocity selection and the source characterization. Both numerical and experimental simulations are conducted on thin plates. The approach needs to be validated for thick plates.

References

- Gorman, M.R. and Prosser, W.H. (1991). "AE Source Orientation by Plate Wave Analysis," *Journal of Acoustic Emission*, **9**, 283-288.
- Hill, R., Forsyth, S.A. and Macey, P. (2004). "Finite Element Modeling of Ultrasound, with Reference to transducers and AE waves," *Ultrasonics*, **42**, 253-258.
- Lysak, M.V. (1996). "Development of the Theory of Acoustic Emission by Propagating Cracks in terms of Fracture Mechanics," *Engineering Fracture Mechanics*, **55**, 443-452.
- Nair, A. and Cai, C.S. (2010). "Acoustic Emission Monitoring of Bridges: Review and Case Studies," *Engineering Structures*, **32**, 1704-1714.
- Ohtsu, M. and Ono, K. (1982). "The Generalized Theory and Source Representations of Acoustic Emission," *Journal of Acoustic Emission*, **5**, (4), 124-133.
- Ohtsu, M. and Ono, K. (1988). "AE Source Location and Orientation Determination of Tensile Cracks from Surface Observation," *NDT International*, **21**, (3), 143-150.
- Oppenheim, A.V. and Willsky, A.S. (1997). *Signals and Systems*. 2nd Edition. Prentice Hall, p.8.

DETECTION OF AE SIGNALS AGAINST BACKGROUND FRICTION NOISE

V. BARAT¹, D. GRISHIN² and M. ROSTOVTSEV¹

¹ Interunis Ltd., Building 3-4, 24/7 Myasnitskaya Str., Moscow 101000, Russia, ² Moscow Power Engineering Institute (Tu), 17 Krasnokazarmennaya Str., Moscow 125000, Russia

Abstract

Noise similar in waveform to AE signals is of particular challenge for filtering. Such noise is generated by various mechanical reasons, impact, impact of foreign objects, and precipitations. Friction is the most sophisticated and irremovable source of noise, as it is complex for filtering. Detection of AE signals against friction noise is possible using advanced digital signal processing methods; non-threshold segmentations, adaptive filtering and principal component analysis. Effective noise filtering is achieved both in *real time* and in *post-processing* mode.

Keywords: AE signal detection, friction noise filtering, principal component analysis.

Introduction

One problem of the acoustic emission (AE) testing is a high level of noise affecting the diagnosis. Electric noise, electromagnetic interference, background acoustic noise, and friction noise are far from the full list of noise present during measurements. Due to the high level of noise, the operator has to increase the recording threshold of the AE signals through reducing the testing sensitivity at the risk of missing a dangerous defect. Lack of the data filtering can result in an incorrect location and erroneous definition of the AE source danger level.

Noise recorded during the AE testing is highly varied. Noise can come from various physical reasons, such as sensor noise, imperfection of a measuring path, and operational noise of the testing object. The noise can have various waveforms. It can be stochastic or deterministic, stationary or non-stationary, and broadband or narrow-band. Noise similar in waveform to AE signals presents particular complexity for filtering. Noise can be generated by various mechanical reasons - impact, impact of foreign objects, and precipitations (such as rain and hail). Friction is the most sophisticated and irremovable reason of noise, and it is difficult for filtering. In the past, automatic or floating threshold was used [1]. However, its analog nature limited response speed, as can be seen in [2].

Detection of AE signals against friction noise is possible with help of advanced digital signal processing methods. Depending on the specific nature of testing procedure, friction noise can be suppressed at all stages of diagnostic information processing, through adaptive modification of the recording threshold or in a post-processing mode through AE signal decomposition, allowing the separation of noise component and AE signals.

Diagnostic Signals Characteristics

This paper considers the AE signals received against constantly present noise or interference. Assembly friction is an inevitable phenomenon for a variety of structures and cannot be eliminated and its influence defies shielding. It arises at the points of movable supports, hinged and cable-stayed fastenings, at pins of flanged couplings, and in movable assemblies of structures.

Examples of the friction-induced AE signals are shown in Fig. 1. Over a long time (more than a second, cf. Fig. 1b), this signal is a quasi-periodic process of deterministic-stochastic nature. The determinancy is defined by physical laws describing the friction process, while the stochasticity is defined by influence of a great number of random factors. With the standard threshold scheme of data recording, the signal characterizing friction is divided into a quantity of similar signals (see Fig. 1a). The signal represented in Fig. 1a has the noise characteristics, and it should be excluded from the subsequent study.

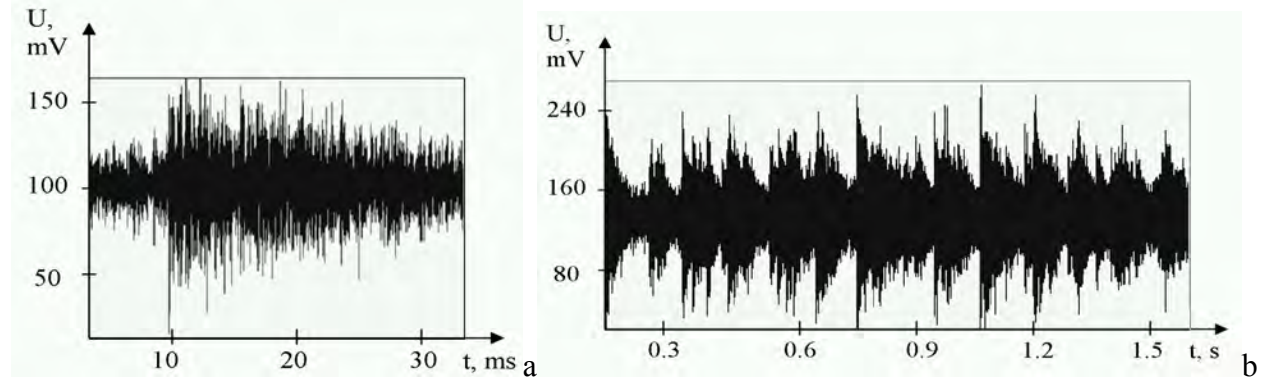


Fig. 1 Signals characterizing a) single rubbing event; b) rubbing process of 1.5-s duration.

The lack of special filtering procedures for the friction noise produces faulty evaluation, namely, overestimate of AE activity. As a consequence, it results in faulty evaluation of the AE source danger level.

Adaptive Threshold of AE Data Recording

For high-speed AE systems, it can be recommended to use the adaptive variable threshold in the data processing algorithm for filtering of constantly operating noise of friction type. Figure 2 illustrates this processing. Here, an AE signal (at ~130 s) is present against the friction-induced noise. In conventional AE threshold processing, it is necessary for excluding the friction noise to select the threshold above the noise level, i.e. in the region of 600-650 mV. With such a threshold value, the testing sensitivity decreases and the risk of missing defect signal arises. In adaptive threshold recording, a threshold value is not specified, but is calculated automatically depending on the local statistical characteristics of the AE signal. In early days of AE instrumentation, this was known as floating threshold and the threshold level was determined via analog processing by averaged rms voltage level. [1]

Here, the adaptive selection of threshold value is based on two principles. The first one defines the rule of local threshold value estimation on the basis of signal median, $median(y(n))$, while the second one allows the selection of an interval size, n , which controls the estimation of $median(y(n))$ [3]. The estimation of threshold value, thr , is based on the local median $median(y)$, and MAD (median absolute deviation); see equations (1) to (3), where γ is an empirically determined coefficient. Here, MAD defined by equation (3) is a robust measure of the data variability.

$$thr = median|y(n)| \pm \gamma \cdot \sigma_y(y(n)) \quad (1)$$

$$\sigma_y = \frac{MAD(y(n))}{0.6745 \cdot \sqrt{2}} \quad (2)$$

$$MAD = median|y(n) - median|y(n)|| \quad (3)$$

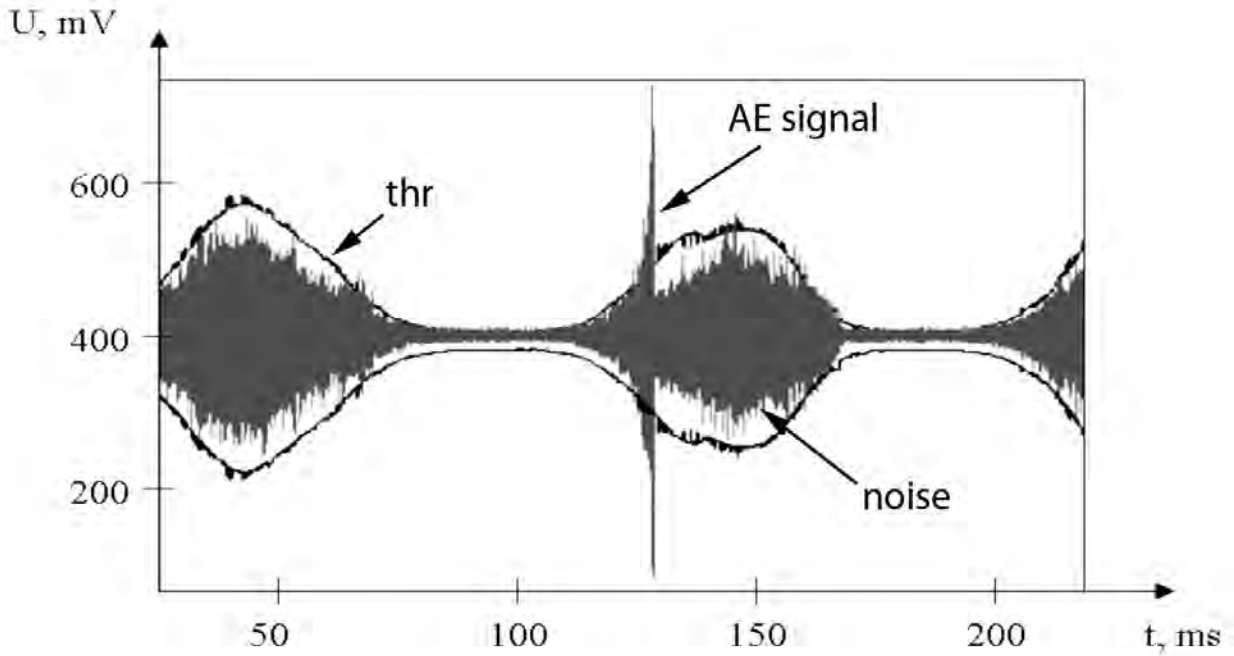


Fig. 2 Result of adaptive threshold segmentation.

In order for the AE local transients to be detected effectively, one should be guided by local estimations of the median and MAD, calculated with the help of a sliding time window. For adaptation of the threshold value to the signal statistical parameters, the time window duration should be variable. If the signal parameters vary, the window duration should be small, for tracking these changes. If the signal parameters are constant, the window duration should be maximal, for reaching effective filtering of the high-frequency and Gaussian noise.

Both signal median and MAD are insensitive to influence of the transient signal components. Therefore, the recording threshold value is defined only by the signal noise component; i.e., in our case, by friction noise. The AE signals representing outliers with a low probability of occurrence are necessarily above the threshold. An example in Fig. 2 illustrates the *thr* curves (above and below noise) accurately following the envelope of noise component. However, the transient (AE) signal at ~130 ms exceeds the local *thr* values.

To select the optimum duration of time window, the principle of intersection of confidence intervals (ICI) is used [3]. The ICI method suggests the selection of window length from the range of *a priori* specified lengths $\{N_i\}$. For each of N_i , the confidence interval $D(N)$ is calculated by equation (4);

$$D(N) = [\text{median}|y(N_i)| \pm \gamma \cdot \sigma(y(N_i))], \quad (4)$$

where

$$\sigma(N) = \sigma_y \sqrt{\frac{\pi}{2N}}. \quad (5)$$

From the selected range of window lengths, N^* is optimum when the set of intersections of interval $D(N^*)$ with intervals corresponding to the smaller windows is not empty.

For illustrating properties of the adaptive threshold, the following signal model can be considered (see Fig. 3a):

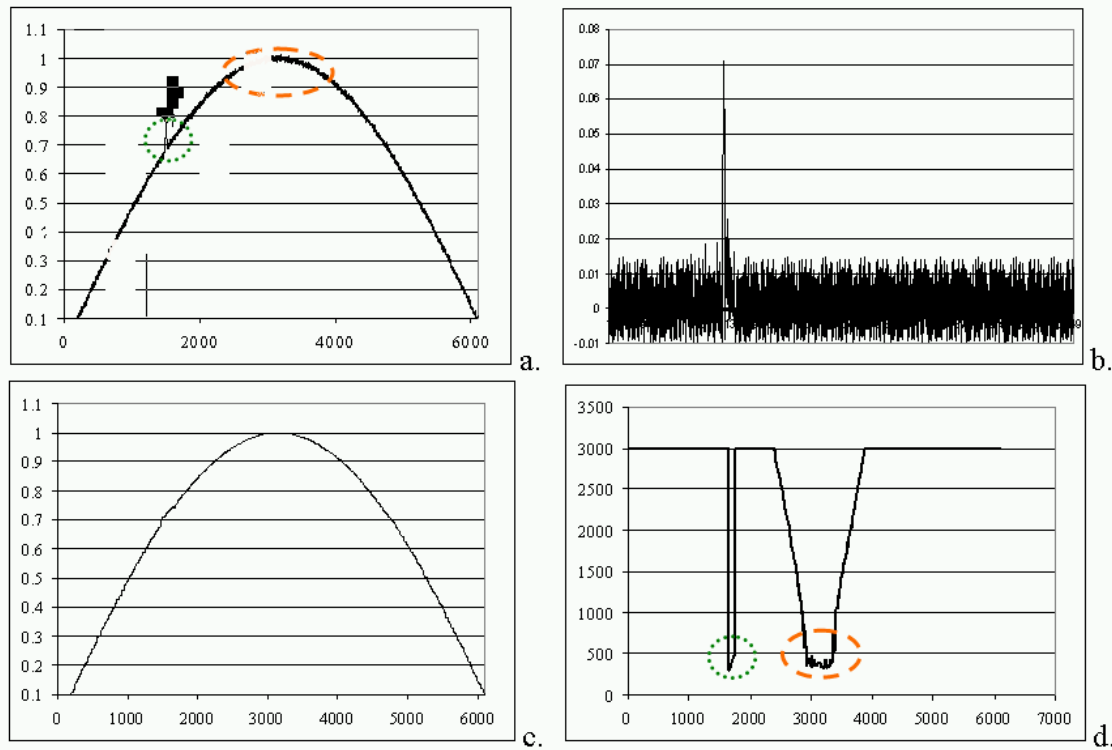


Fig. 3 a. input signal $s(n)$; b. result of filtering; c. threshold values $\sigma(n, N^*)$; d. optimal window length $N^*(n)$.

$$s(n) = A_1 \cdot \sin(\omega n) + A_2 e^{-\frac{(n-x_0)^2}{\sigma^2}} + noise(n)$$

The half-sine pulse is a time trend to which an impulse of small amplitude and duration and a random noise $noise(n)$ are added (second and third terms). The processing is to detect an impulse against a low-frequency trend. Figure 3b shows the result of filtering with adaptation of the threshold value. The adaptation of the filtering algorithm to the signal properties has enabled the slow time trend to be fully excluded from consideration. Figure 3c shows the time dependence of threshold values, which faithfully copy the trend values. This adaptation accuracy is reached by selecting the optimum duration of the time window, N^* . At the portion of signal containing a transient (encircled in green dots) and at the maximum signal part which shows changes in properties (enclosed in red dashed ellipse), the duration of the optimum time window N^* decreases to under 500.

The friction noise filtering is carried out by selecting a number of windows $\{N_i\}$ according to the model of the signal under study. The window minimum duration is selected several times higher than the AE signal duration. The segmentation threshold flexibly was adapted to relatively slow measurements of noise shape, while the small-scale components of the signal, impulses, remain invisible for it.

Optimum Filtering

The simplest and widespread method of optimum filtering is a Wiener filter. The Wiener filter is an optimum filter for the detection of the useful signal, which contains the AE signal along with noise [4, 5]. Prior information on spectral density of signal (or noise) is required for its use. As a criterion of its optimization used is the mean-square deviation of signal at the filter output from the specified waveform of signal (or noise). With the use of this filter, it is supposed that

the noise has an additive character, given in equation (6). The filter coefficients w are calculated in compliance with the optimization criterion on the basis of equation (7), where R_{ff} and R_{nn} are autocorrelation matrices of the AE signal and the noise, respectively. The filter frequency characteristic is set by equation (8), where P_{ff} and P_{nn} are the power spectra of $f(n)$ and $noise(n)$.

$$s(n) = f(n) + noise(n) \quad (6)$$

$$w = (R_{ff} + R_{nn})^{-1} r_{sf} \quad (7)$$

$$W(f) = \frac{P_{ff}(f)}{P_{ff}(f) + P_{nn}(f)} \quad (8)$$

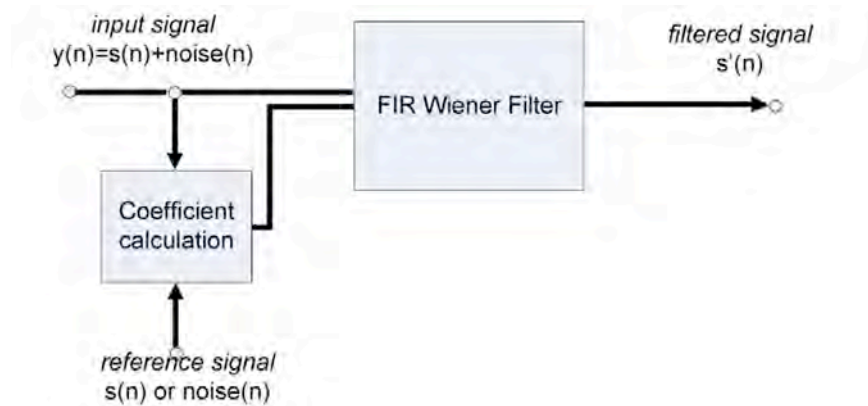


Fig. 4 Wiener filter application scheme.

Figure 4 illustrates the Wiener filter scheme. The filter takes in inputs of an initial signal (which consists of AE signal and noise) and reference signal (which represents the AE signal or noise of known waveform). The coefficients of a Wiener filter w are calculated with equation (7) to minimize the average squared distance between the filter output and reference signal. Application of the Wiener filter to the model signals is described in [4].

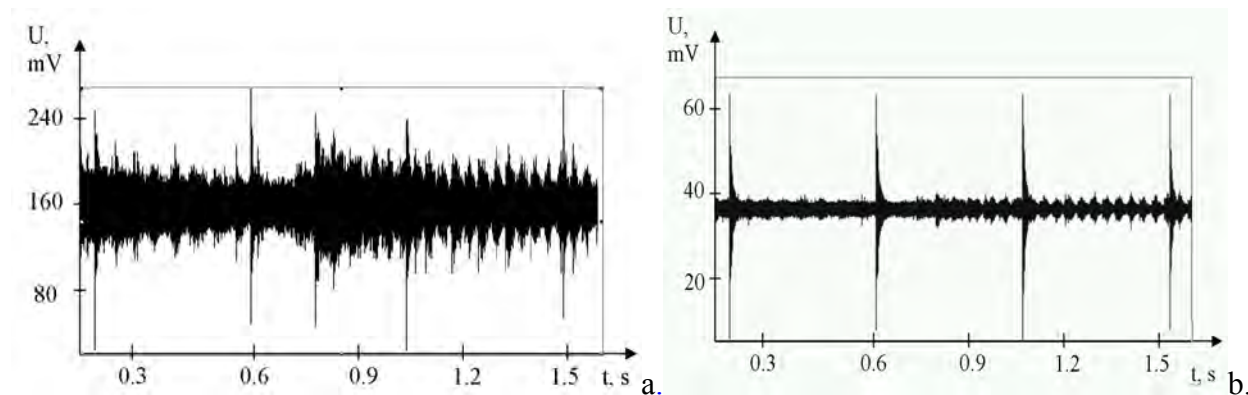


Fig. 5 a) AE signal against the friction noise background: SNR < 0.9; b) result of the Wiener filter application: SNR > 9.

Figure 5a shows the non-filtered input corresponding to the AE signals and friction noise. This signal is received in laboratory simulation. Its duration is approximately 1.5 s with the S/N ratio (SNR) of about 0.9. Figure 5b shows the result of the Wiener filter application. After filtering we can detect with confidence the AE signals against the noise background, and SNR has increased approximately tenfold to 9.

The optimum filtering application makes it possible to filter effectively the friction noise even in the cases of $\text{SNR} < 0.5$. A disadvantage of this method is the necessity to use a priori information on noise characteristics and the necessity to adapt the filtering algorithm to variation in these characteristics.

Method of Principal Components for Friction Noise Filtering

The problem of friction noise filtering can be also solved in a post-processing mode by means of the AE signal decomposition using the method of principal components. To identify processes with a different nature of periodicity, it is possible to employ one of methods of time series analysis, the method of principal components, which allows for dividing the AE signal represented as a time series into several elements (components), periodic components, transients and a trend.

In interpreting of AE signals, the periodic components characterize, as a rule, deterministic noise, white noise corresponds to random electronic noise, and the impulse components characterize the AE signals.

The method of principal components is a method of multidimensional data analysis, but for the time series analysis, the scientists from the St.-Petersburg State University designed its special modification, singular spectrum analysis [6]. This method suggests a transformation of the univariate time series to a set of time series, which represent a large number of fragments of the original signal, cut with a sliding time window; see equation (9). The time window duration shall be selected so that all processes (the noise processes and AE process) are able to become apparent.

$$X_i = (s_{i-1}, \dots, s_{i+L-2}), \quad (9)$$

where L is a window length. When the parameters are selected correctly, the signal is divided into several components, which characterize the various processes generated by various sources, both the noise sources and the AE sources.

The analysis algorithm can be conditionally divided into four stages: embedding, singular decomposition, grouping and reconstruction. The first two stages may be designated together as decomposition, while the last two as recovery. The first stage, embedding, consists in shaping from the signal a trajectory matrix, \mathbf{X} , equation (10). The second stage is a singular decomposition of each component of \mathbf{X} , that is, \mathbf{X}_i for $i = 1$ to d , given as equation (11).

$$\mathbf{X} = \mathbf{X}_1 + \mathbf{X}_2 + \dots + \mathbf{X}_d, \quad (10)$$

$$\mathbf{X}_i = \sqrt{\lambda_i} U_i V_i^T, \quad (11)$$

where $\lambda_1 \geq \lambda_2 \geq \dots \geq \lambda_d > 0$ are ordered nonzero eigenvalues of matrix, \mathbf{X}_i , $U_i \in \mathbf{R}^L$ are eigenvectors corresponding to them, and V_i are factorial vectors, equation (12).

$$V_i = \lambda_i^{-1/2} \mathbf{X}^T U_i \in \mathbf{R}^K \quad (12)$$

At the third stage, the decomposition components are grouped as equation (13),

$$\mathbf{X}_{I_j} = \sum_{k \in I_j} \mathbf{X}_k \quad (13)$$

where I_j are sets of the matrices to be combined. At the fourth stage, the reconstruction is performed by the conversion of the grouped matrices to the analyzed signal components, see (14).

$$s(t) = s_{i1}(t) + s_{i2}(t) + \dots + s_{ij}(t) \tag{14}$$

When the method of principal components is applied to the AE signal containing friction noise, we expect that, as a result of decomposition, noise-related quasiperiodic component and transient signals will appear in various components of decomposition. To reduce the data volume, it is recommended to operate not the signal itself, but its envelope. Such replacement does not result in diminution of algorithm accuracy, since the signal spectrum, in this case, is not informative. The envelope characterizes a low-frequency portion of the signal, and it can be effectively compressed through wavelet-transformation. The data compression ratio depends on the contraction ratio of frequency range. To evaluate the method of principal components, it is reasonable to analyze friction-induced noisy signals and AE signals separately. To reduce the computational burden, not the signals proper, but their envelopes are analyzed.

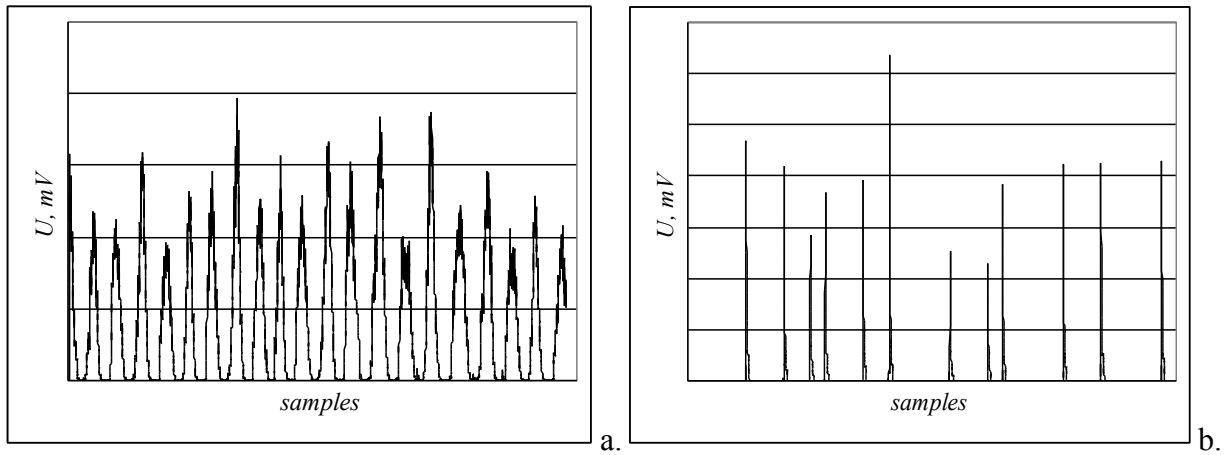
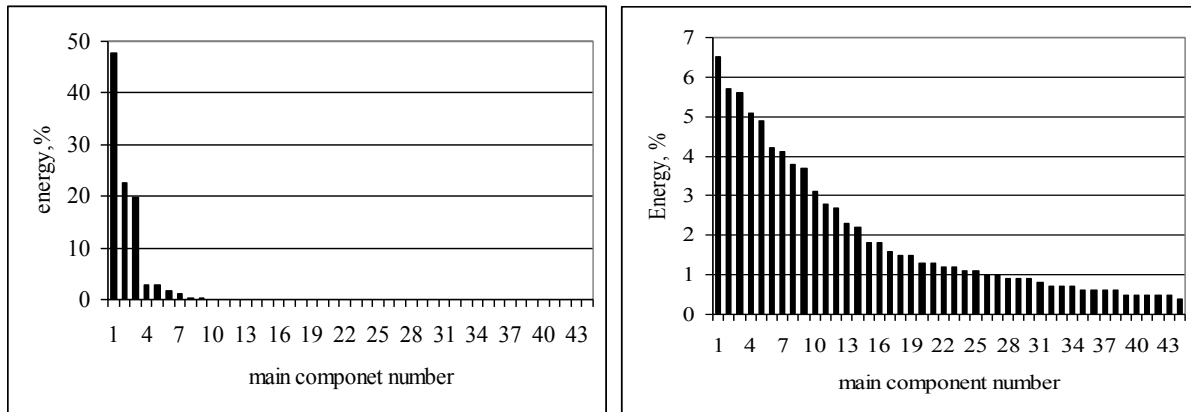


Fig. 6 a) Envelope of friction noise. b) envelope of AE signals.



a) for friction noise. b) for AE signals.

Fig. 7 Energy distribution of principal components decomposition.

The friction-induced noise envelope is shown in Fig. 6a. The harmonic component observed against the background white noise is dominant and Fig. 7a shows the result of decomposition in the form of the signal energy distribution according to the main components of the noise X_i . The time window for constructing a trajectory matrix was selected of the order of the envelope period. A total of seven main components were selected, the first three components containing more than 85% of the signal energy. The result of decomposition of the AE signals (Fig. 6b) is shown in Fig. 7b. In this case, the signal energy is distributed between a large number of

components, and 85% of the signal energy was distributed in 45 components of decomposition. One may draw an analogy between the signal energy distribution according to the main components and the power spectral density. In Fourier analysis, harmonic signals are also localized in the frequency domain, while transient signals have a broadband spectrum distributed according to the coefficients of Fourier transform.

As the energy of friction-induced noise is localized in the low-order component region, while the AE signal energy is distributed according to the decomposition components more uniformly, it is possible to make a conclusion that the method of principal components is useful for detecting an AE signal against the background friction noise.

Next, we examine the case of AE signal-noise combination. The combined signal $s(n)$ defined by equation (15),

$$s(n) = A \cdot Friction(n) + B \cdot Ae(n), \quad (15)$$

which is the sum of friction-induced noise $Friction(n)$ and the AE signal $Ae(n)$. The envelope of the combined signal $s(n)$ is shown in Fig. 8a. The weighting coefficients are selected in such a manner that the SNR value in the combined signal is below 0.1.

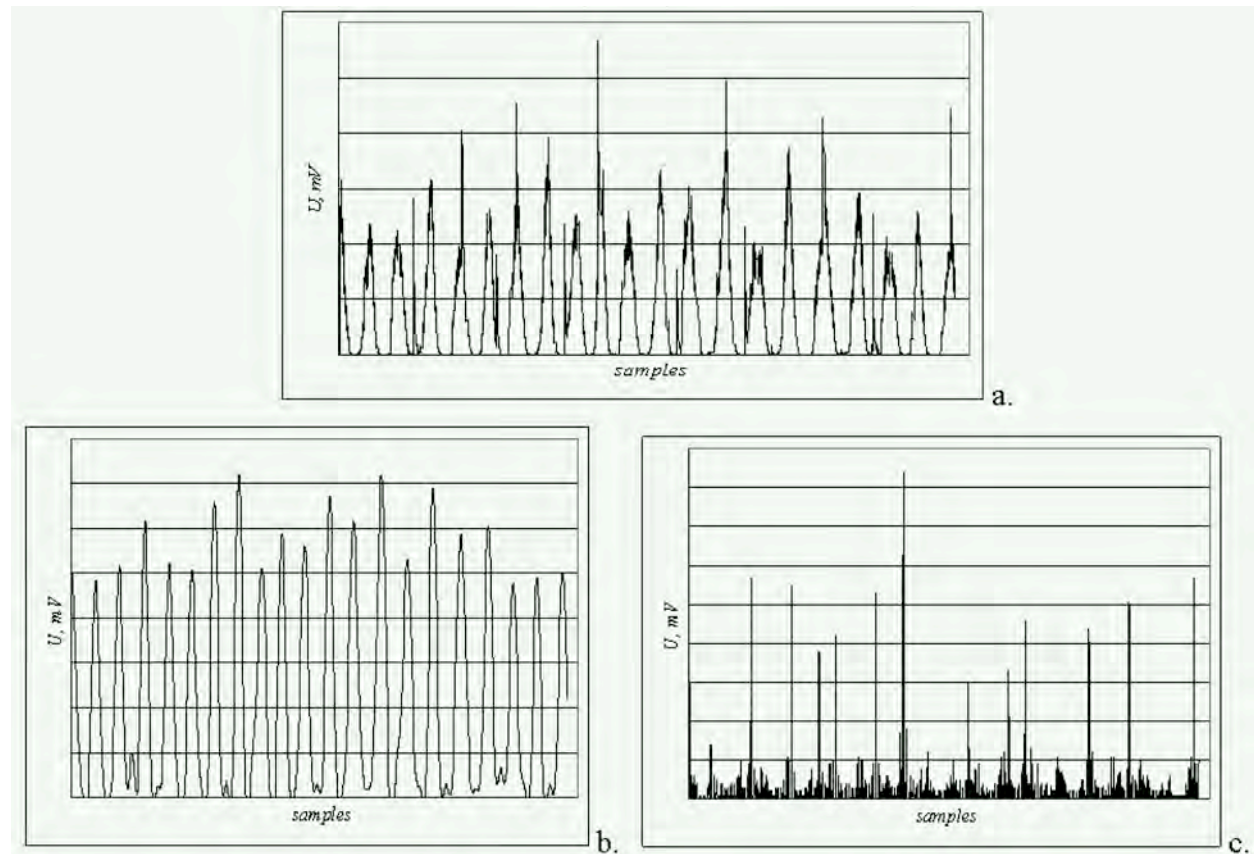


Fig. 8 a. Initial signal $s(n)$; b. reconstructed friction noise $Friction(n)$; c. reconstructed AE signal $Ae(n)$.

Figures 8b and c demonstrate the result of separation of the friction noise and the AE signal by grouping of the low-order main components (Fig. 8b) and the high-order components (Fig. 8c). A quarter of the high-order components (from 33 to 45) were discarded for the sake of filtering random noise.

Conclusion

In this paper, a variety of methods for the friction noise filtering are considered, adaptive selection of the recording threshold, the optimum filtering method, and the signal decomposition by the method of principal components. All three algorithms make it possible to perform effective filtering, both in *real time* mode (adaptive selection of the recording threshold and optimum filtering), and in *post-processing* mode (the method of principal components). Selection of one or other processing method depends on requirements of an operational speed of the AE system and its technical capabilities.

For our future AE systems, the adaptive threshold algorithm will be implemented, since this algorithm does not require excessive time expenditures and complicated procedure of adaptation. This algorithm can be applied not only in case of the friction noise, but also for white noise filtering with various time characteristics, and also for the arbitrary non-stationary noise having a non-transient nature.

Acknowledgement

Authors would like to acknowledge and express their heartfelt gratitude to Professor Kanji Ono for those encouragement and valuable remarks making this article more understandable and correct.

References

- [1] Carroll F. Morais (assigned to AET Corp.), Automatic threshold control means and the use thereof - United States Patent 4036057. July 19, 1977.
- [2] J. Rodgers, The Use of a Floating Threshold for Online Acoustic Emission Monitoring of Fossil High Energy Piping, Newsletter, Acoustic Emission Consulting, Ver. 1.0, Aug. 1994.
- [3] P. Stachel, R. Zivanovic and P. Schegner, Enhanced Segmentation of Disturbance Records by Adaptive Thresholding, *Proceedings of Power Systems Computation Conference (PSCC'08)*, Glasgow, Scotland, July 2008.
- [4] V. Barat, Y. Borodin, A. Kuzmin, Intelligent AE signal filtering methods, *Journal of Acoustic Emission*, **28**, 2010, 109-119.
- [5] Saeed V. Vaseghi, *Advanced Digital Signal Processing and Noise Reduction*, John Wiley & Sons Ltd, 2000.
- [6] N. Golyandina, V. Nekrutkin, A. Zhigljavsky, *Analysis of Time Series Structure. SSA and Related Techniques*, Chapman and Hall/CRC, 2001, 320 p.

GUIDE FOR DEVELOPMENT OF ACOUSTIC EMISSION APPLICATIONS FOR EXAMINATION OF METAL STRUCTURES

BORIS MURAVIN¹ and MARK F. CARLOS²

¹ Israeli Acoustic Emission Group, Association of Engineers, Architects and Graduates of Technological Sciences in Israel, Dizengoff 200, 61063, Tel-Aviv, Israel. ² ASTM Subcommittee E07.04 on Acoustic Emission, 195 Clarksville Rd, Princeton Jct, NJ 08550, USA

Abstract

In this work a guide for development of new AE field applications for examination of metal structures is presented. The practical goal of this guide is to provide a standard model, a master document that can be shared between different AE standards dedicated to different AE metal applications. In addition, this guide may improve the quality and comprehensiveness of new AE field applications and potentially simplify standardization process of AE practices and test methods developed according to this document. The guide provides a typical structure of standards dedicated to AE field applications, recommends considerations that shall be taken into account in new standards and explains their rationale. This guide is useful for anyone planning to perform AE field testing (metal or otherwise) and is a recommended reading for AE Level IIIs.

Introduction

Standardization is an essential step in maturing of every technology. Today, after more than three decades, several dozens of Acoustic Emission (AE) standards have been developed worldwide by international organizations such as ASTM, ISO, EN, ASME and GOST. These standards are dedicated to application of AE technology for examination of different structures. Nevertheless, the variety of modern AE applications is much broader than those described in the existing standards. Also, development of new standards is a long and complicated process. As a result, many AE applications are not standardized today. One of the ways to overcome this limitation is to develop a system of master AE standards covering broad range of aspects related to the AE testing and AE structural health monitoring. The guide proposed below describes considerations that should be addressed during AE field testing or in the process of development of new AE standards for metal structures.

Learning Structure

Before conducting AE examination or AE structural health monitoring [1] of a metal structure, it is necessary to obtain all information available regarding the structure to be examined including:

- The function of the structure and its design including detailed drawings.
- Materials used, their properties and manufacturing processes.
- Previous and current operational/stress/environmental conditions and factors that can contribute to flaw origination and development.
- Wave propagation characteristics in the structure (propagation modes, velocities, attenuation characteristics, etc.).
- Results of previous NDT examinations including visual surveys and results of stress analysis if exist, history of repairs and results of failure analyses, known discontinuities, flaws and leakages in the structure to be examined.

- Statistics of failures of similar structures, common failure mechanisms, possible location of flaws and expected rate of flaw propagation.
- Possible noise sources and other conditions that may affect examination.

Obtaining the above information is required for development of appropriate examination procedure, including: selection of a loading procedure, examination setup, equipment, development of assessment criteria, evaluation of flaw detectability and reliability of examination.

Investigation of Material Properties and Flaw Characteristics

Laboratory and/or full-scale tests shall be conducted on specimens and/or structures with known flaws at known stage of development in order to develop ability to detect, identify and assess or classify specific flaws/faults in intended or “goal” applications.

When small specimen laboratory tests are conducted, they should be performed according to ASTM E1932-07 standard. In addition, the following initial requirements are recommended:

- Type and mode of specimen loading should correspond to those normally present in the goal application. These can be tensile (step-wise or monotonically increasing load), bending, shear or fatigue tests.
- Specimens should be made from the material of the structure to be examined. If no material from the structure is available, it is recommended to obtain material from similar structures that were in operation over comparable time.
- Flawed and/or flawless specimens are examined. Flaws typical for the examined structure can be artificially induced (for example, fatigue cracks, stress corrosion cracking, hydrogen embrittlement) or be a part of the specimen taken directly from a structure.
- If artificial welded specimens are examined, the welding procedure should be similar to the one used in the production of the structure to be examined. This is in order to obtain similar microstructure, inclusion content, residual stress distributions and other factors that may result in different AE characteristics during specimens' examination.
- Material directionality should be considered during specimen preparation and loading.

AE characteristics acquired during the test of small specimens can be significantly affected by reflections, different geometric/size effects on flaw development and other factors. Therefore, in every specimen test, it is necessary to find invariant qualitative or quantitative AE characteristics that can be usefully applied for examination of real structures. Examples of such invariant characteristics are:

- Stress at onset of detectable AE in flawless specimen.
- Stress intensity factor or J -integral value of a flaw at onset of detectable burst AE.
- Presence or absence of Kaiser effect for the specific material.
- Ratio of AE energy released in form of continuous and burst AE.

Mechanical properties acquired during specimens tests should be documented, including yield strength, ultimate strength, stress at onset of continuous and burst AE, fracture toughness (when possible), brittle or ductile behavior, etc.

When statistically sufficient batches of specimens are tested, it is useful to:

- Investigate statistical distribution of mechanical properties and AE parameters/characteristics of the examined specimens.

- If several characteristic statistical groups of specimens according to their mechanical and AE characteristics are observed, it is recommended to perform fractography examinations to identify qualitative or quantitative differences between groups of specimens. Such investigation is useful for separation of specimens subjected to local embrittlement, different inclusion content, and others. Once such differences identified, the obtained information may be used in certain cases for detection of these indications of in goal applications.

Whenever possible, it is recommended to perform full-scale tests on structures with known service-developed or artificially induced flaws. It is important to note that artificially developed flaws may have lower detectability compared with service-developed flaws due to different factors.

Selection of Equipment and Sensor Installation

General rules for selections of equipment described in ASTM E1932 [2] standard shall apply with the following additional considerations:

- Sensor's frequency range should be selected based on investigation of wave propagation characteristics in the structure to be examined. For this purpose, it is necessary to investigate modes of AE waves that can be present, their velocity and attenuation characteristics. For simple geometries like flat plates, one can use analytical solution to predict wave propagation characteristics, and for complex geometries various numerical software packages can be used.
- Wideband sensors can be used whenever it is necessary to perform frequency-based analysis of AE signals in order to separate different processes by their frequency characteristics, for performing advanced AE source location, etc.

Sensor positioning and installation should be performed under the following considerations:

- Sensor position is determined by considering dimensions and the geometry of the examined structures. Sensors shall be placed as close as possible to major welds and welded accessories in welded structures due to the fact that flaws most commonly develop in weld joints.
- Distance between sensors is governed by attenuation of AE waves along the structure, geometrical changes (for example, elbows, tee and wye blocks, heavy valves or other accessories in piping systems) and by AE background noise characteristics. In zones with elevated and/or variable background noise, the distance between sensors can be shortened to allow better detectability, which usually is the primary objective of examination.
- When welded or mechanically attached waveguides are used for installation of AE sensors, it is necessary to evaluate AE wave energy loss at structure-to-waveguide interface. In addition, AE wave modes change as a function of waveguide geometry and this should be investigated.

System Performance Verification

System performance verification should be conducted immediately before the examination. This is in order to ensure that the system is satisfactorily prepared for the examination. Particularly, one must verify that sensors are properly mounted on the structure and maintain required sensitivity level and there are no conditions that reduce sensitivity and reliability of the system. During and immediately after the examination, it is necessary to verify that there is no change in system performance. System channels found to have performance below required minimum should be repaired or replaced. Any significant change in performance during examination

should be documented. System performance verification shall be performed by guidelines provided in ASTM E2374 standard [3].

AE Examination

An optimal examination procedure is considered one that ensures the maximum probability of flaw/fault indication and detection while minimizing false negative findings. This can be achieved by the application of appropriate loading conditions, suitable equipment and methods of data acquisition and data analysis.

Loading/Operational Conditions for Conducting AE Examination

Optimal conditions for performing examination are considered those, under which flaws/faults naturally originate and develop in the examined structure. Therefore, it is recommended to conduct AE examinations under full normal operational load and stress conditions of the structure.

In certain cases, it may be required to perform examination under higher stresses than normal operational stresses, for example, when duration of examination is short and additional stimulus is necessary to intensify flaw development or when a structure is periodically subjected to dynamic overstresses above normal operational stresses. Additional special examinations can be performed under controlled variable stress conditions to evaluate sensitivity of flaws to load/stress changes.

AE examination can be used to identify structural issues. These capabilities can be provided given the examination performed under real operation of the structure. For example, in case of steam piping, it is possible to reveal issues related to thermal shocks, valve leaks, valve malfunctioning, steam fluctuations and turbulence, improper performance of hanger and support systems, impacts, friction due to piping interference, and events of water hammer, thereby providing valuable information for piping maintenance.

Duration of Examination

Duration of examination is governed by probability of flaw/fault detection. The probability of flaw detection depends upon failure mechanisms, examination setup, hit detection techniques, background noise characteristics, stress conditions and other factors. Duration of examination should be such that at least 6 signals related to the least active flaw indication to be revealed will be detected under specific AE background noise conditions using the particular system and examination setup. Thus, for example, in zones with elevated background noise and/or with high thresholds, longer examination times may be required. Examination duration should be increased to achieve consistent and statistically valid results in case of variable stress or elevated/fluctuating AE noise conditions.

Noise Management

Structures can operate under strong and variable AE background noise (for example, rotating machinery, process piping and reactors). This is one of the main challenges of AE examination. In certain cases, minor changes in structure operation can significantly reduce AE background noise. For example, temporary full or partial closure of extraction pipes and/or stabilizing flow can significantly reduce background noise in process piping. Possible approaches for reducing background noise can be discussed with the structure operator and implemented whenever is acceptable and practical. Other means to manage noise effect on examination performance is by selection of optimal equipment, system setup and methods of data acquisition and data analysis.

System Setup

Frequency range. The frequency range for conducting AE examination should be in agreement with the selection of sensors, preamplifier characteristics and noise conditions. In the case of high background noise, the high-pass frequency range can be increased. Nevertheless, this may require shortening the distance between sensors due to increased attenuation. Any increase in the high-pass frequency should be followed by analysis of attenuation and detectability of signals of target amplitude and frequency under specific background conditions and given sensor spacing. Areas of structure with reduced detectability or reliability due to high background noise conditions or any other reasons should be specified in the report.

Hit detection techniques. Detection of AE activity suspected to be from flaw development usually is a problem of statistical outlier detection. Different hit detection techniques, threshold dependent for burst AE signals or threshold independent for continuous AE signals and their combination may be used for structure examination. Among threshold dependent techniques, several float threshold methods are often used for detection of AE burst signals. In order to minimize false positive hit detection by float threshold, additional parametric hit filtration is required. Normally, hits with too short or too long duration and few counts are eliminated. Flaw/deficiency detection in process monitoring or rotating machinery applications requires measurement of continuous characteristics of noise, such as RMS, kurtosis, peak amplitude and others.

Operational Data

Load, pressure, temperature or other relevant operational data can be measured during examination or provided by the structure operator. This data can be used to detect possible correlation between AE activity and relevant operational/stress/environmental conditions.

Documentation of Sensor Installation and of the Structure

Documentation of sensor installation and of the structure should be performed during examination and include information about exact position of the sensors, their spacing and their distance from main elements of the structure, like welds, hangers and supports, tees, wyes, elbows, valves, extraction pipes, thermocouples in case of piping systems or welds, supports, manholes, nozzles, etc. in case of pressure vessels.

Visual Survey

Visual survey of the structure and its accessories should be conducted during examination for any unusual conditions or possible deficiencies. Visual survey may provide important direct and/or indirect information about structure condition, possible overstressed zones, assist in interpretation of some of recorded AE activity, etc. All abnormal findings should be reported.

Preliminary Analysis

Preliminary analysis of the measured data must be performed in the field in order to reveal or rule out any severe conditions that may threaten safety of the examined structure and should be immediately addressed. Although such scenarios are rare, still they happen and therefore the role of preliminary analysis cannot be under evaluated.

DATA ANALYSIS

Location and Clustering

Different methods are applied for evaluation of AE source location. Commonly applied methods are time-difference locations for burst AE signals, zone location, cross-correlation and energy

attenuation-based locations for continuous and burst AE signals. In the case of energy attenuation-based location, noise normalization should be performed to reduce location error due to difference of background noise conditions at different sensors.

Location clustering can be performed to identify AE source characteristics including likely AE origin, number of emissions vs. time vs. physical location, etc. AE activity locations should be compared with position of main structural elements, welds, structural accessories, etc. and findings of visual survey.

Statistical analysis of signal parameters within each cluster should be performed in order to identify possible different groups of AE signals within a cluster, which may identify several physical processes occurring in the same location (for example, general electrochemical corrosion and cracking in pressure vessels).

Location accuracy and reliability can be limited in cases of strong and/or variable background noise and/or complex geometries. Due to these reasons, different location artifacts including location folding and location scattering may be observed. Nevertheless, it is important to note that all AE activity, regardless if it is locatable or not, should be analyzed, documented and reported.

Flaw-Indication Identification and Assessment

When proper methods of data analysis and criteria are developed, AE data can be used for flaw-indication/identification, assessment or classification. AE is flaw/fault-stage-material specific, i.e. different flaws and faults at different stages of their development in different materials have different AE characteristics. Therefore, flaw/fault identification (typification) and assessment is possible when unique AE characteristics characterizing different flaws/faults indications at different stages of their development in the specific material can be identified, effectively distinguished and compared with similar characteristics obtained in similar applications and/or in laboratory tests. Features used in data analysis should have an established relationship with physical phenomena being measured during AE examination in order to ensure correct assessment of the examined structure. Signal parameters used for assessment of indications should be a minimum set of statistically significant features; filtered and normalized whenever is required so influence of background noise is minimized and data measured at different times and different locations is comparable. Comparison of loading/stress/environmental conditions with AE activity and/or AE data parameters can be used to identify conditions causing flaw/fault accumulation, development, acceleration or arrest.

Managing Uncertainties

During data analysis a conservative approach should be taken in case of uncertain results. Flaw/fault indications that can be equally classified into two different groups by their severity level should be attributed to the group corresponding to more severe flaws/faults. Also, all AE activity distinguishable from AE background noise should be considered as flaw/fault related activity unless difference is verified.

Report

Examination report should include the following information:

- History of the structure, repairs and findings of previous NDE examinations.
- Description of examination procedure and test setup.

- Location of flaw/suspected indications, their type and significance specified in isometric drawings and tables. Operational/stress/environmental conditions, under which flaw-indications revealed are most active.
- Findings of the visual survey. Zones with reduced reliability of examination.
- Conclusions and recommendations regarding the interval for the next examination and application of other NDE methods if necessary, when and where.

Re-examination of structure is performed to follow up on the condition of a structure over time. For success of monitoring, it is necessary to identify quantitative and/or qualitative AE characteristics that are changing with flaw/fault development. It is important to perform monitoring at least partially under similar operational conditions as during the previous examination. If a significant change in stress/operational conditions occurs for any reason, it may require change in the monitoring policy and re-inspection interval. In cases when structure is subjected to extreme dynamic event/s and trauma, it should be re-examined immediately after this event occurrence. Optimal re-inspection interval is such that a risk of unexpected failure is reduced to the minimum acceptable probability, defined for the specific structure with specific operational and stress conditions, material and specific flaw mechanisms. Presence of different structural risk factors like history of uncontrolled overstresses should also be taken into consideration. Re-inspection interval can be shortened in case of reduced detectability or reliability of the examination due to high or fluctuating background noise conditions.

Conclusions

In this work, we present a guide for development of new AE field applications for examination of metal structures. This guide provides a general approach that can be shared between different future standard AE applications and may improve their quality and comprehensiveness.

References

- [1] B. Muravin, G. Muravin, L. Lezvinsky, "The Fundamentals of Structural Health Monitoring by the Acoustic Emission Method", *Proceedings of the 20th International Acoustic Emission Symposium*, November 17-19, Kumamoto, Japan, pp. 253-258.
- [2] ASTM E1932 "Standard Guide for Acoustic Emission Examination of Small Parts", *Committee E07 on Nondestructive Testing*, 2007.
- [3] ASTM E2374 "Standard Guide for Acoustic Emission System Performance Verification", *Committee E07 on Nondestructive Testing*, 2004.

ACOUSTIC EMISSION MEASUREMENTS ON PIEZOELECTRIC/ FERROELECTRIC MATERIALS

HIDEAKI ABURATANI

Kitakyushu National College of Technology, Kokura-minami, Kitakyushu, Fukuoka, Japan

Abstract

Ferroelectric materials such as PZT are widely used in many industrial fields because of their excellent piezoelectric properties. The AE method has been applied on the piezoelectric/ferroelectric materials to investigate the domain dynamics, phase transition as well as material fatigue. However, it is important to notice that there are two kinds of AE in the electric field induced AE: AE from within the sample and vibro-AE caused by sample vibration due to electrical coupling between the power supply and the piezoelectric sample. In this study, the electric field induced AE generations in the ferroelectric PZT ceramics and multilayer actuators under unipolar or bipolar electric fields are examined. The vibro-AE that easily conceals the ferroelectric domain related AE is suppressed using an external resistor. The vibro-AE activity is discussed with comparisons of the ferroelectric domain related AE as well as failures, and is also used to evaluate the piezoelectricity of the sample. From these AE activities, AE measurements on piezoelectric/ferroelectric materials and their possibilities for the material evaluation are discussed.

Keywords: Ferroelectric materials, piezoelectric materials, ferroelectric domain, vibro-acoustic emission, PZT ceramics, multilayer actuator

1. Introduction

Ferroelectric materials such as lead zirconate titanate (PZT) are widely used in many industrial fields, such as capacitors, sounders (speakers), mechanical filters and ultrasonic motors, because of their excellent dielectric and piezoelectric properties. The PZT acoustic emission (AE) sensor is one of the best applications of piezoelectric materials. For piezoelectric/ferroelectric materials, the AE method has been used to research ferroelectric domain reorientation processes [1], phase transitions [2], and to detect crack propagation and material fatigue [3-5]. However, in AE measurements of ferroelectric materials under electric fields, there are two possible kinds of AE signals: AE signals from within the ferroelectric sample and vibro-acoustic emission (vibro-AE) signals related to the piezoelectricity of the sample [6]. The former are related to energy loss mechanisms caused by structural changes of the ferroelectric domain or the crack propagation. The latter are generated by mechanical vibration stimulated by electrical coupling between the power supply and the piezoelectric sample; the AE signal is mechanically generated. It should be noted that vibro-AE tends to conceal the AE signals from within the sample. In order to clarify the effect of vibro-AE on the measurement, the AE signal levels before and after poling as well as with and without an applied voltage should be evaluated.

In this study, the AE behaviors in ferroelectric lead zirconate titanate (PZT) ceramics and multilayer actuator under applications of electric fields are examined. The vibro-AE activity is discussed by comparison with ferroelectric domain related AE and AE generated by failures. From these two types of AE activities, the use of the AE method for the piezoelectric/ferroelectric materials and the AE measurement technique for piezoelectric material are discussed.

2. Experimental Method

Figure 1 shows a schematic of the measurement system employed for this study. The AE signal detected by an AE sensor (NF AE-904E) is amplified by up to 90 dB with pre- and main-amplifiers. The amplified AE signals passing through a high-pass filter (>100 kHz) are analyzed using a discriminator (NF AE-9922) and a signal-processing module (NF As-712). The AE signal amplitude and the rms value of the AE signal (AE signal V_{rms}) over a period of 1.0 s are recorded to examine the AE behavior. Unipolar or bipolar voltages with various levels are applied to the samples using a power amplifier (NF HVA-4321). The periods of voltage application is set to be from 100 to 1,000 s. Induced displacements are measured using a linear variable differential transducer (LVDT; Mahr Millimar1300).

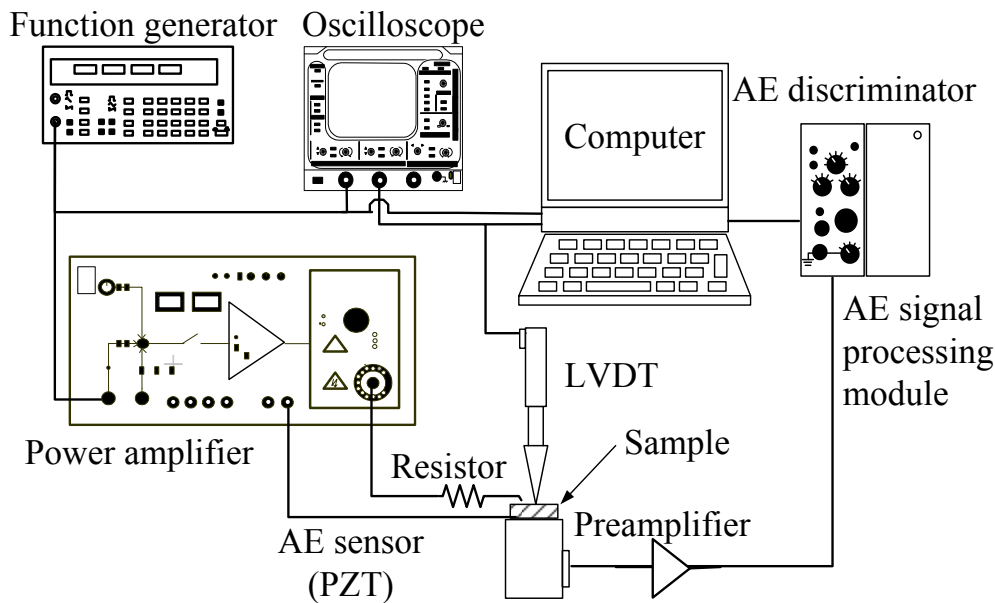


Fig. 1. The induced displacement and AE measurement system.

Silver-electroded disk specimens of commercial soft PZT ceramics (Fuji Ceramics C-6) with 15.0-mm diameter and 0.4-mm thickness and co-fired multilayer actuators (NEC-Tokin AE0203D08F and AE0505D08F) are chosen for this study. The properties of these samples are listed in Tables 1 and 2. Schematic figures of typical multilayer actuator structures are shown in Figs. 2(a) and (b): an interdigital electrode type and a plate-through type. The multilayer actuators employed for this study are the plate-through type; thin layers with thickness of about 100 μm are placed between plate-through electrodes in stacks of layers. Although the high reliability of the commercial multilayer actuators ($>10^{10}$ cycles) is achieved, there are still possible failures from cracking and delamination (i.e. separation of the internal electrode from piezoelectric ceramic layer), since the stress concentration is inevitable in both structures. The interdigital electrode structure (interlocking-finger configuration) is widely used for dielectric devices, because of its simplicity. Electric field and stress concentrations that may lead to failure (cracking) occur at the ends of internal electrodes. Whereas in the plate-through electrode structure, glass insulators that require complex processes to fabricate are positioned on alternate sides of the internal electrodes in order to obtain a uniform electric field distribution and deformation. However, the stress concentration also takes place at the interface between active and inactive layers due to the residual strain caused by the poling process as well as the induced strain during the operation.

Table 1. Properties of PZT disk samples.

	Piezoelectric constant d_{33} (pC/N)	Curie point T_c (°C)	Electromechanical coupling factor k_{33}	Dielectric constant $\epsilon_{33}^T/\epsilon_0$
C-6	472	295	0.76	2270

Table 2. Properties of multilayer actuator samples.

Model	Displacement @ 150 V (μm)	Size (mm)	Resonance frequency (kHz)	Generated force (N)
AE0505D08F	9.1±1.5	6.5x6.5x10	138	850
AE0302D08F	9.1±1.5	3.5x4.5x10	138	200

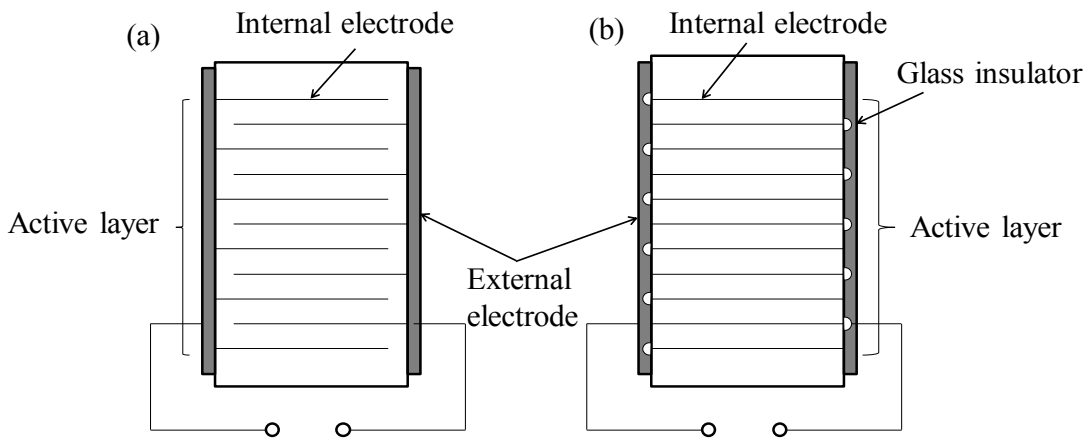


Fig. 2. Typical internal electrode structures for multilayer actuators: (a) an interdigital electrode type and (b) a plate-through type.

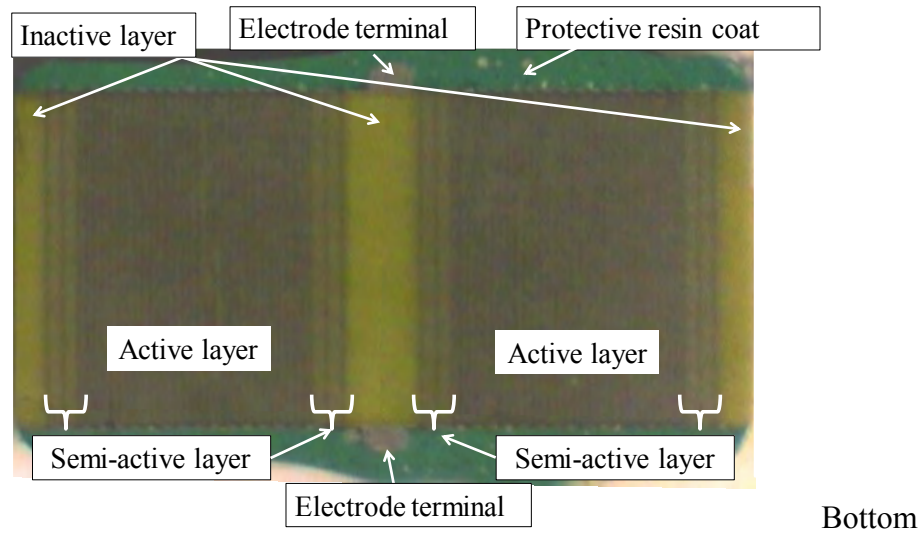


Fig. 3. A cross section of the plate-through type multilayer actuator (AE0505D08).

Figure 3 shows a cross section of the plate-through type multilayer actuator sample. As shown in the figure, semi-active layers with doubled layer thickness are placed between active and inactive layers to reduce the stress. As the strain of piezoelectric layer is proportional to the

applied electric field, the electric field at the semi-active layer is a half of that in the active layer, because the electrode gap is doubled. The inactive areas at both sides are necessary as protection layers for practical use. All sides of the actuator are also covered with a resin coat in order to protect the internal electrode. A relatively large inactive layer is inserted at the center where the cracking due to the ceramic sintering process is found to occur. External electrode terminals are also formed at the center inactive layer to lower the thermal damage to the active layers.

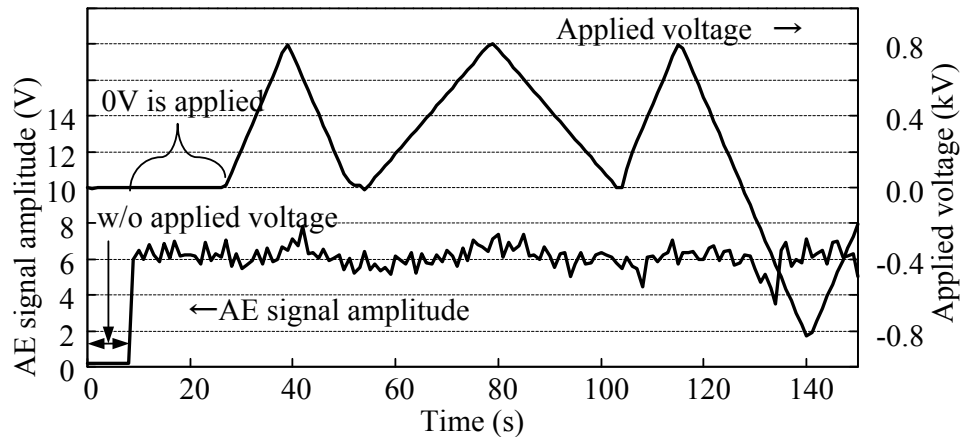


Fig. 4. Applied voltage and vibro-AE signal as functions of time measured at 90 dB.

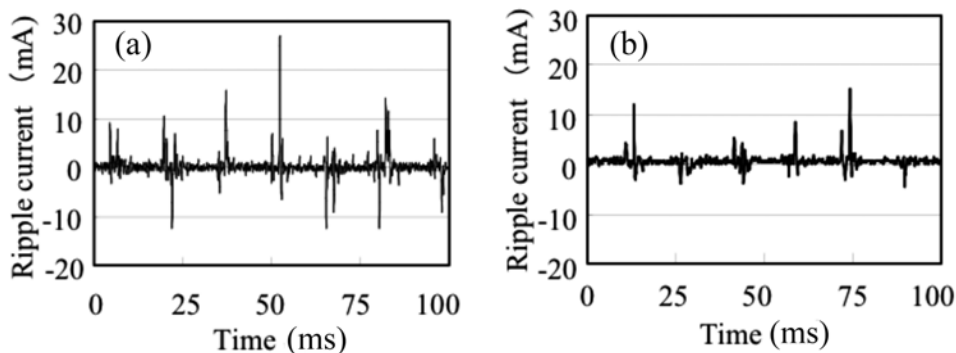


Fig. 5. Ripple current caused by electrical coupling (a) for disk sample and (b) for multilayer actuator.

3. Experimental Results

3.1 Electrical Coupling and Vibro-AE

Figure 4 shows the vibro-AE signals measured at 90 dB when the poled PZT sample is connected to the power amplifier. The signal level is found to increase rapidly as soon as the voltage is applied, even if the voltage is set to 0 V. This rise in the signal level is caused by the ripple current shown in Fig. 5(a). Because of the spontaneous polarization, the ferroelectric sample is electrically self-biased. When the sample is connected to the power amplifier, this electrical bias is changed to a fixed external voltage. The variation of external voltage induces mechanical deformation of the sample through its piezoelectricity. Depending upon the specification of power amplifier, this electrical interaction between the piezoelectric sample and the power amplifier results in stabilized ripple current. Similar ripple current is also observed for the multilayer actuator as shown in Fig. 5(b). The frequency of ripple current is found to be around 65 kHz, close to the frequency limit of the power supply. It should be noted that these ripple current may not cause any serious problems in usual applications except for the AE measurement.

Figures 6(a) and (b) also show a typical power amplifier dependence of the vibro-AE generation. The multilayer actuator is connected to a high-speed bipolar amplifier (NF HSA-4011), of which output voltage is set to 0 V with different amplification levels: 10 times and 50 times. Although a low AE signal amplification of 40 dB is chosen, large vibro-AE signals are easily detected. Since the electrical coupling is caused by the feedback process of amplifier, the larger amplification of amplifier generates the larger ripple current and vibro-AE signal. The vibro-AE is caused by mechanical vibrations of the piezoelectric sample due to the electrical coupling; therefore, the AE sensor signal is found to be continuous.

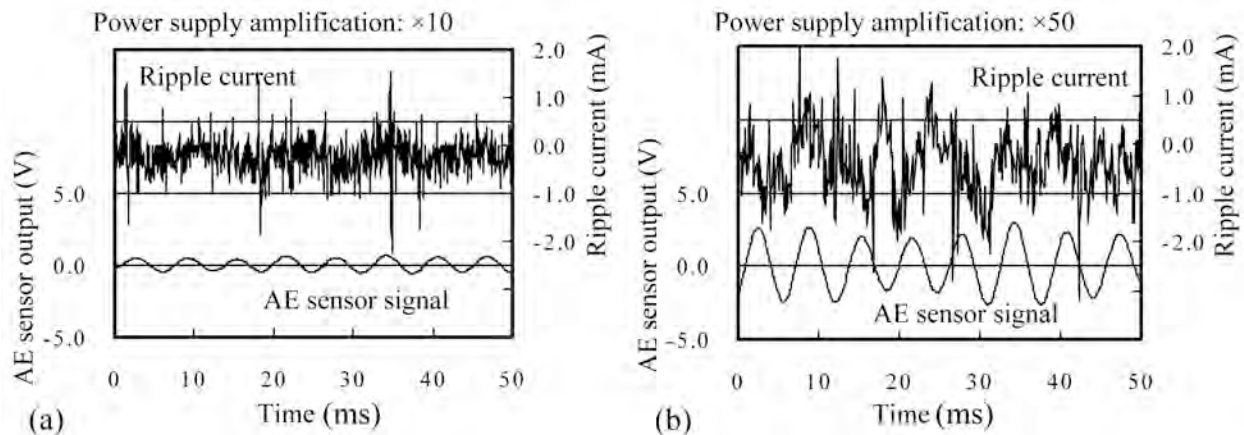


Fig. 6. The vibro-AE signal and ripple current waveforms. (a) Amplification of power supply at 10 times and (b) at 50 times.

In order to reduce the vibro-AE signal level to lower than that of the AE from within the sample, external resistors of 20 M Ω and 1 M Ω are connected in series to the PZT sample and the multilayer actuator, respectively. As the ferroelectric/piezoelectric samples are capacitors, the connected resistor and the sample form a low pass R-C filter. Because the series resistor limits the current, much less electrical coupling between the sample and the power amplifier is obtained, resulting in a suppressed vibro-AE signal level. Since the vibro-AE decreases with the value of resistor, the vibro-AE signals can be lowered to the background level using a very high resistor (e.g. >100 M Ω). However, it is also to be noted that the frequency of applied voltage simply decreases due to the limited current flow. Therefore, the value of resistor should be optimized from the viewpoint of overall performance.

3.2 AE measurements on disk PZT samples

Figure 7(a) shows the AE signal amplitude, AE signal V_{rms} , and the induced strain as functions of time during the poling process and the successive application of an electric field. Total signal amplification is set to be 90 dB for this measurement, and the AE signal level at the unpoled state is equal to the background noise level. It is shown that the AE signal amplitude increases and exhibits high activity until the applied field reaches the maximum level after the strain begins to be induced. It also exhibits low activity while the electric field is decreased. The measured AE activities are supposed to be due to the ferroelectric domain reorientation related to stress reduction. It should be noted that, after the poling, the AE signal amplitude is found to be higher than the previous background noise level. This increase is simply attributed to the vibro-AE signal as a result of the introduced sample piezoelectricity. Since the vibro-AE is continuously generated, the AE signal V_{rms} , the average signal amplitude over a time interval of 1.0 s, tends to reflect the vibro-AE activity. In addition, it is shown that an increase in the AE signal V_{rms} takes place before both the induced strain and the AE signal amplitude begin to

increase. It is supposed that the microscopic piezoelectricity is introduced into the sample by the application of the electric field, even before the major strain is induced. This result indicates the possibility of the vibro-AE measurement for real-time determination of piezoelectricity of the sample. Figure 7(b) shows the AE signal amplitude and the induced strain for a bipolar electric field. A butterfly-shaped induced strain curve is obtained and the AE is observed as sharp peaks in the AE signal amplitude only after strain switching (polarization switching) has occurred. Conflicts among domains in the sequence of domain reorientation from the clamped state to the aligned domain state and the consequent stress relaxations are considered to be the origin of AE [7]. It is also important to note that the base level of AE signal, i.e., the vibro-AE, drops to a minimum of almost the background level at critical fields. The markedly diminished vibro-AE implies low piezoelectricity of the sample. When the applied field is suddenly decreased as soon as it reaches the critical field, the vibro-AE maintains a minimum level of almost the background (i.e., non-piezoelectric) even after the external field is removed as shown in Figure 7(c). Conflicts among ferroelectric domains developed through domain reorientation in the domain structure are suggested to be the origins of the non-piezoelectric state. This result indicates the possibility of electrical depoling process using the vibro-AE measurement as a real-time determination of the sample piezoelectricity and new driving methods of ferroelectric devices [8].

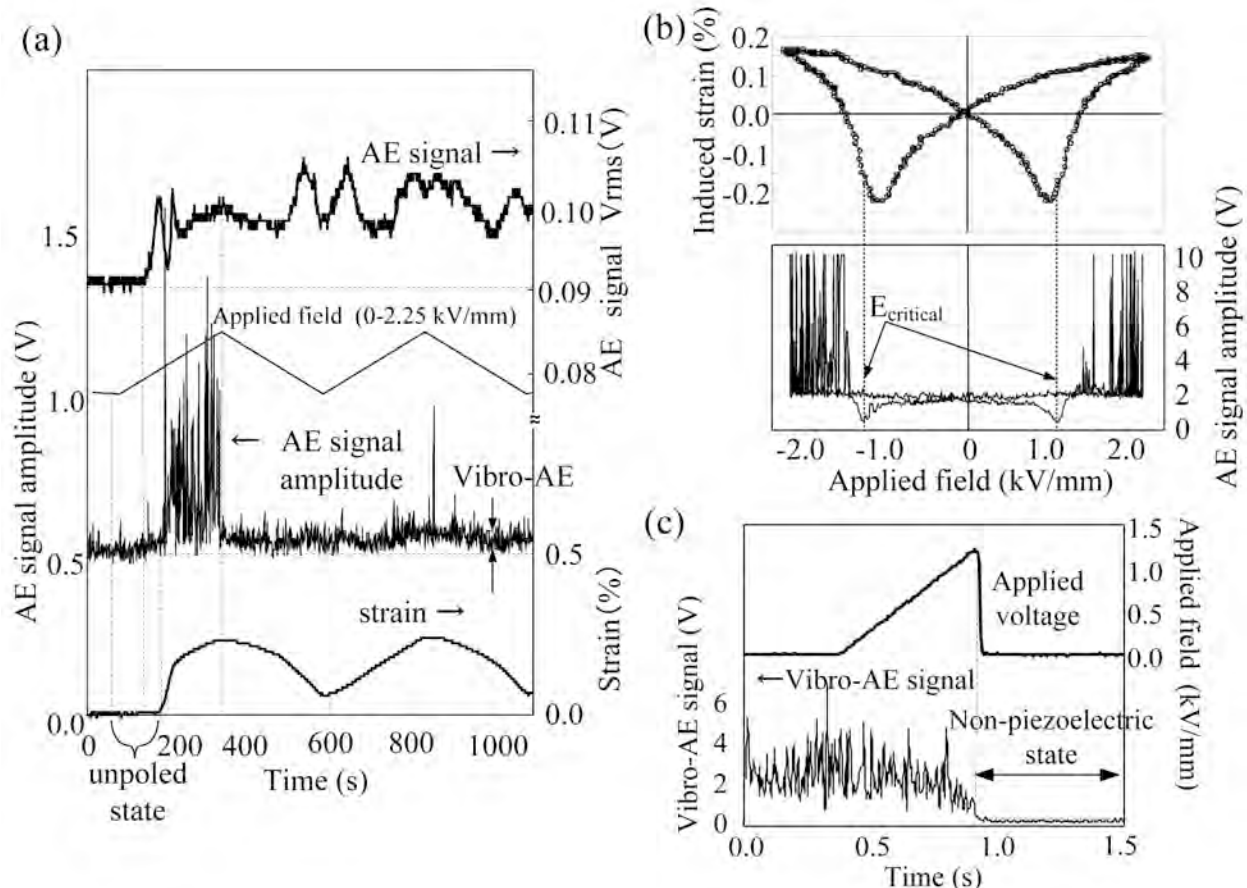


Fig. 7. AE measurement on the PZT sample: (a) During the poling process, (b) for the bipolar field, and (c) non-piezoelectric state obtained using the vibro-AE.

3.3 AE measurements on multilayer samples under unipolar voltages

The multilayer actuators are usually unipolar driven to prevent the polarization switching and consequent displacement switching. Figure 8(a) shows the induced displacement of the multilayer actuator as a function of the applied unipolar voltage. A voltage up to 900 V, six times

larger than the recommended maximum voltage of 150 V, is applied in order to introduce failures (i.e., crack and delamination) in the actuator. The induced displacement is found to exhibit less hysteresis at high voltage and a maximum induced displacement of 20 μm is obtained at 900 V. The AE measurement is conducted at an amplification of 80 dB using the external resistor. As shown in Fig. 8(b), the applied voltage is cyclically increased to 900 V, and then 900 V is applied repeatedly. The AE events occur when the applied voltage exceeds 600 V; Cracking, growth of delamination, and defects at electrodes are supposed to be the origins of AE. In the AE signal, these AE events are detected as peaks of the signal. It should be noted that the base level of the AE signal increases with the applied voltage and these rises are caused by increases in the vibro-AE at higher voltages. Thus, in this measurement, the vibro-AE signals are successfully suppressed to the level lower than that of the AE relevant to the failures within the sample.

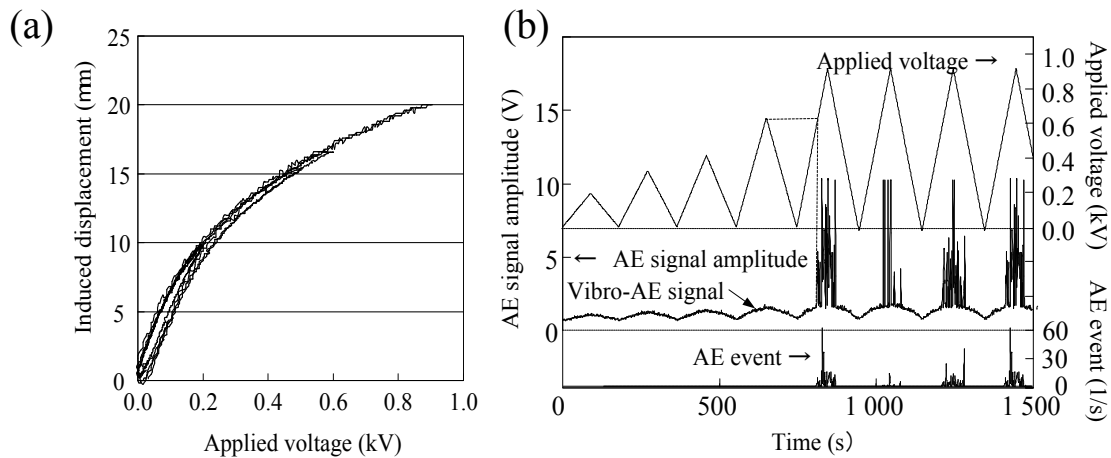


Fig. 8. Measurements on the multilayer actuator: (a) the induced displacement as a function of applied voltage and (b) AE measurements.

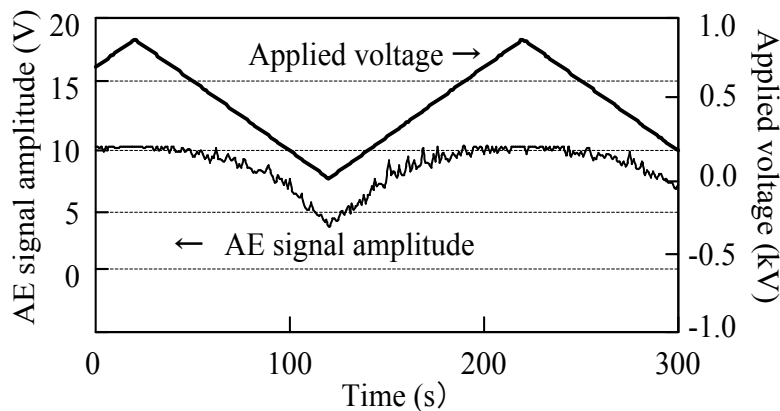


Fig. 9. Applied voltage and vibro-AE as functions of time without the external resistor.

Figure 9 shows the applied voltage and the AE signal as functions of time for the AE measurement without using the external resistor. A lower signal amplification of 60 dB is chosen to avoid saturation of the signal. The signal due to the vibro-AE is found to increase with applied voltage and is about 50 times larger than the suppressed values with the series resistor. However, this signal level is still lower than those obtained using the different amplifier (Figs. 6(a) and (b)). From these results, it is shown that the suppression of vibro-AE is the key technique

for the AE measurement on piezoelectric/ferroelectric samples and the influence of power amplifier on AE measurement should be taken into consideration.

3.4 AE measurements on multilayer samples during poling process

As shown in the previous section, the higher applied voltage to the multilayer actuators increases the probability of failures. In actuality, the multilayer actuators are exposed the highest applied voltage during the poling process (i.e., the poling voltage) and the recommended maximum driving voltage is chosen to be lower than that. The poling voltage is usually determined from the piezoelectric performance and the reliability of actuators.

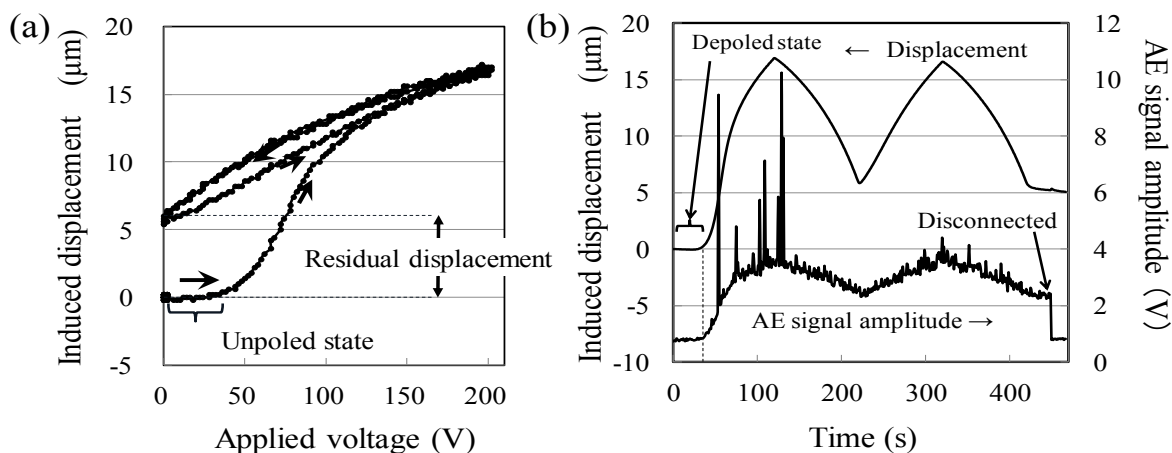


Fig. 10. Displacement and AE during the poling process: (a) The induced displacement as a function of applied voltage, (b) the induced displacement and AE as functions of time.

Figures 10(a) and (b) show the induced displacement and the AE signal amplitude during the poling process and the subsequent applications of a unipolar voltage of 200 V. Since all commercial multilayer actuators are poled, the samples are heated to 200°C to thermally depole for this measurement. The AE signal amplification of 90 dB, used for the poling of disk PZT sample, is also chosen for this measurement. The displacement begins to be induced around 30 V and a residual displacement of 6 μm is obtained after the poling process. The poled actuator exhibits a displacement of 9 μm at 150 V that coincides with the given data. As the residual displacement caused by the poling process is the same order of the practically used maximum displacement, the failures in the multilayer actuators tend to occur during the poling process. Similarly as obtained for the disk samples, the AE signal level at the non-piezoelectric depoled state is equal to the background noise level. The AE signal amplitude is found to increase when the displacement begins to be induced (i.e., the poled state) and exhibits some peaks during the first cycle. The changes in AE signal amplitude similar to the induced displacement are supposed to be caused by the vibro-AE. Therefore, the signal returns to the background level when the sample is disconnected from the power amplifier. The larger signal amplitude than that of disk samples is due to the difference in the effective volume of piezoelectric element and the higher voltage sensitivity of the multilayer actuator. In addition, different from the disk samples, the microscopic piezoelectricity before the major displacement induction is observed not to occur, since the vibro-AE begins to be detected simultaneously when the displacement induction takes place. This result may imply that the multilayer structure including the inactive layers and protective resin coat clamps the actuator itself mechanically and suppresses the microscopic piezoelectricity. As the observed peaks are much larger than those in disk sample, the micro-cracking and stress reduction at the interfaces between active and inactive layers rather than ferroelectric domain reorientations are supposed to be the origins of AE.

3.5 AE measurements on multilayer samples under bipolar voltages

As shown in sec. 3.2, the polarization switching induces a large butterfly-shape displacement. Thus, an application of bipolar voltage with polarization switching will damage the multilayer actuator. Especially for the interdigital electrode type actuators, even a low bipolar voltage may result in the polarization switching at the end of internal electrode due to the electric field concentration. In this section, the AE behavior during the bipolar drive is discussed. Figure 11(a) and (b) shows the induced displacement and AE signal amplitude during the bipolar drive (± 600 V) with polarization switching. The displacement switching caused by the polarization switching is found to occur at ± 80 V and a total displacement of $25 \mu\text{m}$ is obtained.

Different from the disk sample, the AE related to ferroelectric domain reorientation does not appear in the first polarization switching. It is assumed that the multilayer structure with many internal electrodes attenuates the AE signals. It may also imply the thickness and stress dependence on the AE generation in the ferroelectric materials, since the layer thickness is less than that of disk samples and the inactive layers clamp the active layers. At the second cycle, large peaks in the AE signal amplitude are observed after the polarization switching. Thereafter, new peaks of the AE signal begin to appear. Thus, the observed large AE peaks are attributed to fast crack propagations and the subsequent AE activities seem to be caused by additional slow crack growth and the friction at these cracked interfaces. In the multilayer actuators, the displacement is induced through the electric field. Therefore, the generated crack and delamination may reduce the electric field concentration, resulting in a crack arrest and low AE activities as shown in Fig. 11(b).

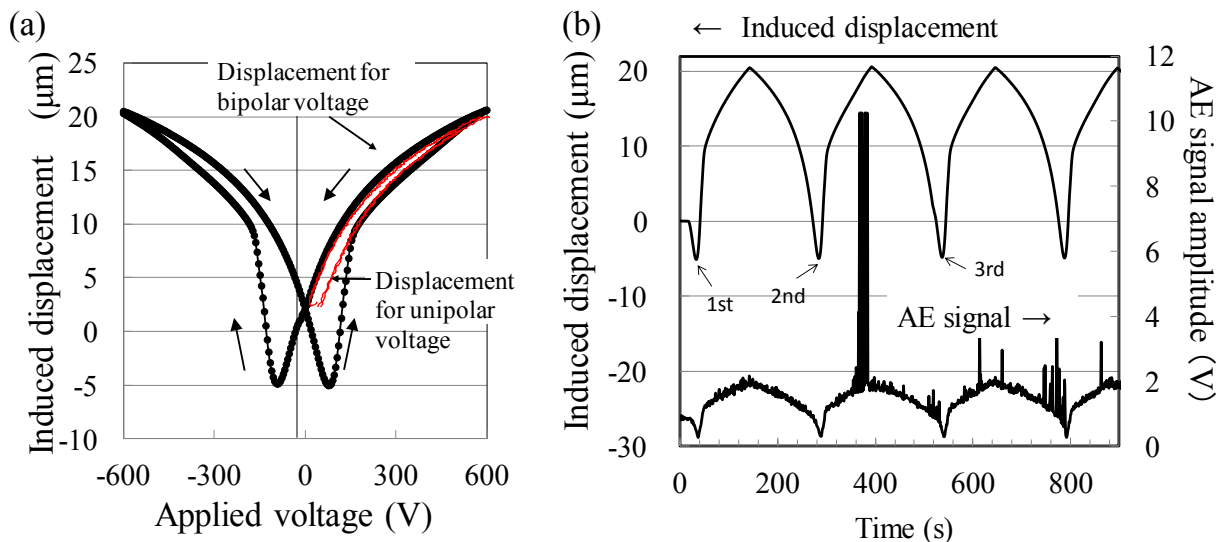


Fig. 11. Displacement and AE during the poling process: (a) The induced displacement as a function of applied voltage, (b) the induced displacement and AE as functions of time.

Figures 12(a), (b) and (c) show cracks and delamination in the bipolar voltage-driven sample (after 50 cycles). These failures tend to be found near the midsection of the samples. At the top and bottom of the actuator, a crack is found to propagate vertically through the active layer and even to penetrate the inactive layer (Fig. 12(a)). This is a typical crack found in the multilayered ferroelectric element caused by the polarization switching [9, 10]. At the center inactive layer, cracks are found to initiate from the external electrode terminal where the pre-damage due to the terminal formation process is supposed to occur and to grow through the layer (Fig. 12(b)). These cracks and delamination (Fig. 12(c)) are supposed to be caused by shrinkage and

expansion of active layer in the transverse direction. It should be noticed that the failure processes occurring through the polarization switching are different from that under the unipolar voltage. The polarization switching takes place where the electric field reaches a critical value (i.e., coercive field). However, the voltage that gives the coercive field is different in each active layer, because of the slight variations in thickness. Therefore, the polarization switching and consequent displacement switching take place non-uniformly, and cause a large stress concentration at the layer interfaces. It is shown that the failure process in the multilayer actuator can be detected using the AE method.

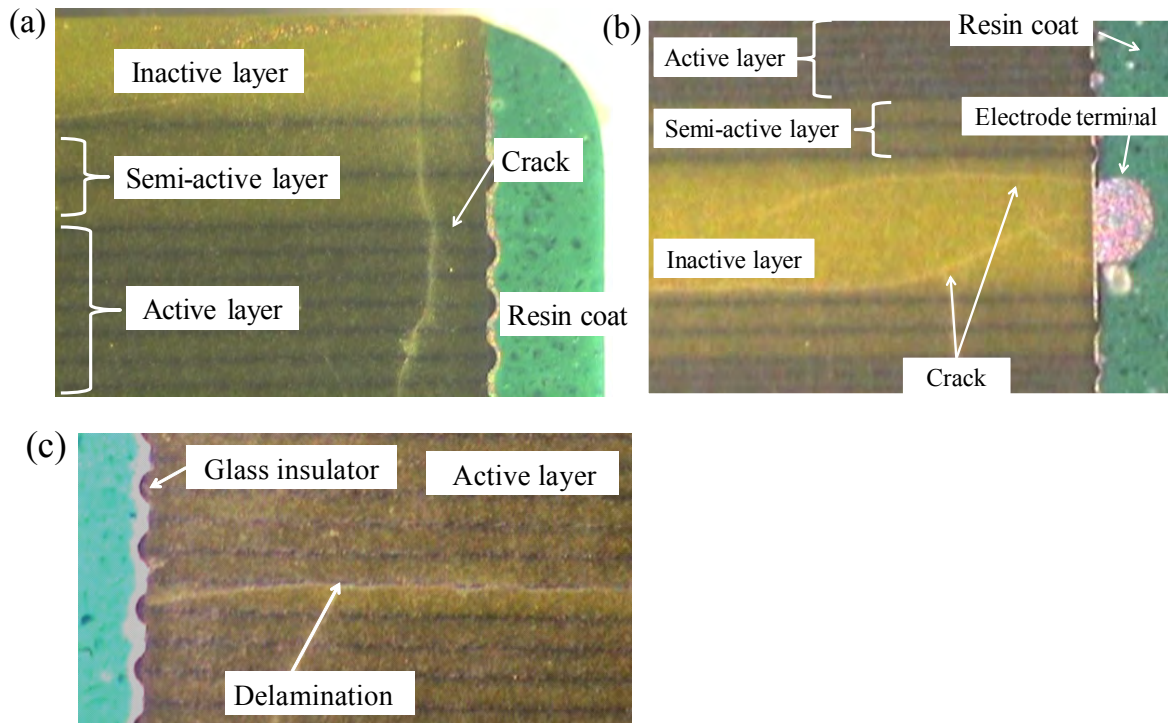


Fig. 12. Failures in the bipolar-driven multilayer sample (AE0505D08): (a) vertically propagated crack, (b) crack at the inactive layer, and (c) delamination along internal electrode.

4. Conclusion

The AE behavior in PZT ceramics and multilayer actuators are examined using two kinds of acoustic emission: vibro-AE and AE from within the sample. It is shown that the ripple current due to the electrical coupling is the origin of the vibro-AE and is dependent on the specification of the power amplifier. It is demonstrated that the suppression of vibro-AE with the use of a series resistor is the key technique for AE measurement on piezoelectric/ferroelectric materials and devices. The AE method is used to determine the ferroelectric domain behavior in the disk PZT samples. In previous studies, the vibro-AE was considered to only cause interference in the AE measurement. However, it is shown that the vibro-AE can be used for the microscopic and real-time detection of the piezoelectricity in the sample. For multilayer actuators, it is demonstrated that the vibro-AE easily conceals the AE signals originated from the failures in the device. In addition, the multilayer structure seems to attenuate the AE signal relevant to the ferroelectric domain reorientation. It is shown that the AE relevant to failures are measurable by suppressing the vibro-AE generation. From these obtained AE activities, it is concluded that the AE method can be utilized for the detection of piezoelectricity, ferroelectric domain behavior, as well as failures in the piezoelectric/ferroelectric materials and devices.

References

- [1] Aburatani, H. and Uchino, K., "A Fractal Analysis on Domain Related Electric Field Induced Acoustic Emission in Ferroelectric Ceramics," *Jpn. J. Appl. Phys.*, November 1998, **37**, 602-605.
- [2] Dul'kin, E., Mojaev, E., Roth, M., Jo, W., and Granzow, T., "Acoustic emission study of domain wall motion and phase transition in $(1-x-y)$ $\text{Bi}_{0.5}\text{Na}_{0.5}\text{TiO}_3-x\text{BaTiO}_3-y\text{K}_{0.5}\text{Na}_{0.5}\text{NbO}_3$ lead-free piezoceramics," *Scripta Materialia*, February 2009, **60**, 251-253.
- [3] Srikantha, V. and Subbarao, E.C., "Acoustic emission in ferroelectric lead titanate ceramics: Origin and recombination of microcracks," *Acta Metallurgica et Materialia*, May 1992, **40**, 1091-1100.
- [4] Aburatani, H., Harada, S., Uchino, K., Furuta, A., and Fuda, Y., "Destruction Mechanisms in Ceramic Multilayer Actuators," *Jpn. J. Appl. Phys.*, February 1994, **33**, 3091-3094.
- [5] Aburatani, H., Yoshikawa, S., Uchino, K. and de Vries, J.W.C., "A Study of Acoustic Emission in Piezoelectric Multilayer Ceramic Actuator," *Jpn. J. Appl. Phys.*, March 1998, **35**, L516-L518.
- [6] Aburatani, H. and Uchino, K., "Acoustic Emission (AE) Measurement Technique in Piezoelectric Ceramics," *Jpn. J. Appl. Phys.*, March 1996, **35**, L516-L518.
- [7] Aburatani, H. "Evaluation of Ferroelectric Domain Behaviors Using Acoustic Emission Method," *Jpn. J. Appl. Phys.*, September 2010, **9**, 09MD05.
- [8] Aburatani, H. "Drive of Piezoelectric Actuators Using an Electrical Depoling Process," *Inter. J. Automation Technology*, 2011, **5**, (4) 601-605.
- [9] Furuta, A. and Uchino, K. "Dynamic Observation of Crack Propagation in Piezoelectric Multilayer Actuators" *J. Amer. Ceram. Soc.*, 1993, **76**, 1615-1617.
- [10] Uchino, K. and Takahashi, S. "Multilayer ceramic actuators," *Curr Opin Solid State Mater. Sci*, October 1996, **1**, (5), 698-705.

INTRINSICALLY SAFE ACOUSTIC EMISSION TRANSDUCERS

RAN ZHOU and STAN HALE

Score Atlanta Inc., 975 Cobb Place Blvd. Suite 202, Kennesaw GA, 30144

Abstract

Intrinsic safety (IS) is a signaling technique that protects plant and personnel from the risk of fire and explosions by ensuring that the energy transferred to a hazardous area is well below the energy required to ignite the explosive gas atmosphere. IS basic principles are presented in this paper. Two intrinsically safe acoustic emission (AE) transducers with integrated 20-dB preamplifier are described. A power adaptor is designed to provide power and signal conditioning for the AE transducers and is to be installed outside the hazardous area. An IS barrier is built into the power adaptor. The power adaptor will be constructed in an IP20 (IEC 60529) enclosure, which will be mounted on standard 35-mm DIN rail. The transducers and power adaptor are developed to meet the requirements of electrical apparatus standards UL 60079-0:2005 and UL 60079-11:2007.

Keywords: Intrinsic safety, transducers, integral preamplifier

Technical Terms

countable fault – fault which occurs in parts of electrical apparatus conforming to the constructional requirements of UL 60079-11.

creepage distance in air – shortest distance along the surface of an insulating medium in contact with air between two conductive parts.

fault – any defect of any component, separation, insulation or connection between components, not defined as infallible by UL 60079-11.

non-countable fault – fault which occurs in parts of electrical apparatus not conforming to the constructional requirements of UL 60079-11.

Introduction

The three ingredients necessary for an explosion (fuel, ignition energy and oxidizer) make up the ignition triangle (see Fig. 1). In order for an explosion to occur, the three ingredients must be present simultaneously in the right proportions. [1]

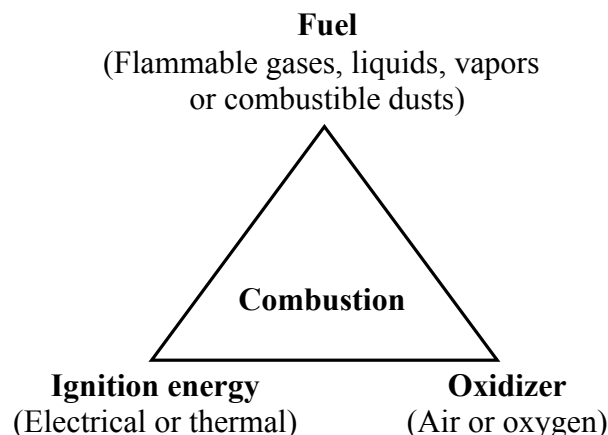


Fig. 1. The ignition triangle.

The first type of ignition source is thermal. A hot surface can cause ignition by spontaneous combustion. Every hazardous area has a temperature classification. The second type of ignition source is the spark. Sparks can be generated by the normal operation of equipment, like motor starters; and also can be produced by electrical equipment failure. Any electronic device, which stores or produces energy can cause a spark. Minimum ignition energy (MIE) exists for every fuel that represents the ideal ratio of fuel to air. At this ratio, the mixture is most easily ignited. Below the MIE, ignition is impossible for any concentration [2].

The simplest method providing effective explosion protection to electronic instrumentation is intrinsic safety (IS). The basic principle of IS is to limit energy into the hazardous area. There are two basic types of intrinsic safety interfaces: Zener barriers and galvanic isolators. Zener barriers have been widely used as safety interfaces to meet the majority of applications in hazardous areas. Based on energy-diversion concept, Zener barrier is a network of components arranged as shown in Fig. 2. Zener barriers have good frequency response and high linearity. They are simple, high-accuracy and low cost devices [3]. Galvanic isolators provide isolation between hazardous and safe area devices, by using components, such as transformers, relays, and optocouplers, which must comply with requirements of safety standards to guarantee safety.

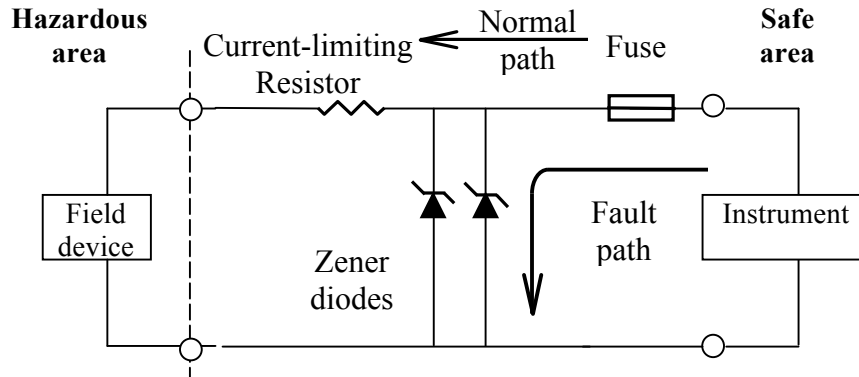


Fig. 2. Zener barrier.

Intrinsic Safety Basic Principles

Intrinsically safe apparatus are electrical apparatus, which are incapable of causing ignition of a given explosive gas atmosphere, when any spark or any thermal effect is produced by the apparatus under normal or specified fault conditions. In intrinsic safety applications, three basic parts have to be considered: hazardous area devices, safety interfaces, and interconnecting cables [2].

Hazardous Area Devices

The field devices used in any hazardous area must be one of two types: simple apparatus, and intrinsically safe certified apparatus.

A simple apparatus is a field device, which meets one of the following requirements [4]:

- Passive components, for example, switches, junction boxes, resistors and simple semiconductor devices;
- Sources of stored energy with well-defined parameters, for example, capacitors or inductors;
- Sources of generated energy, for example, thermocouples and photocells, which do not generate more than 1.5 V, 100 mA, and 25 mW.

Piezoelectric material produces an electrical charge when it is mechanically deformed. Any device, which does not fall into the category of simple apparatus, must be intrinsically safe certified. Piezoelectric acoustic emission (AE) sensors must be protected by intrinsically safe circuits and certified.

Safety Interfaces

Safety interfaces between field devices and instruments protect the hazardous area devices by limiting the flow of energy under normal and fault conditions. Associated apparatus are electrical apparatus, which contain both intrinsically safe circuits and non-intrinsically safe circuits, and are constructed so that the non-intrinsically safe circuits cannot adversely affect the intrinsically safe circuits [4]. Associated apparatus defines maximum allowable safety parameters of the circuits connected to the hazardous area terminals of the safety interfaces. Zener barriers must be designed and certified as associated apparatus.

Zener barriers were developed in the late 1950's as process control computers were more widely applied to the chemical industry. They consist of a fuse, a resistor, and two or three Zener diodes (See Fig. 2). The Zener diodes are connected in the reversed biased direction. Zener barriers block dangerous energy from being transmitted from the instrument to the hazardous area. The energy could be from a power supply, stored in capacitors, stored in inductors, or some combination of the three. This energy could be released due to some combination of faults (open circuits, shorts, grounds, etc.) occurring in the system.

In normal operation, the voltage applied to the hazard area is less than the Zener voltage, and the barrier will be virtually transparent to the control loop. If a fault voltage appears at the safe area terminals of the barrier, the resulting high current flows to ground through the fuse and Zener diodes. The fuse is rated to blow in order to protect the Zener diodes from damage and to prevent the transfer of unacceptably high energy into the hazardous area. During fault transient, the open circuit voltage (V_{oc}) at the hazardous area terminals of the Zener barrier is clamped to the Zener voltage, and the short circuit current (I_{sc}) in hazardous area is limited by the resistor. The two values, V_{oc} and I_{sc} determine the maximum allowable capacitance and inductance at the hazardous area terminals.

Interconnecting Cables

Cables store capacitive energy and inductive energy. The capacitance and inductance values of the cable (generally, given in pF/m and μ H/m) are available from the cable manufacturer. In IS circuits, low voltage V_{oc} and current I_{sc} , allow the use of ordinary instrumentation cables provided that capacitance and inductance are taken into account in assessing the safety of the system; cable parameters seldom are a problem and long distances can be easily achieved [3].

Intrinsically Safe Integral Preamplifier-AE Transducers Design and Construction

The National Electrical Code (NEC) defines hazardous locations as those areas "where fire or explosion hazards may exist due to flammable gases or vapors, flammable liquids, combustible dust, or ignitable fibers or flyings" [5].

Gas Groups and Temperature Classes

Flammable materials are grouped according to the ignition energy (gas groups) and classified for their minimum ignition temperature (temperature class).

Electrical apparatus for explosive gas atmospheres are divided into two groups [6].

- Group I: electrical apparatus for mines susceptible to firedamp;
- Group II: electrical apparatus for places with an explosive gas atmosphere other than mines susceptible to firedamp.

According to the hazardous substance, electrical apparatus of group II are subdivided into

- IIC: acetylene, hydrogen and hydrogen mixes;
- IIB: ethylene, etc.;
- IIA: propane, gasoline, natural gas, etc.

Acetylene is a gas with extremely high explosion pressures. Group IIC has the lowest minimum ignition energy among group II, so apparatus marked IIC are suitable for application requiring apparatus of IIB and IIA.

Maximum surface temperature is the highest temperature, which is attained under the most adverse conditions by any part or surface of an electrical apparatus, which would be able to produce an ignition of the surrounding explosive gas atmosphere [6]. Electrical apparatus of group II shall be marked as a function of its maximum surface temperature (See Table 1).

Area Classifications and Protection Categories

According to the probability of the presence of an explosive mixture, hazardous area can be divided into three zones,

- Zone 0: ignitable concentrations are present continuously or long periods of time under normal operating conditions
- Zone 1: ignitable concentrations likely to exist under normal operations; may exist frequently because of repair, maintenance or leakage;
- Zone 2: ignitable concentrations not likely to exist under normal operations or may exist for a short time only.

Intrinsically safe certified apparatus and intrinsically safe certified parts of associated apparatus shall be placed in category “ia” or “ib” [4]. Generally, the intrinsically safe circuits in electrical apparatus of category “ia” are not capable of causing ignition in normal operation and with the application of non-countable faults or up to two countable faults; those in category “ib” are not be capable of causing ignition in normal operation and with the application of non-countable faults or one countable faults. Apparatus may be specified as both “ia” and “ib”, and may have different parameters for each category. Intrinsically safe electrical apparatus in zone 0 should be in category “ia”, and those in zone 1 can be in “ia” or “ib”.

Requirements of Intrinsically Safe Integral Preamplifier-AE Transducers

Piezoelectric devices use the piezoelectric effect to measure pressure, acceleration, strain or force by converting them to an electrical potential. Here, two AE transducers are developed to be certified as intrinsically safe integral preamplifier-AE transducers. The power adaptor is designed to be an associated apparatus. A diagram of the intrinsically safe system is given in Fig. 3. The intrinsically safe integral preamplifier-AE transducers and power adaptor are developed to be in category “ia”, group IIC, and class T4.

An IS voltage protection circuit is employed in the AE transducers, which have an integral 20-dB preamplifier. Thus, the energy stored by the capacitance of the crystal is limited. To eliminate a current caused by metalwork contacting with other metalwork, the AE transducers are covered with a coat of nonconductive epoxy material.

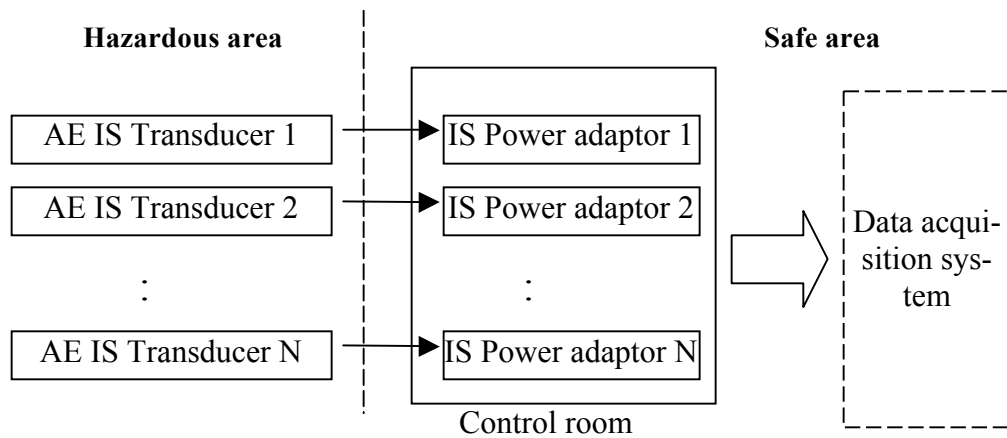


Fig. 3. Block diagram of an AE transducer system for intrinsic safety application.

In principle, associated apparatus do not require an enclosure since the method of protection is embodied within the circuit. While IS can be impaired by access to conducting parts, an enclosure with a protection classification of IP20 (IEC 60529) is able to provide effective protection for the circuits containing infallible creepage distances in air. IP20 enclosures provide protections against test fingers and solid foreign particles of diameter 12.5 mm and greater. The required creepage distances under insulating coatings are much smaller than those in air. A protective coating will reduce the dimensions of the printed circuit boards of IS circuits. The power adaptor with a built-in Zener barrier will be epoxy filled, and constructed in an IP20 enclosure.

A Deutsches Institutes für Normung (DIN, the German institute for standardization) rail is a metal rail of a standard type widely used for mounting circuit breakers and industrial control equipment inside equipment racks. The most popular type is the 35 mm x 7.5 mm top-hat rail (EN 50022, BS 5584, DIN 46277-3). The IP20 enclosure will be mounted on standard 35 mm DIN rail.

Voltage Protection and Zener Barrier

The power adaptor requires a conventional +24~+28 VDC power supply. The voltage protection circuit within the AE transducers enables the peak-to-peak output of the power adaptor up to 20 V. Ideally, Zener diodes would not allow any current in the reverse direction until the Zener voltage has been attained. In practice, Zener diodes conduct only a small leakage current, the value of which increases as the applied voltage is increased. In normal operation, the current flows into the dangerous area is less than 0.02 A, which is much larger than the reverse leakage current value of the chosen Zener diodes.

In general the frequency response of a Zener barrier is determined by the value of the current limiting resistor and the diode capacitance. A Zener barrier is similar to a passive low-pass filter in frequency domain. If a system frequency is higher than 50 kHz, the only solution is to try the system experimentally, attempting if possible to allow for the effects of interconnecting cables [3]. The effect of the Zener barrier on the frequency response of the AE transducers in normal operation has been studied. The frequency responses of the two AE transducers without and with the IS barrier are given in Figs. 4 and 5.

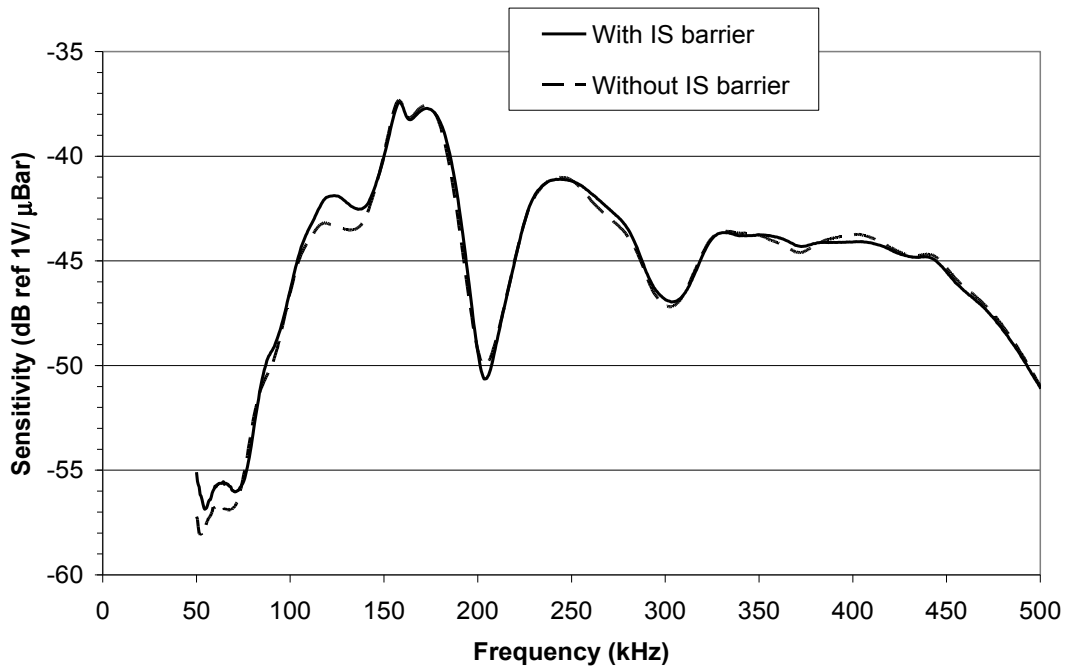


Fig. 4. Frequency responses of the intrinsically safe Score-Dunegan resonant AE transducer with and without IS barrier.

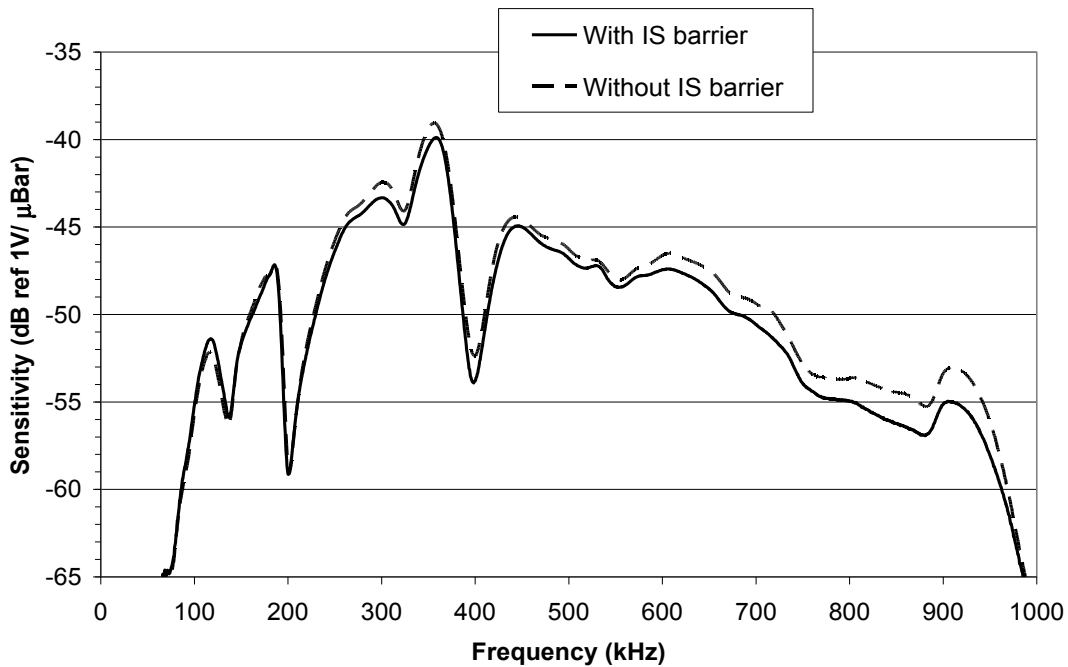


Fig. 5. Frequency responses of the intrinsically safe Score-Dunegan broadband AE transducer with and without IS barrier.

The effect of the designed IS barrier on the frequency response of the AE resonant transducer is negligible within its operating frequency range, see Fig. 4. It is seen that the sensitivity degradation caused by the IS barrier is more obvious for the broadband AE transducer, especially at high frequency. We found that the difference between the two frequency response curves in Fig. 5 is no more than 2 dB below 900 kHz.

Summary

This paper presents a brief introduction of intrinsic safety. The function requirements of two intrinsically safe AE transducers are described. It is shown that the designed IS barrier introduces a small sensitivity degradation below 900 kHz when the AE transducers are in normal operation.

References

- [1] The Art of Intrinsic Safety, URL: <http://www.ronan.com>, Ronan Engineering, April 2011.
- [2] Intrinsic Safety Basic Principles, URL: <http://www.gminternationalsrl.com>, G.M. International srl, April 2011.
- [3] Shunt-Diode Safety Barriers and Galvanic Isolators – a Critical Comparison, URL: <http://www.casuarina.com.sg>, Casuarina Services Pte Ltd., April 2011.
- [4] UL Standard for Safety for Electrical Apparatus for Explosive Gas Atmospheres-Part 11: Intrinsic Safety “i”, UL 60079-11, Underwriters Laboratories Inc.
- [5] Hazardous (Classified) Locations, URL: <http://www.osha.gov>, April 2011.
- [6] UL Standard for Safety for Electrical Apparatus for Explosive Gas Atmospheres-Part 0: General Requirements, UL 60079-0, Underwriters Laboratories Inc.

Table 1. Classification of maximum surface temperatures for group II electrical apparatus [4].

Temperature class	Maximum surface temperature
T1	450°C
T2	300°C
T3	200°C
T4	135°C
T5	100°C
T6	85°C

RE-EXAMINATION OF NIST ACOUSTIC EMISSION SENSOR CALIBRATION: Part I – Modeling the loading from glass capillary fracture

BRIAN BURKS

Mechanical and Materials Engineering Department, University of Denver,
2390 S. York St., Denver, CO 80208

Abstract

The procedure for absolute calibration of acoustic emission (AE) sensors is provided in ASTM E1106. In that test method, a glass capillary is fractured against a large steel cylinder in order to generate an acoustic waveform used for calibration of the sensor. In this work the finite element method was used to investigate the viability of the point source load assumption made in the analytic calculation of the resultant waveform for the glass capillary fracture procedure. It was found that the stress field on the steel cylinder due to elastic deformation was not singular, but approximately ellipsoidal in nature. Part II of this work will highlight the impact that the shape of the stress field had on the resultant waveform, leading to the necessity for revision of ASTM E1106.

Keywords: Absolute AE sensor calibration, ASTM E1106, finite element modeling, glass capillary fracture, NIST steel block

1. Introduction

Recent developments in acoustic emission (AE) techniques based upon the spectral content of AE waveforms have proven to be effective in damage detection and identification [1-4]. These advances have primarily been enabled through ever increasing computational power. However, these analysis techniques necessitate properly, and absolutely calibrated transducers, as an improperly calibrated transducer could potentially distort the waveform of the AE signal and lead to an improper analysis. The ASTM International test method that governs the absolute calibration of AE transducers is E1106. In this test method, a loading screw applies a force to a glass rod, which is in contact and oriented in a perpendicular fashion to a glass capillary. The capillary sits on a thin glass slide, which rests on top of a large steel cylinder as shown in Fig. 1 [5]. The fracture of the glass capillary is intended to simulate a point load on an infinite half-space. Such a set-up for absolutely calibrating AE transducers exists at the National Institute of Standards and Technology in Boulder, CO.

In ASTM E1106-07 two methods are mentioned for determining the resultant waveform that the transducer under test should register upon fracture of the glass capillary. The first method discussed relies on a high fidelity capacitive transducer that measures the absolute out-of-plane surface displacement on the surface of the steel cylinder. The second method mentioned is an analytic calculation of the surface displacement of an infinite half-space subjected to a step load point force; the analytic solution was first derived by Pekeris [6]. For either method mentioned, the waveform recorded by the transducer under test is compared to the waveform determined by either method.

In Fig. 1, it is clear that initially a line contact condition exists between the glass capillary and the glass slide. Considering Hertz's work on bodies in contact [7], as the capillary deforms into the glass slide, the resulting stress field within the glass slide would be expected to be

elliptical in nature. Then, as the load from the glass slide is transferred to the steel cylinder, the expected loading most certainly would not be a point source, but more likely ellipsoidal in nature. Thus, assuming a point source as the loading source to analytically predict the surface displacement of an infinite half space appears debatable.

To analytically solve the multiple bodies in contact problem that the set-up requires is certainly not trivial and would be quite laborious in nature. Hence, the approach adopted in this work was to use a numeric technique. Specifically, the finite element (FE) method was used to approximate the resultant surface stress field on the surface of the steel cylinder as a result of performing the procedure described in ASTM E1106. Additionally, the state of stress within the glass capillary was evaluated, to provide insight on the fracture initiation site within the glass capillary.

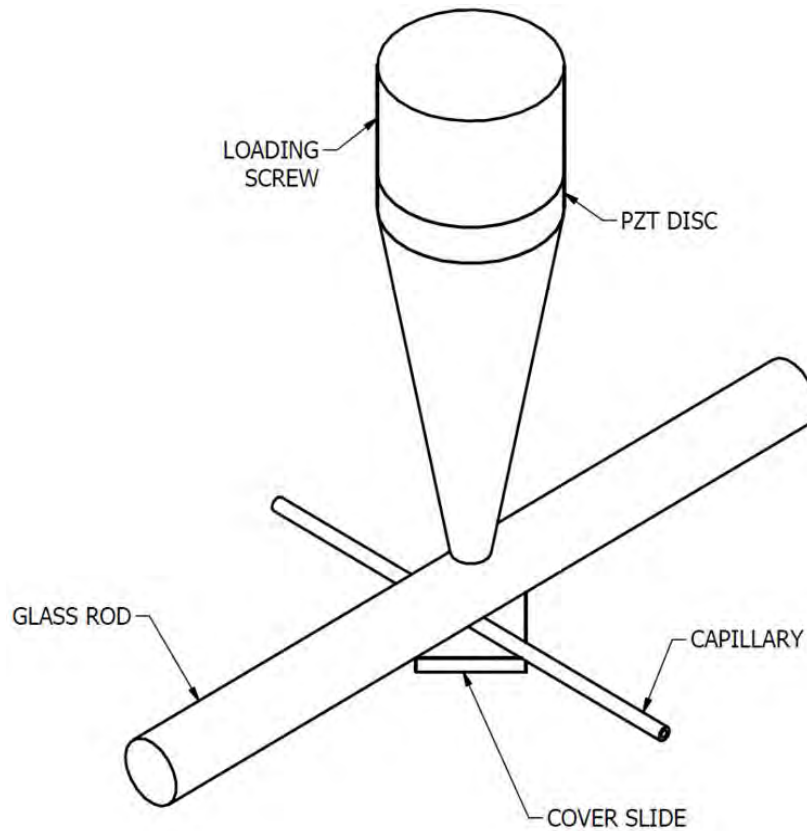


Fig. 1 Schematic of the set-up used for the absolute sensor calibration described in ASTM E1106.

2. Methods

Table 1 summarizes pertinent dimensions of all parts shown in Fig. 1. The large discrepancy in dimensions between the steel cylinder, and the dimensions of the other components presents an issue in developing a numeric model. Attempting to model the entire set-up would result in an extremely large numerical model, requiring an excessive amount of time to solve. For computational efficiency only the near field portion of the steel cylinder was modeled, as stresses are expected to decay to zero in a natural logarithmic fashion in the far field [8]. Thus, for the numeric model the radius of the steel cylinder was modeled as 1.25 mm with a thickness of 1 mm. For further computational efficiency a quarter-volume model was developed as shown in

Fig. 2, with appropriate symmetric boundary conditions applied to represent the full 3D volume. The entire mesh consisted of linearly interpolated three dimensional hexahedral volume elements; both full and reduced integration formulations were considered¹. A mesh biasing scheme was used for the steel cylinder to reduce the characteristic element size and capture the stress field directly under the applied load, but allowed the element size to increase further away from the applied load where little variation in the stress field was present.

Table 1 Summary of pertinent dimensions from the NIST Boulder AE absolute sensor calibration set-up.

Component	Dimensions
Glass Rod	Diameter = 2 mm L = 70 mm
Glass Capillary	Outer Diameter = 0.2 mm Inner Diameter = 0.1 mm L = 50.0 mm
Glass Slide	W = 1.5 mm L = 1.5 mm t = 0.08 mm
Steel Cylinder	Diameter = 900 mm
Loading Screw	Minimum Diameter = 1.6 mm

All materials were assigned isotropic, linear elastic material properties. The glass rod, capillary, and slide were modeled as having a Young’s modulus of 72 GPa and a Poisson’s ratio of 0.22, while the steel cylinder had a Young’s modulus of 200 GPa and a Poisson’s ratio of 0.29. Plane-strain boundary conditions were assigned to both the glass rod and capillary. All nodes on the bottom of the steel cylinder were constrained in the out-of-plane direction to maintain static equilibrium from the force to be applied. The degrees of freedom for the in-plane directions of the center node on the bottom of the steel cylinder were additionally constrained to prevent rigid body modes.

The numeric model was run in force control, with loads of 10 N and 20 N being applied; these loads were selected as they are the common bounds of experimentally reported fracture loads [5]. A concentrated load was applied to a single node, which was rigidly beamed to nodes on the top edge of the glass rod (rigid beam elements are identified in red in Fig. 2). The length of the beamed nodes on the glass rod matched the outer diameter of the loading screw (OD = 1.6 mm) in Fig. 1. By applying the load in this manner “hot-spotting,” of the mesh was avoided. A surface-to-surface, finite sliding contact definition was used to optimize the stress field calculation due to bodies in contact [9]. A tie constraint was assigned to all surfaces that were in contact with one another, before loads were applied. The tie constraint fixes the associated degrees of freedom to the surface that they were initially assigned in contact with, expediting convergence of the non-linear contact solution.

¹ Full and reduced integration refers to the number of evaluation points used for the Gaussian quadrature integration. In order to fully integrate a linearly interpolated hexahedral volume element a 2x2x2 integration rule is necessary, whereas for a reduced integration formulation only a 1x1x1 integration rule is needed. A reduced integration element is less computationally expensive than a fully integrated element.

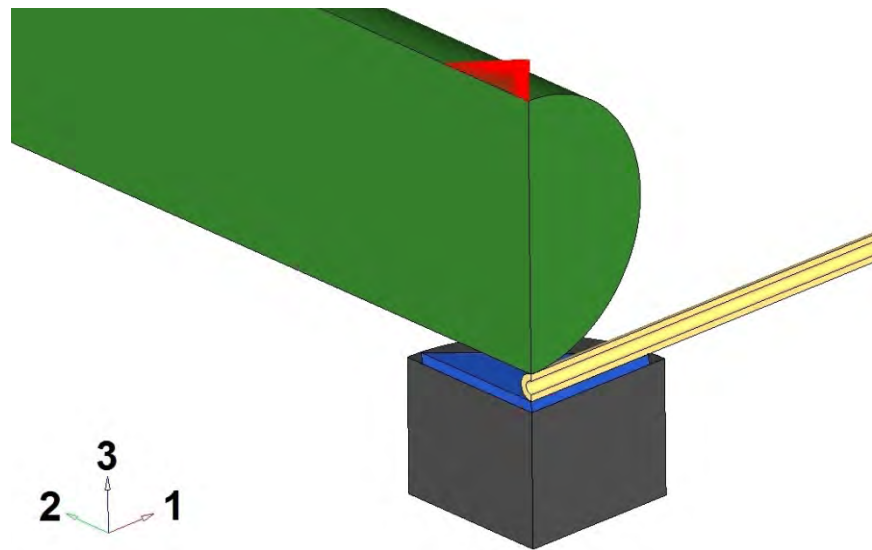


Fig. 2 Quarter volume finite element representation of the absolute calibration set-up of [5]. With appropriate boundary conditions applied, the solution is identical to what would be obtained if the entire volume were modeled.

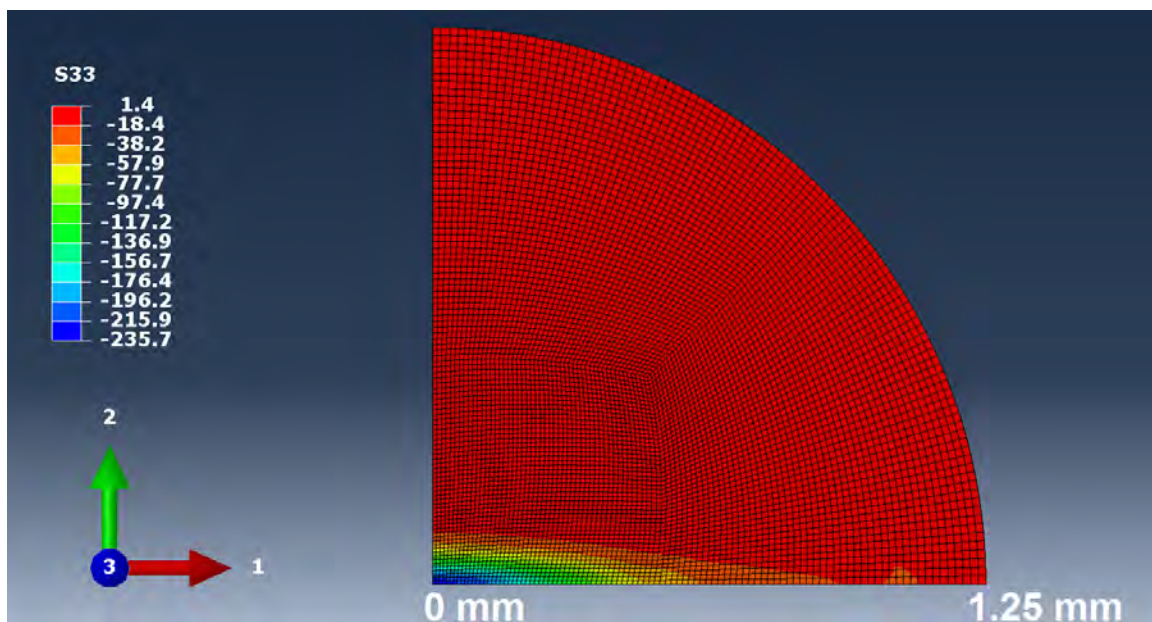


Fig. 3 Out-of-plane stress (σ_{33}) field contour for the 20 N load case. Stresses in the legend are presented in MPa.

3. Results and Discussion

The out-of-plane stress field of the surface of the steel block was found to be predominantly compressive in nature and the stress field contour is shown in Fig. 3. Clearly the stress field was not singular, but was found to be roughly elliptical in nature with a major radius of 1.053 mm, and a minor radius of 0.140 mm. A mesh convergence study was carried out, and the solution was considered converged when the out-of-plane stress did not differ by more than 1% from the previous mesh, while using regular refinement of the near-field elements (the so-called h refinement of [10]).

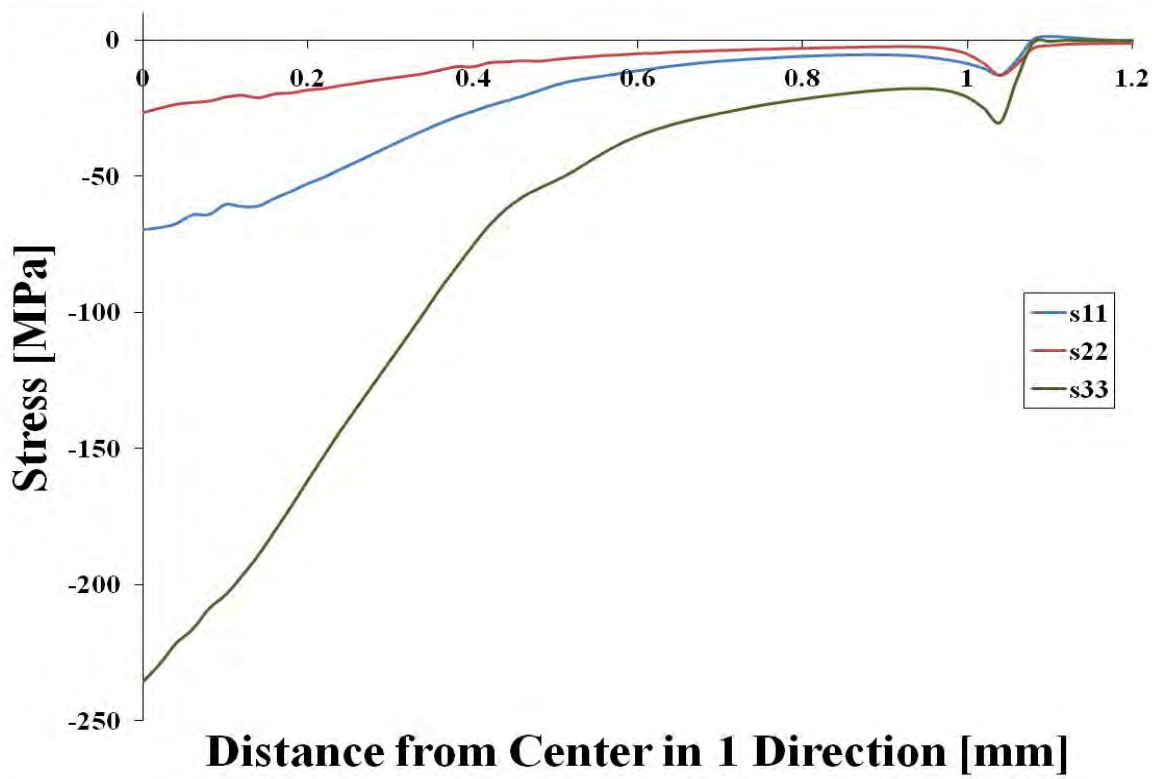


Fig. 4 Normal stresses as a function of distance on the surface of the steel cylinder along a line oriented in a parallel fashion to the glass capillary.

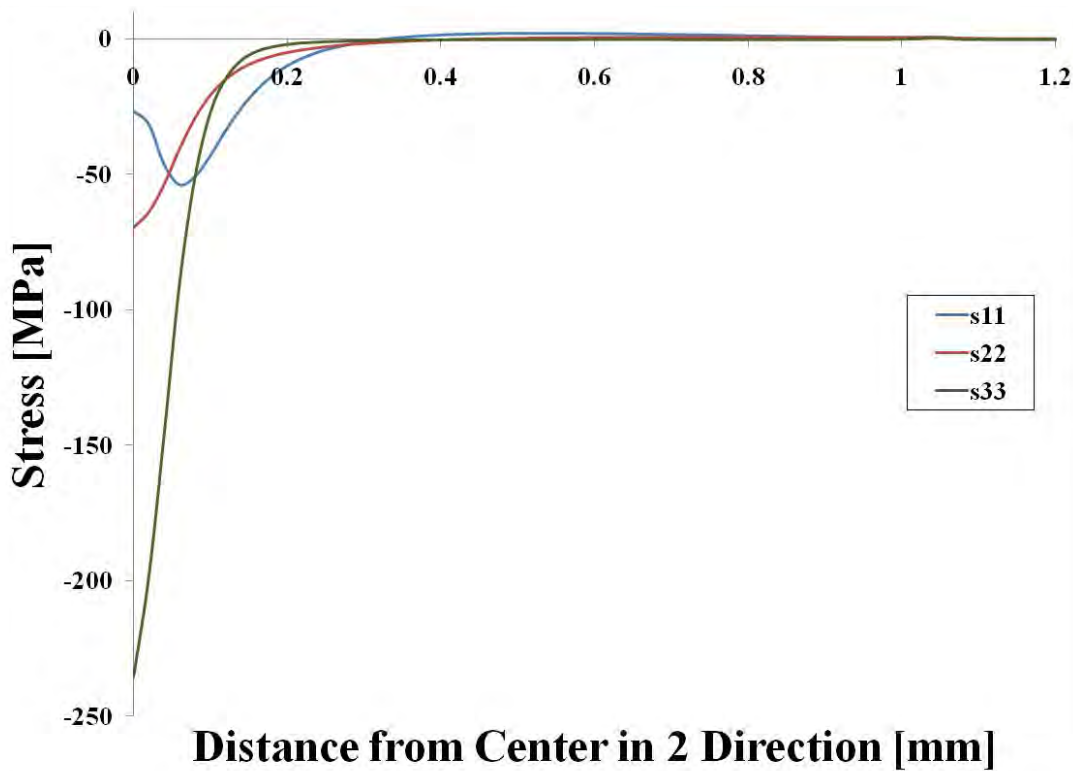


Fig. 5 Normal stresses as a function of distance on the surface of the steel cylinder along a line oriented in a perpendicular fashion to the glass capillary.

Stress as a function of radius for the three normal stress components on the surface of the steel block along lines parallel (in the global 1 direction) and perpendicular (in the global 2 direction) to the axial direction of the glass capillary are shown in Figs. 4 and 5 for an applied load of 20 N, respectively. For the former, the three principal stresses were found to be compressive in nature and maximum at the center of the steel block, decaying to zero with increasing distance from the center. The corner of the glass slide resulted in a geometric stress concentration, which slightly raised the local stress state (Fig. 4). As for the latter, the σ_{11} and σ_{33} stresses were found to again be maximum and compressive at the center of the steel block². The σ_{22} component exhibited a lobed feature that was maximum 60 μm from the center of the top of the steel block, and became slightly tensile in nature before decaying to zero (Fig. 5).

In Part II of this work, Hamstad used a dynamic axi-symmetric finite element code to calculate the surface wave displacement of the steel block subjected to the loading condition determined from this work. The out-of-plane stress field distribution determined in this work was used as input into the axi-symmetric dynamic finite element code. To convert the stress field for the axi-symmetric analysis, the centroidal locations of each element on the surface of the entire steel block were “binned” into 26 consecutive annular discs, and the corresponding stress values were averaged over the area. Figure 6 shows the averaged out-of-plane stress (σ_{AVE}) as a function of the distance from the center of the steel cylinder for both full and reduced integration element formulations. It is clear from Fig. 6 that using a reduced integration element formulation had a negligible effect on the numeric solution, and the analysis run-time was reduced by 18% in comparison to the full integration analysis. Thus, the reduced integration hexahedral element formulation proved to be the more valuable analysis technique for this work.

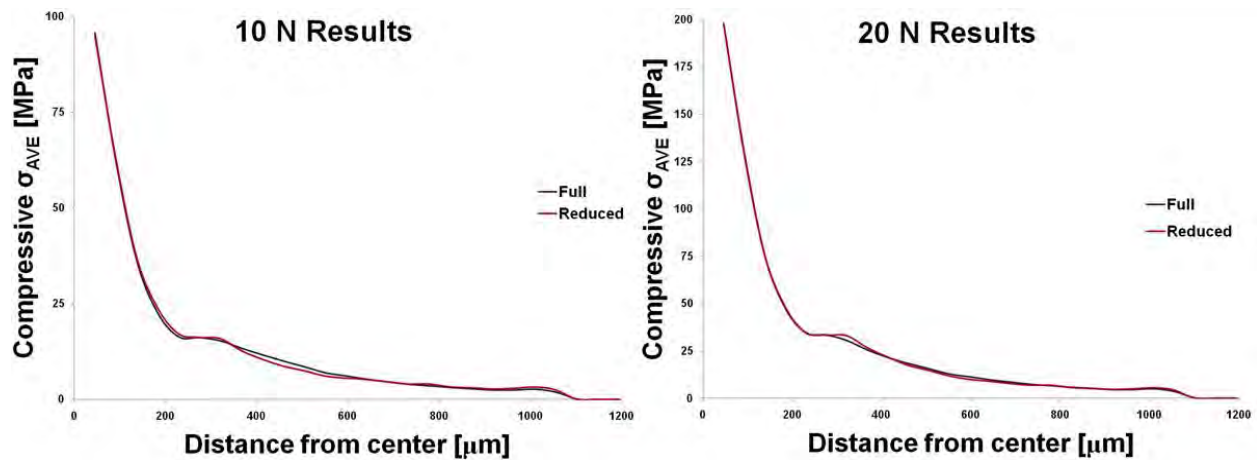


Fig. 6 Comparison of the out-of-plane stress field averaging results on the surface of the steel block for both full and reduced element integration formulation.

Stress contours for the two in-plane principal stresses of the glass capillary are shown for the 20 N load case. A state of bi-axial tension was found on the inner diameter of the glass capillary nearest the glass rod (Fig. 7). Considering the brittle nature of silicate glass (which performs relatively poorly in tension), the inner diameter nearest the glass rod was found to be the most probable point of fracture initiation. Additionally, the maximum values shown in Fig. 7 ($\sigma_{11} = 536.1 \text{ MPa}$ and $\sigma_{22} = 2515.0 \text{ MPa}$) indicate the sensitivity that this experimental set-up has to

² The σ_{ii} and s_{ii} notations are used interchangeably as it is the convention of the FE software Abaqus; the two are identical in meaning, and are to be understood as the i^{th} component of stress.

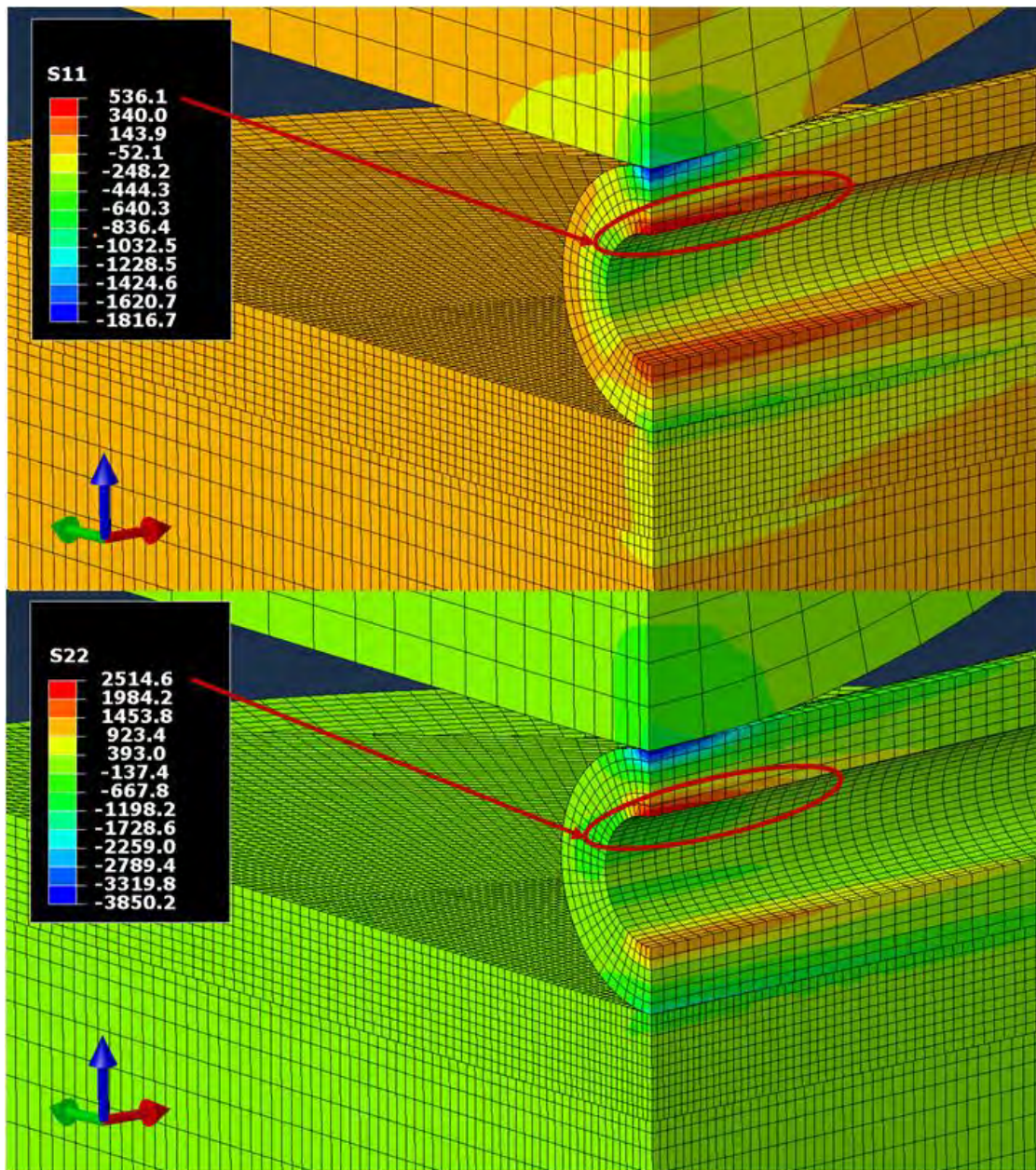


Fig. 7 Principal stress contours for the stresses within the glass capillary for the 20N load case; a state of bi-axial tension was found on the inner diameter of the glass capillary, nearest the glass rod. Stresses in the legend are shown in MPa.

variability. The value of σ_{22} was found to be on the order of the tensile strength of silicate glass [11], thus fracture loads, as well as potentially the actual fracture location, would be significantly affected by surface flaws on the inner diameter of the glass capillary, as well as dimensional variability on the inner and outer diameters of the glass capillary. The variability in typical glass capillaries, as discussed in [5], coupled with this work point out the reason that such large variability is observed in fracture loads (~50%).

4. Conclusion

In this work, it was found that the procedure described in ASTM test method E1106 does not result in a point source load. Rather the out-of-plane stress field on the surface of the steel

cylinder as a result of the applied loading was found to be roughly elliptical in nature (with a major radius of 1.053 mm and a minor radius of 0.140 mm). The solution of this multiple bodies in contact problem was achieved through the use of the finite element method. The significance of this finding will be elaborated upon in Part II of this work. In addition, it was found that the most probable point of glass capillary fracture would initiate on the inner diameter, nearest the glass rod.

In light of the primary findings of this work, and the significance that it has (elaborated upon in Part II), a revision of ASTM E1106 may be in order. A revision of the alternative analytic approach to calibration is necessary, as it was shown in this work that the approximation of a point source is not sufficiently accurate for the loading condition that occurs on the surface of the steel cylinder.

Acknowledgements

The contributions of Dr. Marvin Hamstad of NIST Boulder to this work are gratefully acknowledged.

References

- [1] Prosser, W.H., et al., Finite Element and Plate Theory Modeling of Acoustic Emission Waveforms. *Journal of Nondestructive Evaluation*, 1999, **18**(3), 83-90.
- [2] Hamstad, M.A., Gallagher, A.O. and Gary, J., A wavelet transform applied to acoustic emission signals: part I: source identification. *Journal of Acoustic Emission*, 2002, **20**, 39-61.
- [3] Prosser, W.H., Advanced AE techniques in composite materials research. *Journal of Acoustic Emission*, 1996, **14**(3-4), 1-11.
- [4] Sause, M.G.R. and Horn, S., Simulation of Acoustic Emission in Planar Carbon Fiber Reinforced Plastic Specimens. *Journal of Nondestructive Evaluation*, 2010, **29**, 123-142.
- [5] ASTM International, ASTM E1106-07: Standard test method for primary calibration of acoustic emission sensors. ASTM International, West Conshohocken, PA, 2007.
- [6] Pekeris, C.L., The seismic surface pulse. *Geophysics*, 1955, **41**(7), 469-480.
- [7] Hertz, H., On the Contact of Elastic Solids. *Journal of Mathematics*, 1881, **92**, 156-171.
- [8] Michell, J.H., On the direct determination of stress in an elastic solid, with application to the theory of plates. *Proceedings of the London Mathematical Society*, 1899, **31**, 100-124.
- [9] Dassault Systèmes Simulia Corp., Abaqus v.6.9 Documentation. Providence, RI, 2009.
- [10] Cook, R, et al. *Concepts and Applications of the Finite Element Analysis* 4th Edition. J. Wiley and Sons, Inc., 2002. p. 319.
- [11] Ashby, M.F. and Jones, D.R.H. *Engineering Materials I: An Introduction to Properties, Applications and Design*, 3rd Edition. Elsevier Publishing, San Francisco, 2005.

RE-EXAMINATION OF NIST ACOUSTIC EMISSION ABSOLUTE SENSOR CALIBRATION: Part II - Finite element modeling of acoustic emission signal from glass capillary fracture^{*#}

M. A. HAMSTAD

National Institute of Standards and Technology, Materials Reliability Division (653), 325 Broadway, Boulder, CO 80305-3328 and Mechanical and Materials Engineering Department, School of Engineering and Computer Science, University of Denver, Denver, CO 80208

Abstract

A validated axisymmetric finite-element code was used to model the out-of-plane displacement acoustic emission (AE) signal at 100 mm from a glass capillary fracture on the surface of a large steel block under the control of National Institute of Standards and Technology (NIST). This situation corresponds to the absolute sensor calibration approach described in the test method ASTM E1106-07. A number of source parameters relating to the fracture of the glass capillary source were studied: (i) value of the rise-time of the force release, (ii) temporal shape of the force release, (iii) spatial size and spatial distribution of the normal stress on the block surface, and (iv) the magnitude of the force. The results of the dynamic finite-element model (FEM) were compared to the signal from the capacitance sensor used in the AE sensor calibration at NIST. The FEM results indicate that the magnitude of the signal is a linear function of the force released, and that all other source parameters change the magnitude of the Rayleigh wave that dominates the displacement signal. During calibration, only the force at fracture is measured. It is not clear at present how the other parameters can be measured. Based on the results in this study, recommendations are made relative to the content of ASTM E1106-07.

Keywords: Absolute AE sensor calibration; ASTM E1106-07; finite-element modeling; glass-capillary fracture; NIST steel block; Rayleigh wave

1. Introduction

In late 2009, the large steel cylinder (900 mm diameter by 430 mm long under the control of the National Institute of Standards and Technology (NIST)) referred to in the test method ASTM E1106-07 [1] for absolute calibration of acoustic emission (AE) sensors was moved from NIST-Gaithersburg to NIST-Boulder. Figure 1 shows a photograph of the steel cylinder. As a result of this move, a study was initiated by use of finite element modeling to examine both the surface loading from the glass capillary (used in the calibration procedure described in E1106 [1]) and the subsequent wave generated by the fracture of the glass capillary. Part I of this paper [2] provided the results from the static loading just prior to the capillary fracture. Those results provided key input to the research reported here.

The research presented here examined with dynamic finite-element modeling a number of variables to determine their influence on the wave generated by the fracture of the glass capillary. In particular, the variables examined were the source rise-time (of the force released by the fracture) and its temporal shape, the spatial size and the spatial distribution of the normal surface

* Contribution of the U.S. National Institute of Standards and Technology; not subject to copyright in the United States. # Trade and company names are included only for complete scientific/technical description; endorsement is neither intended nor implied.

loading at the fracture load and the magnitude of the force at fracture. In addition, the finite element approach allowed a study of the “overshoot” (defined at an appropriate point later in this paper) that is observed in the experimental out-of-plane signal recorded by the reference capacitance sensor located 100 mm from the glass capillary source. This distance corresponds to the propagation distance to both the capacitance sensor and the sensor being calibrated.

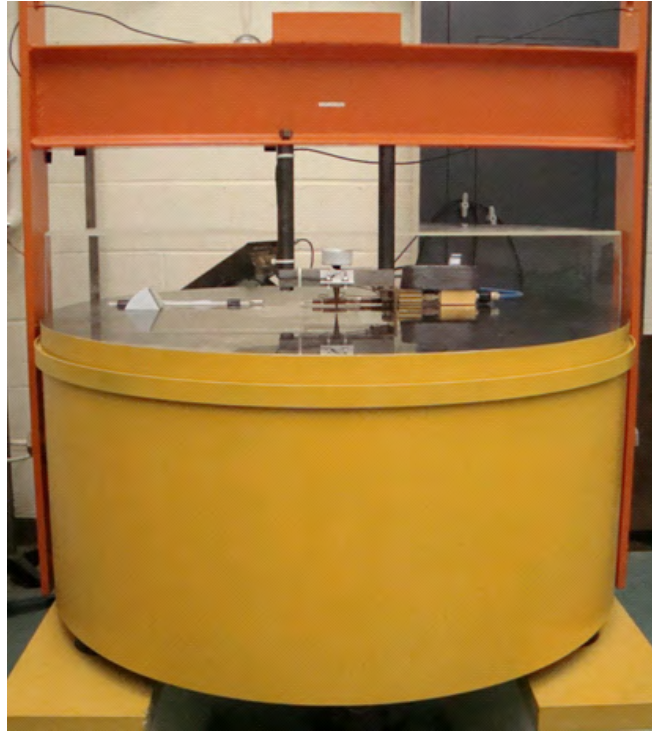


Fig. 1 Cylindrical block of steel has a diameter of 900 mm and a length of 430 mm with a highly polished top surface.

Information on the Finite Element Modeling

A validated axisymmetric finite-element code was used for the current research [3]. The results shown in this paper are the out-of-plane displacement signals versus time (where zero time corresponds to the start of the operation of the source) obtained on the top surface of the steel cylinder at a propagation distance of 100 mm (radial direction) from the capillary fracture. The code uses a uniform cell size (or element size) in both the axial and radial directions. Due to past experience with finite element modeling (FEM) when a Rayleigh wave was present [4], double-precision calculations were made in order to avoid errors due to numerical round-off. The axisymmetric code was used rather than a 3-D code, because much smaller cell sizes could be used while making use of reasonable computing facilities. For most of the FEM runs, the size of the steel block was reduced in order to decrease the size of the domain of the calculation. This decrease in size was limited such that reflections from the block boundaries did not occur until some time after the completion of the full arrival and departure of the Rayleigh wave at the 100 mm propagation distance. The AE source was always located at the center of the top surface of the steel block. Unless specifically stated, the normal surface stress released (to generate the signal) was uniformly distributed over the first 80% of the source radius and linearly decreased to zero over the final 20%. In addition, the total force (that generated the normal stress) for all results shown was 10 N. The bulk velocities used in the FEM code were 5850 m/s and 3188 m/s, respectively, for the longitudinal and shear velocities. These velocities were obtained from the

ultrasonic characterization of the block at NIST Gaithersburg. The density used in the code was 7.8 Mg/m^3 .

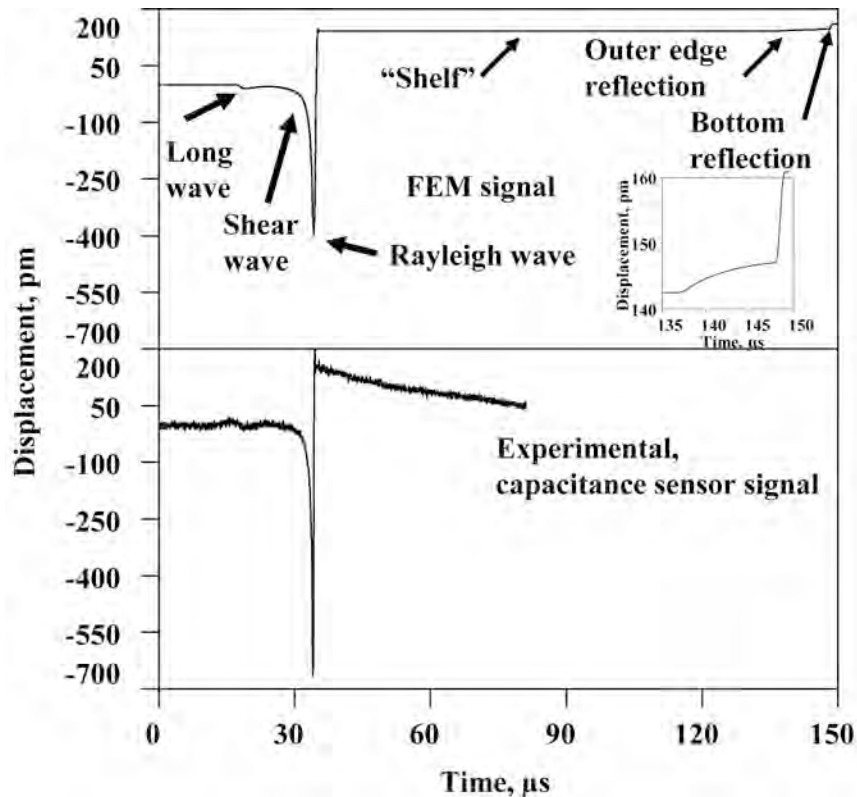


Fig. 2 Comparison of FEM and experimental out-of-plane displacement signals at 100 mm distance for full block. Insert shows expanded scale of bottom reflection arrivals.

Initial FEM Result for the Full-size Steel Block

As an overall check on the FEM-based out-of-plane displacement calculated for the propagation distance of 100 mm, a run was made by use of the full size of the steel block. This result was then compared with a typical experimental signal obtained from the capacitance sensor [5]. The FEM conditions for this run were a total source force of 10 N (corresponding to the measured value in the experiment), a source rise-time of $1 \mu\text{s}$, a source radius of 1 mm, a time-step of $16.3 \mu\text{s}$, and a cell-size of 0.106 mm. The temporal shape of the source rise-time was the “cosine bell” type, which for convenience will be defined by a later equation and shown in a later figure. The longer rise-time (than expected from the glass capillary fracture) allowed modeling of the whole block for a longer time period with reasonable computer resources. The comparison of the FEM signal and experimental results are shown in Fig. 2. This figure shows that the FEM signal was similar in form to the experimental signal for the key features, including arrivals of the bulk longitudinal wave, shear wave and the Rayleigh wave. Due to the long rise-time of the source in this run, the peak amplitude of the Rayleigh wave was reduced. In addition, due to the longer duration of the FEM signal, the expected reflections of the bulk longitudinal wave from the outer edge (radius of the block) and the bottom surface of the block are present in that signal. These arrivals (shown in more detail in the inset in Fig. 2) in the FEM signal are at $137 \mu\text{s}$ for the edge reflection, versus a calculated value of $136.8 \mu\text{s}$, and for the bottom surface reflection the FEM arrival was $148 \mu\text{s}$ versus a calculated value of $148.3 \mu\text{s}$. The calculated values were based on the actual path distances and the previously given bulk longitudinal velocity. It should be noted that

these reflections arrive well after the termination of the experimental signal from the capacitance sensor that is used and specified in the absolute sensor calibration procedure.

The FEM result prior to the reflections has a “shelf” with a constant value after the end of the Rayleigh-wave portion of the signal. This constant “shelf” was also observed in an analytical-calculation result that will be shown in a figure later in this paper. The gradual falloff of the experimental capacitance signal in the “shelf” region is characteristic of such a sensor, and it does not significantly affect the calibration due to the low frequencies involved, which are below those relevant to the AE sensor calibration.

FEM Results from the Source Parameter Studies:

(a) Variation of the Temporal Shape of the Source Rise Time for a Fixed Rise Time

Since the actual temporal shape and the rise time of the source generated by the glass capillary fracture are not known, different shapes and rise times were evaluated. Figure 3 demonstrates the FEM-based signals at the 100 mm propagation distance for three different temporal shapes of the source rise time. These three cases are shown in Fig. 4 for the normalized time dependence, $T(t)$, multiplied by the total force of 10 N and a rise time, τ , of 0.3 μs . The temporal shapes, for other than the “linear” case, are the “cosine bell,” given by equation (1) and “sharp end,” which is given by equations (2) and (3). These temporal shapes have a range from smooth to abrupt starts and finishes.

$$T(t) = \begin{cases} 0 & \text{for } t < 0 \\ (0.5 - 0.5 \cos [\pi t/\tau]) & \text{for } 0 \leq t \leq \tau \\ 1 & \text{for } t > \tau \end{cases} \quad (1)$$

$$T(t) = \begin{cases} 0 & \text{for } t < 0 \\ 1 - \text{erf}(t_2 - t_1)/\text{erf}(t_2) & \text{for } 0 \leq t \leq \tau \\ 1 & \text{for } t > \tau, \end{cases} \quad (2)$$

where

$$\begin{aligned} t_1 &= t a^{1/2} \\ t_2 &= \tau a^{1/2} \end{aligned} \quad (3)$$

and

$$a = -\ln(0.5)/(3\tau/8)^2.$$

The other FEM conditions for the results in Fig. 3 were a source radius of 0.5 mm, cell size of 30 μm , and a time step of 4.5 ns. The time scale in Fig. 3 was expanded to “focus” on the region of the shear and Rayleigh wave arrivals where the amplitudes are significant. In this region, the most important features of the signal appear. The figure demonstrates the changes in the peak amplitude of the Rayleigh wave as the temporal shape of the source changes. Figure 3 also demonstrates the positive “overshoot” prior to the steady-state “shelf.” Finite-element results (not shown) demonstrated that the magnitude of the “shelf” depended only on the total force release of the source, and the amplitude of the complete FEM signal depended linearly on the value of the total force over the range from 10 N to 20 N that is applicable in the calibration process.

(b) Variation of the Source Rise Time for a Fixed Temporal Shape

Figure 5 demonstrates, for the “focus” region of the shear and Rayleigh waves, that the peak magnitude of the Rayleigh wave decreases as the rise time increases from 0.2 μs to 0.4 μs . The net result is a 12% decrease in the Rayleigh wave peak amplitude for the longer rise time com-

pared to that for the shortest rise time. The FEM parameters for these runs were a source radius of 0.5 mm, cell size of 30 μm , a “sharp-end” rise-time temporal shape and a time step of 4.5 ns.

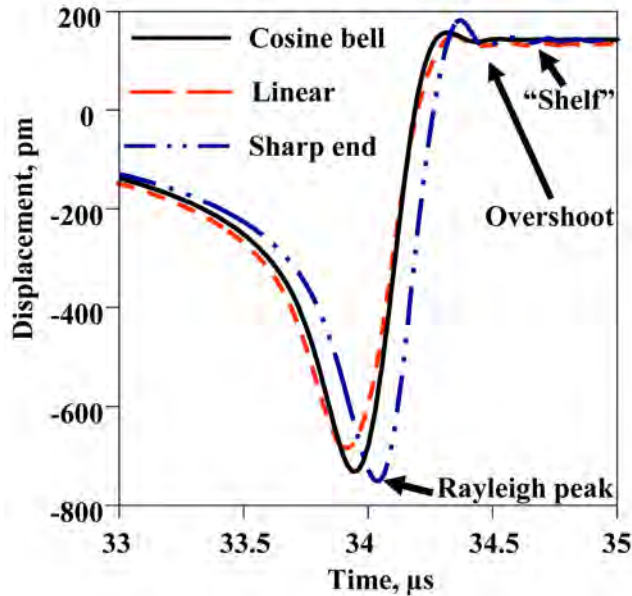


Fig. 3 Changes in shear/Rayleigh wave region as the temporal aspect of the source rise-time changes.

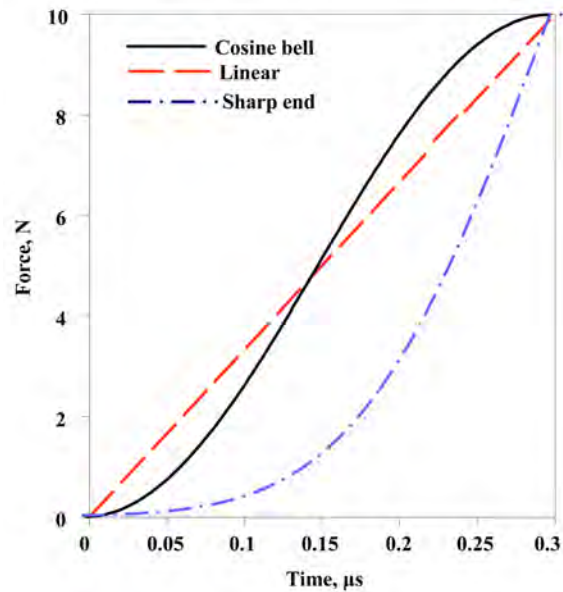


Fig. 4 Temporal shapes of rise time shown for a 0.3 μs rise-time and 10 N force.

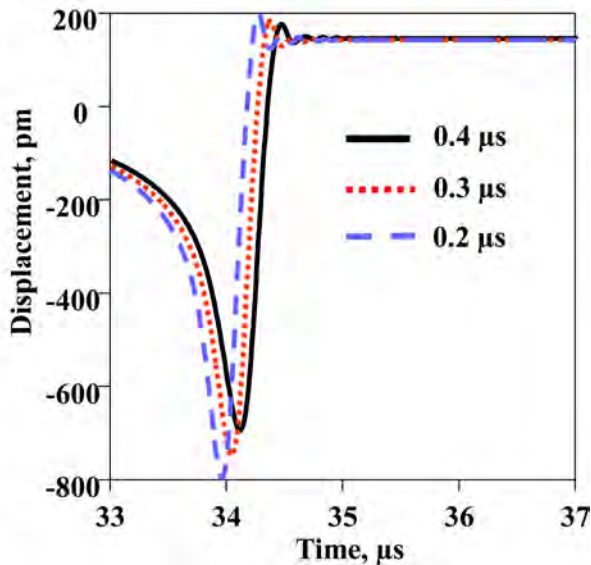


Fig. 5 Increasing the source rise-time (for the three values shown) decreases the peak amplitude of the Rayleigh wave.

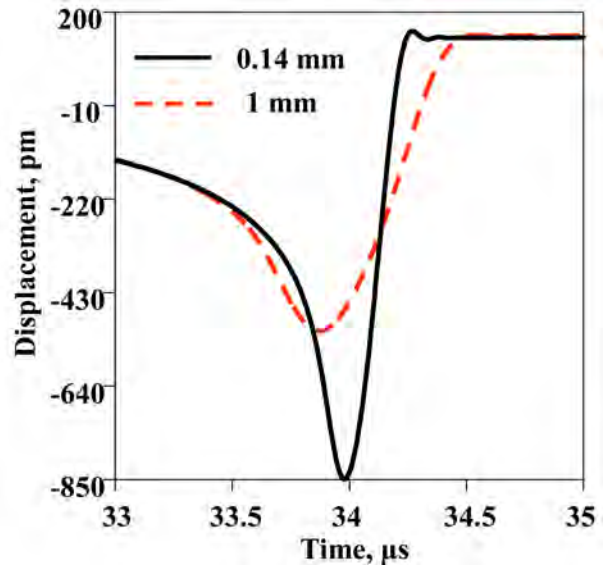


Fig. 6 Two different source radii (values shown) show large differences in the Rayleigh wave peak amplitude.

(c) Variation of the Source Spatial Size

The radius of the source region upon which the normal stress was applied was examined for a 1-mm and a 0.14-mm radius. These values were chosen based on some of the results reported in part I [2]. Part I showed that the loading (from the glass capillary) on the top surface of the block results in a normal stress that is approximately elliptical in shape, with major and minor axis values of about 2 mm by 0.28 mm, respectively, at a total load of 10 N. Figure 6 demonstrates in the

“focus” region a large drop of 39% in the Rayleigh peak amplitude when the source radius increased from 0.14 mm to 1 mm. It should be pointed out that the result for the large radius did not show an “overshoot.” The FEM parameters for these runs were a rise time of 0.35 μs , cell size of 12.5 μm , a “cosine bell” rise-time temporal shape and a time step of 1.9 ns.

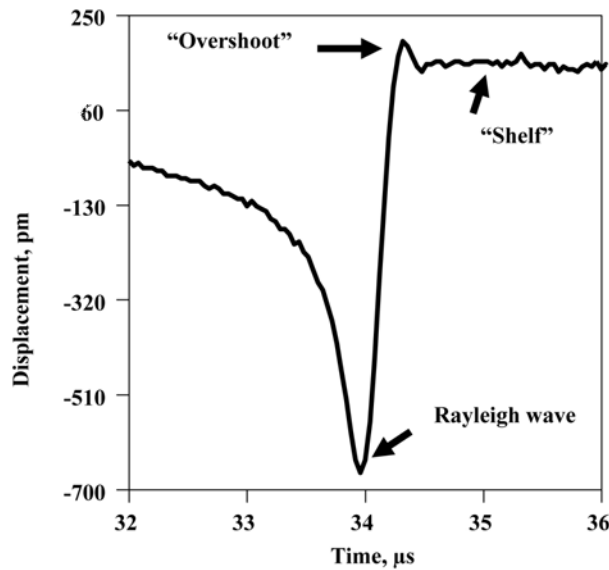


Fig. 7 Reference experimental signal from capacitance sensor with “overshoot” and “shelf.”

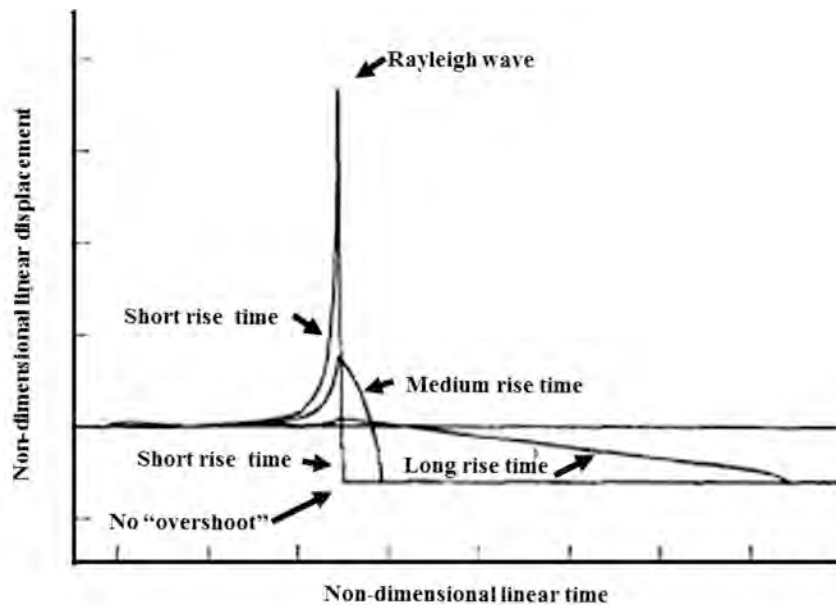


Fig. 8 Analytical result for non-dimensional out-of-plane displacement versus non-dimensional time for various non-dimensional rise times [6].

(d) Examination of the Positive “Overshoot”

Figure 7 shows for the “focus” region the Rayleigh wave, the “overshoot” and the drooping of the “shelf” for the experimental capacitance sensor signal [5]. As shown in Fig. 8, an analytical result [6] for three different finite rise times does not show an “overshoot”. (Note that the polarity of the source function is opposite in this figure versus the other results in this paper.) These analytical results are relevant to the current work, because the results are for finite rise times. To

examine as realistically as possible the “overshoot” by use of the FEM axisymmetric code, the normal stress loading as determined in part I [2] was averaged over 26 circular “rings,” each 0.046 mm wide. By this means, the elliptically shaped region of normal stress loading was approximated in a way that could be used with the axisymmetric code. Figure 9 shows the loading approximation as a function of radius from the center of the surface loading on the steel block. This input spatial loading distribution was used for a “cosine bell” temporal loading with a 0.3- μ s rise time and a series of ever smaller cell sizes until the resultant out-of-plane displacement signal at the 100 mm propagation distance converged with no “overshoot.” The FEM conditions for the converged result were a cell size of 12.5 μ m and a time step of 1.9 ns. It was found that these displacement results could be resampled to a time step of 25 ns without changing the resulting signal. This fact led to a conclusion that the small cell size and time step of the original converged run was required only for the immediate region of the source. Figure 10 shows the 25 ns time-step result (note this time step supports a Nyquist frequency of nearly 20 MHz) as well as the result after a 6 MHz low-pass Butterworth infinite-response filter of order six was applied to the 25 ns time-step data. This filter resulted in no “overshoot” and did not change the Rayleigh wave peak amplitude. It did result in the small time delay shown in Fig. 10.

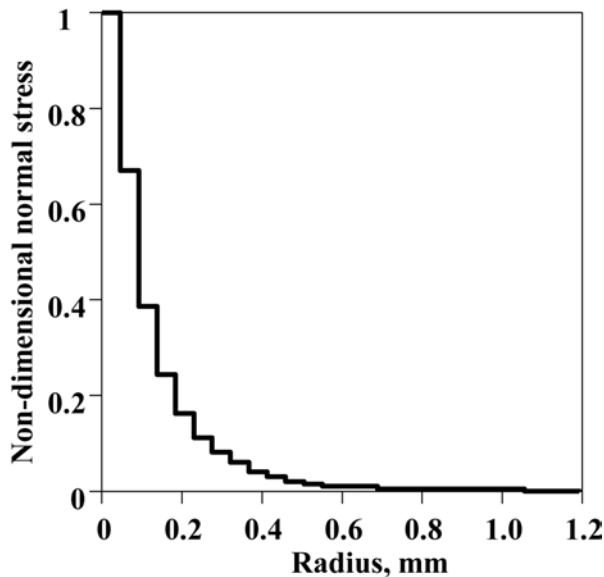


Fig. 9 Distribution of normal stress from averaged “rings” to approximate actual elliptical distribution [2].

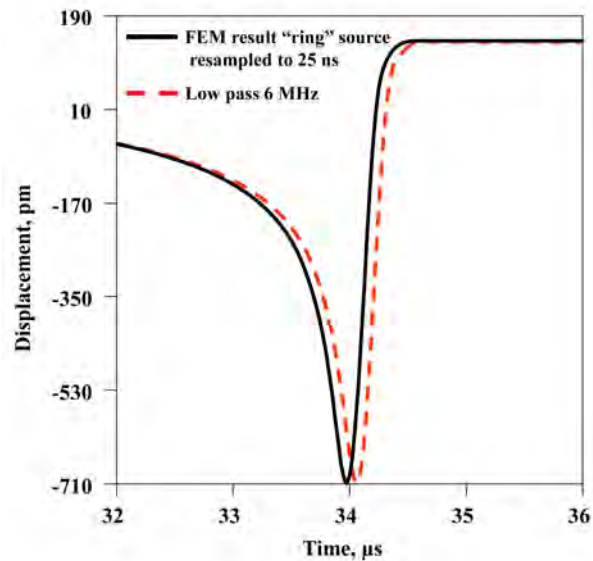


Fig. 10 Resampled “ring” source signal with 25 ns time step compared to the result after filtering the resampled signal at 6 MHz low-pass.

To examine the results for a frequency bandwidth closer to that expected for the experimental system, the same type of low-pass filter was applied (to the 25 ns data) with cutoffs at 3 MHz and also 2 MHz. As Fig. 11 shows, these filters caused the “overshoot” to appear and the amount of “overshoot” to be the largest for the 2 MHz low-pass data. Figure 11 includes the experimental result with an “overshoot” that appears to be similar to that from the 2 MHz low-pass result. Since the sampling rate of the experimental system is 20 MHz, it appears that there is some other hardware aspect of the experimental system that reduces the upper frequency of the bandwidth so as to induce the “overshoot.” Figure 11 also shows that the filtered Rayleigh wave peak amplitudes with the 0.3 μ s rise time are close to that of the experimental result. Thus, it appears that the release of the normal stresses from the glass capillary fracture is not a step in time. This observation is supported by the result in Fig. 5, which shows that a rise time of 0.2 μ s results in

an increase in the peak amplitude of the Rayleigh wave of 6.4 % compared to a rise time of 0.3 μs . It is to be expected that a step rise-time source would result in an even greater increase in the Rayleigh wave peak amplitude, and this amplitude would be much higher than the experimental and 0.3- μs FEM results. This observation is also supported by the fact that a step rise-time for a point source results in infinite amplitude of the Rayleigh wave [7]. It is important to point out that the ASTM test method E1106-07 that describes the absolute AE sensor calibration states that the calibration applies only up to a frequency of 1 MHz. Thus, the upper limitation in the frequency bandwidth of the experimental system does not change the accuracy of the test method calibration.

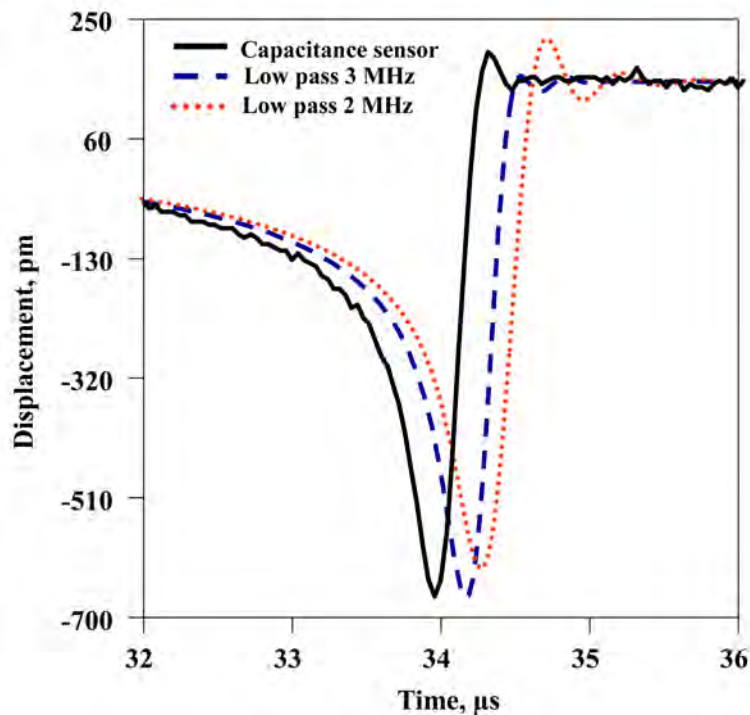


Fig. 11 Comparison of capacitance sensor signal and filtered FEM signal at indicated low-pass frequencies.

Comments relating to the ASTM Absolute AE Sensor Calibration Test Method

ASTM test method E1106-07 [1], as currently written, presents two approaches for absolute calibration of AE sensors. The approach using the output from a capacitance sensor that measures the out-of-plane displacement is described in detail so as to provide a result (which is required for an ASTM test method) for the calibration of a sensor. An alternate approach to the absolute sensor calibration is based on an analytical solution (see, e.g., reference [7]). The specifics of the use of this approach to provide a sensor calibration result are not described in E1106-07 [1]. This analytical solution assumes a point source and step-in-time force release. However, Part I [2] of this paper shows that the glass capillary source is not a point source. The dynamic FEM results shown here demonstrate that changes in the parameters of temporal shape of the source rise time, source rise-time value and dimensions and distribution of the region of the surface normal stress result in changes in the shear/Rayleigh wave (which dominates the wave generated). Since these parameters are unknown in the current calibration procedure and can be expected to vary from one experimental glass-capillary fracture to the next, it is not clear how the analytical solution could be rationally modified to provide a method to achieve a test result (only

the total force released is measured in the calibration). Further, it is not clear how to measure these additional parameters. In addition, as already pointed out, the amplitude of the Rayleigh wave from the analytical solution is infinite [7]. This fact results in another complication with respect to the analytical solution. Thus, it is recommended that the parts of the ASTM test method that refer to the use of an alternate approach for an AE sensor calibration by use of an analytical calculation be modified. The resulting calibration test method would be based on the use of the capacitance sensor, which would in fact have an output that includes the effects of the unknown parameters and thus provides the needed reference signal for the absolute calibration. It is important to point out in this regard that AE sensor calibrations at NIST Gaithersburg from 1982 [8] until the summer of 2009 [5] were done using the output from the capacitance sensor.

Conclusions

- Changes in the spatial distribution and spatial size of the normal-stress source from the glass capillary result in changes in the Rayleigh wave peak amplitude.
- Changes in the temporal rise time and shape also result in changes in the Rayleigh wave peak amplitude.
- Since use of a capacitance reference sensor accounts for the above spatial and temporal aspects for glass capillary fractures, it is recommended that use of an alternate calibration approach using an analytical solution, which presently cannot rationally account for the actual values of these parameters, be modified in E1106-07.

Acknowledgements

The static finite-element computations and input by Mr. Brian Burks, University of Denver, are gratefully acknowledged. The dynamic finite-element computations by Dr. John Gary, NIST retired, are gratefully acknowledged.

References

1. ASTM E1106-07, "Standard Test Method for Primary Calibration of Acoustic Emission Sensors," ASTM International, West Conshohocken, Pennsylvania.
2. Burks, B., "Re-examination of NIST acoustic emission sensor calibration: Part I – modeling the loading from glass capillary fracture," *J. of Acoustic Emission*, **29**, 2011, 167-174.
3. Gary, John and Marvin Hamstad, "On the Far-field Structure of Waves Generated by a Pencil Break on a Thin Plate," *J. Acoustic Emission*, **12**, (3-4), 1994, 157-170.
4. Hamstad, M.A., "Some Observations on Rayleigh Waves and Acoustic Emission in Thick Steel Plates," *J. Acoustic Emission*, **27**, 2009, 114-136.
5. Fick, Steven, NIST, Gaithersburg, Maryland, personal communication, 2009.
6. Afandi, O.F. and R.A. Scott, "A Note on Dynamic Surface Displacements in an Elastic Half Space," *Acta Mechanica*, **17**, 1973, 145-152.
7. Pekeris, Chaim L. and Hanna Lifson, "Motion of the Surface of a Uniform Half-space Produced by a Buried Pulse," *J. Acoust. Soc. Am.*, **29**, (11), 1957, 1233-1238.
8. Proctor, Thomas M., Jr., "Some details on the NBS conical transducer," *J. of Acoustic Emission*, **1**, (3), 1982, 173-178.

INVESTIGATION OF PENCIL-LEAD BREAKS AS ACOUSTIC EMISSION SOURCES

MARKUS G. R. SAUSE

University of Augsburg, Institute for Physics, Experimental Physics II, D-86135 Augsburg, Germany

Abstract

Pencil-lead breaks are widely used as a reproducible source for test signals in acoustic emission (AE) applications. Experimental and numerical studies are presented that focus on the differences in surface displacements obtained from pencil-lead breaks under different angles and free lead lengths. Experimentally, a setup for measurement of rupture forces during pencil-lead breaks was designed. The experiments were carried out with different lead diameters, different free lead lengths and under various angles with respect to an aluminum block. The measured forces were used as parameters for validation of finite element modeling of pencil-lead breakage. The model for the pencil-lead break source was developed using multi-scale modeling and dynamic boundary conditions. Various experimental conditions were simulated, and the resulting surface displacement and forces at the contact between lead and aluminum block were evaluated to obtain numerical source functions for pencil-lead breaks. A comparison is made between source functions of finite element simulation and analytical source functions as proposed in literature. The obtained source functions elucidate the difference in signal magnitudes for the various angles and lead lengths and yield insight in the microscopic processes during lead fracture.

1. Introduction

Pencil-lead breakage (PLB) is a long established standard as a reproducible artificial acoustic emission (AE) source. Often this type of source is also referred to as the Hsu-Nielsen source, based on the original works of Hsu [Hsu1981] and Nielsen. Using a mechanical pencil, the lead is pressed firmly against the structure under investigation until the lead breaks. During pressure application with the lead, the surface of the structure gets deformed. At the moment of lead breakage, the accumulated stress is suddenly released, which causes a microscopic displacement of the surface and causes an acoustic wave that propagates into the structure. Since this type of source is easy to handle in laboratory environments, as well as in field testing, it became the most common type of test source in AE testing.

The test signals obtained from PLBs are very reproducible given the handling of the mechanical pencil is repeated accurately. Unfortunately, slight deviations in the type of handling, the type of pencil and the respective lead cause differences in the test signals and thus make detailed comparisons between reports found in literature more difficult. Since PLBs are typically applied to investigate signal propagation in the structure under investigation, to check sensor couplings and to define threshold values for signal detection, it is of crucial importance to understand how differences in handling of the mechanical pencil and the lead diameter can influence the test signals.

Thus, the intention of this study is a comparison of PLB signals obtained by systematic variation of free lead length, angle of lead relative to the test structure and the choice of lead diameter. This is done in a combined approach of finite element modeling of pencil-lead breakage and respective experiments to validate the model.

2. Finite Element Modeling

For modeling of AE signals, knowledge about the source function is vital. This is the case for the established analytical methods of AE signal modeling [Ohtsu1984, Ohtsu1986, Green1995, Lysak1996, Giordano1999] as well as for more recent attempts using finite element techniques [Gary1994, Prosser1999, Sause2010a]. While finite element modeling of AE signal propagation in solids [Prosser1999, Castaings2004, Greve2005] is already well established, less investigations have been published regarding finite element modeling of the AE source itself. Nevertheless, the characteristics of the source influence the frequency content of the propagating signal [Hamstad2002, Sause2010a] and the formation process of guided waves like those found in plates or cylinders. Modeling of AE sources beyond point-like approximations [Gary1994, Prosser1999, Hamstad1999] requires additional knowledge about the source microstructure and the material properties close to the source [Sause2010a, Sause2010b, Sause2010c].

Various finite element methods are reported that focus on simulation of crack growth in solid materials [Song2008], like the virtual crack closure technique [Krüger2004] or the material point method [Sulsky1995, Nairn2003]. One major drawback of all these methods for simulation of AE signal is the quasi-static conditions for crack growth. Since the origin of AE is the rapid microscopic displacement within a solid, i.e., the deflection and vibration of crack walls, a high temporal resolution is required. This is typically in contrast to the formulation of quasi-static boundary conditions as in the cited approaches.

In the following an alternative finite element modeling approach for simulation of pencil-lead breakage with associated AE excitation will be demonstrated, using the software program “Comsol Multiphysics”. In the following all descriptions only refer to the way of implementation within the module “Structural Mechanics” of this software.

2.1 Simulation methodology

The calculation of stress-strain relationships is based on the structural mechanics constitutive equation. Based on the principle of virtual work the program solves the partial differential equations for equilibrium conditions, expressed in global or local stress and strain components for an external stimulation.

For linear elastic media with elastic coefficients \vec{D} , Hooks law is chosen as constitutive equation.

$$\vec{\sigma} = \vec{D} \cdot \vec{\epsilon} \quad (1)$$

In the general case for anisotropic media the elasticity tensor \vec{D} is a 6 x 6 matrix with 12 independent components. Using the Voigt notation convention, the stress tensor can be written as vector $\vec{\sigma}$ with six independent components composed of normal stresses σ and shear stresses τ . The strain tensor is written similarly as vector $\vec{\epsilon}$, which also has six independent components consisting of normal components ϵ and shear strain components γ . In the case of isotropic media the elasticity tensor is completely described by Young’s modulus E and the Poisson’s ratio, ν .

The principle of virtual work states that the variation of work W induced by forces F_i and virtual displacements du_i in an equilibrium state equals zero:

$$\delta W = \sum_i F_i \cdot \delta u_i = 0 \quad (2)$$

Generally, the external applied virtual work equals the internal virtual work and in the case of a deformable body with volume V and surface S , results in a deformation state with new internal stress and strain components.

$$\int_S \delta \vec{u}^t \cdot \vec{F}_S dS + \int_V \delta \vec{u}^t \cdot \vec{F}_V dV - \int_V \delta \vec{\epsilon}^t \cdot \vec{\sigma} dV = 0 \quad (3)$$

The external applied forces \vec{F}_S and \vec{F}_V act on the surface and volume of the body, respectively. The constraint forces within the material are expressed by consistent internal stress $\vec{\sigma}$ and strain $\vec{\epsilon}$ components, with the superscript t indicating the transposed vectors.

To extend the principle of virtual work for dynamic systems, mass accelerations are introduced. This yields the formulation of the d'Alembert principle, which states that a state of dynamic equilibrium exists if the virtual work for arbitrary virtual displacements vanishes. Taking this into account and introducing the material density ρ equation (3) becomes:

$$\int_S \delta \vec{u}^t \cdot \vec{F}_S dS + \int_V \delta \vec{u}^t \cdot \vec{F}_V dV - \int_V \delta \vec{\epsilon}^t \cdot \vec{\sigma} dV - \int_V \rho \frac{\partial^2 \vec{u}}{\partial t^2} \cdot \delta \vec{u} dV = 0 \quad (4)$$

This defines the basic differential equation solved for every finite element. In order to model structural mechanics problems, a suitable geometry and respective boundary conditions have to be defined.

2.2 Model description

The model geometry consists of the tip of a mechanical pencil (i.e., Pentel P205), which is composed of a fixed (non-sliding) steel collet and the pencil lead. For all simulations, a 2-dimensional setup with plane-strain conditions was used. As illustrated in Fig. 1, the plastic frame of the mechanical pencil is not modeled, since no mechanical or acoustical contribution is expected from this component. In order to simulate pencil-lead breakage, the mechanical pencil is loaded against a test block in the negative y -direction. All values for the elastic properties used in the simulation are summarized in Table 1. The values for a typical high-strength alloy steel and 7075 aluminum alloy were chosen from the built-in material database of the software Comsol. Since no entry was found for pencil-lead or a respective graphite modification, a different approach was chosen to select its properties. Literature values for graphite-based materials span a broad range of properties for density, elastic modulus and fracture strength [Sakai1983, Sakai1988, Allard1991]. Since the exact composition of the pencil-lead used is subject to assumptions, the material properties reported in Table 1 were validated by experimental data as described in section 3.

As the pencil lead and test block form different entities, contact modeling was used to transfer load and displacement between the tip of the pencil lead to the test block. Since contact modeling is restricted to boundary elements, it was necessary to chamfer one of the pencil-lead edges to yield an angled boundary as illustrated in Fig. 1. For all investigations, the length of the chamfer was kept constant at 0.1 mm.

The modeling approach to simulate crack growth within the pencil-lead is illustrated in Fig. 2. Initially, the steel collet and pencil lead form a union and are loaded in negative y -direction. At the time of fracture t_{frac} the internal boundary conditions of the pencil-lead at the tip of the collet are released and contact modeling is enabled. Thus for times $t \geq t_{\text{frac}}$ both boundaries of the

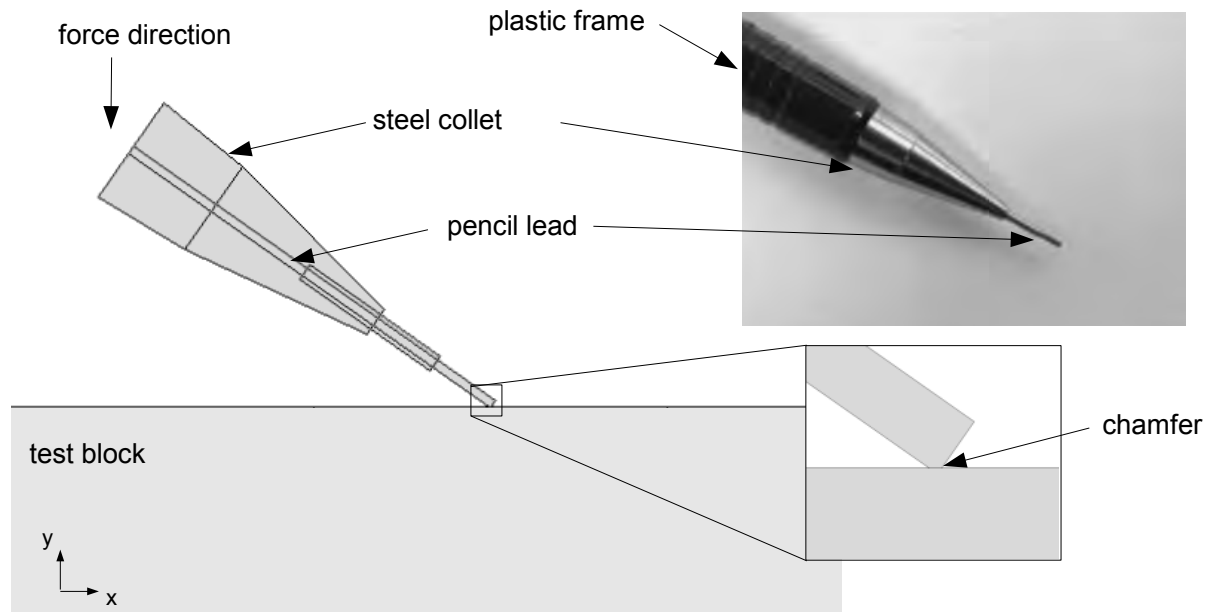


Fig. 1. Illustration of model geometry.

Table 1. Material properties used for simulation.

Property	Aluminum	Pencil lead	Steel
Density [Mg/m ³]	2.720	1.780	7.850
Elastic modulus [GPa]	71.1	10.5	200.0
Poisson's ratio	0.33	0.33	0.33

pencil lead are allowed to move independently but do not penetrate each other. The position for separation of the pencil lead was chosen based on static loading of the mechanical pencil. As indicated by the color range of the von-Mises stress in Fig. 2 the maximum stress occurs at the position, where the pencil lead leaves the collet. This is also the typical position, where fracture is introduced experimentally. For this investigation and all following, the size of the mesh elements was chosen to be less than 0.1 mm and was refined at the interacting boundaries for crack initiation and contact modeling to go down to 2.5 μm . As temporal resolution 0.01 μs was found to be sufficient, i.e., no change in the calculated solutions was found for a change in resolution down to 0.001 μs .

In reality the time for loading of the mechanical pencil is typically a couple of seconds. Computationally it is not feasible to simulate such long loading times with the accuracy in temporal resolution of 0.01 μs . Thus, it was investigated, what loading rate is acceptable to reflect quasi-static loading conditions as faced in the experiment. As long as no time-dependent material law is applied, this condition is fulfilled, if the displacement velocity does not exceed the sound velocity of the material. Thus, any external loading of the structure that results in movements sufficiently slower than the transverse sound velocity of the material can be assumed to ensure quasi-static loading conditions. For the current case a good compromise between this requirement and the computation time was $t_{\text{frac}} = 5 \mu\text{s}$ based on the convergence of the calculated source functions (see section 4).

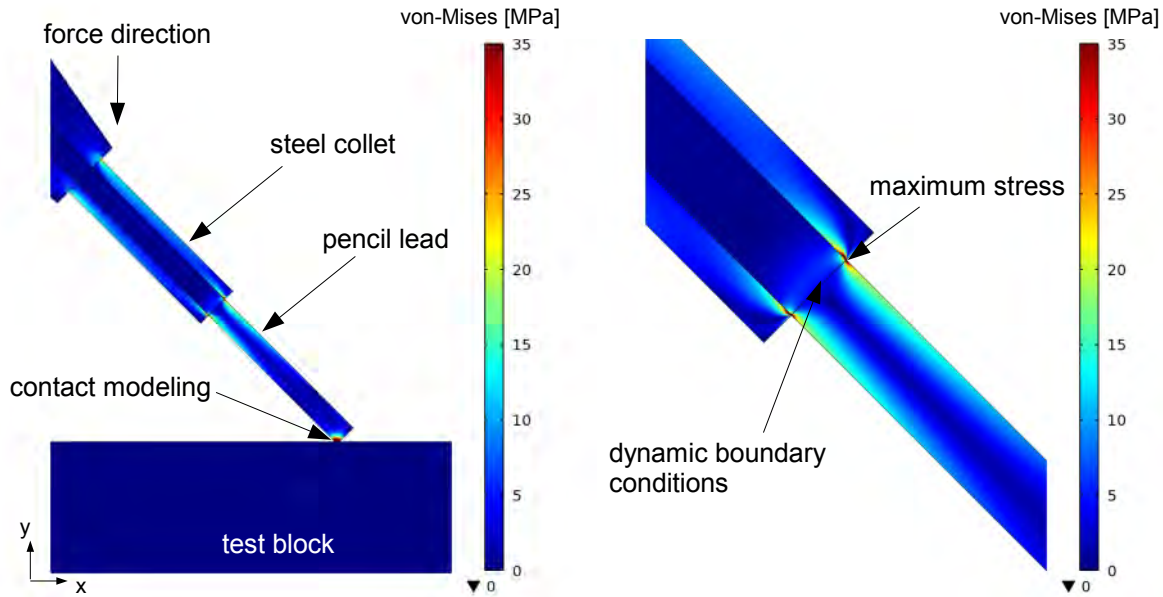


Fig. 2. Definition of boundary conditions and investigation of fracture zone by static loading.

It is worth noting that the present approach is sufficient for modeling of pencil-lead break sources, but not necessarily for modeling of crack propagation. The evolution of the latter is severely influenced by plastic deformation of the fracture zone due to crack propagation. In order to take into account such changes and the according interaction with the stress field, more comprehensive approaches for modeling of crack propagation [Sulsky1995, Nairn2003] have to be extended to allow simultaneous simulation of AE. Also, the von-Mises stress values should be used with care, since their absolute value is influenced by the 2-dimensional representation. For a 3-dimensional model a stronger stress concentration at the position between collet and pencil-lead may be expected.

3. Experimental

In order to validate the proposed modeling approach the rupture force for a variety of PLB configurations were evaluated. As shown at the bottom of Fig. 3, the mechanical pencil was mounted within tensile jaws. The tip of the lead was pressed against a sensitive load cell with 5-N maximum capacity. As defined in Fig. 3, various free lead lengths and contact angles were investigated. In addition, two lead diameters (0.5 mm and 0.3 mm) of hardness 2H were tested. Dimensions of lead diameter, free lead length and contact angle were measured from images like Fig. 3 using a calibrated optical extensometer. Table 2 holds a summary of the chosen parameters and the measurement results.

For comparison a respective simulation of the experimental conditions under static loading conditions was performed. For this purpose the PLB model described in section 2.2 was loaded to the maximum displacement as measured experimentally. As already mentioned in section 2.2, a broad range of properties for graphite modifications is found in literature [Sakai1983, Sakai1988, Allard1991]. Since typical values for pencil leads are beyond the scope of literature, a range of elastic properties was evaluated. For this purpose, the elastic modulus was varied between 9.5 GPa and 13.5 GPa in 0.5 GPa steps and density was varied between 1.50 Mg/m³ and 1.80 Mg/m³ in steps of 20 kg/m³. The best agreement between the calculated force at the pencil-lead tip and experimental values was found for $E = 10.5$ GPa and $\rho = 1.78$ Mg/m³. For better

comparison, results of experiment and simulation are shown in Fig. 4 as a scatterplot. Within the experimental range of scatter, the simulation results show good agreement.

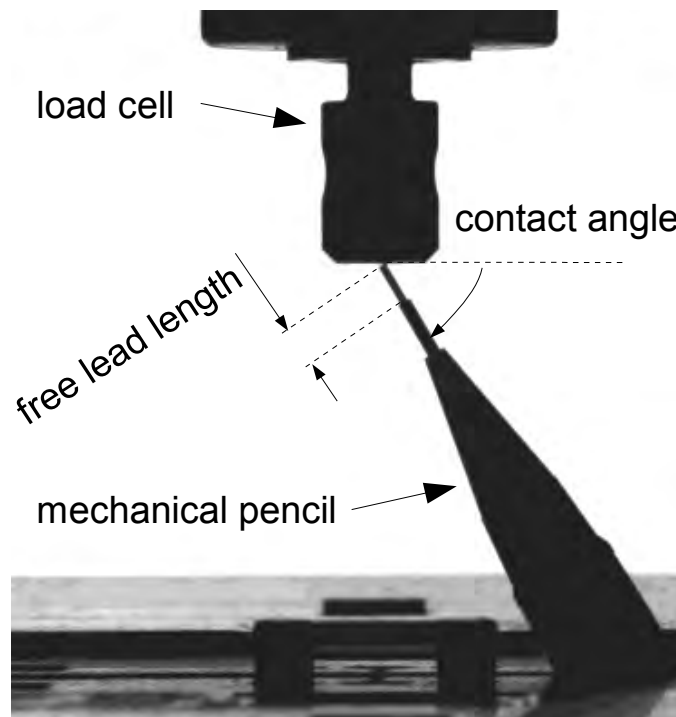


Fig. 3. Image of measurement setup.

Table 2. Measured rupture forces of PLB for various lead diameters, contact angles and lead lengths. For comparison, results of a static simulation of the chosen configuration are reported.

Diameter [mm]	Contact angle [°]	Lead length [mm]	Force (experimental) [N]	Force (simulation) [N]
0.5	23.5	4.0	1.60 ± 0.07	1.61
		3.2	2.08 ± 0.14	2.03
		2.4	2.34 ± 0.41	2.66
	45°	4.0	2.16 ± 0.14	2.31
		3.2	3.25 ± 0.68	2.89
		2.4	3.97 ± 0.15	3.84
	60°	4.0	3.32 ± 0.12	3.39
		3.2	4.03 ± 0.50	4.16
		2.4	> 5.00 ¹	5.14
0.3	45°	4.4	0.47 ± 0.01	0.48
		2.2	1.62 ± 0.36	1.25

¹ force exceeds limit of load cell

4. Results and Discussion

In the following, results of the conducted numerical studies are presented. In Fig. 5 images of the stress distribution around the pencil lead are shown at distinct time steps before and after fracture. For times less than t_{frac} the stress at the fracture zone increases. For $t \leq t_{\text{frac}}$ boundary constraints inhibit independent movement of the lower and upper part of the pencil lead. At $t > t_{\text{frac}}$ boundary conditions at the interface are changed to independent movement using contact modeling. The separation (i.e. cracking) of the pencil lead causes initiation of a flexural wave that propagates along the free pencil lead.

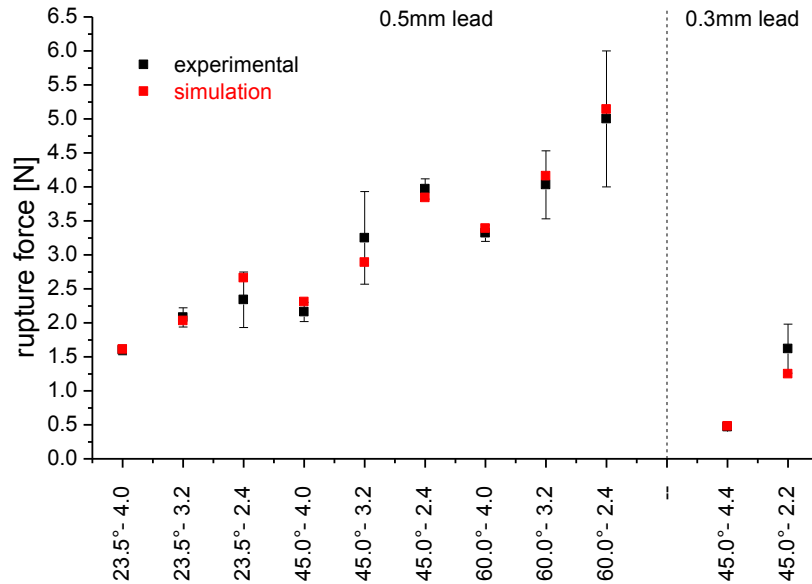


Fig. 4. Comparison of measured rupture forces of PLB configurations and calculated force evaluated at the tip of the pencil lead from the simulation against the angle and free length.

Due to inertial forces, the free pencil lead remains in contact with the test block. For a free lead length of 4 mm the flexural wave reaches the tip of the pencil lead within 1.5 μ s after fracture initiation. At this time the maximum compressive contact force is reached at the tip of the lead. Due to reflection of the flexural wave at the interface between pencil lead and test block, the contact between both is lost. As a consequence, the pencil lead flips away.

In Fig. 6, the maximum of the von-Mises stress at the position of the crack within the pencil lead is shown together with the calculated contact force and surface displacement of the test block at the position of the lead tip. Until the time of fracture initiation t_{frac} the stress at the internal boundary within the pencil lead is increasing linearly, since the pencil is loaded with constant force per time. At $t = t_{\text{frac}}$ boundary conditions are changed and contact modeling is enabled. This causes a sharp drop of the von-Mises stress at this boundary that reaches a steady-state friction stress level after a characteristic time t_{crack} between 150 ns and 400 ns. This corresponds well to the characteristic times for shear waves propagating across the diameter of the pencil-lead as reported by Scruby et al. [Scruby1978]. The friction stress level originates from the friction contact between both boundaries of the pencil lead. As already seen in Fig. 5, a flexural wave propagates along the free pencil-lead and reaches the test block delayed by 1.44 μ s for 4.0 mm lead length. At this time the maximum surface displacement and the maximum contact force is calculated.

Under quasi-static loading conditions, i.e. a couple of seconds loading time, the initial slope of surface displacement and contact force can be assumed to vanish. This is indicated in Fig. 6 by the dashed horizontal lines. Thus the true source function for a PLB should include a small compressive surface displacement and compressive force at the beginning. It is noted, that source functions for pencil-lead breaks as deduced from experimental signals by deconvolution procedures using Green's theorem yield quite similar signals (see Breckenridge et al. [Breckenridge1990]). Also, the signal calculated for the surface displacement is in good agreement to the reports of various other authors [Scruby1978, Breckenridge1990]. The distortion of the contact

force signal around $7.4 \mu\text{s}$ is caused by the settings for contact modeling. Depending on the exact parameters chosen within the software, the distortion is emphasized or gets negligible. It is thus considered to be a numerical issue, rather than a physical effect.

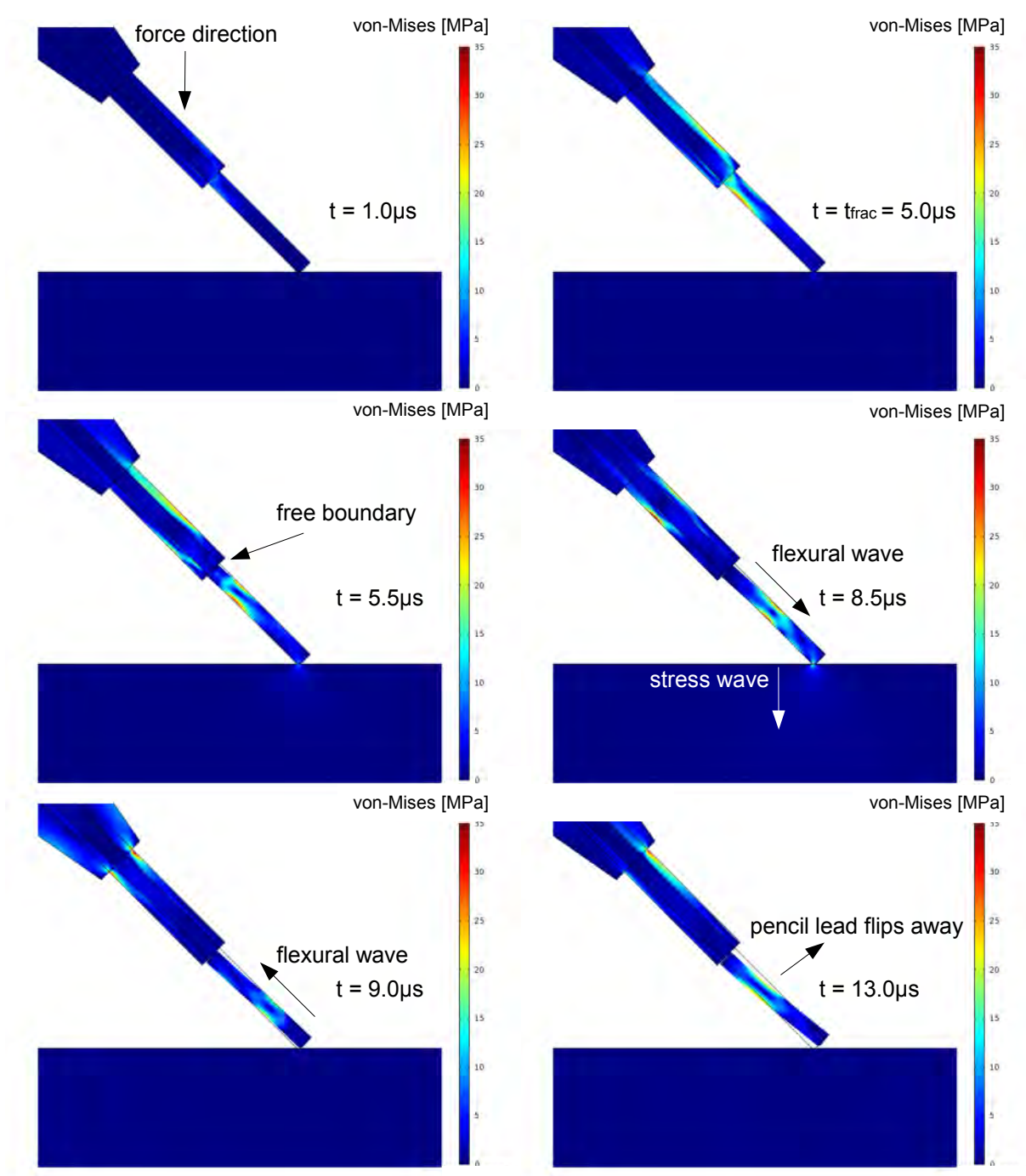


Fig. 5. Stress distribution in vicinity of pencil-lead at distinct time steps before and after fracture. Simulation for 4.0 mm free lead length under 45° contact angle. For the purpose of visualization, deformations are exaggerated by a factor of 10.

4.1 Comparison to analytical source functions

Most of the time analytical source functions are used to introduce acoustic emission sources for numerical or analytical calculations [Gary1994, Lysak1996, Prosser1999, Hamstad1999,

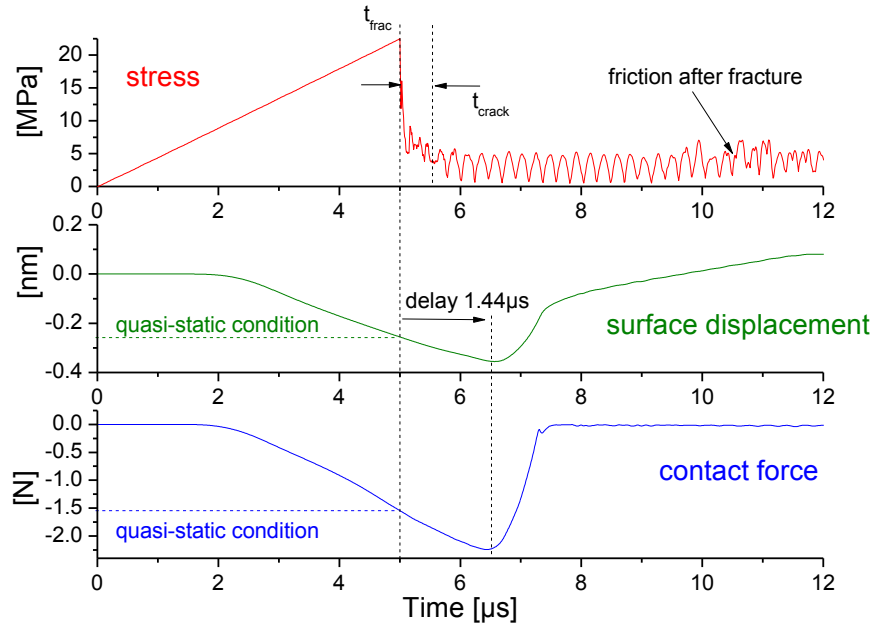


Fig. 6: Evaluation of von-Mises stress at crack position and according surface displacement and contact force between pencil-lead and test block for 50 mm thick aluminum plate, with 4.0 mm free lead length under 45° angle and constrained displacement for bottom surface of test block.

Sause2010a]. Using the PLB model as described above, a comparison of the simulated contact force is made to typical source functions as reported in literature. A direct comparison with respective rise times is shown in Fig. 7 for the FEM result, a step function [Lysak1996], a linear ramp function [Gary1994, Prosser1999, Sause2010a] and a cosine bell function [Hamstad1999]. Among those functions, best agreement between the simulation result and the analytical description is found for the cosine bell function.

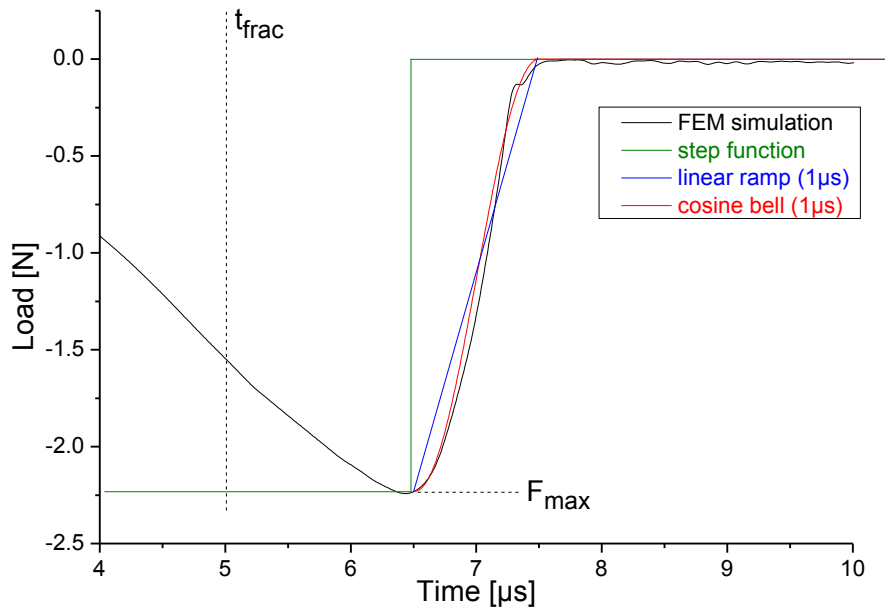


Fig. 7: Simulated force release on 15 mm thick aluminum plate, with 4.0 mm free lead length under 45° angle and 0.5 mm lead diameter. Comparison with analytical source functions used to describe PLB.

Next, a comparison is shown in Figs. 8-a and -b for the calculated surface displacement signals and surface displacement velocity signals obtained from a 15-mm thick plate at a distance of 40 mm away from the simulated PLB. In both figures the black curve shows the signals obtained using the full PLB model as described above. The same plate geometry was loaded at a point corresponding to the midpoint of the chamfer as seen in Fig. 1. As source functions, the linear ramp function and the cosine bell shape were chosen. In both cases a cosine load function was used to reflect the loading conditions for times $t < 6.5 \mu\text{s}$ (see Fig. 7). In experiments the loading occurs under quasi-static conditions, so this contribution is assumed to be negligible in the final shape of the AE signal. Since only negligible difference is found for the simulated surface displacement in Fig. 8-a, the surface displacement velocity was evaluated. Here, minor differences are observed between the PLB model result and the simulations using analytical descriptions. Based on this comparison a slightly better match between 25 μs and 30 μs is found for the description using the cosine bell function. The main difference between the PLB model results and the source model descriptions is attributed to the contribution of friction as seen from Fig. 6.

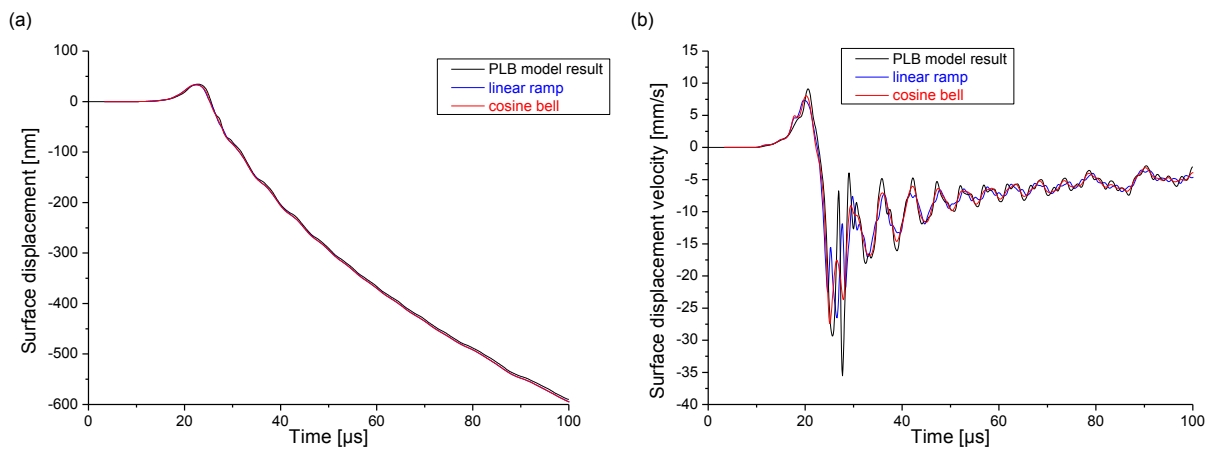


Fig. 8: Comparison of acoustic emission signal from PLB modeling and respective source model descriptions. Surface displacement signal at 40 mm distance from PLB (a) and respective surface displacement velocity (b).

4.2 Variation of test geometry

Since PLBs introduce external loads, it is important to consider the boundary conditions for the test block geometry. Since no displacement constraints act on the surface of the test block it gets accelerated through the load introduced by the PLB. This effect is shown in Figs. 9-a and -b, respectively. While the calculated contact force is almost independent of the plate thickness, the situation is different for the calculated surface displacement. Here, mass inertia dominates the simulated surface displacement curves. That is, for larger masses, the surface displacement response approaches the ideal (constrained) shape as seen from Fig. 6. Thus, for simulations using global coordinate systems, a description of PLBs as load functions is preferred to displacement functions.

4.3 Variation of free lead length

As demonstrated experimentally, the variation of free lead length causes different rupture forces. Figure 10 shows the simulated contact forces for the three different lead lengths used experimentally. The simulations were for a 15-mm thick plate under 45° contact angle. As already expected from the quasi-static simulations, the maximum load introduced at the contact between pencil-lead tip and test block is dependent on the lead length. Also, the time of maximum load is

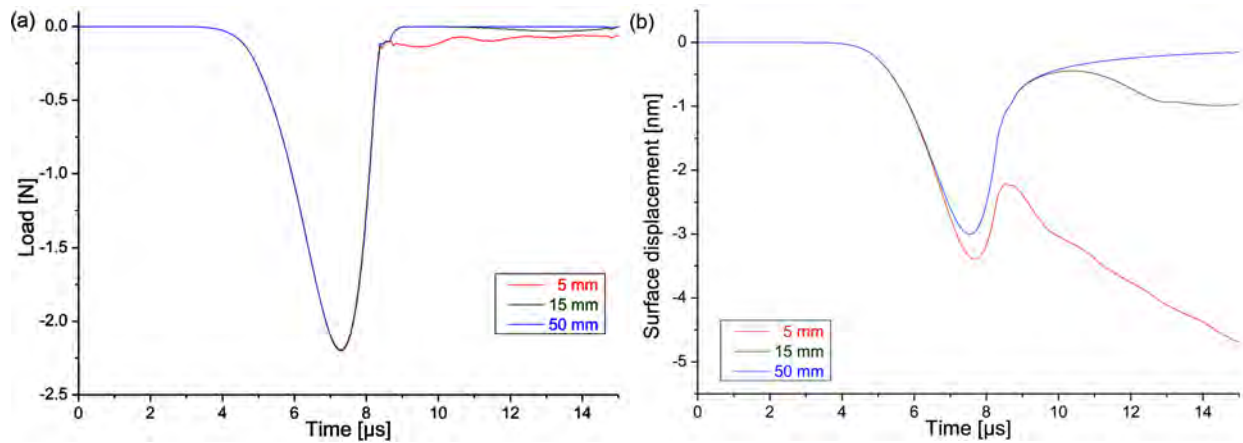


Fig. 9: Simulated force release on aluminum plates with varying thickness (a) and respective surface displacements (b). All simulations for 4.0 mm free lead length under 45° angle.

dependent on the free lead length. This corresponds to the occurrence of the flexural wave as shown in Fig. 6. The arrival time of the wave is obviously linked to the propagation length, which is the length of the pencil lead in this case. The observed difference in arrival times of $0.6 \mu\text{s}$ for 4.0-mm lead length and 2.4-mm lead length corresponds well to the expected sound velocity for the pencil lead.

4.4 Variation of contact angle

Also similar to the experiments, the contact angle between test block and pencil-lead was varied. Figure 11 shows the respective simulations for contact forces under 23.5° , 45.0° and 60.0° contact angles. Similar to the variation of free lead length changes in the force magnitudes are observed. Also, a shift of the arrival times of maximum contact force is found for the three contact angles. Both observations are attributed to the change in structural loading conditions, i.e., stiffness of the mechanical pencil and the pencil lead under vertical loading.

It is worth noting that no substantial changes of the contact force shape were found for the variation of free lead length and variation of contact angle. If the obtained curves are normalized and shifted with respect to their maximum, the falling slope understood as source function in Fig. 7 coincides well for all configurations. Thus, the shape of the source function itself is not affected by variation of free lead length or contact angle, but the magnitude of the excited AE signals will directly depend on the magnitude of the contact force.

5. Conclusions

The current study contributes to the description of pencil-lead breaks as AE sources. It was demonstrated, that slight differences in the usage of mechanical pencil can introduce large differences in the source magnitude. This was confirmed experimentally by measurement of the rupture forces under various contact angles and free lead lengths.

A new finite element modeling approach was set up to dynamically change boundary conditions that simulate crack propagation within a pencil lead. Within the numerical studies, it was observed how cracking of the lead causes the respective contact forces and surface displacements between pencil-lead tip and test block geometry. It was concluded that a flexural wave propagating along the pencil lead causes a characteristic delay between the time of fracture and the maximum contact force and surface displacement. The change in delay was found to be systematical-

ly dependent on the free lead length and the contact angle. The simulated contact force magnitudes showed good agreement to the experimental measurements.

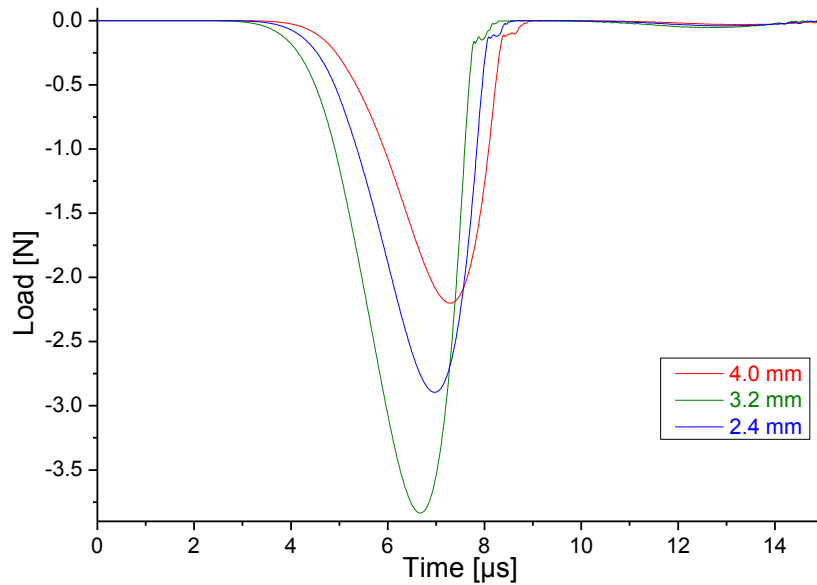


Fig. 10: Simulated force release on aluminum plates with 15 mm thickness for various free lead lengths under 45° angle.

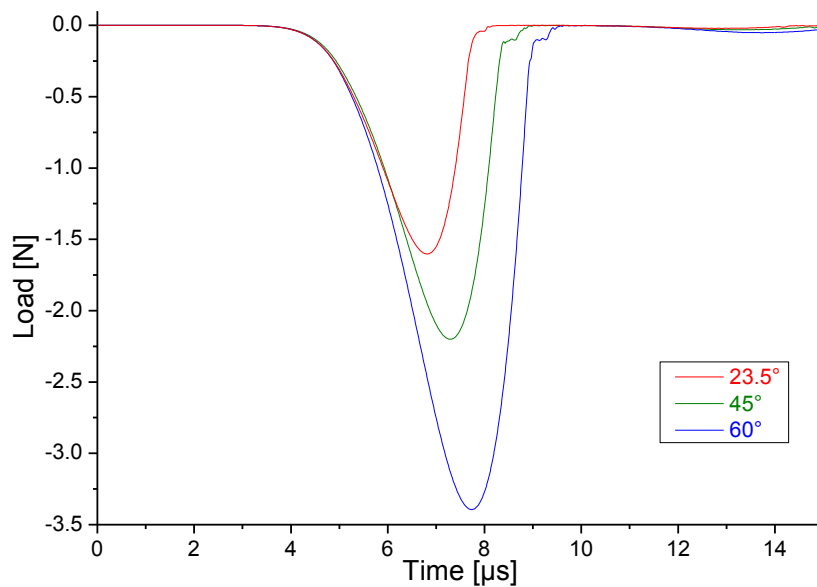


Fig. 11: Simulated force release on aluminum plates with 15 mm thickness for 4.0 mm free lead length under various contact angles.

A comparison was made between the contact force simulation by finite elements and respective analytical descriptions from literature. In summary, the cosine-bell function was found to show best agreement to the contact force simulation. The best match between the simulated AE signals obtained in the far field was found for the cosine-bell shape as well, although a linear ramp source function was found to show almost similar performance. The source rise time for the aluminum plate was found to be $1 \mu\text{s}$ for all free lead lengths and contact angles. However, based on the difference in elastic properties different rise times are expected for other materials.

Thus, similar investigations should be conducted to derive rise times for other materials. Ultimately, a substitution of the complex source model for pencil-lead breakage by analytical source functions seems appropriate given the computational efficiency and ease of implementation.

Acknowledgments

I would like to thank Marvin A. Hamstad for the fruitful discussions on simulation of acoustic emission signals and the recommendations regarding modeling of pencil-lead breakage.

References

- [Allard1991] B. Allard, D. Rouby and G. Fantozzi (1991), *Carbon*, **29**:3, 457-468.
- [Breckenridge1990] F.R. Breckenridge, T.M. Proctor, N.N. Hsu, S.E. Fick and D.G. Eitzen (1990), *Progress in Acoustic Emission V*, eds. K. Yamagushi, H. Takahashi, and H. Niitsuma (Eds.), Tokyo, pp. 20-37.
- [Castaings2004] M. Castaings, C. Bacon, B. Hosten and M. V. Predoi (2004), *J. Acoust. Soc. Am.*, **115**:3, 1125-1133.
- [Gary1994] J. Gary and M.A. Hamstad (1994), *J. Acoustic Emission*, **12**:3-4, 157-170.
- [Green1995] E. R. Green (1995), *Composites Engineering*, **5**, 1453-1469.
- [Greve2005] D.W. Greve, J.J. Neumann, J.H. Nieuwenhuis, I.J. Oppenheim, N.L. Tyson (2005), *Proc. SPIE*, SPIE-5765, pp. 281-292.
- [Giordano1999] M. Giordano, L. Condelli and L. Nicolais (1999), *Comp. Sci. Technol.*, **59**, 1735-1743.
- [Hamstad1999] M.A. Hamstad, A. O’Gallagher and J. Gary (1999), *J. Acoustic Emission*, **17**:3-4, 97-110.
- [Hsu1981] N.N. Hsu, F.R. Breckenridge (1981), *Mat. Eval.*, **39**, 60-68.
- [Krüger2004] R. Krüger (2004), *Appl. Mech. Rev.* **57**:2 109-143.
- [Lysak1996] M. Lysak (1996). *Eng. Frac. Mech.*, **55**:3, 443-452.
- [Nairn2003] J.A. Nairn (2003), *Comput. Method. Appl. M.*, **4**, 649-663.
- [Ohtsu1984] M. Ohtsu and K. Ono (1984), *J. Acoustic Emission*, **3**, 27-40.
- [Ohtsu1986] M. Ohtsu and K. Ono (1986), *J. Acoustic Emission*, **5**, 124-133.
- [Prosser1999] W. H. Prosser, M. A. Hamstad, J. Gary and A. O’Gallagher (1999), *J. Nondest. Eval.* **18**:3, 83-90.
- [Sakai1983] M. Sakai, K. Urashima and M. Inagaki (1983), *J. Am. Ceram. Soc.*, **66**:12, 868-873.
- [Sakai1988] M. Sakai, J.-I. Yoshimura, Y. Goto and M. Inagaki (1988), *J. Am. Ceram. Soc.*, **71**:8, 609-616.
- [Sause2010a] M.G.R. Sause and S. Horn (2010), *J. Nondest. Eval.*, **29**:2, 123-142.
- [Sause2010b] M.G.R. Sause and S. Horn (2010), *J. Acoustic Emission*, **28**, 142-154.
- [Sause2010c] M.G.R. Sause (2010), *Identification of failure mechanisms in hybrid materials utilizing pattern recognition techniques applied to acoustic emission analysis*, PhD-thesis, mbv-Verlag, Berlin.
- [Scruby1978] C.B. Scruby and H.N.G. Wadley (1978), *J. Phys. D. Appl. Phys.*, **11**, 1487-1494.
- [Song2008] J.-H. Song, H. Wang and T. Belytschko (2008). *Comput. Mech.* **42**, 239-250.
- [Sulsky1995] D. Sulsky, S.-J. Zhou and H. Schreyer (1995), *Comput. Phys. Commun.* **87**, 236-252.

NECESSARY CONDITION FOR DELAYED FRACTURE OF METASTABLE 304 STAINLESS STEEL WITH STRAIN-INDUCED MARTENSITE

MIKIO TAKEMOTO, SHUICHI UENO, MOTOAKI NAKAMURA and GUNJI UENO
Kanmeta Engineering Co., Nakanochi-higashi 2-34-5, Tondabayashi, Osaka 584-0022, Japan

Abstract

In order to reveal the necessary condition for shot-peened 304 stainless steel strips to cause delayed fracture, we monitored AE signals during stepwise strain increasing (SSI) tests of the hydrogen-charged strips in flexure and also during hydrogen charging of the bent strips. During the strain holding in the SSI test, we detected less than ten AE signals from the cracks produced in martensite-bearing surface layer. Numbers of AE signals and cracks agreed. This test showed no need for dynamic straining to cause the delayed fracture when sufficient hydrogen is supplied to martensite-bearing layer. Cracks did not propagate beyond the martensite-bearing surface layer of 150-200 μm . We also detected AE signals from the bent strips exposed to hydrogen charging, and estimated apparent diffusion coefficient of hydrogen in martensite-bearing layer from both the charge time for first AE detection and hydrogen diffusion length. It was estimated to be 10^{-9} cm^2/s for austenite layer with strain-induced martensite of 10 mass %.

Introduction

Susceptibility of austenitic stainless steels (SS) to delayed fracture is generally low. However, some types of the stainless steels show susceptibility when they are exposed to wet hydrogen environment. These SS are metastable 300-series (typ. Fe-18Cr-8Ni) and dual phase SS (50% ferrite-50% austenite phase). Also susceptible are high nickel alloys such as Inconel and Hastelloy with nickel content higher than 40%. Dual phase SS was demonstrated to show high susceptibility to the delayed fracture [1].

This paper deals with the delayed fracture of shot-peened 304 SS and as-received dual phase SS. 304 SS produces martensite when it is shot-peened at room temperature. Here, the martensite formation temperature of this steel is calculated as 30 °C (303 K) according to the Md_{30} formulation. The Md_{30} temperature means the temperature at which half of austenite phase at plastic strain of 30% is transformed to ferritic phase. The 304 SS shot-peened by partially stabilized zirconia (PSZ) shots produces up to 10% martensite, depending on the peening intensity.

Delayed fracture of the 304 SS with strain-induced martensite were studied by some researchers [2, 3]. Carpenters group [4, 5] utilized AE technique to study the delayed fracture of sensitized 304 SS under dynamic straining or constant extension rate testing (CERT) in charging solution. They reported that the intergranular (IG) cracking occurs when hydrogen charging was continued till the maximum tensile load, and that AE signals were produced by grain boundary separation. They proposed a hydrogen transport model by moving dislocations. This model implies that both the fast and sufficient supplies of hydrogen to the martensite are possible by gliding dislocations accompanying hydrogen.

We also monitored AE signals from hydrogen related brittle cracking of sensitized 304 and 316 SS [6]. We monitored much AE signals from the 304 SS when it is exposed to both the

dynamic plastic deformation (CERT) and hydrogen charging, simultaneously. AE emission rate increased during plastic loading at higher crosshead speed. No emission from 316 SS suggested that brittle cracking occurs when martensite is formed during dynamic plastic straining. Results by Carpenter and our group suggest that hydrogen-assisted cracking or grain boundary separation occurs when sufficient hydrogen is transported to the martensite by dynamic straining or gliding dislocations. It is noted that the CERT tests in Carpenter study were completed within 1,800 s (30 minutes) and those in our group were 20,000 s (6.6 hrs).

Purpose of this research is to study whether the gliding dislocation is necessary condition for delayed fracture of non-sensitized 304 SS with strain-induced martensite using AE technique. Here, the martensites less than 10% were produced by shot peening at room temperature. We also monitored AE signals from duplex SS under hydrogen charging and estimated apparent diffusion coefficient of hydrogen in the shot-peened 304 stainless steel.

Test Specimen and Test Procedure

Specimens are as-received 304 SS and duplex (0.03C-4.95Ni-21.6Cr) SS with 2-mm thickness, 19-mm width and 76-mm length. One side of the 304 SS strips was shot-peened with 0.6-mm diameter PSZ shots by direct compressed air. Peening strength (expressed by the arc height of Almen strip A, or in mmA) was changed from 0.3 mmA to 0.8 mmA by changing the air pressure and peening time. All specimens were peened so as the coverage is higher than 100% except one sample (#31) with coverage of 40%. The Md_{30} temperature of the 304 SS is calculated as 30 °C. As shown in Fig. 1, temperature of the strip increases rapidly just after the peening starts, and reaches 50 to 60 °C. Thus the martensite is mainly produced during early time of the peening. Amount of the martensite in the peened strips was measured by a magnetic-type ferrite meter, and found to be from 0.5 % to 10 %. Figure 2 shows transverse microphotograph of the peened type-304 SS strip (0.6 mmA) with martensite from 5 to 7.5 %. Here, the martensite (black portion) was revealed by etching in the surface layer up to 0.12 mm.

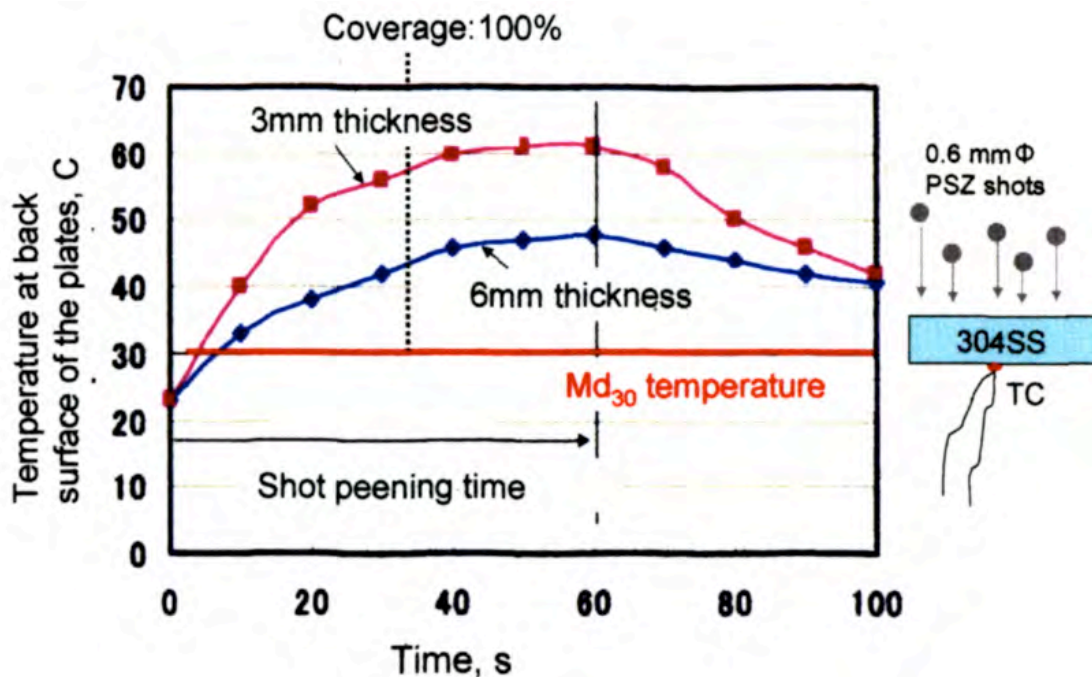


Fig. 1. Change of back surface temperature of the Type-304 SS strip during shot peening.

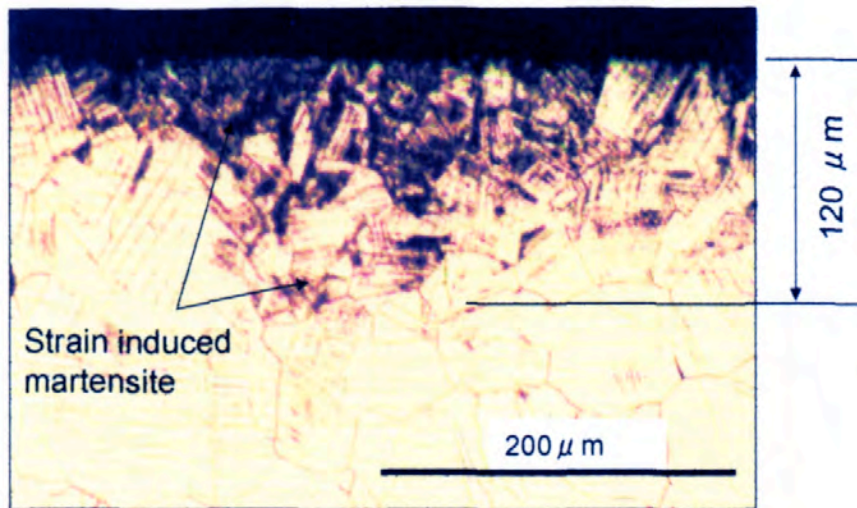


Fig. 2. Transverse structure of peened 304 SS strip.

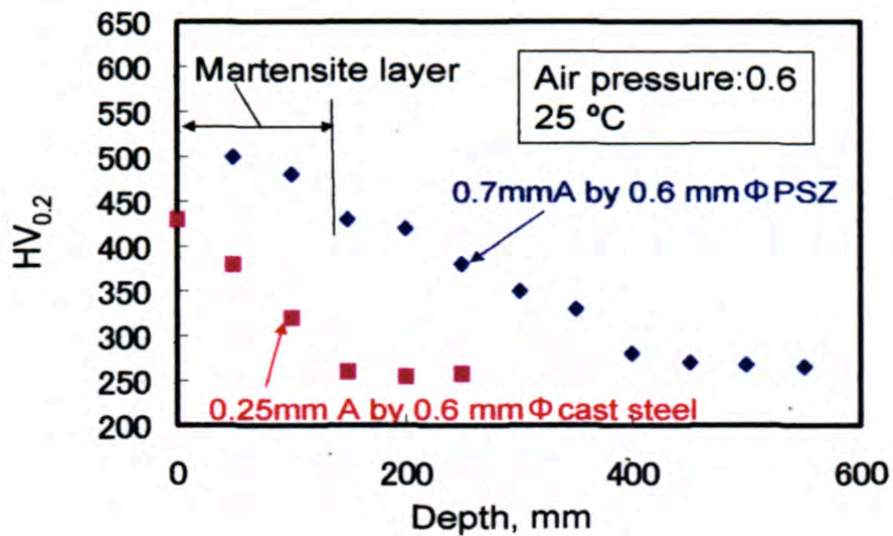


Fig. 3. Comparison of hardness profiles of 304 SS plate shot-peened by PSZ and cast-steel shots at 20°C.

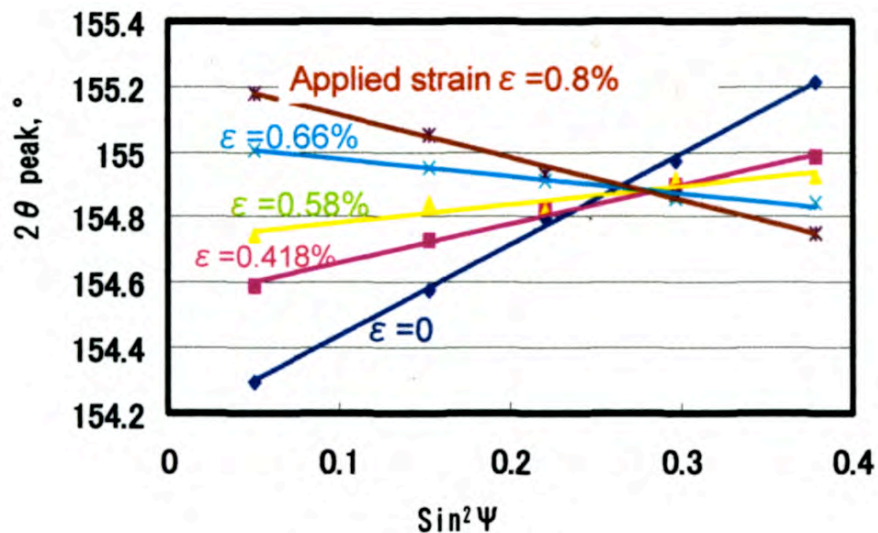


Fig. 4. 2θ peak angle vs. $\sin^2 \Psi$ for shot peened ($\epsilon = 0$) and three point bent strips.

Figure 3 compares the hardness profiles in the depth of peened 304 SS. Here the steel strips were peened by 0.6-mm PSZ shot or cast steel shots. Peening intensity reaches 0.7mmA for the PSZ peening but that by cast steel shot only to 0.25mmA. Higher peening intensity by PSZ shots appears to be due to its high fracture toughness ($K_{IC} = 12 \text{ MPa}\sqrt{\text{m}}$) and hardness. The strain induced martensite exists in the hardened layer with hardness higher than 430 Hv. This implies that the 304 SS peened by cast steel shots does not show susceptibility to the hydrogen cracking with less martensite.

We next measured surface stress of as-peened and three-point bent 304 SS strips since the strips were hydrogen charged while being bent. X-ray diffraction method was used. The stresses were calculated by the $\sin^2 \Psi$ method. Figure 4 shows changes of slopes in 2θ vs. $\sin^2 \Psi$ relation. Here, the negative slope indicates compressive stresses and the positive slope tensile stresses. It can be seen that the outer fiber stress of the as-peened 304 SS strip ($\epsilon = 0$) and bent strips with strain ϵ lower than 0.58% are compressive, while the strips bent at strain higher than 0.66% show tensile stresses. As the delayed fracture occurs under tensile stresses, we bent the strips so that the surface strain, measure by strain gage, is higher than 0.66%. Outer fiber stresses, calculated from the slopes in Fig. 4, are shown in Fig. 5. The stresses increased nonlinearly with bending strain. In most experiments, we applied 500 MPa by giving strips 0.8% strain.

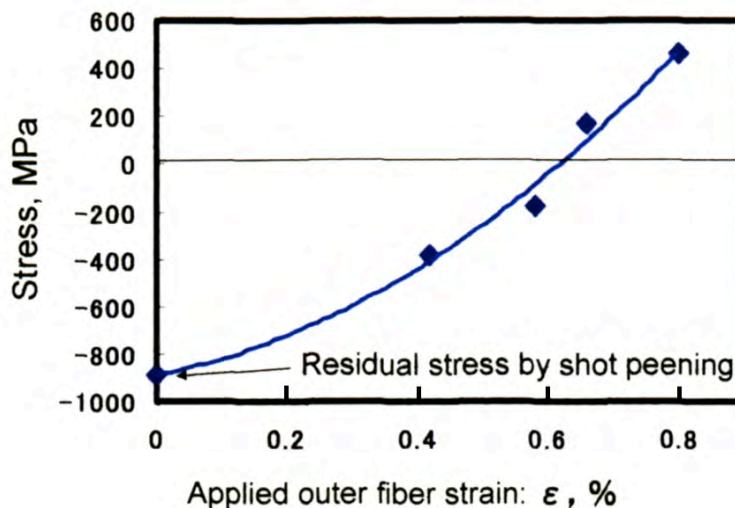


Fig. 5 Change of outer fiber stresses of three point bent strips.

Next we measured the depth distribution of tensile stress using a modified hole-drilling method [7]. In this modified method, stress distribution in depth was calculated from the slope of the released strain by hole drilling. Figure 6 shows depth distribution of residual stresses of peened strip (dashed line) and actual stresses of the bent strip. Axial stresses (blue data) of the bent strip at 0.8% strain are higher than 200 MPa in the surface layer of 0.15 mm, and transverse stresses are compressive. It is noted that the delayed cracks occur, as shown later, in the surface layer less than 0.15 mm thick.

Hydrogen charge and AE monitoring methods are the same as used in our previous study [8]. Bent strips were hydrogen charged using a 20-mm diameter glass cell attached on the convex plane. Cathode charging is performed by direct current at density of 0.6 mA/cm^2 in a 1 N boric acid solution with 0.033 mol/l KCl and 0.02 mol/l thiourea. The thiourea accelerates the hydrogen permeation into the strips by reducing the combination of adsorbed hydrogen ions (H^+) to

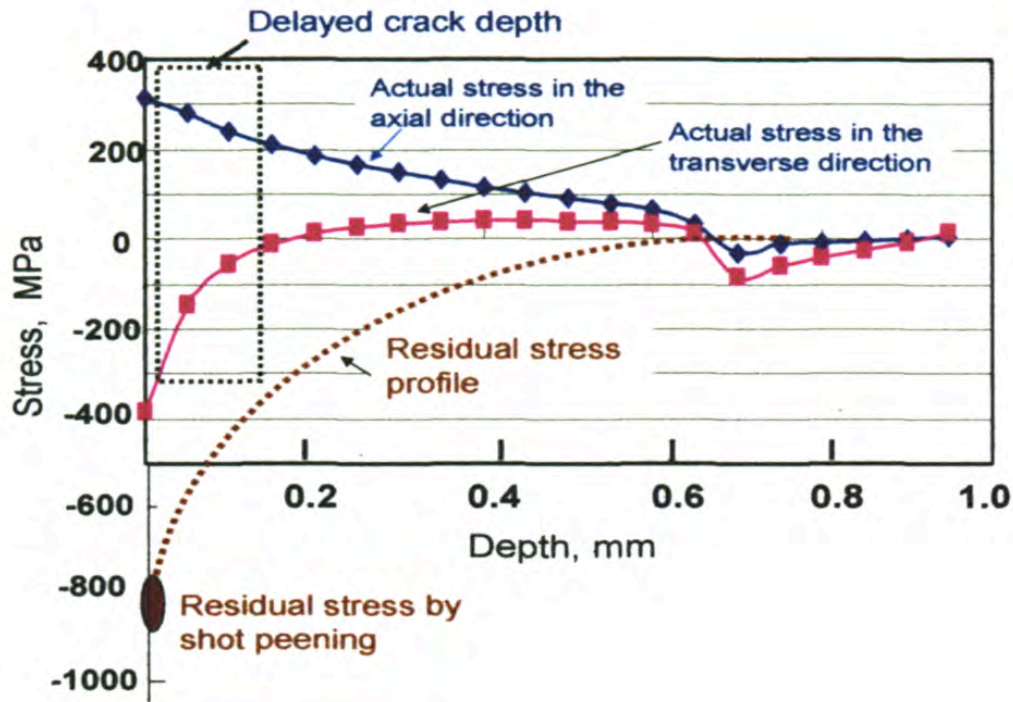


Fig. 6. Stress profile in peened and bent strips to 0.8% outer fiber strain.

hydrogen gas (H_2). AE signals were monitored by two resonant type sensors (PAC Pico) mounted on the concave plane at 18 mm and 36 mm from the center of the glass cell. Outputs of the sensors were amplified 40 dB and acquired as digital data. In addition to in-situ AE monitoring, we used a step-wise strain increasing (SSI) method to detect hidden cracks underneath the surface [7]. It is noted that the strips are hydrogen charged under a statically bent strain. Thus, dislocation gliding during hydrogen charging is less compared to that by the dynamic straining method or the CERT. Hydrogen charge was continued for 2,000 hrs at room temperature.

Test Results

Results of the shot-peened 304 SS strips

Test result is summarized in a diagram (Fig. 7) of charge time (H^+ amount) vs. martensite content of peened strips. The samples that suffered delayed cracks are represented by red solid lines with crack number and length, while the samples free from delayed crack are by black dotted line. Sample-31, out of the plot area, designates the sample with peening coverage of 40%. This sample showed short cracks of less than 100 μm in peened craters. Thus, the sample -31 is located in crack zone. Blue slant line represents a tentative boundary between crack/no-crack regions. Characteristic feature of delayed cracks of samples-1, -2, -3, -11 and -14 are shown below.

For sample-1 with martensite of 7.5-10% with bending strain of 1%, we could not observe any open crack after being charged for 170 hours, as shown in top photo of Fig. 8. However after the SSI test up to strain of 2.2%, we observed several fine cracks, as shown in the bottom photo. Figure 9 shows a relation between step-wise strain and AE generation during the SSI test of sample-1. We detected five events during the first strain increase from 1% to 1.45%. This indicates that the crack produced by hydrogen charging under static strain is buried underneath the surface, and dynamic straining is needed for opening the closed crack. Transverse microphotograph of this sample is shown in Fig. 10. We observed 9 short transverse cracks less than 0.2 mm long.

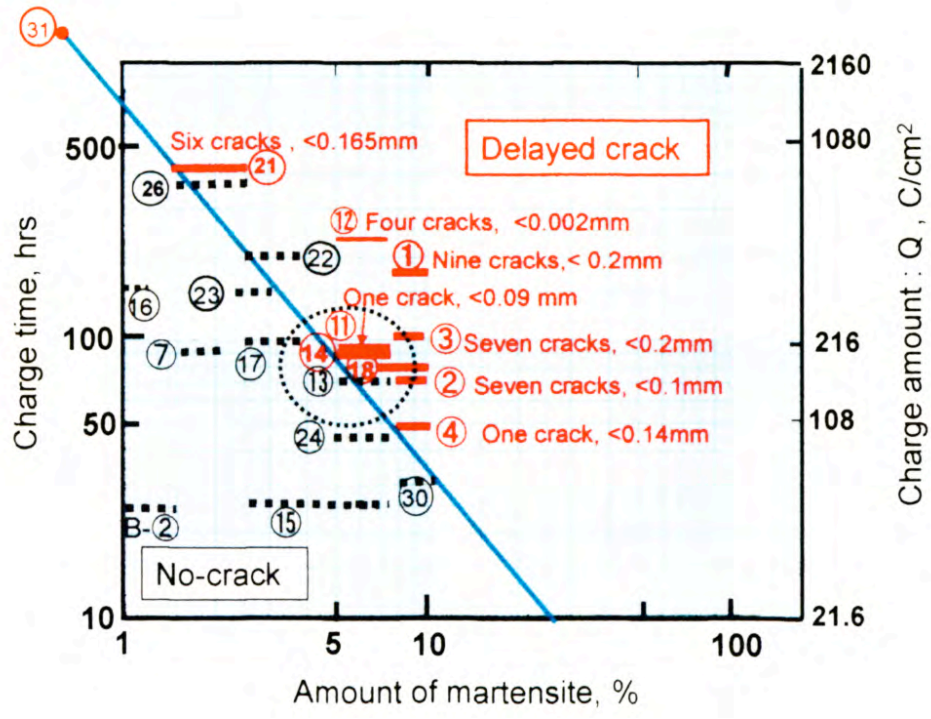


Fig. 7. Tentative boundary for crack/non- crack region in peened strips as function of amounts of martensite and hydrogen charge.

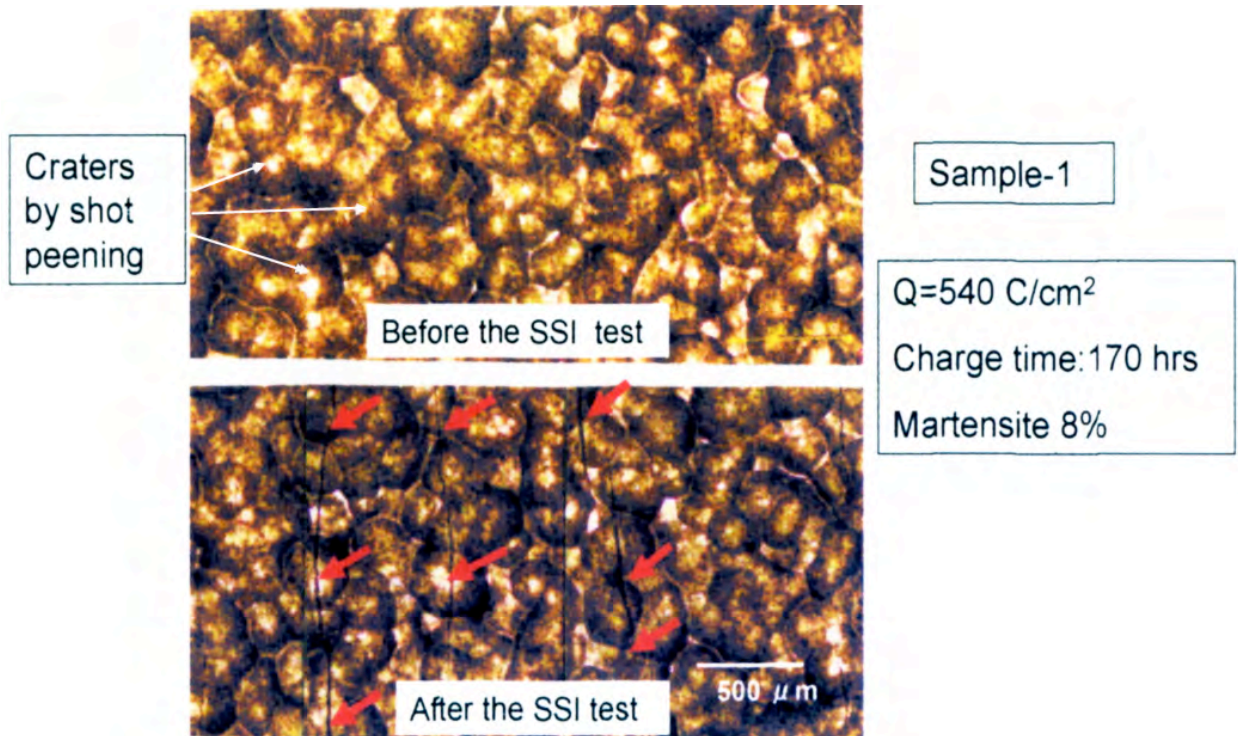


Fig. 8 Surface appearance of sample-1 after being charged for 170 hours (top) and after the SSI test with fine cracks (bottom).

Capturing of short cracks by specimen sectioning to reveal the crack distribution density is generally very difficult work. Successful results for samples-2 and-3 are shown in Fig. 11. Here the central loading point is at 3 mm. Seven cracks were generated over 5 mm width for sample-2,

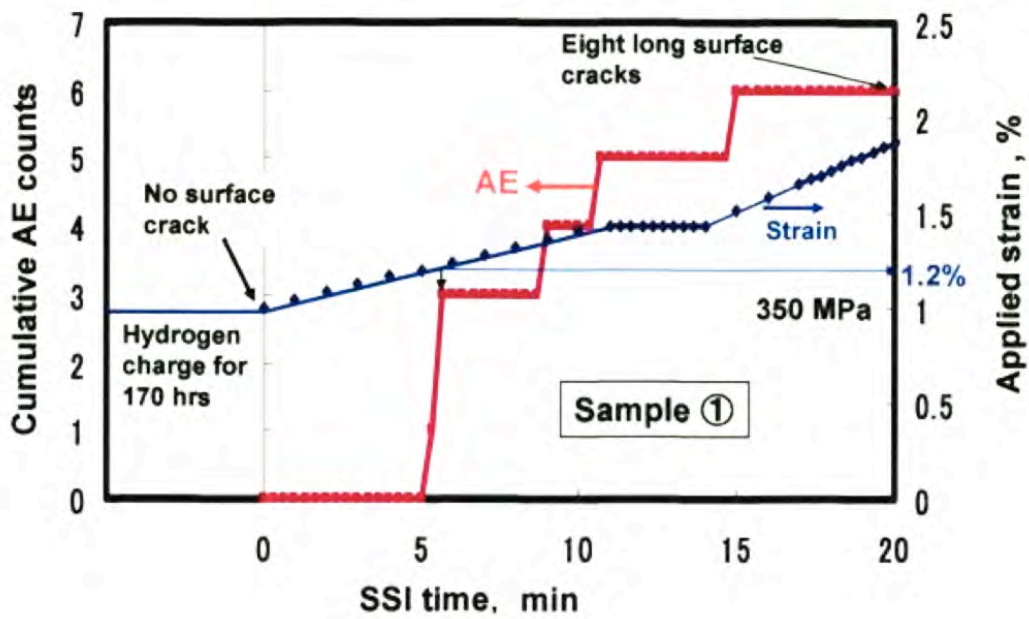


Fig. 9. Relation between step-wise strain and AE generation during the SSI test of sample-1.

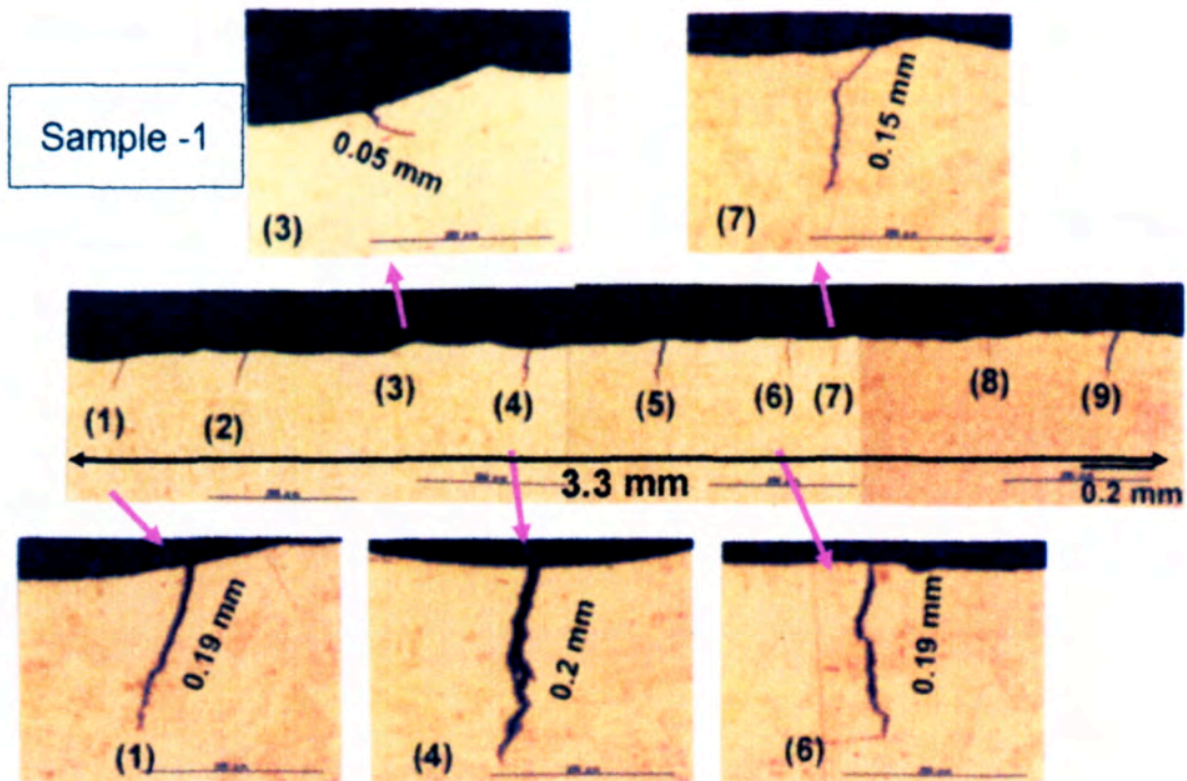


Fig. 10. Nine TG-cracks at transverse section of sample-1 around maximum applied strain. Martensite amount = 8%, charge amount: $Q = 540 \text{ C/cm}^2$.

and over 2 mm for sample-2. Surface crack length after the SSI test of sample-3 were from $80 \mu\text{m}$ to $330 \mu\text{m}$ except one long crack of 8.1 mm. Figure 12 shows SEM of delayed cracks observed in sample-2. Curved and branched cracks were observed. This is in contrast to delayed cracks in high strength ferritic steel, which are generally straight without any branching. Thus, the zigzag and branched cracks in Fig.12 are unique crack observed only for austenitic steel with

martensite. The branching is due to complex distribution of the martensite as shown in Fig. 2 and is indicative of the strain-induced martensite being a path for hydrogen diffusion and crack site.

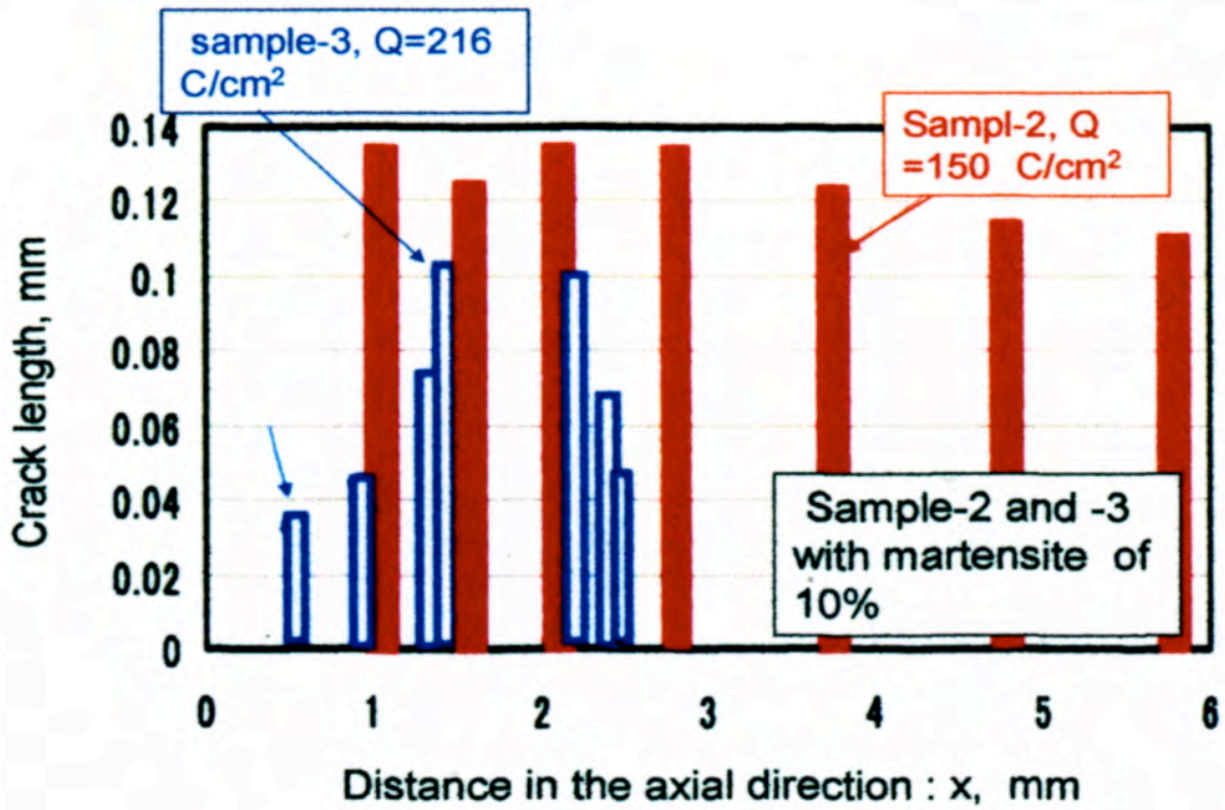


Fig. 11. Distribution of micro-cracks for samples-2 and -3.

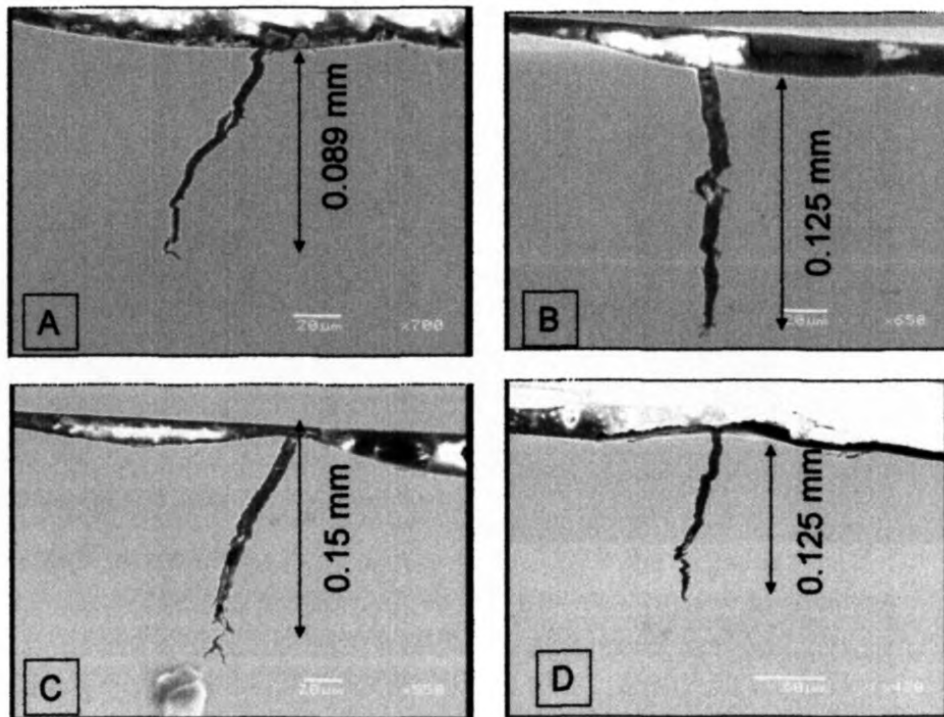


Fig. 12. Some transverse cracks for sample-2.

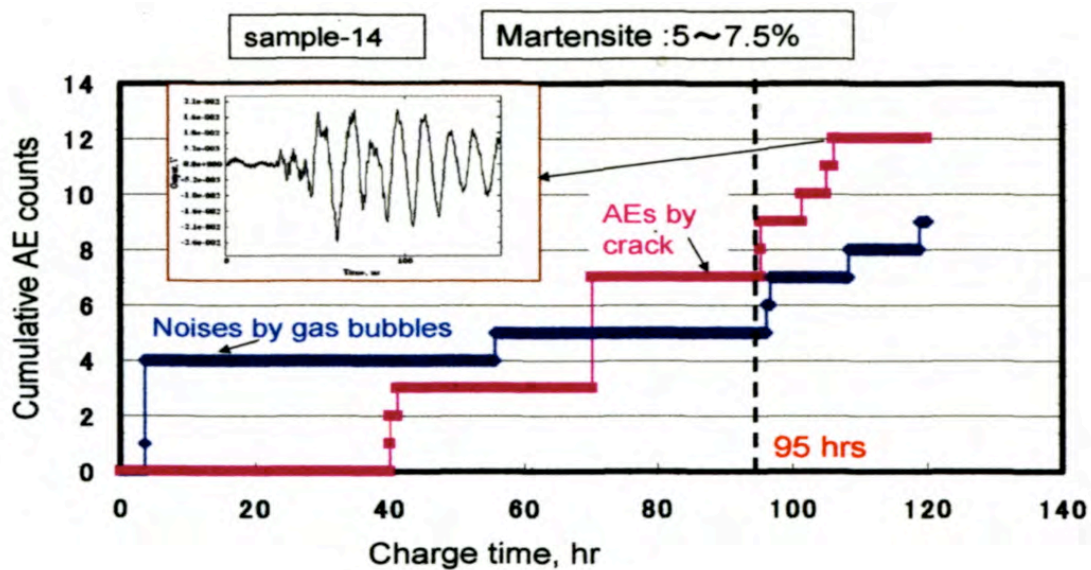


Fig. 13. Change of cumulative AE counts with hydrogen charging time for sample-14.

While small hidden cracks were produced during static charging, we next studied whether AE can be detected during static charging. Figure 13 represents a result for sample-14 with 5-7.5% martensite. We first detected only noise by hydrogen gas bubbles, but after 40 hours, we detected three signals. After 95 hours, intermittent AE signals were emitted. The AE signal from crack generation possesses dispersive Lamb-wave characteristics, while that from gas bubbles is composed of single frequency, as shown in Fig. 14. Though we could not detect any crack by sectioning of this sample, this sample was classified as the sample in cracking zone of Fig. 4 owing to AE signals. Another example for sample-18 with 5-7.5% martensite is shown in Fig. 15. We detected three strong AE signals at 88 hours. Sectioning revealed one crack with 150- μm depth.

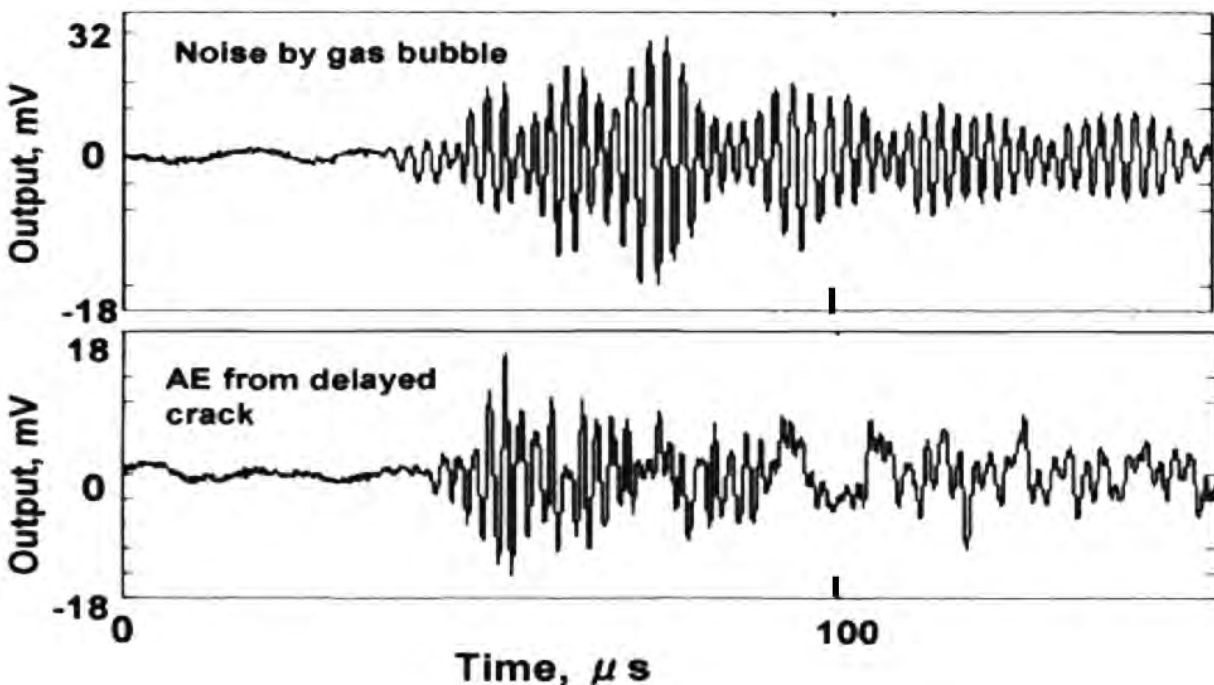


Fig. 14. Typical waveforms from gas bubbles (the upper) and from internal crack.

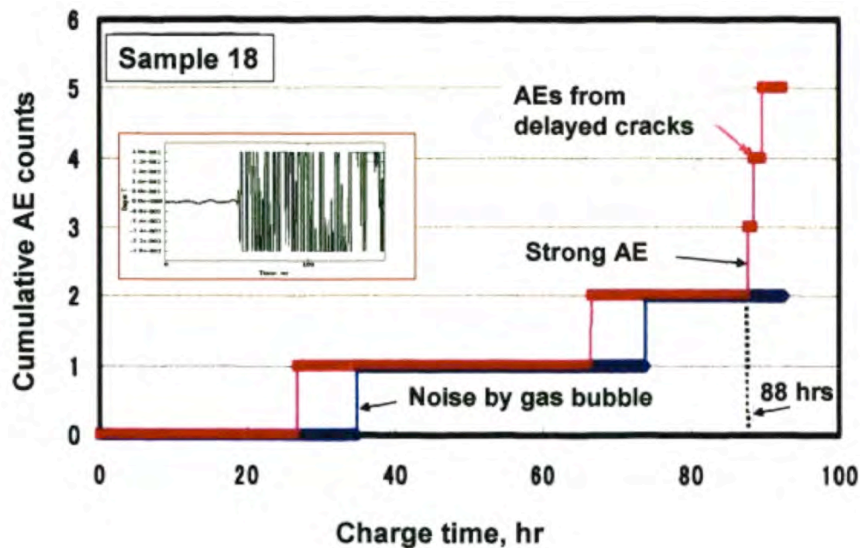


Fig. 15. Change of cumulative AE counts with hydrogen charging time for sample-18.

Based on the fact that 1) the crack length of sample-2 is 100 μm after 70 hours charging, 2) crack length of sample-3 is 200 μm after 100 hours and 3) that of sample-11 is 150 μm after 88 hours, we estimated that hydrogen can diffuse in the martensite-bearing 304 SS up to 140 μm after 90 hours. Thus, apparent diffusion coefficient of hydrogen in martensite (7.5-10%) bearing 304 SS is of the order of $10^{-9} \text{ cm}^2/\text{s}$ at room temperature.

Results of the duplex stainless steel

Duplex stainless steel with 50% ferrite phase is demonstrated to suffer the delayed fracture. Sensitization accelerates the delayed fracture. Our work revealed that the hydrogen could diffuse up to 2 mm ahead of the main crack using K-controlled CT specimen. However, the hydrogen-induced crack of the duplex SS strip at constant bending strain is smaller and different from that observed in the K-controlled CT specimen.

Figure 16 shows the transverse photo of the steel that was hydrogen charged for 40 hours. We see crack-like attack along grain boundary. It is noted that crack number is extraordinarily large, but cracks are shallow and at less than 100 μm . Due to numerous surface cracks, we detected a number of AE during hydrogen charge, as shown in Fig. 17. First AE signal was detected after approximately 10 hours of charging.

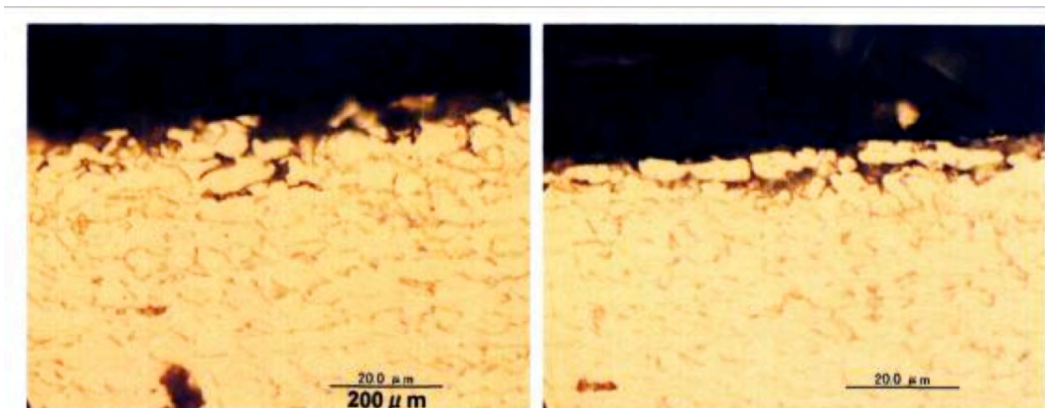


Fig. 16. Transverse photo of the duplex stainless steel absorbed hydrogen for 40 hours at bending strain of 1.3%.

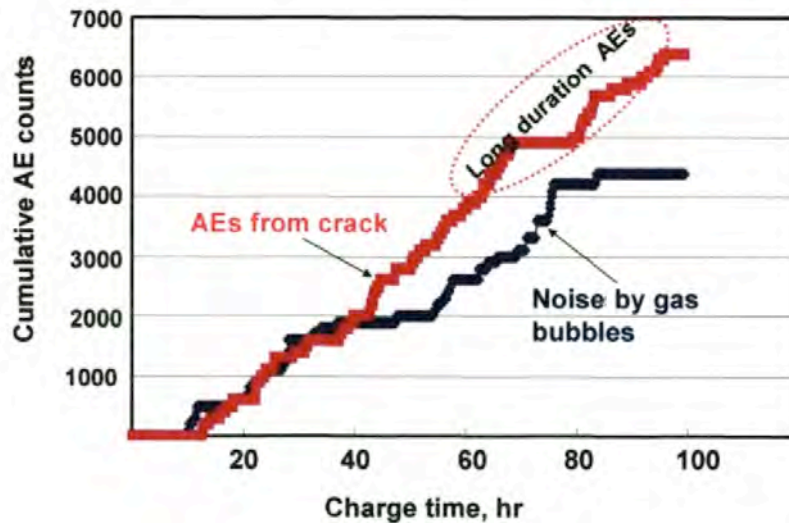


Fig. 17. Change of cumulative AE counts with charge time for the duplex SS at constant bending strain of 1.3%.

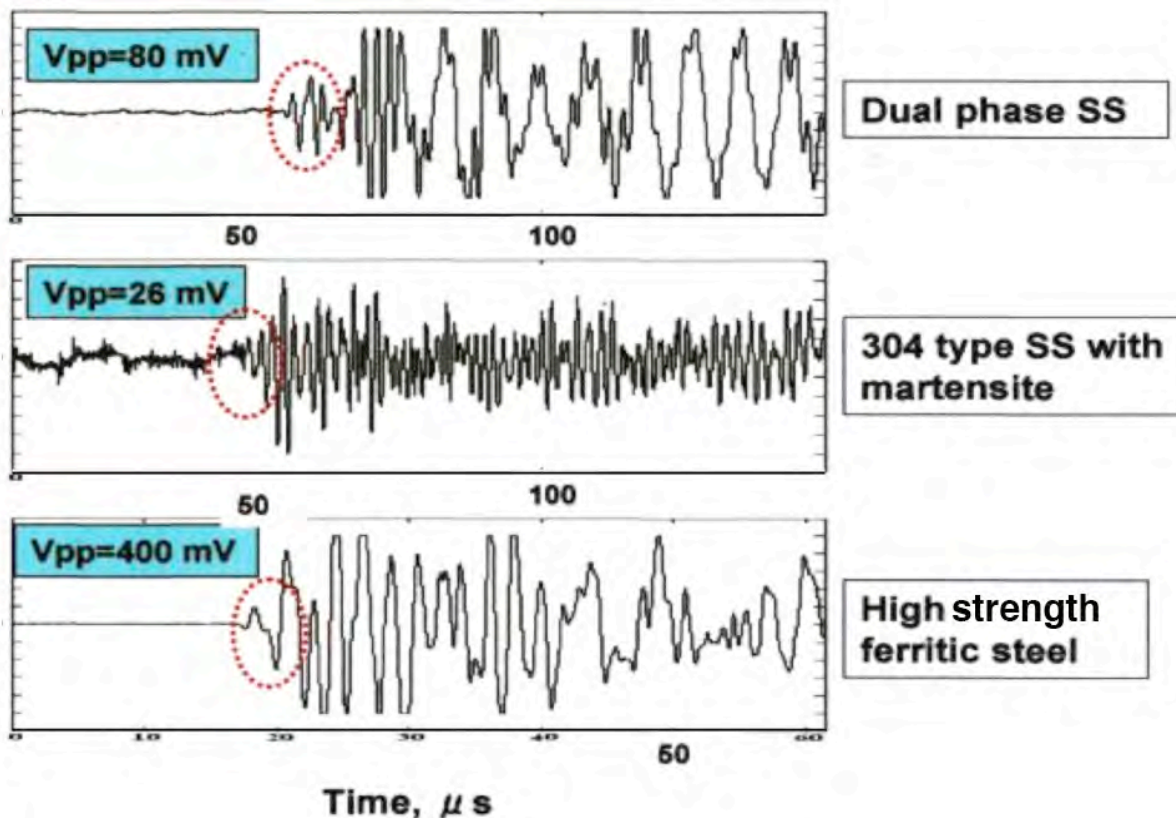


Fig. 18. Comparison of waveforms and amplitudes of AEs detected for two types of SS and high-strength ferritic steel.

Figure 18 compares waveforms and amplitudes of AE signals detected for two types of stainless steels and high-strength ferritic steel. Time scale of the bottom AE is expanded from top two, since it is cited from our previous data [7]. Amplitude or Vpp of the So-mode wave from martensite-bearing 304 SS is smallest among the three. The Vpp of 80 mV from duplex stainless steel is 3 times larger than 304 SS but 5 times smaller than Vpp (400 mV) from the high-strength ferritic steel. It is noted that the high-strength steel strip of 2 mm thickness completely fractured within 2 hours of charging.

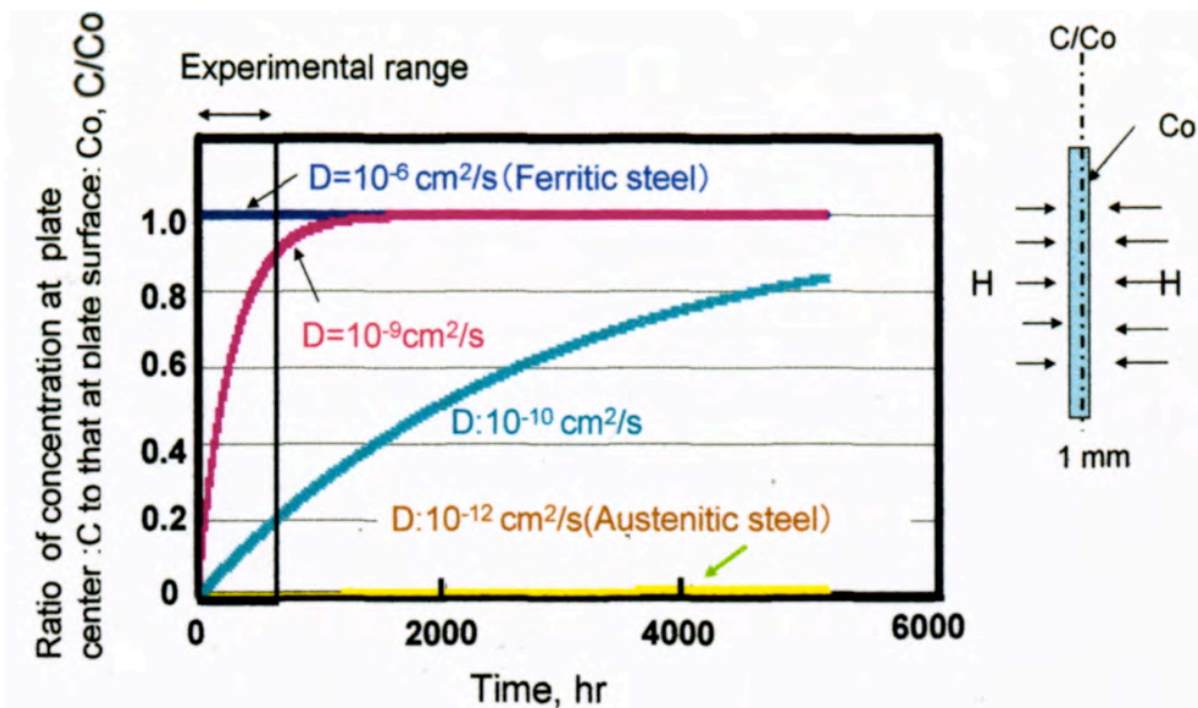


Fig. 19. Transient hydrogen concentration at 1-mm distance from plate surface with different diffusion coefficients.

Apparent hydrogen diffusion coefficient of martensite- or ferrite-bearing austenitic SS

Diffusion coefficient of hydrogen in ferritic steels is reported as $10^{-6} \text{ cm}^2/\text{s}$ that is 10^6 times faster than in the austenitic SS with $10^{-12} \text{ cm}^2/\text{s}$. As shown in Fig. 19, hydrogen hardly diffuses in the austenitic steel within our test time of less than 2000 hours. This figure represents transient hydrogen concentration at mid-section of 2-mm thick plate, which absorbs hydrogen from both surfaces. We estimated above apparent diffusion coefficient of hydrogen in 304 SS with 10% martensite as $10^{-9} \text{ cm}^2/\text{s}$. This estimation is based on the average crack length and charge time. We can roughly estimate the crack time by equating the charge time to the crack time. However, we must remember that the delayed crack in the shot peened 304 SS does not progress beyond 200 μm within 1000 hours.

Conclusion

We studied delayed fracture of shot-peened 304 SS with strain-induced martensite less than 10%. AE technique was successfully utilized for the detection of small cracks during both hydrogen charging of bent strips and SSI test of hydrogen-charged strips. Results are summarized below.

- 1) 304 stainless steel with strain-induced martensite produces subsurface delayed cracks under constant tensile stress. The cracks are not straight, but zigzag and often branched. Neither the gliding dislocation nor sensitization is a necessary condition for the delayed crack of metastable austenitic stainless steel.
- 2) Shot-peening produces less than 10% martensite in the surface layer of 150-200 μm . Delayed cracks occur in the hardened surface layer and does not progress beyond the hardened layer.

- 3) Apparent diffusion coefficient of hydrogen in the shot-peened 304 SS with 10% martensite was estimated as 10^{-9} cm²/s. Strain induced martensite appears to be the path for hydrogen diffusion.

References

- 1) K. Kurose, H. Cho, T. Ogawa and M. Takemoto, *Progress in Acoustic Emission XIV*, (2008) JSNDI, p. 121.
- 2) M.L. Holzworth, *Corrosion*, **25** (1968) 107.
- 3) N. Ohtani, S. Asano, Y. Fujishima and Y. Yamamasu, *J. Japan Inst. Metals*, **37** (1977) 746.
- 4) S.H. Carpenter and D.R. Smith, *Metallurgical Transaction A*, **21A** (1992) 1933.
- 5) S.H. Carpenter, K. Ono and D. Armentrout, *Progress in Acoustic Emission XIII*, (2006) JSNDI, p. 55.
- 6) H. Cho and M. Takemoto, *Advances in Acoustic Emission 2007*, (2007) AEWG, p. 360.
- 7) M. Takemoto, *Corrosion Engineering of Japan (Boshoku-gijyutsu)*, **30** (1981) 203.
- 8) M. Takemoto, M. Nakamura, S. Masano and S. Ueno, *Progress in Acoustic Emission XIV*, (2008) JSNDI, p. 135.

ON THE STRAIN RATE DEPENDENCE OF ACOUSTIC EMISSION DURING HYDROGEN-ASSISTED CRACKING OF HIGH CARBON STEEL

EVGENY D. MERSON¹, DMITRI L. MERSON¹, MIKHAIL M. KRISHTAL¹
and ALEXEI VINOGRADOV^{1,2}

¹ Laboratory for the Physics of Strength of Materials and Intelligent Diagnostic Systems, Togliatti State University, Togliatti, 445667, Russia. ² Department of Intelligent Materials Engineering Osaka City University, Osaka, 558-8585, Japan

Abstract

The classic problem of hydrogen-assisted cracking (HAC) is revisited in the present work aiming at clarification of damage mechanisms leading to failure of hydrogen charged high-carbon steels under load. Plastic deformation and hydrogen-assisted intergranular and transgranular fracture have been clearly distinguished by acoustic emission (AE) at different strain rates. AE features corresponding to these major mechanisms are discussed.

Keywords: Hydrogen-assisted cracking, strain rate, high carbon steel.

Introduction

Hydrogen-assisted cracking (HAC) is a well-known phenomenon causing substantial degradation of properties in steels and high strength alloys. The term “*hydrogen-assisted cracking (HAC)*” has been loosely defined and encompasses a number of different mechanisms. It is often considered to be interchangeable with “*hydrogen-induced cracking (HIC)*” and/or “*hydrogen embrittlement (HE)*”. In this article, HAC refers to a generic class of phenomena where hydrogen plays a significant role in the initiation or propagation of cracks. Terms *HIC* and *HE* are left for narrower definitions of cracking, which commonly occurs under direct influence of hydrogen (e.g., blistering) and a general loss of ductility of a metal resulting from absorption of hydrogen, respectively. Besides, the deteriorative influence of hydrogen is important for fracture toughness, fatigue crack growth resistance, etc. [1]

Being the root cause of many service-related failures and technological catastrophes, HAC attracted much attention from scientists and engineers aiming at failure risk reduction and alleviation of the damage effects induced by hydrogen. Eventually, the prevention of hydrogen-affected technological catastrophes relies heavily on in-depth understanding of a HAC phenomenon on one hand and on the success in developing a viable technique capable of in-situ monitoring of hydrogen-induced damage accumulation in loaded metallic articles on the other. Acoustic emission (AE) is among the most promising techniques for this purpose. The high sensitivity of AE technique to HAC has been convincingly demonstrated in a large number of publications, e.g. [2-7]. A vast majority of AE tests associated with HAC have been performed so far using either constant load (stress) conditions in stress corrosion cracking (SSC) testing [8, 9], slow strain rate tests (SSRT, with nominal extension rate in the range of 1×10^{-7} to 1×10^{-5} s⁻¹) utilizing smooth samples or fracture toughness and crack propagation tests on notched and/or pre-cracked samples [10]. These conditions are most often met in the industry. However, HAC is strain-rate dependent [1]. At room temperature HAC is particularly pronounced at relatively low strain rates, ($\sim 10^{-5}$ s⁻¹ for low carbon steels) [11]. Despite this fact, the strain-rate dependence of HAC has been just scarcely studied [12, 13]. No AE studies concerning the strain-rate depend-

ence of hydrogen-assisted damage accumulation have been performed so far to the author's knowledge. Understanding of the interaction between the mechanisms involved in HAC under different strain rates is supposed to shed some light on the mutual role of these mechanisms.

The objective of this work is to determine the effect of strain rate on fracture mechanisms of hydrogen-charged high carbon steel with help of acoustic emission.

Experimental

High carbon steel 70 in Russian designation (AISI 1070 is a close analogue) was chosen for the present study because it is widely used industrially as spring steel, which is known to be prone to premature failure due to HAC [14]. The chemical composition of this steel is shown in Table 1. The samples were machined to have a rectangular shape of 120 mm length and 20 mm width. The samples with different thickness $\delta = 1.5, 1.8$ or 2.5 mm were tested. They were thermally treated using a schedule that is commonly used for this type steels: 1) quenching from $850 \pm 10^\circ\text{C}$ in oil; 2) low tempering at temperature of $240 \pm 10^\circ\text{C}$ for 1 h; 3) primary tempering at $450 \pm 10^\circ\text{C}$ for 2 h followed by cooling in air. The hardness after this treatment was of 49 ± 2 HRC.

For hydrogen charging, some of the specimens were electrolytically plated with a Zn layer of 10- μm thick from an alkaline solution containing 110-120 g/l NaOH and 12-14 g/l ZnO. The plating (and hydrogen charging) was performed at current density of 8 A/dm^2 for 20 min. Reference specimens were left unplated for comparison.

Three-point bending mechanical testing of the samples with and without coating was performed at room temperature using a screw driven Instron-type frame. Loading was performed at three different crosshead velocities resulting in three different initial strain rates: "slow" - $\dot{\epsilon} = 3 \times 10^{-6} \text{ s}^{-1}$, "middle" - $\dot{\epsilon} = 3 \times 10^{-4} \text{ s}^{-1}$ and "high" - $\dot{\epsilon} = 3 \times 10^{-3} \text{ s}^{-1}$. The slowest strain rate corresponds to the upper bound of the strain rates used typically during SSRT. The ductility was characterized by the maximum value of the deflection at break Δ_{max} .

Table 1. Chemical composition of steel 70.

C	Si	Mn	Cr	S	P	Cu	Ni	Fe
0.70	0.29	0.72	0.03	0.006	0.013	0.06	0.02	balance

AE was recorded using a home-made PC-controlled system with a 12-bit ADC at the core. The broadband piezoelectric transducer MSAE-L2 (Microsensors AE, Russia) with a low noise built-in 27-dB preamplifier was mounted on the specimen with vacuum oil as a couplant. The signal from the sensor's preamplifier output was transferred through a main filter-amplifier FA-010 with the 40-dB gain and the frequency band 50-1200 kHz. The laboratory noise did not exceed 30 μV (peak-to-peak). The burst AE signals with relatively high amplitude above 1 mV (30-dB threshold) were recorded and counted synchronously with the load signal. The waveforms of 4096 readings were stored on hard disk. The true root-mean-square voltage U_{rms} with 100 ms integration time was measured by the FA-010 unit. The U_{rms} signal was fed to a 14-bit ADC for continuous acquisition at 1 kHz sampling rate.

Hydrogen content of the samples was measured by a hydrogen analyzer LECO RH-402; the concentration of hydrogen C_{H} was evaluated with a nominal accuracy of less than 2 ppm. (In

Table 2, C_H is given in $\text{cm}^3/100 \text{ g}$ of steel. 1 ppm = 1.11 $\text{cm}^3/100 \text{ g}$.) The specimens of $3 \times 3 \times \delta$ mm (with $\delta = 1.5$ or 2.5 mm thickness) were prepared from charged and uncharged plates. The fracture surface was observed by a scanning electron microscope LEO1455VP.

Results

Results of measurements of the hydrogen content are shown in Table 2. It is evident that a small amount of dissolved hydrogen is present even in the as-received commercial grade steel (reference specimens). However, cathodic charging significantly increases the hydrogen amount (by an order of magnitude). After hydrogenation the ductility in bending Δ_{\max} notably reduces at all strain rates, including the highest one $3 \times 10^{-3} \text{ s}^{-1}$. The effect of embrittlement is more pronounced at slower strain rates, as is reasonably expected. In fact, a similar negative strain rate dependence of Δ_{\max} is also visible for the uncharged reference specimens despite a substantially smaller amount of hydrogen dissolved in these specimens. Of course, this apparent dependence of Δ_{\max} on $\dot{\epsilon}$ is less pronounced in uncharged reference specimens.

Table 2. Concentration of hydrogen, C_H , maximum deflection Δ_{\max} and cumulative AE count N_{Σ} .

Specimen thickness, δ , mm	Specimen state	C_H , $\text{cm}^3/100\text{g}$	Strain rate $\dot{\epsilon}$, s^{-1}					
			$3 \cdot 10^{-3}$		$3 \cdot 10^{-4}$		$3 \cdot 10^{-6}$	
			Δ_{\max} , mm	N_{Σ}	Δ_{\max} , mm	N_{Σ}	Δ_{\max} , mm	N_{Σ}
1.5	reference	1.0	25.7	39	27.4	73	18.9	241
	charged	14.5	11.5	53	8.1	383	6.3	2609
1.8	reference	-	18.3	32	17.3	60	16.9	317
	charged	-	14.6	84	10.1	385	6.5	5172
2.5	reference	1.1	18.4	-	13.8	102	12.9	279
	charged	12.4	10.3	-	11.7	624	7.0	3552

The scanning micrographs of the fracture surface shown in Fig. 1 reveal mixed ductile-brittle fracture patterns. The fraction of brittle and ductile components of the relief, however, varies strongly depending on testing conditions. Commonly, the decrease in $\dot{\epsilon}$ and/or the increase of C_H gives rise to the increasing fraction of brittle facets in the fracture relief. The fracture surface of the reference specimens tested at highest strain rate of $3 \times 10^{-3} \text{ s}^{-1}$ is almost entirely ductile; ductile dimples are dominant although some transgranular microcracks with brittle features can also be seen as typical “steps” between the MnS inclusions, Fig. 1a. Figure 2a illustrates the brittle steps at the surface associated with sulphide decohesion. The X-ray energy-dispersive analysis, Fig. 2b, revealed an excess amount of S and Mn atoms in the selected area marked “A”. The fracture surface of coated specimens is distinctly different. This is particularly clear for the specimens tested at the slow strain rate $3 \times 10^{-6} \text{ s}^{-1}$, Fig. 1f, where a typical brittle fracture pattern with some ductile dimples is seen. The crack propagates in the intergranular manner across the whole fracture surface while the signatures of sulphide decohesion, such as those seen in Fig. 2a, are very rare. Fracture surface patterns of other specimens, Figs. 1b-e, are of mixed type between the two extremes (Fig. 1a and f) discussed above. Hence, one can see that the area fraction of ductile or brittle component is controlled by the strain rate and the amount of dissolved hydrogen.

Uniform plastic deformation caused by dislocation motion in annealed single- and polycrystals of pure metals generates a continuous noise-like AE signal [15]. Hardened or embrittled

materials with restricted or impeded dislocation motion are prone to micro- and macro-cracking since cracks serve as primary mechanisms responsible for local stress relaxation instead of dislocations. Hence, with increased hardening and reduced ductility the continuous AE component, such as that exemplified in Fig. 3a, should decrease while the discrete, burst component, Fig. 3b, should increase. Indeed this is observed clearly in the present work. The ductility reduction caused either by hydrogen charging or low strain rate results in the remarkable increase of the burst type AE signals during testing (c.f. N_{Σ} in Table 2). This trend of the dependence of N_{Σ}/Δ_{max} on $\dot{\epsilon}$ is shown in Fig. 4 with different thickness δ . The N_{Σ}/Δ_{max} ratio does not depend on δ .

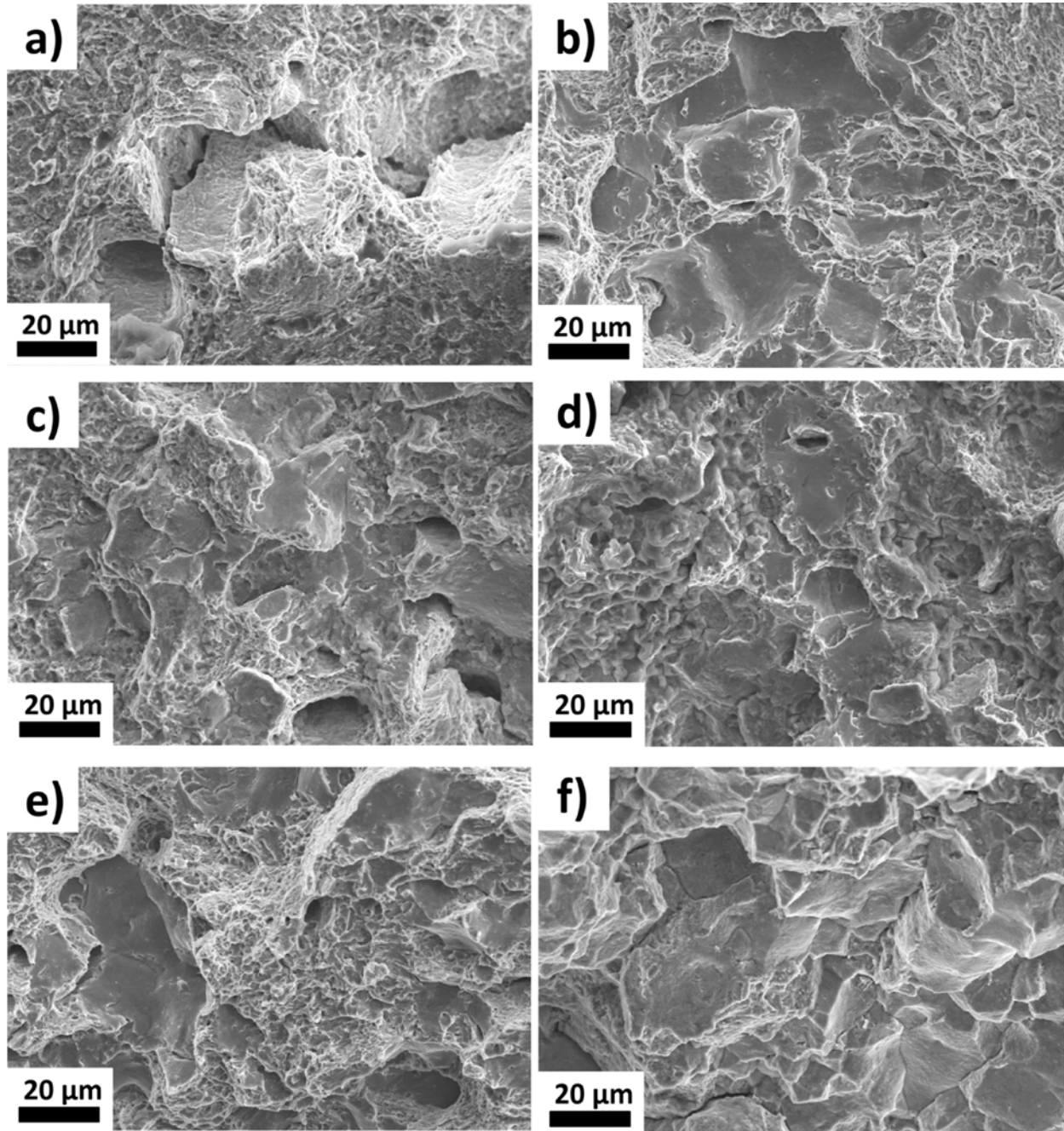


Fig. 1 SEM images showing fragments of fracture surface of the samples without coating (a, c, e) and with coating (b, d, f), fractured at different strain rates: fast (a, b), medium (c, d), slow (e, f).

The *rms* voltage, U_{RMS} , reveals a characteristic AE peak in the quasi-elastic part of the loading curve for all specimens at high and middle strain rates of 3×10^{-3} and $3 \times 10^{-4} \text{ s}^{-1}$, respectively, Figs. 5a-d. However, the AE peak for charged specimens is 5-10 times higher than that for the reference specimens, c.f. also Table 3. Furthermore, the position of the peak is shifted to significantly lower loads after hydrogenation.

When $\dot{\epsilon}$ is reduced from 3×10^{-3} to $3 \times 10^{-4} \text{ s}^{-1}$ the AE peak height, U_{RMS}^* , is reduced for all specimens, Fig. 5 a-d. This is a common trend in AE [15, 16]. However, U_{RMS}^* reduction occurs significantly differently for two types of specimens: in the reference specimens, U_{RMS}^* decreased by a factor of 10 whereas in the charged specimens, this reduction was much smaller, Table 3.

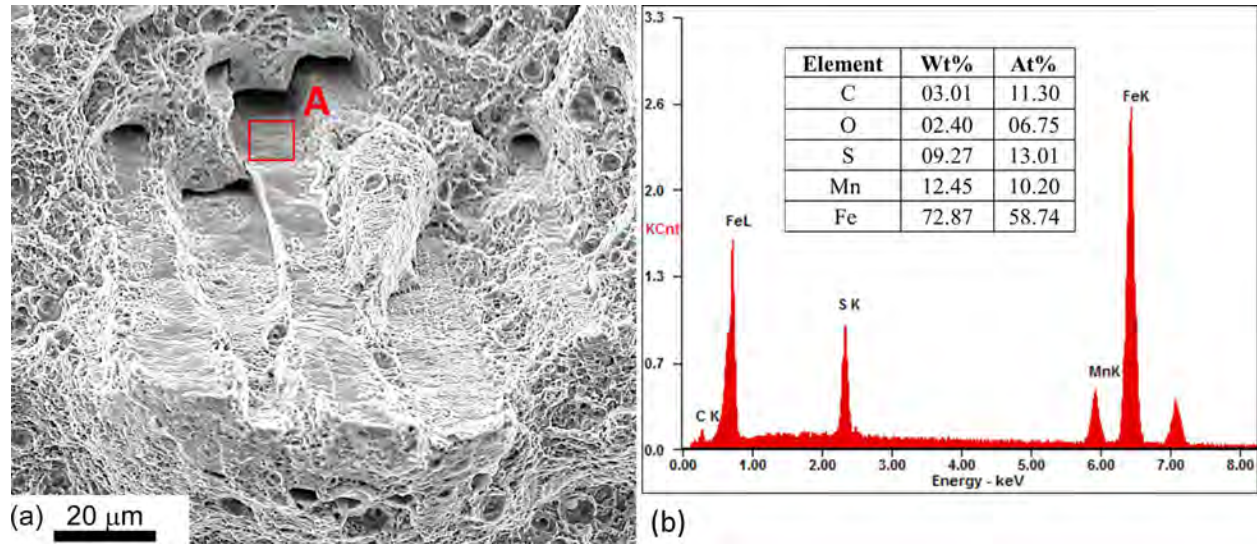


Fig. 2 (a) SEM image showing a fragment of the fracture surface of hydrogen charged specimen fractured at high strain rate; decohesion of sulfide inclusions is seen at steps. (b) EDS spectrum taken from the selected area A marked on (a), illustrating that fracture occurred along the sulfide boundary. The numeric values corresponding to respective concentrations of elements of interest in wt.% and at.% are shown in the inset.

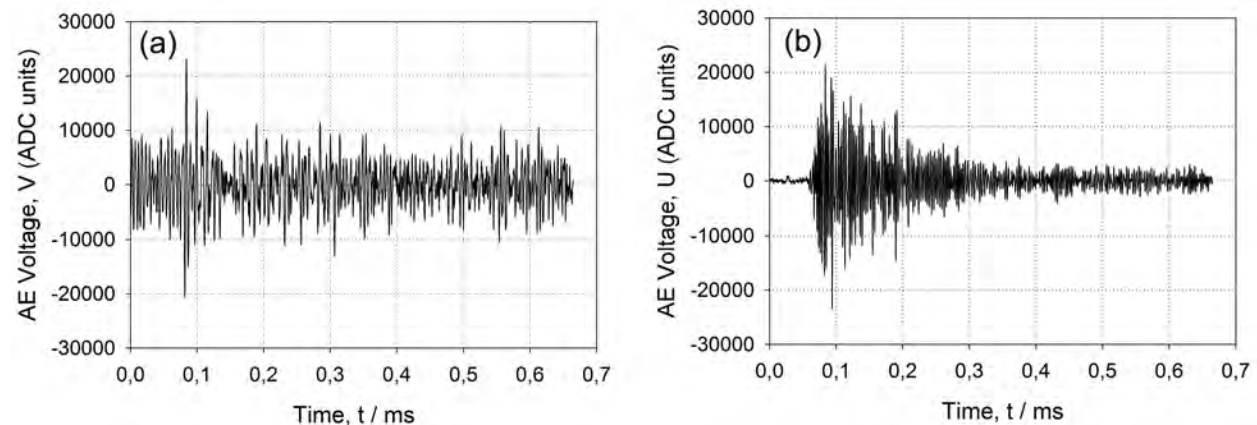


Fig. 3 Typical AE waveforms in hydrogen charged specimens: (a) continuous AE realization. (b) discrete AE “burst”-type signal,

The position of the U_{RMS}^* peak with respect to the loading curve does not change substantially. However, the load corresponding to the AE onset, P_{AE}^* increases when the strain rate decreases. This load and load of U_{RMS} peak in hydrogen charged specimens is consistently smaller

than that in reference specimens. In all cases, the high-energy AE bursts, such as those shown in Fig. 3b, are seen. Their “instant” amplitudes or *rms* values usually exceed by far the average height of the AE *rms* peak seen at the onset of deformation, Figs. 5c and d.

Further decrease in $\dot{\epsilon}$ by two orders of magnitude to $3 \times 10^{-6} \text{ s}^{-1}$ completely eliminates continuous AE for both types of samples. The U_{RMS} magnitude also is reduced for the discrete AE bursts, Figs. 5e and f. However, the hydrogen-charged specimens still exhibit a pronounced AE peak, which is created by a large amount of intensive bursts. If compared to a higher strain rate $\dot{\epsilon} = 3 \times 10^{-4} \text{ s}^{-1}$ the height of the peak is lower by a factor of 2 or 4, while the position of the peak corresponds to a smaller stress; see Fig. 5f, and Table 3.

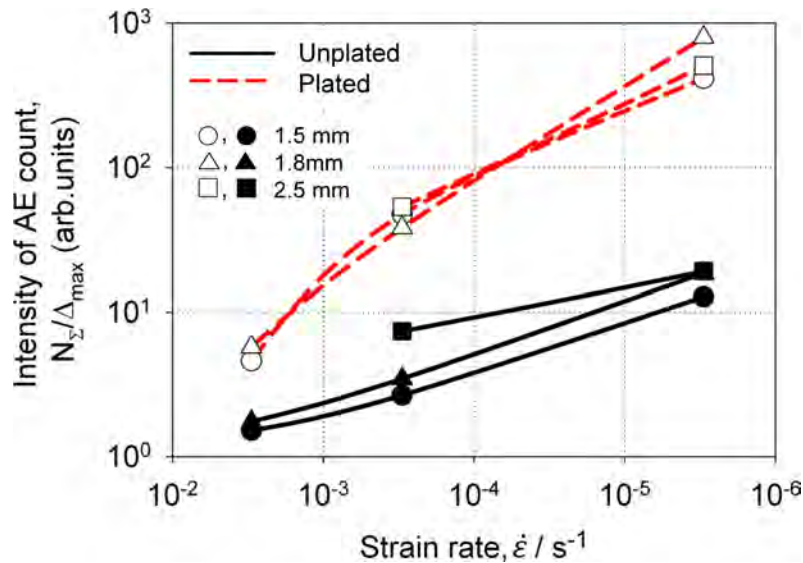


Fig. 4. Average intensity of discrete AE accumulation per deflection during test.

Table 3 Acoustic emission parameters as functions of the hydrogen charging and strain rate.

Specimen thickness, δ , mm	State of the specimen	Strain rate $\dot{\epsilon}$, s^{-1}								
		$3 \cdot 10^{-3}$			$3 \cdot 10^{-4}$			$3 \cdot 10^{-6}$		
		AE peak height, U_{RMS}^* , V	Load corresponding to AE onset, P_{AE} , N	Load corresponding to AE maximum, P_{AE}^* , N	AE peak height, U_{RMS}^* , V	Load corresponding to AE onset, P_{AE} , N	Load corresponding to AE maximum, P_{AE}^* , N	AE peak height, U_{RMS}^* , V	Load corresponding to AE onset, P_{AE} , N	Load corresponding to AE maximum, P_{AE}^* , N
1.5	reference	0.27	544	935	0.02	706	1021	-	-	-
	charged	1.47	180	700	0.30	313	631	0.13	417	569
1.8	reference	0.35	731	1266	0.04	1166	1284	-	-	-
	charged	2.10	150	590	0.33	700	984	0.08	256	631
2.5	reference	-	-	-	0.04	1946	2698	-	-	-
	charged	-	-	-	0.32	675	1580	0.16	580	1098

Discussion

We have seen that the ductility reduction caused by hydrogenation or/and strain rate reduction is accompanied by increasing of brittle fraction, Fig. 1, and amount of discrete type AE recorded during testing. It is therefore plausible to state that these AE transient signals are originated from microscopic fracture processes such as intergranular cracking along the boundaries separating austenitic grains and decohesion of non-metallic inclusions. The role of sulfide inclusions in the AE accompanying fracture of steels has been highlighted in [17-19]. In these works

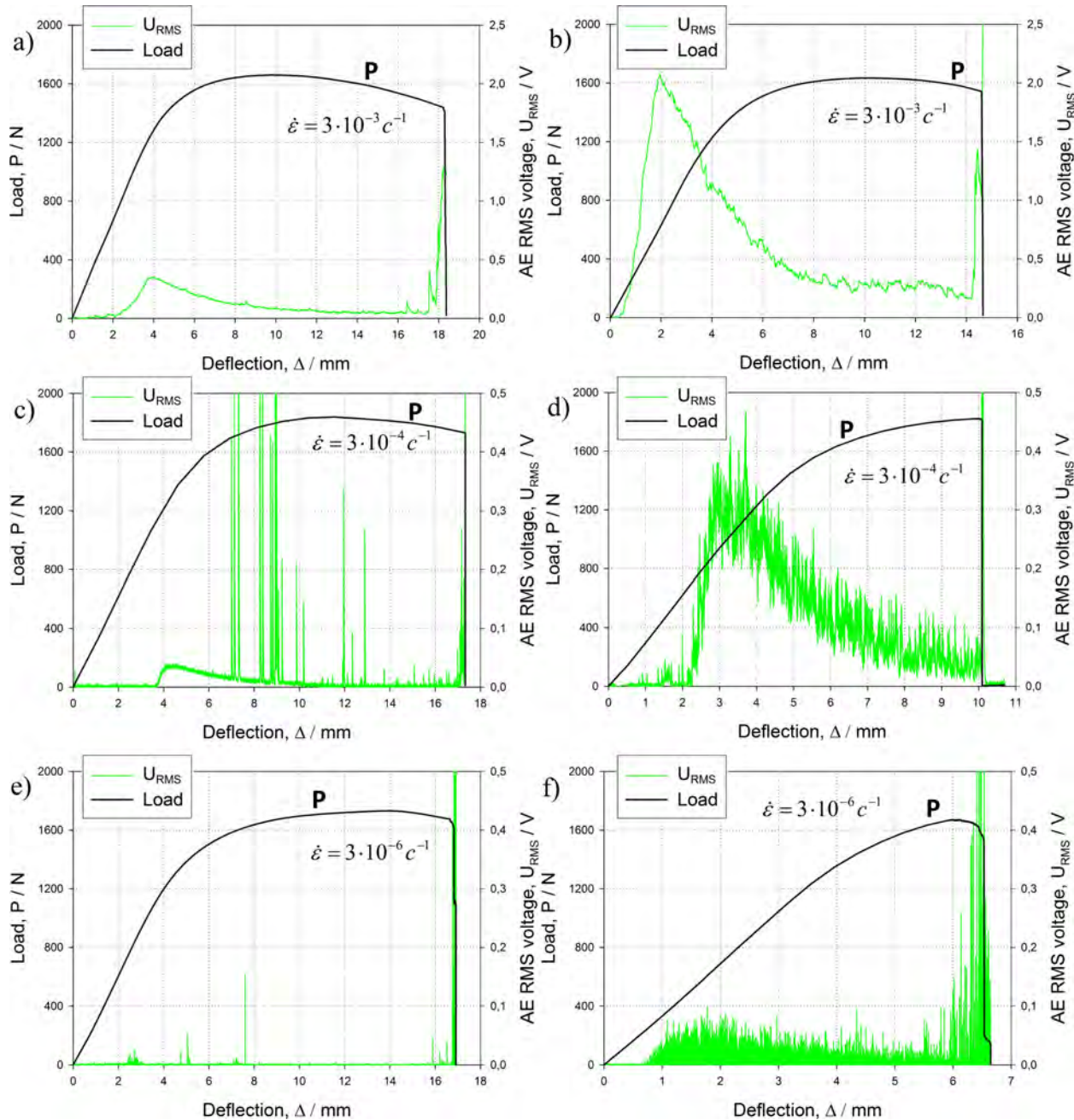


Fig. 5 Typical three-point bending loading curves and AE rms voltage for the specimens tested at different nominal strain rates: $\dot{\epsilon} = 3 \times 10^{-3} \text{ s}^{-1}$ (a) reference (uncoated) and (b) cathodically charged; $\dot{\epsilon} = 3 \times 10^{-4} \text{ s}^{-1}$ (c) reference and (d) cathodically charged; $\dot{\epsilon} = 3 \times 10^{-6} \text{ s}^{-1}$, (e) reference and (f) cathodically charged.

decohesion of sulphide inclusions has long been recognized as a powerful source of burst type AE in high strength steels and this can be reasonably responsible for the high amplitude burst type AE signals (see Fig. 3b, for example) which are commonly observed in steel 70 at all strain rate. The EDS analysis in SEM confirmed that decohesion of MnS inclusions is a primary damaging process in the present steel. Apparently, the number of transient events should scale with intensity of HAC. The strain rate dependence of N_{Σ} and Δ_{\max} for reference samples is less pronounced than that for hydrogen charged ones. However, the fact that this dependence does take place shows that the reversible HAC which is caused by crack initiation and propagation facilitated by diffusion-active hydrogen [20] can be observed in high strength steels even at very low initial concentration of H atoms which present in steel before plating.

Continuous AE is observed at two faster strain rates. This continuous AE forms a pronounced peak in the quasi-elastic region as is commonly observed for a wide range of metals due to plastic (or micro-plastic) deformation [15]. Moreover, it has been well established that the rms voltage of AE caused by uniform plastic deformation should be proportional to $\sqrt{\dot{\epsilon}}$ [16]. This dependence is however not seen in the reference samples the AE energy appears to be proportional to $\dot{\epsilon}^2$ and not to $\dot{\epsilon}$ as could be expected for uniform plastic deformation. The conclusion is that the continuous AE, which is observed in the present work, is not associated with uniform plastic deformation. This seems to be quite reasonable for the present high strength steel. The AE peak vanishes in the reference specimen at $\dot{\epsilon} = 3 \times 10^{-6} \text{ s}^{-1}$. In view of the above, the latter is not surprising because with strain rate reduction by two orders of magnitude, the AE rms peak should decrease by a factor of 100 or so, i.e. the U_{RMS}^* is expected to fall below 40 μV that is less than the laboratory noise level in the current experiments (of 1 mV after amplification), c.f. Fig. 6.

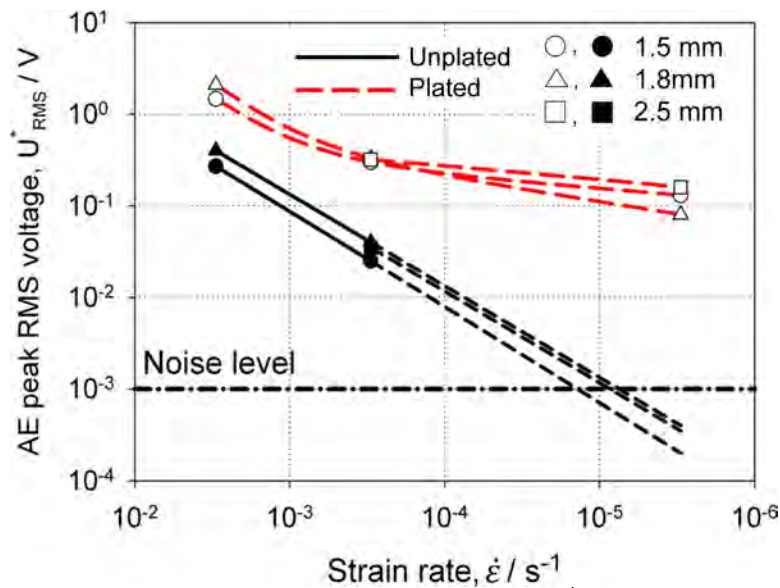


Fig. 6 Dependence of the AE peak height U_{RMS}^* on the strain rate.

Fractograph of the present high strength steel is featured by a large volume fraction of MnS inclusion serving as a root cause for microcrack nucleation. Besides, as these sulfides are natural stress risers, plastic deformation tend to localize around and to commence at lower far field stresses than in the rest of the sample. Since the onset of the AE U_{RMS} peak is observed during the quasi elastic loading stage, it is plausible to associate the continuous AE observed during deformation of the steel 70 with plastic deformation localized at inclusions.

While in the reference specimens the AE peak is poorly defined at the slow strain rate, the hydrogen charged specimens exhibit a clear AE maximum, compare Figs. 5e and f. In the charged samples the AE peak consists of a large number of discrete bursts, which are originated from HAC. At higher strain rates the AE peak in hydrogen charged specimens is also significantly higher than in the reference specimens. This is explained by superposition of continuous AE caused by strongly localized plastic deformation at the tips of the cracks and at inclusions and burst-type AE associated with brittle crack advance. This superposition of two processes accounts, in particular, for the lack in proportionality between the AE energy peak magnitude and the strain rate in hydrogenated specimens. The intensity of microcracking increases with strain-rate reduction in the hydrogen charged specimens, i.e. the contribution of this process to the resultant AE increases while the continuous AE component reasonably decreases with decreasing strain rate.

Hence, we can conclude that two competitive mechanisms operate during the deformation of the high carbon steel 70: (i) highly localized plastic deformation and (ii) brittle intergranular and transgranular (through non-metallic inclusions) cracking promoted by the hydrogen influence. Both these mechanisms generate AE with markedly different features. The contribution of each mechanism varies depending on metallographic and loading factors. When the hydrogen-induced embrittlement effect is relatively low (e.g. at high strain rate in reference specimens), the continuous AE associated with plastic deformation is dominant, Figs. 5a and 3a. In contrast, when the effect of hydrogen is significant (at low strain rate in hydrogenated specimens) AE appears as high rates of high amplitude pulses, Figs. 5f and 3b. In the case when both plastic deformation and brittle fracture take place in approximately equal proportions the AE U_{RMS}^* either increase, Figs. 5b and d, or one can see a peak of continues AE superimposed with high energy burst signals, Fig. 5c.

Conclusions

1. The electrochemical Zn-plating results in hydrogen charging and consequent ductility reduction of a high-carbon steel, steel 70. The embrittlement is more pronounced with strain rate reduction. This picture is typical of the so-called *reversible hydrogen embrittlement*, which is caused by crack initiation and propagation facilitated by diffusion-active hydrogen [20]. HAC can occur even at very small concentration of dissolved hydrogen.
2. The cumulative AE event count, N_{Σ} , during three-point bending test of steel 70 specimens depends on their apparent ductility and the fraction of brittle component on the fracture surface. AE “burst” signals are originated from microscopic fracture processes such as intergranular cracking along the boundaries separating austenitic grains and decohesion of non-metallic inclusions.
3. Two competitive mechanisms operate during three-point bending deformation of steel 70: (i) localized plastic deformation and (ii) brittle intergranular and transgranular cracking promoted by hydrogen influence. Both these mechanisms generate AE with markedly different features. When the hydrogen-assisted embrittlement effect is relatively low, the continuous AE associated with strongly localized plastic deformation is dominant. In contrast, when the effect of hydrogen is significant, AE appears as high rates of high amplitude pulses. In case when both plastic deformation and brittle fracture take place in approximately equal proportions, the mixture of two types AE results either in U_{RMS}^* increase or in continues AE superimposed with high energy burst signals.

Acknowledgements

Financial support from the Russian Ministry of Education and Science through the grant-in-aid № 11.G34.31.0031 is greatly appreciated.

References

- [1] M. Louthan, *Journal of Failure Analysis and Prevention*, **8** (2008) 289-307.
- [2] D.L. Merson, D.E. Mesheryakov, A. Vinogradov, *Progress in acoustic emission XIV*. The Japanese Society for NDI, (2008) 115-120.
- [3] H.L. Dunegan, A.S. Tetelman, *Engineering Fracture Mechanics*, **2** (1971) 387-402.
- [4] A.K. Bhattacharya, N. Parida, P.C. Gope, *Journal of Materials Science*, **27** (1992) 1421-1427.
- [5] S. Carpenter, D. Smith, *Metallurgical and Materials Transactions A*, **21** (1990) 1933-1939.
- [6] D.D. Dedhia, W.E. Wood, *Materials Science and Engineering*, **49** (1981) 263-273.
- [7] R. Padmanabhan, N. Suriyayothin, W. Wood, *Metallurgical and Materials Transactions A*, **14** (1983) 2357-2362.
- [8] F. Ferrer, E. Schille, D. Verardo, J. Goudiakas, *Journal of Materials Science*, **37** (2002) 2707-2712.
- [9] W.W. Gerberich, R.H. Jones, M.A. Friesel, A. Nozue, *Materials Science and Engineering: A*, **103** (1988) 185-191.
- [10] S.L. Chou, W.T. Tsai, *Materials Science and Engineering: A*, **270** (1999) 219-224.
- [11] X.Q. Wu, I.S. Kim, *Materials Science and Engineering: A*, **348** (2003) 309-318.
- [12] A.H.M. Krom, H.J. Maier, R.W.J. Koers, A. Bakker, *Materials Science and Engineering: A*, **271** (1999) 22-30.
- [13] L.M. Young, M.R. Eggleston, H.D. Solomon, L.R. Kaisand, *Materials Science and Engineering: A*, **203** (1995) 377-387.
- [14] M. Krishtal, I. Yasnikov, A. Eremichev, A. Karavanova, *Metal Science and Heat Treatment*, **49** (2007) 490-496.
- [15] C.R. Heiple, S.H. Carpenter, *J. Acoustic Emission.*, **6** (1987) 177-237.
- [16] H. Hatano, *Journal of Applied Physics*, **47** (1976) 3873-3876.
- [17] K. Ono, M. Yamamoto, *Materials Science and Engineering*, **47** (1981) 247-263.
- [18] H.B. Teoh, K. Ono, E. Kobayashi, *J. Acoustic Emission*, **3** (1984) 130-143.
- [19] H.B. Teoh, K. Ono, *J. Acoustic Emission*, **6** (1987) 1-12.
- [20] B.A. Kolachev, *Materials Science*, **15** (1979) 202-207.

AE TECHNIQUE FOR DETECTING THE DELAYED CRACKS UNDER THERMAL SPRAYED COATING

MIKIO TAKEMOTO, GUNJI UENO, SHUICHI UENO, SEIJI MASANO
and MOTOAKI NAKAMURA

Kanmeta Engineering Co., Nakanocho-higashi 2-34-5, Tondabayashi, Osaka 584-0022, Japan

Abstract

This study investigates how the sprayed coating protects metal substrates from delayed fracture. One surface of spring steel strips (0.6% carbon steel, 1.4-GPa tensile strength) was coated by flame spraying of 50Ni-50Cr and titania and exposed to cathodic charging or corrosion in strongly acidic solution under three-point bending load. AE technique was utilized to determine the threshold strain for the delayed fracture. We used stepwise strain increasing method (SSI) to separate AE signals from delayed crack and from coating damage. Here the AE detected during a strain-increasing stage was classified as coating damage and those during strain holding as the delayed crack in the strip. The threshold strain determined by AE technique was correlated with concentration of diffusible hydrogen in the strip. Coated strips shows lower hydrogen concentration and higher threshold strain than strips without coating. Coating was found to act as diffusion barrier and to reduce hydrogen concentration significantly. Even the coating damaged at higher applied strain can reduce the hydrogen concentration in limited area and convert the break-before-leak fracture to leak-before-break fracture.

Introduction

Delayed fracture or hydrogen induced cracking of ferritic steels occurs when the hydrogen concentration in the steel becomes higher than a critical level. The critical level depends on the strength level of the steel and is as low as 3-4 ppm for high strength steel of >1 GPa. When the hydrogen concentration is higher than 4 ppm over a wide area, the fracture tends to be catastrophic since unstable through-wall crack rapidly propagates over the wide area. Thus, the delayed fracture is known as a break-before-leak (BBL) type fracture. When the hydrogen concentration is low in a limited area, we can detect the leak-before-break (LBB) type fracture and avoid the BBL by appropriate operation.

Accidents of chemical process equipment by the delayed fracture is becoming lower since the steels with tensile strengths lower than 600 MPa have been widely used. Nevertheless, we are often asked to remedy chemical equipment damaged by the delayed fracture. Two effective countermeasures against the delayed fracture are available. One is coating with a metal having lower hydrogen over-potentials, such as Pt, Au, Ni, Cr, and letting the adsorbed atomic hydrogen or proton leave into solution as hydrogen gas. High Cr-Ni austenitic alloy steels possess both low hydrogen over-potential and low diffusion coefficient of hydrogen. It is noted that the diffusion coefficient (10^{-12} cm²/s) of hydrogen in austenitic steel is one million times smaller than that (10^{-6} cm²/s) in ferritic steel. The other method is a coating of diffusion barrier to the hydrogen. Oxide ceramics like titania or polymers is known as effective barrier material. However, polymer coatings are not widely used in process equipment due to their chemical and thermal degradation [1]. For such severe applications, we recommend a dual layer coating of 50Ni-50Cr alloy as a bond coat and titania (TiO₂) as a top coat by thermal spraying. This coating has been commercially demonstrated to be a quite effective method and acts as diffusion barrier of hydrogen. However, we have no scientific data on the diffusion barrier capability and hydrogen concentra-

tion in the substrate. Thus, we conducted some fundamental research on delayed fracture of the Almen strip (quenched and tempered spring steel with tensile strength of 1.4 GPa) with and without sprayed coating.

Difficulty in the delayed fracture test of sprayed coatings is that we cannot detect small cracks hidden under the coating. We used AE technique to detect the small cracks produced during SSI (step-wise strain increasing) test of the coated material submitted to delayed fracture tests. Both the waveform analyses and delayed response of AE make it possible to separate the AE from cracks in the coating and delayed fractures in the steel substrate. The AE from the delayed fracture were detected during strain holding and those from coating cracks were detected during strain-increasing stage.

This paper reports a relation between the delayed cracks and hydrogen concentration in the substrate steel under coating. We used two types of test method, i.e., cathode charging in non-corrosive electrolyte and corrosion in a strongly acidified sulfuric acid solution.

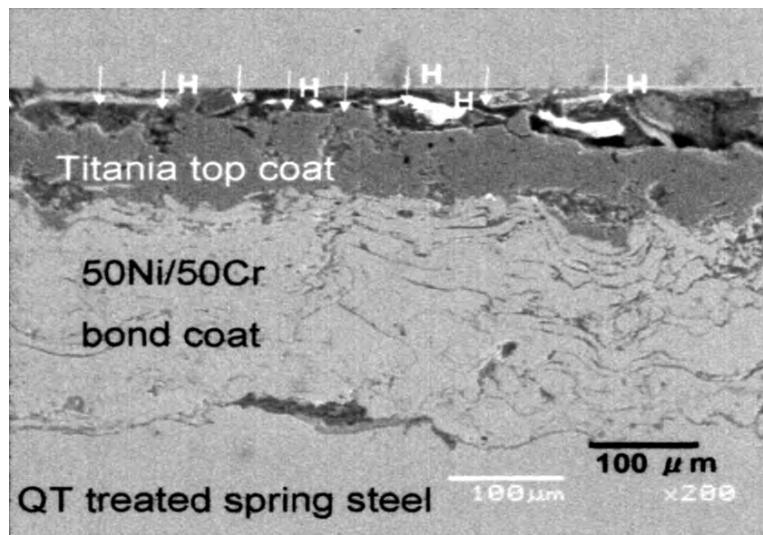


Fig. 1. Transverse microstructure of dual layer coating with SEM: TS-A deposited on sand-blasted spring steel strip.

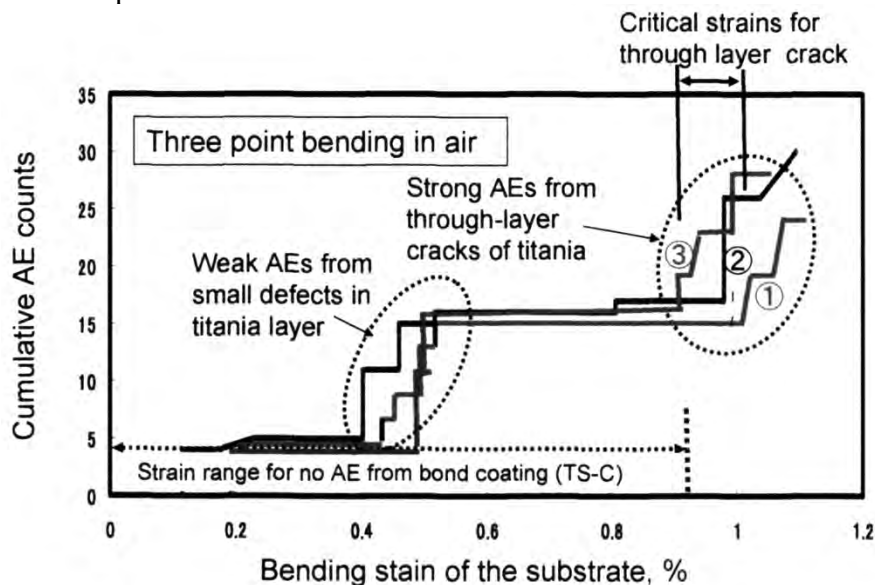


Fig. 2. Relation between bending strain and cumulative AE counts for three TS-A specimens.

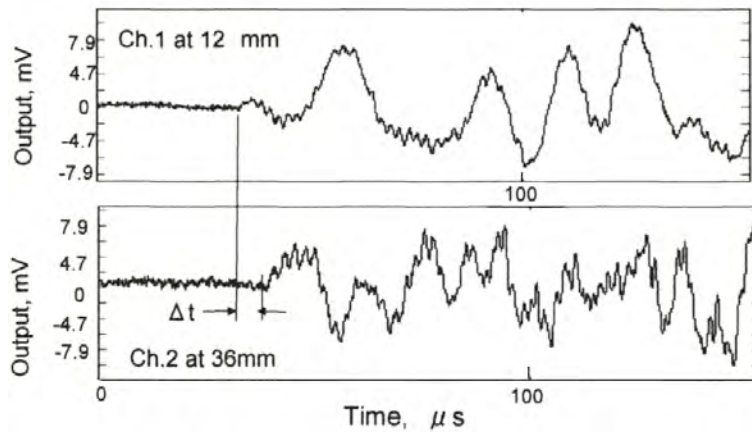


Fig. 3. Lamb wave AE from small cracks at strain of 0.45% for TS-A coating during bending.

Test Specimen

We deposited coating on the sand-blasted Almen-C strips (2.3-mm thick, QT-treated 0.6% carbon spring steel) by acetylene-oxygen flame spraying of 50Ni-50Cr and/or titania. The 50Ni-50Cr layer of 100 μm was used as a bond coat and titania of 100 μm as a top coat. Both coatings have low hydrogen over-potential and low diffusion coefficient of hydrogen. Three types of coatings (TS-A, B and C) were tested. Sprayed titania is TiO_{2-x} and electrically conductive.

TS-A: Silicone sealing of NiCr/Titania

TS-B: Non-sealing of NiCr/Titania

TS-C: Sealing of NiCr

Transverse structure of TS-A is shown in Fig. 1. Pores in the top-coat is sealed by silicone but we cannot see the sealed silicone in the photo.

We first studied AE characteristics of TS-A coating during three-point bending. Test method is the same as that in our previous paper on the delayed fracture test [2]. Figure 2 shows AE behavior for three TS-A coatings. Result for the TS-C is shown in lower portion of the figure. We observed two steps of rapid increases of AE for the TS-A. The first increase at around 0.4% strain is due to the generation of small defects in titania layer, since we observed no AE for the bond-coating only TS-C coating up to 0.9% strain. Waveform of the Lamb AE detected at 0.45% strain is shown in Fig. 3. Amplitude of the wave is low at a few mV. Arrival time difference Δt of the So-mode wave indicates a crack generation at the maximum strain or central loading point. AE from coating damage is the low frequency Lamb waves, seen along with superposed high frequency and low amplitude ripple waves. This is supposed to be due to stacked and porous structure of the sprayed coating. At around 0.9 to 1% strain, we observed the second increase of AE due to through-layer cracks. These AE signals are strong with a few tens of mV. Here, the critical strain of through-layer cracks causing the second increase for the three samples changes from 0.9 % to 1%, suggesting structure variation of the sprayed coatings.

Delayed Fracture Test

Delayed fracture tests were conducted by the following two methods at ambient temperature.

- Method I: Cathodic charge at 500 $\mu\text{A}/\text{cm}^2$ in a solution of (1 N H_3BO_4 + 0.033 mol/l KCl + 0.02 mol/l thiourea).
- Method II: Corrosion in pH = 0.4 sulfuric acid solution

In each method, charging electrolyte solution or corrodant was filled in a 16-mm diameter and 70-mm long glass cell attached on the sprayed surface (convex plane), as shown in Fig. 4. It is noted that hydrogen diffuses in the convex side of an uncoated specimen and diffuses out from the concave free surface. This method simulates the actual process equipment, which absorb hydrogen from process fluid (inside) and easily release the hydrogen from the outside, open to air. As the hydrogen diffusion rate in the ferritic steel is very fast, its concentration in the steel is determined by the rates of diffuse-in and -out of diffusible hydrogen.

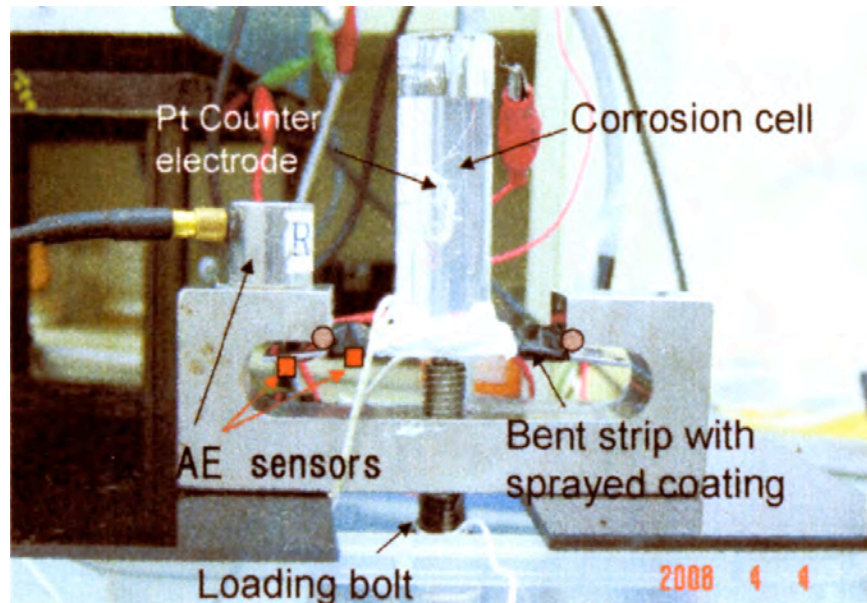


Fig. 4. Delayed fracture test method and AE monitoring.

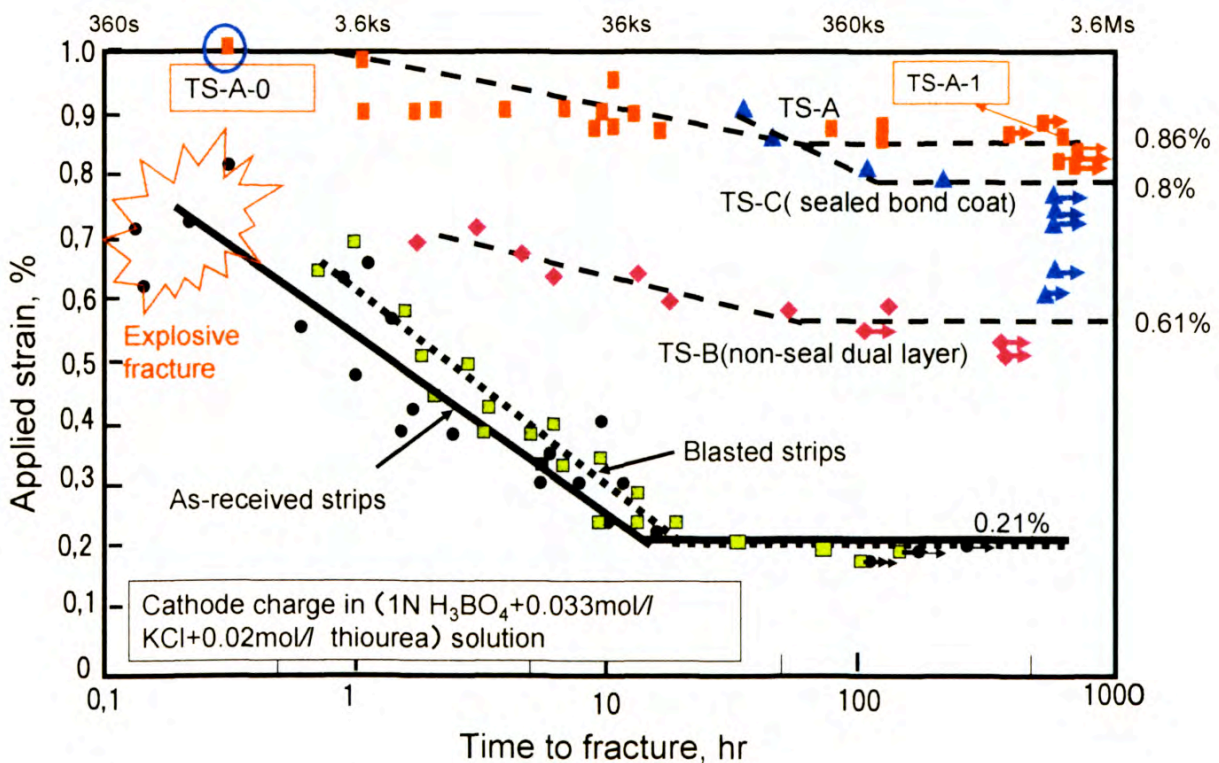


Fig. 5. Delayed fracture curves of as-received, sand-blasted and spray-coated strips under cathodic charging.

AE events were monitored by two small sensors (PAC Type-PICO) mounted on the concave surface (without coating). Outputs of the sensors are amplified 40 dB and digitized by an A/D converter (Alazer). We adopted two monitoring methods. One is simultaneous monitoring during delayed fracture test (DFT), and the other is the monitoring during stepwise strain increasing (SSI) test after the DFT. The latter was mainly utilized in this research since we have only one monitoring system in spite of long DFT (20 days) of many samples. The SSI takes only 30 minutes. Detail of the SSI can be seen elsewhere [2].

Hydrogen concentration in the strips was measured by the glycerol method. In this method, strips with coating were dipped in glycerol at 30°C for the maximum 30 days and measured the hydrogen volume released from the strips using a special capillary. Hydrogen concentration in the strip was expressed as mass of hydrogen per strip mass. Thus, the concentration in this paper is the concentration of diffusible hydrogen in the strip and coating.

We are not interested in the fracture times at high applied strains, but rather interested in the threshold strains of coated samples. For this purpose, we used the SSI to examine whether delayed cracks exist in the substrate steel. Here the delayed cracks are generally smaller than 400 μm due to lower hydrogen concentration in the substrate.

Test Results

Results by Cathode Charge Method (Method-I)

Time of fracture curves for coated samples, TS-A, -B and -C, are shown in Fig. 5 as well as those of as-received and sand-blasted strips. Threshold strain of the as-received and blasted strips is as low as 0.21%. These results are basically the same as previous studies on the delayed fracture of shot-peened spring steel [1, 2]. Blasting produced large compressive residual stresses of 1.2 GPa; however, the threshold strain was not improved by the compressive stresses, but is slightly lower than that of the as-received one possibly due to notch effect of rough surface and lattice defects. It is noted that hydrogen can easily diffuse into the metal with compressive residual stresses. In contrast, the threshold strain (0.86%) of TS-A samples (sealed dual layer coating) is slightly higher than that (0.80%) of the TS-C samples (sealed NiCr layer). These strains agree well with the critical strains of through-wall cracks in Fig. 2.

The fact that the threshold strain (0.61%) of TS-B samples (non-sealed dual-layer coating) is lower than the other two types of coated samples suggests that the sealing of the sprayed coating is important for producing an effective barrier against hydrogen diffusion. Lower threshold strain of the TS-B is due to impregnation of electrolyte through connected pores, and diffusion of the hydrogen into the steel substrate. Figure 6 shows the transverse section of the fractured TS-A-0 sample at applied strain of 1%. Both the through-wall crack and delayed cracks in the substrate are apparent. This is a typical example of delayed fracture produced by coating fracture. Fractures at higher strains are explosive and we can hear loud fracture sound. Broken specimens sometimes fly off over 30 cm. This is due to high hydrogen concentration and rapid crack propagation over wide area.

Determination of the threshold strain of coated samples is very difficult since we cannot hear the sound or observe visually the crack under the coating. Thus, we used the SSI method for all samples charged for longer than 400 hrs. We monitored AE by applying static strains step-wise to the samples in air. The SSI test was performed within 1 hour after the termination of delayed fracture test. Figure 7 is the result for the sample TS-A-1 tested at strain 0.87% (see Fig. 5).

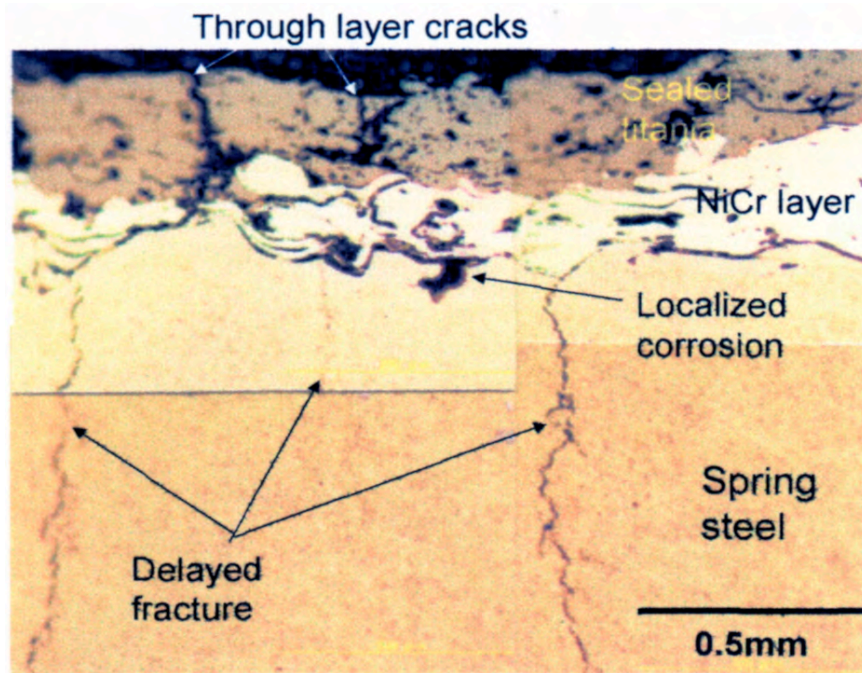


Fig. 6. Transverse photo of the TS-A-0 sample, hydrogen-charged for 0.42 hr at applied strain of 1%.

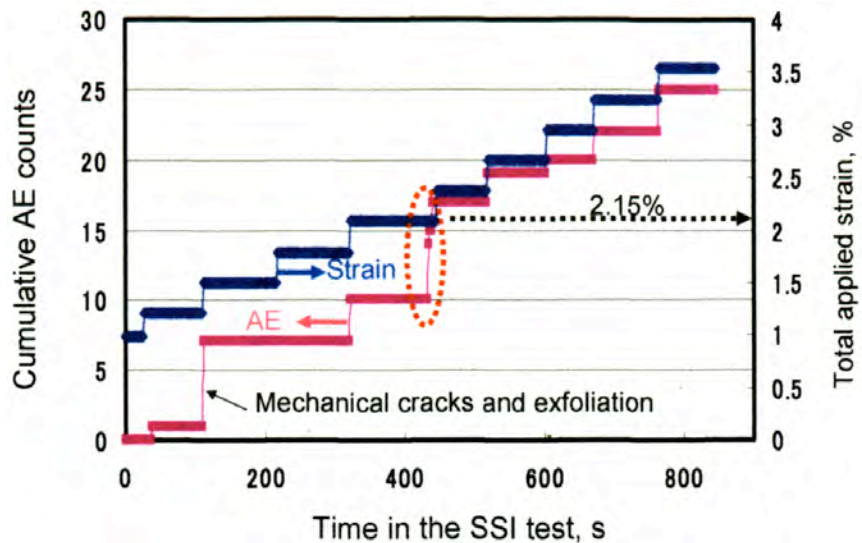


Fig. 7. Relation between step-wise strain change and AE generation during the SSI test of TS-A-1 sample, which was charged for 580 hrs at applied strain of 0.86%.

During the SSI test, we first observed simultaneous step-wise increases of AE and strain. These AE signals were produced by small cracks and exfoliation in the coating. At the end of applied strain of 2.15%, we detected seven AE signals produced by delayed cracks. Weak AE signals suggested small size cracks, possibly due to low concentration of hydrogen. Important technology in the SSI method is that we have to wait AE for 5-6 min. or sometimes 10 or more min. If hydrogen concentration in the strip is high enough to cause the delayed fracture, hydrogen in the strip diffuse into the initiation site of crack quickly and produce a brittle crack. Thus, the delayed AE during strain holding implies AE from delayed fracture. This AE is clearly separated from the AE signals by micro defects in the coating and noise. Another important element is to conduct quick SSI tests so as to prevent the hydrogen from diffusing out of the strip. The delayed AE at 2.15% strain in Fig. 7 implies the occurrence of delayed cracking without any doubt.

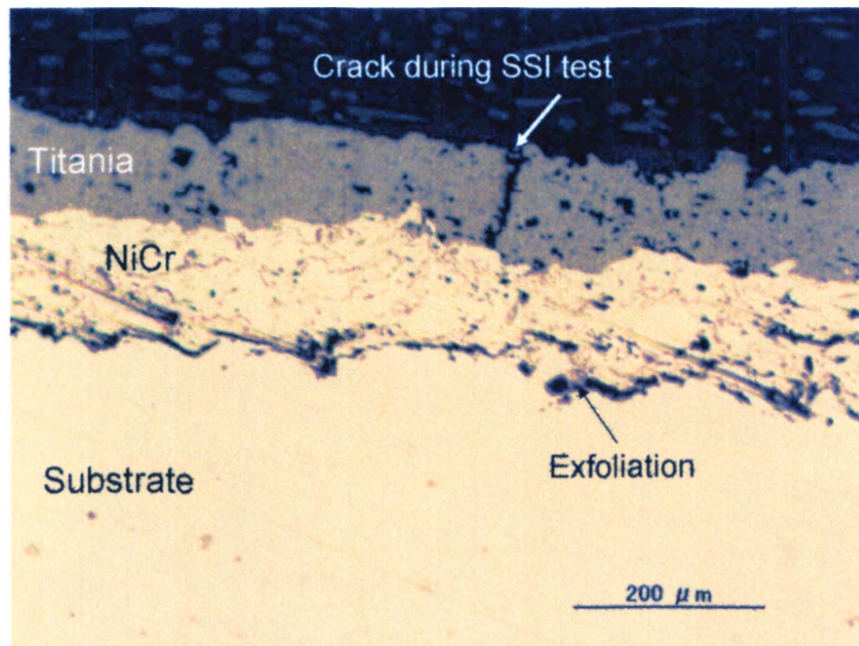


Fig. 8. Transverse photo of TS-A-1 sample, hydrogen charged for 800 hrs at 0.86% strain and then submitted to the SSI test to 3.5% strain.

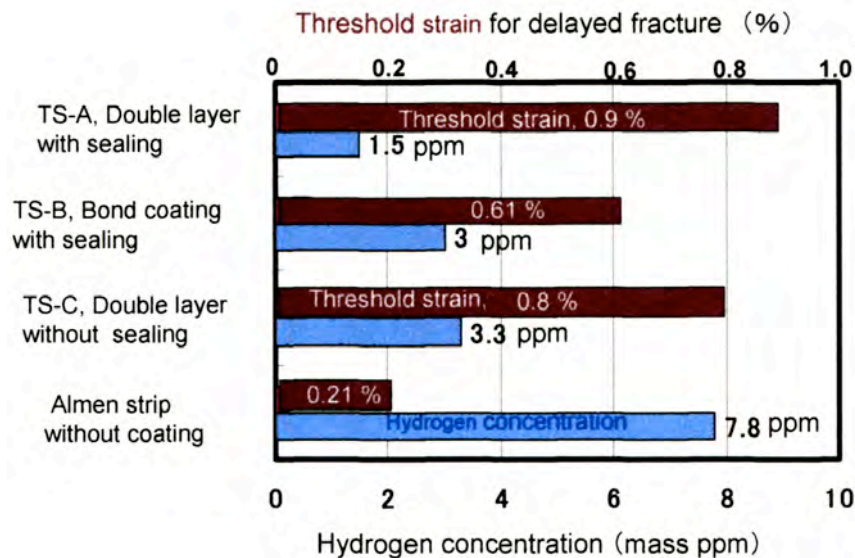


Fig. 9. Hydrogen concentration and threshold strain for four samples charged for 76 hrs.

We then sectioned the sample repeatedly and examined the transverse section. As shown in Fig. 8, we observed crack in titania coat and small exfoliation of NiCr layer, but could not detect delayed cracks in the strip. This means that the delayed cracks of this sample are too small to appear on the cut sections. However, delayed AE at 2.15% strain in Fig. 7 definitely demonstrates the delayed fracture in the strip, thus we determined the threshold strain of the TS-A samples as 0.86%. Threshold strain of TS-A sample is four times larger than that (0.21%) of as-received strips.

Detail mechanism for protective or preventive effect of thermal spray coating are not well known, but we now consider if it is due to diffusion barrier against hydrogen, based on the following facts. Figure 9 compares the diffusible hydrogen concentration in the strip with and

without coating and threshold strain for delayed fracture. It is noted the hydrogen concentration in the TS-A strips charged for 76 hrs is as low as 1.5 ppm. This concentration is lower than the critical concentration (3 ppm) for 1.5 GPa steel [3]. Hydrogen concentrations in TS-B, and -C samples are 3 and 3.3 ppm, respectively. These concentrations are lower than that (7.8 ppm) of bare strip, but are supposed to be still higher than the critical hydrogen concentration of this steel. Delayed fracture pattern on the back surface of bare strip at 0.25% strain and TS-A strip at 0.91% are compared in Fig. 10. We observed catastrophic brittle fracture for the bare strip at low applied strain (0.25%). For the coated TS-A strips, however, we observed a branched and zigzag crack, which often stopped its propagation. The latter is due to low concentration of hydrogen in the strip and suggests that spray coating can convert the BBL (break before leak) type fracture to the LBB (leak before break) type. As the thermal spray coating acts as diffusion barrier of hydrogen, it significantly reduces the hydrogen concentration in the steel substrate. If the coating is locally damaged, hydrogen diffusion is limited in a small area. Rapid diffusion-out of impregnated hydrogen leads to low concentration, and can avoid the BBL-type fracture.

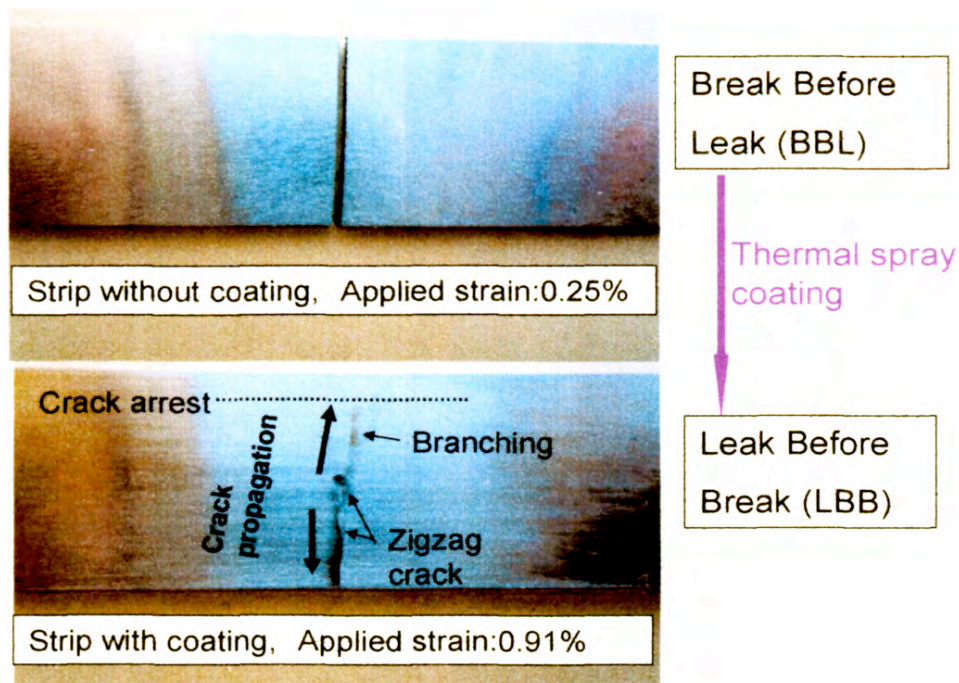


Fig. 10. Back surface crack of the bare Almen strip (upper) and strip with sprayed coating subjected to cathodic charge test (lower).

Results of Corrosion Tests (Method-II)

This test was intended to study the performance of the sprayed coatings in severe corrosive environment. However, the selection of acid concentration was a difficult problem. Adoption of a weak acid solution needs time-consuming test, while a strongly acidified solution may give the coating unexpected damages. As we have no reference data on the corrosion rate of spring steel strip in acidic solution, we adopted a solution of 4-N sulfuric acid (pH=0.4 at 298 K). This solution was once used as an SCC-test solution of austenitic stainless steel by adding 0.4-N NaCl. Sand-blasted or shot-peened 304 stainless steel suffers severe local corrosion at room temperature. Therefore, the sulfuric acid solution of pH=0.4 is noted as a severe corrosive solution. We first measured corrosion rate of bare strip in pH=0.4 sulfuric acid solution at 25°C. The corrosion rate reached 1 to 1.2 μ m/hr, and the 2.3 mm thick strip completely dissolved after 2000 hrs. We next evaluated the corrosion resistance of the coating in pH=0.4 sulfuric acid and then

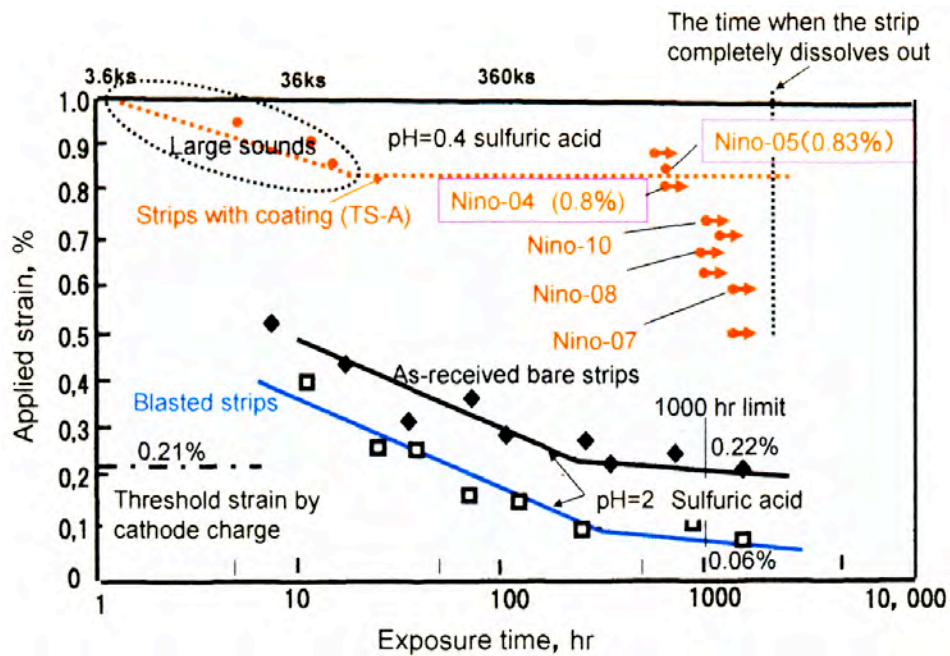


Fig. 11. Time to crack curves of Almen strips with coating (TS-A) in pH=0.4 sulfuric acid and bare strips in pH=2 sulfuric acid solutions.

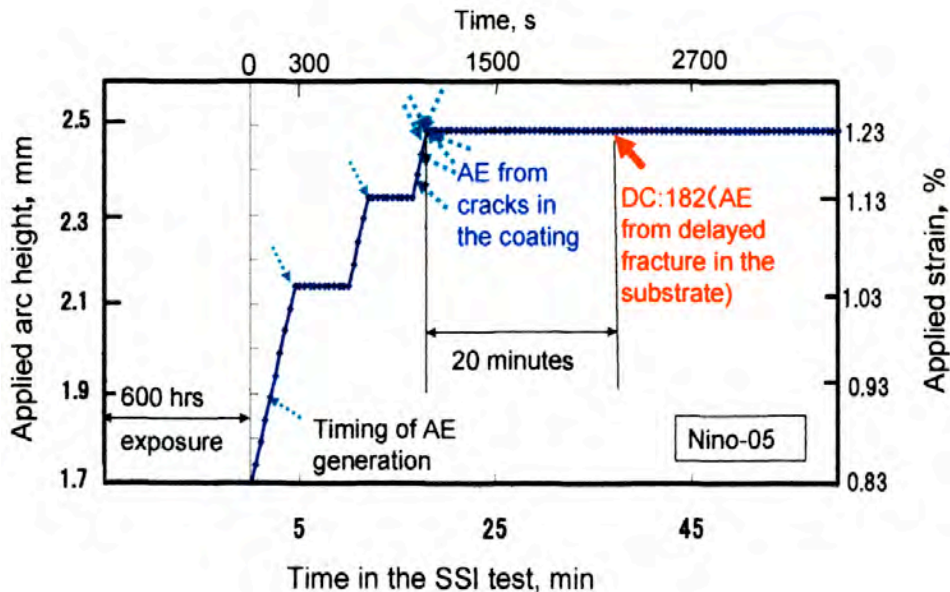


Fig. 12. AE timing during the SSI test of Nino-05 sample exposed to pH=0.4 sulfuric acid solution for 600 hrs at applied strain of 0.83%.

measured the threshold strain if the coating shows some resistance to this solution. We also measured the time-limited threshold strain of as-received and sand-blasted strips in pH=2 sulfuric acids. The corrosion rate of the strip in pH=2 solution is 50 times lower than that in pH=0.4 solution.

Figure 11 shows delayed fracture data in pH=2 and 0.4 sulfuric acid solution at 298 K. As both the bare and blasted strips suffer continuous general corrosion in pH=2 solution, they showed no clear threshold strain. Time-limited threshold strain at 1000 hr is measured as 0.22% for as-received bare strip and 0.06% for blasted strips. It must be noted that sand-blasting and

possibly shot-peening give negative effect for the hydrogen induced cracking in acidic solution. The negative effect appears to be due to rapid dissolution rate of hardened layer and higher lattice defects acting as trap sites for hydrogen.

Exposure tests for the TS-A samples in pH=0.4 solution were conducted up to 1200 hrs. Threshold strain was determined by the SSI-test for the samples named Nino-04, -05, -07, -08 and -10. Here only Nino-05 sample, exposed for 600 hrs at strain of 0.83%, emitted the delayed AE. Figure 12 shows AE timing during the SSI test of Nino-05 sample. The dotted arrows, detected during strain increasing stage, designate the AE signals from small damages in the coating. We detected one delayed fracture AE event (data count: 182) during strain holding at 1.23%. This AE was detected at 1200 s of strain holding, and indicated a single delayed crack in the substrate. Figure 13 shows waveforms of this AE signal (DC 182). Amplitude of So-mode is relatively large compared to that of Ao-mode, indicating a sub-surface crack as the origin. Frequency of this wave is much higher than that of AE signals from coating damage (Fig. 3).

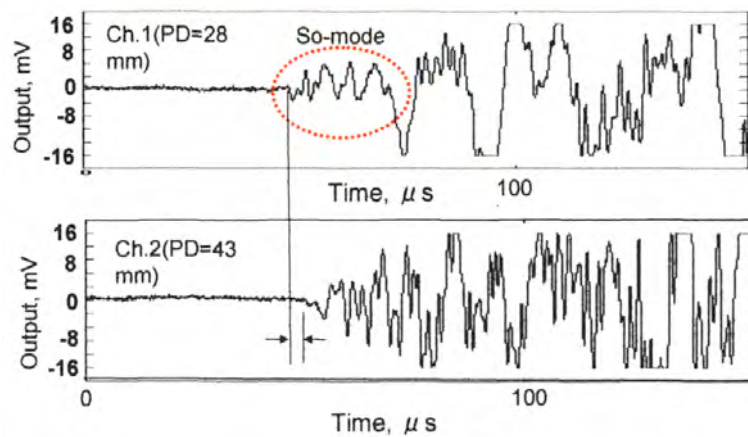


Fig. 13. Waveform of AE (DC-182) detected during strain holding at 1.23% for Nino-05 sample.

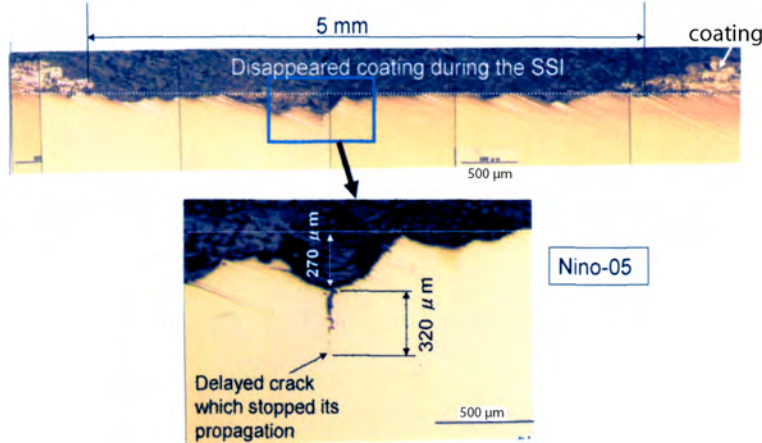


Fig. 14. Transverse section of Nino-05 after the SSI test. Nino-5 was originally exposed to pH = 0.4 sulfuric acid for 600 hrs at 0.83%.

We then examined the transverse section of Nino-05 sample, and found one crack of 320- μm length (see Fig. 14). The steel substrate suffered localized corrosion of 270 μm and coating layer was damaged over 5 mm by straining to 1.23 %. We assume the loss of coating over 5 mm around the central loading point occurred during the strain-increasing stage in the SSI test. We, however, can observe remaining coating on the right and left edges of Fig. 14. This means that the sprayed coating was corrosion resistant in pH=0.4 sulfuric acid when it is not heavily loaded.

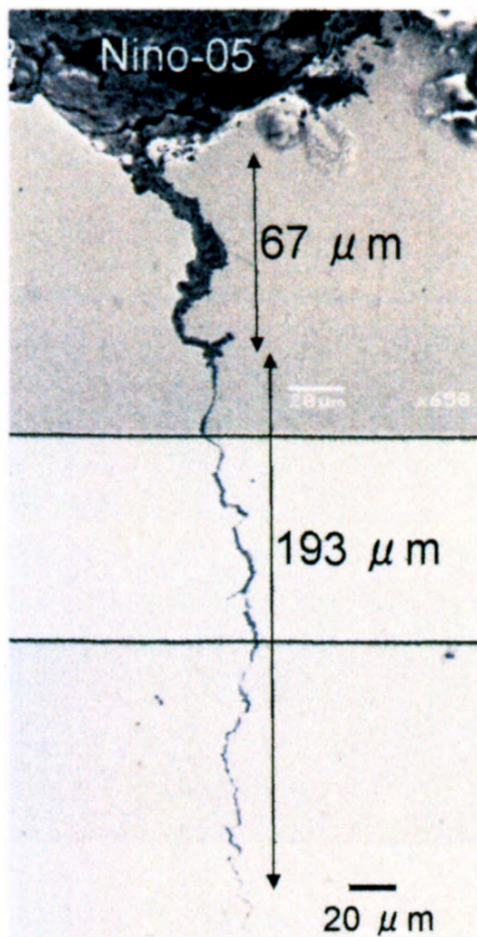


Fig. 15. SEM of delayed crack in sample Nino-05.

Substrate steel at loading point was attacked to the depth of 270 μm . As the corrosion rate of this steel in pH=0.4 acid solution is 1 ~1.2 $\mu\text{m/hr}$, the coating was corroded for the last 225 ~270 hrs exposure. In other word, the coating prevented the substrate from corrosion for the first 330 ~375 hrs even at strain of 0.83%.

For Nino-05 sample, we can observe a delayed crack at the bottom of the deepest local attack. SEM of this crack is shown in Fig. 15. We can see both the open crack of 67- μm long and closed crack of 193- μm long. The open crack, filled with corrosion product, appears to be generated during the immersion test in pH=0.4 solution for 600 hrs, while the closed crack was produced during the SSI test. This closed crack produced a delayed AE (DC 182) in Fig. 12, but stopped its propagation, due to a low hydrogen concentration in the steel.

Figures 16 and 17 are for the case for Nino-04 sample (TS-A), which was immersed in acid for 600 hrs at 0.8% strain. The SSI test of this sample (Fig. 16) emitted no delayed fracture AE even at 1.4% strain. Steel subst-

rate suffered a wall reduction of 230 μm over a 2-mm wide section. As the damage width (2 mm) of this coating is approximately half that (5 mm) of Nino-05, hydrogen concentration in the steel stayed at a low level, and cannot produce a delayed crack. Good information for us is that the sprayed coating, except at the central loading portion under 0.8% strain, protected the steel substrate almost perfectly from severe acid corrosion. We do not observe accelerated corrosion loss of the steel by galvanic action with noble 50Ni-50Cr coating. This dual-layer coating sealed by silicone (TS-A) is demonstrated to be an excellent barrier against corrosion and hydrogen diffusion when excess strain is not applied. It should be noted that the applied strain of 0.8% is extremely large in actual process equipment, corresponding the applied stress of 1.7 GPa.

Conclusion

The utility of thermal spray coating against delayed fracture of high strength steel was studied by determining the threshold strain under hydrogen exposure. Difficulty of detecting small cracks in the coated substrate can be overcome by using AE technique during SSI test. Delayed AE signals during strain holding accurately predict the existence of a small crack and help us determine the threshold strain for delayed fracture test. Threshold strain of the strips coated by dual layers of NiCr and titania were significantly improved, possibly by its diffusion barrier performance to hydrogen. Sealing of sprayed coating seems to be essential for excellent barrier performance against hydrogen diffusion and solution impregnation.

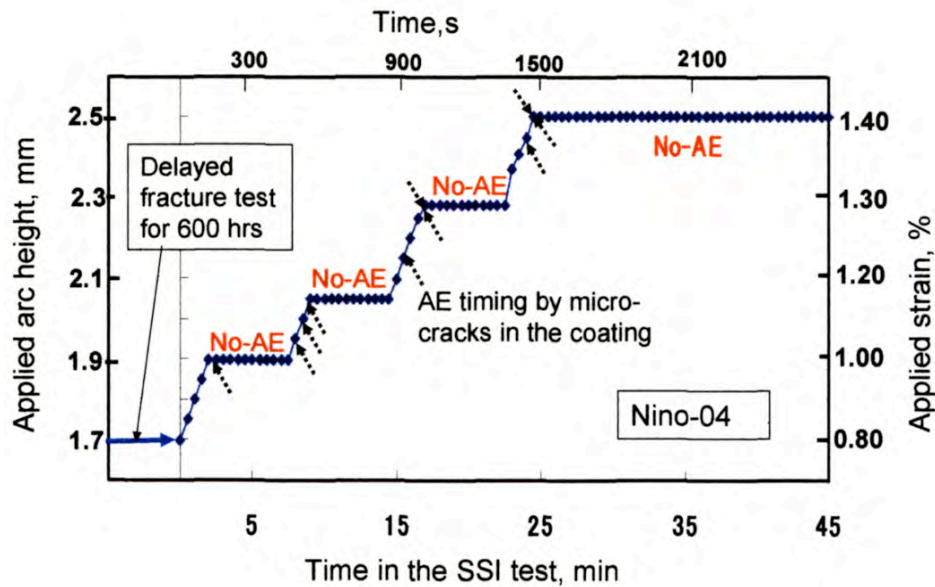


Fig. 16. SSI data of Nino-04, initially exposed to pH=0.4 sulfuric acid solution at 0.8% strain for 600 hrs.

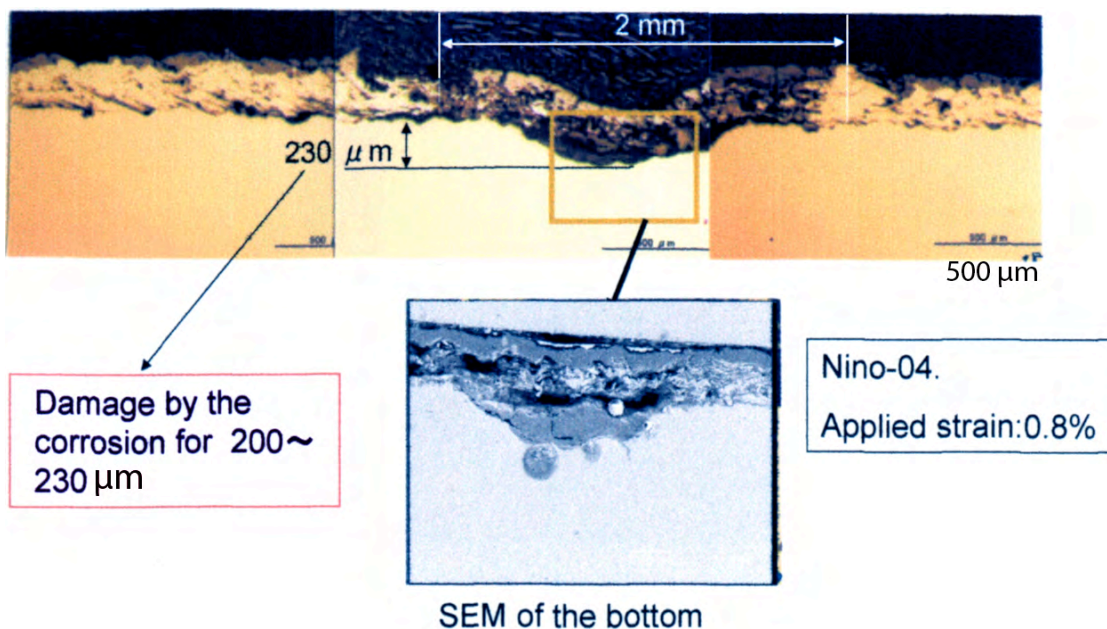


Fig. 17. Transverse section of Nino-04 sample after the SSI test.

References

1. K. Yamakawa, Typical Examples of Failure due to Hydrogen Embrittlement, Materials Science (in Japanese), **25**, (1976) 1110-1117.
2. M. Takemoto, M. Nakamura, S. Masano and S. Ueno, Effect of Shot Peening on the Delayed Fracture using the Almen Strip and AE Technique, J. Acoustic Emission, **27**, (2009) 241-243.
3. K. Yamakawa, Y. Minamino, K. Matsumoto, S. Yonezawa and S. Yoshizawa, Hydrogen Absorbability of SCM Steels and Its Effect on Cracking Behavior, Materials Science (in Japanese), **29**, (1981) 1102-1107.

THE EXTRACTION METHOD FOR DISPERSION CURVES FROM SPECTROGRAMS USING HOUGH TRANSFORM

D.A. TERENTYEV, V.A. BARAT and K.A. BULYGIN

Interunis Ltd., Build. 3-4, 24/7, Myasnitskaya str., Moscow 101000, Russia

Abstract

A Hough transform-based method is developed for the extraction of dispersion curves from spectrograms. This method has been successfully tested using experimental data from both an acoustic emission (AE) signal simulator, and actual AE sources. The method determines the distance to the signal source with an accuracy from 1 to 10% even when the signal arrives only to one sensor.

Keywords: Dispersion curves, spectrogram, extraction, Lamb waves, source location

Introduction

The main purpose of new research in the field of acoustic emission (AE) is development of techniques based on intelligent processing of waveforms, rather than on analysis of a limited set of AE parameters. Typically AE testing is performed on thin-walled metal structures with the wall thickness of 3 to 50 mm, AE signals are emitted by cracks as wideband impulses with the length of order of 1 μ s, working frequencies of AE sensors are within the range of 20-1000 kHz, and the distances between AE sources and sensors are much larger than the wall thickness. In this situation the signals arrive to sensors in the form of Lamb waves [1]; in most cases, in the form of combination of fundamental modes, namely, S_0 and A_0 . The main feature of this type of waves is dispersion, the frequency dependence of the propagation velocity, resulting in arrival of the different frequency components of the impulse to an AE sensor with a spread of tens and hundreds μ s (Fig. 1). This substantially impairs an accuracy of conventional AE source location, based on the calculation of arrival time differences and affected by the level of threshold and the average value of velocity measured in several times at the tested structures with the use of AE signal simulators.

The promising method for analyzing AE signals propagating as Lamb waves is application of spectrograms, which give a signal energy distribution in the time-frequency plane $\{t, f\}$ [2-5]. Hence, on the spectrogram $W(t, f)$ of the AE signal emitted by the source as a wideband impulse at the time point t_0 , which propagates along the infinite plate of h thickness in the form of combination of S_0 and A_0 Lamb waves, and received by the AE sensor being at L distance from the source, there are distinctive portions of two curves, which are specified by equations,

$$t(f) = \begin{cases} t_0 + L/V_{S_0}(f, h, V_L, V_T) \\ t_0 + L/V_{A_0}(f, h, V_L, V_T) \end{cases} \quad (1)$$

Here, V_{S_0} and V_{A_0} are group velocities of S_0 and A_0 waves, V_L and V_T are velocities of bulk longitudinal and transverse waves in the material. The intensity of dispersion curves portions pertaining to different frequencies varies due to signal attenuation in the structure and non-uniformity of the sensor frequency characteristics.

As a rule, during the AE testing, the values of V_L , V_T and h are known. Thus, knowing the distance to source L and the source operation time t_0 , it is possible to characterize the AE signal spectrogram; alternatively, the signal spectrogram contains information about L and t_0 . Use of such information substantially increases the reliability and the accuracy of AE source location in comparison with the traditional threshold crossing method. Thus, the problem of developing an algorithm of dispersion curves extraction from the AE signal spectrogram is urgent.

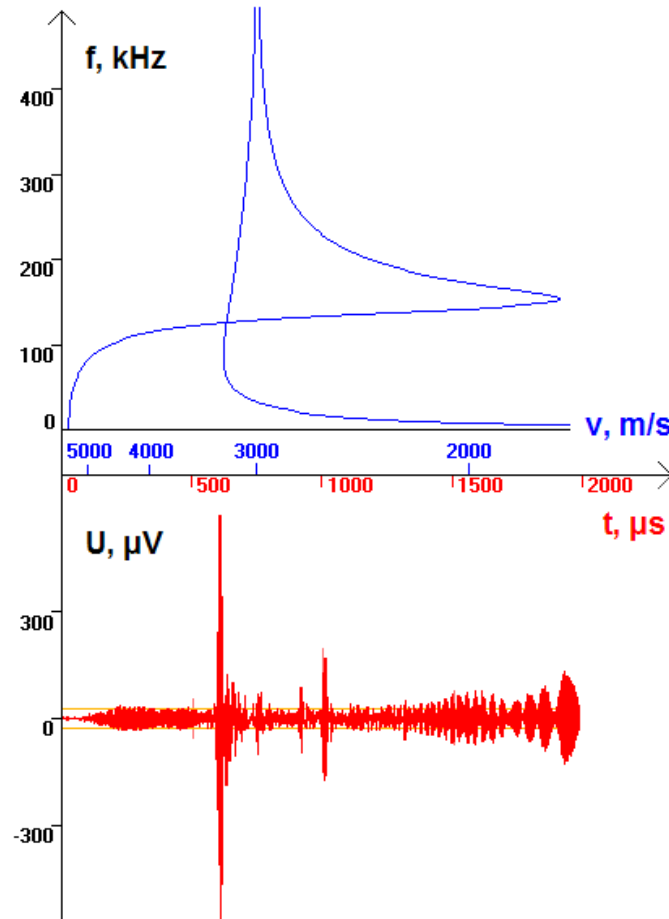


Fig. 1. The relationship between the group velocities and arrival times of different components of the AE signal.

Extraction Method

In addition to the parameters specified above, the AE waveform and signal spectrogram are influenced by crack type, radiation direction, signal attenuation, frequency characteristic of AE sensor, noise, and edge reflections. These significantly complicate the AE signal spectrogram with the result that the extraction of dispersion curves is more complex and not always resolvable problem [6].

We selected to use the generalized Hough transform method of extraction [7], offered in paper [8] for the case of arbitrary curves. As is evident from equation (1), any pair of plots of the dispersion curves of fundamental Lamb modes on the spectrogram is specified by two parameters previously unknown, namely, source operation time and distance of propagation. Thus, a number of the dispersion curves constitute a two-parameter family. Let us associate the two-dimensional parameter space $\{L, t_0\}$ with this family. Each point in the parameter space corre-

sponds to a pair of dispersion curves of S_0 and A_0 modes in the time-frequency plane $\{t, f\}$ (Fig. 2).

The problem of extraction reduces to search a set of parameters $\{L_{Hough}, t_{Hough}\}$, such that the dispersion curve plots (1) superimposed on the AE signal spectrogram in the widest frequency range falls on regions, where absolute values of the spectrogram coefficients exceed some threshold. As a threshold we have used the maximum absolute value of the spectrogram coefficients, which is multiplied by some factor ε to be selected as required by the noise level.

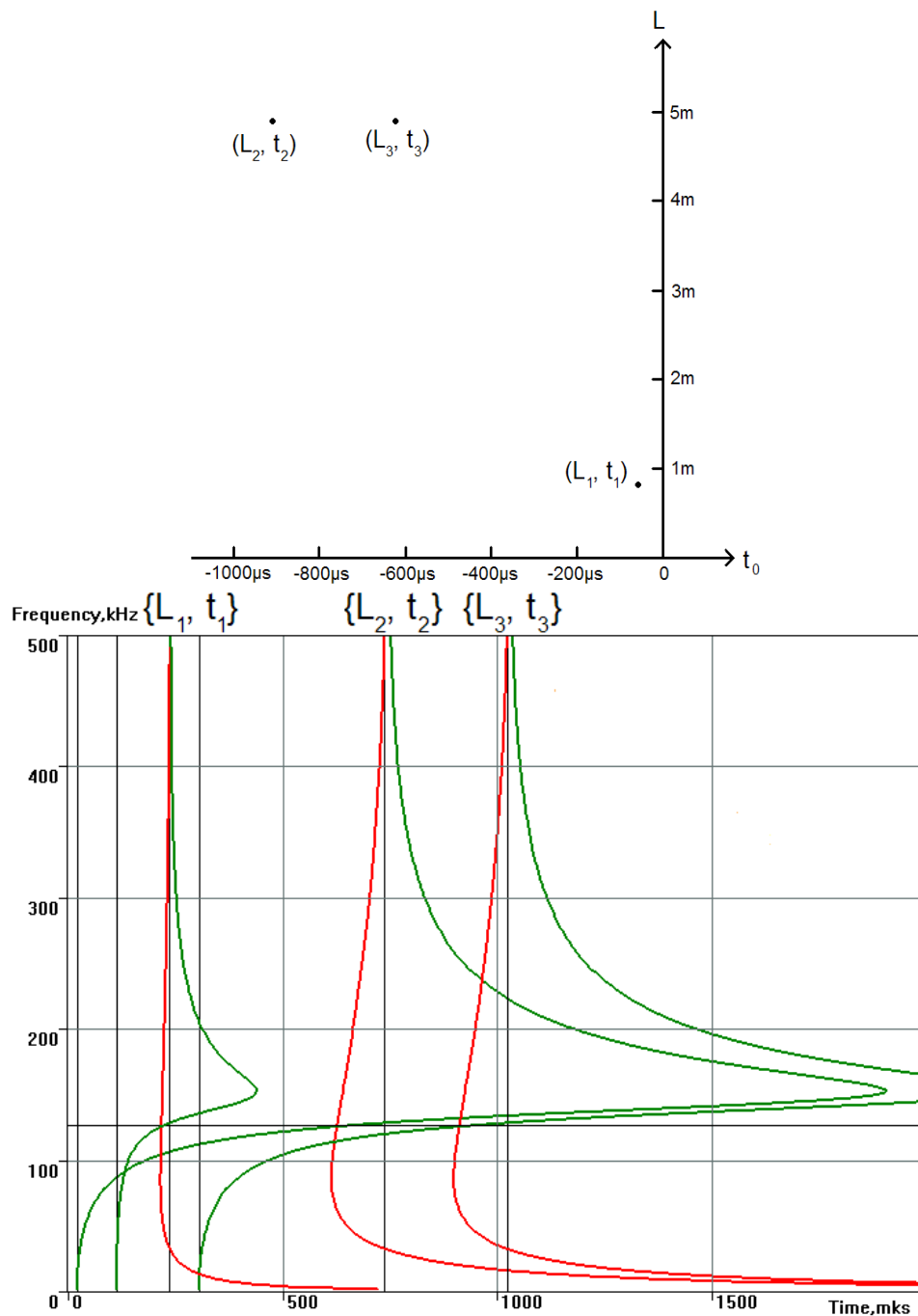


Fig. 2. An example of three points in parameter space $\{L, t_0\}$ and three corresponding pairs of dispersion curves in the time-frequency plane $\{t, f\}$.

Because a waveform recorded by a digital AE system is a one-dimensional array, whose elements are signal values at the sensor input at the discrete set of time points, the spectrogram calculated on its basis is a two-dimensional array, whose elements correspond to combinations of time and frequency values, pertaining to some discrete sets. To search parameters L_{Hough} and t_{Hough} , it was decided to organize two discrete sets of L and t_0 values. The values L were searched within the range from 0 to the value L_{max} . L_{max} is equal to the distance between the neighboring sensors or to the size of the tested structure. The values t_0 were searched within the range from $t_{min} = -L_{max} / V_{A_0}(\bar{f}_{min}, h, V_L, V_T)$ to the pre-triggering value $t_{max} = t_{pretrigg}$. Here, \bar{f}_{min} is the lowest operating frequency of sensor rounded to the nearest frequency on the spectrogram, and $t = 0$ corresponds to the beginning of the waveform. The quantity of elements in the array of distance values L was based on the required accuracy of distance measurement, the time values t_0 , as a rule, were searched with a step equal to the reciprocal of the sampling frequency.

The so-called accumulator two-dimensional array was organized so that each element should correspond to the quantity of spectrogram elements being on the S_0 and A_0 dispersion curves at corresponding combination of L and t_0 values from the discrete arrays described above and having values, exceeding the threshold in absolute value. To calculate values of the accumulator array elements, all combinations of variables L , t_0 and f from three appropriate arrays were searched. For each combination of the variables the value $t(f)$ was calculated by equation (1), and this value was rounded to a multiple to the reciprocal sampling frequency. The absolute value of spectrogram element corresponding to f and $t(f)$ was compared with the threshold, and in case of threshold-crossing a unity was added to the corresponding element of the accumulator array. Comparison of the accumulator array elements values permits to find the desired pair of S_0 and A_0 dispersion curves containing the greatest quantity of spectrogram points with absolute values above the threshold.

In a shorter form the algorithm used may be described as follows: parameters $\{L_{Hough}, t_{Hough}\}$ are searched such that

$$H(L_{Hough}, t_{Hough}) = \max_{i=1, I, j=J_1, J_2} H(L_i, t_j),$$

where

$$H(L_i, t_j) = \sum_{k=K_1}^{K_2} \left[\theta \left(\left| W \left(t_j + \frac{L_i}{V_{S_0}(f_k, h, V_L, V_T)}, f_k \right) \right| - \varepsilon \max(|W|) \right) + \theta \left(\left| W \left(t_j + \frac{L_i}{V_{A_0}(f_k, h, V_L, V_T)}, f_k \right) \right| - \varepsilon \max(|W|) \right) \right],$$

$$\theta(x) = \begin{cases} 1, & x \geq 0 \\ 0, & x < 0 \end{cases} \text{ - Heaviside step function, } \max(|W|) = \max_{n=1, J, m=1, K} (|W(t_n, f_m)|),$$

$L_i = L_{max} \frac{i}{I}$, I is user-defined quantity of elements in the array of distance values L ,

$J_1 = [t_{min} \cdot f_s]$, $J_2 = [t_{max} \cdot f_s]$, f_s = sampling frequency, $[x]$ is integer part of x ,

$|x|$ is absolute value of x , $f_k = \frac{k}{K} F$, $K_1 = \left[\frac{f_{min}}{F} K \right]$, $K_2 = \left[\frac{f_{max}}{F} K \right]$,

K is number of indexes on the frequency axis in the treated spectrogram,

F is the highest frequency on the treated spectrogram, f_{\max} is the highest operating frequency of sensor,
 $t_j = j / f_c$, $J = [T \cdot f_s]$, T is duration of the waveform.

The following major disadvantages of Hough transform-based method should be mentioned. First, the result depends on the threshold that should frequently be corrected manually on the basis of the noise level. Second, for any input signal, including a purely noise signal, this method gives some result, and no criteria for eliminating such results, frequently senseless, are involved in the Hough transform-based method.

Experimental Verification of the Present Technique

To evaluate the validity of the present technique, a series of experiments using a Hsu-Nielsen pencil-lead break and an electronic simulators of AE signals were applied on pipelines and cut portions of pipes having a wall of 8–17 mm thickness and 530–1220 mm diameter with and without insulation, liquid-filled and empty (Fig. 3). The distances between the signal source and the sensor were up to 56 m. Three types of AE sensors with the operating frequency ranges equal to 3-60, 40-100 and 130-200 kHz were used. Sampling frequency varied from 1 to 2 MHz.



Fig. 3. An experiment using an electronic simulator of AE signals.

It has been found that the spectrograms based on Wigner-Ville [9] and Choi-Williams [4] transforms are the most suitable for the experimental data analysis. The spectrograms on the basis of continuous wavelet-transform allowed for revealing dispersive curves of Lamb waves with worse resolution [4] that had an adverse effect on the accuracy of measurement of the distance to the signal source.

The accuracy of distance measurement was typically within the range from 1 to 10% (Table 1) depending on what frequency portions and what Lamb modes were observed on the spectrogram (Fig. 4). The best results in steel structures were obtained when the spectrogram exhibited the S_0 dispersion curve portions corresponding to the range of frequency from 1.5 to 4 MHz·mm/h. In this range, derivative of S_0 group velocity with respect to frequency is large

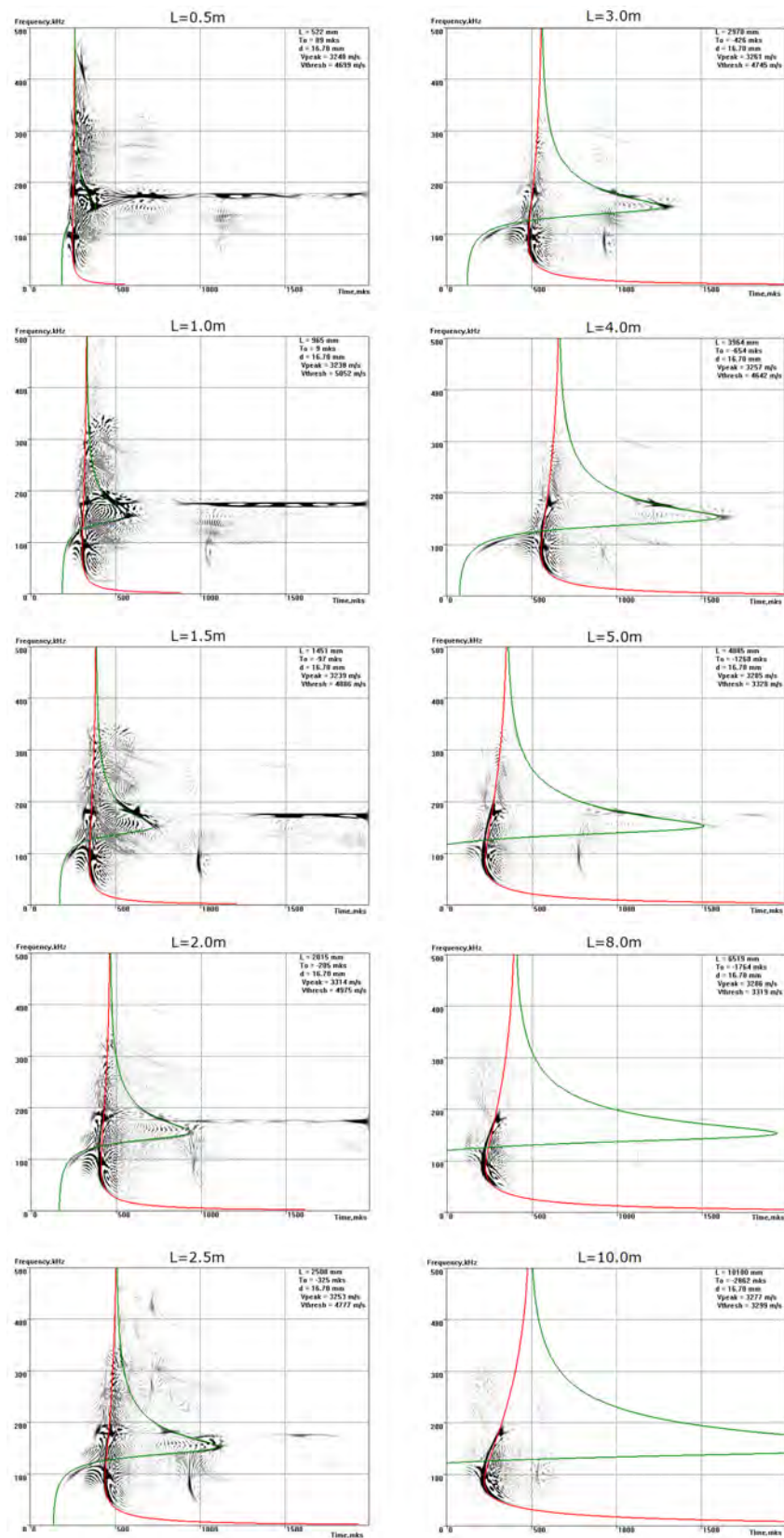


Fig. 4. An experiment on a pipeline without insulation. Hsu-Nielsen source is located at different distances from the AE sensor. Spectrograms based on Wigner-Ville transform, the results of dispersion curves extraction ($\epsilon = 0.05$, $f_{\min} = 30$ kHz, $f_{\max} = 200$ kHz) and corresponding dispersion curves.

enough in absolute value. The portions of the dispersion curve of the A_0 mode corresponding to 0 to 1 MHz·mm/h range possess the similar property, but did not yield high accuracy of distance measurement, since the ratio of the width of the dispersion curve observed on the spectrogram to the corresponding frequency was substantially higher than in case of the S_0 mode.

Table 1. An experiment on pipeline without insulation. The actual values of the distance between the Hsu-Nielsen source and the AE sensor vs. the results of dispersion curves extraction at different values of the threshold. $f_{\min} = 30$ kHz, $f_{\max} = 200$ kHz.

Actual values of the distance, m	Results of extraction at $\varepsilon=0.01$, m	Results of extraction at $\varepsilon=0.02$, m	Results of extraction at $\varepsilon=0.05$, m
0.5	0.52	0.52	0.52
1.0	0.94	0.92	0.97
1.5	1.44	1.41	1.45
2.0	1.99	2.10	2.01
2.5	2.32	2.51	2.51
3.0	2.72	2.97	2.97
4.0	3.55	3.52	3.96
5.0	4.74	4.74	4.89
8.0	0.98	9.51	6.52
10.0	0.95	0.92	10.10

It has been revealed, that the present method is inoperative when the distances between AE sources and sensors are less than 0.5–1 m, because in this case the different portions of dispersing curves are insufficiently separated from each other along the time axis (Fig. 5). At the same time, this method has appeared to be efficient at the distances at least up to 56 m.

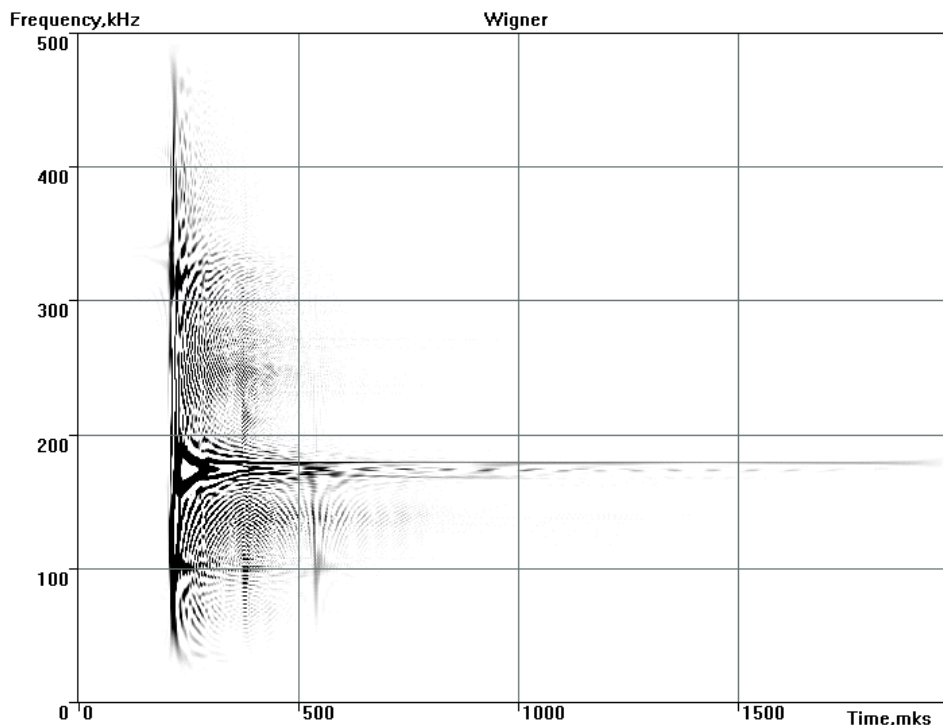


Fig. 5. A spectrogram of a signal from AE simulator, located at 0.15 m from AE sensor.

The coefficient ϵ specifying the threshold level, as a rule, was selected within the range from 0.001 to 0.05, depending on the noise level. No universal threshold level suitable for analyzing any AE signals was found. Therefore, as a rule, when going from one test piece to another, the threshold should be selected anew, since at the arbitrarily selected threshold level the method frequently produced evidently incorrect results (Fig. 6).

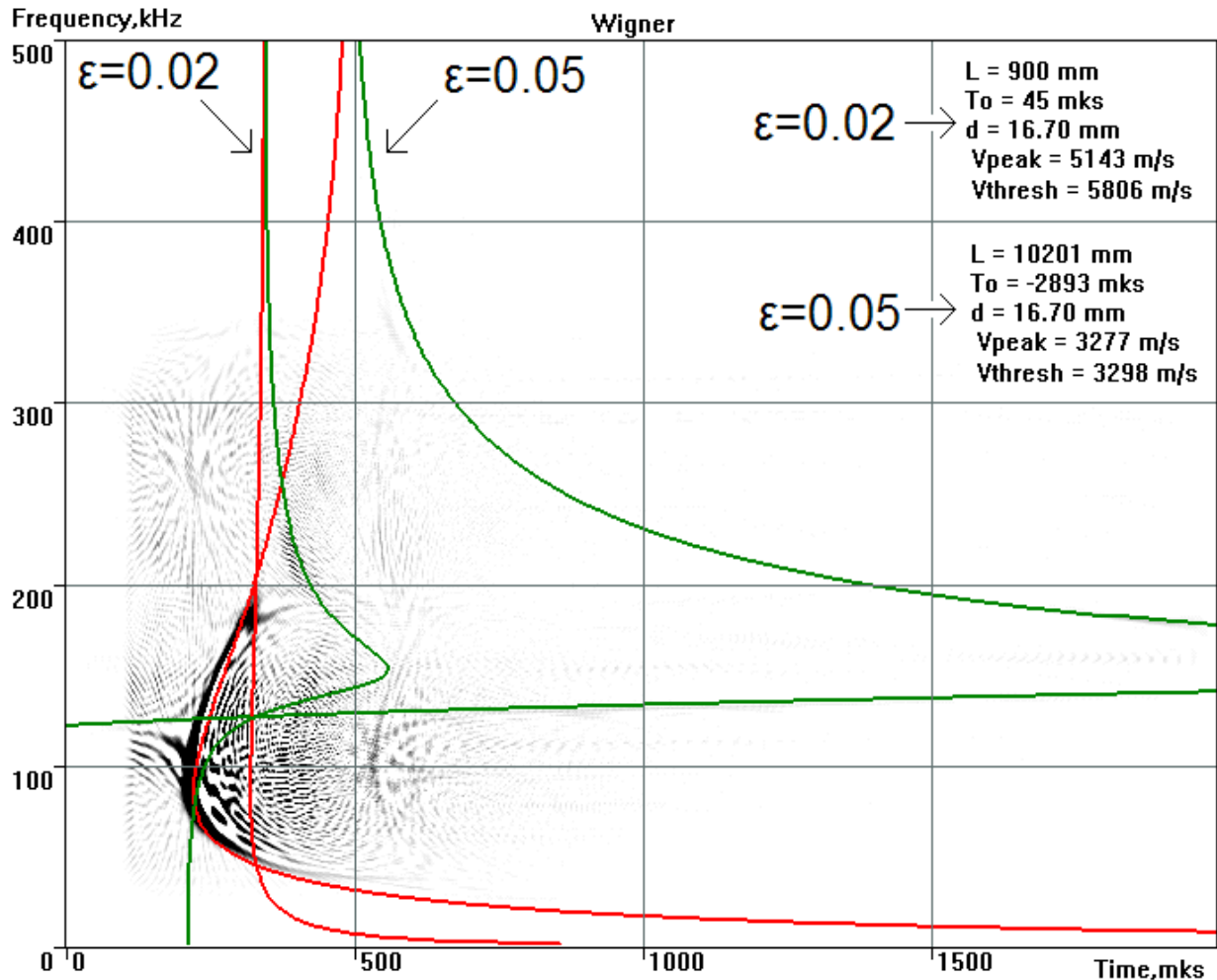


Fig. 6. The influence of the threshold level factor ϵ on the results of the dispersion curves extraction. Spectrogram of AE signal, incorrect results of dispersion curves extraction at $\epsilon = 0.02$, correct results of dispersion curves extraction at $\epsilon = 0.05$ and corresponding dispersion curves.

It was found, that the pipe curvature had no significant effect on the values of group velocity and this made it possible to use the Lamb wave model instead of the more complicated Pochhammer-Chree model [10, 11]. However, when analyzing the spectrograms, the substantial problem was in signals arriving not by the shortest routes, but by helixes, once or several times rounding the pipe. Existence of such signals resulted in occurrence of one or several additional curves on the spectrogram, which in contrast to electromagnetic interferences or other noises, are indistinguishable in their shape from the true dispersion curves. As a result, there could be a situation when at the threshold level selected incorrectly, the Hough transform method of extraction produces the value of distance between the AE signal source and the sensor, measured not along the shortest route, but along one of the helixes (Fig. 7).

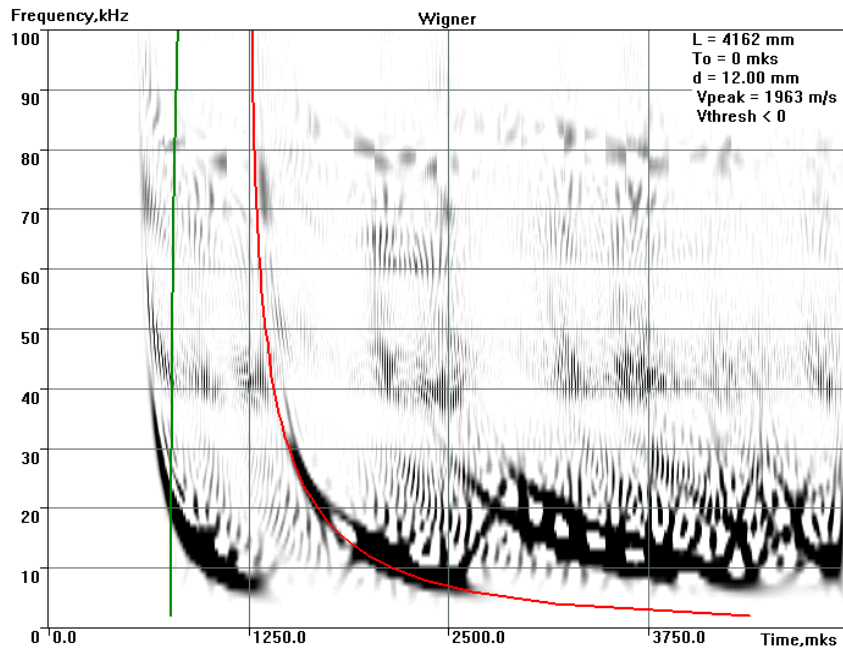


Fig. 7. A spectrogram of AE signal propagating by the helices, incorrect results of dispersion curves extraction and corresponding incorrect dispersion curves.

Next, this technique was used during testing of a buried gas pipeline with the distance between pits of about 40 m. In inspecting the pipeline, a number of AE signals arrived only to one of the mounted AE sensors. The lack of data for the time of arrival to the second AE sensor gave no way of measuring the source coordinates, which in turn did not allow for classifying AE sources. The location executed by the present method showed that the sources were separated from the AE sensor by 1.0 to 3.5 m (Fig. 8), and it was possible to classify the AE sources as the “noncritical active sources”.

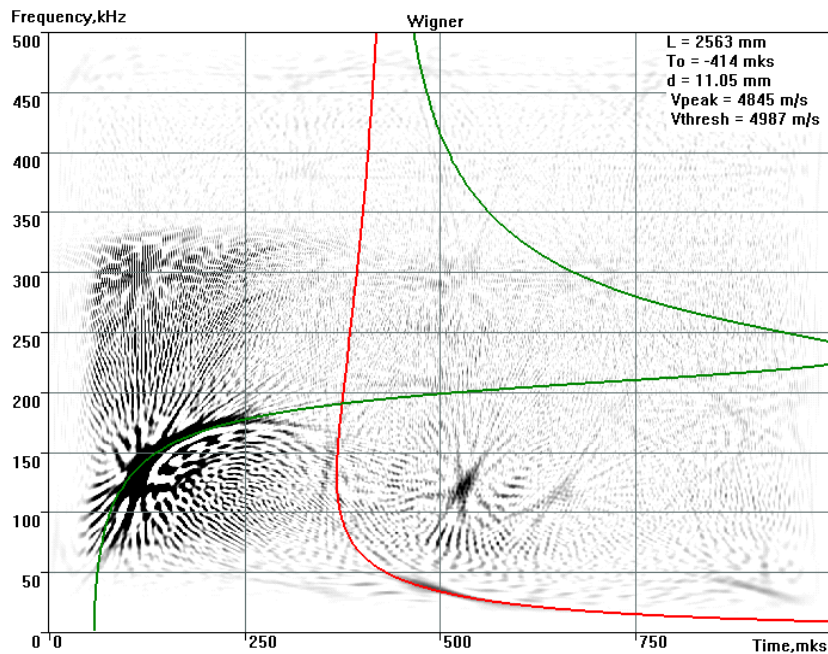


Fig. 8. A spectrogram of AE signal from a buried gas pipeline with the large distance between pits, results of dispersion curves extraction and corresponding dispersion curves.

With the successful results of the experimental check, the Hough transform method of extraction was added (Fig. 9) to the software complex of AE systems "A-Line" [5, 12].

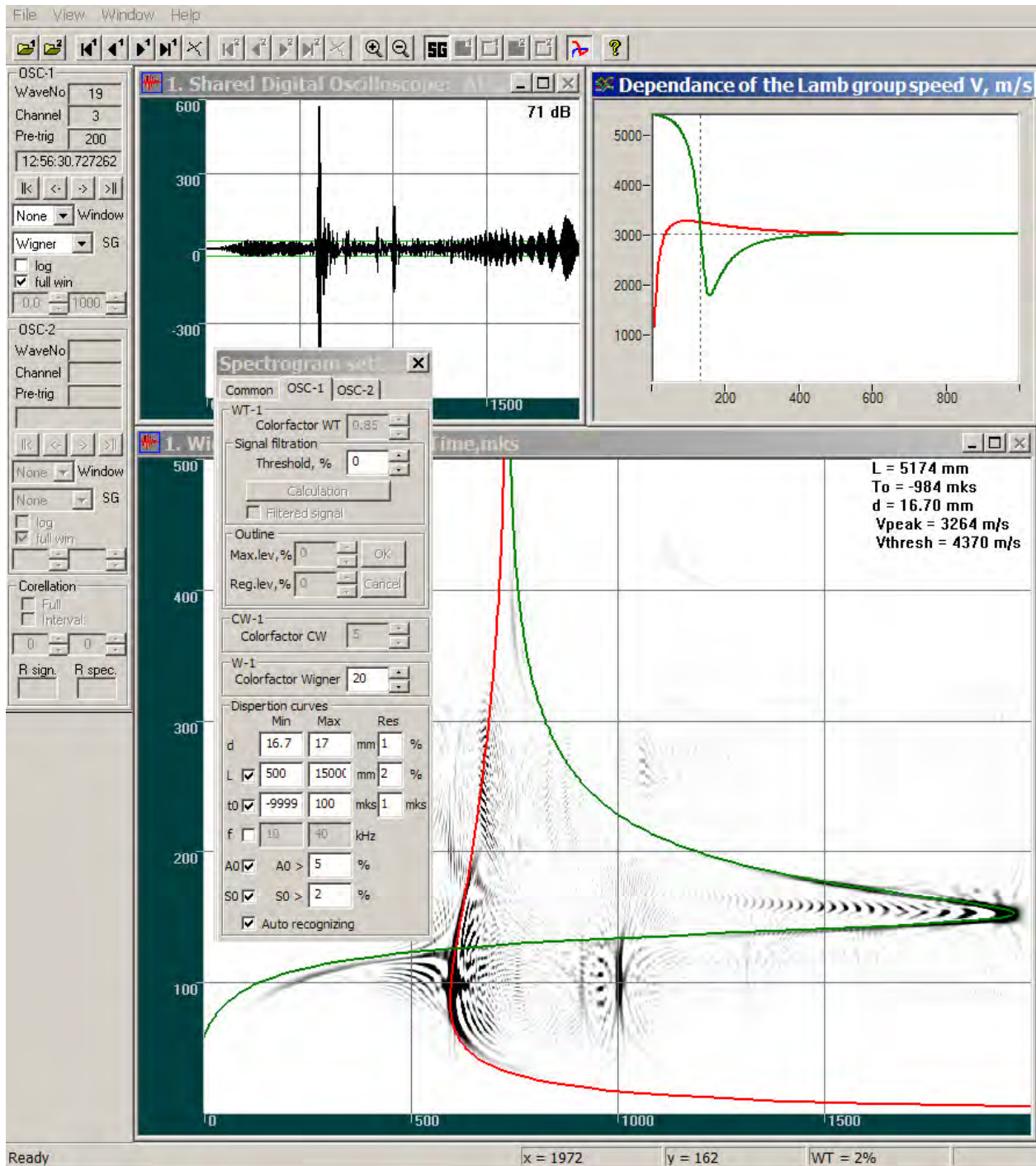


Fig. 9. "A-Line OSC Processing" software.

Conclusions

1. The Hough transform-based method is developed for automatic dispersion curve extraction from spectrogram with evaluation of their parameters, namely, the distance to the AE source and the source operation time.

2. The technique has been successfully tested using experimental data from both the AE signal simulator, and the actual AE sources.

3. The developed technique allows for calculating the distance to the signal source with an accuracy from 1 to 10% even when the signal arrives only to one sensor, giving the chance to perform the AE testing both in case of buried pipelines with the large distance between pits, and in case of one-sided access to a particular extended test piece.

References

1. Viktorov, I. A., “*Rayleigh and Lamb Waves: Physical Theory and Applications*”, Plenum Press, New York, 1967.
2. Suzuki H., Kinjo T., Hayashi Y., Takemoto M., Ono K., Appendix by Hayashi Y., "Wavelet Transform of Acoustic Emission Signals", *Journal of Acoustic Emission*, **14**, 1996, 69–84.
3. Hamstad, M. A., O’Gallagher A., Gary J., “Examination of the Application of a Wavelet Transform to Acoustic Emission Signals”, *Journal of Acoustic Emission*, **20**, 2002, 39–81.
4. Hamstad, M. A., “Comparison of Wavelet Transform and Choi-Williams Distribution to Determine Group Velocities For Different Acoustic Emission Sensors”, *Journal of Acoustic Emission*, **26**, 2008, 40–59.
5. Elizarov S., Bukatin A., Rostovtsev M. and Terentyev D., “New Developments of Software for A-Line Family AE Systems”, *Journal of Acoustic Emission*, **26**, 2008, 311–317.
6. Hamstad, M. A., “Acoustic Emission Signals Generated By Monopole (Pencil Lead Break) Versus Dipole Sources: Finite Element Modeling and Experiments”, *Journal of Acoustic Emission*, **25**, 2007, 92–106.
7. US Patent 3069654.
8. Duda R.O. and P.E. Hart, “Use of the Hough Transformation to Detect Lines and Curves in Pictures”, *Communications of the ACM*, **15**, January 1972, 11–15.
9. B. Allen et al, “*GRASP, a Data Analysis Package for Gravitational Wave Detection*”. Manual and package at: <http://www.lsc-group.phys.uwm.edu/~ballen/grasp-distribution/>
10. Gazis D. C., “Three-Dimension of the Propagation of Waves in Hollow Circular Cylinders”, *J. Acoust. Soc. Amer.*, Vol. **31**, 1959, №3, pp. 568–578.
11. PCdisp - Propagation of Ultrasound in Cylindrical Waveguides:
<http://www.iai.csic.es/users/fseco/pcdisp/pcdisp.htm>
12. “INTERUNIS” company official website: <http://eng.interunis.ru/products/pci>

STUDY OF ACOUSTIC EMISSION DATA ANALYSIS TOOLS FOR STRUCTURAL HEALTH MONITORING APPLICATIONS

MANINDRA R. KAPHLE, ANDY C.C. TAN, DAVID P. THAMBIRATNAM
and TOMMY H.T. CHAN

Queensland University of Technology, 2 George St, Brisbane, Australia

Abstract

Though acoustic emission (AE) is becoming a popular non-destructive testing (NDT) technique for structural health monitoring (SHM) of civil, mechanical and aerospace structures, challenge of effective analysis of recorded data still exists. This paper explores various tools for analysis of recorded AE data to address two primary challenges: discriminating signals from different sources and quantifying damage levels for severity assessment. It is believed such analysis will help in better understanding of mechanisms of AE generation and help enhance the monitoring capability of AE technique.

1. Introduction

Acoustic emission (AE) technique is one of the several diagnostic techniques used for structural health monitoring (SHM) applications. AE technique involves recording the stress waves by means of sensors and appropriate data acquisition system and subsequent analysis of the recorded signals to gather information about the nature of the source of emission [1]. AE technique is highly sensitive to crack activity (active cracks generate while dormant ones do not) and can provide continuous in-situ monitoring. Despite the advantages, successful use of AE technique for structural health monitoring applications has several challenges. A number of spurious sources can also produce AE signals, which can mask genuine damage related signals; hence, it is important to accurately sort extraneous noise from crack based AE [2]. Another important challenge is quantifying the level of damage to assess severity of sources.

Recording and analysis of the complete AE signal waveforms is now common. Though the signals captured by sensors are affected by the medium of propagation and the sensor characteristics, the signals still contain some information about the nature of the source [3]. Hence, complete waveform based analysis approach is believed to yield better results than traditional approach of using parameters alone in source discrimination. To analyse the recorded waveforms, frequency analysis using Fourier transform and time-frequency analysis using short-time Fourier transform (STFT) and wavelet analysis are popular tools. Ratios of energy distribution in different frequency bands from wavelet analysis has been used to identify different potential failure modes in composites [4]. Further, as similar source mechanisms emit similar signals, search for similarity also helps in source discrimination. Cross-correlation coefficients in time domain and magnitude squared coherence (MSC) in frequency domain can be used to check if signals are similar or not [3, 5, 6]. Quantifying damage level is usually attempted using different AE signal parameters or a combination of these. A traditional approach is the b-value analysis, see [7, 8]. It has been found to change during different stages of damage, for example when microcracks occur in the early stages of damage, the b-value is high but becomes low when macrocracks begin to occur [8], making the b-value a candidate to judge damage progress [9]. The b-value has been recently modified by using statistical values of amplitude distribution (mean and standard deviation) and the newer method is referred as improved b-value (Ib-value) [10]. Ib value improves calculation by selecting the amplitude limits of the linear range of the cumulative

frequency distribution data of AE [11]. Ib-value is usually calculated for a certain number of events (generally ranging from 50 to 100) during the test.

This paper aims to explore different data analysis approaches for source discrimination and severity assessment, by analysing AE data recorded from testing in laboratory.

2. EXPERIMENTATION

2.1 Source differentiation

For source differentiation experiments, two sources of AE signals were generated by (a) breaking 0.5-mm pencil leads (Hsu-Nielsen source) and (b) dropping steel balls (6-mm diameter) from a height of 15 cm on a 4 m long steel beam. Ten sets of each test were carried out. A four-channel μ -disp PAC (Physical Acoustics Corporation) system along with two R15 α sensors (made by PAC, resonant at 150 kHz) placed at distances of 1.5 m (Sensor S1) and 3 m (Sensor S2) from the source were used for data acquisition. The sensors were coupled using vacuum grease and magnetic holders. Preamplifiers were used with gain set at 40 dB. The signals were bandpass filtered between 20-400 kHz, as most signals were expected in this range. For each hit, data was acquired at a sampling rate of 1 MHz and recorded for 15-ms duration.

Recorded signals were analysed, first by calculating energy distributions in different frequency bands from STFT analysis. Next, cross-correlation coefficient and magnitude-squared coherence were calculated using Matlab commands 'xcorr' and 'mscohere' to check signal similarity in time and frequency domains, respectively. The command 'xcorr' gives the value of 1 for two identical signals. Similarly, 'mscohere' gives values lying between 0 and 1, which indicate how well two signals correspond to each other at each frequency; with the value of 1 indicating exact match [12].

2.2 Severity assessment

For damage quantification experiment, three-point bending tests were carried on steel pieces (300-mm long, 25-mm wide and 10-mm thick, with a small 45° V-notch in the middle to initiate the crack growth). Instron tensile machine with 100 kN load-cell was used to apply loads to three specimens at loading rates of 1, 2 and 3 mm/min each. To set the threshold value for recording and ensure sensors were performing correctly, pencil-lead breaks (0.5-mm diameter HB leads) were carried out near the crack tip. The value of 60 dB was used as the threshold value in each case, as this value was found to prevent the recording of lower amplitude reflected signals from the pencil-lead break tests. Same system and settings were used for AE data acquisition. Two R15 α resonant sensors were placed at the ends of the specimens equidistant from the crack in order to record signals.

3. Results and Discussion

3.1 Source differentiation

Typical pencil-lead break (PLB) and ball-drop (BD) signals recorded by sensor S1 along with their time-frequency STFT representation calculated using Time-frequency toolbox [13] are shown in Figs. 1 and 2, respectively. Only initial 2 ms of data were used for analysis purposes. The BD signal shows higher energy levels but at lower frequency bands compared to the PLB signal. To study energy distribution with frequency, energies across the total time were summed and the values normalized with respect to total energy across all times and frequencies. Values of these energy ratios against frequencies for ten PLBs and ten BDs are shown in Fig. 3.

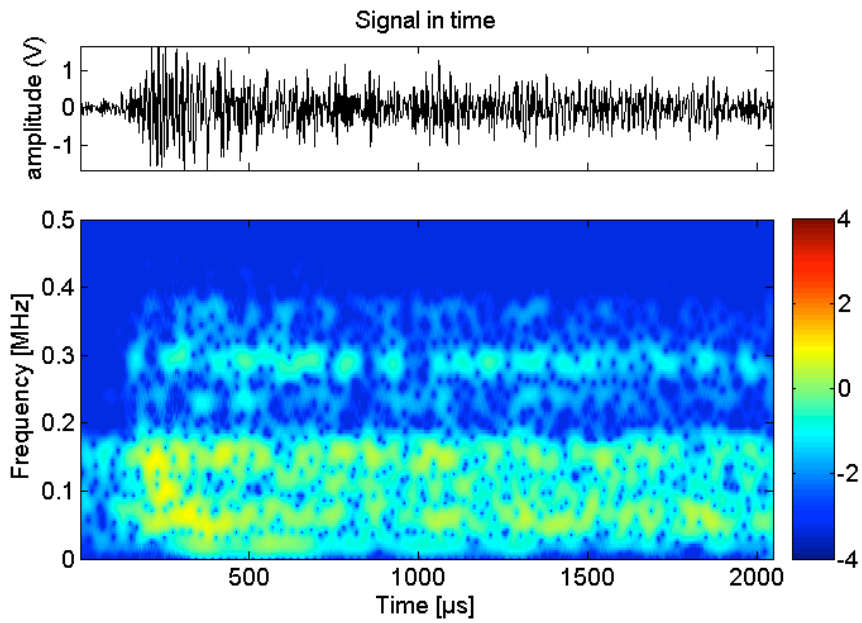


Fig. 1. PLB signal (upper) along with its STFT representation (below).

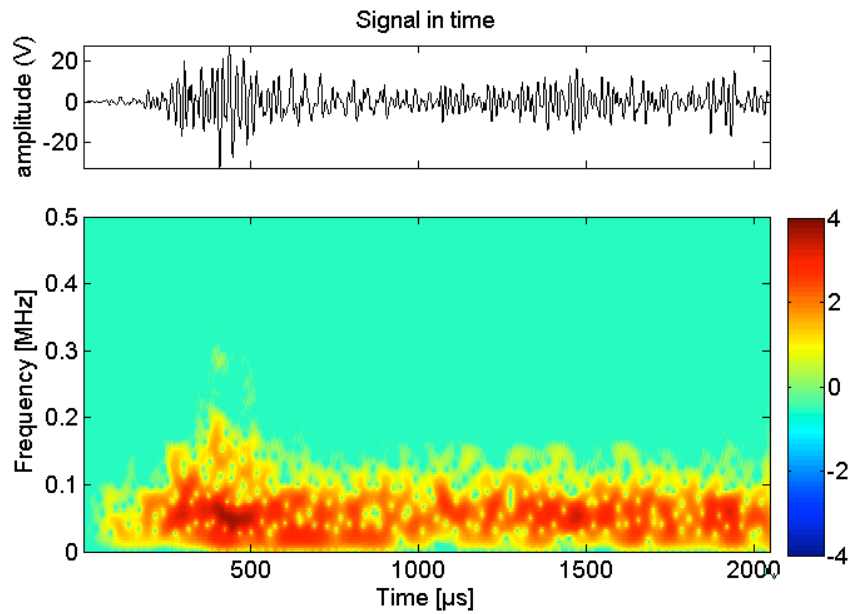


Fig. 2. BD signal (upper) along with its STFT representation (below).

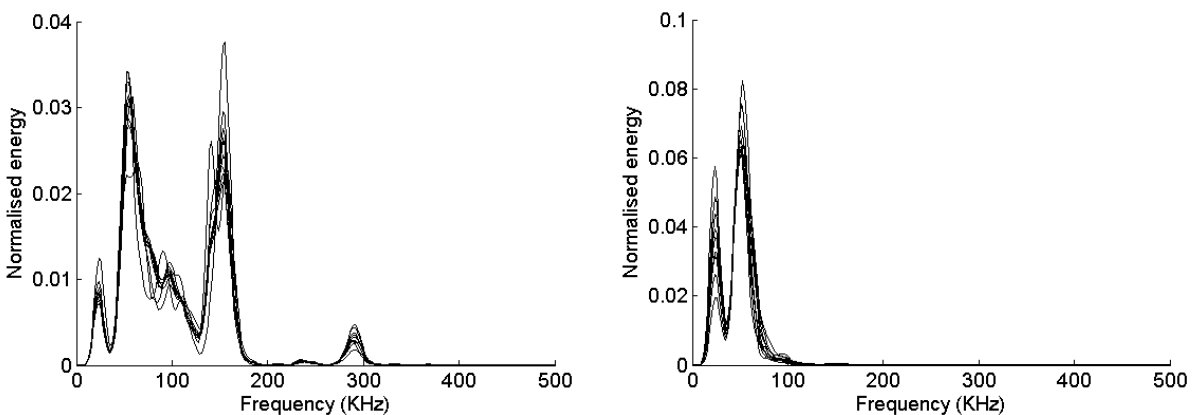


Fig. 3 Distribution of energy against frequencies for PLB and BD signals.

For PLB signals, most energy lies around two peak frequencies of 70 kHz and 170 kHz and small peak at 300 kHz. For BD signals energy is distributed around 70 kHz only. This distinct distribution of energy can differentiate sources.

Cross-correlation analysis: Using the PLB signal (Fig. 1) as the template signal, cross-correlation was performed with the remaining nine PLB signals recorded by S1 and with the ten BD signals, also recorded by S1. A sample result is shown in Fig. 4.

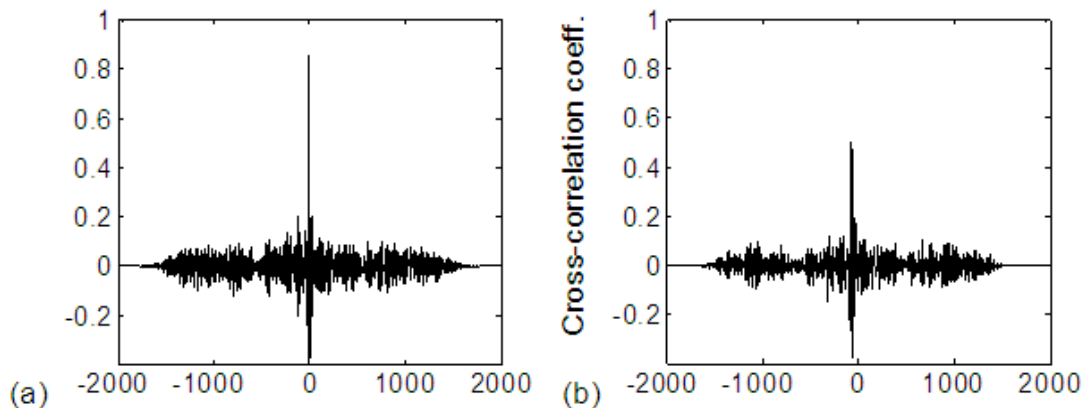


Fig. 4(a) Cross-correlation between two PLB signals (b) Cross-correlation between PLB and BD signals

High cross-correlation (maximum value 0.86) is seen for two PLB signals in Fig. 4a while in Fig. 4b the maximum value is only about 0.5. Cross-correlation of the template PLB signal with remaining nine PLB tests gave an average maximum value of 0.87 (actual: 0.80-0.91) while that for PLB-BD correlation was 0.48 (actual: 0.38-0.54). This difference in maximum cross-correlation values can be used as a criterion for signal discrimination.

Magnitude squared coherence analysis: Magnitude-squared coherence (MSC) analysis was performed using the same template PLB (Fig. 1) and rest of the signals recorded by the sensor S1. A typical plot of MSC values versus frequencies with a PLB signal is shown in Fig. 5a and that with a BD signal is shown in Fig. 5b. Figure 5a indicates closer match of frequencies between the PLB signals in the range 20 - 400 kHz (bandpass range), with an average value of 0.73. On the other hand, Fig. 5b indicates less coherence in that range, with an average MSC value of 0.27.

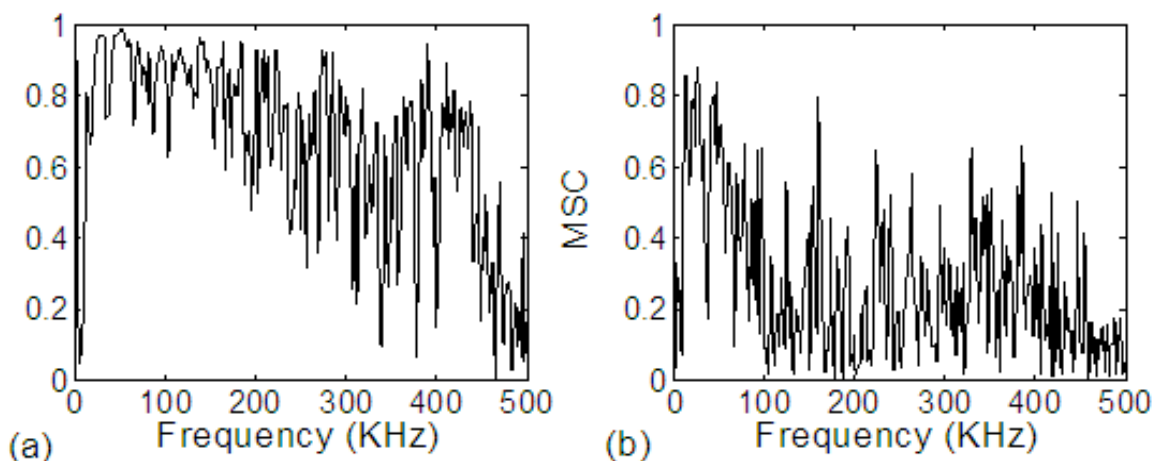


Fig. 5. MSC values versus frequencies. (a) two PLB signals, (b) PLB and BD signals.

While calculating MSC values of the template PLB with the other PLB signals, mean values lie in the range 0.71–0.75, while mean MSC values of the PLB signal with other ten BD signals lie in the much smaller range of 0.25–0.35 with a mean value of 0.29. Again, this distinct difference shows the usefulness of MSC values in signal discrimination.

It is noted that while performing cross-correlation and MSC between the template PLB-S1 signal (Fig. 1) and ten PLBs of sensor S2, very low values were obtained (less than the values obtained in earlier analysis between the PLB and BD signals recorded by the same sensor S1). Nevertheless, cross-correlation and MSC could identify same sources from same distance and this has significant advantage in SHM applications. For example, while monitoring the activity of a crack (finding it is active or benign) in gusset plate of a bridge in real time, being able to automatically filter out AE signals due to traffic using a template signal will significantly reduce the data load.

3.2 Severity assessment

The variation of load with time (to 500 s) for a three-point bending test along with the amplitudes of the hits for one sensor is shown in Fig. 6. When yielding starts, a large number of AE signals with higher amplitudes and energies were recorded in the region of transition between the elastic and plastic deformation. The first visual signs of crack occurred after most of the AE hits, generally when the load reached the peak value. After this, the load decreased and the crack continued to grow but few new AE hits occurred. It is noted that these findings have been well known and have been reported previously.

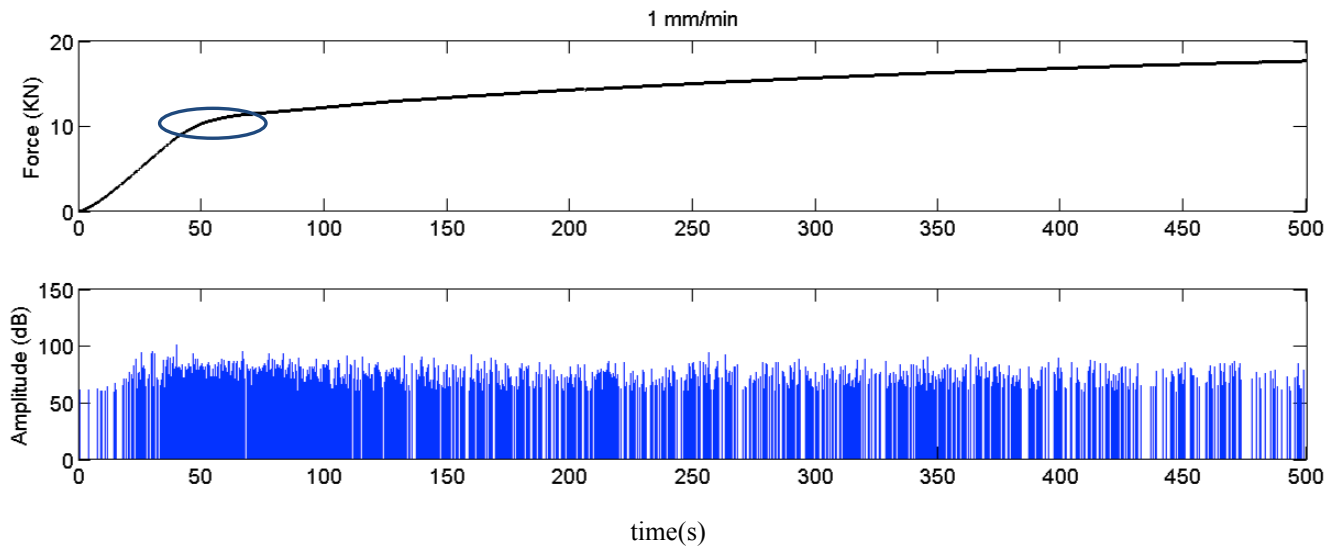


Fig. 6. Variation of force and AE amplitude with time for 1 mm/min loading.

b and Ib value analysis: The cumulative amplitude distribution (number of events vs. amplitude), showed that the linearity exists only in the earlier to middle portion of the distribution. For example, the distribution of amplitudes for 1 mm/min loading case is shown in Fig. 7.

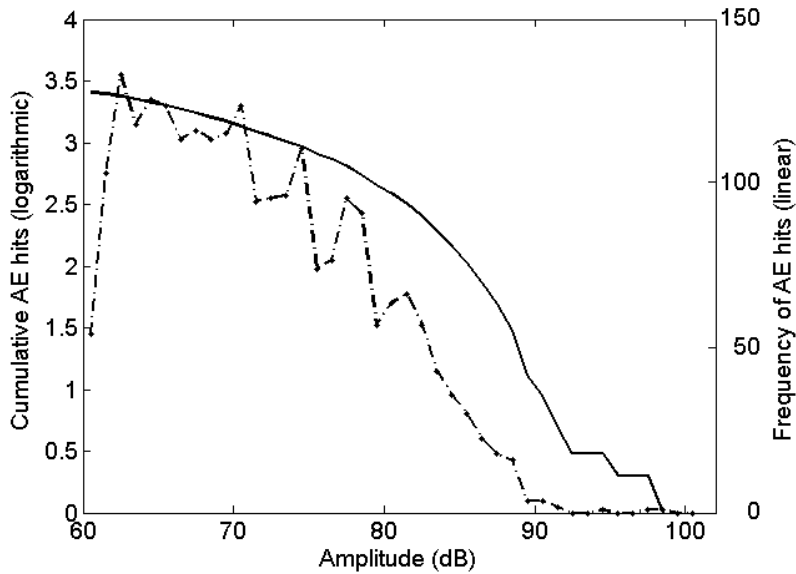


Fig. 7. Frequency (linear, dashed line) and cumulative frequency (logarithmic, solid line) of AE hits against amplitude.

Ib-value was utilized to calculate the slope in this linear region [10] using sets of 100 events with a lag of 20 events as done in [14], that is, the Ib value is first calculated for the group of the events 1-100, then 21-120, followed by 41-140 and so on. A sample Ib value calculation for first set of 1 mm/loading case is shown in Fig. 8. The results showing the variation in Ib-value (multiplied by 20 as suggested) with time for the three loading cases are shown in Fig. 9.

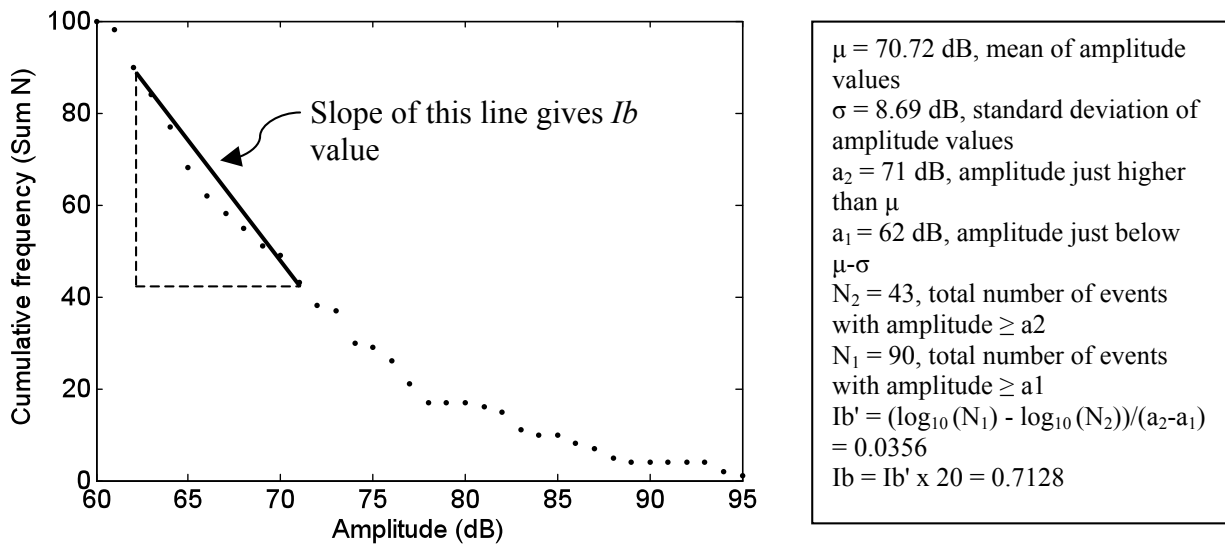


Fig. 8. Ib value calculation for first set of 100 events for 1 mm/min loading.

The plots in Fig. 9 show that the lowest Ib values are around 0.5 and occur at the yielding region (marked by an ellipse). As this region is known to be the areas of significant AE generation [15, 16], the occurrence of lowest Ib value has provided an accurate indication of damage occurrence. Further, higher activity (large number of AE event rates) and higher intensity events (events with higher amplitude) are also seen at the same time. These observations indicate that the instance of damage initiation is predicted by the lowest Ib-value.

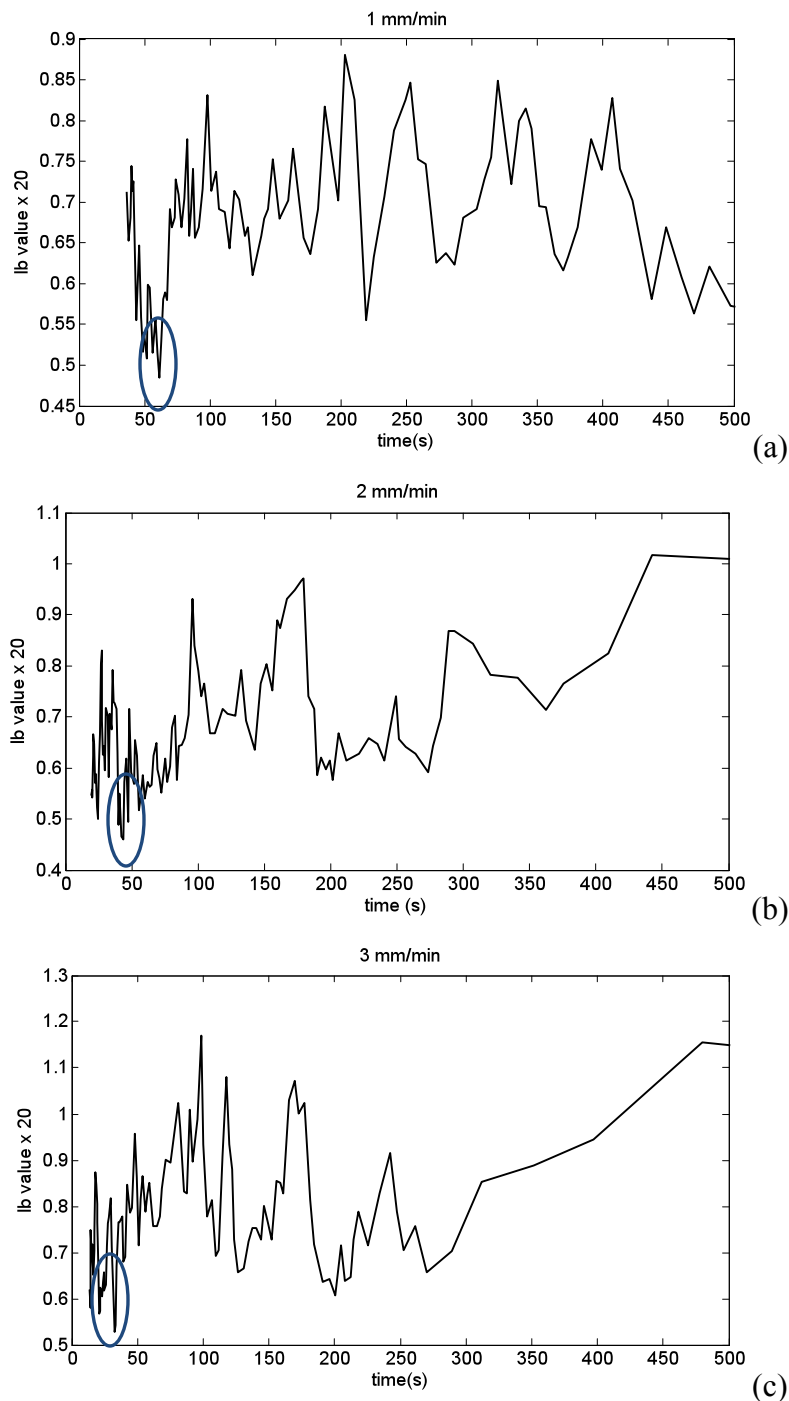


Fig. 9. Ib-values for three loading conditions.

Conclusions

The main aims of this study were to study some aspects of two important issues in application of AE technique for SHM of engineering structures, namely source differentiation and damage quantification. The results from the tests indicate that energy distribution in different frequency bands can be a suitable tool for differentiating signals from different sources. Further, if a template signal from a known source is available, it can be compared with subsequently obtained experimental signals using maximum cross-correlation value and average magnitude coherence values to judge signal similarity, thus performing source differentiation.

Regarding damage quantification, use of I_b -value to analyse recorded AE data from three-point bending load gave promising results. The studies on the use of I_b -value in brittle materials such as concrete and rock have found the value of around 1 at around the fracture point. The observations in the study show that the onset of plasticity, indicating the instance of damage initiation, was predicted by the lowest I_b -value.

More study on data analysis tools for source differentiation and damage quantification will further increase the effectiveness of AE technique for SHM of engineering structures.

References

1. Holford, K.M. and R.J. Lark, *Acoustic emission testing of bridges*, in *Inspection and monitoring techniques for bridges and civil structures*, G. Fu, ed. 2005, Woodhead, pp. 183-215.
2. Hamstad, M.A. and J.D. McColskey, *Detectability of slow crack growth in bridge steels by acoustic emission*. *Materials Evaluation*, 1999. **57**(11): 1165-1174.
3. Grosse, C.U., et al., *Improvements of AE technique using wavelet algorithms, coherence functions and automatic data analysis*. *Construction and building Materials*, 2004. **18**(3): p. 203-213.
4. Qi, G., *Wavelet-based AE characterization of composite materials*. *NDT&E International*, 2000. **33**(3): 133-144.
5. Eaton, M., et al., *Use of macro fibre composite transducers as acoustic emission sensors*. *Remote Sensing*, 2009. **1**(2): 68-79.
6. Kurz, J.H., et al. *Similarity matrices as a new feature for acoustic emission analysis of concrete*. in *26th European Conference on Acoustic Emission Testing*. 2004. Berlin: DGZfP. pp. 769-775.
7. Carpinteri, A., G. Lacidogna, and G. Niccolini, *Critical behaviour in concrete structures and damage localization by acoustic emission*. *Key Engineering Materials*, 2006. **312**: 305-310.
8. Colombo, S., I.G. Main, and M.C. Forde, *Assessing damage of reinforced concrete beam using 'b-value' analysis of acoustic emission signals*. *Journal of materials in civil engineering*, 2003. **15**(3): 280-286.
9. Carpinteri, A., G. Lacidogna, and S. Puzzi, *From criticality to final collapse: Evolution of the 'b-value' from 1.5 to 1.0*. *Chaos, Solitons and Fractals*, 2009. **41**(2): 843-853.
10. Shiotani, T., et al., *Application of AE improved b-value to quantitative evaluation of fracture process in concrete materials*. *Journal of acoustic emission*, 2001. **19**: 118-133.
11. Rao, M.V.M.S. and K.J.P. Lakshmi, *Analysis of b-value and improved b-value of acoustic emissions accompanying rock fracture*. *Current Science*, 2005. **89**(9). 1577-1582.
12. Mathworks, *MATLAB Users Guide*. 2009: Natick, MA.
13. Auger, F., et al., *Time-Frequency Toolbox - For use with MATLAB*. 1996, CNRS (France) and Rice University (USA).
14. Kurz, J.H., et al., *Stress drop and stress redistribution in concrete quantified over time by the b-value analysis*. *Structural health monitoring*, 2006. **5**(1): 69-81.
15. Mukhopadhyay, C.K., et al., *Acoustic emission during tensile deformation of annealed and cold-worked AISI type 304 austenitic stainless steel*. *Journal of materials science*, 1993. **28**: 145-154.
16. Han, Z., H. Luo, and H. Wang, *Effects of strain rate and notch on acoustic emission during the tensile deformation of a discontinuous yielding material*. *Materials Science and Engineering A*, 2011. **528**(13-14): 4372-4380.

NEURAL NETWORK FATIGUE LIFE PREDICTION IN NOTCHED BRIDGE STEEL I-BEAMS FROM ACOUSTIC EMISSION AMPLITUDE DATA

FADY F. BARSOUM, ERIC V. K. HILL, JAMIL SULEMAN, ANDREJ KORCAK
and YI ZHANG

Multidisciplinary NDE Group, Embry-Riddle Aeronautical University,
Daytona Beach, FL 32114

Abstract

Ten notched I-beams of A572-G50 bridge steel were loaded in three-point bending, and back-propagation neural network (BPNN) fatigue life predictions were performed on the acoustic emission (AE) amplitude histogram data taken during fatigue cycling. BPNN fatigue life predictions based on the AE data from the first (0-25%), second (25-50%), and third (50-75%) quarters of the fatigue life data yielded worst-case errors of 18.4%, 16.8% and 5.3%, respectively, for training on five beams and testing (predicting) on the remaining five. The worst-case prediction errors decreased to -12.4%, -13.4%, and 4.5% when trained on the AE data from six beams and tested on four. Thus, it was found that BPNN prediction accuracy was improved both by using more training data (six beams rather than five) and by training on AE data taken later (third quarter) in the fatigue life of the notched I-beams. Moreover, in an effort to simulate actual AE structural health monitoring (SHM) of bridges, AE fatigue data taken at semi-random time intervals after fatigue crack initiation were used to predict fatigue lives, which resulted in a worst case prediction error of 5.1% using five beams for training and five for testing. From all the above, it can be concluded that BPNNs trained on the AE amplitude histogram data from either the third quarter of the fatigue life or at semi-random time intervals after crack initiation can predict fatigue lives in A572-G50 bridge steel I-beams with worst case errors of $\leq 5\%$ by training on the data from at least six beams.

Keywords: A572-G50 bridge steel, back-propagation neural network, fatigue life prediction, I-beams, structural health monitoring, three-point bending

Introduction

This paper is a continuation of previous research on the fatigue life prediction of axially loaded, notched bridge steel bars using acoustic emission (AE) data and neural networks [1]. Back-propagation neural networks (BPNNs), when trained properly, are able to predict fatigue or residual life of cyclically loaded structures.

Previously, twenty notched A572-G50 steel bars were axially fatigue tested using an MTS machine. Fatigue life predictions were performed on the bars using AE amplitude histogram data as the input to the BPNNs. This yielded worst-case prediction errors within $\pm 20\%$ for first quarter of data and $\pm 12\%$ for third quarter of data [2]. Here this research was extended to three-point bending fatigue of notched A572-G50 steel I-beams, which are typical structural members used in bridge construction. BPNNs were used to process the AE data occurring during the first, second and third quarters of the fatigue life with the goal of reducing the worst-case errors, hopefully to within the $\pm 5\%$ range.

Experimental Setup

Ten notched A572-G50 bridge steel I-beams were simply supported on a large-scale testing frame with a transverse load acting at the midpoint of the span (three-point bending), simulating the loading condition of actual bridge members. Each S4 x 7.7 standard I-beam had a height of 101.6 mm (4") and span of 2.85 m. A 45 kN MTS actuator was used to apply the loading, which ranged from 1.36 to 17 kN at a frequency of 1 Hz and had a maximum deflection of approximately 13 mm. The actual loading was approximately sinusoidal, as the structure was stiff and the actuator would reach its resonant frequency when tasked to match the controller input exactly [3]. The hydraulic pump, located ~1 m behind the setup, generated noise, which was picked up by the AE analyzer but subsequently edited out of the data set. A plastic block was placed between the actuator and test specimen to reduce this noise coming from the actuator (in steel-steel connection, noise emissions will be transferred). Two 150 kHz AE transducers were mounted on the notched bottom flange of each I-beam. The Physical Acoustics Corporation Pocket AE[®] analyzer with imbedded AEWin[®] software was used to record the AE data from the two transducers as the beam was fatigued to failure. The experimental setup is shown in Fig. 1.

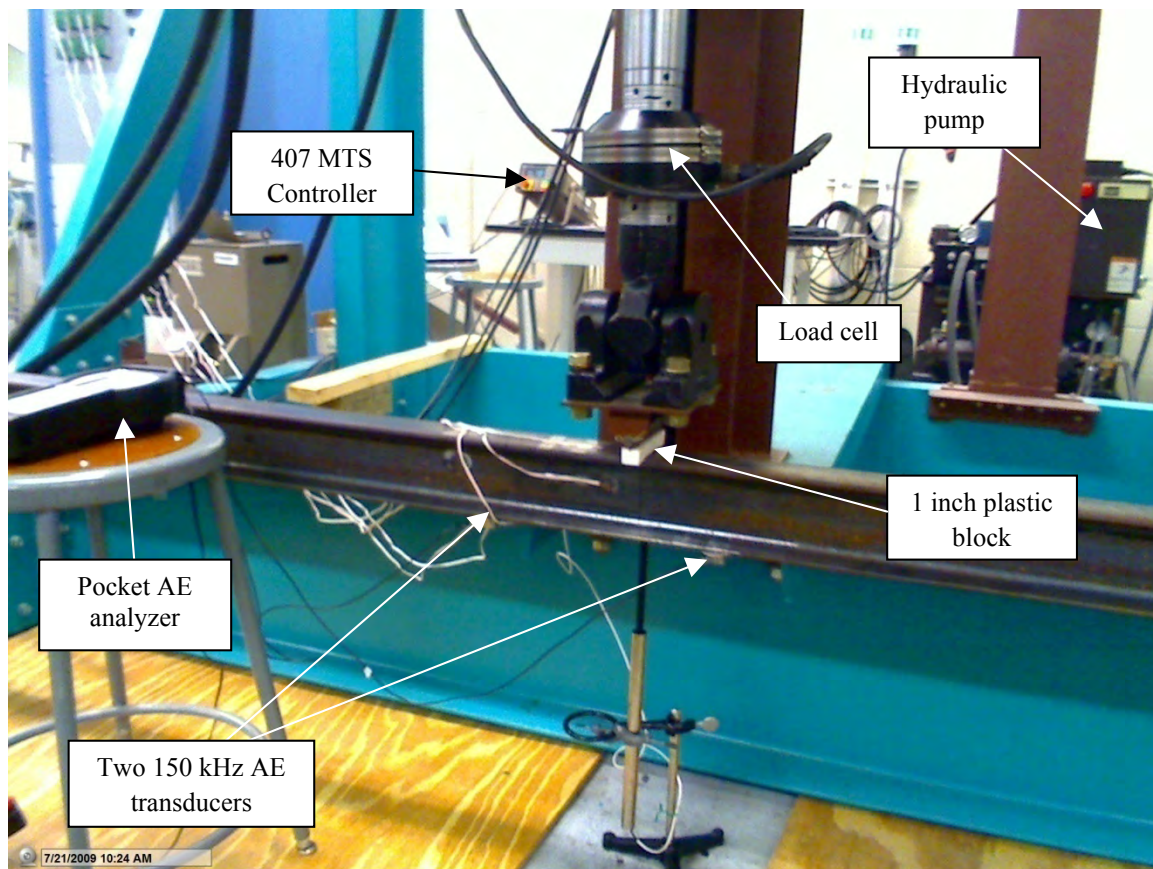


Fig. 1. Experimental setup.

A 2.5-mm deep 45° angle V-notch was machined on the bottom flange of the beam to ensure that fatigue cracking would initiate on the bottom, instead of on the top where the stress concentration was formed due to the load application, as shown in Fig. 2. The AE transducers were mounted on each side of the notch using hot melt glue as an adhesive/couplant. This setup allows verification of the location of the source of the AE activity to ensure that the AE data collected are from the known crack location at the center of the I-beam bottom flange.

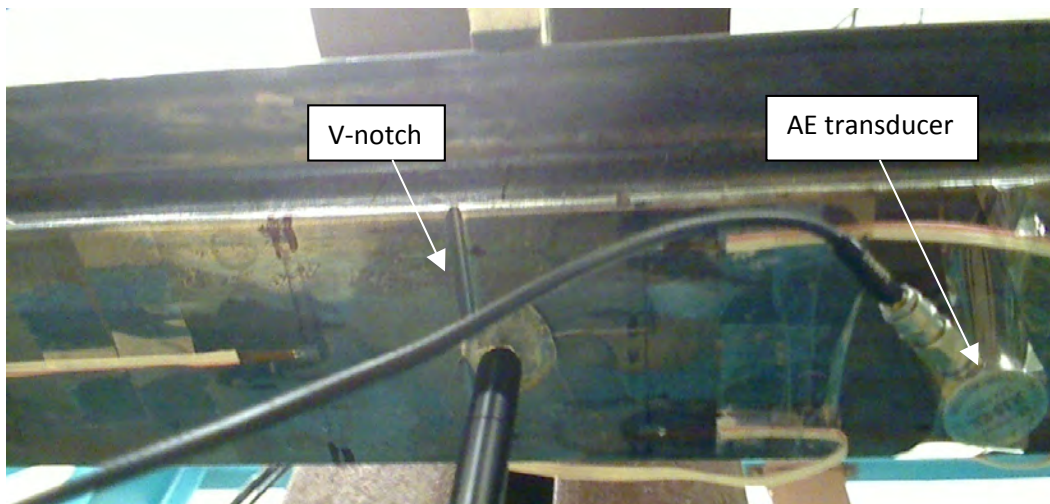


Fig. 2. Bottom view of the notched beam.

Noise Filtering and AE Settings

The noise involved in this experiment includes that from the MTS servo-hydraulic actuator, rubbing at the point of force application, ambient noise and electromagnetic interference from the AE analyzer/charger interface. Various noise was removed by the appropriate setting of the signal threshold within the AE analyzer and the application of filters on the average frequency and the count characteristics of the incoming signals. In order to investigate noise behaviors, several ambient noise tests were run without loading (the MTS machine switched on, but both the mean cyclic load and the span setting were set to zero) prior to the actual experiment. These AE ambient noise data were recorded and analyzed. The amplitude histogram and duration vs. count graphs were subsequently plotted.

The amplitude histogram of the noise data is shown in Fig. 3, which displays constant noise signals ranging from 30 to 43 dB. This noise was probably a combination of the coupled hydraulic pump noise and other ambient noise. The threshold of AE analyzer was then set to 40 dB to eliminate this noise, meaning that the signals of amplitude below 40 dB would not be recorded. Here, the risk of losing data of interest was introduced, which is a typical issue involved in the AE nondestructive testing method. Therefore, to be on the safe side, the highest amplitude ambient noise signals (41 through 43 dB) were not filtered out at this point.

A duration vs. count graph using the above noise data was also plotted, as shown in Fig. 4, where the ratio of counts divided by duration is the average frequency of each signal. It can be seen from the graph that the noise was mostly confined to average frequencies (AFs) of 15 kHz or less, except for the long duration hits at the top. An average frequency filter was thus applied to eliminate the noise of AFs less than 15 kHz. Here again, the AFs from 15-30 kHz were not eliminated at this point so as not to eliminate any data of interest. Figure 5 is the same plot as Fig. 4 but with the AF filter applied. Note that the noise from 16-30 kHz is still present. It can also be seen from Fig. 5 that there is a cluster of several thousand short duration, low counts signals close to the origin. This was removed by filtering on AE hits with counts less than 5.

In addition, AE hits with zero duration or rise time, or extra long duration (due to continuous rubbing or hydraulics) are either noise or incomplete data hits, both of which were removed manually from the individual data files recorded from the actual testing. After the noise tests

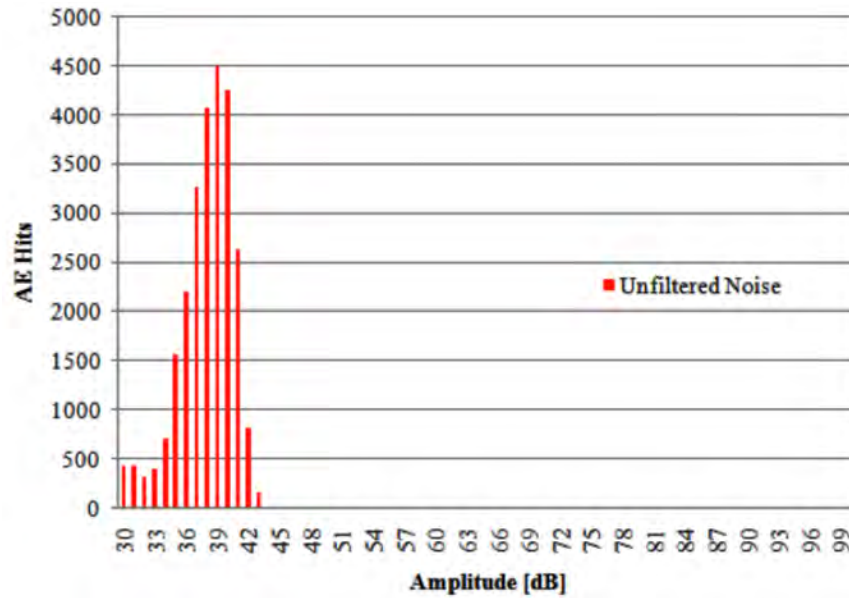


Fig. 3. Amplitude histogram of unfiltered noise.

were performed, the amplitude threshold of AE analyzer was set to be 40 dB for both channels, and the maximum duration was set to 2 ms to allow all data of interest to be captured. The waveform parameters, peak definition time (PDT), hit definition time (HDT), and hit lock-out time (HLT), were set to separate noise from fatigue data according to the recommended values [4].

Beam Experimental Results

The experimental fatigue lives of the ten I-beams ranged from 11,811 to 19,653 cycles with the typical large variability of fatigue lives evident. The mean and standard deviation were 16,229 and 2,324 cycles, respectively. In this research, the AE amplitude histograms were utilized as inputs to the BPNN for fatigue life prediction. The amplitude histograms for all ten I-beams are plotted in Fig. 6. It can be observed that the AE fatigue cracking data for all the beams are in the same amplitude band but have different magnitudes (some beams produce more AE than others).

Three BPNN networks were constructed to predict the fatigue lives of tested I-beams based on the AE amplitude histograms from the first quarter (0-25%), second quarter (25-50%) and third quarter (50-75%) of the cyclic life data. Predictions using either five or six training specimens (beams) were then investigated.

Fatigue Life Prediction Results

BPNN Predictions Based on First Quarter (0-25%) of Life AE Data

NeuralWorks Professional II/Plus Software was used for prediction. Two BPNNs were trained and tested based on the AE data of the first quarter (0-25%) of fatigue lives. The first network was trained on five samples (beams 5, 6, 7, 8, 9) and tested on the other five, while the second network was trained on six (beams 5, 6, 7, 8, 9, 11) and tested on four. The training specimens were selected to include the beams having the highest and lowest fatigue lives plus some in between for best prediction results. The BPNN parameters were optimized to the parameters

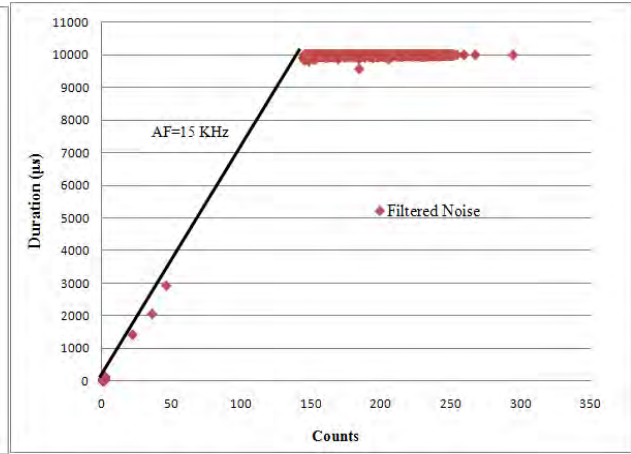
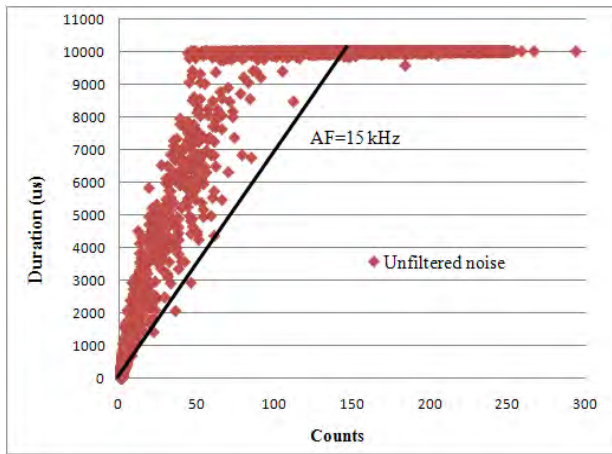


Fig. 4. Duration vs. count plot, unfiltered noise. Fig. 5. Duration vs. count plot, filtered noise.

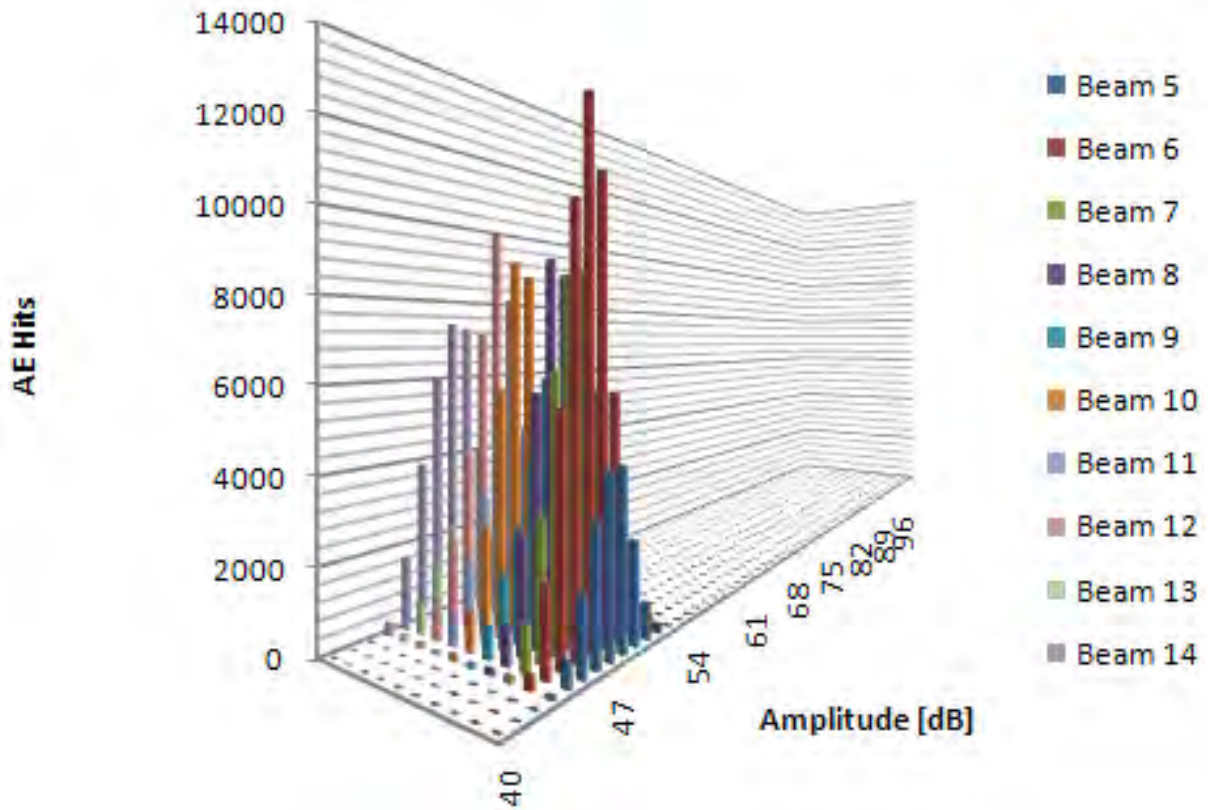


Fig. 6. Amplitude histograms of all tested beams [3].

shown in Table 1. Prediction results based on five training files are shown in Table 2, where the maximum prediction error was 18.4%. Table 3 shows the prediction results based on six training files, where the maximum error was -12.4%.

BPNN Predictions Based on Second Quarter (25-50%) of Life AE Data

This network predicts the fatigue life using AE data from the second quarter of fatigue life. Again both networks using five training files and six training files were investigated. The BPNN parameters are shown in Table 4. The prediction results from these networks are shown in Tables

5 and 6, where the worst case error were 16.8% based on five training files and -13.4% based on six training files.

Table 1. First quarter BPNN parameters.

BPNN Parameter	Train on Five	Train on Six
Hidden Layer Neurons	3	3
Hidden Layer Learning Coefficient	0.8	0.5
Output Layer Learning Coefficient	0.05	0.05
Transition Point	90	85
Learning Coefficient Ratio	0.5	0.2
Learning Rule	Norm-Cum-Delta	Norm-Cum-Delta
Transfer Function	TanH	TanH

Table 2. First quarter prediction results (five training files).

Specimen	Experimental Fatigue Life	Predicted Fatigue Life	% Error
Beam 10	19,188	17,636	-8.1
Beam 11	13,573	16,068	18.4
Beam 12	15,833	15,753	-0.5
Beam 13	15,710	12,824	-18.4
Beam 14	16,084	17,412	8.3

Table 3. First quarter prediction results (six training files).

Specimen	Experimental Fatigue Life	Predicted Fatigue Life	% Error
Beam 10	19,188	16,805	-12.4
Beam 12	15,833	15,499	-2.1
Beam 13	15,710	14,234	-9.4
Beam 14	16,084	16,996	5.7

Table 4. Second quarter BPNN parameters.

BPNN Parameter	Train on Five	Train on Six
Hidden Layer Neurons	3	3
Hidden Layer Learning Coefficient	0.01	0.02
Output Layer Learning Coefficient	0.01	0.01
Transition Point	1000	950
Learning Coefficient Ratio	0.5	0.5
Learning Rule	Norm-Cum-Delta	Norm-Cum-Delta
Transfer Function	TanH	TanH

Table 5. Second quarter prediction results (five training files).

Specimen	Experimental Fatigue Life	Predicted Fatigue Life	% Error
Beam 10	19,188	16,586	-13.6
Beam 11	13,573	15,851	16.8
Beam 12	15,833	17,496	10.5
Beam 13	15,710	14,020	-10.8
Beam 14	16,084	15,431	-4.1

Table 6. Second quarter prediction results (six training files).

Specimen	Experimental Fatigue Life	Predicted Fatigue Life	% Error
Beam 10	19,188	16,629	-13.3
Beam 12	15,833	17,270	9.1
Beam 13	15,710	13,604	-13.4
Beam 14	16,084	15,340	-4.6

BPNN Predictions Based on Third Quarter (50-75%) of Life AE Data

Another set of BPNN networks was setup using the AE data from the third quarter of fatigue life for predictions. The network parameter setups are shown in Table 7. The prediction results are shown in Tables 8 and 9, where the worst-case error of 5.3% was based on five training files and the 4.5% error was based on six training files. It can be seen that the prediction becomes more accurate when using the AE data from the later part of fatigue life.

Table 7. Third quarter BPNN parameters.

BPNN Parameter	Train on Five	Train on Six
Hidden Layer Neurons	3	3
Hidden Layer Learning Coefficient	0.8	0.5
Output Layer Learning Coefficient	0.05	0.05
Transition Point	90	85
Learning Coefficient Ratio	0.5	0.2
Learning Rule	Norm-Cum-Delta	Norm-Cum-Delta
Transfer Function	TanH	TanH

Table 8. Third quarter prediction results (five training files).

Specimen	Experimental Fatigue Life	Predicted Fatigue Life	% Error
Beam 10	19,188	19,568	2.0
Beam 11	13,573	13,876	2.2
Beam 12	15,833	16,667	5.3
Beam 13	15,710	16,195	3.1
Beam 14	16,084	16,249	1.0

BPNN Prediction Based on Semi-Random Time Interval AE Data

In order to simulate the prediction capability of a BPNN in actual field testing, another network was constructed using AE data that were selected semi-randomly but after initiation of the fatigue crack. AE data intervals used were all from the early part of the cyclic lives, as shown in Fig. 7, and they did not have the same start times or lengths.

Table 9. Third quarter prediction results (six training files).

Specimen	Experimental Fatigue Life	Predicted Fatigue Life	% Error
Beam 10	19,188	19,550	1.9
Beam 12	15,833	16,485	4.1
Beam 13	15,710	16,419	4.5
Beam 14	16,084	16,362	1.7

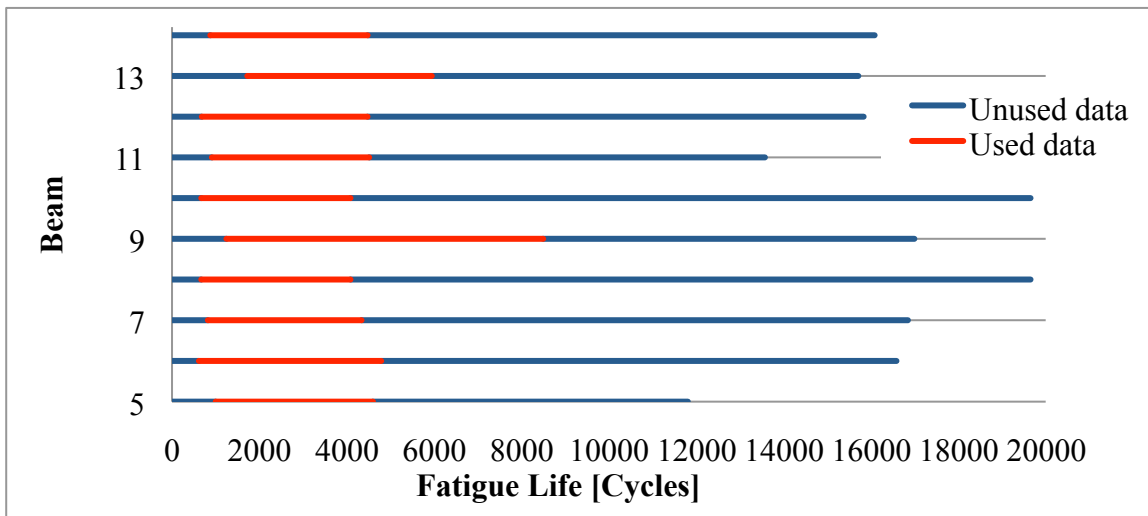


Fig. 9. Graphical illustration of semi-arbitrary AE data used for training and testing [3].

The network was trained on five beams and tested on the other five. The BPNN parameters are shown in Table 10 with the prediction results in Table 11. The worst-case prediction error for this network was 5.1%, which suggests the viability of BPNN in an actual structural health-monitoring scenario.

Table 10. BPNN parameters for semi-random time interval AE data.

BPNN Parameter	Train on Five
Hidden Layer Neurons	3
Hidden Layer Learning Coefficient	0.35
Output Layer Learning Coefficient	0.01
Transition Point	800
Learning Coefficient Ratio	0.5
Learning Rule	Norm-Cum-Delta
Transfer Function	TanH

Table 11. Prediction results for semi-random time interval AE data (five training files)

Specimen	Experimental Fatigue Life	Predicted Fatigue Life	% Error
Beam 10	19,188	19,016	-0.9
Beam 11	13,573	14,163	4.3
Beam 12	15,833	16,286	2.9
Beam 13	15,710	16,506	5.1
Beam 14	16,084	16,611	3.3

Conclusions

First, it was seen that the more training data files (beams), the more accurate the BPNN were in predicting fatigue lives. The fatigue life predictions based on the third quarter of fatigue life AE data had worst-case prediction errors within $\pm 5\%$. This is good in that AE testing during the third quarter is preferable for structural health monitoring (SHM) of bridges, in that fatigue cracks are typically observed as the structure approaches the later part of its useful life. Second,

the predictions based on AE data of semi-random time intervals (after fatigue crack initiation) were performed to simulate the actual testing scenario, i.e., AE fatigue crack SHM subsequent to a fatigue crack being observed. Here, using five beams for BPNN training and five beams for testing (predicting), the worst-case error was found to be 5.1%. Thus, it can be concluded that BPNNs trained on AE amplitude histogram data from either the third quarter of the fatigue life or at semi-random time intervals after crack initiation can predict fatigue lives in bridge steel I-beams with worst-case errors of approximately 5% or less by training on the data from at least six beams.

References

1. Miller, R.K., Hill, E.v.K., and Moore, P.O., *Nondestructive Testing Handbook, 3rd Ed., Vol. 6. Acoustic Emission Testing*. Columbus, OH: American Society for Nondestructive Testing, 2005, p. 32.
2. Barsoum, F.F., Suleman, J., Korcak, A., and Hill, E.v.K. (2009) Acoustic Emission Fatigue Life Prediction in Axially Loaded Notched Steel Specimens, *J. of Acoustic Emission*, **27**, 40-52.
3. Korcak, A., Fatigue Life Prediction in Steel Using Acoustic Emission Amplitude Histograms and Back Propagation Neural Networks. MSAE Thesis, Embry-Riddle Aeronautical University, FL, 2010.
4. Physical Acoustics Corporation website, MISTRAS Group Inc. Princeton, NJ. <http://www.pacndt.com>; <http://www.pacndt.com/index.aspx?go=products&focus=Pocket%20AE.htm>.

NUMERICAL SIMULATION TO EXAMINE ACCURACY OF AE SOURCE LOCATION AND ITS APPLICATIONS TO *IN-SITU* ROCK MONITORING

TSUYOSHI ISHIDA¹ and SHUNJI SASAKI²

¹ Kyoto University, Nishikyo, Kyoto 615-8540, Japan; ² Association for the Development of Earthquake Prediction, Sarugaku 1-5-18, Chiyoda, Tokyo 101-0064, Japan

Abstract

The location of an AE event is the most useful information obtained by AE monitoring. The accuracy is important for not only reliability of the source location itself, but also the analysis of crack mechanism depends on an accurate source location. In order to examine an arrangement of sensor positions based on the iterative method with the least-square principle, a simple simulation method using a random number is proposed. In addition, the method is applied to two cases where the sensor network cannot enclose a monitoring region three-dimensionally due to respective monitoring restrictions. The first case is the monitoring of *in-situ* direct shear test of rock in underground chamber that we actually made. The second is a case to examine an arrangement of drilling holes in advance to monitor hydraulic fracturing in deep underground. Through the examples, advantage and applicability of the method are elucidated for three-dimensional monitoring in a semi-infinite medium, which we often encounter in *in-situ* rock monitoring.

Keywords: Source location, accuracy, sensor arrangement, numerical simulation, *in-situ* direct shear test, hydraulic fracturing.

Introduction

The location of an AE event is the most useful information obtained by AE monitoring. The accuracy is important for not only reliability of the source location itself, but also the analysis of crack mechanism depends on an accurate source location. Factors influencing the accuracy of AE source locations are wave arrival time determination, arrangement of sensor positions, wave velocity and isotropy, signal attenuation and reflection, and transducer size and configuration. On the wave arrival time determination, Landis et al. (1992), Sedlak et al. (2008) and others discussed and developed automated determination methods for a large volume of AE data. An accuracy of AE source location influenced by an arrangement of sensor positions depends on the principles of source location methods. Ge (2003a and 2003b) classified the principles of source location methods into tri-axial sensor methods, zonal location methods, and iterative and non-iterative methods. The accuracy by an arrangement of sensor positions for the zonal location methods was examined by Catty (2009 and 2010). On the accuracy for the most popular iterative method, Salamon and Wiebols (1974) pointed out that a "blind spot" exists in neighborhood of the apex on the axis of a right circular cone when all sensors positioned on one of the sheets of the cone. For structures such as pressure vessels, storage tanks and piping composed of flat or curved planes, cylinder, cone, torus and sphere, Nakasa (1986 and 1994) made numerical experiments for accuracy of source location due to errors of P-wave arrival time determination, P wave velocity and others. However, a method to examine the accuracy for a general arrangement of sensor positions has not been discussed to our knowledge.

In this paper, for a general arrangement of sensor positions based on the iterative method, we propose a simple examination method using a random number, and show two examples applied to the cases where the sensor network cannot enclose a monitoring region three-dimensionally due to respective monitoring restrictions. The first example is the monitoring of an *in-situ* direct shear test of rock in underground chamber that we made (Ishida and Kanagawa, 2008; Ishida et al., 2010). The other is an example to examine an arrangement of drilling holes in advance to monitor hydraulic fracturing in deep underground. In this paper, the discussion is made under the assumption that the iterative method with the least square principle, which is classified into Geiger's method (Geiger, 1910 and 1912) by Ge (2003a and 2003b), is used as source location method and only P-wave arrival times are used for the source location.

Examination Method

We conducted the examination by a simple numerical simulation using a random number. By assuming positions of AE sensors and an average measuring error on the determination of P-wave arrival time, we examined how located sources distribute around the assumed source with the measuring error under the arrangement of AE sensors. Even under the same location of the assumed source and the same average measuring error, the distribution of located sources is quite different with changes of AE sensor arrangement. Under the same average of the measuring error, a sensor arrangement to make less scattering of sources around the assumed source is considered to be better. Procedure of the numerical simulation is as follows.

First Step

At first, an arrangement of AE sensors is assumed, i.e., N sets of three-dimensional coordinates of AE sensor positions, $O_i(x_i, y_i, z_i)$ where $i = 1, 2, 3, \dots, N$, are assumed as shown in Fig. 1. Next, an AE event is assumed to occur at a location, $S(x_s, y_s, z_s)$, and at a time, t_s . A distance, O_iS , from the assumed source, S , to the i -th AE sensor, O_i , and the P-wave arrival times at the respective AE sensors, t_i , with P-wave velocity, V_p , are represented as follow,

$$O_iS = \sqrt{(x_i - x_s)^2 + (y_i - y_s)^2 + (z_i - z_s)^2} \quad (1)$$

$$t_i = \frac{O_iS}{V_p} + t_s = \frac{\sqrt{(x_i - x_s)^2 + (y_i - y_s)^2 + (z_i - z_s)^2}}{V_p} + t_s \quad (2)$$

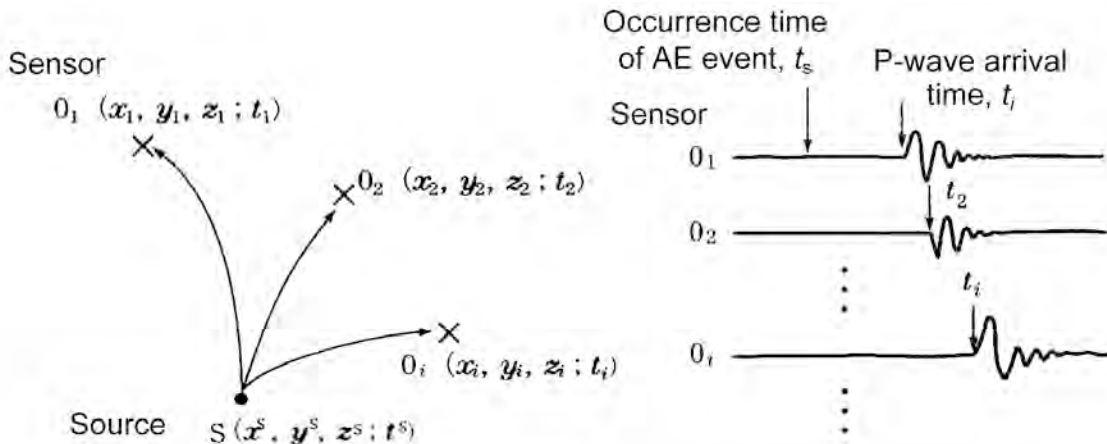


Fig. 1 Coordinates of a source and sensors, and a set of recorded waveforms.

Since the arrival times, t_i , is used in the calculation for source location only as relative differences among the respective AE sensors, an actual value of the occurrence time, t_s , is unimportant. By assuming the value, t_s , to be any constant or zero, the respective times, t_i , are obtained. Afterwards, a random number made by the method explained in the third step and Appendix is added to the respective time, t_i , as a measuring error on the P-wave arrival time determination.

Second Step

The measuring error can be estimated from a dominant frequency of a measuring AE signal, the resolution of measuring equipment and others. For example, an error at reading a P-wave arrival time on a recorded wave trace is estimated within a quarter of a period of the arrival initial motion. In other words, when the wave trace is assumed to be a sine curve, the error is estimated within a time length from its arrival to the peak, as shown in Fig. 2. Since we can usually consider that a dominant period of the arrival initial motion is the same as a resonance period of the AE sensor, we can roughly estimate the measuring error to be a quarter of the resonance period of the AE sensor. Needless to say, when other factors are expected to cause an error on the P-wave arrival time determination, the errors estimated by the factors should be considered as well.

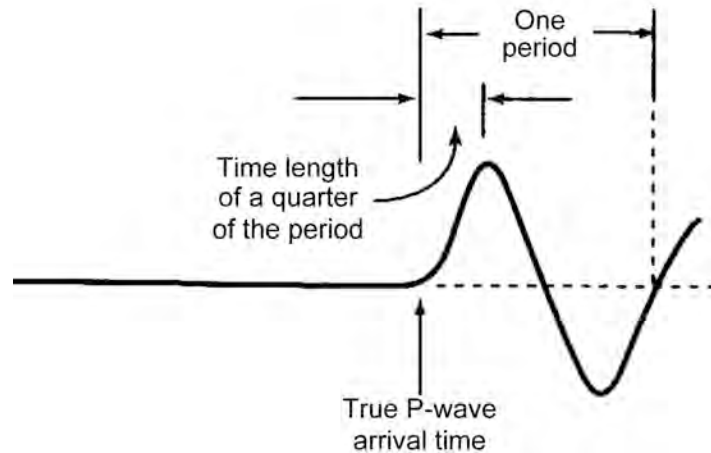


Fig. 2 Estimation of an error at reading P-wave.

Third Step

We make a set of random numbers, $z_i = (z_1, z_2, \dots, z_n)$, having a standard deviation, a , and an average, b , which were produced by the method explained in Appendix, and add the random number, z_i to the arrival time, t_i , as the measuring error at the AE sensor O_i . As described in the second step, when we consider a quarter of the resonance period of the AE sensor as an average of the measuring errors, we put the time length to be a value of the standard deviation, a . Usually, we put a value of the average, b , to be zero. Next, by considering the value, t'_i , shown in equation (3), as the P-wave arrival time at the AE sensor O_i , we obtain source coordinates of the AE event, by following a usual iterative method with the least square principle for source location.

$$t'_i = t_i + z_i \quad (3)$$

Fourth Step

When 10 to 20 AE sources are located by considering the time, t'_i , containing the random number as a P-wave arrival time, they distribute around the assumed source. For example, when

an AE sensor arrangement does not have good accuracy for the source location in the vertical direction, the sources distribute over a large distance in the vertical direction. Since the sources are scattered in the low accuracy direction, we can find a problem of the AE sensor arrangement for the source location. By repeating the simulation with changing the AE sensor arrangement, when we find the sensor arrangement that provides the least scattering of the source distribution around the assumed source, we consider that is the optimal sensor arrangement. Since an error of the source location can be estimated from a size of the scattering, the simulation results also give us the margin of the measuring error on the P-wave arrival time determination in relation to the accuracy needed in the monitoring.

Application to *In-Situ* Direct Shear Test of Rock

As the first example, we show an examination of AE sensor arrangement for an *in-situ* direct shear test of rock, which was conducted to obtain strength of the rock mass for designing an underground power station (Ishida and Kanagawa, 2008; Ishida et al., 2010).

Sensor Arrangement

The specimen in our experiment was a slate-dominant alternation of slate and sandstone measuring 0.5 m long, 0.5 m wide and 0.2 m high, as shown in Fig. 3. The specimen for the test block was made from the rock mass under the ground surface of the chamber by removing surrounding rocks outside the specimen using a small rotational boring machine and a mechanical breaker. The test block for the direct shear test was constructed by encapsulating the specimen in 0.1 m thick reinforced concrete. A shear load was applied to the test block in the direction having an angle 17° from the horizontal and the load was increased up to the final failure, while the vertical load was kept constant during the test.

As shown in Fig. 3, eight AE sensors from No. 1 through 8 were affixed with cement paste on the bottom of the holes that were drilled around the test block. Fracture was expected to occur in a thin layer of a few cm along the expected shear plane, which was the plane at the base of the specimen that extended from the ground surface around the specimen. Due to the limitation of the test configuration, we could not place an AE sensor just above or below the expected shear plane. All sensors were set lower than the expected shear plane around the test block. The AE sensor arrangement is expected to cause low accuracy of the source location in the vertical direction.

Simulation and Result

We assume an AE source at the location of the closed circle in Fig. 3, and we calculate the P-wave travel time from the assumed source to the seven sensors. No. 5 sensor was not used in the source location due to its position far from the specimen. In the calculation, the P-wave velocity value of 5.0 km/s, which is measured by using PZT transmitters set at both lateral sides of the test block, was used. Following the method explained previously, the random numbers having the average of 0 μ s and the standard deviation of 10 μ s were added to the calculated theoretical P-wave arrival times of the respective AE sensors, and coordinates of a source was obtained using the times including the additional random numbers. The standard deviation of 10 μ s corresponds to the largest error that we expected in the monitoring, because the resonant frequency of the AE sensors was around 25 kHz.

The sources obtained are shown by open circles in Fig. 4(a). The figure shows that the sources distribute more in the vertical direction than in the horizontal direction. Consequently,

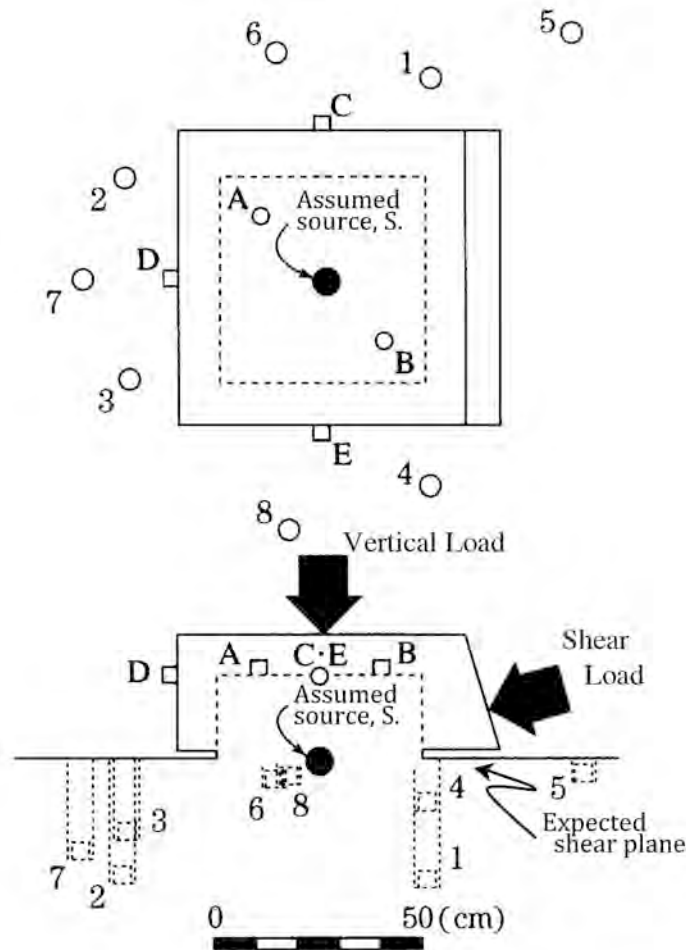


Fig. 3 AE sensor arrangement for the *in-situ* direct shear test. The closed circle, S, indicates a position of the assumed source.

the results indicate that, in the sensor arrangement, we cannot rely on the vertical locations of the sources, while the horizontal locations are reliable.

Next, consider a case where the sensor numbers 1, 2, 4, 6, 7, A and B are used for the source location, by replacing the sensors Nos. 3 and 8 with the sensors A and B. Scatter of the located sources for the same error is shown in Fig. 4(b). Comparison between Fig. 4(a) and (b) clearly indicates improvement of the accuracy in the vertical direction. Actually it is not easy to set the sensors in the positions A and B, because they are under the loading plate and inside of the 0.1-m thick reinforced concrete encapsulating the specimen. Figure 4(c) shows the scatter of the located sources when we use the eight sensors, Nos. 1, 2, 4, 6, 7, C, D and E, by adding the sensors C, D and E set on the outside surfaces of the encapsulating concrete instead of the sensors A and B. Results in Fig. 4(c) indicate that the accuracy in the vertical direction is much better than that shown in (a) although it is slightly worse than that in (b). The results demonstrate that it is necessary to enclose a specimen with AE sensors three-dimensionally to locate an AE source three-dimensionally with good accuracy.

Advantage of the Simulation Results

The examination of the sensor arrangement for the *in-situ* direct shear test was made after our AE monitoring. When we started the AE source location after the monitoring, we found that the

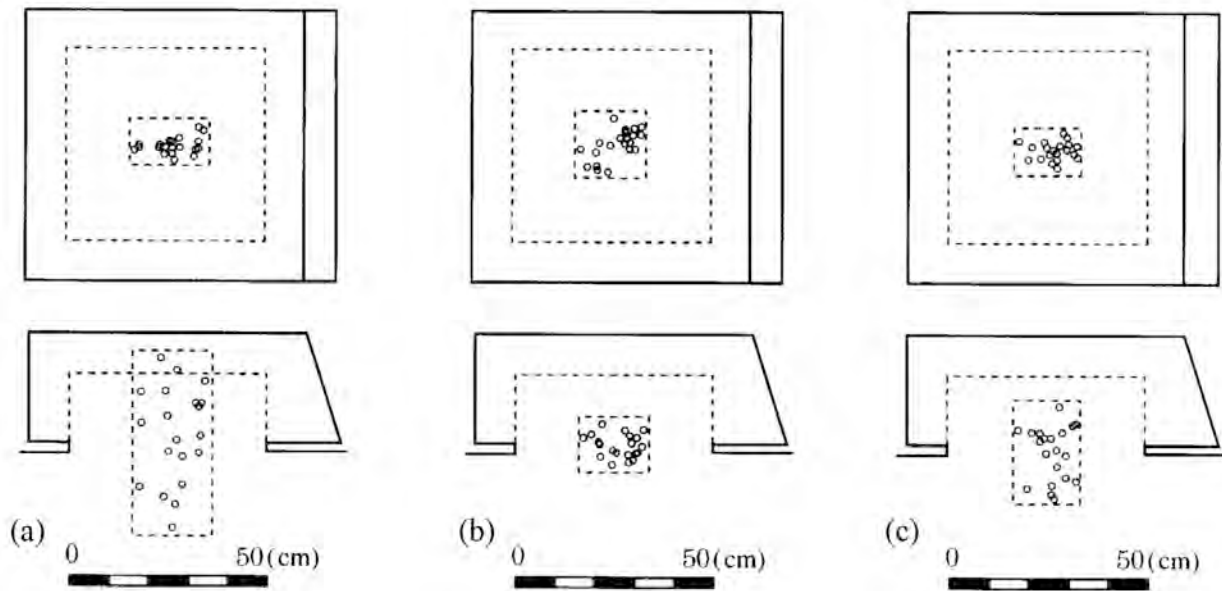


Fig. 4 Source distributions of the simulation results for the *in-situ* direct shear test. (a) Sensors Nos. 1, 2, 3, 4, 6, 7 and 8 used. (b) Sensors Nos. 1, 2, 4, 6, 7, A and B used. (c) Sensors Nos. 1, 2, 4, 6, 7, C, D and E used.

located sources scattered, particularly in the vertical direction. Since this distribution seems to indicate a low accuracy of the source location, we need to evaluate the accuracy by the numerical simulation. We realized from the simulation results that our sensor arrangement is not sufficient for the source location. If we knew the simulation results before the monitoring, we could add easily the sensors D, E and F on the surfaces of the encapsulating concrete and get more reliable and accurate located sources of the AE events. Fortunately, however, all AE events that occurred in this test appear to have been generated in a thin layer, only a few cm thick, parallel to the expected shear plane including the assumed source, S, in Fig. 3, since heights of the fractured plane measured after the test range within -3 to $+5$ cm of the expected shear plane. Consequently, the AE sources were located two-dimensionally under the assumption that they were generated on the expected shear plane. Since the simulation results allow us to avoid wasting time to make effort to locate the sources three-dimensionally, we could concentrate discussion on two-dimensional fracture extension from the located AE sources (Ishida and Kanagawa, 2008; Ishida et al., 2010). On this point, the simulation helped us discuss the monitoring results.

Application to Deep Underground Hydraulic Fracturing

As the second example, we show an examination of sensor arrangement to monitor AE events induced by hydraulic fracturing at the depth of 300 m with many AE sensors set on the surface and a limited number of downhole AE sensors. Through the examination, we can obtain information on the number, depths and horizontal position of the downhole sensors that are necessary to get locations of the AE events with a sufficient accuracy. In a field experiment like this, since a cost for drilling holes to monitor AE events usually amounts to a large part of the total cost, results of the examination are helpful to estimate the budget necessary for the experiment, especially at the planning stage.

Sensor Arrangement

Assume a source at the position of a closed circle in Fig. 5, which is at the depth of 300 m in the hole, "f". Also assume to set AE sensors on the bottoms of the holes drilled at the vertex positions of the regular hexagon. From now on, we call a set of the six surface sensors "a surface net". Of the six sensors, three sensors, Nos. 1, 3 and 5, are placed at the depth of 25 m, while the other three sensors, Nos. 2, 4 and 6, are set at the depth of 50 m. For deep downhole sensors, first, we consider a case that the sensor A is set at the same position as that of the assumed source. Next, we consider a case that the sensors B and C are placed at the respective depths of 250 m and 350 m in the hole, "g", which is drilled at a position 50 m from the epicenter of the assumed source, (50, 0), in the coordinate system shown in Fig. 5.

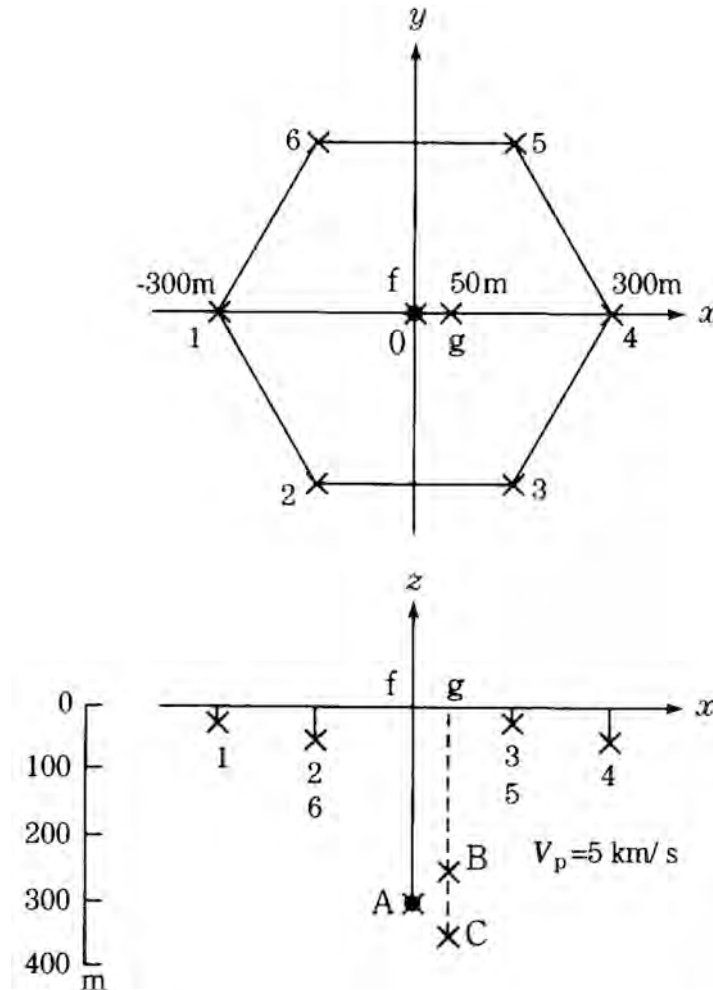


Fig. 5 AE sensor arrangement for hydraulic fracturing at the depth of 300 m. The closed circle, A, indicates the position of the assumed source, while the crosses indicate positions of AE sensors.

Simulation and Result

P-wave travel times, t_i , from the assumed source to the respective sensors are calculated, under the assumption that the rock mass is homogeneous and isotropic, and its P-wave velocity, V_p , is 5 km/s. The random number, z_i , are added to the travel times, and times t'_i ($t'_i = t_i + z_i$) are obtained for respective sensors by following equation (3). By considering the time, t'_i , containing a random number as P-wave arrival time, an AE source is back-calculated.

First, for a data set of the P-wave arrival time having the average of 0 ms and the standard deviation of 1 ms as the errors, we show changes of source distributions depending on a different set of the sensors. Figure 6(a) shows the result of the case using only the surface net. The sources concentrating around the epicenter of the assumed source indicates that the accuracy is sufficient on the horizontal direction. However, in the vertical direction, a large scattering from 100 to 800 m in depth in spite of the assumed source being at 300 m indicates low accuracy, necessitating an improvement.

Tanaka et al. (1997), Ishida (2001) and Manthei et al. (2003) have developed hydraulic fracturing sondes incorporating AE sensors. By setting a sonde in the hole in the vicinity of the point where the hydraulic fracturing is induced, the accuracy of source location could be improved without drilling an additional hole for monitoring. Figure 6(b) shows the result of the case using the sensor A set at the same point of the hydraulic fracturing along with the surface net. The scattering of the located sources is limited from 250 to 350 m having the center at 300 m, which is the depth of the assumed source. The result indicates that the accuracy in the vertical direction is improved using the sensor A in addition to the surface net.

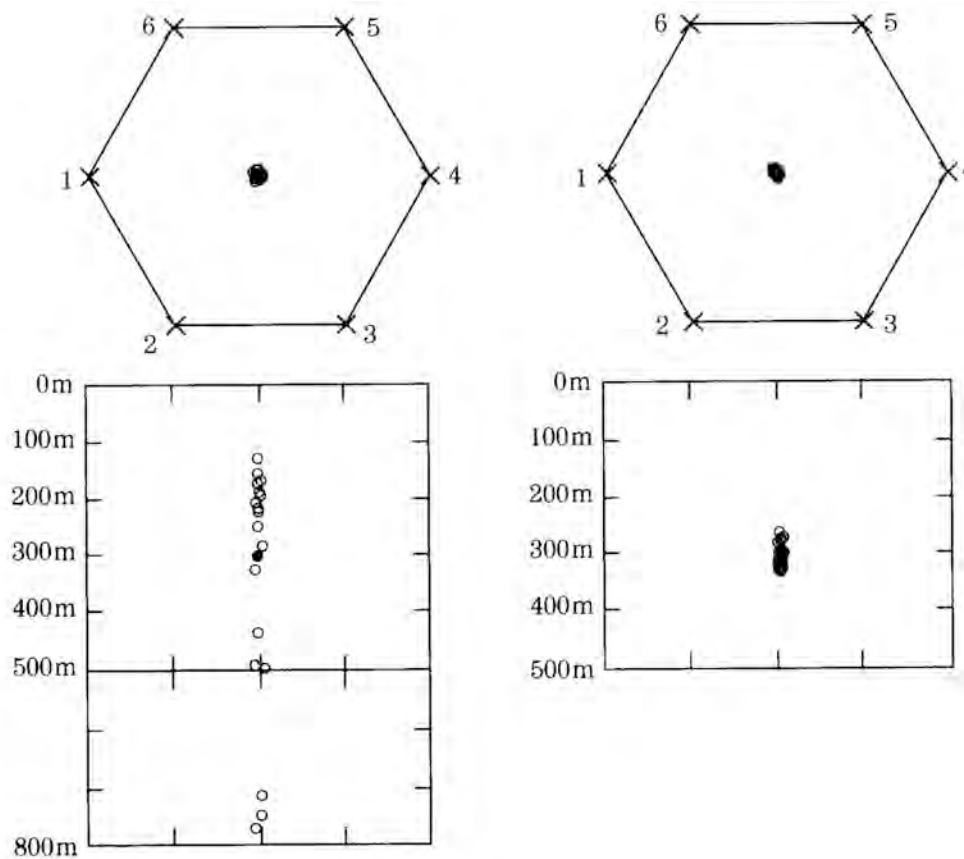


Fig. 6(a) Source distribution using only the surface net sensors (Nos. 1 through 6). (b) Source distribution using the sensor A at the same point of the hydraulic fracturing together with the surface net sensors.

Figures 6(c) and (d) show the respective results using the sensor B placed at 250 m and the sensor C separately at 350 m with the surface net. The accuracy in the case using the sensor C set below the assumed source is better than that in the case using the sensor B set above the assumed source. This is because the sensor C and surface net in the latter case surround the assumed source three-dimensionally.

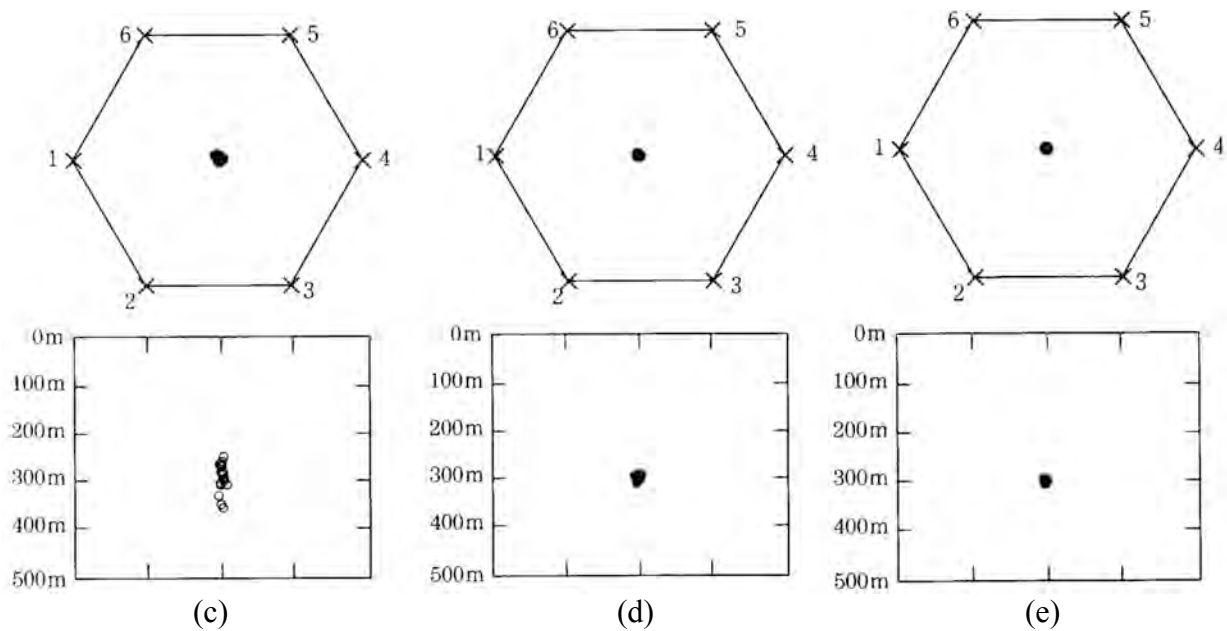


Fig. 6(c) Source distribution using the deep sensor B set above the assumed source with the surface net sensors. (d) Source distribution using the deep sensor C set below the assumed source with the surface net sensors. (e) Source distribution using the all downhole sensors A, B and C together with the surface net sensors.

Figure 6 (e) shows the result in the case using all three deep downhole sensors A, B and C with the surface net, indicating no distinct difference from that in the case showed in Fig. 6(d) using only the sensor C. This result demonstrates that it is desired for a single deep downhole sensor to be set lower than the point of hydraulic fracturing, and that no other underground sensors are necessary as one deep sensor provides good source location data.

Figure 7 shows the result when a standard deviation of the random numbers is 10 ms, which is ten times larger than in the previous cases. The result indicates that the scattering becomes larger with such a large error, even if we use all deep downhole sensors A, B and C with the surface net. This result shows that we should control the error lower than approximately 1 ms for AE monitoring of hydraulic fracturing made at the depth of around 300 m.

Effect of Setting Depth Distribution of the Surface Net Sensors

So far, the sensor numbers 1, 3 and 5 of the surface net were set at the depth of 25 m, and the other sensors, Nos. 2, 4 and 6, were set at the depth of 50 m. If the scattering does not change when all six sensors are set at the same depth of 25 m, cost to drill the 50-m holes can be saved. Thus, we examine the case that the entire six surface sensors are set at the same depth of 25 m. First, when we tried to locate sources using the downhole sensor C (at 350 m) and the surface net sensors, all six at 25 m, we could not locate any sources due to divergence of the calculation. In this case, a standard deviation of the random number given as the error was 1 ms. As the result is quite different from that shown in Fig. 6(a), it indicates that we should not set the surface net sensors at the same depth. However, when we add the downhole sensor B to these sensors, the sources can be located in good accuracy without large scattering, as shown in Fig. 8. These results demonstrate that more than two deep downhole sensors are needed if the surface net sensors are set at a same depth.

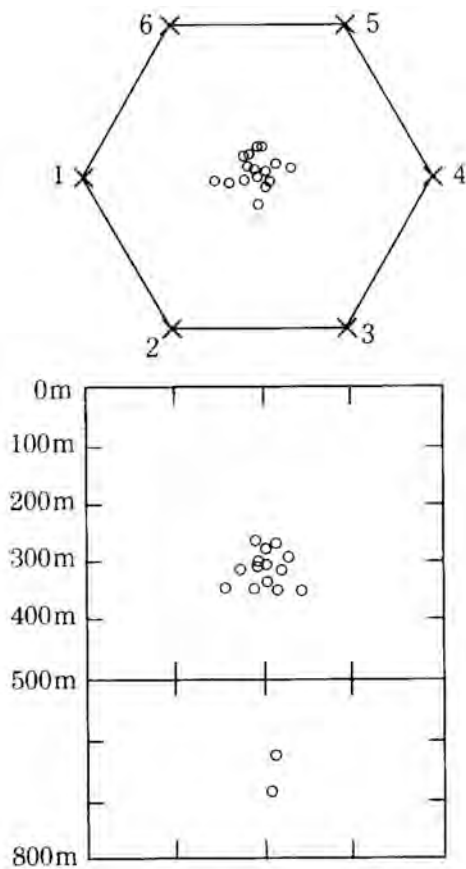


Fig. 7 Source distribution when the standard deviation is 10 ms. All downhole sensors A, B and C and the surface net sensors are used.

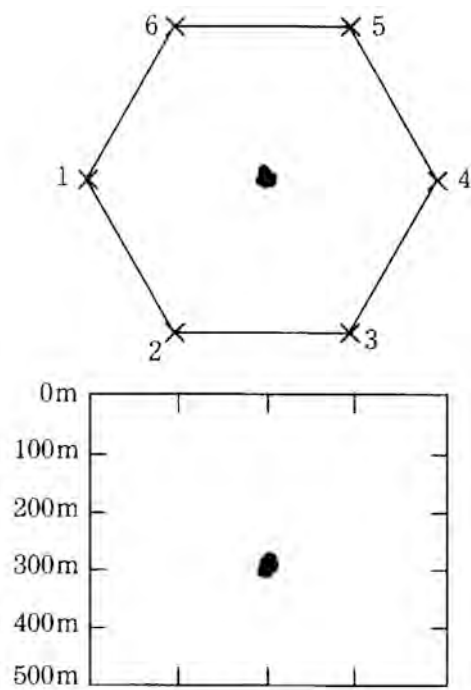


Fig. 8 Source distribution using the downhole sensors B and C with the six surface sensors set at the same depth of 25 m. Standard deviation of the given errors is 10 ms. As noted in text, we could not locate any sources due to divergence, using only sensor C and the six surface net sensors at the same depth of 25 m.

Concluding Remarks

We propose a simple examination method for an arrangement of sensor positions based on the iterative method using a random number with the least-square principle. We show two examples applied to the cases where the sensor network cannot surround a monitoring region three-dimensionally due to respective monitoring restrictions.

The first example of *in-situ* direct shear test of rock in underground chamber produced the following results.

- (1) From the simulation results, we found that our sensor arrangement is insufficient for the three-dimensional source locations for the expected error of 10 μ s in the determination of P-wave arrival time.
- (2) All AE events that occurred in this test are presumably generated in a thin layer, only a few cm thick, parallel to the expected shear plane. Consequently, the AE sources were located two-dimensionally under the assumption that they are generated on the expected shear plane.
- (3) The simulation results helped us concentrate to discuss two-dimensional fracture extension from the located AE sources without wasting time to locate the sources three-dimensionally.

From the second example to examine an arrangement of monitoring hydraulic fracturing at the depth of 300 m, the following recommendations were obtained.

- (4) Depths at which AE sensors in the surface net are set should be more than two levels, for example, 25 m and 50 m.
- (5) Even if the surface net satisfies the above condition, it is necessary to set, at least, one deep downhole sensor. The deep downhole sensor should be set lower than the depth, at which AE events are expected to occur.

Through the two examples, the following facts were clarified.

- (6) To locate an AE source three-dimensionally with sufficient accuracy using only P-wave arrival time, it is necessary for AE sensors to surround a source three-dimensionally.
- (7) Advantage and applicability of the proposed method are elucidated for three-dimensional monitoring in a semi-infinite medium, which we often encounter in *in-situ* rock monitoring.

Acknowledgement

The content of this paper will be included in a book entitled "Microcracking in Rock as Acoustic Emission" by Tsuyoshi Ishida and Joseph F. Labuz, which will be published from Taylor & Francis. The authors appreciate Taylor & Francis to permit to present the contents in this paper.

References

- Catty, J. (2009), "Acoustic emission testing - Defining a new standard of acoustic emission testing for pressure vessels, Part 1. Quantitative and comparative performance analysis of zonal location and triangulation methods", *Journal of Acoustic Emission*, **27**, 299-313.
- Catty, J. (2010), "Acoustic emission testing - Defining a new standard of acoustic emission testing for pressure vessels, Part 2. Performance analysis of different configurations of real case testing and recommendations for developing a new guide for the application of acoustic emission", *Journal of Acoustic Emission*, **28**, 11-31.
- Ge, M. (2003a), "Analysis of source location algorithms--Part I: Overview and non-iterative methods", *Journal of Acoustic Emission*, **21**, 21-28.
- Ge, M. (2003b), "Analysis of source location algorithms--Part II: Iterative methods", *Journal of Acoustic Emission*, **21**, 29-51.
- Geiger, L. (1910), "Herbsetimmung bei Erdbeben aus den Aukunfzeiten", *K. Gessell. Will. Goett.* **4**, 331-349.
- Geiger, L. (1912), "Probability method for the determination of earthquake epicentres from the arrival time only", *Bull. St. Louis. Univ.*, **8**, 60-71.
- Ishida, T. (2001), "Acoustic emission monitoring of hydraulic fracturing in laboratory and field", *Construction and Building Materials*, **15**, 283-295.
- Ishida, T. and Kanagawa, T. (2008), "Acoustic emission monitoring during *in-situ* direct shear test of rock", *Progress in Acoustic Emission XIV* (Proc. of 19th International Acoustic Emission Symposium), pp. 399-406, Kyoto, Japan, December.
- Ishida, T., Kanagawa, T. and Kanaori, Y. (2010), "Source distribution of acoustic emission during an *in-situ* direct shear test: Implication for an analog model of inhomogeneous rock-mass fracturing", *Engineering Geology*, **110**, 66-76.

Landis, E., Ouyang, C. and Shah, S. P. (1992), "Automated determination of first P-wave arrival and acoustic emission source location", *Journal of Acoustic Emission*, **10**, S97-S103.

Manthei, G, Eisenblatter, J. and Kamlot, P. (2003), "Stress measurements in salt mines using a special hydraulic fracturing borehole tool", *Proc. of International Symposium on Geotechnical Measurements and Modelling*, pp. 355-360, Karlsruhe, Germany.

Nakasa, H. (1986), "Acoustic emission source location for 3-dimensional structural components", *Progress in Acoustic Emission III* (Proc. of 8th International Acoustic Emission Symposium), pp. 34-41, Tokyo, Japan.

Nakasa, H. (1994), "High-accuracy AE source location method using numerical analysis", *Progress in Acoustic Emission VII* (Proc. of 12th International Acoustic Emission Symposium), pp. 559-564, Sapporo, Japan.

Salamon, M.D.G. and Wiebols, G.A. (1974), "Digital location of seismic events by an underground network of seismometers using the arrival times of compressional waves", *Rock Mechanics*, **6**, 141-166.

Sedlak, P., Hirose, V., Enoki, M. and Sikura, J. (2008), "Arrival time detection in this multilayer plates on the basis of Akaike information criterion", *Journal of Acoustic Emission*, **26**, 181-188.

Tanaka, M., Kuwabara, K., Honma, M., Ishida, T., Kanagawa, T. and Mizuta, Y.(1997) , "Determination of crack direction in hydraulic fracturing by borehole acoustic emission sonde", *Proc. of 4th International Symposium on Rockburst and Seismicity in Mines*, pp. 409-413, Krakow, Poland.

Appendix

We can make a set of random numbers having any desired mean value and standard deviation by the following procedure. At first, we generate a set of uniform random numbers, $x=(x_1, x_2, \dots, x_n)$, using a function in our personal computer, for example, the function "RAND" in the program "Excel" of Microsoft, and calculate its mean value and standard deviation in the following equations.

$$\bar{x} = \sum x_i / n \quad (\text{A-1})$$

$$\sigma_x = \sqrt{\sum (x_i - \bar{x})^2 / n} \quad (\text{A-2})$$

where n is a number of the random numbers.

Next, we make the second set of random numbers, $y=(y_1, y_2, \dots, y_n)$, from the first random numbers, $x=(x_1, x_2, \dots, x_n)$, using the following equation.

$$y_i = (x_i - \bar{x}) / \sigma_x \quad (\text{A-3})$$

The random numbers, $y = (y_1, y_2, \dots, y_n)$, have the mean value, \bar{y} , of zero and the standard deviation, σ_y , of one. The facts are proved as follows.

$$\bar{y} = \frac{\sum y_i}{n} = \frac{1}{n} \sum \left(\frac{x_i - \bar{x}}{\sigma_x} \right) = \frac{1}{n\sigma_x} (\sum x_i - n\bar{x}) = \frac{1}{\sigma_x} \left(\frac{\sum x_i}{n} - \bar{x} \right) = \frac{1}{\sigma_x} (\bar{x} - \bar{x}) = 0 \quad (\text{A-4})$$

$$\sigma_y = \sqrt{\frac{1}{n} \sum (y_i - \bar{y})^2} = \sqrt{\frac{1}{n} \sum y_i^2} \quad (\because \bar{y} = 0) \quad (\text{A-5})$$

From equation (A-3), and using equation (A-2),

$$\sum y_i^2 = \sum \frac{(x_i - \bar{x})^2}{\sigma_x^2} = \frac{1}{\sigma_x^2} \sum (x_i - \bar{x})^2 = \frac{\sum (x_i - \bar{x})^2}{\sum (x_i - \bar{x})^2 / n} = n \quad (\text{A-6})$$

By substituting the result for the term in equation (A-5),

$$\therefore \sigma_y = \sqrt{\frac{1}{n}} = 1 \quad (\text{A-7})$$

Finally, we make the third set of random numbers, $z = (z_1, z_2, \dots, z_n)$, from the second random numbers, $y = (y_1, y_2, \dots, y_n)$, using the following equation.

$$z_i = ay_i + b \quad (\text{A-8})$$

The random numbers, $z = (z_1, z_2, \dots, z_n)$, has the mean value, \bar{z} , of b and the standard deviation, σ_z , of a . The facts are proved as follows.

$$\bar{z} = \frac{\sum z_i}{n} = \frac{\sum (ay_i + b)}{n} = \frac{a \sum y_i + nb}{n} = a \frac{\sum y_i}{n} + b = a\bar{y} + b = b \quad (\bar{y} = 0) \quad (\text{A-9})$$

$$\sigma_z = \sqrt{\frac{1}{n} \sum (z_i - \bar{z})^2} = \sqrt{\frac{1}{n} \sum (z_i - b)^2} = \sqrt{\frac{1}{n} \sum (ay_i + b - b)^2} = \sqrt{\frac{a^2}{n} \sum y_i^2} \quad (\text{A-10})$$

Here, since equation (A-6) indicates that $\sum y_i^2 = n$,

$$\therefore \sigma_z = \sqrt{\frac{a^2}{n} n} = a \quad (\text{A-11})$$

Thus, we can make a set of random numbers having any desired mean value, b , and standard deviation, a .

RESEARCH ON GAS PIPELINE LEAK LOCATION METHOD BASED ON EMPIRICAL MODE DECOMPOSITION

XIANYONG QIN, GONGTIAN SHEN, RENYANG HE, TAO MENG
and YONG XIAO

China Special Equipment Inspection and Research Institute, Beijing 100013, China

Abstract

Leak location is one of the most important technologies for gas pipeline leak detection; the normal location method is to calculate the time difference with cross-correlation analysis method. However, the dispersive leak signals propagate with different sound speeds in different frequency ranges and a large positioning error results in the cross-correlation method for leak location. The gas pipeline leak location method based on empirical mode decomposition (EMD) is presented. The EMD method allows reconstruction of signals, which are then subjected to cross-correlation location method. Simulations and field tests indicate that this location method is effective, with significantly improved location accuracy of 1-2% over distances up to 27 m.

Keywords: Empirical mode decomposition (EMD); gas pipeline; leak location

1. Introduction

Municipal gas pipeline is one of the important infrastructures providing energy supply and comprising basic conditions for people's life and for industry. In the operation process, the gas pipeline will inevitably burst or leak because of natural aging, corrosion, third party damage and other reasons, which may cause explosions and wide range of fire with great harm to society. Therefore, detecting the gas pipeline leak effectively and quickly is important to ensure the safe operation.

Pipeline leak signals propagate along the pipe wall as guided waves, leading to different sound speeds for leak signals in different frequency ranges and a large positioning error in the cross-correlation method for leak location. The gas pipeline leak location method based on empirical mode decomposition (EMD) is presented. The optimized inherent mode components are selected and reconstructed after leak signals are decomposed with EMD method. The reconstructed signals are then subjected to cross-correlation location method. Simulations of gas pipeline leakage and field gas pipeline leak detection applications indicate that this location method is effective.

2. Pipeline Leak Location Method Based on EMD Correlation Analysis

2.1 EMD algorithm theory

EMD algorithm is a kind of numerical algorithm for decomposition of time signal on the scale of the frequency, and the components will be different scales of fluctuation signal or trend by gradually decomposing out. EMD will produce a series of intrinsic mode functions (IMFs) with different feature scales. Similar as wavelet transformation, EMD can be seen as Q value filter. The difference is that wavelet transformation needs to choose the optimum wavelet basis function, but EMD is adaptive decomposition according to the feature time scale on the basis of signal characteristics themselves. The decomposed IMF must meet the following two conditions:

- (1) The number of extreme points and zero points of a function should be equal or differ by one at most; (2) In the function, mean value of maximum value points and enveloped minimum value points is zero [1 - 3].

In the conditions assumed above, the natural modes of a leak AE signal can be separated with EMD method [4]. The procedure is as follows:

(1) Find out all the local extreme value points of the signal. All of the local maximum value points and local minimum points are connected with a cubic spline lines (see Fig. 3, ref. [3]) to form the upper and lower envelope curves, which should enclose all data points. Mean value of the two envelope curves is recorded as m_1 , the difference of data X and m_1 is:

$$h_1(t) = X(t) - m_1(t) \quad (1)$$

If $h_1(t)$ meets the definition of the IMF, then $h_1(t)$ is an IMF1 and the first component of $X(t)$.

(2) If $h_1(t)$ does not meet the definition of the IMF, $h_1(t)$ is considered as the original data, and repeating the above steps, we get that:

$$h_{11}(t) = h_1(t) - m_{11}(t) \quad (2)$$

where $m_{11}(t)$ is the mean value of the upper and lower envelope curves of $h_1(t)$; Judging whether $h_{11}(t)$ meets the definition of IMF, and then repeating calculation k times, if not, we get that:

$$h_{1k}(t) = h_{1(k-1)}(t) - m_{1k}(t) \quad (3)$$

make $m_{1k}(t)$ meet the definition of IMF, remembering $c_1 = h_{1k}$.

(3) Separate c_1 from data X :

$$r_1(t) = X(t) - c_1(t) \quad (4)$$

Then considering $r_1(t)$ as the new original data, repeat the above (1) and (2) steps, and we get the second component c_2 meeting the IMF definition, with repetition to get

$$r_{j-1}(t) - c_j(t) = r_j(t); \quad j = 2, 3, 4, \dots, n. \quad (5)$$

The loop ends until $r_n(t)$ becomes a monotonic function and there will be no more IMF component to extract from it. So the original data can be expressed by the sum of IMF components and finally residual term (Res):

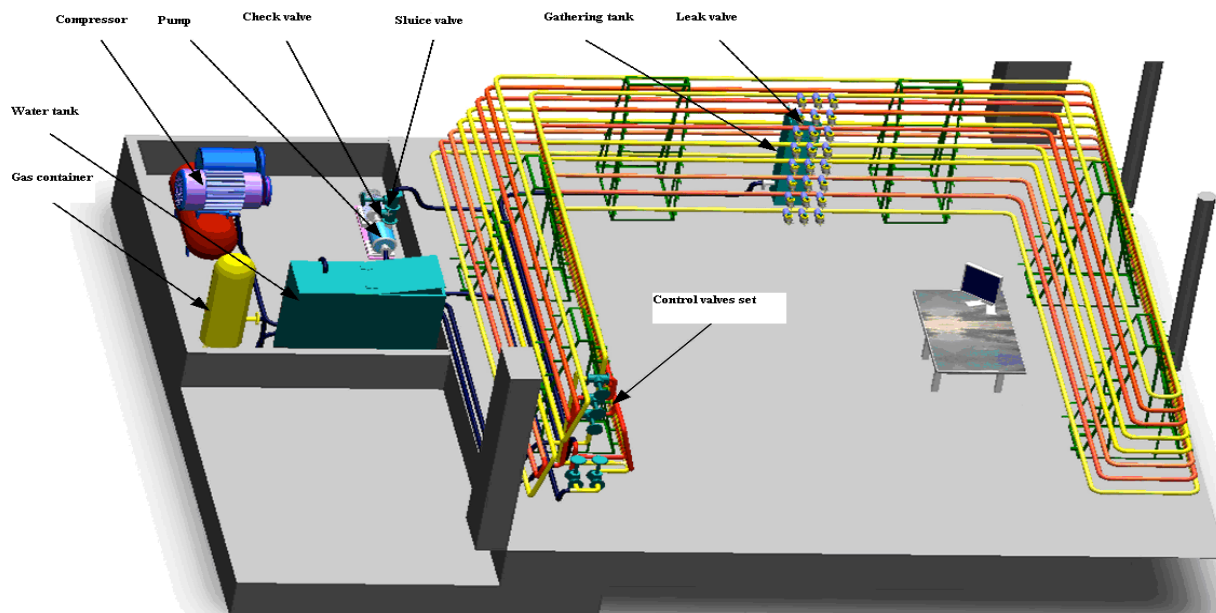


Fig. 1 Test pipeline structure scheme.

$$X(t) = \sum_{j=1}^n c_j(t) + r_n(t) \quad (6)$$

Any signal can be decomposed to n IMF components and one residual r_n ; among them $c_1, c_2, c_3, \dots, c_n$ components contain the different ingredients of signal from high to low frequency bands, respectively. From the EMD screening process, we can see that IMF successive extraction always reflects the high frequency first, and then a lower frequency, and an even lower frequency, etc. The goal is to eliminate the mode superposition of wave and to make the wave outline more symmetrical from the characteristics of the time scale, and to gradually separate signals containing the relevant modes. In the final step, we get the highest order single-component intrinsic mode function (corresponding to IMF13 in Fig. 4 below) and the residual term. The EMD decomposition results retain nonlinear and unsteady characteristics of original signals, suitable for nonlinear signal processing [5].

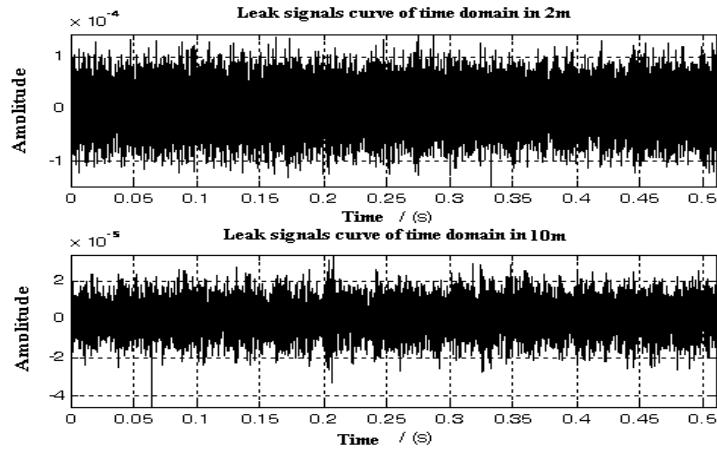


Fig. 2 Raw leak signals.

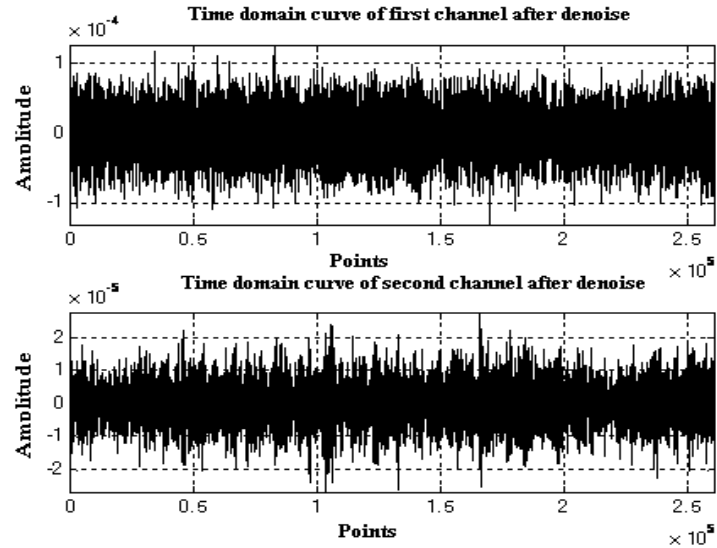


Fig. 3 Denoised leak signals.

2.2 Leak signal correlation analysis based on EMD

Pipeline leak AE signals have very obvious non-stationary characteristics, so the EMD method can be used for pipeline leak signal correlation analysis. In signal correlation analysis process, the leakage signal is considered as sound sources, two sensors are installed along the pipe in a certain distance from a sound source; GPS is used to control the two sensors for synchronous

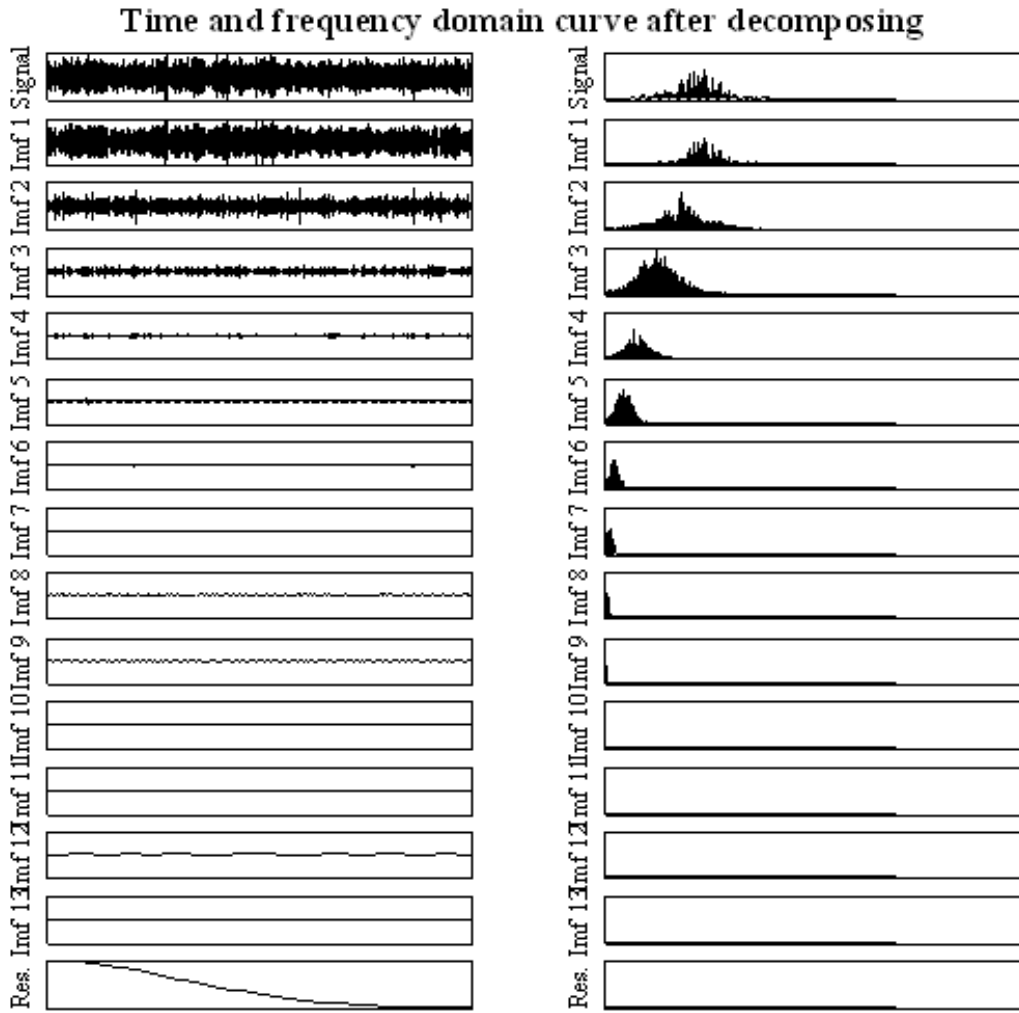


Fig. 4 Time- and frequency-domain curves after decomposition of first channel signal.

collection. The inherent mode components are optimized, selected and reconstructed after EMD decomposition of leak signals, and using the reconstructed signals for cross-correlation location.

(1) *Pipeline leak AE signal collection*: The test pipeline length is 150 m, diameter is 50 mm, and pipe wall is 3 mm. The scheme of the test pipeline structure is shown in Fig. 1. Data collecting and analysis system is a Gas Pipeline Leak Detecting and Locating System, which we developed internally. It contains data collecting module, sensors, GPS antenna, computer and data collecting and analysis software. The digitization frequency was 500 kHz, and the raw leak signals and denoised leak signals are shown in Figs. 2 and 3. The raw signals were denoised using discrete wavelet analysis method.

(2) *EMD decomposition and reconstruction of leak signals*: Leak AE signals collected by two sensors are decomposed with EMD method. The time- and frequency-domain curves after decomposition are shown in Figs. 4 and 5. The EMD decomposition is applied in order to obtain the optimized inherent mode components and reconstructed them. After the time-domain and frequency-domain feature analysis of each component, we find that IMF1, IMF2, and IMF3 components have obvious impact strength and strongest energy and finally choose these three components as the optimized inherent modes. In contrast, the energy of low-frequency IMF components (IMF4 - IMF13) is weak. These components have long cycles and slower spread

speeds and can be regarded as echo. The IMF1, IMF2 and IMF3 components are shown as Fig. 6. After reconstructing them as effective natural modes using equation (6), the reconstructed signals and their frequency-domain analysis as shown in Fig. 7 and Fig. 8, respectively.

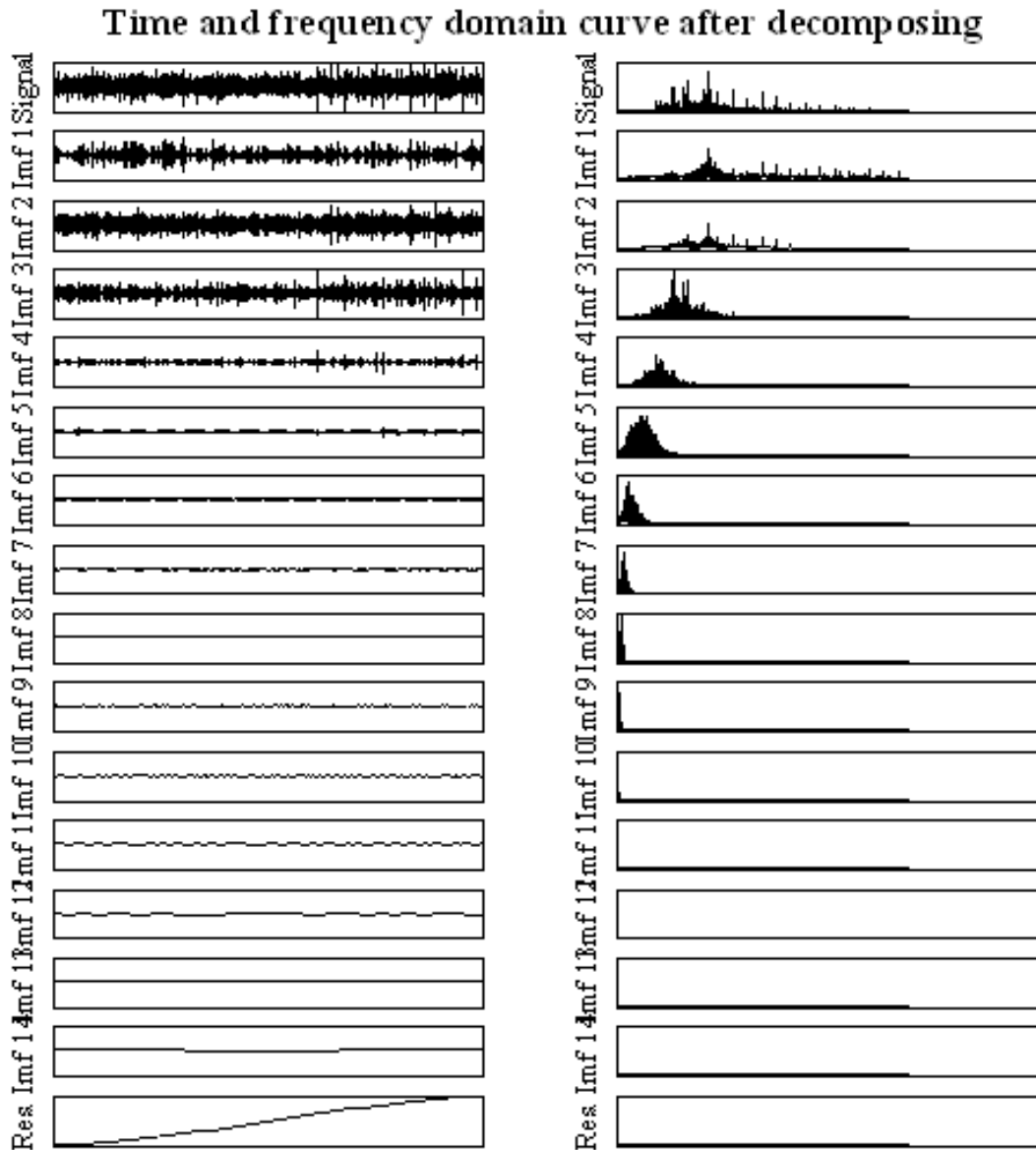


Fig. 5 Time- and frequency-domain curves after decomposition of second channel signal.

The cross-correlation maximum of this set of denoised leak AE signals (Fig. 9) directly is 0.087, and the time difference is 6.2 ms. Since the distance between two sensors and leak point is 2 m and 10 m, the location error is 0.68 m according the wave velocity of 1071 m/s. Using the reconstructed denoised leak signals with EMD method, cross-correlation maximum is 0.103, time difference is 8.5 ms and the positioning error is 0.55 m. Two cross-correlation function curves are shown as Figs. 9 and 10. Figure 10 used reconstructed denoised leak signals with EMD method.

Direct cross-correlation location and with EMD decomposition and reconstruction with multiple sets of leak AE signals are analyzed and results are given in Table 1.

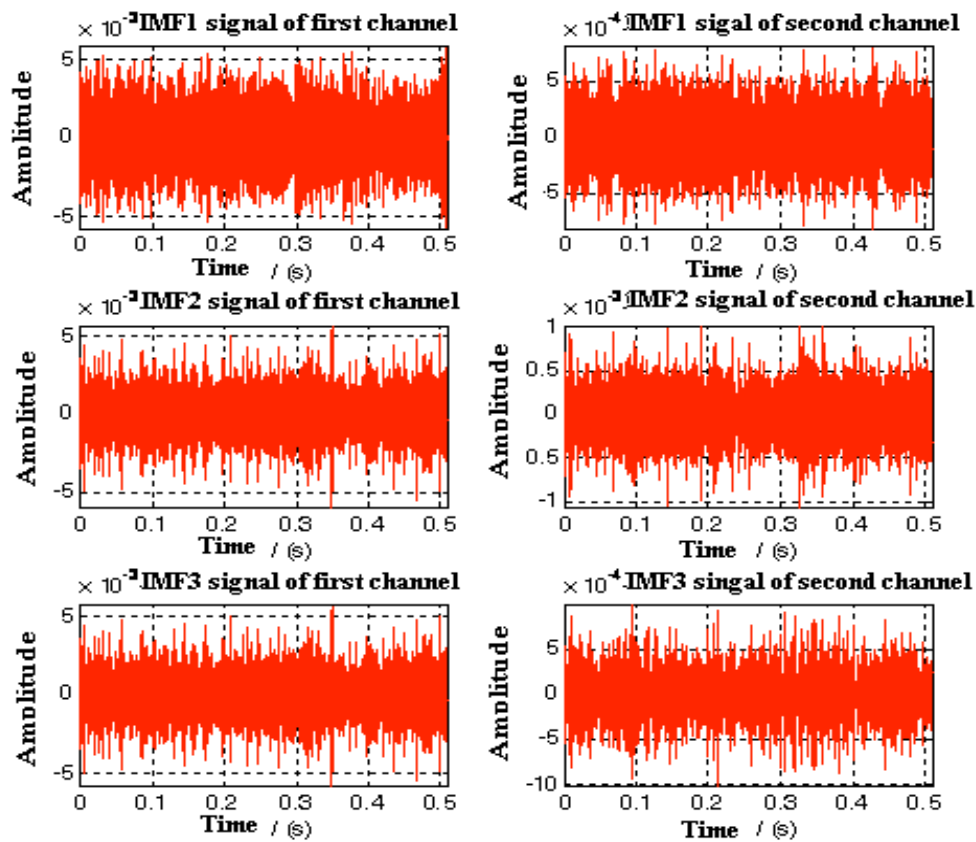


Fig. 6 The IMF1, IMF2 and IMF3 components.

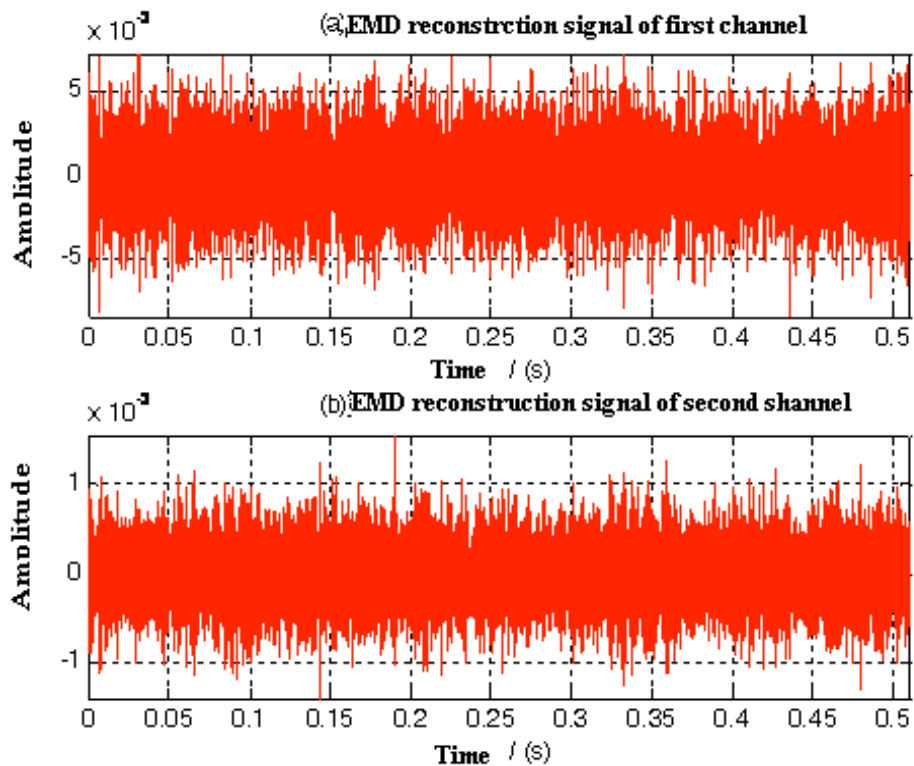


Fig. 7 Reconstructed leak signals after EMD decomposition and reconstruction using only IMF1-IMF3.

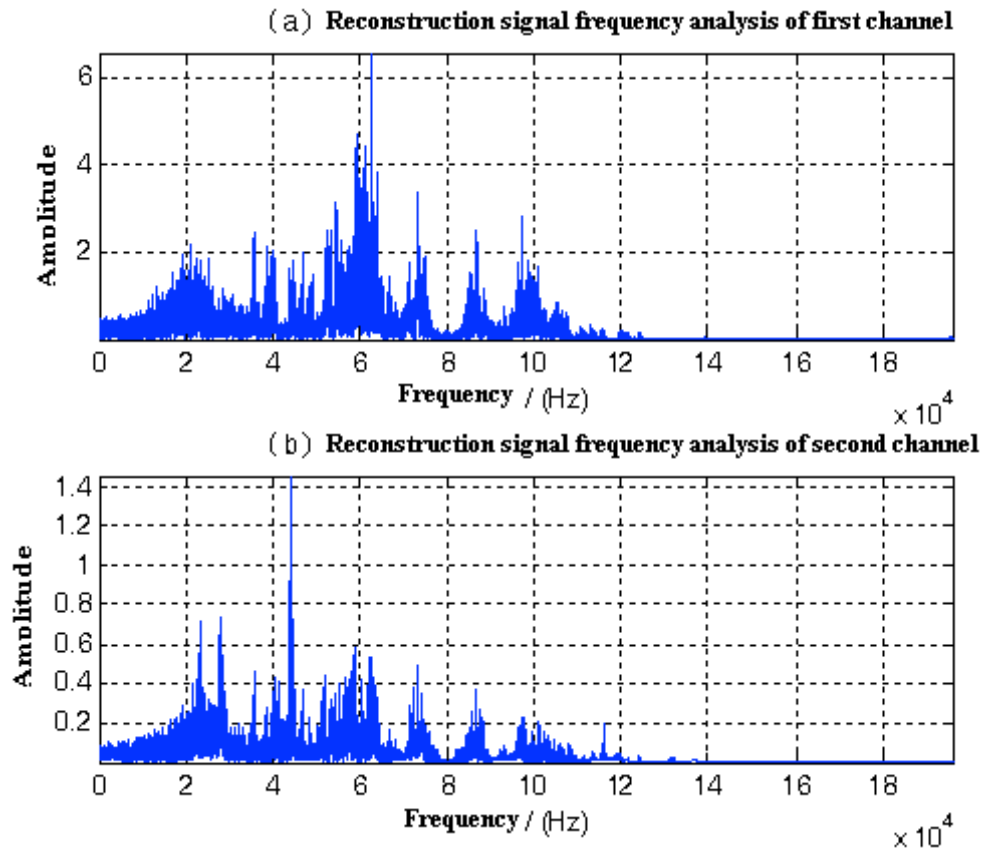


Fig. 8 Frequency domain analysis of reconstructed signals.

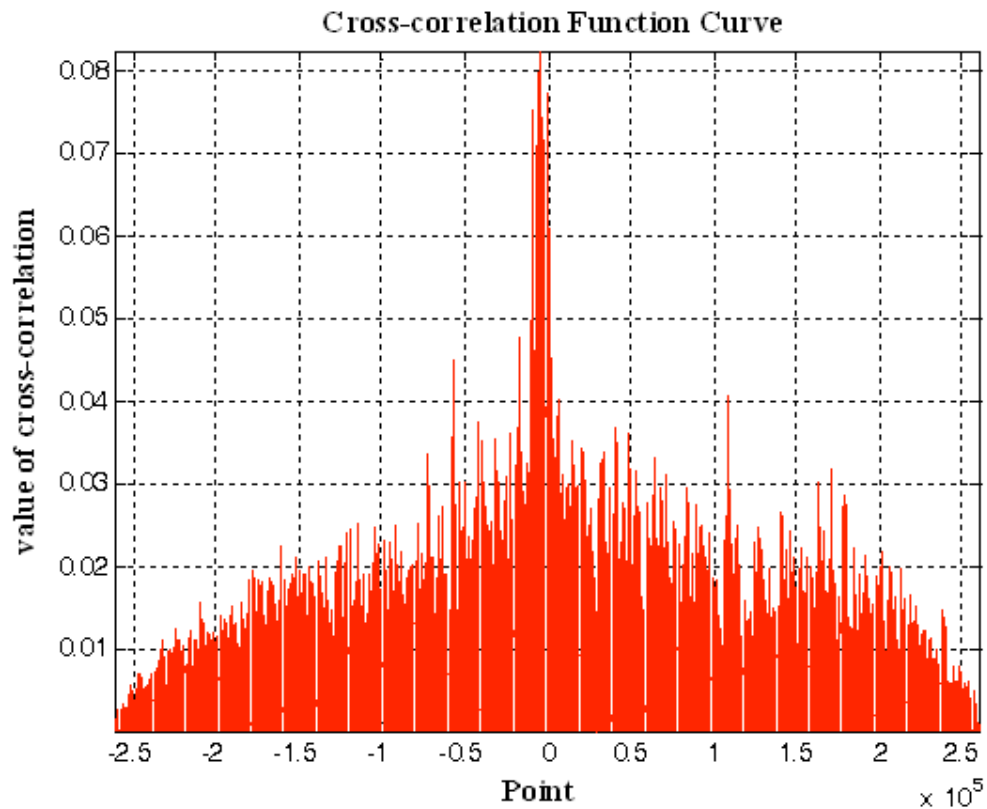


Fig. 9. Direct cross-correlation function curve of denoised only signals.

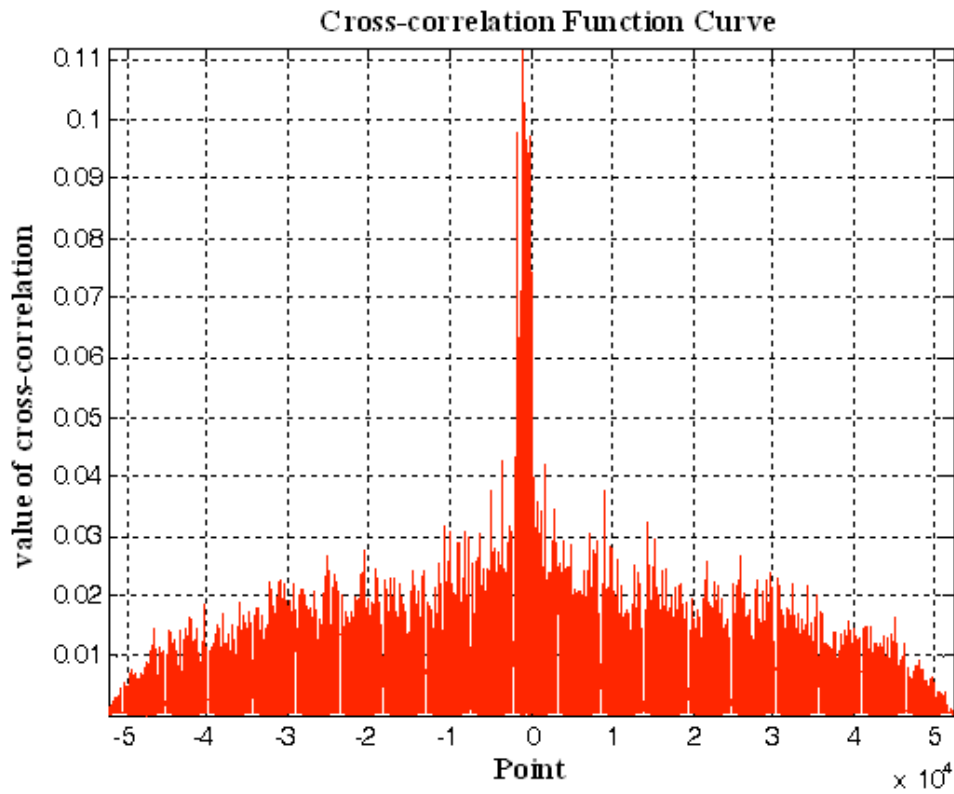


Fig. 10. Cross-correlation function curve using EMD-reconstructed signals.

Table 1. Comparison of direct location and EMD-reconstructed location.

Set		Cross-correlation maximum	Time difference /s	Location error /%	Distance of two sensors /m
1	Location direct	0.128	0.0011	4.4	5
	Location with EMD	0.168	0.0010	2.2	5
2	Location direct	0.123	0.0031	6.1	7
	Location with EMD	0.156	0.0028	1.6	7
3	Location direct	0.083	0.0094	24.8	12
	Location with EMD	0.112	0.0081	1.5	12
4	Location direct	0.090	0.0110	11.3	16
	Location with EMD	0.115	0.0118	1.8	16
5	Location direct	0.101	0.0186	5.2	27
	Location with EMD	0.125	0.0202	1.5	27

Results of several sets of experimental data analysis show that the cross-correlation analysis with EMD method can improve the correlation maximum and reduce the mean positioning error of the above experiments from 1.37 m to 0.22 m. With EMD method, the percent location error was consistent (1.5 – 2.2%) and averaged only 1.72%. This improved significantly over the direct correlation method, which showed an error as high as 25%, averaging at 10.4% or six-times higher.

3. Field Gas Pipeline Leak Detection Application

3.1 Anhui Wuhu Jinghu pedestrian street gas pipeline leak detection

The gas pipeline lies in Jinghu pedestrian street in Wuhu city of Anhui Province. The inner pressure of the pipeline is about 100 kPa; Pipe size is 300 mm OD × 12 mm wall thickness; The length of test pipe segment is 43.5 m, and the buried depth is 1~2 m. Sensors arrangement is shown in Fig. 11. Because the pipeline lies in downtown, so we detect leaks of the pipeline at night. The sound velocity on this pipeline is measured as 1109 m/s. One of raw leak signals and the analysis result are shown in Fig. 12.

From the analysis results, we get the leak point at 19.0 m from A point. The measured distance between leak point and A point is 18.5 m after excavation; the positioning error is 1.2%. While two leak points were noted, in practice, we usually consider the leak location point with cross-correlation maximum as the best result.

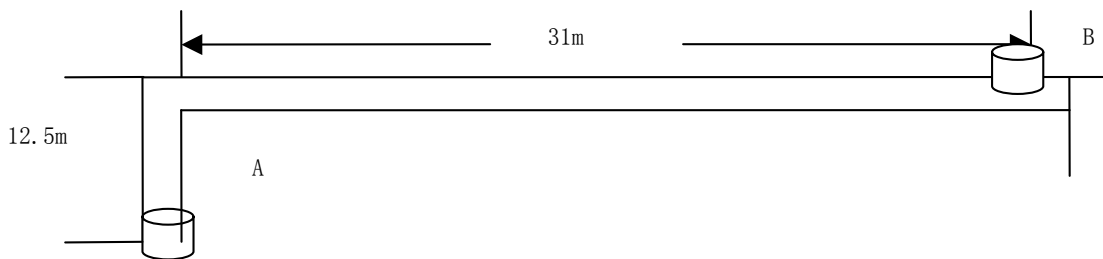
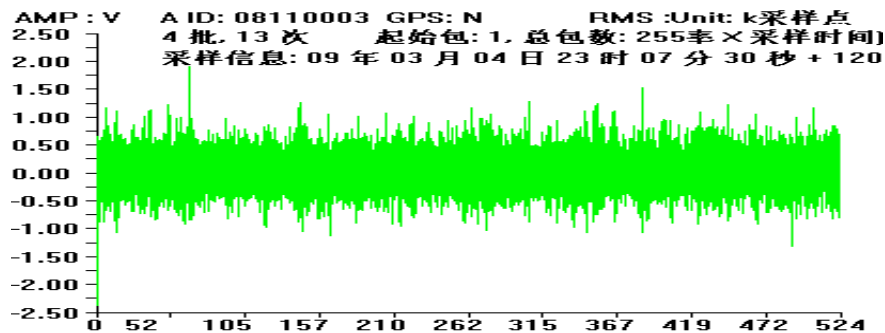
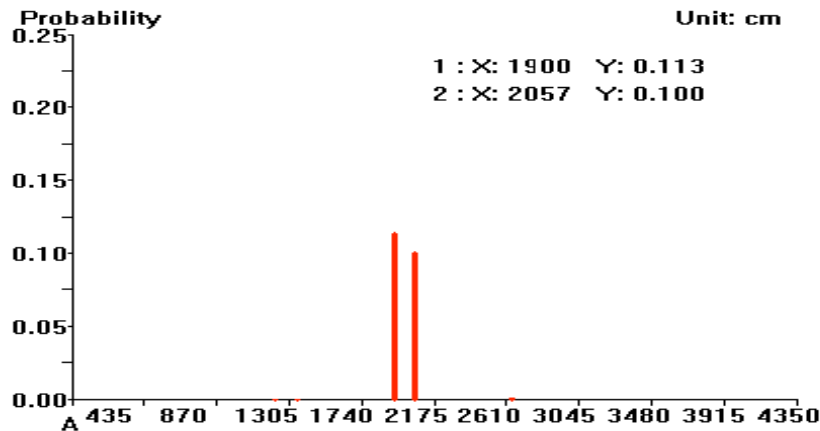


Fig. 11. Sensors arrangement.



(a) Original leak signal of first channel.

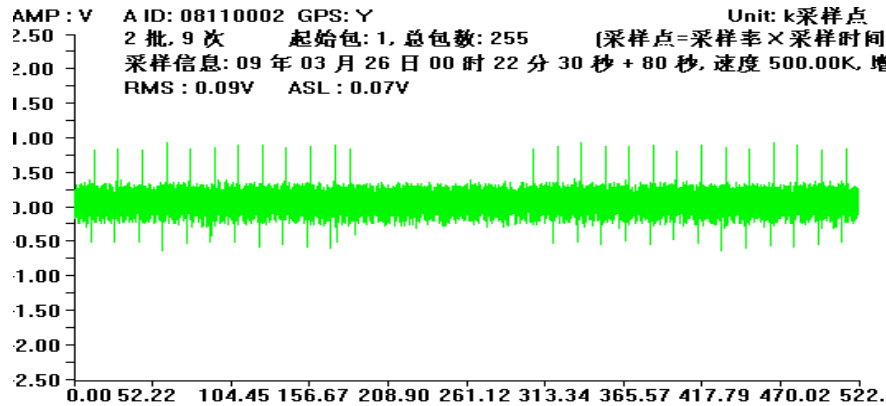


(b) Leak point location.

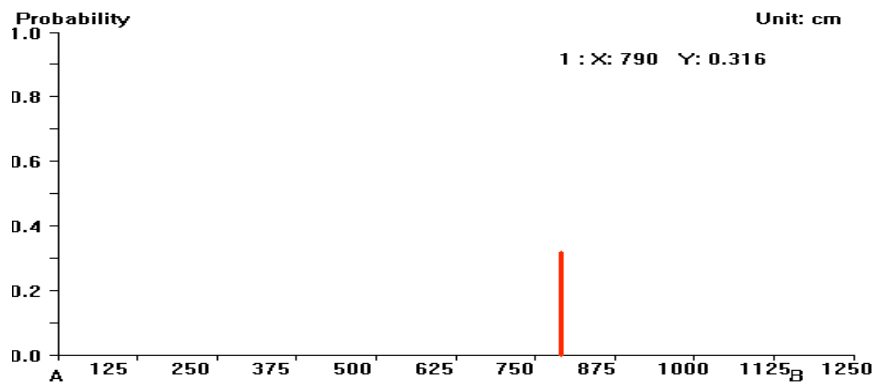
Fig. 12. a) Raw leak signal and b) result of EMD location analysis.

3.2 Anhui Wuhu Zhesan middle street gas pipeline leak detection

The gas pipeline lies in Zhesan middle street in Wuhu city of Anhui Province. The inner pressure of pipeline is about 50 kPa; Pipe size is 500 mm OD × 12 mm thickness; The length of test pipe segment is 12.5 m, and the buried depth is 1~2 m. Again, we tested the pipeline at night. The sound velocity on this pipeline measured is 1109 m/s. Raw signal and the analysis result is shown in Fig. 14.



(a) Original leak signal of first channel.



(b) Leak point location.

Fig. 14 Location analysis.

From the analysis results, we get the leak point is 7.9 m from A point. The measured distance between leak point and A point is 8.0 m after excavation; the positioning error is 1.25%. Thus, the EMD-based leak locating method can accurately detect leaks.

4. Conclusions

The gas pipeline leak location method based on empirical mode decomposition (EMD) is presented. After the empirical mode decomposition (EMD) of leak AE signals, we optimized the selection to the first three inherent modal (IMFs) components. The leak signals were reconstructed from the optimization modals and the reconstructed signals are used for cross-correlation location. Simulations of gas pipeline leakage and field gas pipeline leak detection applications indicate that this method is effective for the gas pipeline leak location with a significantly improved location accuracy of 1-2% over distances up to 27 m.

Acknowledgement

The authors are grateful to support provided by the National Science and Technology planning project of China (2011BAK06B01) and China Special Equipment Inspection and Research Institute support planning (2010 Inner-12).

References*

- [1] Li-ying Sun, Yi-bo Li, Zhi-gang Qu, Wei-kui Wang. Study on Acoustic Emission Pipeline Leakage Detection Based on EMD Signal Analysis Method, *Piezoelectrics & Acousto-optics*, 2008, **30** (2), 239-241.
- [2] Guan-fang Li, An-bang Zhao, Jun-ying Hui. Correlation peak detection and azimuth estimation based on empirical mode decomposition. *Journal of Harbin Engineering University*, 2008, **29** (9), 957-962.
- [3] N.E. Huang, Z. Shen, S.R. Long, et al., The empirical mode decomposition and the Hilbert spectrum for nonlinear and non-stationary time series analysis. *Proc. R. Soc. London A*, **454** (1998), 903-995.
- [4] Xiao-hong Gu, Di-bo Hou, Ze-kui Zhou. Measurement of leak location in buried iron water pipe with acoustic emission and EMD. *Journal of Zhejiang University (Engineering Science)*, 2006, **40** (7), 1105-1108.
- [5] Hui Sun. Research on Empirical Mode Decomposition Theory and Its Application. Zhejiang University, Ph.D. Dissertation, August 2005.

ACOUSTIC EMISSION IN MATERIALS RESEARCH – A REVIEW

KANJI ONO

Department of Materials Science and Engineering, University of California,
Los Angeles, CA 90095-1595

Abstract

This paper reviews progress in methods of signal analysis used in acoustic emission (AE) as applied to materials research field. The achievement and inadequacy in understanding of AE from materials during the deformation, fracture and other processes are examined systematically. New goals for the future are also discussed in view of new analytical tools and vastly advanced instrumentation.

Keywords: Signal analysis, sensors, simulation analysis, source function, transfer function, plastic deformation, fracture, phase transformation, coating, film, corrosion, SCC.

Introduction

Acoustic emission (AE) is used widely in non-destructive evaluation/structural health monitoring to detect the presence of dangerous flaws and to locate the positions of such flaws in structures of various kinds. It is also indispensable for the investigation of dynamic behavior of materials. During the second half of the 20th century, AE from materials, especially AE from deformation and fracture, was studied extensively, cf., Journal of Acoustic Emission (1982-) and conference proceedings of IAES (Japan), ICAE (US), EWGAE (Europe) and AECM (US/Europe). Two recent books are also valuable in understanding the current status of this broad field [1, 2].

From these past studies, we have gained substantial knowledge on the origins of AE signals and can utilize it effectively in most NDE applications. However, our knowledge on the science of AE is hardly complete because of the limitation of experimental and theoretical resources at the time these studies were made. This article builds on reviews by the present author [3, 4], examines new methods of AE signal analysis and attempts to summarize the progress on subjects related to materials research.

Methods of AE Signal Analysis

When one records an AE signal, it contains the information on its source, the propagation medium (sample or structure), AE sensor and electrical instrument used. These can be expressed by the characteristic or transfer functions of the source, propagation medium, sensor and electronics (H_s , H_m , H_t , and H_e). In the frequency domain, the transfer function of the AE signal, H_{AE} , is given by the product of the four transfer functions above:

$$H_{AE} = H_s \times H_m \times H_t \times H_e. \quad (1)$$

This can be performed easier as summation in the logarithmic scale and Fig. 1 shows an example from Sause [5; Fig. 2.20], who modeled a signal from a fiber composite. While AE source is given as a smooth function decreasing with frequency (-6 dB at 1.8 MHz), the medium has the major effect on the final signal detected. In this example system, even a large change in H_s (e.g., -6 dB at 900 kHz) is hardly distinct.

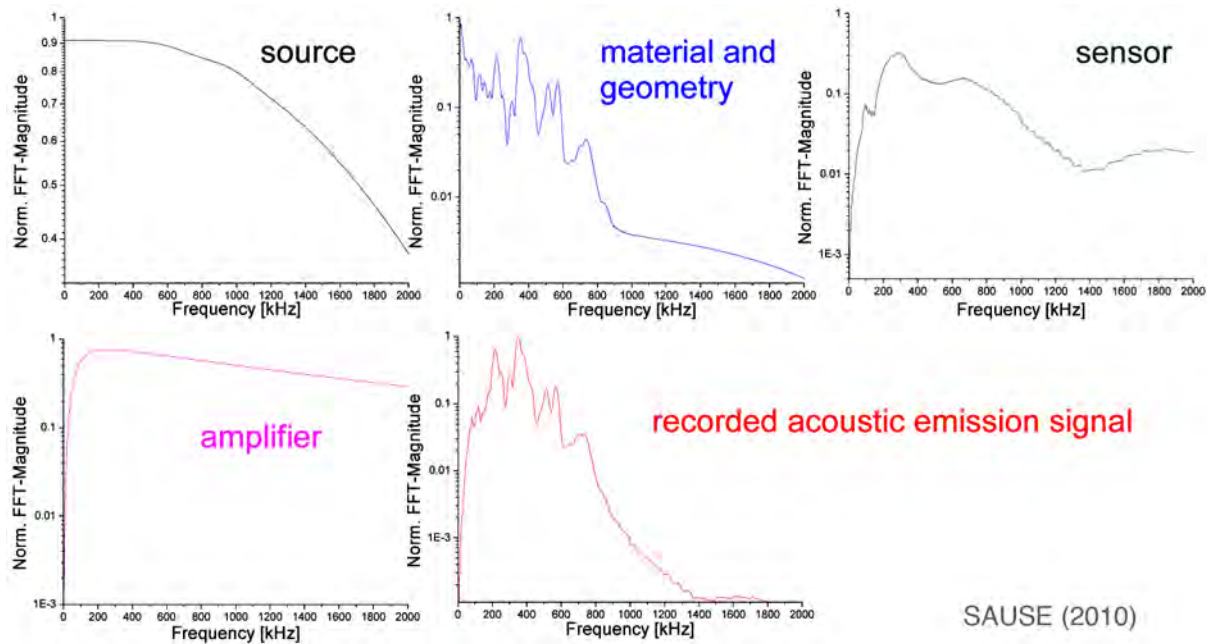


Fig. 1 Magnitude of various H functions in log scale vs. frequency (0-2 MHz) [5].

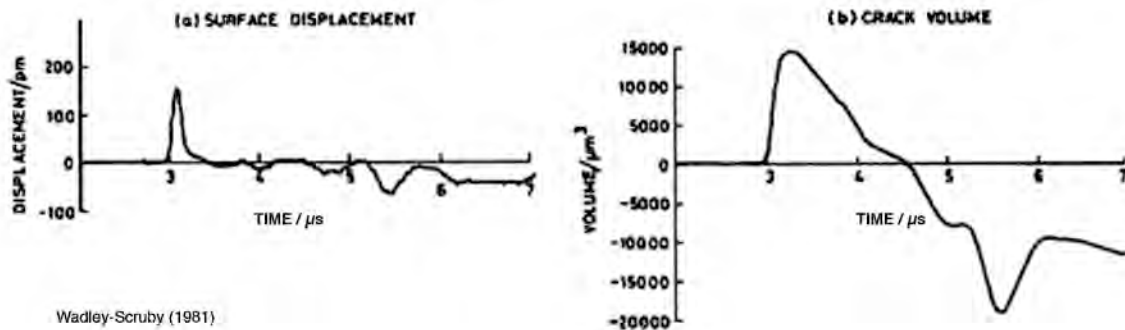


Fig. 2 Cleavage-induced AE (displacement) signal and its deconvolution result [7].

Although the frequency spectra are often adequate in NDE applications of AE, it is essential to examine the time-domain features of AE sources and signals in order to understand the physical basis of AE. From complete transfer functions (inclusive of phase behavior), we can inverse-Fourier transform H 's and gain their time-domain equivalent (denoted as h 's here), i.e., waveforms. In the time domain, however, we need to utilize convolution integral (or deconvolution) instead of frequency-domain multiplication (or division); see [6] for details, but a convolution integral of h_1 and h_2 yielding h_3 is written as (2) below.

$$h_3 = h_1 \odot h_2 = \int_0^t h_1(s)h_2(t-s)ds \quad 0 < t < \infty \quad (2)$$

Implementing convolution and deconvolution procedures with typically large AE signal files requires considerable expertise in software development. Sause [5] recently changed this situation by making AWARE++ software available as freeware. (<http://www.physik.uni-augsburg.de/exp2/downloads/aware.html>)

Applying the above principles requires careful consideration and many simplifying assumptions. Initial successful work to determine H_{AE} was developed in the 1980's and is collectively known as "deconvolution analysis". This method evaluated AE from crack advances on compact

tension samples for fracture toughness tests. See [3, 7, 8]. Outcome was the knowledge of H_s , or specifically, the crack dynamics and crack volume. Wadley and Scruby [7] examined low temperature fracture of iron (intergranular) and mild steel (cleavage) using a special specimen shape, called Yobell. Figure 2 shows two cases for brittle fracture, giving the displacement (measured by a capacitive sensor) and deduced crack volume vs. t . In these studies, the crack plane is known and a calibrated sensor with H_t was at the epicenter position. Theoretical Green's function for H_m was used. The key step is to get H_s from H_{AE} via inverse (deconvolution) processing using known H_m , H_t , and H_e . However, this is prone to instability due to the superimposed noise in H_{AE} [3]. This approach is also restricted severely because H_m is unavailable for most test geometries and was seldom used since around 1990.

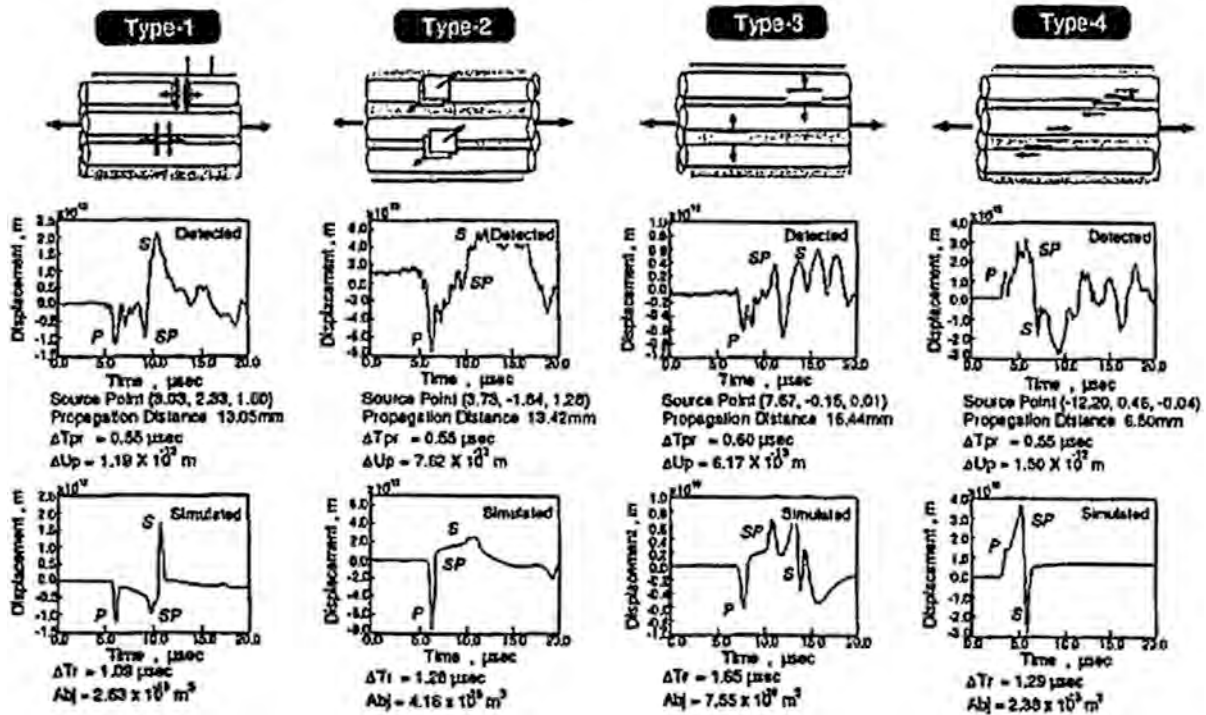


Fig. 3 Fiber-composite failure, types 1-4 (top row); observed and calculated AE waveforms. Source location was conducted first and displacement signal simulated (bottom row) and compared to the detected (middle row) [11].

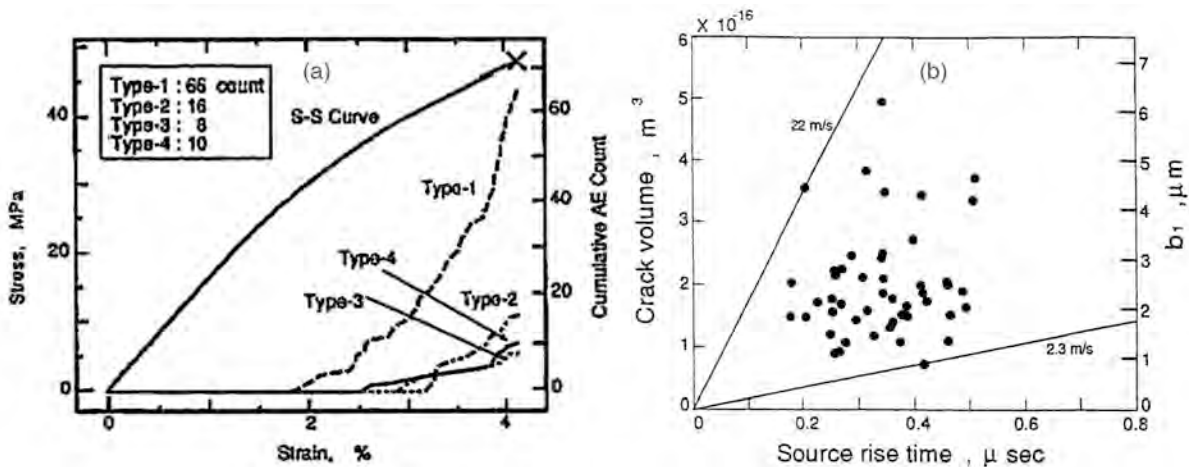


Fig. 4 a) Stress-strain curve and cumulative AE events of 4 types [11]. b) Source parameters of analyzed AE signals from a glass-fiber composite [10a].

First principle elastodynamic calculations of AE waveforms are possible for simple geometries. Ohtsu and Ono [9a,b] formulated displacement solutions assuming smooth-rising source functions of varying rise time, that is, $h_s \otimes h_m$. Here, sources are described in terms of dislocation motion, which can also be given using a moment tensor, commonly used in geophysics. Such modeling or simulation process is most useful in obtaining details of a source by seeking a good match with experimental waveform, i.e., source parameters are used as variables to get the best fit of calculated and observed waveforms, thus, avoiding the deconvolution procedure. Takemoto and coworkers [10a,b, 11] have developed this forward-processing scheme and used it in various AE analyses in composite materials under loading. For example, Fig. 3 shows four types of failure, displacement signals observed and matched simulated waveforms for a unidirectional glass-fiber composite. This led to signal classification as a function of loading. From the source function, crack velocity estimates were also obtained. See Fig. 4. This source function analysis proved its utility in many areas.

A useful development from the moment-tensor representation of source motion is “moment tensor analysis” or moment tensor inversion. This method relies on the first arriving P-waves at multiple sensor locations and obtains the tensile and shear components of the source motion. This approach (available as “PACspecial moment tensor” software package: <http://www.acousticemission.com/index.aspx>) is most suited for large civil engineering structures, and has recently been reviewed elsewhere [in Chaps. 5 and 8, ref. 2]. In concrete and rock testing, the source types of AE during crack propagation have been identified. In most other materials testing, however, sample sizes are too small to use this method.

The use of 3D finite element analysis (FEA) is the next step in characterizing AE signals. Hamstad and coworkers have conducted a wide range of calculations, mainly directing their attention to AE signals generated and propagated on a plate. Starting from the modeling of Lamb waves generated by pencil-lead fracture in thin and thick plates [12a,b], FEA results were compared with modal superposition method [13a], and effects of source rise time, monopole vs. dipole sources, plate thickness and plate width were examined [13b, 14, 15]. FEA method is especially valuable for modeling interior AE sources as these cannot be simulated experimentally. See also <http://www.engr.du.edu/profile/Marvin.htm>. Figure 5 shows a comparison between experimental and computed out-of-plane displacement from a pencil-lead break source at distance of 203 mm [12b]. 50-kHz high-pass filter was applied numerically.

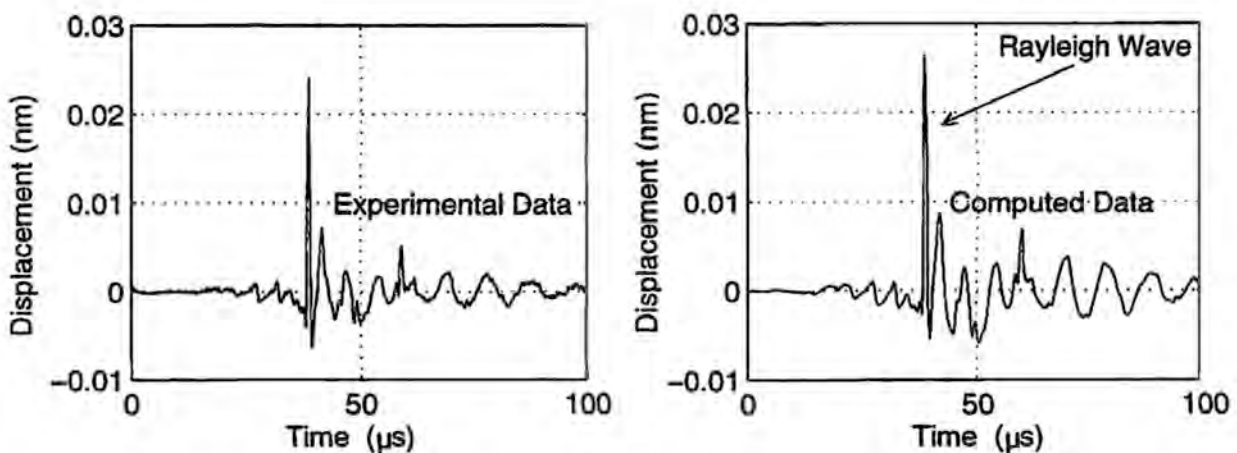


Fig. 5 Experimental (L) and computed (R) out-of-plane displacements from a pencil-lead break source at 203 mm distance. [12b]

Another subject of critical importance is AE sensors and their transfer functions, H_t . Circular capacitive sensors used in [7] have good displacement responses to plane waves, but develop a high-frequency limit for spherical waves and have low sensitivity [7]. Commonly used piezoelectric disc sensors have complex responses due to cross coupling of radial and thickness vibration modes, especially when incident waves are spherical or Rayleigh or Lamb waves. We have examined the sensor characteristics using laser interferometer as reference standard [16a,b]. Sensor responses depend on the wave types, i.e., plane waves, and spherical waves with different radius of curvature. The sensor responses were determined by the excitation of input waves using an ultrasonic transmitter or pulse-laser in conjunction with a transfer block. In addition, it was noted that the ultrasonic transmitter generated radial waves that excited the radial mode of sensor under test. Displacement due to the input waves was obtained using laser interferometer, with which the deconvolution of sensor output yields the transfer function. Because of the source-sensor distance dependence of the transfer function, H_t , its use in equation (1) is much more complex. It is further anticipated that the incident angle of waves also changes sensor responses. An example of source-sensor distance dependence for PAC-WD sensor is shown in Fig. 6, where upper graph is for a plane-wave input and bottom one is for a 25-mm radius spherical wave input [16a].

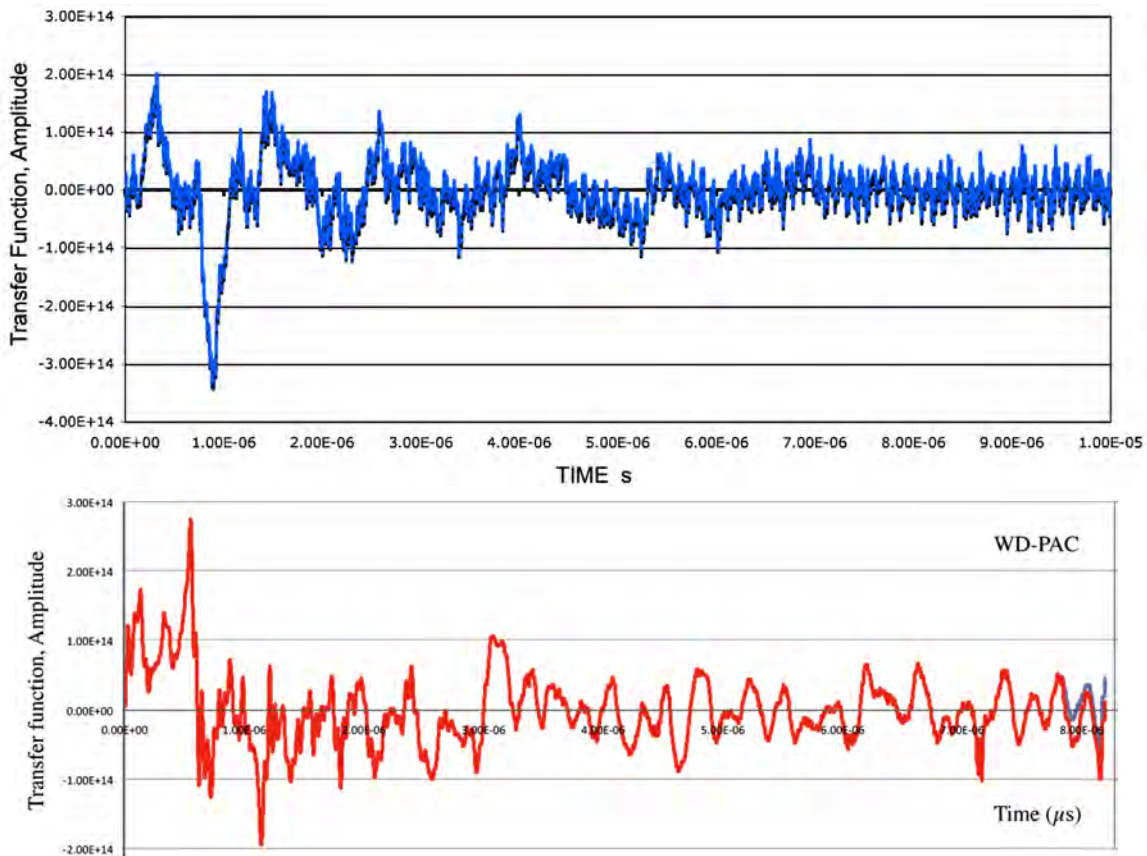


Fig. 6 Transfer functions of PAC-WD sensor; (top) excited by FC500-generated plane wave with 100-mm Al; (bottom) excited by a laser pulse through 25-mm Al [16a].

This behavior of AE sensors based on common piezoelectric discs and rings makes it impractical to broaden the usage of H_t beyond specialized research. It is still essential to develop suitable calibration methods that respond to AE waves encountered in laboratory and field applications. In particular, one must take into account radial mode excitation in commonly used face-to-face sensor calibration. A new method, the bar-wave based approach of sensor evaluation, is

recently demonstrated [16b]. We utilized bar waves with a long flat metal bar. The waves are excited using an ultrasonic transmitter and displacements of the bar are characterized with a laser interferometer as before. Frequency from 20 kHz to 1 MHz is used for characterization purpose. Using FFT, the power spectral density of AE sensors was obtained. Figure 7 shows the bar-wave calibration of PAC-R15 sensor thus obtained. Note the excitation of the radial component of this sensor at 150 kHz.

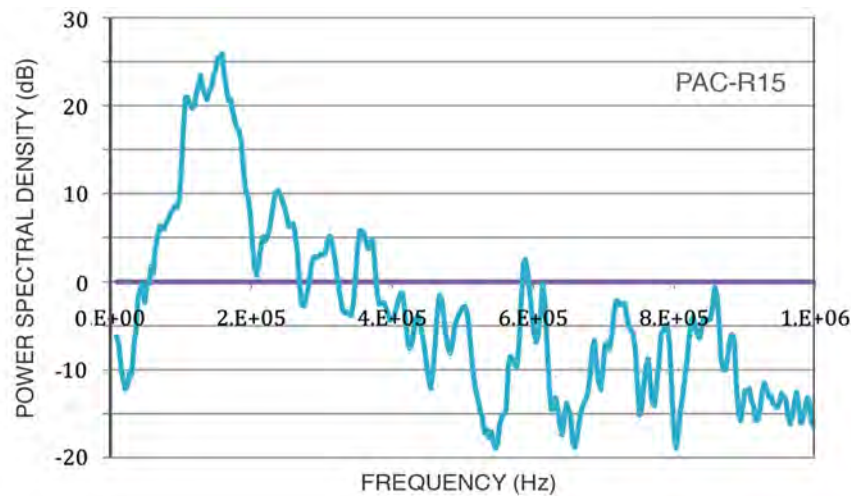


Fig. 7 Bar-wave calibration of an R15 sensor [16b].

The most advanced scheme for understanding the nature of AE signals relies on full-scale modeling of AE sources, propagation and sensing. Sause [5] conducted a detailed study of composite failure covering the entire sequence from the modeling of fracture, wave propagation and piezoelectric sensing, all utilizing finite element analysis. His analysis of fracture takes into account the finite extent of AE sources and the inhomogeneous elastic properties in its vicinity. In the planar specimen geometries employed, the source model excites Lamb waves with symmetric and antisymmetric modes, incorporating established procedures for Lamb wave modeling (see Hamstad above). A 3D model of the used sensor, PAC-WD including piezoelectric conversion was developed, simulating frequency dependent sensitivity of this sensor, but with a computationally more efficient sensor model. He demonstrated that the shape and frequency content of the simulated sensor signal are critically dependent on the aperture of the PZT-elements of the sensor.

Simulations of various source mechanisms result in excitations exhibiting different ratios of S_0 - and A_0 -modes in line with earlier work of Gorman and Prosser [17]. Sause's results also show that a distinction of matrix-cracking and fiber-breakage at the same source position is possible based on different intensity ratios of symmetric and antisymmetric Lamb wave modes. Strong antisymmetric modes contribute to a strong lower frequency contribution, while strong symmetric modes correspond to high frequency intensity. These characteristics for matrix cracking (lower frequencies) and fiber breakage (higher frequencies) have been known based on experimental observations [17-19]. The different geometries, represented by homogenized plies with rotated elastic properties, significantly influence the simulated AE signals, yet a distinct dependency of the signal characteristics on the source mechanism is still retained. However, at larger (>50 mm) propagation distances, false attribution of failure mechanisms tends to increase due to Lamb wave dispersion. Figure 8 gives an example of fiber-breakage signals simulated for two stacking sequences [Fig. 3.26, ref. 5].

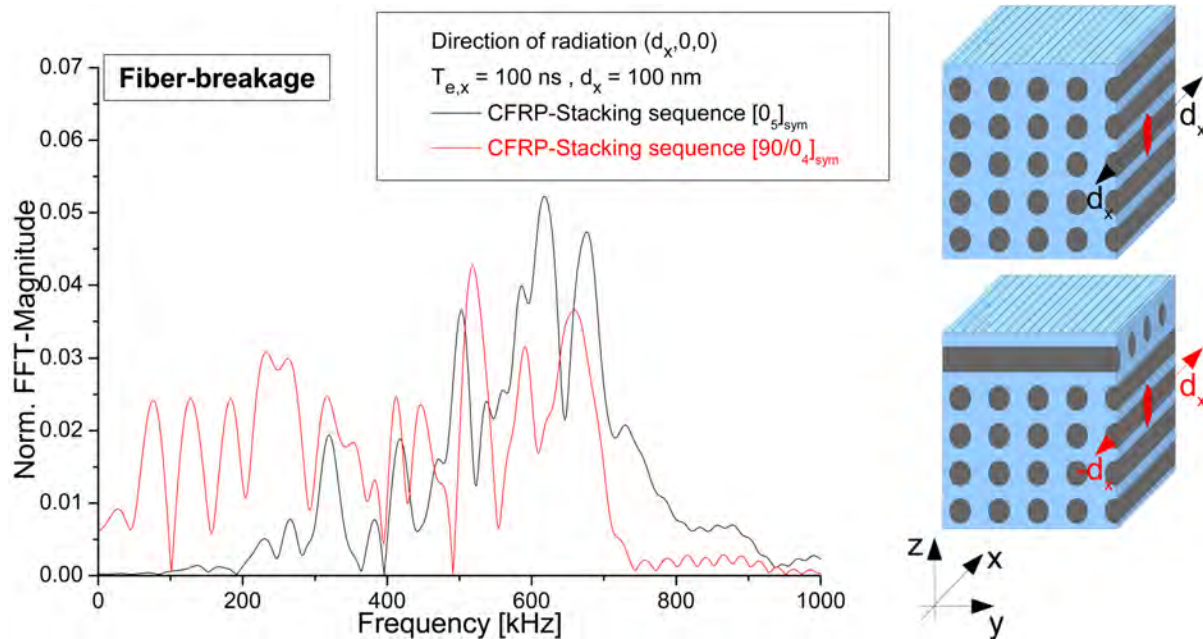


Fig. 8 Simulated AE signal due to fiber breakage in two lay-ups (UD and cross-ply). Resultant displacement of 100 nm was along the fiber with source rise time of 100 ns [5].

Developing own codes for full-scale FEA modeling is not for non-specialists, but it is noted that a software package, such as PZFlex [20], deals with sensor and propagation analysis. Fracture and vibration FEA packages are common. Thus, we hope to see further AE analysis development in the direction Sause superbly pioneered in his doctoral dissertation.

Wavelet transform (WT) has changed how we examine AE signals in the last 15 years. While this author was aware of WT's potential from an article in *Dr. Dobb's Journal* (April 1992) as digital equivalent of audio spectrograms (developed at Bell Labs and used for AE analysis of rocket motorcases at Aerojet by Green et al. in 1964 [21]), early books of Daubechies and Kaiser were of little help for self-implementation. In 1995, Yasuhisa Hayashi (Shizuoka University, Japan) completed a program for WT computation, the source code of which was published in 1996 [22] with his former colleagues at Aoyama Gakuin University (AGU). Its uses were initially limited to Takemoto group [11], but became worldwide once collaboration between AGU and Jochen Vallen (Vallen Systeme, Germany) produced a freeware called, *AGU-Vallen Wavelet* in the past decade. This software now includes Choi-Williams transform calculation as well and has become an indispensable tool of AE workers everywhere. The utility of *AGU-Vallen Wavelet* is demonstrated broadly, so we show an example of another WT software, applied to AE signals from an SiC-SiC ceramic matrix composite. Here, projection of WT coefficients (left figure) and the FFT of the entire signal (right) are shown in Fig. 9. Hayashi and Wakayama [23] extracted the first and second major frequencies from the projected WT diagrams and correlated these to initiation and propagation of micro-damages, such as cracks in SiC matrix, crack propagation along thickness and fiber buckling. Different time segments of a WT diagram are projected and the major frequencies are obtained as shown. (In a WT diagram, the center frequency of the most (or second most) intense peak is defined as the first (or second) major frequency, but such peaks are obscured in a regular FFT spectrum. This feature of WT projection display is now available in *AGU-Vallen Wavelet* as well.

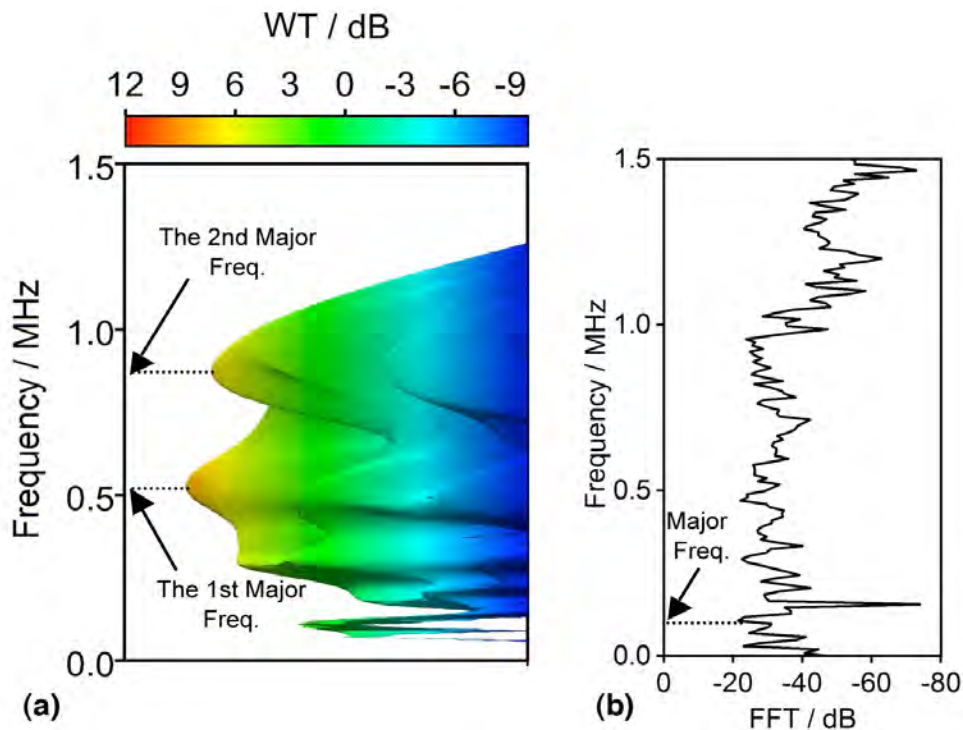


Fig. 9 The major and second major frequencies in (a) projected WT-frequency curve. Note FFT fails to recognize the major frequencies [Fig. 5 in ref. 23].

A new parameter for quantifying the unpredictability of fluctuations in time-series signals (i.e., AE waveforms) has recently appeared. Pincus [24] introduced a feature called approximate entropy, or ApEn, which expresses the likelihood of a similar pattern *not* being repeated subsequently. ApEn is small when many repetitive patterns exist in AE signals, while less predictable signals have higher values of ApEn. This was initially used in physiology and other biomedical fields (cf., <http://www.physionet.org/physiotools/ApEn/>; a link to an ApEn software is given), but its applications to AE signal analysis have been published [25, 26]. The utility of ApEn for AE analysis needs to be established for various conditions, but it is clearly shown in Fig. 10 [25] that ApEn quantifies “noisyness” and that such a parameter was previously unavailable. Bearing defect size is shown to correlate well with ApEn in Fig. 11.

SNR	Waveform	Spectrum	ApEn
Base Signal			0.073
100 dB			0.074
50 dB			0.075
20 dB			0.154
15 dB			0.259
10 dB			0.430
5 dB			0.577
0 dB			0.653
White Noise			1.400

Fig. 10 ApEn for signals with various signal-to-noise ratios (SNR) [25].

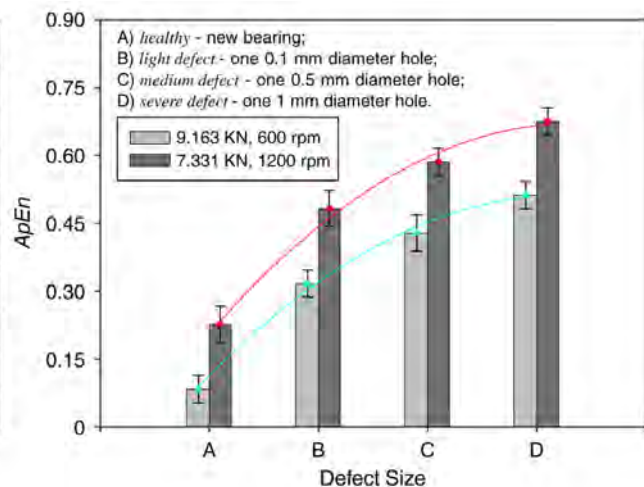


Fig. 11 ApEn values vs. defect size on bearings for two conditions [25].

Another feature of AE signals worth examining is time statistic or temporal distribution of AE events. Manthei and Eisenblätter [27] reviewed works starting from Mogi's paper [28], giving indications of two types of statistics (Poisson or independent and Polya or prior-event dependent processes). This parameter may provide a useful angle in AE analysis.

While most AE signals can be described as burst events, certain phenomena produce “continuous” AE signals. These resemble white (broadband) noise or pink (frequency limited) noise and often found during plastic deformation due to dislocation glide, fracture/decohesion of inclusions, fluid/gas leaks and magnetization. Only their rms voltage levels provided a means of characterization. Ono et al. [29] evaluated continuous AE signals from a steel and found their fractal dimension to increase toward random (from 1.4 to 1.65, with 2.0 being white noise) as yielding is reached. Amplitude distribution also indicated Gaussian behavior. However, Lyapunov exponent and correlation dimension showed no apparent correlation. They also simulated Gaussian behavior from a laser-pulse input on a typical round-bar tensile sample, forming the basis of continuous AE signals via superposition. The origin of continuous AE signals with Gaussian distribution can be traced to the small source size and the irregular reflections and refractions of sample geometry. This produces spreading waves that are randomized through bouncing at the shoulders and enlarged grip regions.

Vinogradov and coworkers systematically examined AE from plastic deformation, including single crystal studies and successfully extracted a useful parameter in connection to dislocation theory of glide, i.e., median frequency, f_m [30-32]. It is defined as [30]

$$\int_0^{f_m} G(f)df = \int_{f_m}^{\infty} G(f)df \quad (3)$$

where $G(f)$ is the power spectral density function of signal segment being considered. They also use the integrated $G(f)$ over the detected frequency range as AE energy, E . Figure 12 gives plots of f_m and E with the stress-strain curve of a copper single crystal [30]. E values rose with strain during Stage I, followed by steady decrease during Stage II. The median frequency was ~250 kHz in Stage I (with a slight increasing trend), but f_m increased to 550 kHz at 40% strain. This finding is in common with previous results for single crystals and polycrystals tested in tension where the AE power spectral density shifts to higher frequencies with increasing strain [e.g., 34]. This trend is viewed in terms of reduced glide distance of dislocations, and resultant increase in the number of glide loops. In a dilute Cu-Ge alloy [31] and in Fe [32], however, f_m is essentially unchanged with strain and other rationales are needed. (cf., Fig. 13) Work on Ge-alloying of Cu [31] shows the reduction in the rms voltage of AE, attributed to the raised frictional stress due to solution hardening (in turn, increasing f_m as more dislocations are needed to account for the reduced dislocation velocity). Another alloying effect appeared in the power density spectra, even though the experimental setups are basically identical, but twinning becomes active with higher Ge content. Work on Fe [32] demonstrates the presence of two types of strain instability and their consequences on AE behavior during yielding and necking. Recent activity in simulating work hardening with phase-field theory [cf., ref. 34] resulted in some reasonable predictions, such as increasing dislocation density with stress squared and increasing fractal dimensions [29]. However, some tried to introduce dislocation avalanches, invoking burst AE observed in ice deformed near melting point [35]. This has no physical basis. Earlier, such bursts were definitively linked to micro-crack observation [36]. It is probably wishful thinking that these computational physicists examine complex reality of deformation and AE results.

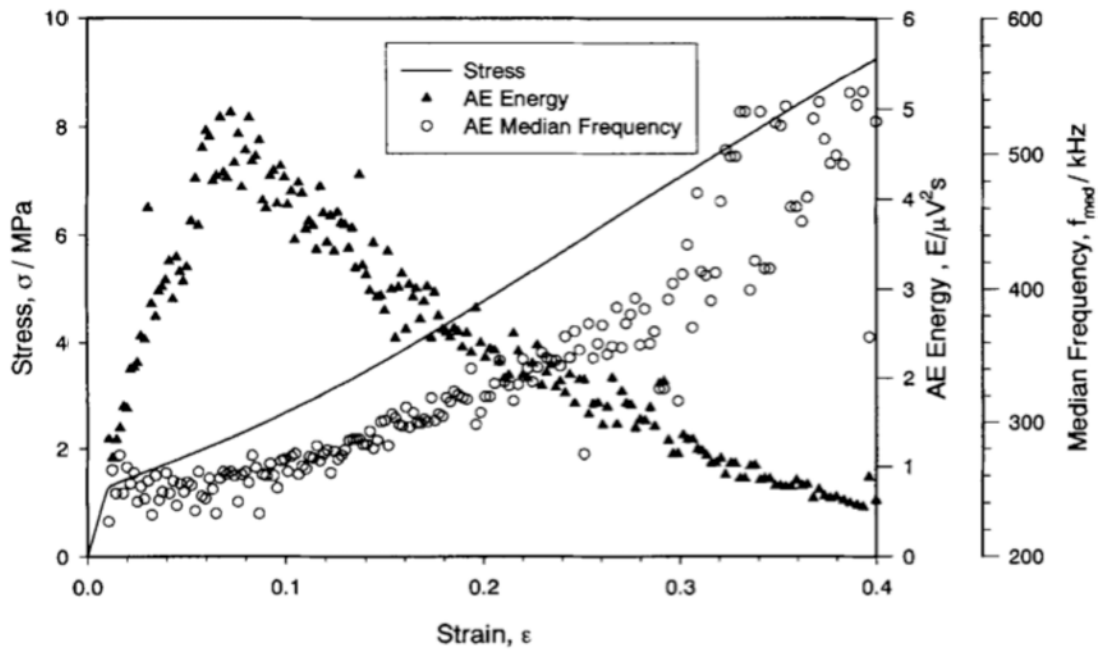


Fig. 12 Values of f_m and E with the stress-strain curve of a copper single crystal. (The stress scale was corrected per author.) [30]

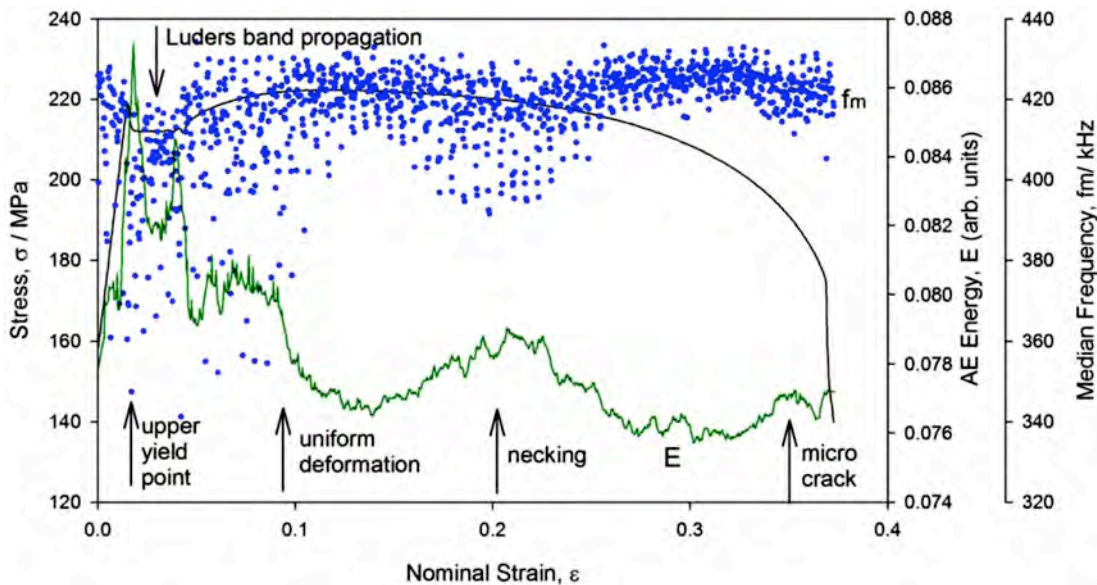


Fig. 13 Values of f_m and E with the stress-strain curve of 3N-iron [32].

AE in Materials Research

Deformation and Fracture

In the last decade, AE studies of plastic deformation have been limited with the exception of hcp alloys of Mg (and Ti and Zr to lesser extent). These materials deform via mechanical twinning, which has previously received much less attention than research on dislocation glide. For Mg alloys, see [37-41]; Ti alloy [42] and Zr alloy [43]. Most of the AE work on Mg alloys unfortunately used just AE counts, so only indications of AE activities are monitored.

The most recent paper [37] used modern AE methods (getting PSD, f_m and V_{rms} digitally) and obtained corresponding *in situ* measurement of deformation twins with a third-generation

ENGIN-X stress-strain diffractometer at a spallation neutron source in the UK. They used annealed ZM20 alloys (2Zn-0.5Mn) with fine (FG=17 μm) and coarse (CG=114 μm) grain sizes. Stress-strain curves and AE (V_{rms}) are shown in Fig. 14 for both grain sizes in compression (a,b) and tension (c,d). Beside the usual high AE activities at yield, AE reflects the nature of the deformation twinning, which is more active in compression, and both exhibit tension-compression asymmetry. Observed work-hardening behavior is significantly different in tension and compression, long attributed to twinning. Neutron diffraction provided the twinning volume and residual stress during interrupted testing while keeping stress/strain as samples were deformed in the diffractometer. They found that most of the twin nucleation occurred at the onset of plasticity at strains $<1.5\%$ in both FG and CG samples, whereas plastic deformation at higher strains is governed by twin growth and dislocation glide. Grain size affected the twin developments with strain; in FG, twinning begins cooperatively in many parent grains simultaneously: in CG, twins increased progressively over a larger strain range. AE results show the instability of the microstructure upon stress relaxation at strains $<2\%$ and a gradual stabilization of the microstructure at higher strains. This seems to be due to the effect of an increasing number of twins, which act as barriers to the dislocation's movement. This, the authors noted, is only feasible to determine from AE study.

Lou et al. [38] conducted tension-compression cycling experiments and reported untwining (or reversal of twinning) activities when stress direction is reversed. Chmelik et al. [39,40] showed increased twinning at higher temperatures (Fig. 15) and little effect on AE of having ultra-fine grain sizes.

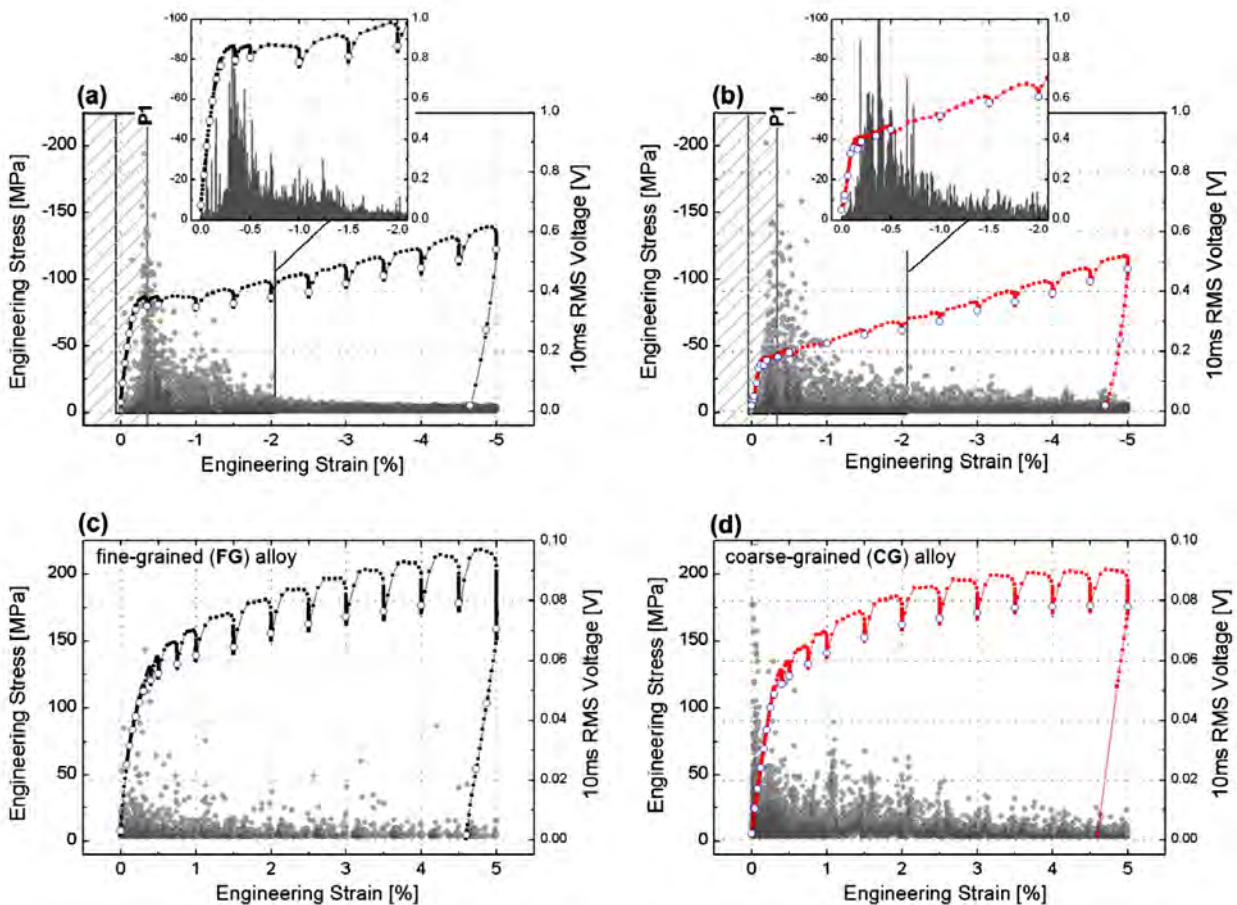


Fig. 14 Stress-strain curves of FG/CG ZM20 alloys with V_{rms} values (with averaging time of 10 ms). Top inserts give V_{rms} values as bar charts [37].

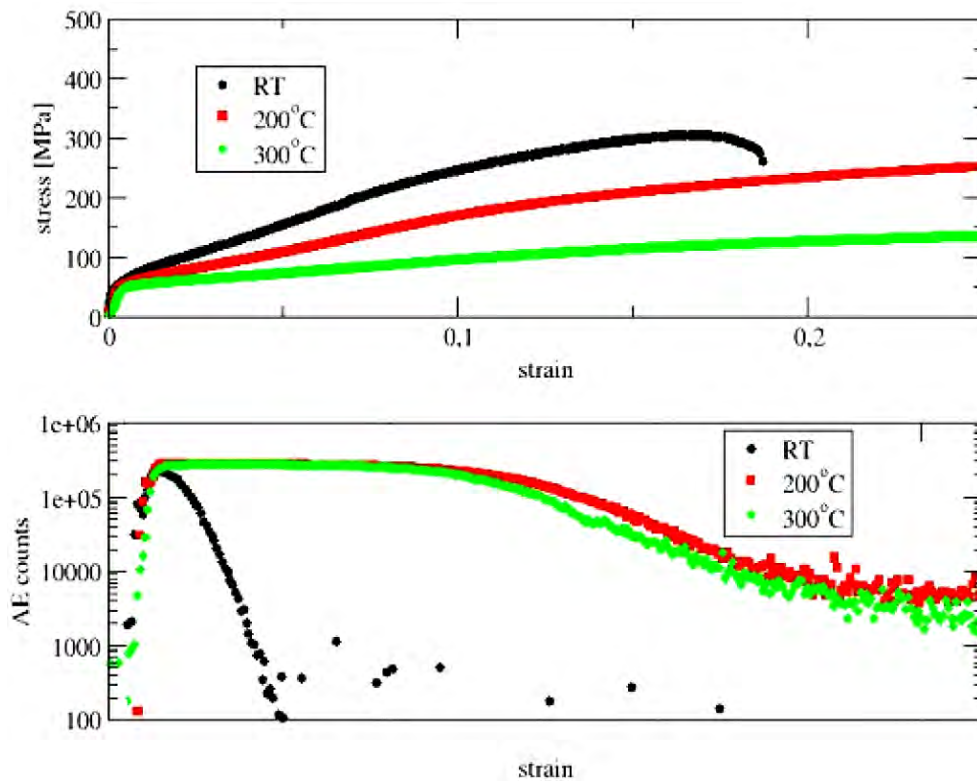


Fig. 15 Temperature effects on compressive stress-strain curves and AE counts for AZ31 Mg alloy (3Al-1Zn) [40].

Taniyama et al. [42] utilized advance AE instrumentation to identify the deformation mode of AE events observed. They used a Grade 1 Ti (commercially pure Ti) plate with a spherical indentation, mounting four small sensors (PAC Pico) on the edges and cooled it to 200 K. At below 230 K (esp. <210 K), twinning started from the area around the indentation. Figure 16 shows the waveforms recorded from one such event. The initial P-wave arrivals have two positive and two negative polarity results. This fact (and Ch5 waveform from a displacement sensor at the epicenter position under the plate) implies the source of this AE event is of Mode-2 shear motion. This agrees with the expected twinning. From this figure, the rise time of P-waves is $\sim\mu\text{s}$ and grain size is several hundred μm [42], thus implying the twin velocity of several hundred m/s. Further examination of twin dynamics should be worthwhile in Ti and other hcp alloys at various temperatures.

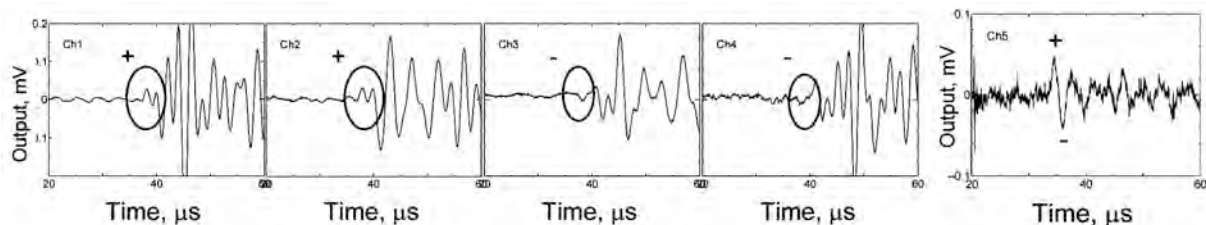


Fig. 16 Waveforms from a twinning event in Ti-Pd alloy, showing Mode-2 shear [42].

Yoshida et al. [44, 45] examined AE behavior of gamma-prime or Ni_3Al in single crystals or in directionally solidified (DS) condition, some with B additions. With B additions, AE at yield increased, but AE in later part of work-hardening stage decreased. In DS samples, AE from the work-hardening stage was much more active due to the presence of grain boundaries. The authors suggested frictional drag from B and dissociation of APB obstacles for the two types of

AE, but no concrete evidence is available. Since this material (also superalloys that contain high γ' content) is used at elevated temperature, AE at their peak strength condition at >1000 K should be most interesting. No such study has been done to date.

Fukaura et al. [46a,b,c] used AE to evaluate the stress, at which constituent carbide particles fracture in ultra-high strength steels (JIS SDK11 and its modification, M-SKD11) in connection to the fatigue strength study. AE showed that carbide fracture stress increased from 1.1 to 1.8 GPa with the modification of the composition (reducing C and Cr and increasing Mo and V).

Reed and Walter [41] correlated AE serrated flow (due to twinning, but labeled as Portevin-Le Chatelier or PLC effect) in a Mg alloy. Sophisticated models have been published to account for the physics of PLC [47, 48]. AE is used to justify some of the assumptions. It remains to be seen if the models are valid in explaining various observations. Another theory [49] provides the lattice dynamics analysis of plastic deformation. Ravi-Chandler [50] reviewed dynamic fracture models and Minozzi et al. [51] used a lattice model for dynamic fracture in a disordered medium to correlate AE to internal damage evolution. They find that the cumulative AE amplitudes are directly related by a power law to the cumulative damage, namely, the distribution of the AE burst energies follows a power law and its exponent being related to the exponent describing failure avalanches in quasi-static models.

Waveform simulation procedure [10, 11] was applied to fatigue tests of high strength (SUJ2: 1C-1.5Cr) steel. Using an experimental transfer function with source rise time and volume that best match observed waveforms, Yonezu et al. [52] obtained AE source parameters (crack volume and speed). Figure 17 shows that AE begins at the start of da/dN -Stage II and the crack is transgranular. AE rises sharply above $8 \text{ MPa}\sqrt{\text{m}}$ (near Stage III) in this steel and the crack becomes intergranular. Microscopic source analysis indicated that fatigue crack progresses along a few grain boundaries accompanied by strong AE signals. As shown in Fig. 18, crack volumes are typically several times that of a single grain IG crack.

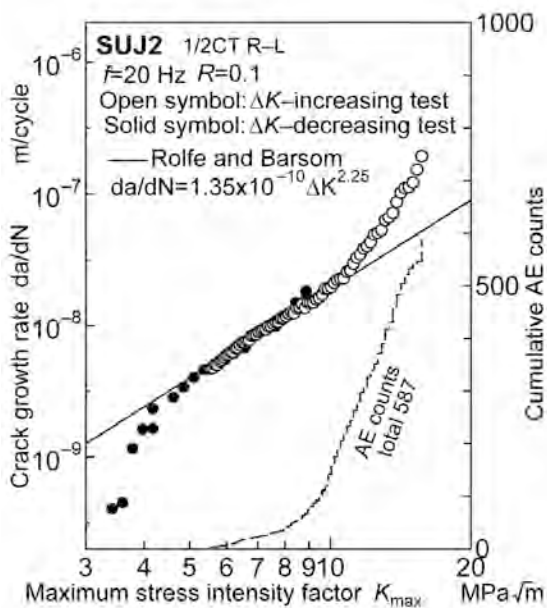


Fig. 17 da/dN and AE event counts vs. K_{\max} [52].

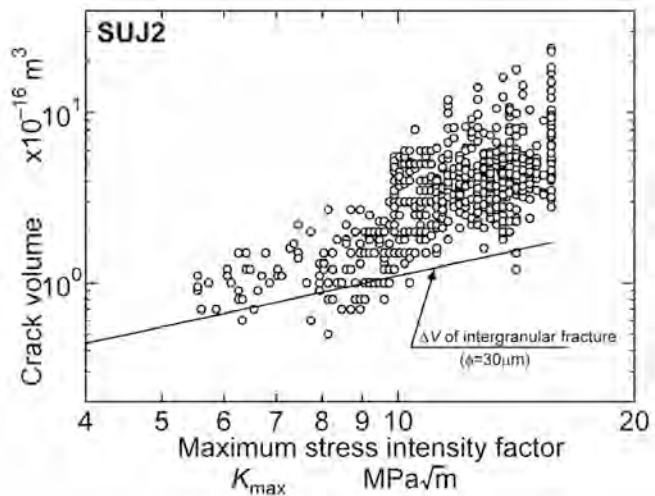


Fig. 18 Crack volume vs. K_{\max} [52].

Another work [53] examined torsional fatigue of stainless steel cylinders. AE behavior was correlated to microscopic fracture surface observations. Fatigue of Ti alloys was examined by classical AE method [54]. Soboyejo et al. [55] introduced mechanistic models for Ti fatigue life prediction using AE parameters. They claim that AE counts are related directly to the crack driving force, ΔK , and the measured AE parameters are also related directly to fatigue fracture mechanisms. No evidence is given in support, however, and readers should use caution. A thesis [56] used NIST sensors to get Rayleigh waves from fracture toughness samples undergoing crack growth. Only wavelet spectrograms are shown and meaningful conclusions cannot be drawn. Another guided wave AE work was given at EWGAE27. Using a 2D FE model, Lee et al. [57] capably showed that emissions from fatigue crack growth in a plate are Lamb waves and that for crack growth of up to 86% of the plate thickness, the A_0 -mode signal had larger amplitude than the S_0 -mode signal. Above that, the A_0 -mode amplitude drops steeply and the S_0 becomes larger. See Fig. 19 for this behavior.

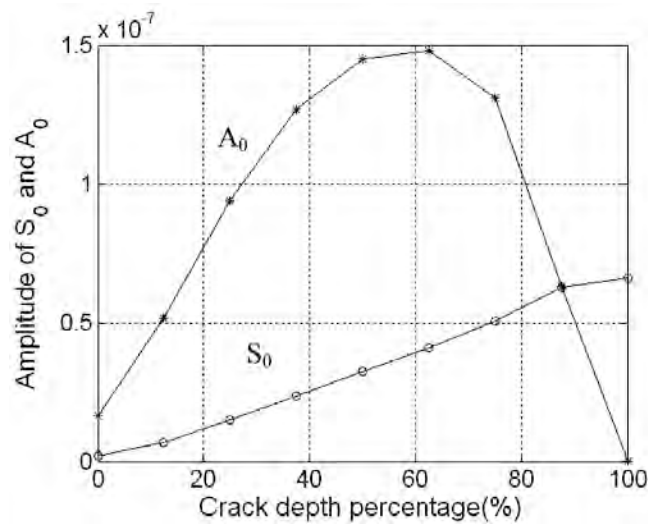


Fig. 19 Amplitude of the S_0 and A_0 modes from different fatigue crack depths [57].

Aggelis et al. [58] used AE parameters commonly used in concrete studies for Al fatigue evaluation. Changes in RA values, for instance, increased sharply prior to final fracture, signaling failure mode shift. Shiwa et al. [59] examined ultrasonic fatigue using AE and nonlinearity parameters. On application side, [60] reported fatigue crack detection work on full-size steel girders for a bridge.

Phase Transformation

AE from martensitic transformation has been studied since the 1930's and has attracted continued attention in connection with shape memory effects. Van Bohemaen [61] recently established that bainitic transformation in steel is also displacive type, like martensitic one. For many years, it has been argued that bainite also is a displacive transformation because of surface reliefs observed, but definitive proof has eluded researchers. See [62, 63]. Here, AE from martensitic and bainitic transformation was characterized with C45 (0.45C medium carbon steel) and 16MnSi (0.16C-1.7Mn-1.6Si) steels using a spot welding machine and wideband AE sensing (PAC WD; 4 MHz sampling). AE parameters obtained include V_{rms} , mean frequency, defined by (4) as

$$\bar{f} = \int G(f) f df / \int G(f) df \quad (4)$$

calculated from waveforms recorded ($G = \text{PSD}$), and peak amplitude. Figure 20 shows results from C45 steel: a) Averaged V_{rms} of AE signals generated during bainite and martensite forma-

tion in steel after spot welding (indicated by W). First peak (B) is bainite formation, and second peak (M) is martensite formation. b) The mean frequency is higher during bainite formation. c) Peak signal amplitude is shown. The observed difference in the mean frequency has been attributed to the characteristics of the (jerky) interface movement of the two transformations: the mean life time of events is shorter for bainite, and the mean free path is less for bainite if the mean velocity is similar in both.

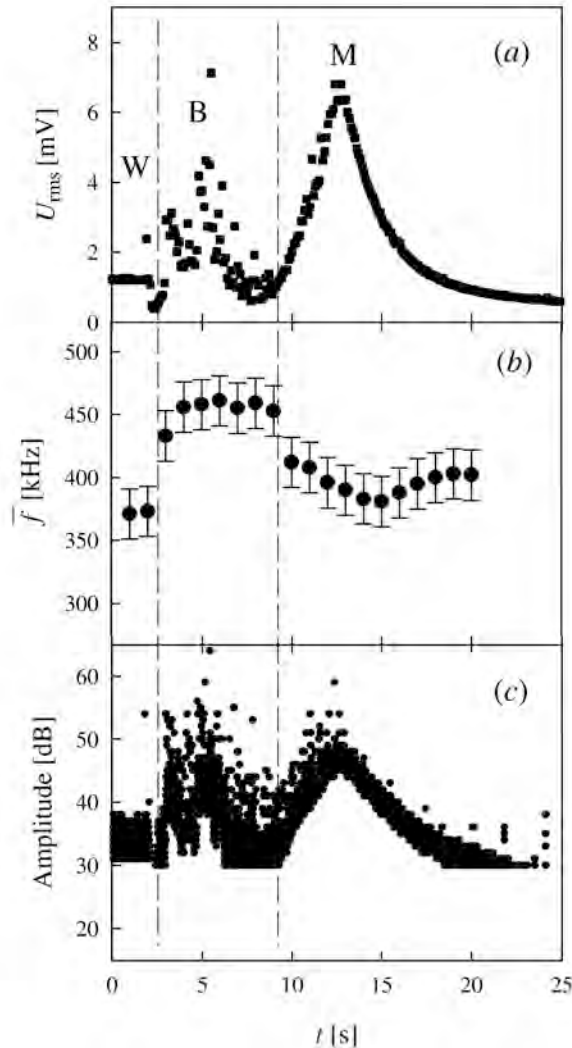


Fig. 20 Phase transformation of C45 steel: a) V_{rms} of AE signals. B: bainite formation, M: martensite formation. b) The mean frequency. c) Peak amplitude [61].

Yoshida and coworkers have examined AE from Cu-Al-Ni single crystals (one of shape memory alloys or SMA) [64a,b], showing systematic variations between two types (super-elastic and thermoelastic) of martensitic phase changes under stressing. Event rise times were $\sim 1 \mu\text{s}$ in most cases. Inamura et al. [65] reported pre-martensitic transformation phenomena of α' -martensitic transformation in 304 stainless steel just above the martensite start temperature. This corresponds to the formation of fine α' -martensite particles. A model was presented for martensitic transformation due to thermal cycling, monitored by AE in Cu-Zn-Al [66]. This model exhibits the repetitive bursts of energy under successive thermal cycles in a small temperature interval as observed in AE experiments. It is interesting to note the existence of thermal emissions, paralleling AE [67].

AE from ferroelectrics is an active field of study. Dul'kin et al. [68a] examined using AE multiferoic ceramic solid solution of relaxor ferroelectric PFW with ferroelectric PbTiO_3 (PT) together with dielectric measurement. AE response appeared at Burns temperature, at ferroelectric phase transition temperatures, and at Néel antiferromagnetic phase transitions. Based on detected AE responses, they modified existing phase diagram for PFW-PT system. The same group [68b] studied a PZT-based ferroelectric and found that the AE peak intensity is generally proportional to the temperature derivative of the dielectric permittivity, in agreement with a model proposed for a thermally cycled small elastic dipole. Prabakar and Rao [69] suggested a sudden appearance of burst AE under an applied dc field during temperature decrease cycle indicates the structural phase transition from cubic to tetragonal in soft PZT ceramics (PZT-5A, 5J and 5H). Phase transition temperature is dependent on applied field, which produced many AE signals in the ferroelectric phase. These resulted in two clusters in pattern recognition analysis indicating two different source mechanisms, piezoelectric strain (at <2 kV/cm) and strain due to domain alignment (2–10 kV/cm). Pérez-Reche et al. [70] conducted AE study of a giant magnetocaloric material, $\text{Gd}_5\text{Si}_2\text{Ge}_2$, during the paramagnetic-monoclinic \leftrightarrow ferromagnetic-orthorhombic magnetostructural phase transition. The detected AE signals showed that avalanches between metastable states control the transition kinetics.

Coating, Film, Friction and Wear

AE study of plasma-sprayed thermal barrier coating (TBC) started in 1979 with indentation and thermal resistance evaluation [71a,b], but soon extended to that of the thermal cycling performance for TBC in gas turbine applications [72]. AE has recently been used in finding the nature of thermal cycling damages; [73,74] used AE with 4-point bending of thermal fatigued samples, trying to evaluate effects of thermally grown oxide (TGO), a critical concern without suitable NDE methods available. Park et al. [74] reported that, with longer thermal fatigue, TGO layer grew and AE was generated earlier. However, with more cracks and micro-porosity, AE events, coefficients, energy and amplitudes decreased. The same authors also showed changes in laser-induced AE signals as a function of TGO thickness. Such changes may be from the structural changes in the TGO, but can be a useful NDE method if confirmed. On this subject, a few doctoral dissertations [75a-c] appeared, but their AE approach is conventional.

Ma and Takemoto [76] quantitatively evaluated thermal shock behavior of plasma-sprayed TBC. Bond coat of this TBC was NiCoCrAlTaY (AMDRY997) and top coat, Y-stabilized zirconia, PSZ (Metco204NS). Two of the samples were also PSZ only, thin and thick. Laser provided heating source and waveform simulation analysis of AE signals (discussed earlier) was used to determine the fracture dynamics of TBC. They used an off-epicenter displacement-sensitive sensor to detect AE signals. These are compared with calculated waveforms corresponding to five types of cracking sources, schematically shown in Fig. 21 together with expected waveforms. In Fig. 22, simulated and detected waveforms of type A, C and E cracks are compared side-by-side. For the simulation, crack volume ($1\sim 7 \times 10^{-15} \text{ m}^3$) and rise time ($1\sim 3 \mu\text{s}$) were adjusted to best match the observed signals. They found that vertical Mode-I fracture to be the major fracture mode under low heat-flux laser power conditions. Lateral or interfacial fracture (Mode-I or II) was prevalent under high heat-flux conditions. Delamination (or decohesion) was responsible for the eventual coating failure in thin (or thick) TBC. A bond coat is beneficial for improving the thermal shock resistance, as expected.

AE-instrumented scratch tests have been used for adhesion testing of coatings and films for some time. Piotrkowski et al. [77, 78] examined this established technique using wavelet transform (WT) analysis. WT of AE signals obtained from scratch tests on hot dip galvanized steel

samples with different corrosion levels was determined. Depending on damage mechanisms, wavelet power was distributed in different frequency bands, which were automatically obtained by searching for the relative minima of the wavelet entropy of signals and appropriate clustering methods. Correlation between the different mechanisms was corroborated by bispectrum analysis (BA). Coating damage was evaluated via the evolution of the wavelet power in a specific frequency band, corresponding to the fracture of the intermetallic phase of the galvanized coating. Damage increased with the level of corrosion, but adherence was not dramatically affected. The application of two signal-processing techniques, WT and BA, contributed to the consistency of the results.

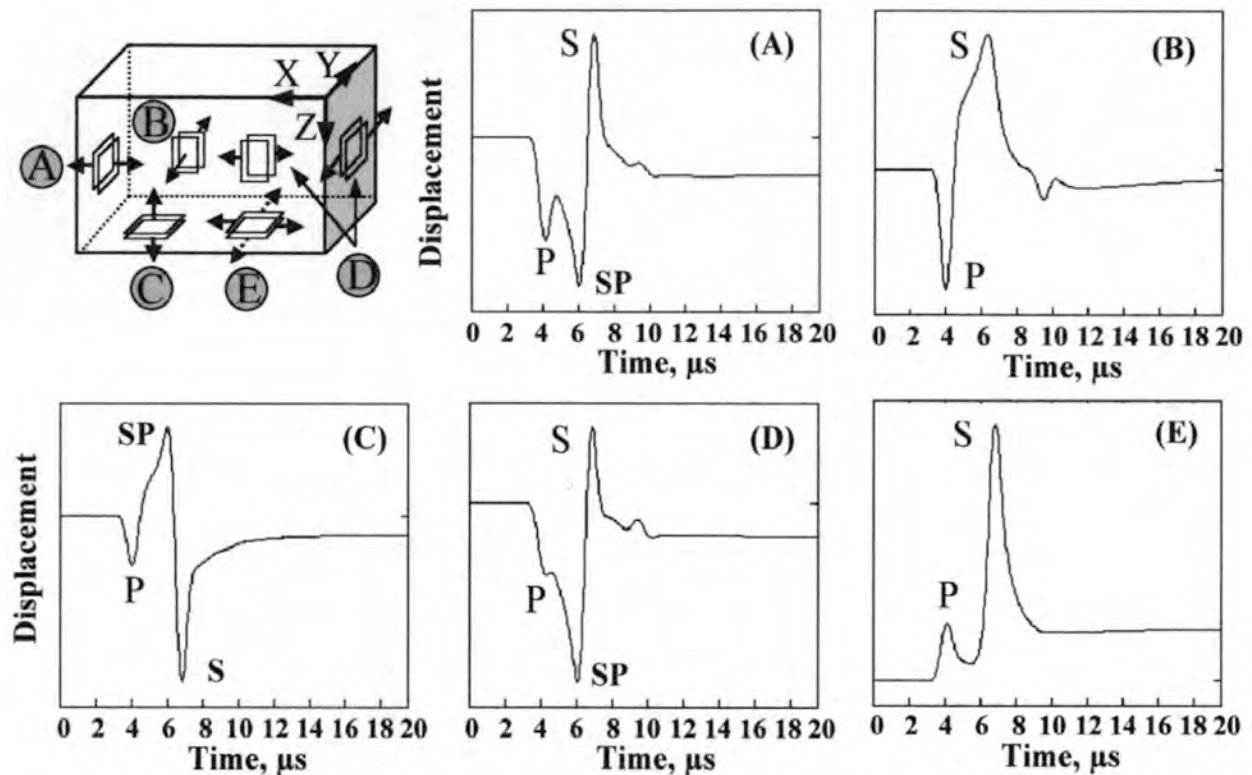


Fig. 21 Five types of cracking sources, A-E, and simulated out-of-plane displacement waveforms [rearranged Fig. 4, ref. 76].

AE is used in examining other films and coatings. Ikeda et al. [79] evaluated polycrystalline diamond films with AE to detect ring cracks in indentation test. This led to finding the static strength of 3.6~4.0 GPa. The strength under cyclic loading was found as 1.4~3.2 GPa, distinctly smaller than the static value. AE method with laser excitation can measure the adhesive strength of coating, used for CVD diamond [80]. The same method was used for PSZ and 316L stainless steel coating by plasma spray [81].

Sause [5, 82] applied his FEM modeling to the analysis of coating failure on composite plates. AE from coating failure consists of crack initiation, crack growth and delamination and is distinguishable from signals arising from failure of CFRP substrate. Experiment was compared to FEM models of AE signals and pattern recognition analysis was applied to separate different types of AE signals.

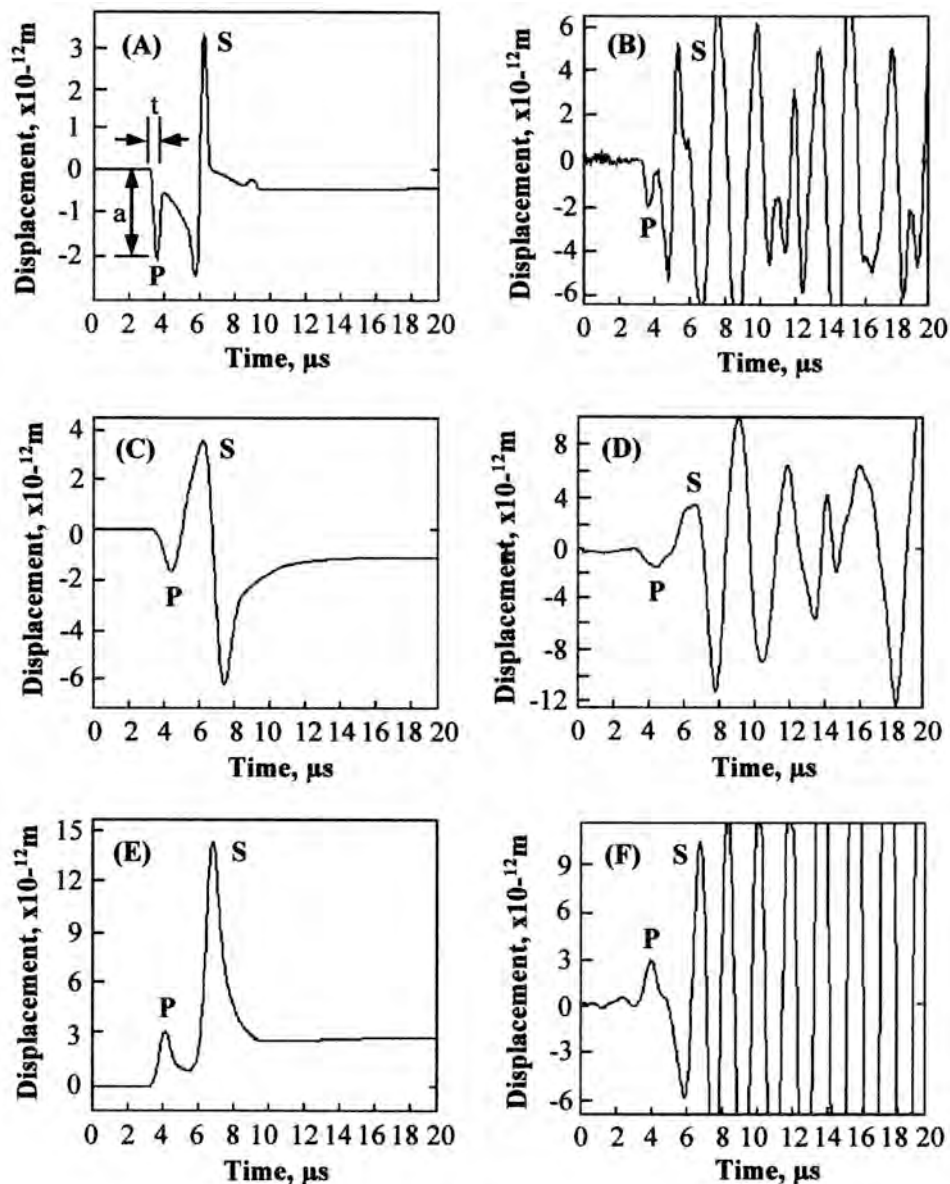


Fig. 22 Simulated (left) and detected (right) waveforms for the TBC. Type A crack (A, B); Type C crack (C,D); Type E crack (E,F) [Fig. 6, ref. 76].

A final note of interest on film/coating is anodized Al under strain. R.G. Liptai's 1963 dissertation [83a] dealt with anodized surfaces as barrier to dislocation glide. A recent work [83b] again showed even thin films (2-20 μm thick) contributes to AE in the elastic range.

Friction and wear have benefitted from the use of AE for a long time. A book on "AE in Friction" [84] is out recently. Early work on AE was on monitoring magnetic hard disk [85] and this still continues with [86] studying the contact behavior of sub-ambient pressure tri-pad sliders during start/stop and constant speed operations and finding contact forces to be a few mN. [87] studied lubricated sliding contacts with AE detecting the presence of wear-reducing additives and the predominant wear process. [88] evaluated tribological behavior with AE of alumina, silicon nitride and 52100 steel under dry sliding with a ball-on-flat-disc. Correlations exist between the wear rate and the integrated AE V_{rms} signal, but strong influence of the sliding speed on the wear rate was found. [89] conducted wear-life tests of different diamond-like carbon (DLC) coatings on a steel substrate (100Cr6) under slip-rolling friction. AE turned out to be an excellent

tool for an *in situ* estimation of the end of the wear life of the DLC coatings. Under lubricated conditions, if a high AE activity was detected, the respective coating failed later in the tests. When no high AE activity was recorded, the respective coatings did not reach the failure criterion and were labeled ‘resistant’ to wear. [90] provided a review of the application of AE techniques for monitoring forming and grinding processes. AE generated during the forming processes is useful for detecting die wear and cracking, friction properties, state of lubrication, galling, stick-slip, etc.

Corrosion and Stress Corrosion

Use of AE in corrosion and stress corrosion cracking (SCC) studies started early [91]. (Note “cracking” in SCC is most often not from mechanical stress, but stress-assisted rapid chemical dissolution, but we will use the conventional term.) Okada et al. [91] showed SCC of 304 austenitic and 25Cr-5Ni-3Mo ferritic stainless steels in boiling MgCl_2 produced no AE because active-path corrosion (APC) is the cause. From our present knowledge, this is transgranular (TG) type SCC with the use of 143°C-boiling MgCl_2 . In contrast, SCC of high strength martensitic stainless steel (13Cr-Ni-Mo) in 3%NaCl and in boiling MgCl_2 is from hydrogen embrittlement and accompanied by AE. Hydrogen evolution in corrosive reaction is detectable with AE [92,93a], has steep amplitude dependence [94] and shows resonating waveforms [93b]. Suezawa, et al. [92] also measured corrosion potential in AE-SCC study of 304 stainless steel. (It is interesting to note they found a shift to higher frequency in deformation-induced AE of 304, as discussed earlier [30, 32].)

Early corrosion research was reviewed by Yuyama et al. [94] Most of the early SCC work failed to control corrosion potential, however, making it difficult to assess electrochemical conditions. Takemoto [95, 96] reviewed more recent AE work on SCC centering on stainless steels. General corrosion contributes to increased AE rms voltage levels and can be distinguished from localized corrosion (pitting, crevice, exfoliation, SCC, etc) [97]. Corrosion AE studies are complemented well by the use of corrosion potential fluctuation (CPF) [98] or electrochemical noise (EN) [97]. CPF and EN are identical parameters. Pitting in Al alloys generates AE by the release of hydrogen micro-bubbles [99a,b]. Initiation of pits is quiet, but growth stage shows two types of AE signals [99a]. Jones and Friesel [99c] found no bubbles in pitting of 304 stainless steel and suggested that rupture of an oxide or salt cap during pit growth is a possible source of the AE with only 1-3% of the pits, or pits larger than 10 μm being active. Yuyama [94] attributed 304 stainless steel crevice corrosion to hydrogen bubble evolution. Crevice corrosion in spot-welded 304 stainless steel in 3.5% NaCl at noble potential emitted two types of AE, one from rust cracking, giving broadband signals and the other from hydrogen bubbles with narrow band AE [100]. AE is shown to detect the early development of exfoliation corrosion in Al alloys [101]. Differences in T6 and T7 conditions are evident and Al-2024 is more resistant than Al-7449. Again, hydrogen bubble release is the active AE source. A few other AE mechanisms were suggested.

Taking advantage of the source function analysis method [10, 11], Hayashi and Takemoto [102] showed the high-speed nature of molten chloride attack on stressed 304 stainless steel at 600°C to be as high as 67 m/s and discovered fall-off of grains and Mode I and II AE sources. Similarly, Fujimoto et al. [103] examined APC type chloride-SCC of 304 austenitic stainless steel and showed no AE from TG-SCC produced in 35% MgCl_2 at 98°C, but detected AE from IG-SCC, also APC type, in sensitized 304 (caused by 38% MgCl_2 at 95°C, increasing-stress test) with fast rise time of 0.17 to 1.0 μs . They used Lamb waves for the analysis. This APC type IG-SCC is the active one, operative in high-temperature, high-pressure water. This is also caused by dilute fluoride and tetrathionic acid ($\text{H}_2\text{S}_4\text{O}_6$) solutions at room temperature [96]. Yonezu et al.

[104] demonstrated the cause of this AE to come from grain fall-off by local corrosion of Cr-depleted grain boundaries. Here, three types of AE were identified with the source function analysis method and CPF: AE from falling-off of grains, fracture of corrosion product and hydrogen gas evolution. Figure 23 shows examples of surface and cross section of 304 stainless steel that underwent IG-SCC in $MgCl_2$ [96]. Most recently, Kovac et al. [105] reported on AE from IG-SCC, attributing ductile fracture ligament as the cause of this AE. In austenitic steels, AE from ductile fracture is known to be weak, so their suggested mechanism is not persuasive.

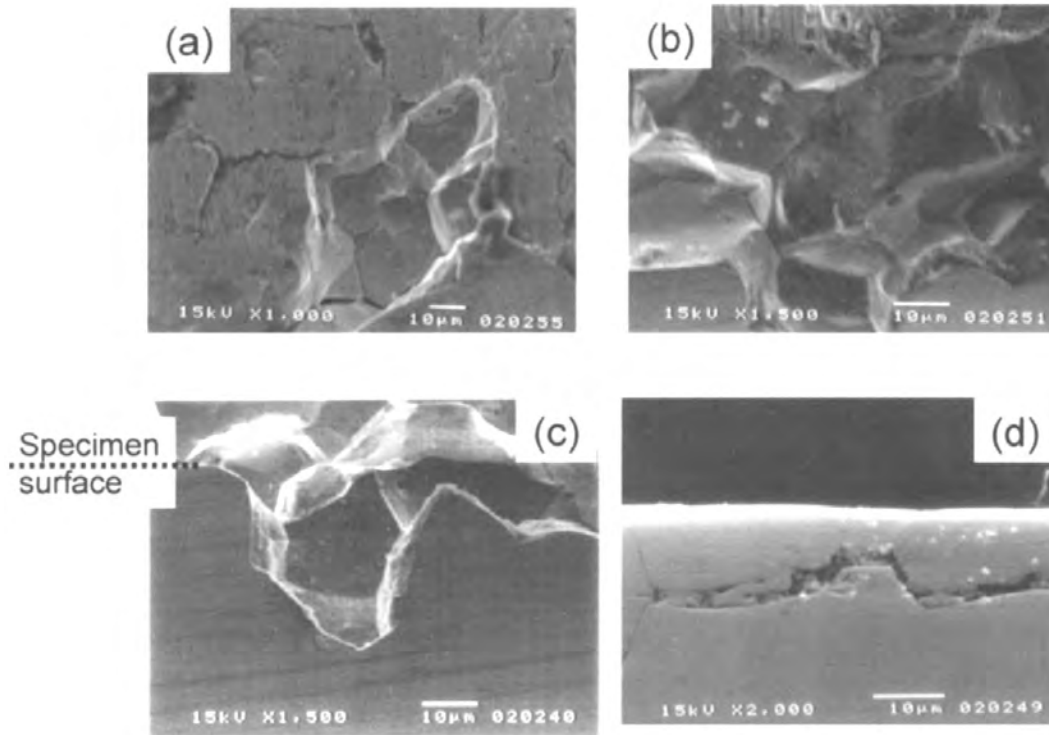


Fig. 23 Surface morphology of austenitic steel after IG-SCC [96].

SCC behavior of a dual phase stainless steel (DP3) in $MgCl_2$ showed APC-type SCC in 42% $MgCl_2$ solution without primary AE [106a]. When this APC-SCC occurs, solution in narrow grooves or cracks is changed to strong acidic solution due to hydrolysis reaction of chromium chloride with water, and the hydrogen gas evolution takes place in the crack. Though they did not confirm hydrogen gas evolution visually, this is consistent with the expected small size of hydrogen bubbles. For this material, hydrogen assisted cracking in 35% $MgCl_2$ solution occurred with AE [106]. SCC due to ammonia in brass, caused in contact with Mattsson's solution (NACE G37-73) was APC-type and IG-SCC, giving AE as above [106b].

Aluminum alloys, especially 7000-series with Zn, suffer from SCC in moist air and from salt water. This SCC is due to hydrogen effects [107, 108] and is controlled by the Cu content of grain boundary precipitates (GBP). SCC rate in NaCl solutions is determined by the rate of anodic dissolution/de-alloying of GBP, which controls the rate of cathodic hydrogen charging of grain-boundary regions just ahead of crack tips. For SCC in moist air, anodic dissolution is unlikely as matching crack-arrest markings accompanying AE are found. Hydrogen generation occurs during crack arrest periods, hydrogen diffusing in along boundaries ahead of crack-tips for 0.1-0.3 μm , causing rapid crack-growth due to hydrogen-induced weakening of atomic bonds with film rupture and/or the hydrogen concentration at a critical level, and crack-arrest and blunting result [108-110].

Studies of hydrogen embrittlement (HE) of high-strength steels were of critical importance to space technology in early days of AE [111]. Recent work applied the source function analysis and deduced details of source mechanisms and their size (source volume) as a function of sensitization in 329 dual phase stainless steel [112]. This steel possesses hardened ferrite phase and suffered HE ahead of main crack, while austenite phase exhibited ductile fracture, while the steels sensitized at 750° and 800°C showed HE in the ferrite and sigma phases. Hydrogen charging effects on sensitized 304 [113a,b] are consistent with grain boundary separation due to hydrogen gas accumulation being the cause of observed IG failure [111]. Hydrogen charging in Ti behaves differently [42]. Micro-fractures of titanium hydride produced by hydrogen charging into tensile loaded titanium caused AE of the Mode-I fracture. Crack opening time was 0.1-0.4 μs , and crack volume was $0.3-1.9 \times 10^{-15} \text{ m}^3$. Finally, AE is used to evaluate the delayed fracture susceptibility of high-strength steels [114]. Elastically loaded strip (Almen strip: SAE J4542) and slow strain-rate tests (with immersion in aggressive solutions) are used successfully to detect the threshold strain to induce the subsurface micro-cracks in the steels. This test method is applicable to evaluate shot-peening effects and trapped and diffusible hydrogen.

Summary

This paper reviewed recent progress in methods of signal analysis used in acoustic emission as applied to materials research. The achievements in understanding of AE from materials during deformation and fracture, phase transformation, coating, film, friction and wear, and corrosion and stress corrosion were examined systematically (but not exhaustively). There are many important areas of AE research that this review could not cover, but it is evident that AE has advanced substantially and contributes to various areas of materials research with increased depth. This makes it mandatory for every AE worker to thoroughly survey available literature before embarking on a new study. All current and future researchers should take advantage of accumulated body of knowledge, which has become much more accessible via the Internet. They can also benefit from the availability of new analytical tools and vastly advanced instrumentation. It is hoped that they successfully resolve many of outstanding issues in the near future.

References

- [1] T. Kishi, M. Ohtsu and S. Yuyama, eds., *Acoustic Emission – Beyond the Millenium*, Elsevier, 213 p., 2000.
- [2] C.U. Grosse and M. Ohtsu, eds., *Acoustic Emission Testing, Basics for Research – Applications in Civil Engineering*, Springer, 414 p., 2008.
- [3] K. Ono, New goals for acoustic emission in materials research, *Acoustic Emission – Beyond the Millenium*, 2000, Elsevier, pp. 57-76.
- [4] K. Ono, Current understanding of mechanisms of acoustic emission, *J. Strain Analysis for Engineering Design*, **40** (1), 2005, 1-15.
- [5] M. Sause, Identification of failure mechanisms in hybrid materials utilizing pattern recognition techniques applied to acoustic emission signals, Augsburg Univ. doctoral dissertation, Mensch und Buch Verlag, 2010, 305 p.
- [6] Convolution: <http://en.wikipedia.org/wiki/Convolution>.
- [7] H. N. G. Wadley and C. B. Scruby, *Proc. Intl Conf. on Acoustic Emission*, Dunhart, 1981, pp. 125-153.
- [8] M. Enoki and T. Kishi, *Acoustic Emission – Beyond the Millenium*, 2000, Elsevier, pp. 1-18.
- [9] a) M. Ohtsu and K. Ono, *J. Acoustic Emission*, **3**, 1984, 27-40. b) *J. Acoustic Emission*, **5**, 1986, 124-133.

- [10] a) H. Suzuki, M. Takemoto and K. Ono, *J. Acoustic Emission*, **11**, 1993, 117; b) *J. Acoustic Emission*, **14**, 1996, 35.
- [11] M. Takemoto, H. Nishino and K. Ono, *Acoustic Emission – Beyond the Millenium*, 2000, Elsevier, pp. 35-56.
- [12] a) J. Gary and M. Hamstad, *J. Acoustic Emission*, **12** (3-4), 1994, 157-170; b) M.A. Hamstad, J. Gary, A. O’Gallagher, *J. Acoustic Emission*, **14** (2), 1996, 103-114.
- [13] a) D. Guo, A. K. Mal and M.A. Hamstad, *J. Acoustic Emission*, **16**, 1998, S222-S232. b) M.A. Hamstad, J. Gary, A. O’Gallagher, *J. Acoustic Emission*, **16**, 1998, S251-S259.
- [14] W. H. Prosser, M.A. Hamstad, J. Gary and A. O’Gallagher, *J. Acoustic Emission*, **17** (1-2), 1999, 37-47.
- [15] M. A. Hamstad, A. O’Gallagher and J. Gary, *J. Acoustic Emission*, **19**, 2001, 258-274.
- [16] a) K. Ono, H. Cho, T. Matsuo, *J. Acoustic Emission*, **26**, 2008, 72-90. b) **28**, 2010, 256-277.
- [17] M. R. Gorman, W. H. Prosser, *J. Acoustic Emission*, **9**, 1991, 283-288.
- [18] K. Ono and Q. Huang, "Pattern Recognition Analysis of Acoustic Emission Signals", *Progress in Acoustic Emission VII*, eds. T. Kishi et al., JSNDI, Tokyo, 1994, pp. 69-78.
- [19] J. Bohse, *J. Acoustic Emission*, **22**, 2004, 208-223.
- [20] PZFlex: <http://www.pzflex.com/about.aspx>.
- [21] A. Green, C.S. Lockman, R.K. Steele, *Modern Plastics*, **41**, 1964, 137-139, 178, 180.
- [22] H. Suzuki, T. Kinjo, Y. Hayashi, M. Takemoto and K. Ono with Appendix by Y. Hayashi, *J. Acoustic Emission*, **14**, 1996, 69-84.
- [23] T. Hayashi and S. Wakayama, *J. Acoustic Emission*, **26**, 2008, 160-171.
- [24] S.M. Pincus, *Proc. National Academy of Sciences of the USA*, **88** (6), 1991, 2297–2301.
- [25] R. Yan and R.X. Gao, *Mechanical Systems and Signal Processing*, **21**, 2007, 824-839.
- [26] Li Lin and Fulei Chu, *Nondestructive Testing and Evaluation*, **26** (2), 2011, 119-128.
- [27] G. Manthei and J. Eisenblätter, ref. 2, pages 284-286.
- [28] K. Mogi, *Bull. Earthquake Res. Inst.*, **40**, 1962, 125-173.
- [29] K. Ono, H. Cho and M. Takuma, *J. Acoustic Emission*, **23**, 2005, 206-214.
- [30] A. Vinogradov, V. Patlan, S. Hashimoto, *Phil. Mag. A*, **81**, 2001, 1427.
- [31] A. Vinogradov, D. L. Merson, V. Patlan, S. Hashimoto, *Materials Science and Engineering*, **A341**, 2003, 57-73.
- [32] A. Razarev and A. Vinogradov, *J. Acoustic Emission*, **27**, 2009, 144-156.
- [33] D. Rouby, P. Fleishmann and C. Duvergier, *Phil. Mag.*, **37**, 1983, 689-705.
- [34] a) M. Koslowski, R. LeSar, R. Thomson, *Phys. Rev. Letters*, **93**, 2004, 265503; b) M. Koslowski, *Phil. Mag.*, **87**, 2007, 1175-1184.
- [35] T. Richeton, J. Weiss, F. Louchet, *Acta Materialia* **53**, 2005, 4463–4471.
- [36] D. Bowles and W. St. Lawrence, *Proc. Western Snow Conf.* 1977, April 18-21, Albuquerque, NM, pp. 88-94; N. Sinha, *Proc. 1982 SESA/JSME Conf., Pt II*, 1982, pp. 767-772.
- [37] O. Muránsky, M.R. Barnett, D.G. Carr, S.C. Vogel, E.C. Oliver, *Acta Materialia*, **58**, 2010, 1503–1517.
- [38] X.Y. Lou, M. Li, R.K. Boger, S.R. Agnew, R.H. Wagoner, *Intl J. Plasticity* **23**, 2007, 44–86.
- [39] F. Chmelík, F. Moll, J. Kiehn, K. Mathis, P. Lukác, K-U. Kainer and T. G. Langdon, *J. Acoustic Emission*, **20**, 2002, 108-128.
- [40] M. Janecek and F. Chmelík, *Magnesium Alloys - Design, Processing and Properties*, ed. F. Czerwinski, InTech, 2011, pp. 43-68.
- [41] J. M. Reed, M. E. Walter, *Materials Science and Engineering*, **A359**, 2003, 1-10.
- [42] Y. Taniyama, T. Matsuo, H. Cho, M. Takemoto and G. Nakayama, *Proc. IAESI8*, JSNDI, pp. 295-302.
- [43] P.K. Chaurasia, C.K. Mukhopadhyay, S. Murugan, P. Muralidharan, K. Chandran, V. Ganesan, T. Jayakumar, P.V. Kumar, *J. Nuclear Materials*, **322**, 2003, 217–227.

- [44] K. Yoshida, T. Saito, A. Zhu, H. Takagi and K. Sakamaki, *Intermetallics*, **6**, 1998, 1-5.
- [45] K. Yoshida, Y. Masui, T. Nagamachi and H. Nishino, *J. Acoustic Emission*, **23**, 2005, 189-195.
- [46] a) K. Fukaura, Y. Yokoyama, D. Yokoi, N. Tsujii, and K. Ono, *Met. Mater. Trans.*, **35A**, 2004, 1289-1300; b) K. Fukaura and K. Ono, *J. Acoustic Emission*, **19**, 2001, 91-99; H. Cho, K. Fukaura and K. Ono, *J. Acoustic Emission*, **21**, 2003, 112-119.
- [47] M.A. Lebyodkin, T.A. Lebedkina, F. Chmelik, T.T. Lamark, Y. Estrin, C. Fressengeas, and J. Weiss, *Phys. Rev. B* **79**, 2009, 174114-9.
- [48] J. Kumar and G. Ananthakrishna, *Phys. Rev. Lett.* **106**, 2011, 106001-4.
- [49] A. Trochidis and B. Polyzos, *J. Appl. Phys.*, **78**, 1995, 170-173.
- [50] K. Ravi-Chandler, *Intl J. Fracture*, **90**, 1998, 83-102.
- [51] M. Minozzi, G. Caldarelli, L. Pietronero and S. Zapperi, *Eur. Phys. J.*, **B36**, 2003, 203-207.
- [52] A. Yonezu, T. Ogawa and M. Takemoto, *Proc. IAESI8*, JSNDI, 2006, pp. 463-470.
- [53] Z. Shi, J. Jarzynski, S. Bair, S. Hurlbaus and L.J. Jacobs, *J. Mech. Engineering Sciences*, **214**, Part C, 2000, 1141-1149.
- [54] D.H. Korn, P. Ducheyne and J. Awerbuch, *J. Mat. Sci.*, **27**, 1992, 3133-3142.
- [55] W.O. Soboyejo, B. Rabeeh, Y. Li, A.B.O. Soboyejo and S. Rokhlin, *Fatigue & Fracture of Engineering Materials & Structures*, **21**, 1998, 557-568.
- [56] M.R. Horne, PhD dissertation, Virginia Polytechnic Institute and State University, 2003.
- [57] C.K. Lee, J.J. Scholey, P.D. Wilcox, M.R. Wisnom, M.I. Friswell and B.W. Drinkwater, *Advanced Materials Research*, **13-14**, 2006, 23-28.
- [58] D. G. Aggelis, E. Z. Kordatos, T. E. Matikas, *Proc. IAES20*, 2010, pp. 73-78.
- [59] M. Shiwa, Y. Furuya, H. Yamawaki, K. Ito and M. Enoki, *Proc. IAES20*, 2010, pp. 319-324.
- [60] J. McKeefry and C. Shield, *Acoustic Emission Monitoring Of Fatigue Cracks In Steel Bridge Girders*, MN-DOT report, MN/RC-1999-36, 1999, 138 p.
- [61] S.M.C. Van Bohemen, J. Sietsma, M.J.M. Hermans, I.M. Richardson, *Phil. Mag.*, **85** (16), 2005, 1791 -1804.
- [62] R.W. Cahn and P. Haasen, *Physical Metallurgy*, 4th ed., N. Holland, 1996, p. 1469.
- [63] H.K.D.H. Bhadeshia, *Bainite in Steels*, Inst. Materials, 2001, 460 p.
- [64] a) T. Yasuda, S. Kondo, H. Nishino and K. Yoshida, *J. Acoustic Emission*, **26**, 2006, 270-278; b) T. Yasuda, B. Pang, H. Nishino and K. Yoshida, *Materials Transactions*, **52** (3) 2011, 397-405.
- [65] T. Inamura, S. Nagano, M. Shimojo, K. Takashima and Y. Higo, *J. Acoustic Emission*, **19**, 2001, 85-90.
- [66] S. Sreekala and G. Ananthakrishna, *Phys. Rev. Lett.*, **90**, 2003, 135501-1.
- [67] L. Carrillo and J. Ortín, *Phys. Rev.* **B56**, 1997, 11508-11517.
- [68] a) E. Dul'kin, E. Mojaev, M. Roth, S. Kamba, and P. M. Vilarinho, *J. Appl. Phys.*, **103**, 2008, 083542; b) E. Dul'kin, E. Mojaev, M. Roth, O. Khamman and X. Tan, *Appl. Phys. Lett.*, **95**, 2009, 252903.
- [69] K. Prabakar and S. P. Mallikarjun Rao, *Ferroelectrics Letters Section*, **32** (5-6), 2005, 99-110.
- [70] F-J. Pérez-Reche, F. Casanova, E. Vives, L. Mañosa, A. Planes, J. Marcos, X. Batlle and A. Labarta, *Phys. Rev. B* **73**, 2006, 014110.
- [71] a) S. Safai, H. Herman and K. Ono, *Am. Ceram. Soc. Bull.*, **58** (6), 1979, 624; b) *Proc. 9th. Int. Thermal Spraying Conf.*, The Hague, 19-23 May, Netherlands Inst. Lasteniek, 1980, pp. 129-132.
- [72] C.C. Berndt, *J. Engineering for Gas Turbines and Power*, **107**, 1985, 142-146.

- [73] J. Voyer, F. Gitzhofer, M.I. Boulos, J. Dionne, *Thermal Spray 1996: Practical Solutions for Engineering Problems*, ASM International, 1996, pp. 303-310.
- [74] J.H. Park, J.S. Kim, K.H. Lee, *J. Materials Processing Technology* **187-188**, 2007, 537-541.
- [75] a) S. Chang, Purdue University, 2005; b) N.H. Faisal, Heriot-Watt University, 2009; c) S. Nekkanty, Ohio State University, 2009.
- [76] X.Q. Ma and M. Takemoto, *Materials Science and Engineering A*, **308**, 2001, 101-110.
- [77] R. Piotrkowski, A. Gallego, E. Castro, M.T. García-Hernandez, J.E. Ruzzante, *NDT&E International*, **38**, 2005, 260–267.
- [78] R. Piotrkowski, E. Castro, A. Gallego, *Mechanical Systems and Signal Processing*, **23**, 2009, 432–445.
- [79] R. Ikeda, M. Hayashi, A. Yonezu, H. Cho, T. Ogawa and M. Takemoto, *Proc. IAESI8*, JSNDI, 2006, pp. 455-462.
- [80] R. Ikeda, H. Cho, A. Sawabe and M. Takemoto, *Diamond and Related Materials*, **14**, 2005, 631-636.
- [81] T. Uchiyama, R. Ikeda, H. Cho and M. Takemoto, *Proc. IAESI8*, JSNDI, 2006, pp. 303-462.
- [82] M.G.R. Sause, D. Schultheiß and S. Horn, *J. Acoustic Emission*, **26**, 2008, 1-13.
- [83] a) R.G. Liptai. *An Investigation of the Acoustic Emission Phenomenon*. PhD dissertation, Michigan State University, East Lansing, Michigan. 1963. b) J.M. Goetz, Honors thesis, Ohio State University, 2005.
- [84] V. Baranov, E. Kudryavtsev, G. Sarychev, V. Schavelin, *Acoustic Emission in Friction*, Elsevier, 2007, 232 p.
- [85] M-K. Tse, J. Leifer and A.F. Lewis, *J. Acoustic Emission*, **4**, 1985, S127-S131.
- [86] A. G. Khurshudov and F. E. Talke, *J. Tribol.* **120**, 1998, 54-59.
- [87] R.J. Boness and S.L. McBride, *Wear*. **149**, 1991, 41-53.
- [88] H.S. Benabdallah, *J. Materials Science*, **34**, 1999, 4995-5004.
- [89] M. Löhr, D. Spaltmann, S. Binkowski, E. Santner, M. Woydt, *Wear* **260**, 2006, 469-478.
- [90] T. Jayakumar, C.K. Mukhopadhyay, S. Venugopal, S.L. Mannan, Baldev Raj, *J. Materials Processing Technology* **159**, 2005, 48–61.
- [91] H. Okada, K-I. Yukawa and H. Tamura, *Corrosion*. **30**, 1974, 253-255.
- [92] Y. Suezawa, H. Takemoto, and T. Tanaka, *Boshoku Gijutsu (J. Japan Soc. Corrosion Engr.)*, **24**, 1975, 239-248.
- [93] a) O. Takano and K. Ono, *Proc. IAES2*, 1974, p. VI-31; b) T. Morikawa and K. Ono, *Plating & Surface Finishing*, **89** (12), 2002, 50-54.
- [94] S. Yuyama, T. Kishi and Y. Hisamatsu, *J. Acoustic Emission*, **2**, 71-93.
- [95] M. Takemoto, H. Cho, K. Ono, *Proc. 26th European Conference of AE*, DGfZP, Berlin, 2004, pp. 617-629.
- [96] M. Takemoto, *Proc. ICAE6*, AEWG, 2007, pp. 415-424.
- [97] M. Winkelmann, U. Müller and H.-J. Bassler, *Materials and Corrosion*, **58** (12), 2007, 907-915.
- [98] R.C. Newman, K. Sieradzki, *Scripta Metall. Mater.* **17**, 1983, 621–624.
- [99] a) H. Idrissi, J. Derenne, H. Mazille, *J. Acoustic Emission*, **18**, 2000, 299-306; b) S. Krakowiak and K. Darowicki, *J. Solid State Electrochem*, **13**, 2009, 1653–1657; c) R.H. Jones and M.A. Friesel, *Corrosion NACE*, **48** (9), 1992, 751-758.
- [100] H. Cho and M. Takemoto, *Proc. IAESI8*, JSNDI, 2006, pp. 287-294.
- [101] F. Bellenger, H. Mazille, H. Idrissi, *NDT&E International*, **35** (6), 2002, 385–92.
- [102] K. Hayashi and M. Takemoto, *Proc. IAESI3*, JSNDI, 1996, pp. 76-81.
- [103] S. Fujimoto, M. Takemoto and K. Ono, *J. Acoustic Emission*, **19**, 2001, 63-74.
- [104] A. Yonezu, H. Cho and M. Takemoto, *Advanced Material Research*, **13**, 2006, 243-250.

- [105] J. Kovac, C. Alaux, T.J. Marrow, E. Govekar, A. Legat, *Corrosion Science*, **52**, 2010, 2015–2025.
- [106] a) K. Kagayama, T. Ogawa, A. Yonezu, H. Cho and M. Takemoto, *J. Acoustic Emission*, **24**, 2006, 127-138; b) F. Uchida, H. Nishino, M. Takemoto and K. Ono, *J. Acoustic Emission*, **19**, 2001, 75-84.
- [107] N.J.H. Holroyd, in *Environment-Induced Cracking of Metals*, R.P. Gangloff and M.B. Ives, eds., NACE, Houston, 1989, pp. 311-345.
- [108] S.P. Lynch, S.P. Knight, N. Birbilis, B.C. Muddle, in *Effects of hydrogen on materials, Proc. 2008 Intl Hydrogen Conference*, B. Somerday et al. eds., ASM International, 2008, pp. 243–250.
- [109] G.M. Scamans, *Metall. Trans.*, **11A**, 1980, 846-850.
- [110] P. Martin, J.L. Dickson, J.-P. Bâillon, *Materials Science and Engineering*, **69** (1), 1985, L9-L13.
- [111] H.L. Dunegan and A.S. Tetelman, *Engineering Fracture Mechanics*, **2**, 1971, 387-390.
- [112] K. Kurose, H. Cho, T. Ogawa and M. Takemoto, *Proc. IAESI9*, JSNDI, 2008, pp. 121-127.
- [113] a) S.H. Carpenter and D.R. Smith, Jr., *Metall. Trans.*, **21A**, 1990, 1933-1939; b) S.H. Carpenter, K. Ono and D. Armentrout, *J. Acoustic Emission*, **24**, 2006, 119-126.
- [114] M. Takemoto, M. Nakamura, S. Masano and S. Ueno, *J. Acoustic Emission*, **27**, 2009, 241-253.

Note

This paper is an edited version of a paper published in the *Proceedings of World Conference on Acoustic Emission, 2011*, Beijing, China, held in Beijing, August 24-26, 2011. It was presented via video recording as a keynote lecture.

PATTERN RECOGNITION STUDY OF ACOUSTIC EMISSION SIGNALS OF AIRCRAFT FATIGUE CRACKING BASED ON WAVEFORM ANALYSIS AND ARTIFICIAL NEURAL NETWORKS

ZHEN-LONG HU^{1,2}, GONG-TIAN SHEN¹, GUAN-HUA WU², SHI-FENG LIU³, and ZHAN-WEN WU¹

¹ China Special Equipment Inspection and Research Institute, Beijing 100013, China, ² Key Lab of Nondestructive Testing, Ministry of Education, Nanchang Hangkong University, Nanchang 330063, China, ³ Beijing Soundwel Technology Co. Ltd., Beijing 100029, China

Abstract

In this paper, SOM neural network was used to identify the AE signal waveforms of aircraft fatigue test, which produced a group of suspected crack signals. Three peaks of relatively large energy appear simultaneously in frequency spectra. The frequency of peak 3 (168.5 kHz) was consistent with previous result (175.8 kHz), showing characteristics of crack AE signal.

Keywords: Waveform analysis; fatigue crack; WPD; SOM neural network; spectrum analysis

1. Introduction

Use of acoustic emission (AE) technology for the monitoring of aircraft fatigue crack initiation and growth has important practical significance [1-4]. In the past, due to the limited ability of waveform recording and storage of AE instrument, people made the judgment of crack generation dependent on AE parameters analysis [5-7]. However, AE waveforms contain more information than parameters [8-9]. Therefore, a full waveform AE system was used to monitor the aircraft fatigue-crack initiation and propagation with waveform analysis.

Some references point out that the automatic processing of AE signals can be achieved by methods of artificial neural network pattern recognition [10-11]. However, the traditional neural network methods (supervised neural network) need to determine the input vector and output vector. It means that the typical crack signal should be obtained first as an input vector, but this is difficult to achieve due to the interference of noise, which comes from the fatigue test itself. Therefore, in this paper, SOM neural network (Self-Organizing Feature Map, unsupervised neural network) was used to identify the AE waveforms of aircraft fatigue test. A group of suspected crack signals and their characteristics were obtained. Due to the serious interference of noise, which comes from both the aircraft structure itself and the surrounding environment in the process of fatigue test, the filtering process of collected signal is necessary.

2. Test Equipment and the Acquisition of AE Signals

In this study, SEAU2S full waveform AE system, which was provided by Beijing Soundwel Technology Co Ltd., was used to monitor the airfoil AE signals. The sampling frequency is 10 Ms/s. The sensor model is SR150, with 150-kHz resonant frequency, and the arrangement is shown in Fig. 1. Before the start of the fatigue test, the airfoil was inspected by normal NDT methods and no defect was found. Therefore, the collected AE signals in the early stages of test can be defined as noise signal (pure noise). By the same token, in the middle and late stages of the fatigue test, it can be considered that the collected AE signals containing both crack and noise signals, since the crack was found at this time and eventually broken. The extraction of

these two types of signal has important implications to the accuracy of the SOM algorithm classification results.

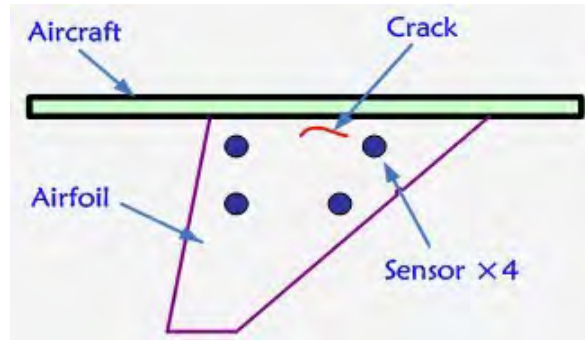


Fig. 1 Fatigue test device and sensor arrangement.

3. Wavelet Packet Noise Reduction Processing Method

Due to the existence of large amplitude and broad frequency band noise, individually detecting the weak crack AE signal is difficult. The interference of noise was mainly reflected in the following two aspects:

- (1) More noise, low percentage of the useful crack signal, which accounted for the total signal;
- (2) In the useful crack AE signals, noise component occupied a very high percentage of the total waveform energy.

Therefore, the selection of the useful crack AE signal from the noise faces the following two problems:

- (1) Since the useful crack AE signals appear at low percentage, an approach to consider signals to be crack signals over an entire period is not likely to be realistic.
- (2) Even in the useful crack signal, noise occupied greater proportion of energy, which leads to the serious distortion of the original crack signal, and it is difficult to distinguish a crack AE signal from noise subjectively.

Based on previous experiences that although the frequency distribution of noise is broad, but its energy is mainly concentrated at low frequency; although the frequency of crack AE signal is high, but affected by the signal attenuation and the frequency response of the sensor. The high frequency always means serious signal attenuation and waveform distortion. Therefore, the selection the appropriate filter range can reduce the interference of noise on crack AE signals, while increasing the classification accuracy of SOM.

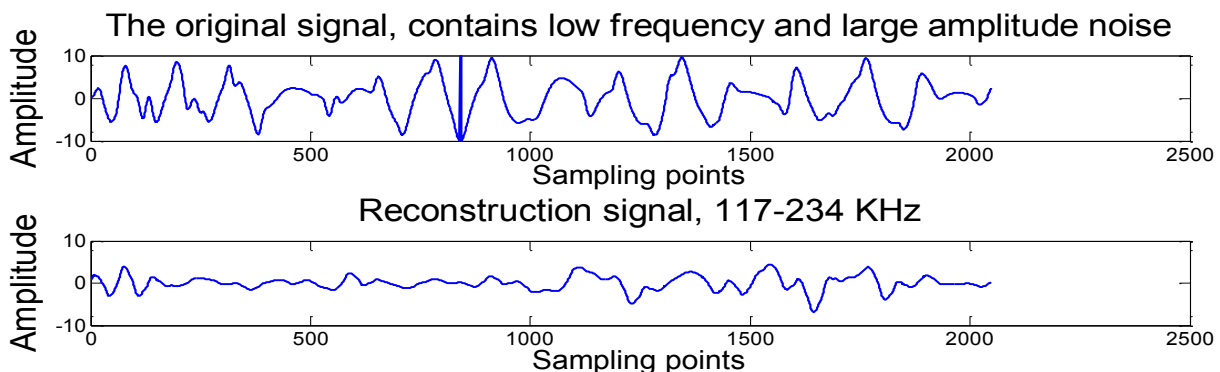


Fig. 2 Wavelet packet noise reduction processing.

According to Wang et al. [12], the center frequency of cracking in a similar test on an aircraft component was around 175 kHz. Therefore, the filtering program of 7-layer wavelet packet decomposition was selected and 117-234 kHz band-pass filtering effect was achieved by the reconstruction of its 4, 5 and 6 layers. As shown in Fig. 2, the use of wavelet packet decomposition and reconstruction reduced the low-frequency part of the original signal (usually large amplitude), making the filtered signal “simpler”.

4. SOM Neural Network Pattern Recognition Methods

SOM neural network is a competitive neural network, proposed by Finnish scholar Kohonen in 1981, and a network structure is shown in Fig. 3. SOM neural network, also known as “Unsupervised” neural network, has obvious differences from commonly used methods, can classify input patterns automatically according to learning rules. It means that, in the case of no expected output vector, SOM can capture the mode characteristics of each input vector through repeated learning, and finally show the classification results in the competition layer. Based on the characteristics that SOM can classify automatically, two AE signals from different periods, one from the initial signal (pure noise, called Set A) and the other from a certain period after a crack was discovered (a mixture of crack and noise, called Set B), are fed to the SOM. Set A and Set B have the following characteristics.

Set A

- a) Set A contains noise only;
- b) Because of the diversity and uncertainty of noise, the noise signal in Set A may contain signals similar to the crack AE.

Set B

- a) Set B certainly contains crack AE signals;
- b) Set B also contains noise.

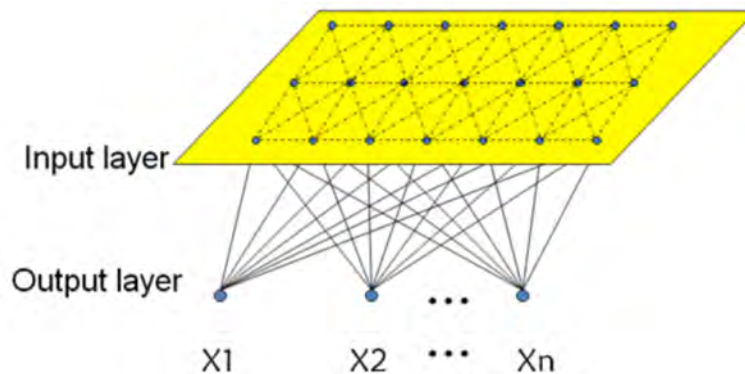


Fig. 3 SOM neural network structure.

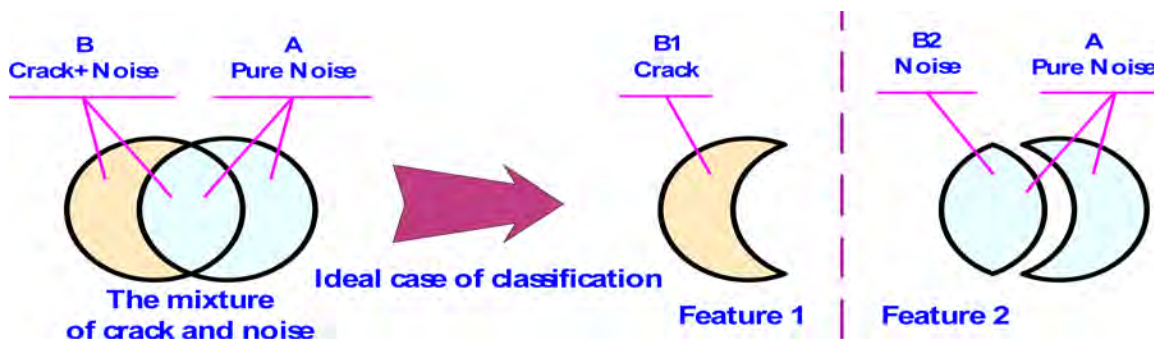


Fig. 4 SOM ideal classifications (two categories).

Ideally, SOM algorithm is capable of classifying the signal with similar characteristics automatically when Set A and Set B are randomly mixed and combined. The classification may result in two categories, for example, as shown in Fig. 4. However, due to the lack of such capability, SOM can only classify but not distinguish the crack AE signal. Therefore, additional “criteria” are needed to enhance the classification results and identify the possible crack AE signals:

Criterion 1: If all the signals in a set come from set B, then define it as Set C, which represents a potential set of crack AE signals;

Criterion 2: When all the signals come from Set A, then define it as Set D, which represents a set of noise samples;

Criterion 3: If a large percentage (80%, for example) of the signals in a set come from set B, also regard it as Set C.

5. AE Signals Classification and Characterization

(1) SOM network training and classification

The construction of SOM network was achieved by the function called “newsom”. Among the parameters provided are the numbers of neurons in competitive layer set to $6 \times 8 = 40$, with the remaining parameters using the default values. 2454 waveform signals were selected randomly as noise (set A) in the initial test, and 4416 waveform signals were selected continuously as the collection of crack and noise (Set B) taken after the detection of a crack. After randomly mixing Set A and B, the mixture was used as the input vector of the network, which was trained for 100 cycles and the classification results are shown in Table 1.

Table 1. The classification results from Set A and Set B and ratio B/(A+B).

Classification	Total amount	From Set A (pure noise)	From Set B (crack + noise)	B / (A + B)
1*	1344	1	1343	99.92%
2	581	492	89	
3	269	174	95	
4*	1237	9	1228	99.27%
5*	373	73	300	80.42%
6	198	44	154	
7	1086	812	274	
8*	109	1	108	99.08%
9	227	219	8	
10	1181	568	613	
11*	10	0	10	100%
12	245	51	194	
13	10	10	0	

From Table 1, it can be found that the categories of 1, 4, 5, 8 and 11 have a high percentage of signals coming from Set B. These could be respectively considered as potential crack AE sets. Subsequently, all the waveforms in categories, especially c1, c4, c5, c8 and c11, were analyzed for their spectra.

(2) Spectrum analysis of the potential crack AE signals

From the spectrum analysis, most of the waveforms do not have obviously features, and their energy is not high and is concentrated in the low-frequency parts (<60kHz), as shown in Fig. 5.

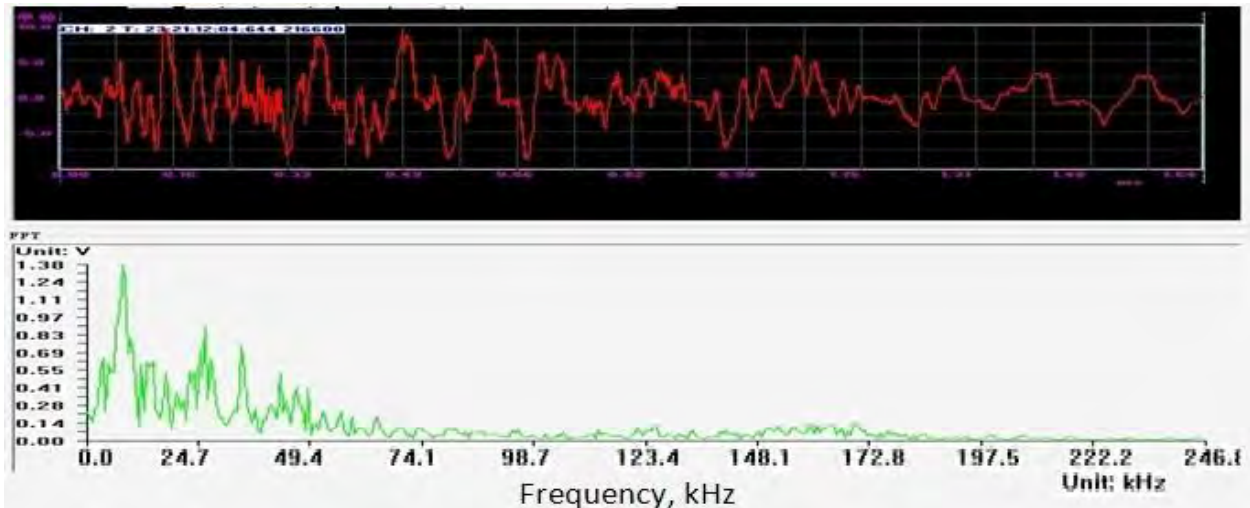


Fig. 5 A waveform from c1 set with its FFT spectrum.

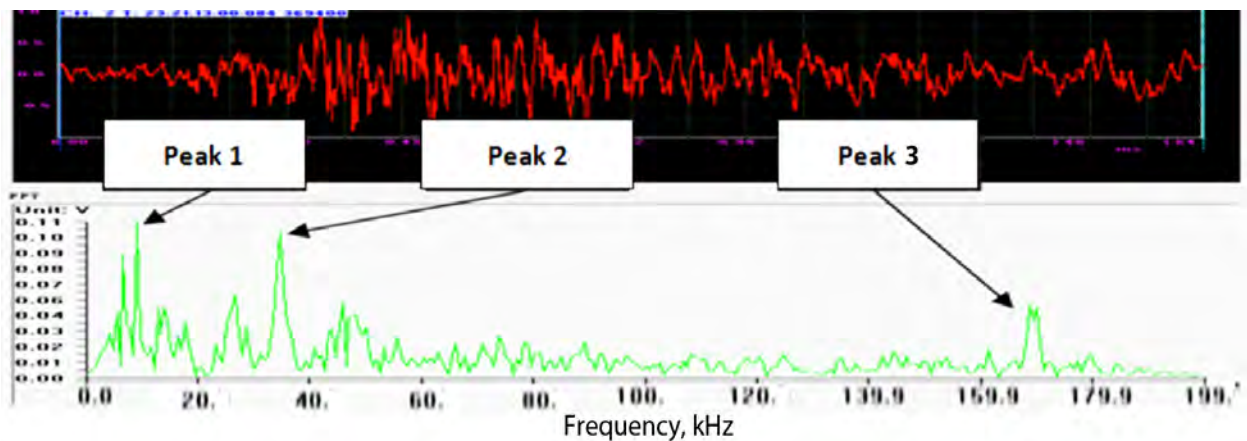


Fig. 6 A waveform from c5 set with its FFT spectrum with three distinct peaks.

In the potential set of crack AE signals (c1, c4, c5, c8 and c11), only 300 waveforms from c5 sample set showed 3 distinct peaks on the FFT spectrum. Such peaks were absent in the waveforms of the remaining four sample sets. The three peaks in the c5 set appear in the frequency range of 0 - 20 kHz, 20 - 120 kHz, 120 - 240 kHz, and called peak 1, 2 and 3, respectively, as shown in Fig. 6. Further statistical analysis found that these 3 peaks have the following rules.

The 300 waveforms in c5 set come from Set B were judged to have 3 distinct peaks in the spectrum, because the peak energy is much greater than the average band energy. The ratio of the peak energy to average band energy is shown in Fig. 7. The average values of the ratio for each peak are 4.5, 4.6 and 5.3, as indicated in the figure.

Frequency of the three peaks is plotted against sample number for 300 waveforms in c5 set in Fig. 8. The position of the three peaks is relatively fixed, and the mean frequency was, respectively: 13.4 kHz, 46.2 kHz and 168.5 kHz. The frequency of peak 3 (168.5 kHz) was consistent with the previous result (175.8 kHz), and reflects that of the sensor used. It was previously attributed to crack AE signal [12]. Relative peak energies of the three peaks are shown in Fig. 9.

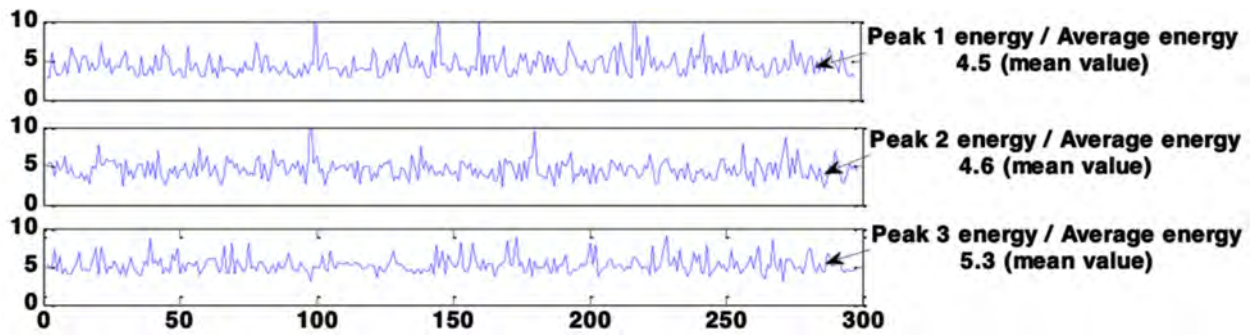


Fig. 7 Ratio of peak energy to average band energy vs. sample number for 300 waveforms in c5 set.

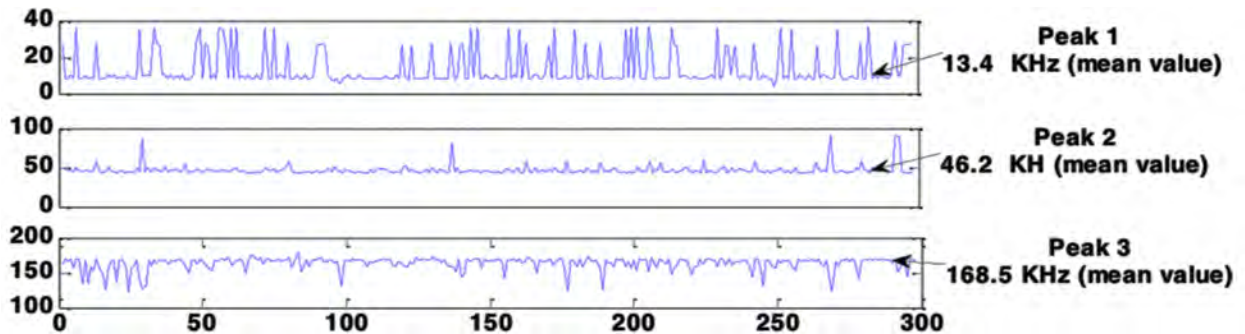


Fig. 8 The distribution of peak frequency for 300 waveforms in c5 set.

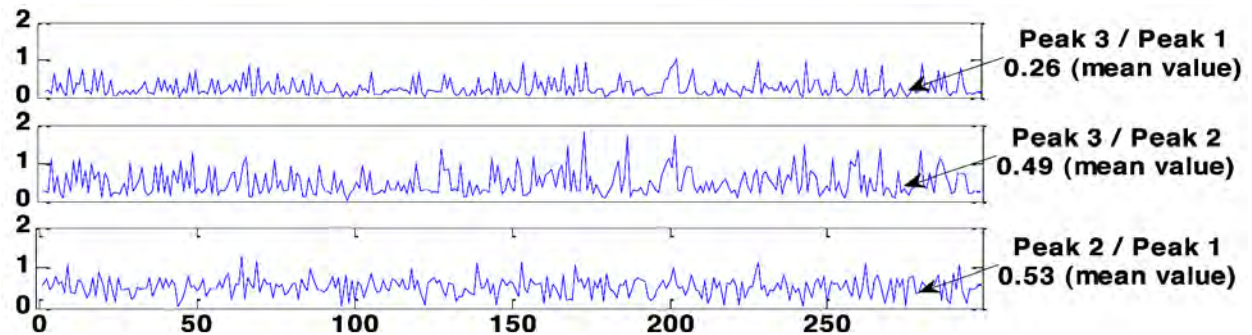


Fig. 9 Ratio of peak energy among 3 peaks for 300 waveforms in c5 set.

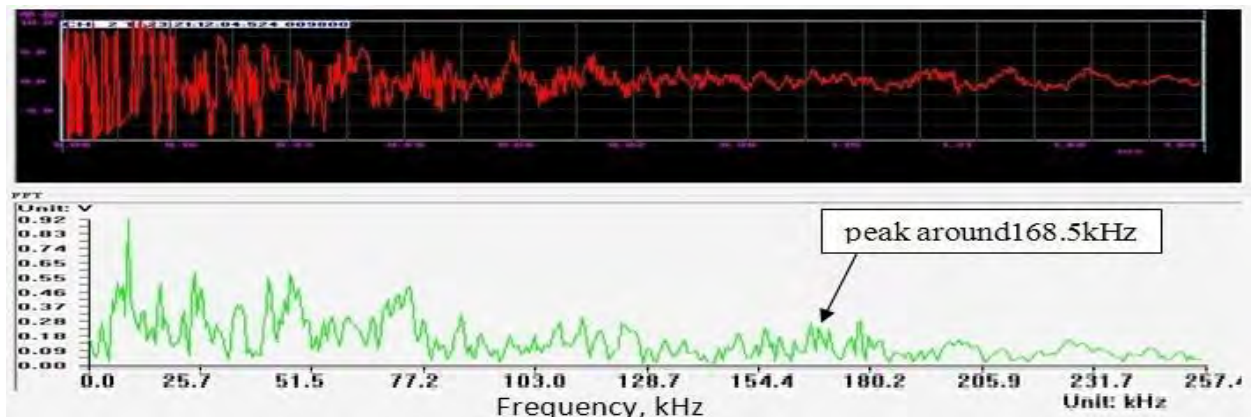


Fig. 10 A waveform from category of 12 with its FFT spectrum.

These appear simultaneously in a frequency spectrum and it is the obvious difference between these 300 waveforms and others that show no peaks. Therefore, it can be assumed that

these ratios of peak energies are another important basis for the identification of these 300 waveforms. The mean values of the ratios (3/1, 3/2, and 2/1) are 0.26, 0.49 and 0.53 (Fig. 9).

Outside of these five sample sets, the existence of the peak of around 168.5 kHz also can be found on the FFT spectrum in the category of 12 (194 waveforms). All these waveforms are "overflowing" signals as their signal amplitude is greater than 100 dB, exceeding the instrument's maximum dynamic range, as indicated in the Fig. 10.

(3) Possible origins of these frequency peaks

AE signals generated under large cyclic load were often accompanied by noise due to collision and mechanical friction. Therefore, the crack AE signals collected were actually the combination of pure crack signals and noise. They have the characteristics of both crack AE signals and noise, which are likely to be reflected in the frequency spectrum. We can expect both frequency peaks due to cracking and noise.

According to Kaiser Effect, AE signals from the same crack cannot be obtained again until the stress exceeds its highest previous value. That is, the generation of crack AE signals is often accompanied by the larger load. However, larger load usually means larger low-frequency mechanical noise and this is the mainly cause of peak 1 and peak 2 in the spectrum in the two low frequency ranges. In the c5 sample set (300 waveforms), the appearance of peak 3 is always accompanied by peak 1 and peak 2 simultaneously. That may be interpreted as that the large load not only produces crack AE signals of specific frequency (168.5 kHz), but also generate noise, which may be caused by friction. These noise waveforms were easy to identify and concentrated in the low frequency part (13.4 kHz, 46.2 kHz). Thus, the ratio of 3 peaks energy can be considered as an important feature to identify crack AE signals.

Similar to the peak 3 in c5, the peak in the category of 12 may also be generated by cracks. As mentioned earlier, a larger load (large amplitude) usually means larger noise, and the crack signals may be annihilated in the noise, leading to the incorrectly classification results because of the relatively weak contribution of crack characteristics to the entire waveform. Due to the random distribution of large load, the overflow signals may appear at any period during the entire experiment, not only at the time of cracking. That is why the waveforms of category 12 are distributed both in Set A and Set B.

6. Conclusions

(1) Utilizing an SOM neural network with the use of reasonable choice of data sample, and the support of some selection "criteria", the useful crack AE signals can be extracted from a large number of waveforms. These methods are feasible and confirmed by spectrum analysis.

(2) The classification results of SOM algorithm could be more reliable after applying wavelet packet noise reduction processing method.

(3) Currently, it is unable to meet the requirements of real-time monitoring of crack, since the calculation of SOM algorithm needs post-processing.

(4) The waveform characteristics of fatigue crack signals, such as the frequency, energy and ratios of three peaks, can become an important basis for the identification of crack.

(5) It is very possible that some of the crack signals in Set B (4416 waveforms) may appear outside c5, for example, the category of 12. The main reason is the noise. Therefore, the further study of denoising algorithm is very necessary.

(6) With the progress of the test, if the crack depth analyses can become feasible using waveform characteristics of fatigue crack AE signals, a special AE system would be developed for AE real-time monitoring of aircraft fatigue.

Acknowledgement

This study was financially supported by Chinese 11th five-year project 2009BAK58802-03.

References

- [1] Matthew G, Baxter R, Pullin K, et al. Detection of Fatigue Crack Growth in Aircraft Landing Gear [C]. Proceedings of the 26th EWGAE, Berlin, 2004.
- [2] A. N. Ser'eznov, A. V. Mal'tsev, L. N. Stepanova, et al. Inspection of Fatigue Defects in Endurance Testing of Half-Axles of Maneuverable Aircraft's Stabilizers by Means of Acoustic Emission and Tensometry [J]. Russian J. Nondestructive Testing, 2004, **40**(9) 573-579.
- [3] Geng Rong-sheng, Jing Peng. The State Monitoring for Aircraft Structure Using Trend Analysis Technique [C]. The 7th National Acoustic Emission Symposium. Shanghai: The AE Committee of Chinese Society for NDT, 1997: 142- 145.
- [4] Zhang Feng-lin, Han Wei, Hu Guo-cai, et al. Research on the Application of AE in the Field of Aviation [J]. Nondestructive Testing, 2000, **22** (4): 157-161.
- [5] Wu Ke-qin, Geng Ron-sheng, Xie Li-yang, Wu Ning-xiang. Acoustic Emission Real - Time Monitoring for Fatigue Damage to Horizontal Tails of a Certain Plane During Functional Test [J]. Journal of Northeastern University (Natural Science), 2007, **28**(8): 1167-1170.
- [6] Feng Jian-fei, Geng Rong-sheng, Wu Guan-hua, Wu Wei. AE Characteristic Analysis in Aircraft Fatigue Test under Flight Loading Condition [J]. J. Mechanical Engineering, 2010, **46**(8): 6-11.
- [7] Wang Bing-yang, Geng Rong-sheng, Wu Guan-hua. The Application of Acoustic Emission Technology in Aircraft Main Landing Gear Fatigue Test [J]. Nondestructive Testing, 2011, **33**(4): 22-25.
- [8] Liu Shi-feng, Geng Rong-sheng. Analysis of Acoustic Emission Monitoring Crack in Aircraft Fatigue Test [C]. The 11th National Acoustic Emission Symposium. Hangzhou: The AE Committee of Chinese Society for NDT. 2006, **7**: 86-89.
- [9] Geng Rong-sheng, Shen G.T., Liu Shi-feng. Acoustic Emission Signal Processing Technique Based on Waveform Analysis [J]. Nondestructive Testing, 2002, **24**(6): 257-261.
- [10] Shen G.T., Duan Qing-ru, Zhou Yu-feng, Li Bang-xian, et al. Investigation of Artificial Neural Network Pattern Recognition of Acoustic Emission Signals for Pressure Vessels [J]. Nondestructive Testing, 2001, **23**(4): 144-149.
- [11] Luo jijun, Hou Suxia, Xu Jun, Li Juanjuan. Study on Acoustic Emission Signal Identification Based on Neural Network Technology [J]. Chinese Journal of Scientific Instrument, 2007, **28**(4): 678-680.
- [12] Wang Xin-jian, Wu Ke-qin, Wang Ben-zhi, Geng Rong-sheng. The Real-Time Monitoring for Axle Condition to Horizontal Tails of a Certain Plane using Acoustic Emission Technology [C]. The 11th National Acoustic Emission Symposium. Hangzhou: The AE Committee of Chinese Society for NDT, 2006, **7**: 90- 96.
- [13] S. H. Lee and D. Lee. In-process Monitoring of Drilling Burr Formation Using Acoustic Emission and a Wavelet-based Artificial Neural Network [J]. International Journal of Production Research, **46**, (17), 2008, 4871–4888.
- [14] R. de Oliveira, A.T. Marques. Health Monitoring of FRP Using Acoustic Emission and Artificial Neural Networks [J]. Computers and Structures **86** (2008) 367–373.

ACOUSTIC EMISSION RESPONSE OF REINFORCED LIGHTWEIGHT METAL MATRIX COMPOSITES DURING TENSILE AND CYCLIC LOADING

MATTHIAS MERZKIRCH, ANDREAS REEB, KAY ANDRÉ WEIDENMANN,
ALEXANDER WANNER and VOLKER SCHULZE

Karlsruhe Institute of Technology (KIT), Institute for Applied Materials - Materials Science and Engineering (IAM–WK), 76131 Karlsruhe, Germany

Abstract

In the field of lightweight construction for transportation means, hybrid structures composed of high-strength and low-density materials exhibit a high application potential. As a viable approach to increase the stiffness, strength and fatigue life of light-metal sections, spring steel (301SS) wires are incorporated into the matrix material via composite extrusion. This work investigated the deformation and damage behavior of wire-reinforced hybrid samples with aluminum (EN AW-6082) and magnesium (AZ31) matrices under quasi-static and cyclic loads. The mechanical tests are accompanied by acoustic emission (AE) analysis. The results show that the AE analysis allows for the detection of the plastic deformation under pure tensile as well as under cyclic load for both composites. Furthermore, the damage can be detected and located so that the AE analyses lead to a detailed insight to damage mechanisms like crack growth, debonding of the matrix material from the interface and fracture of the components.

Keywords: MMC, unidirectional, EN AW-6082, AZ31, tensile testing, fatigue testing

1. Introduction

For the application of hybrid materials for lightweight structural parts in, e.g. aeronautical and automotive sector, it is essential to get a detailed insight into the damage behavior in order to realize a fail-safe dimensioning. The mechanical behavior and the occurring damage mechanisms of aluminum sections unidirectionally reinforced with metallic wires, produced via composite extrusion [1] have already been investigated in detail for quasi-static tensile [2] and cyclic [3] loading. Some insight into the damage mechanisms like necking, debonding between matrix and reinforcement, crack initiation and crack growth can be obtained by analyzing the evolution of strain and shape of the sample. Acoustic emission (AE) analysis is a viable technique to obtain additional information about the on-going processes inside the sample subjected to quasi-static or cyclic testing. The investigation within this work focuses on the AE response during tensile and cyclic loading of spring steel wire reinforced EN AW-6082 and AZ31.

The quasi-static and fatigue behavior of AZ31 in longitudinal and transverse extrusion direction has been determined by [4]. The quasistatic behavior in combination with the AE response of the magnesium alloy AZ31 has been investigated in detail by [5,6]. Here, most of the AE activity occurred before the macroscopic yield strength of the material was reached, which was not further discussed by [5,6]. In [7] this effect was attributed to micro yielding by activation basal slip in the hexagonal lattice structure.

Acoustic emission analysis during fatigue testing of AZ31 at a testing frequency of 1 Hz has been carried out by [8]. Three stages of fatigue crack propagation were observed: The crack initiation in the beginning of the test causes high AE activity represented by an increase of the

cumulative AE (ring down) counts, whereas the following slow crack propagation only causes a low AE activity compared to stage I. The final steep increase in the cumulative counts during stage III is caused by fast crack propagation [8].

2. Materials and Specimen Geometry

The specimens were taken out of composite extruded profiles with a 40 x 10 mm² section each reinforced with 4 spring steel wires [1]. The aluminum EN AW-6082 composite has been extruded with a billet temperature of 570°C and quenched with moving air after extrusion, resulting in T4 temper. The magnesium AZ31 composite has been extruded with a billet temperature of 360°C and was cooled in stationary air. The reinforcing elements were 301 stainless steel (301SS) spring wires with a diameter of 1 mm. Figure 1 shows metallographic sections of the embedded wires in the particular matrix material (left: EN AW-6082, right: AZ31), showing a good bonding between wire and matrix. The apparent gap between wire and AZ31 matrix is a metallographic artifact. The specimens for tensile and cyclic testing were manufactured according to the geometries shown in Fig. 2 where the loading direction is parallel to the extrusion direction. The gauge diameter was 3 mm resulting in a fiber fraction of 11.1 vol.-% in the gauge length. The specimen ends were face-turned for proper application of AE sensors.

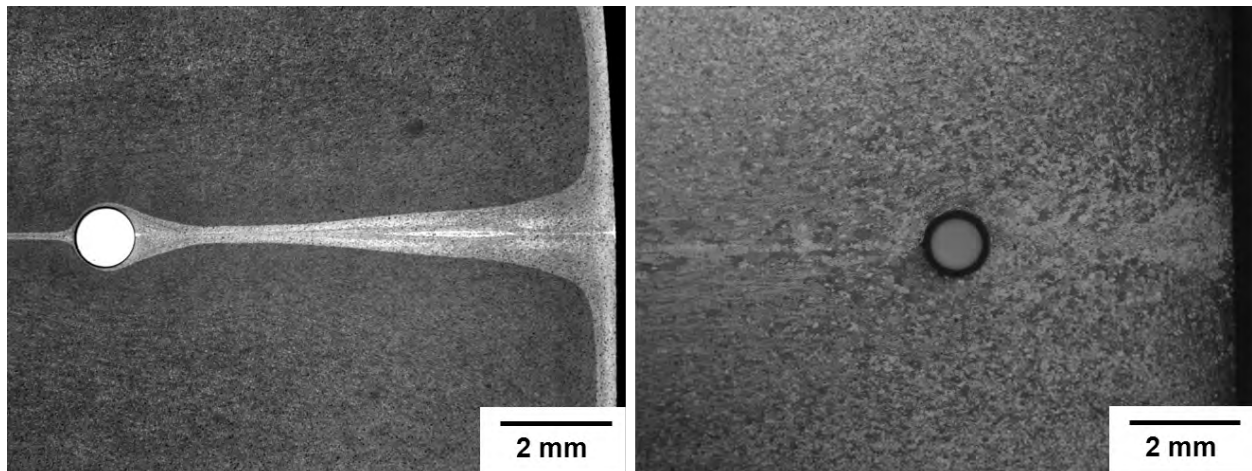


Fig. 1. Cross sections of 301SS-wire reinforced materials used, left: EN AW-6082, right: AZ31.

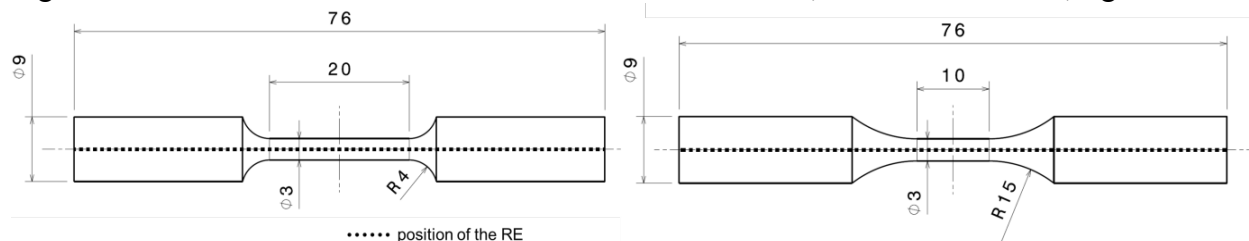


Fig. 2. Geometries of the specimens for the tensile (left) and cyclic (right) tests.

3. Experimental Setup

3.1 Tensile Tests

The quasistatic tests were carried out on a Zwick 200 kN electromechanical testing machine. The crosshead velocity was set to 1 mm/min ($d\varepsilon/dt \approx 16 \times 10^{-4} \text{ s}^{-1}$). The strain was measured over a length of 10 mm by an extensometer attached to the specimen. The hydraulic mounting of the specimen was realized by specially designed clamping allowing for the attachment of the AE sensors on the specimen ends, see Fig. 3.

3.2 Fatigue Tests

The fatigue tests were carried out on an Instron E3000 electro-dynamic testing machine with the same clamping design as above. The tests were load-controlled with a stress ratio of $R = -1$ with a loading frequency of 10 Hz. The strain was measured using a capacitive clip gauge within a length of 10 mm.

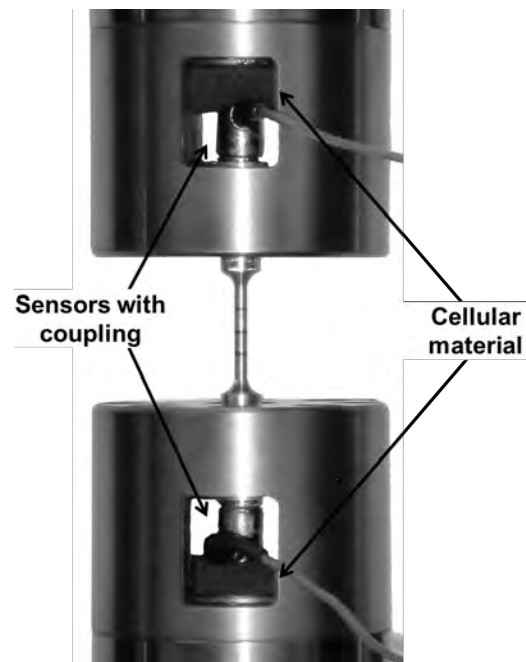


Fig. 3. Experimental setup for the tensile and cyclic tests with AE.

3.3 AE Equipment / Setup

The AE system was a Vallen AMSY-4/AMSY-5 with AEP3 preamplifiers with integrated band-pass filters of 95 – 1,000 kHz and a variable gain (34 – 49 dB), set to 49 dB. The system offered adjustable band-pass filters to suppress background noise. The adjustment of the experimental setup was reported previously [3]. Resonant sensors Vallen VS600-Z1 and broadband sensors Digital Wave (DWC) B-1025 have been used. For a good acoustic coupling, vacuum grease was applied to the sensors before attachment and cellular material was used to fix the sensors (Fig. 3). Two sensors placed on opposite ends of the specimen were used for localization of the AE sources along the specimen axis. The required velocity of sound was determined by pulsing before the tests. Table 1 gives the AE parameters used during the quasistatic (modified settings for rearm time and duration discrimination time) and cyclic tests (Vallen default values). The parametric inputs of the AE system were used to correlate the load and the elongation with the detected acoustic emissions.

Table. 1 AE acquisition parameters.

Testing	Threshold in dB	Bandpass-filter in kHz	Rearm time in ms	Duration Discrimination time in ms
Tensile tests	11.1	100 – 1,000	0.4	0.2
Fatigue tests	22 - 23.7	180 – 1,000	3.2	0.4

4. Results

4.1 Quasistatic tensile tests

EN AW-6082: Figure 4 shows exemplarily the stress-strain curve for an 11.1 vol.-% reinforced specimen correlating the mechanical and AE data; cumulative (AE ring down) counts C_{cum} (left) and the RMS value (right). The stress-strain curve is in agreement with the theoretical model by [9] and exhibits four stages of deformation and damage. After [9] within stage I, the deformation is characterized by an elastic behavior of both components. The plastic deformation of the matrix material defines the onset of stage II while the reinforcement still deforms elastically. Stage III is

identified by plastic deformation of both components. The reinforcement exceeds at this stage its total strain to fracture ($\varepsilon_{fr} = 1.8\%$) by multiple necking and debonding of both components. In stage IV, the remaining matrix material deforms by necking until ultimate fracture.

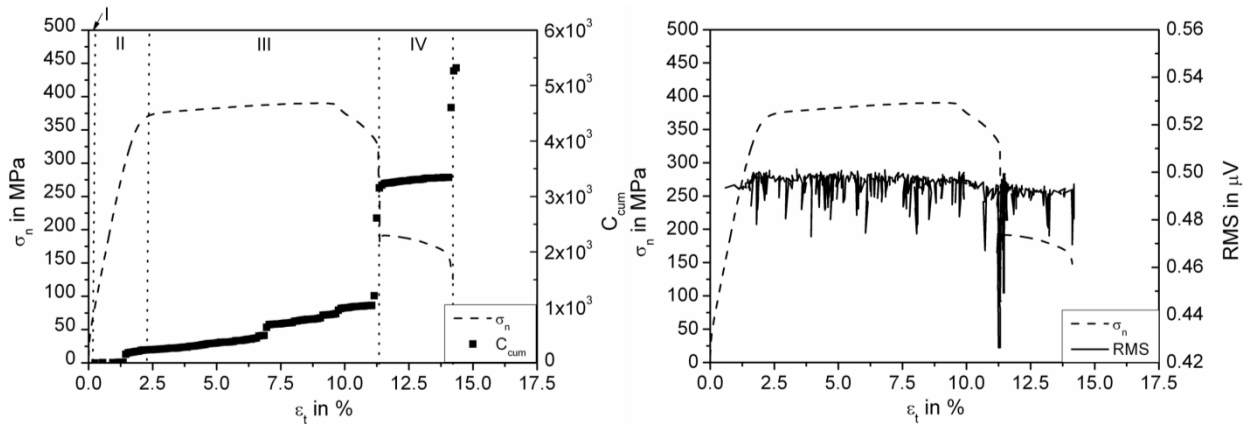


Fig. 4 AE data during quasistatic tensile loading of reinforced EN AW-6082, left: cumulative counts C_{cum} , right: RMS.

The AE activity via the cumulative counts C_{cum} starts at the beginning of stage II whereas stage III shows only a slight rise followed by a steep increase at a strain of $\varepsilon_t \approx 11.3\%$ where the fracture of the reinforcing element occurs. During the continuing plastic deformation and necking of the matrix material (stage IV) a slight increase of the cumulative counts C_{cum} can be attested whereas at the final fracture of the specimen ($\varepsilon_t \approx 14.2\%$) a sudden increase of C_{cum} can be recognized. On Fig. 4 (right) the RMS value shows a relatively constant progression with fluctuations starting at the end of stage II until large peaks appear at the fracture of the reinforcement at a strain of $\varepsilon_t \approx 11.3\%$. Regarding stage IV a larger peak in RMS sets in at the final failure of the composite.

Figure 5 (left) shows the global source location of the hits within the specimen compared to the stress-strain curve. The detected location along the specimen axis has been modified by implementing the elongation of the gauge length ($l_0 = 20$ mm, see dotted lines) during the tensile test:

$$x_{loc,mod} = \frac{x_1 + (x_2 + 2 \cdot \Delta l) - v \cdot \Delta t}{2}$$

where x_1 and x_2 represent the sensor positions. The sensor at location x_2 is shifted to $x_2 + 2\Delta l$, where Δl represents the elongation measured within the initial length of $l_0 = 10$ mm. The influence of the localized elongation due to necking of the specimen is neglected.

It can be seen that only a few of the recorded hits could be located within stage III during plastic deformation and debonding of both components. Close to the fracture of the reinforcing element at $\varepsilon_t \approx 11.3\%$, more hits can be located, which show a cluster in the lower part of the gauge length. Figure 5 (right) shows the distribution of hits just prior to the large load drop of the composite ($9.6\% < \varepsilon_t < 11.4\%$) within the gauge length. By comparing the longitudinal section of 20-mm gauge length with the Gaussian fit, a good localization of the wire fracture to ~ 1 mm can be attested.

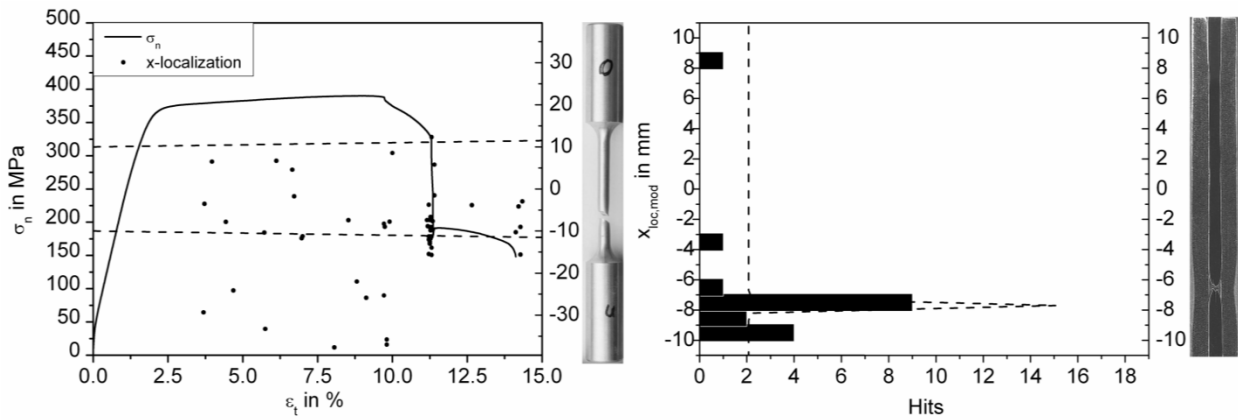


Fig. 5 Localization of deformation and damage in reinforced EN AW-6082 (auto calibration, $v = 4,871$ m/s).

AZ31: Figure 6 shows the exemplary results of a tensile test of a reinforced AZ31 specimen. The deformation and damage behavior can be subdivided in 3 stages (the 4th stage is missing due to simultaneous matrix fracture at reinforcement failure).

From both cumulative counts C_{cum} and RMS value, AE activity increases from the beginning of the test within the elastic stage. This is also observed for the AZ31 matrix material. Here, the rearm time (RT) and the duration discrimination time (DDT) have been modified in comparison to the default values, see Table 1, in order to accommodate the continuous character of the signal. This is indicated by the increase of the RMS value during stage II, see Fig. 6 (right). The AE activity decreases and is nearly constant in stage III until an increase of the RMS value occurs at the final fracture of the composite at $\epsilon_t \approx 7.4\%$.

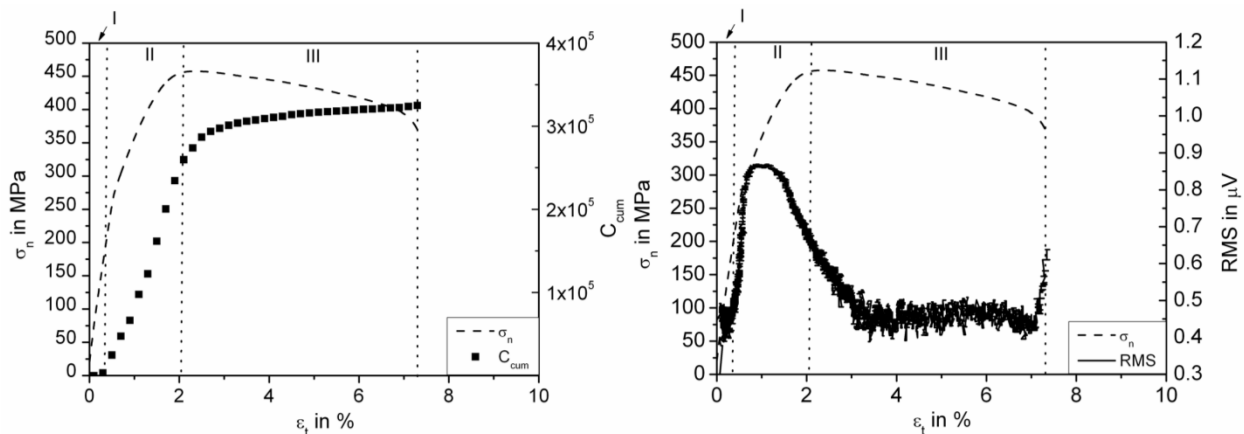


Fig. 6. AE data during quasistatic tensile loading of reinforced AZ31, left: cumulative counts C_{cum} , right: RMS.

Figure 7 shows the located hits during deformation and damage. The located hits show a broad scatter within the gauge length and partially at the specimen heads. The distribution of the located hits within stage III starting at about $\epsilon_t = 2\%$ show that most of the detected hits were located within the gauge section of the specimen, see Gaussian fit, Fig. 7 (right). The global specimen failure cannot be located from the hit locations since they are widely distributed along the specimen axis.

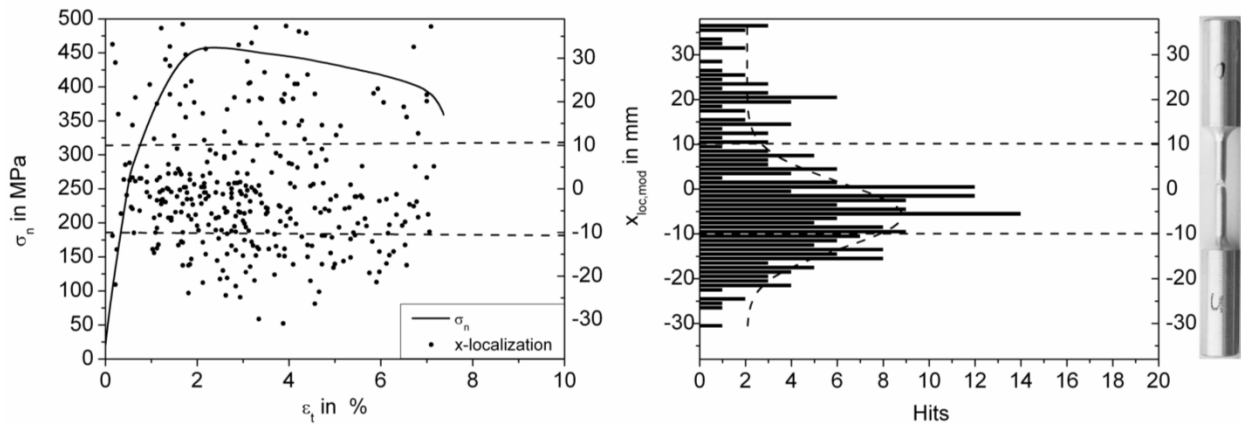


Fig. 7 Localization of deformation and damage in reinforced AZ31 (auto calibration, $v = 4,222$ m/s).

4.2 Fatigue tests

EN AW-6082: Figure 8 shows the results of a fatigue test with stress amplitude of 175 MPa. Figure 8 (left) shows the change of the plastic strain amplitude $\epsilon_{pl,a}$ and the RMS value versus the fractional lifetime, ratio of the number of cycles to that of fracture, N/N_f . The decrease of the plastic strain amplitude $\epsilon_{pl,a}$ in stage I indicates the cyclic hardening of the material due to the formation and pile-up of dislocations resulting in a decrease of the dislocation activity. The hardening of the material continues with increasing cycles at a lower rate. Stage III characterizes the onset of crack growth within the matrix material resulting in an increase of the plastic strain amplitude $\epsilon_{pl,a}$. Figure 8 (right) shows a more detailed view in stage III and IV. The increase of the plastic strain amplitude $\epsilon_{pl,a}$ is due to crack growth within the matrix material. At the end of stage III, the matrix material fractures resulting in a local maximum of the plastic strain amplitude $\epsilon_{pl,a}$. The fatigue of the reinforcing element continues in stage IV where the decrease of the plastic strain amplitude $\epsilon_{pl,a}$ indicates the hardening of the reinforcing element whereas the slight increase at the end of lifetime can be attributed to macroscopic crack growth.

The evolution of the RMS values shows a decrease within the hardening stage I and a steady state within the saturation stage II. In stage III, a more continuous and increasing behavior can be observed. Figure 8 (right) shows a local maximum of the RMS value close to the transition to stage IV followed by a decrease. Prior to fracture of the reinforcement, a slight increase of the RMS value can be observed.

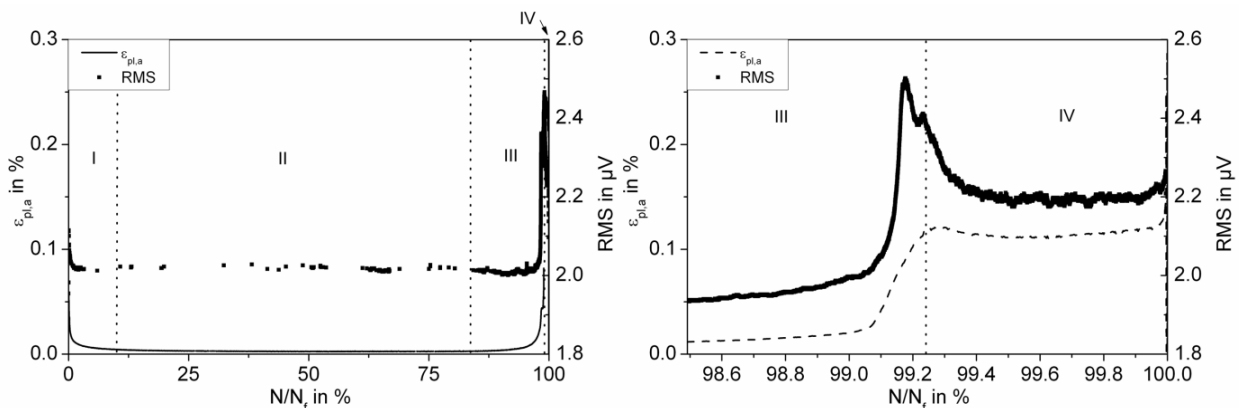


Fig. 8 EN AW-6082 + 301SS plastic strain amplitude $\epsilon_{pl,a}$ and RMS vs. relative number of cycles to fracture N/N_f , right: zoom in ($\sigma_a = 175$ MPa).

In order to describe the evolution of damage, a parameter D based on the loss in stiffness (increase of compliance) in tension [3] due to crack growth is shown in Fig. 9. D is defined by the following equation:

$$D [\%] = \frac{S_{\text{unl(ave1-100)}} - S_{\text{unl}(i)}}{S_{\text{unl(ave1-100)}}}$$

where S_{unl} characterizes the unloading stiffness in tension; the index i stands for the current cycle and (ave1-100) for the average value of the first 100 cycles as reference for the start value. The increase of the damage parameter D resulting from crack growth within the matrix material defines the beginning of stage III. Similarly, the cumulative counts C_{cum} indicated a slight increase at nearly the same fractional lifetime. The further increase of the damage parameter D results from the crack propagation within the matrix material and the interaction between the crack and the reinforcing element along the interface (debonding). A steep increase of the damage parameter D resulting from the fracture of the matrix material can be seen upon reaching stage IV. After matrix failure within stage IV, the cumulative counts C_{cum} show a steady increase, Fig. 9 (right).

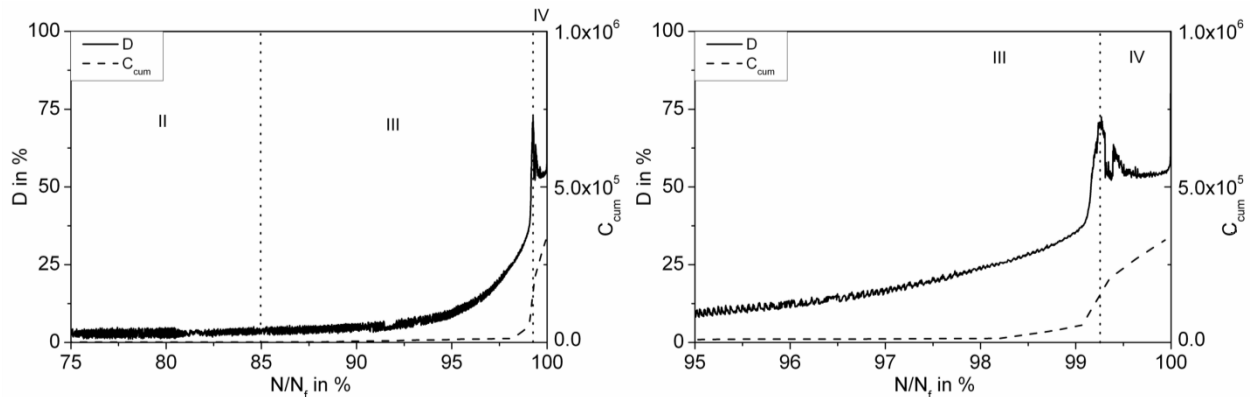


Fig. 9 EN AW-6082 + 301SS, Damage parameter D and cumulative counts C_{cum} left: transcending stage II to III, right: detail stages III and IV ($\sigma_a = 150$ MPa).

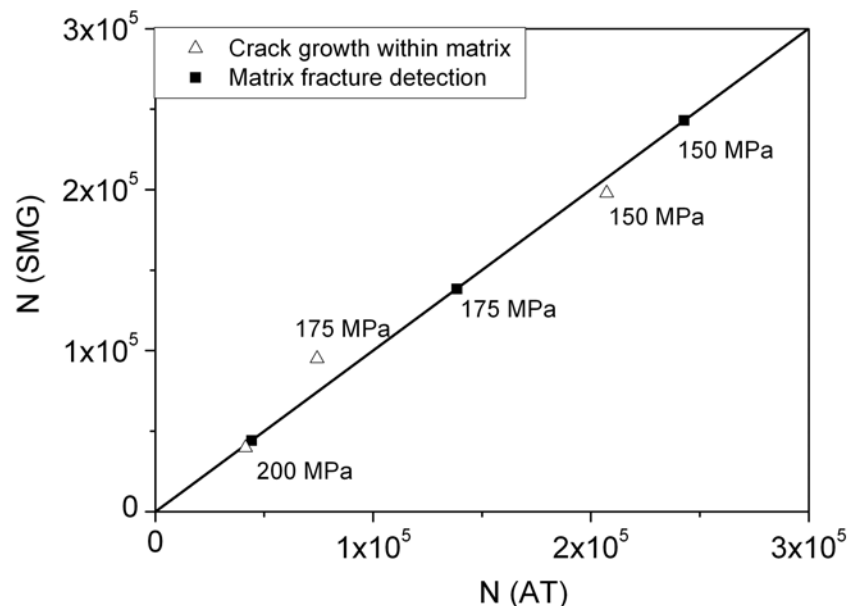


Fig. 10 EN AW-6082 + 301SS. Comparison of the load cycle numbers at which the beginnings of characteristic damage processes are identified via strain measuring gauge (SMG) or via AE testing (AT) for different stress amplitudes.

In order to compare the detection of damage, namely crack growth within the matrix material and the fracture of the matrix material via an increase of the mechanical damage parameter D (measured with a strain measuring clip gauge – SMG) and the acoustic emission response via an increase of the cumulative counts and the RMS value (AT), multiple tests at different stress amplitudes (150 MPa, 175 MPa, 200 MPa) have been carried out. Figure 10 shows the comparison with the bisecting line where a comparable sensitivity especially for matrix fracture detection can be concluded.

Figure 11 shows the results of the localization of detected hits over lifetime. Matrix fracture can be optically observed, in consequence only hits recorded before matrix fracture (up to stage IV) were considered for localization. The best results have been achieved by an eccentric placement of the small ($\Phi = 4.8$ mm) resonant sensors onto the specimen ends so that the sensor plate was set on the pure matrix material. Just before matrix fracture the spreading of hit locations gets very large, which can be attributed to the matrix crack surface fretting and the resulting acoustic noise. It can be seen that most of the located hits can be found at the lower part of the specimen gauge section. The concentration of hits on the lower part of the specimen is in good agreement with the real fracture location (Fig. 11 right).

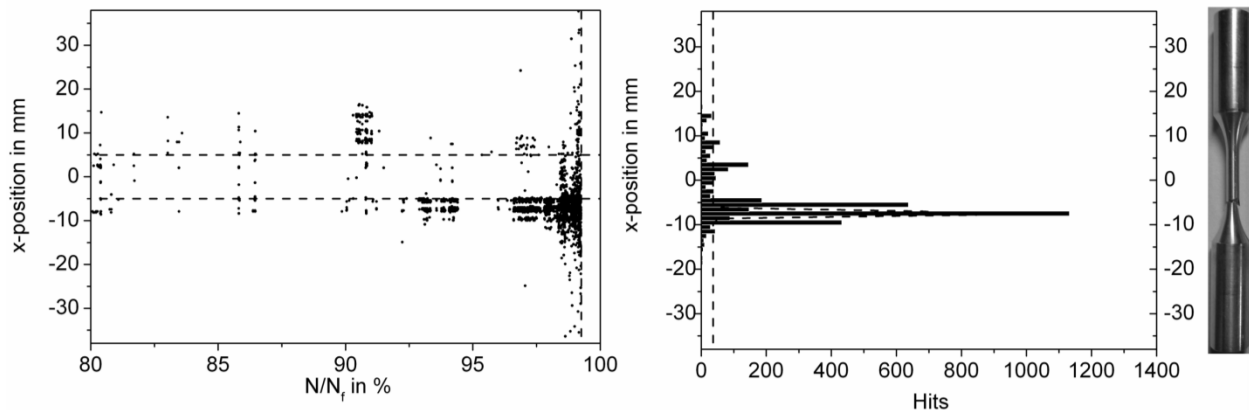


Fig. 11 Localization of deformation and damage of reinforced EN AW-6082 ($\sigma_a = 175$ MPa, $v = 4,250$ m/s).

AZ31: The AE measurements on AZ31 fatigue testing was done with broadband sensors DWC B-1025, with a threshold set to 22.7 dB since the cyclic hardening at the beginning of the test leads to a much higher AE activity, which can be seen in Fig. 12. In Fig. 12 (left) the plastic strain amplitude $\epsilon_{pl,a}$ and the RMS value are plotted against fractional lifetime. Near the end of lifetime at about 83% a clear increase in plastic strain amplitude $\epsilon_{pl,a}$ is observed, whereas the RMS value shows a significant increase at about 93% of lifetime. At the beginning of stage IV the decrease of RMS and the plastic strain amplitude $\epsilon_{pl,a}$ due to cyclic hardening of the reinforcing element can be observed.

In Fig 12 (right), the damage parameter D is compared with the cumulative counts C_{cum} . D shows a relatively large spread and the first noticeable increase at about 83% of lifetime. For the cumulative counts C_{cum} there is a steep increase at the beginning of the test, during cyclic hardening within stage I. Within stage II a nearly linear accumulation up to 93% lifetime can be seen, where matrix fracture occurs and a considerable increase of the cumulative counts can be observed. The disadvantage of using broadband sensors is the undefined onset of damage detection via the cumulative counts C_{cum} .

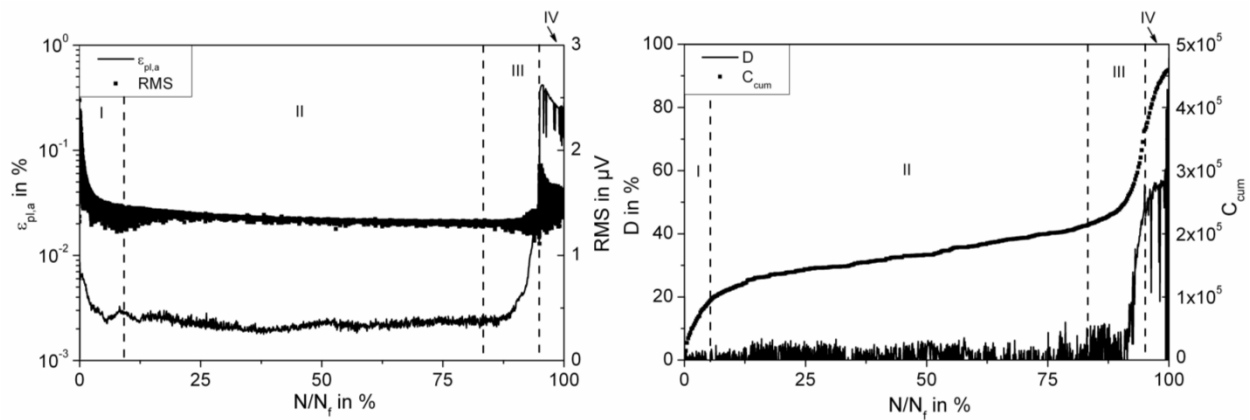


Fig. 12 AZ31 + 301SS left: plastic strain amplitude and RMS vs. relative number of cycles to fracture N/N_f , right: damage parameter D and cumulative counts C_{cum} vs. relative number of cycles to fracture N/N_f ($\sigma_a = 120$ MPa).

In order to understand the origin of the step increase of the cumulative counts, Fig. 13 shows the cumulative counts C_{cum} during tension and compression. It can be deduced that most of the measured hits during cyclic hardening are observed at negative loads. Furthermore, the increase of the cumulative counts for negative loads is observed earlier than for positive loads. A possible explanation is that full crack closure leads to higher AE activity. In addition, friction between the matrix material and the reinforcement can also contribute to an increase of the measured hits.

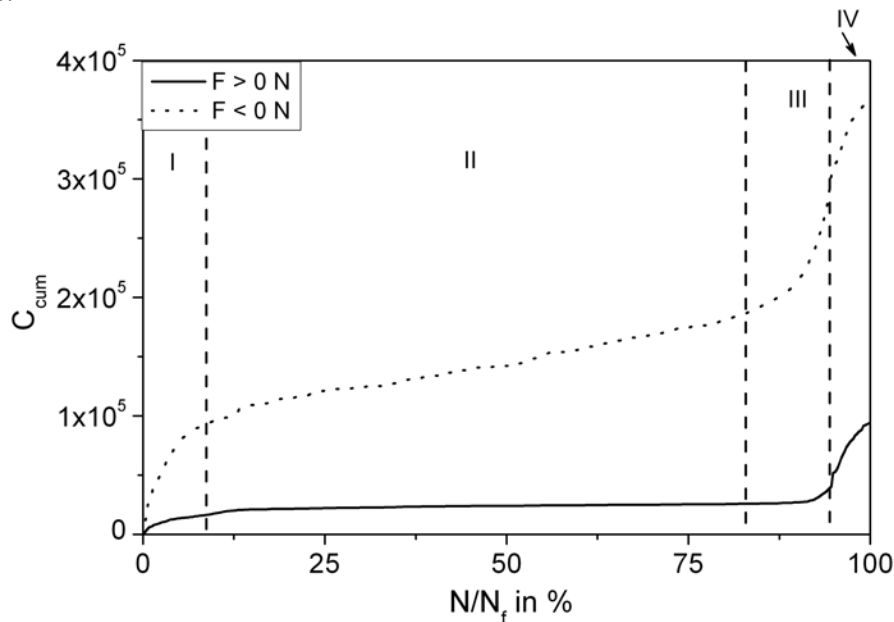


Fig. 13. Detection of counts during tension ($F > 0$) and compression ($F < 0$, $\sigma_a = 120$ MPa).

Figure 14 shows the localization of hits over fatigue life until matrix fracture becomes visible (end of stage III). The filtering of the hits shown is focused on hits detected during compression ($F < 0$) since investigations of located hits without filtering showed a wider distribution of located hits. Thus, it can be seen that the detected hits during hardening of the matrix material show a wide spread. From about 70% relative lifetime on, the AE hits are concentrated in the lower part of the gauge length where also the ultimate fracture of the specimen is observed at 100% relative lifetime. On Fig. 14 (right), the cumulative hits detected until matrix fracture are shown. From this cumulative data set, the global fracture site cannot be identified accurately.

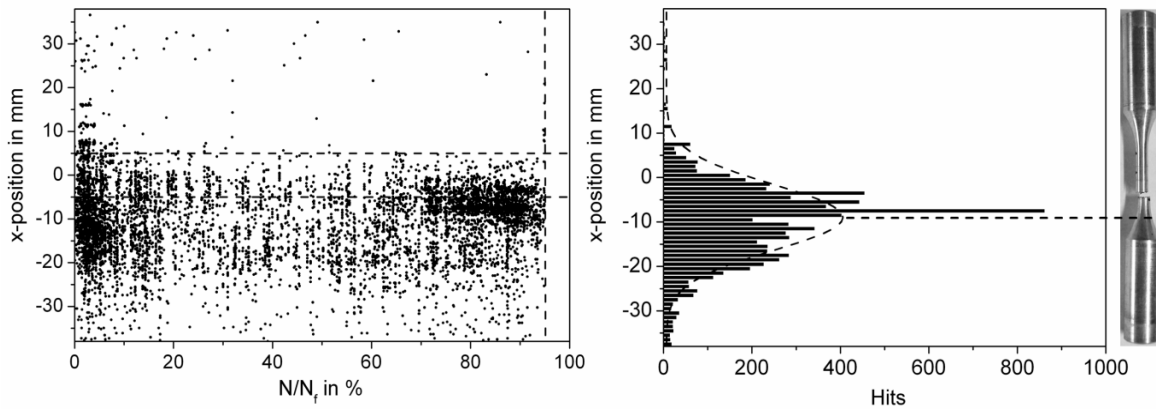


Fig. 14 Localization of deformation and damage of reinforced AZ31 ($F < 0$ N, $\sigma_a = 120$ MPa, auto calibration $v = 4,691$ m/s)

5. Discussion and Outlook

Regarding the results from tensile testing, it can be concluded that for spring steel reinforced EN AW-6082, the RMS value and the cumulative counts C_{cum} can be used to determine deformation and damage, such as fracture of the reinforcement and the complete failure of the specimen. The plastic deformation of the components as well as the necking and debonding can be acoustically registered by an increase in C_{cum} whereas a precise separation of individual damage mechanisms appears impossible. The localization results showed that debonding and necking cannot be detected whereas the localization of the reinforcement failure is relatively precise.

The mechanical deformation behavior and AE data of AZ31 differ from those of EN AW-6082. Since the fracture of the matrix occurred simultaneous to fracture of the reinforcement, no stage IV exists. Comparing C_{cum} and RMS, high AE activity can be observed within the elastic stage I, which was already investigated for AZ31 in [10]. In order to discuss further details about the deformation behavior influenced by gliding of dislocations in basal planes, orientated parallel to the extrusion direction, as well as twinning [11-14], more knowledge about the crystallographic texture and grain size [15] is needed. Comparable to the AE results of the EN AW-6082, composite debonding and necking in stage III cannot be identified from the AE results. The localization of the fracture of the reinforcing element was very inaccurate. Further investigations about the origin of the detected hits during debonding and necking in stage III should be done. This could lead to an *in situ* view on the deformation behavior under tensile loads.

In cyclic testing both AE values are also applicable. The RMS value allows for a detection of cyclic hardening at the beginning of the test and crack growth in both reinforced materials. Although the constraints are not as clearly visible as in mechanical measurement of the plastic strain amplitude, the *in situ* monitoring offers a large benefit, so that the time of the matrix fracture detection is very accurate (local maximum in RMS). C_{cum} is mainly important for monitoring the damage evolution in stage III, where crack growth in the matrix material and debonding and necking of the wire occurs, although the AE response cannot be attributed to individual damage mechanisms. Compared to the mechanically determined parameter D , the beginning of damage detection is visible through AE. In case of AZ31 the damage parameter D allows slightly earlier damage detection than C_{cum} , which may be attributed to the use of broadband sensors of a lower sensitivity. For both composites the hardening of the reinforcing element as well as the following crack growth could be detected after matrix fracture, which results in a bumping of the matrix crack surfaces during the fully reversed testing.

The four different stages of deformation of spring steel reinforced AZ31 are identified acoustically by AE cumulative counts. The slowing increase of the cumulative counts can be attributed to the microscopic yielding whereas the exact crystallographic deformation behavior should be investigated in detail. The second stage with a nearly linear increase of the cumulative counts can be attributed to small amounts of hardening whereas stage III with a progressive increase of the cumulative counts is based on crack growth within the matrix material. The three stages detected by AE are equivalent to those registered for the pure matrix material and are different from the investigations shown in [8]. Reference [16] gives a more quantitative interpretation of the evolution of cumulative counts over fatigue life, influenced by several AE parameters such as gain and threshold and mechanical parameters, such as stress amplitude and stress ratio. For the reinforced material, at the end of stage III, the fracture of the matrix material causes a steep increase of the cumulative counts resulting from fretting of the crack surfaces of the matrix material. The difference in cumulative counts registered during compressive and tensile loading can be attributed to the different deformation behavior for AZ31, which is explained in detail in [13-15].

The localization of damage-induced AE hits on EN AW-6082/301SS proved to be precise within the theoretical measuring accuracy ($\pm 0.5\text{--}1$ mm), depending on the sampling frequency. The precision of the localization is reduced due to deflection of acoustic waves at the interface, which results in an improper localization.

The current study showed that AE is an appropriate means for characterization methods in testing reinforced lightweight alloys in quasistatic as well as in cyclic loading. The comparison of AE characteristics with measured mechanical values showed that a large benefit from additional *in situ* AE monitoring can be reached for cyclic testing, since the damage parameter and the plastic strain amplitude suffer from being *ex post* interpretation methods. Important damage hits like reinforcement or matrix fracture (tensile and cyclic) and crack growth (cyclic) can be clearly recognized. Further the fast rise of the RMS value at wire fracture (quasistatic) or matrix fracture (cyclic) allows defining a threshold for automatic matrix fracture detection. A shutdown algorithm built into the AE software could be programmed to automatically stop the test for metallographic investigations. Future investigations should focus on pattern recognition features or clustering of the recorded AE data so that other damage mechanisms like debonding or necking could be recognized from the AE signals.

Acknowledgment

This paper is based on investigations of the subproject A3 “Material systems for reinforced and functional extruded profiles” of the Transregional Collaborative Research Center/Transregio 10, which is kindly supported by the German Research Foundation (DFG). The authors would like to thank A. Henschel for contributing to the experiments on AZ31.

References

- [1] M. Kleiner, M. Schomäcker, M. Schikorra, A. Klaus, *Mat.-wiss. u. Werkstofftechn.*, **35** [7], (2004), 431-439.
- [2] K.A. Weidenmann, E. Kerscher, V. Schulze, D. Löhle, *Advanced Materials Research*, **10**, (2006), 23-34.
- [3] K.A. Weidenmann, E. Kerscher, M. Merzkirch, *Advanced Engineering Materials*, **12** [1], (2010), 637-640.

- [4] A.N. Chamos, Sp. G. Pantelakis, G.N. Haidemenopoulos, E. Kamoutsi, *Fatigue Fract Engng Mater Struct*, **31**, (2008), 812–821.
- [5] J. Bohlen, F. Chmelik, P. Dobron, D. Letzig, P. Lukác, K.U. Kainer, *Journal of Alloys and Compounds*, **378**, (2004), 214–219.
- [6] P. Dobron, F. Chmelik, J. Bohlen, K. Hantzsche, D. Letzig, K.U. Kainer, *Int. J. Mat. Res.*, **6**, (2009), 889-891.
- [7] S.R. Agnew, *Magnesium Technology 2002*, TMS Annual Meeting, Seattle, (2002),
- [8] H. Zhou, J. Wang, Q. Zang, E. Han, W. Ke, *Materials Science Forum*, **546-549**, (2007), 579-584.
- [9] Th. Courtney, *Mechanical Behavior of Materials*, 2nd Edition, (2000).
- [10] M. Friesel, S. H. Carpenter, *Journal of acoustic emission*, **3** [1], (1984), 11-17.
- [11] C.R. Heiple and S.H. Carpenter, *Journal of Acoustic Emission*, **6** [3], (1987), 177-204.
- [12] C.R. Heiple and S.H. Carpenter, *Journal of Acoustic Emission*, **6** [4], (1987), 215-237.
- [13] M.R. Barnett, *Materials Science and Engineering A*, **464**, (2007), 1-7.
- [14] M.R. Barnett, *Materials Science and Engineering A*, **464**, (2007), 8–16.
- [15] J. Bohlen, P. Dobron, J. Swiostek, D. Letzig, F. Chmelik, P. Lukac, K.U. Kainer, *Materials Science and Engineering A*, **462**, (2007), 302–306.
- [16] D. Fang, A. Berkovits, *Fatigue Fract. Engng Mater. Struct.*, **17** [9], (1994), 1057-1067.